Synthesis and theoretical studies of heterometallic complexes based on divalent lanthanides and transition metals

Valeriu Cemortan

INSTITUT POLYTECHNIQUE DE PARIS

ÉCOLE POLYTECHNIQUE

IP PARIS

NNT : 2022IPPAX016

Thèse de doctorat

Synthèse et études théoriques de complexes hétérométalliques à base de lanthanides divalents et de métaux de transition

Thèse de doctorat de l'Institut Polytechnique de Paris
préparée à l'École Polytechnique

École doctorale n°626 Ecole Doctorale de l'Institut Polytechnique de Paris (ED IP Paris)

Spécialité de doctorat: Chimie

Thèse présentée et soutenue à Palaiseau, le 11 mars 2022, par

Valeriu Cemortan

Composition du Jury :

Nicolas Mézailles Directeur de Recherche, Université Paul Sabatier	Président du Jury
Stephen Liddle Professeur des Universités, University of Manchester	Rapporteur
Lionel Perrin Directeur de Recherche, Université Lyon I	Rapporteur
Sophie Bezzenine Maître de Conférences, Université Paris-Saclay	Examinatrice
Grégory Nocton Chargé de Recherche, École Polytechnique	Directeur de thèse
Carine Clavaguéra Directrice de Recherche, Université Paris-Saclay	Co-Directrice de thèse
Sébastien Blanchard Maître de Conférences, Sorbonne Université	Invité

Synthesis and theoretical studies of heterometallic complexes based on divalent lanthanides and transition metals

Valeriu Cemortan

Chemistry

Ecole Polytechnique, IP Paris

A thesis for the degree of

Doctor of Philosophy

11th of March 2022

Acknowledgements

"The road will not come to you in visions in the darkness
The road is selfish, and the road can be hard
The road can be long, the road can be far
The road will mean struggle, the road will leave scars"

This is it. The end of a 3 year journey. Yet, despite the intrinsically solitary nature of this *road*, I was never lonely. This small section is dedicated to all those who have helped me make it to the starting line, pushed me during the race and were there to greet me at the finish line. It is dedicated to those who made merry many a day and to those with whom I shared the intense camaraderie and sense of belonging all throughout my stay at the LCM. Often the two overlap.

It is an abstract and daunting task to try to meaningfully compress the experience of north of 1000 days in a few short pages. Here's my best go at it :

My first and humblest words go to my very talented PhD supervisors, Greg and Carine. I am very grateful that you decided to trust me with a challenging project four years ago. I owe my evolution as a scientist to your different, but complementary approaches.

I thank you, Greg, for showing me the richly textured domain of lanthanide chemistry and for teaching me rigour, independence and the benefit of a resolute approach to defending a scientific belief. I will remember with great pleasure our passionate discussions about science[*] during group meetings and other, more trivial matters, at the unofficial Lab 1 headquarters.

I thank you, Carine, for the supervision that was peppered with great tips about computations, and full of generosity and encouragement. You've taught me so much, despite our infrequent meetings and the remote conditions that we often had to resort to. I'm also grateful for giving me the chance to learn even more during the post-doc to come.

It is in the same spirit that I would like to thank my jury – referees Steve Liddle, Lionel Perrin and examiners Sophie Bezzenine, Sébastien Blanchard and Nicolas Mézailles – for having agreed to evaluate my work and to take part in my PhD defense. Additionally, I thank Professors Mézailles and Blanchard for their input at the half-way point of my thesis and for their encouragement which, at the time, was invaluable to me.

I would like to address a warm thank you to Drs Corinne Gosmini and Cédric Tard as chiefs of the lab for their structural and administrative support throughout this PhD and for having maintained a pleasant climate for the student corps. It was a pleasure being part of the lab council for two (peaceful and uneventful) years. In particular, Cédric, I congratulate you on your

[*] It's possible that my memory is a bit hazy after all these years, but I can't **definitively** exclude Greg paraphrasing Bill Shankly : "Some people believe chemistry is a matter of life and death. I am very disappointed with that attitude. I can assure you that it is much, much more important than that."

strong start in the hotseat and wish you well for the future. Your diplomacy and quiet encouragement make you a good fit for the job.

Despite the difficult physical separation between us (two flights of stairs, to be exact), I would like to thank Sylvaine, Édith, Christophe, Olivier, Gilles, Cindy and Élodie for their consistently cheerful and lovely company. You lit up the Christmas parties and lab barbecues.

Anne-Flo deserves a particular mention, for her kind heart and ample patience when dealing with administrative misfits with needlessly complicated affiliations and funding, such as myself.

As if to prove that research in academia should be a collaborative effort, the research staff at LCM were available for extending a helping hand when needed. Stéphane, thank you for being such a wonderful host for those memorable parties. I hope we see each other again for other guitar blind tests. I would like to thank Audrey for the pleasant conversations in the coffee room, as well as for her subtle nudges of encouragement during the final weeks of my writing. I would like to thank Louis Ricard for having patiently taught me some XRD survival skills and for helping me out with the bug-ridden clusters. Bibi, your honesty, positive vibes and colourful language were a breath of fresh air when we always needed it. Duncan, thank you for showing me that one can still find polymaths at Polytechnique. I very much appreciated our talks about football, classical music and the occurrence of assholes in academia. It's just a shame that you lost your Scouse accent.

Ultimately, life in the lab flows through the students' distillations, the Dewar refills and, for the unlucky ones, through the mind-numbing boredom of doing manual columns.

I'll start with those who strain the criteria the most. Nicolas, you're a gentle, exceedingly handsome soul with a razor-sharp mind… and, soon, a new XRD machine. You have my full confidence in being able to walk the delicate tightrope from the students' hall across the enemy lines. Thomas, you might be an incoming junior researcher, but I will always remember you as the kind-hearted and unreasonably responsible post-doc. You were always quite stubbornly the smartest and nicest person in the room. Thank you very much for being there when I needed it most. I'm sure you'll do brilliantly in your new position.

I'll continue with the Lab Elders. Although I didn't have the chance to be part of the working crew, Mathieu "Le Capitaine" left a tight and smoothly running ship. It was a pleasure to meet you in less militarily-charged circumstances after your PhD. Loulou, you may have quit academia to do [insert bullshit job here], but there's a proud heritage of *joie de vivre* and a questionable affection for *franglais* in the lab that traces straight back to you. When PSG play Real next time in the Champions League, hit me up. Céline, thanks for temporarily pulling me in the LCM Running Club's orbit with your cheerful nature. It was almost enough to convince me that running can be fun.

Thanks to interns Poonam, Audrey P., Zeyu, Lamise, Carla, Noemi, Jules, Marie and Ingrid for their fun, but ultimately ephemeral and meaningless contributions. You've been good sports and you always took the intern jokes well. Mathilde, if only we could discover a way to use your megawatt-smile and laughter to solve the energy crisis, we'd probably have a terrible PhD project idea. The LCM would be a much better place with you in its ranks. Rafaela, you have a contagious propensity to make everybody feel warm and fuzzy. Your South American cheer and tactile

affection rubbed off on all of us (well, with a few exceptions…). I thank Jean-Christophe for his exemplary attitude, willingness to chase an almost sprinting supervisor down the hallways and the very engaging discussions that we've had.

I'd like to thank all the student group for these very fun and lively three years. In between the bars, the Melted Cheese Nights and our now predictable birthday surprises, I couldn't have asked for a more cheerful gang. I thank Manu, Anju, Julien, Silvia, Zsuzsanna, Nomad and Ling Hui for the good times we've had.

Cate, thank you for your abundant good spirits and kind words. I hope you have fun during your French adventure. Radhika, the computational chemistry lineage of the lab died off (at least for now) with our departures. We gave it a damn good send-off. To Oleh, the foremost Ukrainian French nationalist (and, maybe soon, the other way around !), I wish you the best of luck for the future and thanks for setting me up at the Préfécture more than once. I thank Mengyu, the soft-spoken and generous colleague for all these years. I wish you good luck for the end of your PhD and I encourage you to assert yourself to the degree that your talent deserves. P-A, I distinctly remember being informed of you having a "short stay" in our lab in the summer of '19. Yet, here we are, in the year of the Lord 2022, and you're still anchored in the hearts and minds of the lab. It's been really fun sharing the playground with you. Thibault, the recurrent nerf drive-by victim of the above, it's brilliant to have someone to dump all the football-related content on. You're a great guy and I hope you don't mind us often crash-landing at your place. Pauline, it would seem that luck wasn't always on your side in terms of discreet office mates and intern reports. But it's been a pleasure seeing you grow into a confident, competent scientist – by far the most mature in the kindergarten – who will soon depart for the dark side.

Onto the renowned "crazy lanthanide team". I thank you all for helping me ease in to the PhD life whilst also pushing each other to high standards. I thank Jules for having shared his mantra of "If you do your PhD without leaving a part of yourself on the table, you haven't done it right." early on, whilst also seamlessly marshalling us new PhD students with a cheerful and fun attitude. Ding was mine and Maxime's big brother, who showed us the ropes and helped us grow into our roles as organometallic chemists. I can only hope that my good wishes cross the Great Firewall of China. Maxime, I congratulate you on your brilliant performance for your PhD defence and for keeping your admirable record of invincibility against manual columns intact all throughout these four years. You've been a phenomenal and gracious partner in crime, despite the fact that you're head and shoulders above us (figuratively and quite literally). Good luck in Switzerland !

To the next generation of lanthanide students, we've left behind solid foundations and we will be watching your careers with great interest. Nolwenn, the lab is basically your responsibility now, enjoy ! It's been a real blast to observe your transformation from shy intern to bossy PhD student. I wish you luck for the future in controlling your tricky Cnt ligands and your temper-

ature-dependent hapticity switches. Kuba, you've taught me something important throughout our brief time in the office – you can be a very good scientist, no matter how wildly the quality of your jokes fluctuates, how you dress or how messy your hair looks. Keep rocking that BoJo vibe ! The very endearingly self-deprecating Adrien will soon complete his transformation from tall intern to tall PhD candidate. I know you'll be taking your project very Ceriumsly and I'm sure you'll do a splendid job.

Outside of the lab, I will cherish the numerous moments of levity, hearty laughter, daring jokes, shamelessly ignored curfews, passionate discussions, tennis and football matches (both played and shouted at), homemade cooking and 3 am wisdom shared with Amanda, Andrei, Babou, Carlos, Cezar, Cyril, Horia, Iacob, Ileana, Irina, Jenea, João, Kera, Laura, Mahdi, Mariana, Maxime, Monica, Oliver, Radu, Sandu, Valeria, Vera, Vica, Vlad, Vladimir. You are arranged alphabetically, because, quite honestly… it would have been a bit too on the nose to sort you out in descending order of how much I like you.

I would like to thank my second family – Ded, Magali, Marion, Lucie – for their always warm and delightful welcome in Saint-Dolay. You've given me nothing but kindness and a true *tour de force* of delicious French home-cooked meals for the past five years.

Îmi rezerv dreptul să-mi mulțumesc propria familie într-un grai mai mioritic. Ați fost piatra de căpătâi și punctul de pornire al acestei lucrări. Îmi mulțumesc bunicii – doi Ioni (adecvat, dat fiind turnura chimică a educației mele), Aglaia și Elena – pe care tata îi numește, pe bună dreptate, stejarii familiei. Le mulțumesc mămunei și lui tătunea pentru iubirea pe care ne-au purtat-o tuturor de-a lungul anilor. Mâca e, din punct de vedere caloric, persoana cea mai responsabilă pentru faptul că sunt în viață. Bunelu a fost primul doctor în familie. Dincolo de întâietate în domeniu, a avut și grijă să ocupe treapta cea mai de sus a științelor (matematica). Le mulțumesc tuturor rudelor – Tolea, Snejana (și adorabilele mele nepoțele), nana Ala, nanu Andrei, Natașa, Lenuța, Andreea, Mișa și mulți, mulți alții – pentru afecțiunea continuă, sprijinul și încurajările necontenite. Vă iubesc.

La drept vorbind, le-aș putea mulțumi părinților pentru o suită întreagă de lucruri. Dar la vârful listei se află faptul că mi-au creat condițiile pentru a prospera peste hotare, exemplul demn de urmat de etică de lucru și disciplină, imboldul (și presiunea !) de a mă ameliora și, pur și simplu, iubirea necondiționată de care am avut parte tot timpul. Vă iubesc.

John, ale noastre două teze diferă. Eu câștig la precizie, tu la stil; figurile mele îmi aparțin, ale tale sunt mai frumoase; a mea e de doctor, a ta de-abia clipocește a masterat. Declar amorsată cursa pentru cine va avea primul un număr de cititori cu doua cifre. Dacă tu mi-ai atribuit "the power to increase the options", ți-aș da "the dominion over the verb". Îți datorez faptul că nu mi-e rușine de manuscris și, respectiv, o bună parte din criticile juriului meu de teză. Îți sunt recunoscător că m-ai tras de guler și nu mi-ai dat voie să fiu copleșit de doctorat acești trei ani. Te iubesc.

Sarah, les derniers mots t'appartiennent. Nous voilà les deux docteurs. Malgré le faible lien entre nos deux mondes chimiques, je suis fier de voir qu'on a su être un appui l'un pour l'autre. Ces années de thèse auraient été plus compliquées, moins joyeuses, plus épuisantes, moins souriantes sans ton soutien et tes encouragements quotidiens. Tu m'aides à trouver du sens, de la motivation et des motifs pour sourire. Je t'en remercie.

Cette page de thèse se tourne, la suivante doit encore être écrite. Ma seule certitude est que je veux l'écrire avec toi. Je t'aime.

And, lastly… Mike

Contents

List of abbreviations

18-C-6 – 18-Crown-6 or 1,4,7,10,13,16-hexaoxacyclooctadecane

AE – all-electron calculation

BAr^F_4 – tetrakis[3,5-bis(trifluoromethyl)phenyl]borate

bipy – 2,2'-bipyridine

bipym – 2,2'-bipyrimidine

COD – 1,5-cyclooctadiene

COE – cyclooctene

Cp – cyclopentadienyl

Cp* – pentamethylcyclopentadienyl

Cp^{ttt} – 1,2,4-tri(tert-butyl)-cyclopentadienyl

DCM - dichloromethane

DFT – Density Functional Theory

dppz – dipyrido[3,2-a:2',3'-c]phenazine

Eh – Hartree (unit of energy; 1 Eh ≈ 27.21 eV ≈ 627.51 kcal/mol)

eq – equivalent(s)

Et_2O – diethyl ether

eV – electronvolt

GS – Ground State

Hbimpym – 2-(2-pyrimidyl)benzimidazolate

HOMO – Highest Occupied Molecular Orbital

KHMDS – potassium bis(trimethylsilyl)amide

LUMO – Lowest Unoccupied Molecular Orbital

ORTEP – Oak Ridge Thermal Ellipsoid Plot

RAL – Redox-Active Ligand

(R)ECP – relativistic effective core potential

r.t. – room temperature

py / py-d_5 / pyr – pyridine / deuterated pyridine / pyridyl

quin – quinolyl

SIR – Sterically Induced Reductions

SPE – single-point energy

TD-DFT – Time-dependent Density Functional Theory

THF / THF-d_8 – tetrahydrofuran / deuterated tetrahydrofuran

TM – transition metal

tmeda – tetramethylethylenediamine

tol / tol-d_8 – toluene / deuterated toluene

TS – Transition State

VT NMR – variable temperature Nuclear Magnetic Resonance

(SC-)XRD – (Single Crystal) X-Ray Diffraction

Index of synthesised, computed and pertinent complexes

Chapter 1

dppz-based complexes

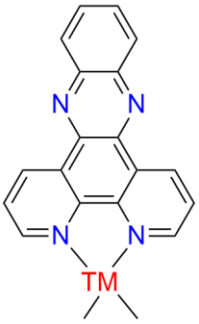

TM = Pd (**1.1**), Ni (**1.2**), Pt (**1.3**)

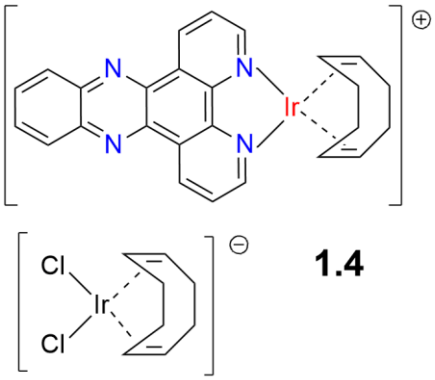

1.4

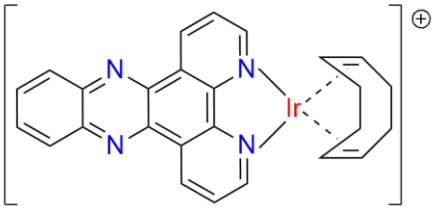

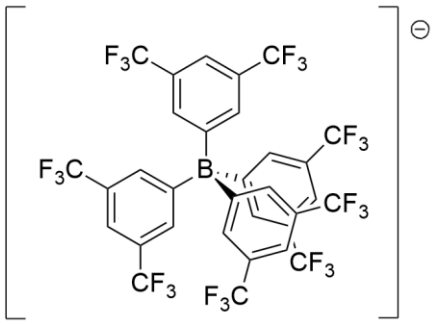

1.5

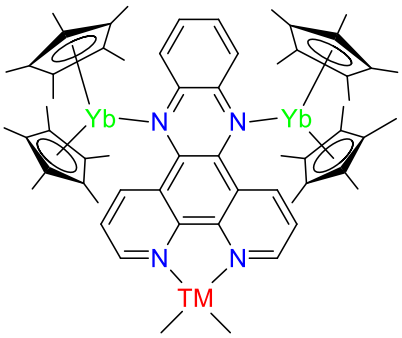

TM = Pd (**1.6**), Pt (**1.7**)

K(bimpym)-based complexes

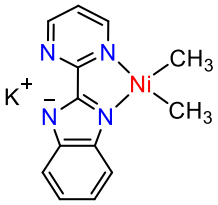

K(bimpym)NiMe$_2$

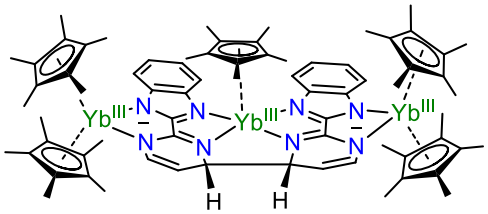

Yb$_3$(bimpym)$_2$

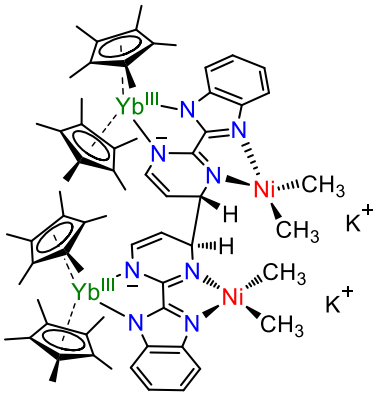

[Yb(bimpym)Ni]$_2$

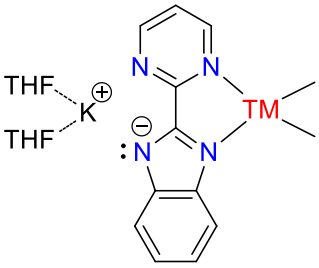

TM = Pd (**1.9**)
Pt (**1.8**)

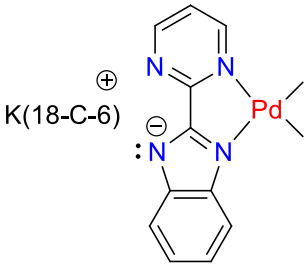

1.10

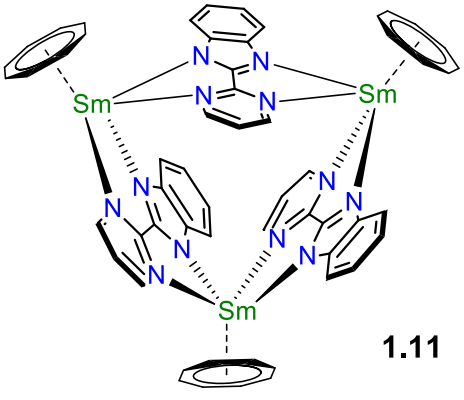

1.11

(bimpym)-based complexes

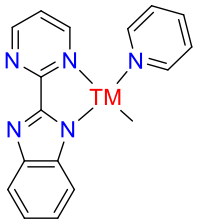

TM = Pd (**1.12**)
Pt (**1.13**)

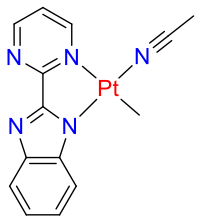

1.14

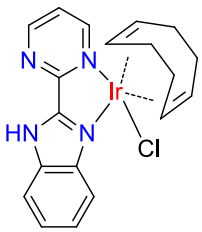

1.15

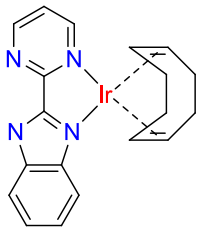

1.16

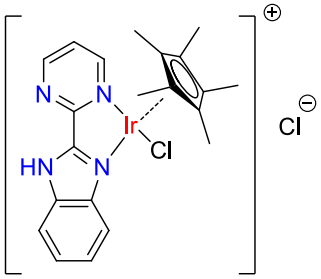

1.17

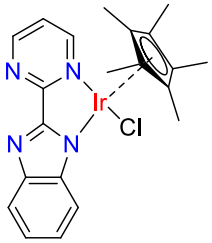

1.18

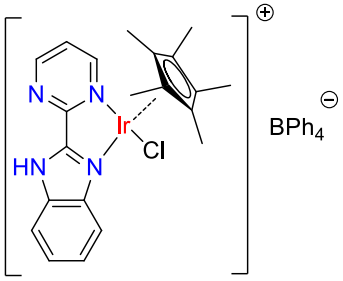

1.19

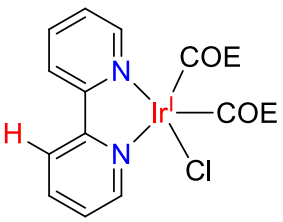

1.20

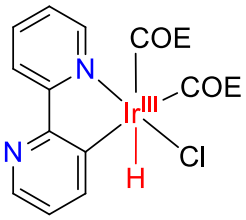

1.21

Computed complexes

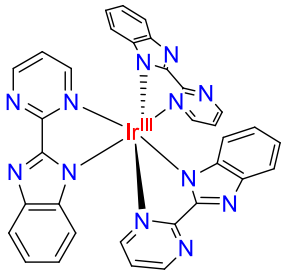

Ir(bimpym)$_3$

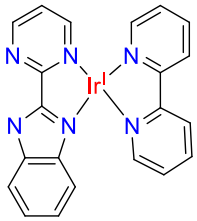

(bimpym)Ir(bipy)

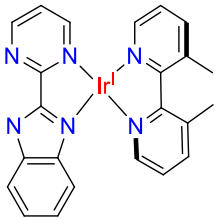

(bimpym)Ir(3,3'-bipy)

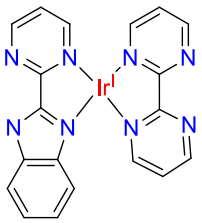

(bimpym)Ir(bipym)

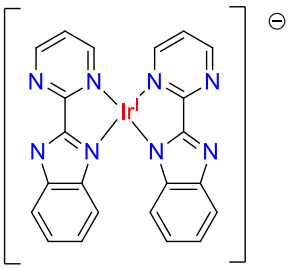

[(bimpym)$_2$Ir]$^-$

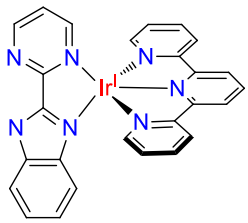

(bimpym)Ir(terpy)

Chapter 2

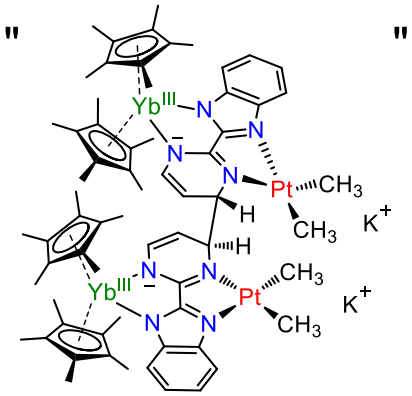

Yb(bimpym)Pt

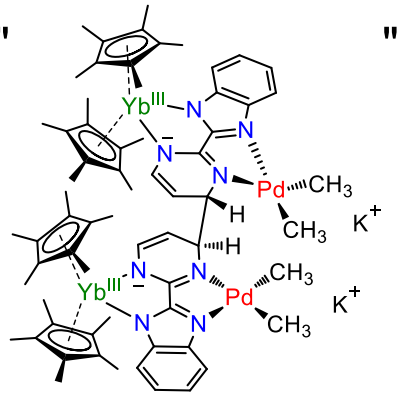

Yb(bimpym)Pd

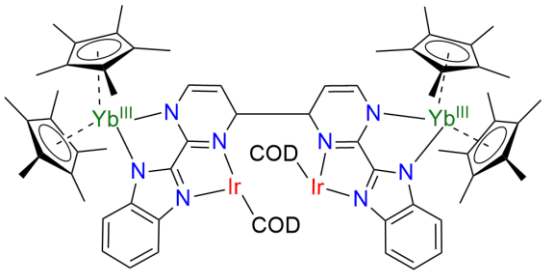

2.1

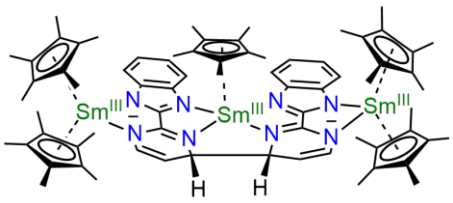

2.3

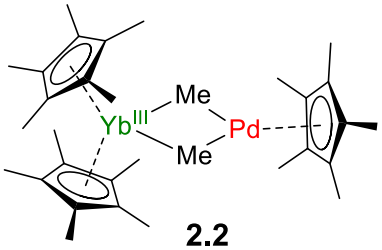

2.2

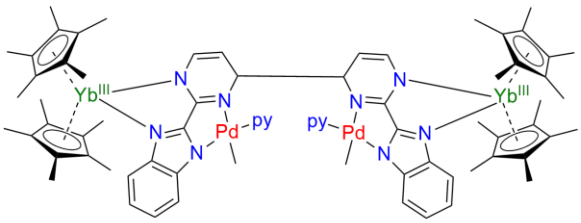

2.4

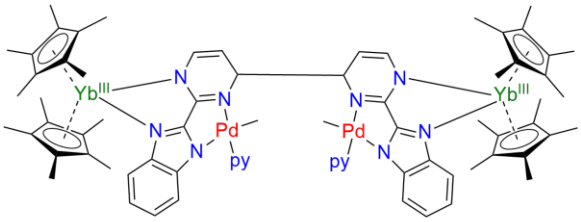

2.5

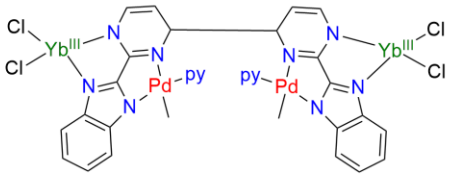

2.4$_{Cl}$

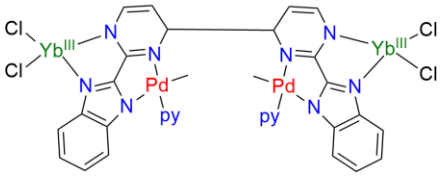

2.5$_{Cl}$

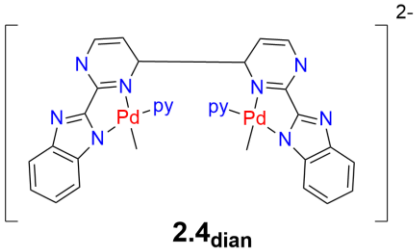

2.4$_{dian}$

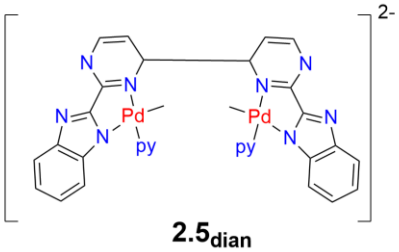

2.5$_{dian}$

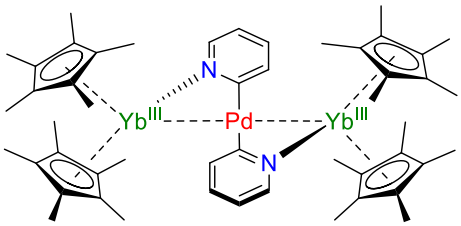

2.6

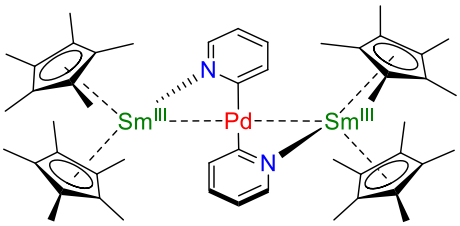

2.7

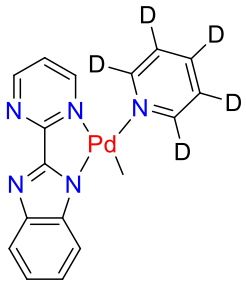

1.12-py-d$_5$

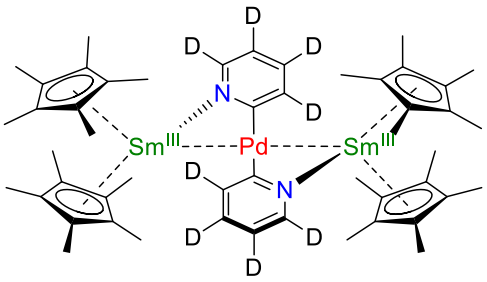

2.7-pyr-d$_4$

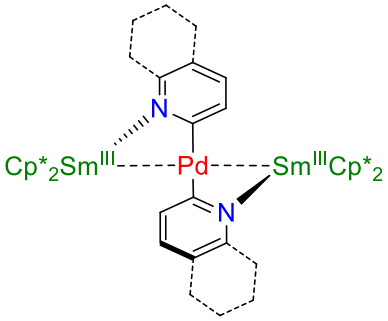

2.8

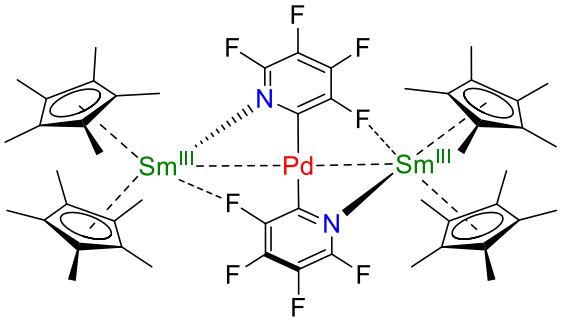

2.9

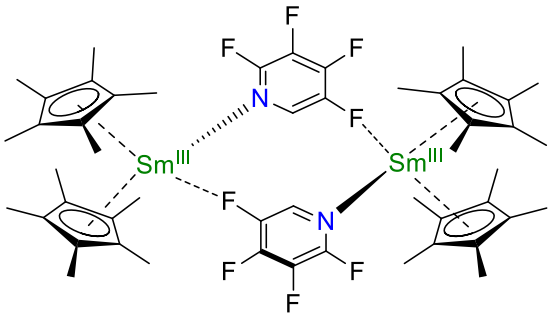

2.10

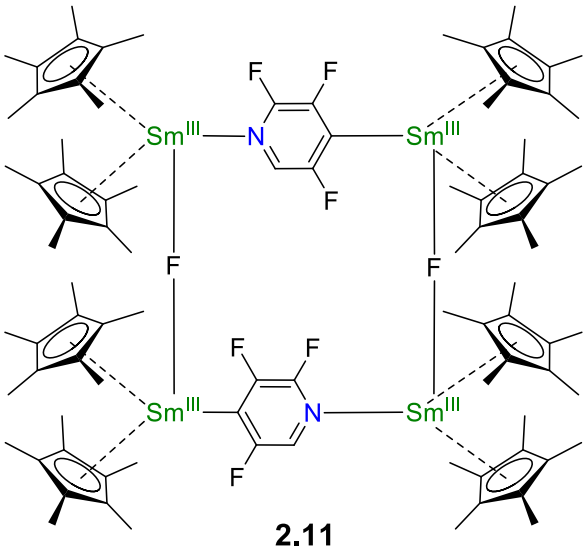

2.11

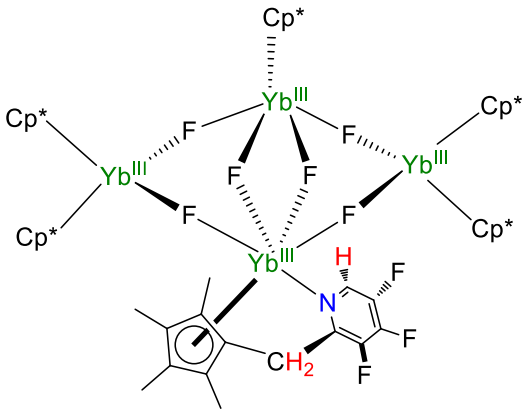

2.12

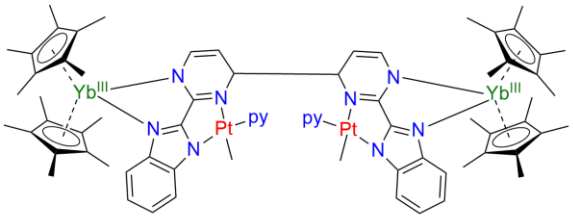

2.13

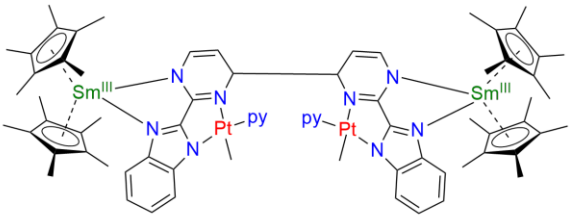

2.14

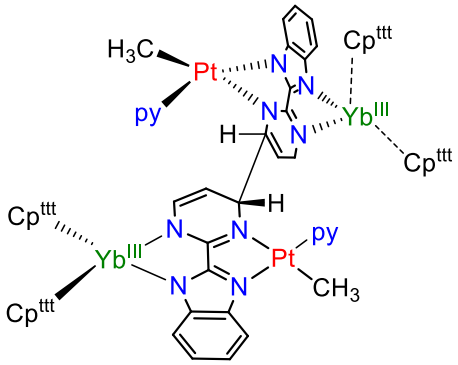

2.15

Chapter 3

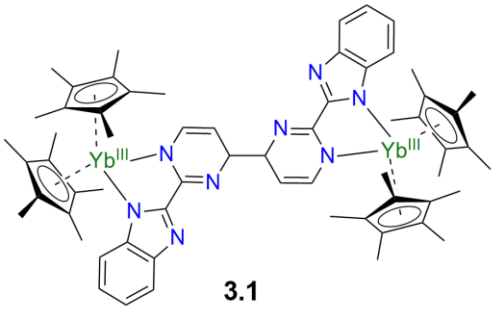

3.1

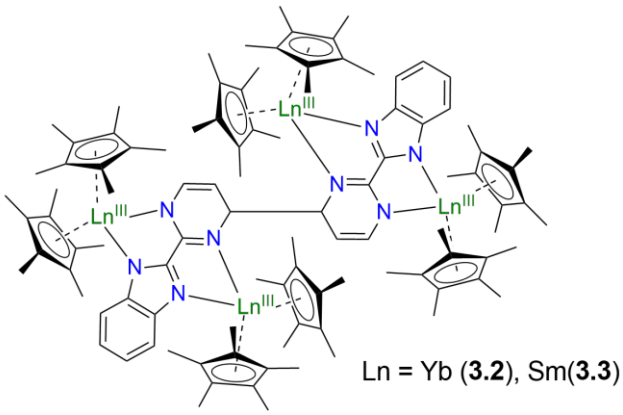

Ln = Yb (**3.2**), Sm(**3.3**)

Computed complexes

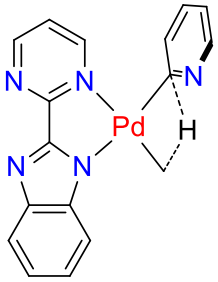

1.12-TS

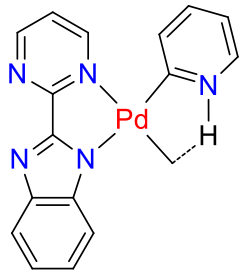

1.12-TS2

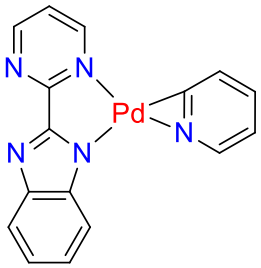

1.12-η^2

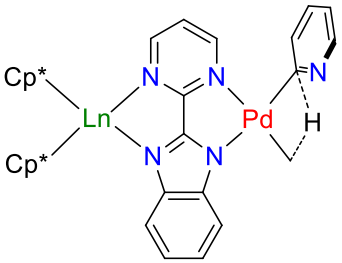

Ln-TS
Ln = Yb or Sm

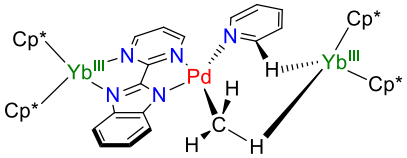

1.12-Yb_2

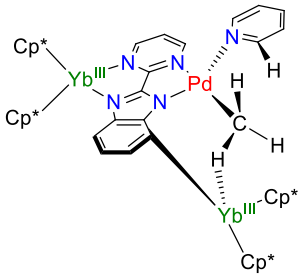

1.12-Yb_2'

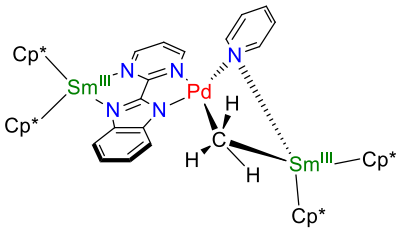

1.12-Sm_2

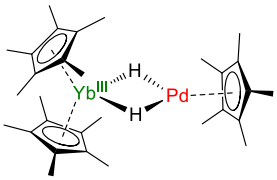

YbH_2Pd

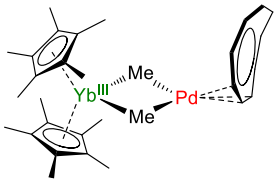

YbPdCNT

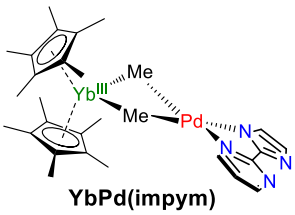

YbPd(impym)

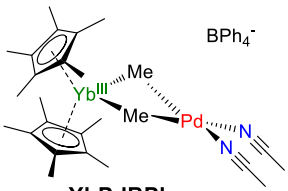

$YbPdBPh_4$

Introduction.

I. Preface

The wider domain of chemistry has an important role to play in the societal challenges facing us at present and in the future. Issues such as energy storage[1] or generation,[2–5] efficient utilisation of the necessary materials thereof,[6] discovery, development and delivery of new drugs[7] and, most importantly, carbon capture and transformation[8–10] all require chemical expertise. Within these areas, the skills mainly concern the extraction, recycling and transformation of matter. Chemical transformations are more and more synonymous nowadays with the concept of catalysis – the art of enabling and accelerating reactions that would otherwise be difficult, if not inaccessible. Catalytic breakthroughs have been rewarded at the highest level – four Nobel prizes in catalysis-related fields in this century alone (2001, 2005, 2010, 2021) – recognising its importance from both a fundamental and practical point of view.

Organometallic chemistry has been one of the key players[11–14] in this area. Although tremendous progress has been made in this field since its first steps at the end of the 19th century, there are still a number of important limitations that need to be surpassed. One of the more prominent targets of the field is to extend the reactivity normally reserved for noble metals – which tend to be more expensive and more sporadically found in the Earth's crust – to the more earth-abundant transition metals (TM).[15,16] Improvements in the catalytic systems may come from a better understanding of their mechanisms and in terms of the control of the regio- and stereoselectivity of the reactions.[17–21]

Another vector in the development of organometallic chemistry has been the expansion of the tool kit available to chemists. Breakthroughs have been made in fields such as sustainable solvents,[22,23] photocatalysis[24,25] or main group catalysis,[26–29] the increase in accuracy and availability of theoretical computations, recently associated to machine learning algorithms,[30] to name but a few. In consequence, there are numerous options and angles from which a chemical problem can be tackled.

The subject of the ERC project, to which this doctoral project is subordinate, is an extension of this theme, since its ultimate goal is to enhance organometallic catalysis *via* single electron transfer (SET) originating from a divalent lanthanide towards the transition metal (TM) fragment, bridged by redox-active ligands (RAL). Each of the core concepts – the use of lanthanides or of RALs in catalysis or the use of a one-electron pathway – are relatively new to this field. A brief description of the specifics associated to each of these will follow, before the overall context and state-of-the-art at the beginning of this PhD is delineated. The main objectives of the doctoral project will then be clarified.

II. Generalities about lanthanides

The lanthanide series (often abbreviated to "Ln") comprise the fifteen metallic elements (Z=57-71), whose main oxidation states are 0, +2 and +3. The etymology of this class of metals comes from the Greek λανθανειν (*lanthanein*), meaning "to lie hidden". This name reflects the difficulty in isolating pure lanthanides, since they tend to be found in minerals, where anywhere from three to all fifteen

of the series can be found simultaneously. In fact, lanthanides are relatively abundant, especially compared to some of the more often used transition metals (Figure 1). Their numerous and ever-increasing fields of applications make the lanthanide series elements of high strategic importance.[31]

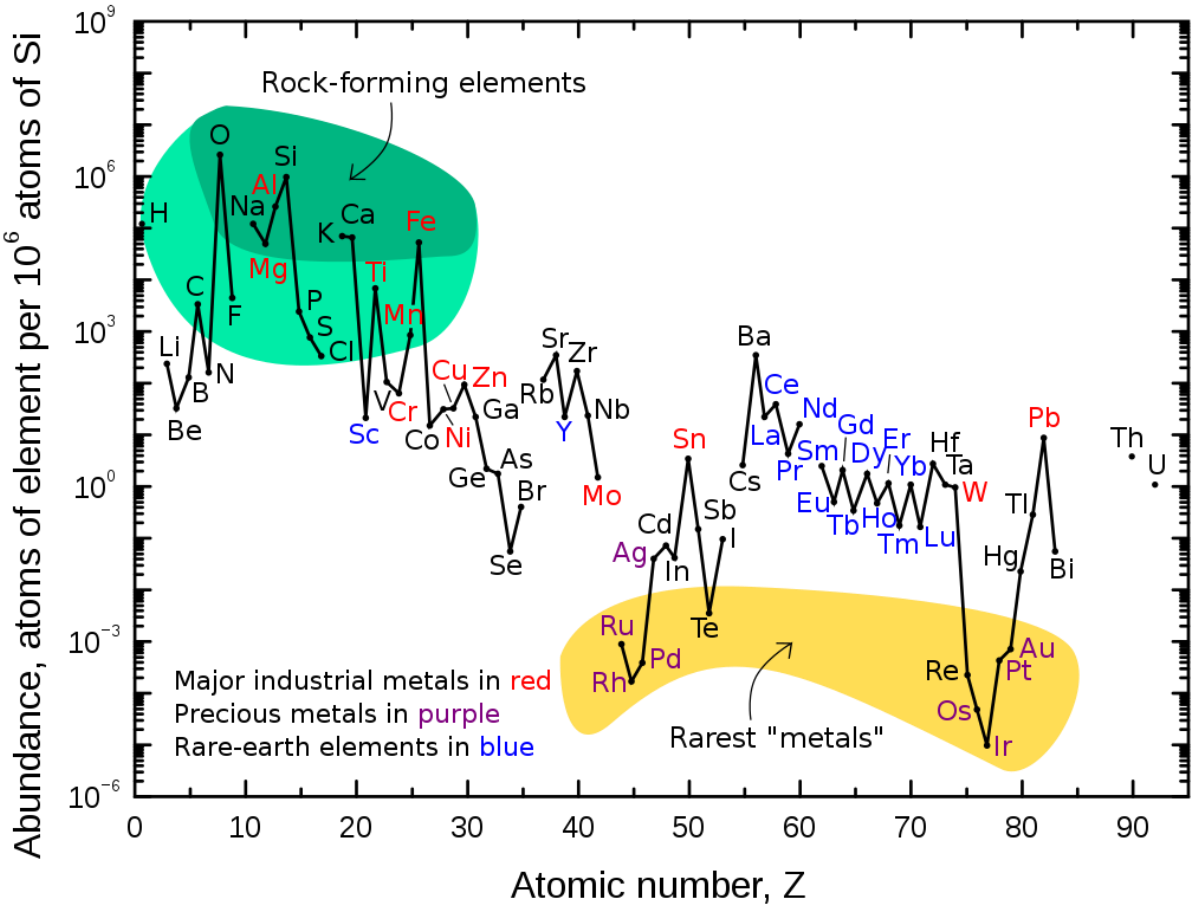

Figure 1: Relative abundance of the natural elements in the Earth's upper crust.[31]

One of the commonly held beliefs surrounding the series relates to their nearly identical chemical nature. This is chiefly due to the most common oxidation state, inherent to all the series – +3. The preference for the +3 oxidation state can be deduced from the electronic configuration of the atom, which are either $4f^n5d^06s^2$ or $4f^{n-1}5d^16s^2$ at the zerovalent state.

For example, the configuration of cerium is $4f^15d^16s^2$ and therefore has four stable oxidation states: 0, +2, +3, and +4, while that of ytterbium is $4f^{14}5d^06s^2$ and has two stable oxidation states – +2 and +3. Removing more than one electron from the 4f orbitals is very energetically costly, which rationalises why the lanthanides favour the +3 oxidation state.[32] However, more exotic tetra- and pentavalent states are occasionally found (Table 1).[33,34] Notably, molecular adducts of Tb^{4+} and Pr^{4+} have been recently described by the Mazzanti and La Pierre groups.[35–38]

	La	Ce	Pr	Nd	Pm	Sm	Eu	Gd	Tb	Dy	Ho	Er	Tm	Yb	Lu
5			G												
4		X	X	S					X	S					
3	X	X	X	X	X	X	X	X	X	X	X	X	X	X	X
2	X	X	X	X		X	X	X	X	X	X	X	X	X	X

Table 1: The oxidation states found for the lanthanides. G – gas phase, S – solid state, green X – classical divalent Ln

The 4f orbitals are contracted, quasi-degenerate and have mostly core-like behaviour. The spin-orbit effect is more important than the crystal field splitting for the removal of this degeneracy. The opposite is true for TM. This has one important consequence: when the 5d sub-shell is populated, the 5d orbitals are impacted by the crystal field splitting, enhancing the bonding interaction with the lanthanide ion.[39] When the 5d orbitals are vacant, the 4f orbitals will favour an ionic interaction. The rarity of the population of the 5d shell (mainly in non-classical divalent lanthanides, discussed below) has fuelled the belief that Ln can only form ionic bond.

Among the organometallic lanthanide adducts, the divalent complexes have been steadily gaining traction.[40] The diiodides (LnI_2) have been known since the 60s and provide an eloquent demonstration of the nature of the divalent state.[41] These complexes can be classified as either "metallic" (with Ln = La, Ce, Pr and Gd), since the metals are better described as $(Ln^{3+})(e\text{-})(I_2)^{2-}$, which possess metallic behaviour because of the presence of free electrons in the lattice, or as "salt-like" (Ln = Nd, Sm, Eu, Dy, Tm and Yb), in which the oxidation state of the metal is 2+.

Among these, divalent europium, samarium and ytterbium are significantly more stable and are hereafter referred to as the "classical divalent lanthanides". The more reductive elements will be designated as "non-classical divalent lanthanides". All of the lanthanides (except for the radioactive Pm) have been isolated and characterised at the divalent state.[42,43]

The solubility of the diiodides has been exploited in organic reactions as SET agents, thanks to the pioneering work of the likes of Kagan and Flowers.[44–46] The non-classical Ln have found more limited use due to their instability in solutions.[47–49]

The organometallic complexes of divalent lanthanides took off in earnest since the use of the pentamethylcyclopentadienyl ligand (Cp*) became ubiquitous.[50,51] These adducts offered important advantages with respect to the Cp-based adducts, as they could be obtained by simple salt metathesis and were highly soluble.

As mentioned above, lanthanide compounds have found numerous applications, as a result of their optical and magnetic properties.[52–55] From a reactivity standpoint, they have been employed as catalysts[56,57] or as reductive or oxidative agents when they are at their divalent oxidation state[44,46,58] or at their tetravalent state,[59] respectively.

III. Redox active ligands (RAL).

The need for high added value products in domains such as medicine, material chemistry and energy have pushed for improvements in the control of reactivity, selectivity, as well as the development of methods that enable or facilitate previously inaccessible reactions. Many catalytic processes require metal-based two-electron redox transformations to assist in the completion of chemical transformations.[60] In parallel, growing concerns over the carbon footprint of human activity have naturally permeated the field of research, requiring greater consideration over energy and atom efficiency in chemical processes. Accordingly, the development of the tools capable of delivering such sought-after goals have flourished.

The properties of metal complexes are the result of the interactions between the metal centre and its ligand sphere.[61] It is in this context that redox-active ligands (RALs) in metal complexes have emerged as effective means for chemical efficiency and versatility. The resulting interplay between the metal and the ligand results in the facilitation of a chemical process in a synergistic manner. Thus, these typical ligands have challenged traditional approaches, where the ligand was used to mediate and

tune the properties of the metal, but generally played a spectator role in the catalytic reactivity.[62] Furthermore, the ability of RALs to act as electron reservoirs[63,64] has enabled one-electron redox events in metals whose oxidation degrees tend to vary by two electrons,[65,66] or, conversely, two-electron pathways in metals whose oxidation degrees tend to vary only by one.[67]

In the context of organometallic chemistry, RAL have been one of the more useful tools in the arsenal, generating much interest in the past decade or so.[68–70] Some of the more frequently used RALs include (bis-)imino pyridine derivatives,[71–73] dithions,[74] diimines,[75] quinones,[60,76] o-aminophenols,[77,78] among others. A common objective of the research into RAL is to achieve better control over the catalytic reactivity of first-row transition metal complexes, with the ultimate goal to replace the scarce, expensive noble metals currently used in a variety of catalytic processes by cheap and abundant first-row transition metals.[61,79]

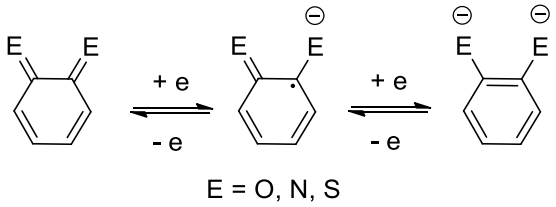

Scheme 1: Behaviour of quinone-type systems.

Their main utility stems from the ability to modify the electronic properties of a complex (and especially of the reactive metal site) in a straightforward manner. Such modifications are usually accomplished by significant chemical changes on the ligand (introduction or removal of electron-withdrawing or donating substituents at the ligand), which are often time-consuming and synthetically challenging. The RALs achieve this by oxidising or reducing the metal itself.

Furthermore, the ligands can serve not only as a redox non-innocent entity,[80] which tunes the properties of the metal, but can also participate chemically themselves in a transformation in multiple ways.[62,81] Broadly speaking, as defined by de Bruin, there are two main types of reactivity in which RALs are involved: the ligand participates in the reactivity only by accepting / donating electrons,[82–85] or the ligand actively participates in the formation / breaking of substrate covalent bonds.[86,87]

The flexibility of a RAL scaffolding was demonstrated by van der Vlugt with the $Pd^{II}Cl(NNO^{ISQ})$ complex (**1** in Scheme 2),[88] where the RAL is an *o*-aminophenol-derived ligand with a pendant pyridine. The starting complex can be both oxidised and reduced (**1**^{ox} and **1**^{red}, respectively), with all three compounds characterized in both solid state and in solution. The reduced complex successfully converted a 4-phenylbutyl azide to 2-phenylpyrrolidine, in a notable example of a radical-type transformation promoted by a ligand-to substrate single-electron transfer.

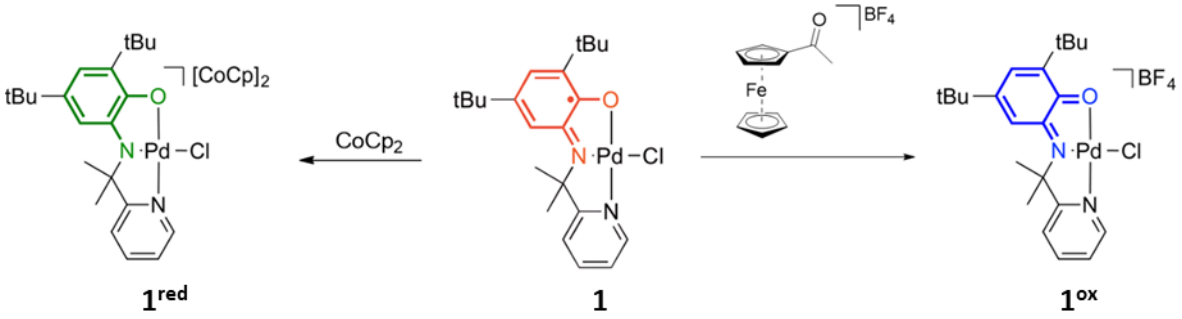

Scheme 2: The chemical transformations yielding the iminoquinone ligand via oxidation (right) or the aminophenolate ligand via reduction (left), starting from the iminosemiquinonato ligand. Adapted from ref 88.

A homologous compound using a Fe^{III} species (**2**) was also characterised by van der Vlugt[89] and its reaction with the same azide yielded a better TON with an efficient recovery of the pre-catalyst (Figure 2, left). A Cu-based bis(thiosemicarbazonato) complex (**3**) promotes dihydrogen formation under electrocatalytic conditions with mild overpotentials with impressive catalytic performances (Figure 2, centre).[90] Other examples of challenging reactivity[91–96] include cycloaddition reactions,[97] the reversible selective hydrogenation of vitamins K2 and K3 under mild conditions[98] or the production of H_2 from formaldehyde and water in the presence of a base (**4**, Figure 2, right).[99]

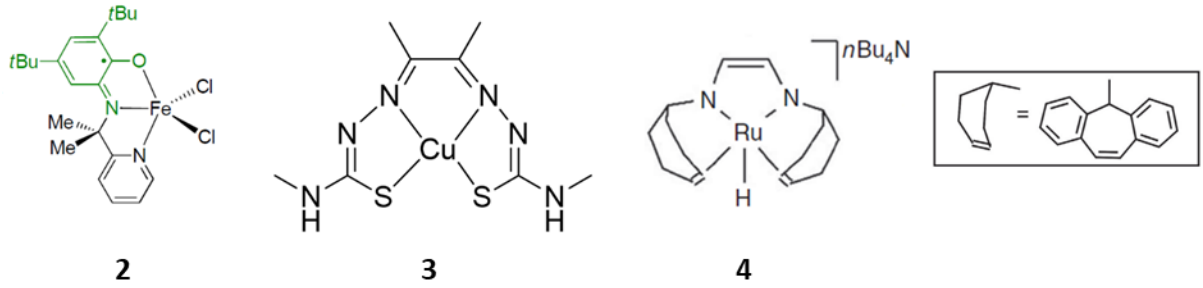

2 **3** **4**

Figure 2: Selected examples of RAL-based complexes with good catalytic activity.

The last example, employing a $[Ru^0(trop_2dad)(L)]$ (L = none, THF) architecture, was shown, via DFT and CASSCF calculations, to be multiconfigurational,[100] with a ground state mixture comprising both a closed-shell singlet ($[d^8\text{-}Ru^0(trop_2dad)(L)] \leftrightarrow [d^6\text{-}Ru^{II}(trop_2dad^{2-})(L)]$) and an open-shell metallo-radical singlet ($[d^7\text{-}Ru^{I}(trop_2dad^{\bullet-})(L)]$) with an antiferromagnetic coupling. The closed-shell singlet wavefunction dominates, but all the studied complexes have a significant (~8-16%) open-shell singlet contribution mixed into the ground state. The triplet configuration $[d^7\text{-}Ru^{I}(trop_2dad^{\cdot\cdot-})(L)]$, where the two unpaired electrons in the complex have parallel spins, is shown to be the least stable from an electronic standpoint, as expected. In agreement with their ambivalent electronic structure, these complexes reveal both metal and ligand centred reactivity.

RAL are therefore shown to actively participate in compounds which have multiconfigurational electronic structures.[101] Not only are such structures fascinating study subjects, their energetically accessible excited states are arguably one of the main reasons why such compounds are capable of inducing either metal-centred or ligand-centred reactivity, which wouldn't occur *in absentia* of the RALs. As such, the compatibility between an adequate RAL and a divalent lanthanide, in order to promote unusual reactivity, is evident.

IV. Complexes bearing lanthanides and RALs.

RAL complexes of lanthanides are intriguing and promising objects in organometallic chemistry, whose study has been increasingly gaining momentum over the past 30 years. During this period, important know-hows have been acquired in order to better control the interaction between the ligand and the metal centre. This is clearly a pre-requisite for controlling phenomena such as electron transfer towards the redox active ligand or the stabilisation of the lanthanide centre in an otherwise inaccessible electronic state, so that ligand-based reactivity can occur. Two main strategies for harnessing the potential of RAL-lanthanide systems exist: triggering an electron transfer from a divalent lanthanide towards the ligand or performing ligand-based chemistry, thereby exploiting the stability the trivalent oxidation state of most lanthanides.

Considering the strong reductive properties of divalent lanthanides, the literal interpretation of "redox-active ligand"– species that can accept or donate one or several electrons – would qualify a

large number of compounds for this discussion. For example, the groups of Evans and Long have isolated remarkable isostructural lanthanide compounds **5-Ln** with a bridging N_2^{3-} radical ligand (Figure 3).[102,103] **5-Gd** couples very strongly with the ligand, with a value of J = -27 cm^{-1}, whilst the terbium adduct **5-Tb** exhibited magnetic hysteresis up to 14 K. Despite the fact that the electrons are obviously stored on the ligand, the use of dinitrogen constitutes an exception rather than the norm and similar examples will therefore not be discussed in detail.

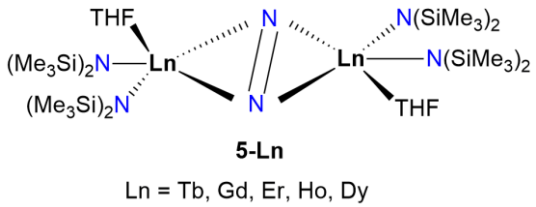

5-Ln

Ln = Tb, Gd, Er, Ho, Dy

Figure 3: Lanthanide-based compounds with a bridging N_2^{3-} radical ligand.

Lanthanide complexes with ligand classes such as arenes,[104–106] amine bis(phenolates),[107,108] tetracyano,[109–111] phthalocyanines[112,113] and numerous radical-based ligands[114–116] (among many others[117]), all of which are redox-flexible, have been isolated and are highlighted for the curious reader. The main breakthroughs in the domain have concerned quinones, semiquinones, diimines, diazadienes,[118,119] imino- and bis(imino)pyridines, nitroxides[120–122] and, in particular, N-heterocycles. Some of the more salient examples will be discussed below in order to establish some of the more frequently encountered phenomena associated with Ln-RAL complexes.

The breakthrough in iminoquinone complexes with lanthanides was achieved by the group of Bochkarev[123] in 2010, employing a phenantren-*o*-iminoquinone system. The addition of the ligand to metallic shavings of Sc and Yb yielded the $Ln(isq)_3$ compounds **6-Ln** (isq = iminosemiquinonate, the singly reduced form).

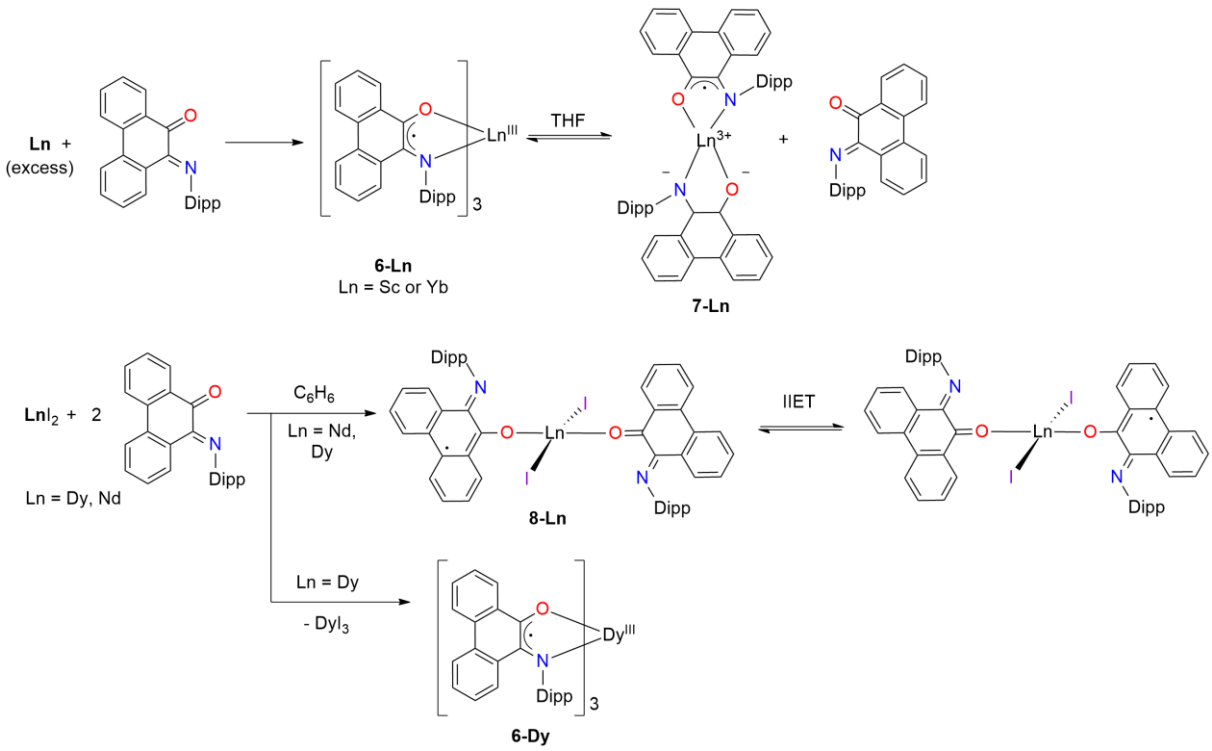

Scheme 3: Formation and reactivity of Ln-based compounds with iminoquinones.[123]

Curiously, the ^{1}H NMR spectra of these compounds in THF-d_8 showed two sets of signals – one corresponding to the neutral free iminoquinone and another set, broadened and paramagnetically shifted, belonging to the singly and doubly reduced ligand. An in-solution equilibrium with **7-Ln** was therefore inferred (Scheme 3).

The addition of the highly reductive Nd^{II} and Dy^{II} iodides to the iminoquinone led to the unusual η^1-coordination of two ligands via the oxygen atom and did not lead to the substitution of the halides (**8-Ln**). Magnetic data collected for these two complexes allowed the unambiguous confirmation of the trivalent oxidation state of the metal centres. Therefore, one of the ligands in the coordination sphere is reduced. NMR and IR data confirmed the existence of a rapid intramolecular inter-ligand electron transfer (IIET). In the case of the Dy system, a disproportionation of the compound led to the formation of DyI_3 and the compound, whose IR spectra was identical to the corresponding spectra of the aforementioned Yb and Sc complexes (**6-Dy**). The equivalent homoleptic compound with Nd was proposed, due to the formation of NdI_3, but was not isolated.

The group of Konchenko examined the reactivity of the iminoquinone motif with zerovalent and divalent Eu and Yb. The addition of iodine-activated metals to a stoichiometric quantity of the fully oxidised ligand led to dimeric compounds featuring intermolecular interactions, with the ligand doubly reduced by the metal (**9-Ln**, Scheme 4, reaction i).[124] The same compounds could be accessed by salt metathesis between the lanthanide diiodides and the potassium salt of the doubly reduced amidophenolate ligand (reaction ii). The addition of a stoichiometric amount of the fully oxidised iminoquinone ligand to the dimeric adduct (first row, middle) prompted a one-electron reduction by the heretofore divalent lanthanide (**10-Ln**, reaction iii). Interestingly, the same mixed ligand species was obtained upon the reaction of LnI_2 with two equivalents of an iminosemiquinonato (singly reduced iminoquinone) salt (reaction iv). The attribution of both the iminosemiquinone and amidophenolate motifs was corroborated by solid-state magnetism, electronic absorption spectra and IR.

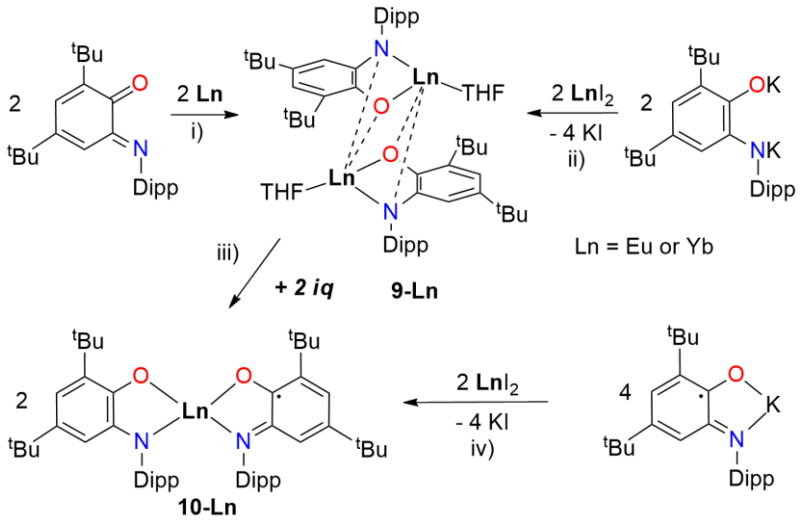

Scheme 4: Formation of Ln compounds with iminoquinone-based ligands.[124] "iq" = iminoquinone (singly reduced form)

Fedushkin and co-workers have contributed enormously to the development of the field of diamine-based Ln complexes, having researched and characterised instances of redox isomerism (also known as valence tautomerism). The Yb and Eu adducts of the bis(imino)acenaphtalene (bian) ligand were obtained starting from the activated metals and the fully oxidised ligand (**11-Ln** Step 1 in Scheme 5).[125,126] Full reduction of the ligand by the metals was confirmed by analysis of the structural parameters of the resulting crystals.

The addition of halogen-based oxidants resulted in the formation of dimeric species (**12-Br**, Step 2 in Scheme 5). In the case of Yb, electron absorption spectroscopy studies showed a temperature-dependent interconversion between two redox isomers: $[(bian)^{\cdot}Yb^{II}Br]_2$, which is predominant at lower temperatures, and $[(bian)^{2-}Yb^{III}Br]_2$, which is formed above 30 °C. These conclusions were corroborated by magnetic susceptibility data in solution.[125] The importance of the reductive potential of divalent lanthanides with respect to the bian ligand was demonstrated by a study on the homologous bridged Eu-bian systems (**14-X**), which exhibited no such behaviour. The complexes remained in the $[(bian)^{\cdot}Eu^{II}X]_2$ configuration all throughout the examined temperature range.[126,127]

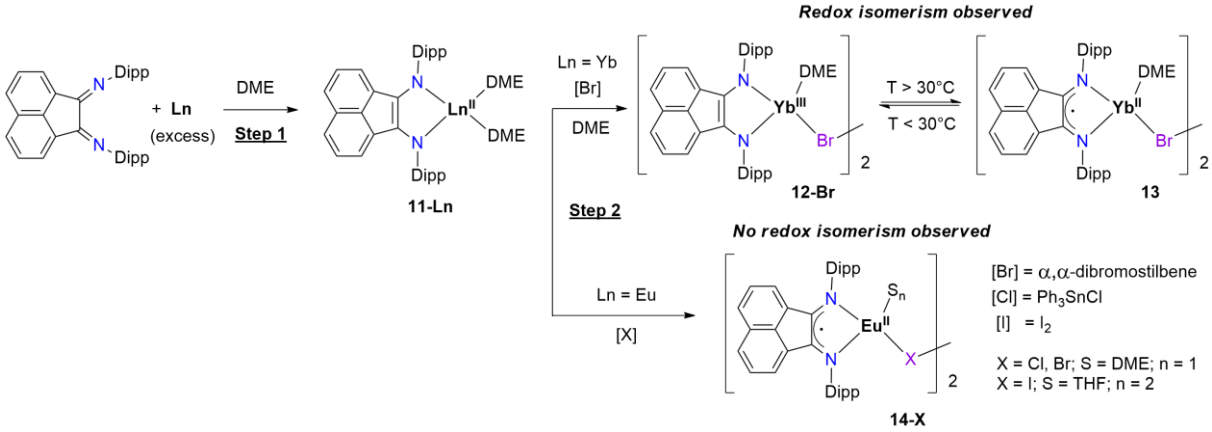

Scheme 5: Lanthanide-dependent redox isomerism in the Ln-bian system.[125–127]

A continuation of this work was based on a similar Yb-bian Cl-bridged system (**12-Cl**). The compound crystallised in three different configurations: two were polymorphous and the third had a supplementary solvent molecule in the unit cell. Of the three, changes in the unit cell parameters upon temperature variation were observed for only one of the modifications. Increasing the temperature past 150 K elongates the bond lengths between the Yb and the coordinating N of one of the bian ligands, which is indicative of ligand oxidation (Scheme 6). Therefore, an equilibrium exists between the $[(bian)^{2-}Yb^{III}(\mu\text{-}Cl)_2Yb^{II}(bian)^{\cdot-}]$ (**15**) and $[(bian)^{2-}Yb^{III}(\mu\text{-}Cl)_2Yb^{III}(bian)^{2-}]$ states.[128]

Magnetic data acquired on a single crystal, corresponding to the only configuration where redox isomerism was observed, indicated an increase of the magnetic susceptibility, due to the transition from diamagnetic Yb^{II} to paramagnetic Yb^{III}. Furthermore, a hysteresis of the magnetic susceptibility was observed when temperature scans were performed. The presumed third redox isomer – $[(bian)^{\cdot}Yb^{II}(\mu\text{-}Cl)_2Yb^{II}(bian)^{\cdot-}]$ – was not observed due to the decomposition of the compound at temperatures above 300 K.

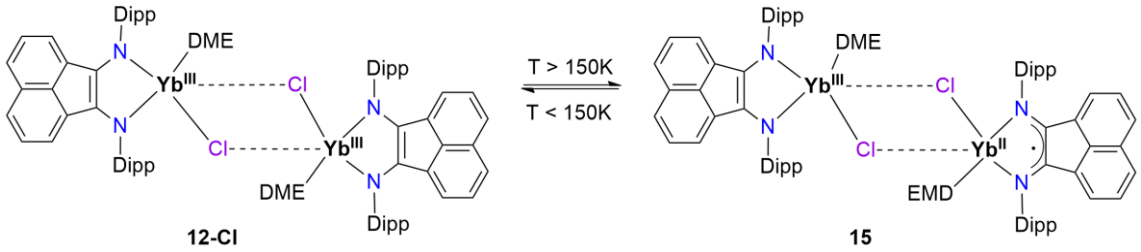

Scheme 6: Redox isomerism observed for one half of the [(bian)YbCl] dimer.[128]

The N-heterocyclic adducts have been, by far, the most used class of RAL in combination with Ln centres. Within this group, the 2,2'-bipyridine ligand (abbreviated henceforth to bipy) is one of the more emblematic redox-active ligands. This ligand has found near ubiquitous use in transition metal

chemistry. Herzog *et al*. prepared the first examples of 4f-block metal bipy compounds in the 1960s, by reaction of trivalent lanthanide halides and Li(bipy), leading to neutral compounds of general formula $Ln(bipy)_4$ with Ln = La, Ce and Nd (Scheme 7).[129,130] This work was expanded upon by the group of Bochkarev in the mid-to-late 1990s, who explored the reactivity of divalent lanthanide precursors (equations i) and ii) in Scheme 7) and characterised the complexes for the remainder of the lanthanide series (equation iii).[131,132]

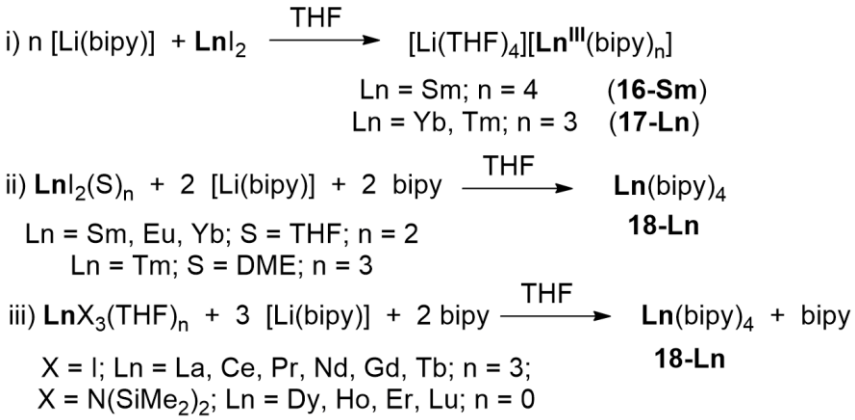

Scheme 7: Preparation of neutral or anionic $Ln(bipy)_4$ complexes.[129–132]

The electronic states of the metal centre and of the bipy ligands in the neutral $Ln(bipy)_4$ complexes – initially believed to be zerovalent and neutral, respectively – has been the subject of some controversy. Bochkarev and co-workers argued for the presence of two electronic configurations: $[Ln(bipy^{\bullet-})_3(bipy^0)]$ and $[Ln(bipy^{2-})(bipy^{\bullet-})(bipy^0)_2]$ on the basis of solid-state magnetic data, IR spectra and of the structural features observed in the available crystal structures (Figure 4).[132] The sole exception is the europium complex, in which the metal centre remains in the divalent state. Its electronic configuration is, therefore, unequivocally $[Eu(bipy^{\bullet-})_2(bipy^0)_2]$. The reduced nature of the ligand can be qualitatively assessed by IR measurements, where strong absorption bands in the regions 800-1000 cm^{-1} and 1490-1575 cm^{-1} are typical for a bipyridyl radical anion.[133] Inconsistencies in their model remained, however. The authors noted, for example, that the twofold rotation axis, which generates two pairs of symmetrically equivalent bipy ligands in the samarium complex, is incompatible with the two proposed electronic configurations.

Further insight was provided almost twenty years afterwards in a detailed theoretical study proposed by Andersen *et al*. L_{III}-edge XANES data obtained for the cerium and ytterbium complexes (whose well-established propensity for multiconfigurational ground states (discussed below) could be the source of ambiguity) substantiated the claim that the metals were trivalent.[134] The results highlighted subtle differences to Bochkarev's interpretation: the isostructural lanthanum and cerium compounds present two sets of M-N distances, which are consistent with the radical anionic ligand ($bipy^{\bullet-}$) and with a ligand electronic configuration in between the neutral and radical forms (assigned as $bipy^{-0.5}$), respectively. As such, their formula would be presented as $[Ln(bipy^{\bullet-})_2(bipy^{-0.5})_2]$. This rationale has been extended to the samarium complex, thereby resolving the aforementioned inconsistency. Multireference quantum mechanical calculations performed for the La, Ce, Yb and Lu complexes showed that the ground-state electronic structures of these compounds are multiconfigurational. This model was extrapolated to the neutral (Sm, Eu) and anionic (Tb, Dy) lanthanide bipy compounds in order to rationalize their physical properties (Figure 4). In this model, the electronic ground states for La/Lu and Ce/Yb are doublets and triplets, respectively, rather than the singlets and the doublets found in the vast number of compounds known for these compounds.

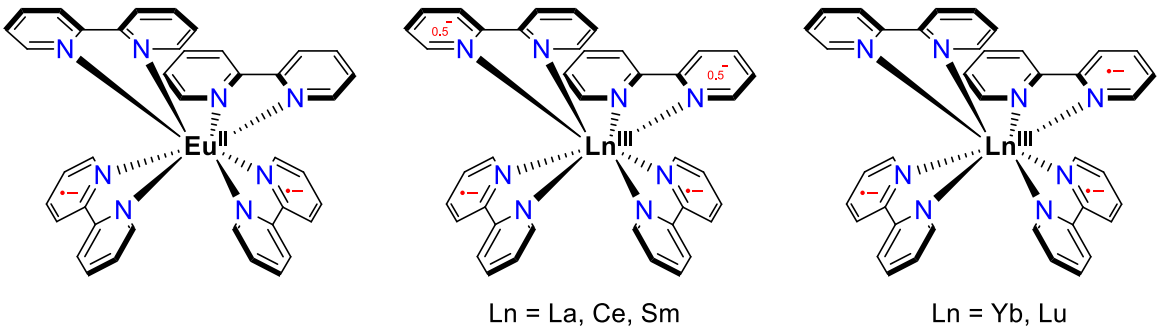

Figure 4: Electronic structures of the [Ln(bipy$_4$)] compounds with known crystal structures.

The bipy ligand arguably owes its iconic status in lanthanide organometallic chemistry to its reactivity with divalent ytterbium compounds, particularly the Cp*$_2$Yb(bipy) complex. Andersen reported a series of compounds obtained following the addition of a RAL to a Cp'$_2$Yb-type starting complex. According to the IR spectra, some of the complexes feature the signature absorptions for the radical anionic ligand.[135] The presence of the bipy$^{\bullet-}$ ligand indicates an electron transfer from the divalent ytterbium to the ligand.

The first publication of the Cp*$_2$Yb(bipy) (**19**) complex[135] in 2002 was followed by a flurry of studies that aimed to explain the anomalous magnetic behaviour initially observed. One of the initial hypotheses invoked to explain the magnetic data was that of temperature-dependent valence tautomerism. In such systems, the electron transfer is temperature-dependent; the ytterbium remains divalent at low temperature, but is oxidised when the temperature increases. This had been previously observed in systems such as Co/dioxolene.[136,137] However, this explanation was dispelled upon the acquisition of L$_{III}$-edge XANES data for a series of Cp*$_2$Yb(L) complexes, where L = bipy and a variety of diazadiene ligands.[138] The spectra showed the signatures of both Yb^{II} and Yb^{III} for all compounds but, crucially, the intensities of these signatures were not temperature-dependent. The fit of the data indicated that the Cp*$_2$Yb(bipy) complex had 83% Yb^{III} character, while the diazadiene-based complexes had 89-95% trivalent character.

Three main configurations were envisioned: the closed-shell singlet (**CSS** in Scheme 8) (f^{14}-$(\pi^*)^0$, where π^* is the LUMO of the bipy ligand), the open-shell singlet (**OSS**) configuration (f^{13}-$(\pi^*)^1$, where the spins couple antiferromagnetically) and the triplet (**T**; also f^{13}-$(\pi^*)^1$) configuration. These computations show that the ground-state wave function is multiconfigurational with an admixture of the open-shell and the close-shell singlets.

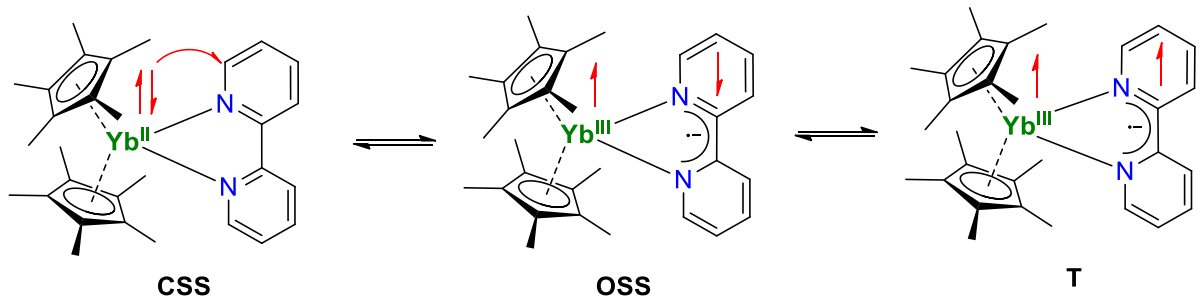

Scheme 8: Representation of the possible electronic configurations of the Yb-bipy system.

Since the lanthanide molecules cannot form primarily covalent bonds, due to limitations in orbital overlap, charge transfer from Yb^{II} to the π^* orbital on bipy is not an available mechanism by which the molecule can alleviate the electron-electron repulsion in the 4f shell. Instead, the molecule mixes the

two singlet configurations forming an intermediate valence configuration and thus lowers the total energy of the molecule (see Scheme 9 for a simplified representation of this phenomenon). The formation of multiconfigurational ground states mimics covalency in systems where the valence electrons are core electrons.[138,139] It is worth noting, however, that examples of covalent character in the bonds in 4f-based compounds are not unheard of, but they remain, as a rule, non-dominant contributions to the overall bonding.[140–143]

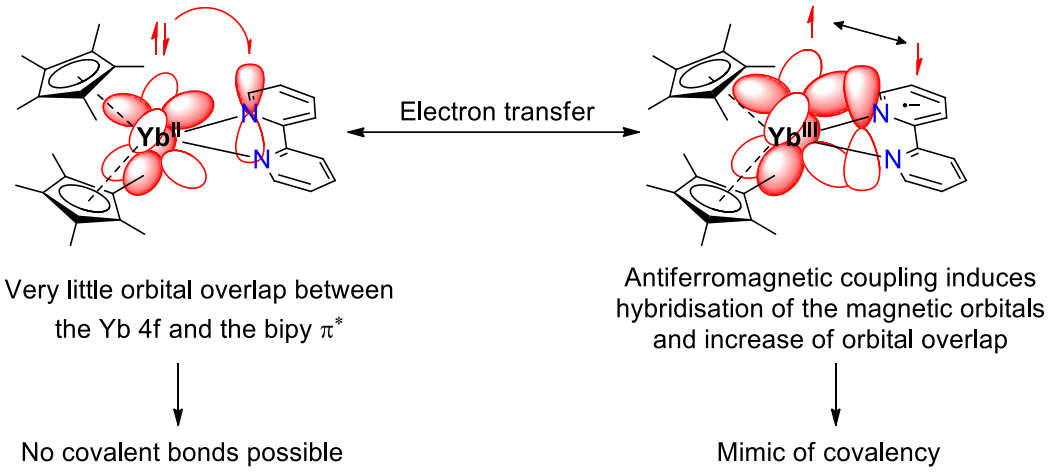

Scheme 9: Representation of the formation of the closed-shell singlet upon electron transfer in the Cp$_2$Yb(bipy) complex.*

Whether the triplet or the multiconfigurational singlet state is favoured is the result of a couple of factors: first of all, it depends on the energy difference between the two orbitals involved in the open-shell singlet – in this case, the 4f orbital of Yb and the π* of the bipy ligand. Second, the symmetry of the orbitals is crucial; a singlet state requires that the orbitals be of the same symmetry within the point group of the molecule.

Another way to visualise this unusual physical phenomenon is to view it as a molecular equivalent to a Kondo singlet, an analogy first used by Neumann and Fulde to describe cerocene.[144,145] The Kondo effect describes coupling of a local magnetic moment to electrons in a conduction band. The coupling occurs when the magnetic orbitals hybridise with the conduction band, causing the formation of a quasi-bound singlet state, known as the "Kondo singlet". In this case, some of the electron weight is projected onto the conduction band and some of the electronic density in the conduction band is localized into the quasi-bound state. Using this analogy, the Kondo interaction in Cp*$_2$Yb(bipy) and similar adducts corresponds to antiferromagnetic coupling between the magnetic moments on the ytterbium and the aromatic, conjugated π orbitals of the ligand. Additionally, using the Hubbard model, it was possible to determine an exchange coupling value of –920 cm^{-1} for Cp*$_2$Yb(bipy) between the metal ion and the ligand radical,[146] which is more than one order of magnitude higher than those of other known molecules with strong coupling.[102]

The electron transfer from the Cp*$_2$Yb(OEt$_2$) complex was studied on a number of complexes bearing different N-heterocycles.[147–150] A summary of the results is presented in Figure 5. The dissimilar outcomes that were observed depended on the reaction stoichiometry, the size of the ligand, as well as the number of available coordination sites. The ability of a ligand to accept one or two electrons is related to its reduction potential; as mentioned above, on the basis of the reported reduction potential of Cp*$_2$Yb, very few of these nitrogen bases should be reduced. However, the extent to which the reduction potentials of the heterocyclic bases are lowered by coordination can be estimated. For example, Cp*$_2$Yb(pyridine)$_2$ is a diamagnetic adduct, where no electron transfer occurs, whilst the Cp*$_2$Yb(pyridazine)$_2$ complex is paramagnetic and contains a Cp*$_2$Yb^{III} fragment. Thus, the work of

Andersen revealed that when the reduction potential of the ligand is about -2.2 V or higher, Cp^*_2Yb can reduce the ligand (illustrated in Scheme 10).[147]

In ligand motifs which have at least two nitrogen atoms that are sterically accessible to two Cp^*_2Yb fragments, the transfer of two electrons to form a dianionic ligand occurs if the reduction potential of the ligand is approximately -2.4 V or higher. Once the two electrons are paired, their polarizability determines whether the two $Cp^*_2Yb^{III}$ fragments communicate electronically: antiferromagnetic coupling results when this value is more negative than about -2 V, as in azobenzene and 2,2'-bipyrimidine, while when the potential is higher, as in the case of phenazine, no coupling results.[147]

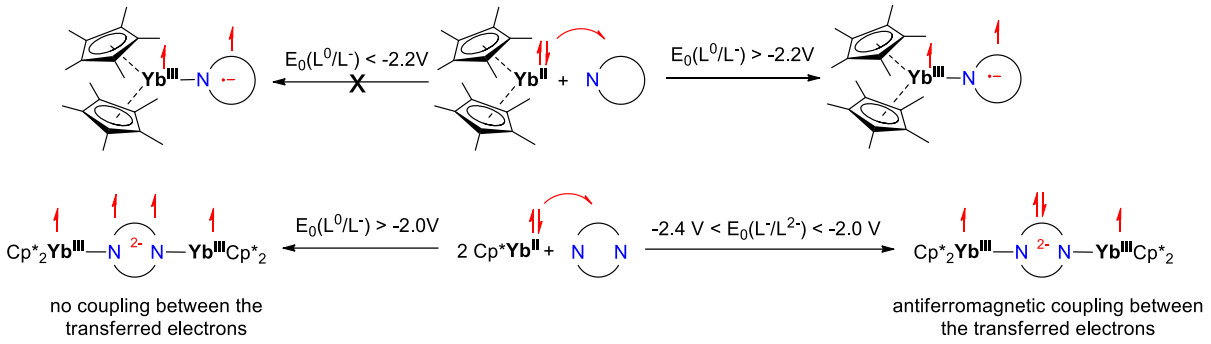

Scheme 10: Dependence of the electron transfer on the N-heterocyclic ligand reduction potential. The relative orientations of the spins of the Yb^{III} centre and the radical anionic ligand are purely schematic and not necessarily representative of the determined electronic configuration.

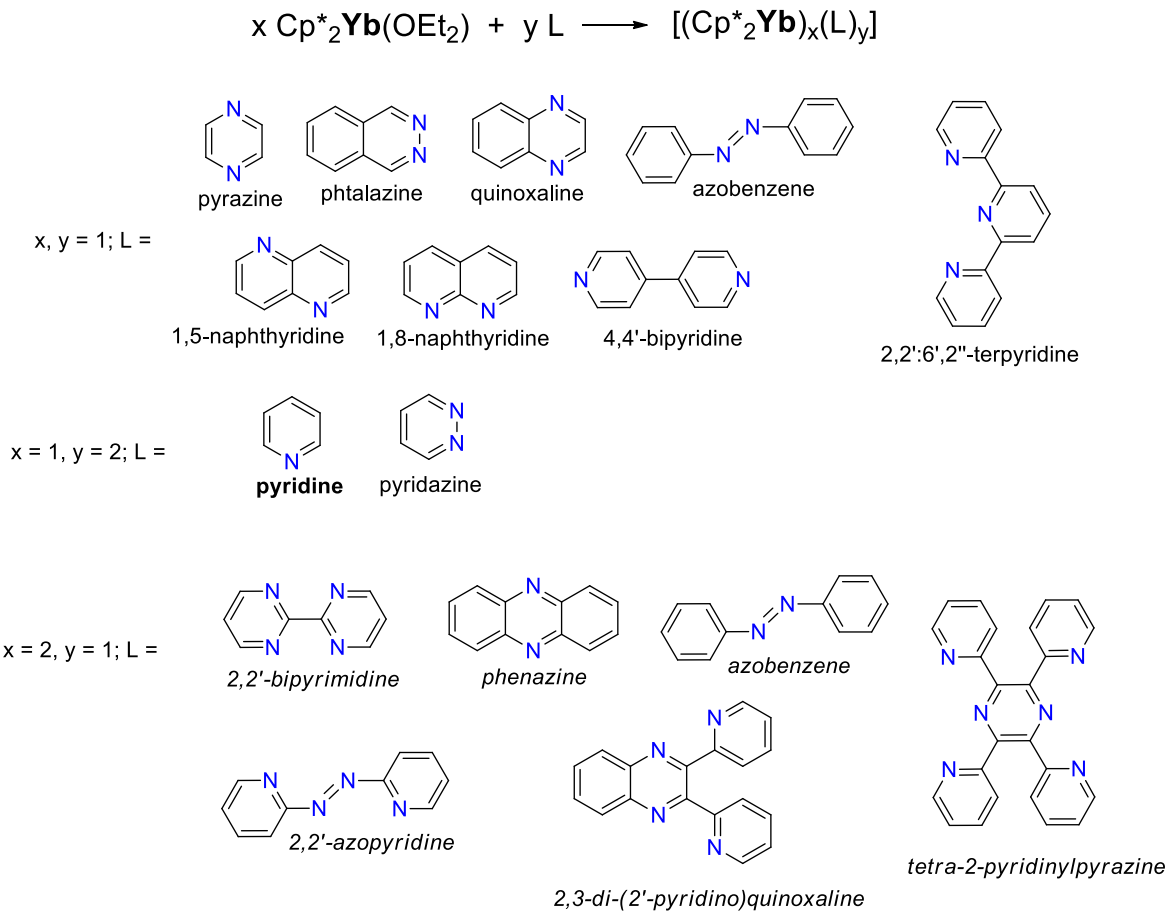

Figure 5: Selection of ytterbocene adducts of various stoichiometry. Names of ligands in bold indicate no electron transfer; in italics indicate double reduction.

The 1,10-phenantroline (phen) adduct of ytterbocene (**20**), as well as the **20-(3,8-Me$_2$)** and **20-(5,6-Me$_2$)** homologues, are ground-state triplets.[151] The chemical ramification is that Cp*$_2$Yb(phen) (**20**) is a dimer when crystallised in solution and a monomer when sublimed at higher temperatures. Cp*$_2$Yb(3,8-Me$_2$phen) (**20-(3,8-Me$_2$)**) exists in solution as a dimer-monomer equilibrium at room temperature. The dimerization proceeds with the formation of a reversible C-C bond between the two phenanthroline groups at the 4,4' positions (**21-a** and **21-b**). Other phen adducts have also been described and present a breadth of different behaviours: depending upon the substituents and their positions, the ground state can be either a triplet or intermediate-valent. The numbering scheme and the chemical reactivity[152] of the Yb-phen compounds are presented in Scheme 11.

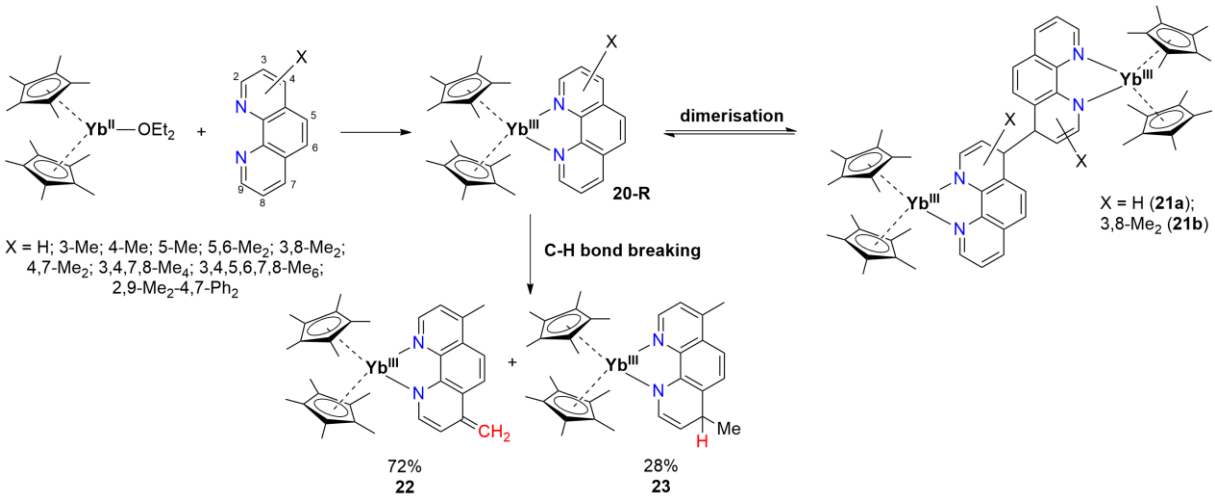

Scheme 11: Formation and reactivity of Yb-phen compounds. The numbering scheme of the substituents is presented as reference.

The difference in behaviour can be rationalised by the electronic structure of the ligand, which is known to possess two empty π orbitals of similar energy that have two very different symmetries. These two orbitals have b_1 and a_2 symmetry in C_{2v} symmetry: b_1 is similar to the equivalent orbital of bipyridine and has density concentrated on the nitrogen atoms, which coordinate the ytterbium centre; conversely, a_2 has very little density on the nitrogen atoms (Figure 6). A molecular orbital diagram of the f-shell orbitals indicated that the singly-occupied f-orbital possesses b_1 symmetry in C_{2v} symmetry, whilst the vacant 5d orbitals are of a_2 symmetry.

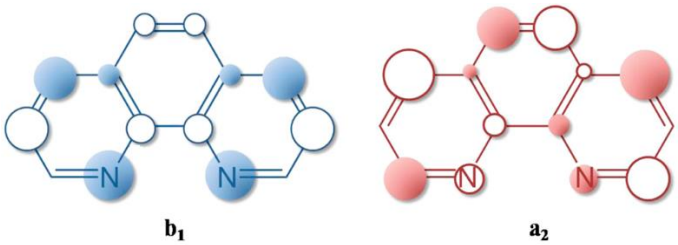

Figure 6: Representations of the LUMO (b_1 symmetry) and LUMO+1 (a_2 symmetry) orbitals. Adapted from ref 151.

The modulation of the relative energies of the orbitals can be summarised as follows: if the ligand b_1 orbital is lower in energy than the a_2 orbital, an open-shell singlet ground state is favoured. If, however, the ligand a_2 and b_1 orbitals are close in energy, the final a_2 orbital ends up lower in energy, stabilising the triplet ground state. The implication is that the b_1-a_2 gap can be tuned by the presence of methyl substituents. The population of the a_2 orbital results in an increased spin density at the C4 and C7 positions – the former is the site of the coupling. However, when the phenanthroline is

substituted at precisely these positions, the reactivity of the ensuing compound is different: an intermolecular hydrogen atom transfer occurs between two complexes (Scheme 11). The electronic configuration of this complex is a multiconfigurational open-shell singlet ground state.[152]

N-aromatic heterocycles were employed with other lanthanides, as well. The group of Long exploited the strong exchange coupling that is characteristic to these systems to probe for promising magnetic properties. The ligands used for these studies had multiple accessible coordination sites that permitted the formations of bimetallic and trimetallic edifices (Scheme 12, equation i and ii, respectively). In all cases, the lanthanide precursors were tetraphenylborates salts of gadolinium, terbium and dysprosium. The reactions were carried out in the presence of potassium graphite and featured ligand-centred reductions, yielding either monoanionic (in the case of the bipyrimidine (bipym) ligand, complexes **24-28**,[153,154] and 2,3,5,6-tetra(2-pyridyl)pyrazine (tppz),[155] leading to **29-Ln**) or trianionic radical ligands following further reduction (for example, the tppz complex **30-Ln** or the hexaazatrinaphthylene complex **31-Ln**[156]).

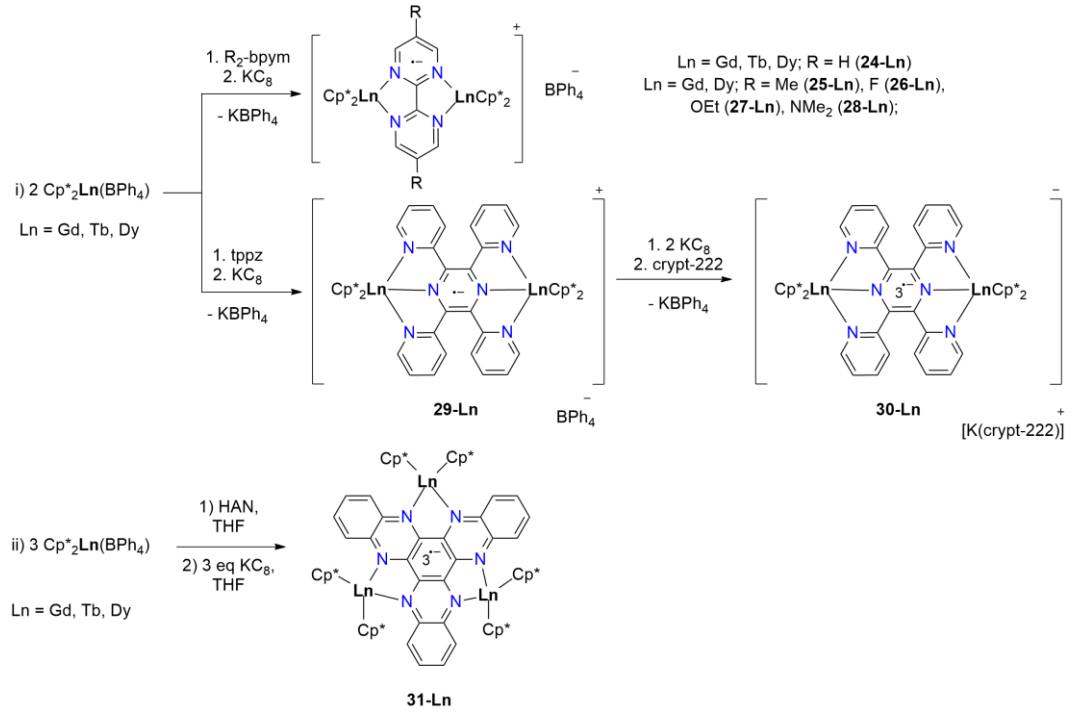

Scheme 12: Synthesis of bi- and trimetallic radical ligand systems.[153–156] "HAN" = hexaazatrinaphthylene.

Ln^{III}-$L^{\bullet-}$ exchange coupling is observed for all species. **24-Tb** and **24-Dy** demonstrate single-molecule magnet behaviour due to the large magnetic anisotropies imparted by these ions. Similar observations were made for the tppz-bridged complexes. The introduction of substituents in the 5,5' positions in the bipym for the Gd and Dy adducts allowed for an up to a fourfold increase of the magnetic exchange coupling constant (by going from an electron-donating to an electron-withdrawing group).[154] The strong magnetic exchange coupling induced by the radical bridging ligand in **31-Dy** facilitates enhanced magnetic hysteresis and comparatively long magnetic relaxation times.

V. Complexes bearing lanthanides, RALs and transition metals.

On a similar line, the group of Nocton investigated the formation and reactivity of heterobimetallic adducts based on divalent ytterbium and transition metals. Two Yb-Pd^{II} compounds were synthesised, bridged by different RALs – bipyrimidine (bipym, **36-Pd**) and 4,5,9,10-tetraazaphenanthrene (taphen;

33-Pd). Upon the oxidative addition of methyl iodide, two different behaviours were observed: the taphen complex **34** undergoes rapid reductive elimination of ethane to revert to a Pd^{II} species **35** (Scheme 13).[157] The analogous bipym complex **37** is sufficiently stable – even at room temperature – to allow isolation and characterisation. Spectroscopic and theoretical studies indicated different electronic ground states for the Yb-Pd^{II} adducts. Analogous to the disparity between phenanthroline and bipyridine, the taphen complex **33-Pd** is a ground ground-state triplet, where the electron lies on the ligand with little participation of the Yb metal centre. In contrast, **36-Pd** has a multi-configurational singlet ground state, where the Yb metal centre has a strong influence on the electron located on the ligand. As opposed to the taphen complex, the electron from the ytterbium is transferred to an orbital that has significant spin density on the N-atoms coordinated to the Pd centre in the bipym complex. This allows the stabilisation of the Pd^{IV} species in **37**.

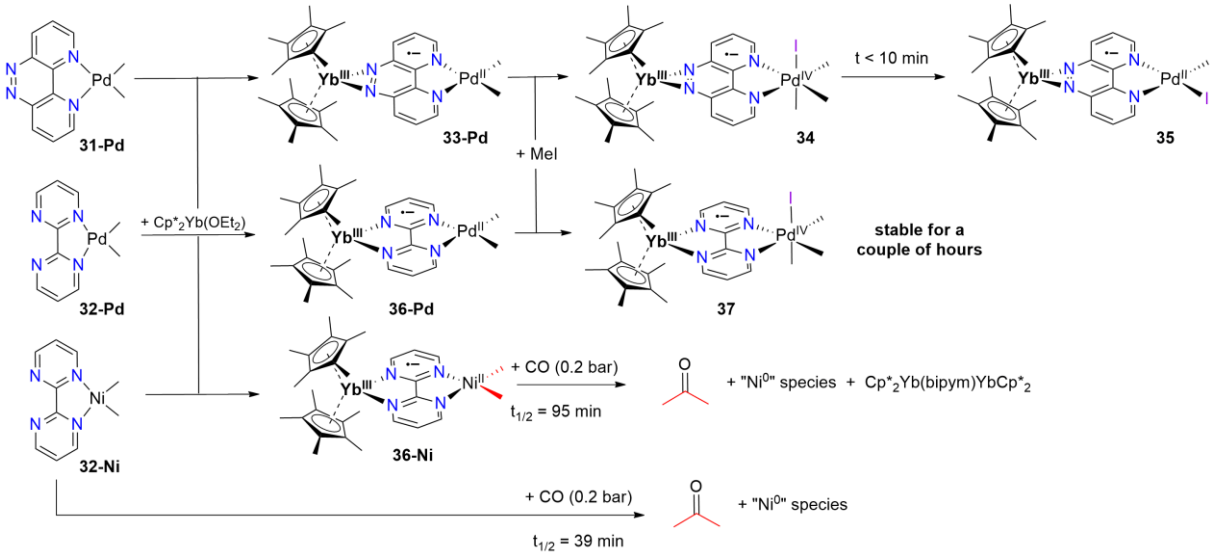

Scheme 13: Reactivity of heterobimetallic species of divalent ytterbium and transition metals.[157,158]

The analogous Yb-Ni^{II} compound **36-Ni** was the subject of a comparative reactivity study and its reactivity with carbon monoxide was investigated. The low-pressure addition (0.2 bar) of the gas was investigated in both the bimetallic compound **36-Ni** and in the nickel precursor **32-Ni**. The new signals observed in the NMR spectra over time and the rapid formation of acetone were interpreted as the results of CO migratory insertion reactions in the Ni–Me bond.[158] The formation of acetone indicates a reductive elimination from the divalent nickel centre to form Ni^0 species. The key role of the lanthanide fragment was demonstrated by the difference in reaction kinetics: the half-time of the reaction was more than doubled in the $YbNi^{II}$ species, compared to that of **32-Ni**, which highlights the stability of the bimetallic intermediate.

Further work on the taphen ligand system demonstrated that the addition of a second equivalent of a divalent ytterbium fragment was possible on the previously characterised architecture, yielding heterotrimetallic complexes {[$Cp^*_2Yb(taphen^{2-})MMe_2$]($Cp^*_2Yb$)} (**38-M**, M = Pd, Pt), in which the divalent ytterbium fragment is coordinated through the methyl groups of the transition metal and in which the taphen ligand underwent a second reduction (Scheme 14). The second reduction is in good agreement with the observed structural features for both trinuclear complexes and occurs only in non-coordinating solvent, such as toluene, and is reversed upon addition of THF – a coordinating solvent.[159] Magnetic data and theoretical computations corroborated the presence of two Yb^{III} centres and of a dianionic, diamagnetic ligand in **38-M**. The observed reactivity validates the concept that the stored

electrons in redox non-innocent ligands can be back-transferred upon coordination-chemistry engineering.

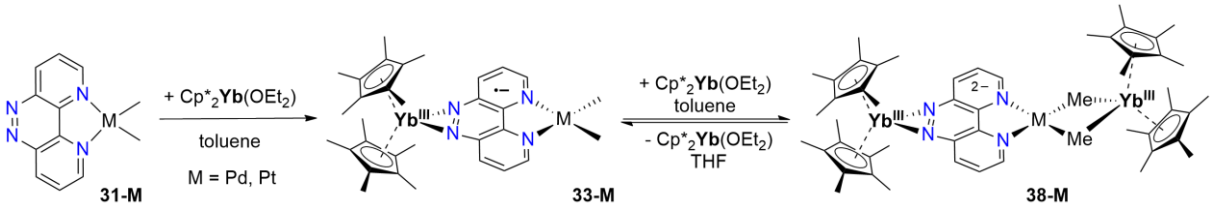

Scheme 14: Reversible electron transfer in taphen complexes.[159]

The group of Farnaby has synthesised conceptually similar structures,[160–162] underlining the premise that lanthanides are valuable partners in such complexes.

VI. Introduction on theoretical computations.

The systems described above are often quite complex and can present a plethora of differing behaviours – solvent-dependent electron transfer, multiconfigurational ground states, magnetic properties, etc. Even the formation of such species is often not anodyne and the mechanisms involved must be described carefully. Spectroscopic characterisation in such cases is often complicated by factors such as instability under ambient conditions (be it air sensitivity or thermally-induced decomposition). To circumnavigate these issues, organometallic chemists have increasingly resorted to theoretical computations as both a means to validate experimental observations and as a tool to try to fill the gaps, where sufficient information cannot be gathered on the laboratory benches. The section below will try to summarise the theoretical background, the main methods used and, crucially, their validity.

Quantum chemistry treatment of molecular systems has been under massive development over the last decades. It would not at all be an exaggeration to say that interest in the field has exploded within the last few decades, even considering the general progress in gross number of publications per annum (Figure 7). This has been enabled by the development of both the methods and time-saving algorithms, as well as by the spectacular growth of computer processing power. It is now possible to perform advanced calculations on molecules comprising hundreds of atoms, and, more pertinently, a significant number of electrons (inherent to heavy elements). Another factor likely to have contributed is the increasing number of (commercially) available software, adapted for either specialised or general methods. Some of the more notable examples are ACES,[163] Dirac,[164] GAMESS,[165] Gaussian,[166] MOLCAS,[167] MOLPRO,[168] ORCA,[169] Turbomole[170] or VASP.[171] It has, thus, never been more accessible to perform quantum chemical computations. Case in point: DFT, arguably the most famous and most used method in organometallic chemistry, was a term found in only 190 publications in 1990[†]. That number rose to more than 52 thousand within 30 years, corresponding to a blistering 275-fold increase. To put that into perspective, the other terms shown in the graph rose between 10-15 times (Figure 7). Some of the reasons justifying the increasing use of these types of computations will be presented below.

[†] According to the Reaxys search engine.

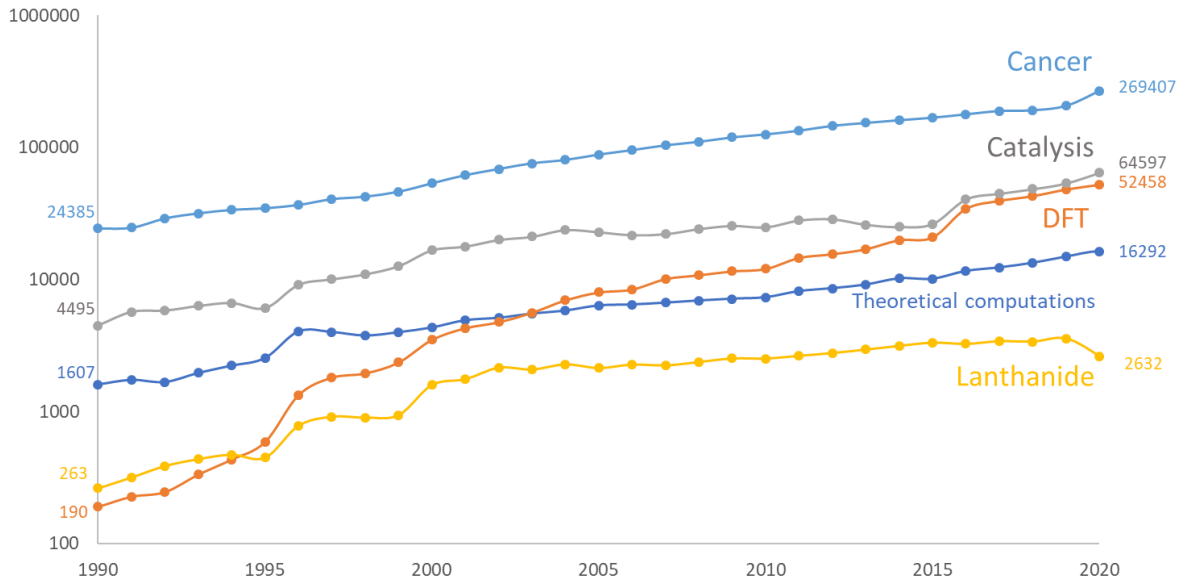

Figure 7: Number of publications containing several prominent keywords in the period 1990-2020. The exact numbers are given, in accordance with the colour code, for the first and last years.

VI.1. Theoretical background

Non-relativistic quantum calculations are based on solving the Schrödinger equation. The time independent Schrödinger equation links the wave-function to the total energy of a system. Its expression can be written as:

$$\hat{H}|\psi\rangle = E|\psi\rangle \quad (1)$$

where E is the stationary energy, $\hat{H}$ is the Hamiltonian, and ψ the wave-function for a system of N nuclei and n electrons. The Hamiltonian is the sum of the kinetic and potential energies and can be written as:

$$\hat{H} = \hat{T}_e + \hat{T}_n + \hat{V}_{NN} + \hat{V}_{Ne} + \hat{V}_{ee} \quad (2)$$

where $\hat{T}_e$ is the electron kinetic energy, $\hat{T}_n$ the nuclei kinetic energy, $\hat{V}_{Ne}$ the interaction between the nuclei and the electron, $\hat{V}_{ee}$ the interaction between the electrons and $\hat{V}_{NN}$ the interaction between the nuclei. The potential terms in Eq 2 are Coulomb potentials and a recent study showed that, while they do not offer exact solutions, are accurate to 40 digits.[172] However, for systems of more than a few atoms and, inherently, for transition metal complexes, calculations rely on several approximations. One of the most important is the Born-Oppenheimer (BO) approximation, which posits that the motion of the nuclei (1836 times heavier than the electron) is much slower than that of the electron and can therefore be decorrelated from the latter.[173] This simplifies calculations, as the interaction term between the nuclei and the electron $\hat{V}_{Ne}$ can be neglected. To put things into perspective, non-BO calculations are limited to very simple systems.[174,175] The BO approximation is quite robust for the description of ground states, but is inadequate for the calculation of excited states.[176]

The non-relativistic approximation is insufficient for very precise calculations, as relativistic energy contributions are already needed for H_2^+ or H_2. Given that the relativistic effect is proportional to the atomic number, they become indispensable for the heavier elements (broadly speaking, from Ag

onwards).[177] The core electrons for such elements are also affected, as they approach the speed of light, which would imply that an accurate description of all the electrons in a rare earth atom need to be correctly described with an all-electron (AE) calculation. This is computationally very costly, both in terms of time and of required memory, which spurred the development of other options.

The approach most commonly used in relativistic calculations revolves around introducing relativity to the Schrödinger equation by using the Dirac equation. The Dirac equation uses a 4-component formalism in order to characterise the particles under investigation, since the formalism describes coupled particle-antiparticle pairs, where the spin of the fermions and the effects of spin-orbit coupling are treated explicitly. Four-component approaches are computationally intensive, severely limiting the scope of the molecules that can be studied.[178] Due to these constraints, there have been significant efforts invested in finding solutions that reduce the computational cost of the calculations. Some of the main advances shall be presented.

The complexity of the four-component formalism prompted the development of algorithms that effectively decouple the particle anti-particle pairs, retaining only the electronic components. The four-component, Dirac formalism can be loosened by decoupling the particle-antiparticle pairs and treating them separately. The spin-orbit coupling can still be treated explicitly, as within the Dirac formalism, or added *a posteriori* by considering the scalar relativistic components in the Hamiltonian.

Two of the more popular approaches used to simplify proceedings are the Zeroth Order Regular Approximation (ZORA) or the Douglas-Kroll-Hess (DKH) Hamiltonian. In the first case, the ZORA[179] formalism affords a relativistic correction to the kinetic energy, which depends on the inverse of the potential V. This is called the gauge dependence. One of the consequences of the gauge dependence is that shifting the electrostatic potential by a certain amount, the ZORA energy decreases faster than it should and does not result in exactly the same shift in eigenenergies. In molecular calculations such a gauge non-invariance may result in unrealistic geometry structures, or wrong electron affinity, due to the appearance of nonphysical attractive forces between nuclei.[180,181] Different ways exist in order to lessen or remove this gauge dependence, by using the higher order expansions of the ZORA method, such as FORA or IORA (first and infinite order, respectively). Alternative theories have replaced the potential with a model potential (ZORA-MP), thereby removing the gauge dependence, which leads to better estimations of the energy.[182,183]

The DKH Hamiltonian relies on another approximation for the evaluation of the Hamiltonian. The guiding principle is to use a unitary transformation that provides an approximate decoupling between the large and the small components in the Dirac formalism.[184] The exact expression of the unitary transformation is not known, but it was shown that it was not necessary to know the exact square root parametrisation initially introduced by Douglas and Kroll. Rather, this matrix can be decomposed in an infinite set of unitary transformations. The decomposition can be done using n unitary transformations, where n designates the order of the DKH Hamiltonian. DKH2 is the most used version of the Hamiltonian and it has been applied to both DFT and *ab initio* methods.

Other prominent solutions employed to further reduce computational cost involved the creation of time-saving density fitting algorithms. Some of the techniques developed are the Choleski Decomposition,[185,186] Resolution of the Identity (RI),[187,188] chain-of-spheres algorithm (COSX),[189] the pair-atomic resolution of-identity (PARI-K) method[190] or the auxiliary density matrix method (ADMM).[191,192] The saved computational cost brought by both the relativistic Hamiltonians and the density fitting algorithms mean that precise computations on large systems are rendered more feasible.

In addition, the rigour imposed by calculations at the AE level can be further simplified by a change of paradigm, based on the approximation that only the valence electrons are pertinent from a chemical standpoint, as the core electrons remain, by and large, chemically inert.[193] Their chief contribution is forming an electrostatic effective potential perceived by the valence electrons. Therefore, one of the ways of expediting theoretical computations has been the use of relativistic effective core potentials (RECP), whose use in the lanthanide series was pioneered by the group of Dolg.[193] The principle involves treating the core electrons as a mean field potential, whilst the valence electrons are treated explicitly. They offer excellent accuracy (up to chemical accuracy), as the RECP have been fitted on AE computations. Within this category, two types of RECP exist for lanthanide elements, depending on how the 4f electrons are considered – Small Core RECP[194] (SC-RECP), with the 4f electrons treated explicitly, and a Large Core RECP[195] (LC-RECP), with the 4f electrons in-the-core of the pseudopotential. The use of LC-RECP can be justified by the low radial extension of the 4f manifold in the lanthanides, which means that the corresponding electrons are largely core-like, unlike the behaviour of the early actinides, which may engage in covalent bonding.[196] The use of LC-RECP is more controversial when computing divalent lanthanides, as the 4f orbitals can be close to the frontier orbitals, which means that they should be treated explicitly in such cases.[143]

The last term in Eq 2, that determines the interaction between any two electrons is still not known analytically: $\hat{V}_{ee}$. Two main families of calculations have been developed in order to solve the Schrödinger equation: wave-function theories (or *ab initio* methods) and Density Functional Theory (DFT). A brief introduction of both methods follows, before detailing the exact parameters used throughout this work.

VI.2. The main types of computations.

VI.2.1. *Ab initio.*

Wave-function theory is based on the Hartree-Fock (HF) formalism. In this formalism, the wave-function is described as a single Slater determinant, and the electron-electron interaction is expressed as a mean field potential described as a Coulomb and an exchange potential. The latter is particularly important and is related to the interaction between two electrons of opposite spin. The set of HF equations is solved by an iterative procedure to better approximate the molecular orbitals, whose exact expression is not known. After an initial resolution of the equations, the resulting orbitals are reinserted into the equations themselves in order to achieve self-consistency (this procedure is called Self-Consistent Field (SCF)).[197]

HF methods often gives a very realistic qualitative description of the ground state of a system in an equilibrium geometry, but are insufficient in cases, where a good description of electronic correlation is required. HF is also deficient in molecules where the wave function is not a single closed-shell configuration state function. The errors chiefly originate in the fact that neither the static, nor the dynamic electronic correlation are treated by the HF method. In such cases, more accurate schemes can be applied to the Hartree–Fock wave function, used as a reference function, to improve the results. The various tools available to computational chemists to resolve the deficiencies of HF is not the focus of this work, but a selection of references is provided for the curious reader.[198–205]

One of the most prominently used solutions is Complete Active Space Self Consistent Field (CASSCF) theory, where the ground state wave-function is described as a combination of multiple Slater determinants.[206] The CASSCF method allows the separation of the core-like molecular orbitals (inactive space) and the definition of the active space, where the molecular orbitals more pertinent to

the electronic structure (or reactivity) are populated by a pre-defined number of electrons. In the active space, the electrons are distributed among the orbitals and all possible occupancies are considered to obtain a multiconfigurational description of the system (Figure 8).[207]

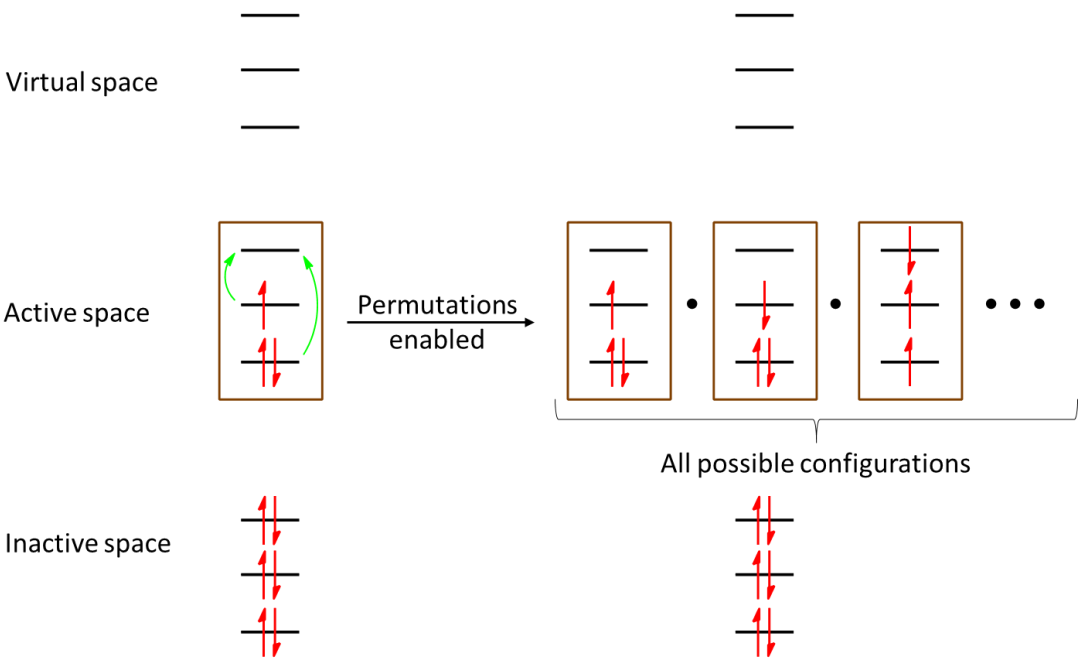

Figure 8: Representation of the principle of multireference CASSCF computations.

This method is not a universal solution in computational chemistry, due to some of its constitutional drawbacks. For one, it does not treat dynamic correlation. Another one of the limitations inherent to this method is that the computational cost increases very rapidly as the number of active orbitals and electrons inserted in the active space is augmented. This is particularly salient in organometallic complexes of lanthanides, as orbitals from the ligand or the lanthanide 5d orbitals are likely to also contribute to the final evaluation of the electronic structure of the complex, in addition to the seven 4f orbitals that need to be taken into the active space. Even more so, Roos recommended the addition of the 6s and 6p in the active space for lanthanide molecules.[208] These considerations would impose a computationally unfeasible active space. Nevertheless, CASSCF studies of lanthanide molecules have been performed with smaller active spaces to corroborate different types of physico-chemical properties, such as multiconfigurational ground states, magnetism or luminescence.[138,209–212]

The high computational cost of *ab initio* methods can be an obstacle in the case of large systems, which makes methods based on Density Functional Theory (described below) more appealing. Recent work shows that DFT provides satisfying accuracy in reproducing the geometrical features of organolanthanide complexes[35,36] and in describing reaction mechanisms.[213–215] As a result, DFT is often the best way to evaluate lanthanide molecules, as it is fast and provides reliable results for energies and electron densities.

However, DFT might be inadequate in more complicated cases, as the degenerate lanthanide 4f orbitals are not accurately described by DFT. This specificity is important in some cases,[138,216] as shall be demonstrated throughout this work as well, while in other traditional DFT methods can be used.[217]

Throughout this work, CASSCF computations were performed using the OpenMolcas software, a DKH2 Hamiltonian, and a large gaussian basis set ANO-RCC-VDZP.[218,219] The notation (X,Y) shall be used for the studied compounds homogenously and designates an active space composed of X electrons in Y orbitals.

VI.2.2. DFT.

One of the alternatives to the HF formalism relies on a simple premise: the electron density could be a better variable for solving the Schrödinger equation than the coordinates of the electron itself. This stands to reason: the electron density only depends on the three spatial coordinates, while each electron requires three spatial coordinates in wave-function theories. According to the seminal work of Hohenberg and Kohn,[220] the energy is a functional of the density. In order to solve analytically the density dependant Schrödinger equation, Kohn and Sham (KS) developed a framework that consists in replacing the electronic system in interaction with a system of independent electrons in an external field.[221] The fictitious system has the same energy as the real one, and can be written as:

$$E = T_{KS}[\rho] + V_{Ne}[\rho] + J[\rho] + E_{xc}[\rho] \quad (3)$$

where ρ is the electronic density, T_{KS} is the kinetic energy and J is the Coulomb interaction in this putative system and E_{xc} is the Exchange-Correlation potential. The last term of the equation is the only one not known analytically and precludes an exact description of the system. As a result, several expressions for this term have been developed over the years.[222]

At the centre of the first advances in the field was the hypothesis of a uniform electron gas – adequate for simple metals such as sodium. This situation is pretty far from realistic in atoms or molecules, which are usually characterized by rapidly varying densities. This gave rise to the local density approximation (LDA). The assumption is that we can write $E_{xc}[\rho]$ as the density-dependent exchange-correlation energy per particle of a uniform electron gas of density ρ(r), weighted with the probability of finding an electron at a given position in space. The LDA family of functionals gives accurate results for systems close to the aforementioned homogeneous electron gas, but is off the mark for systems where there are strong interactions between atoms.

Due to the limits of LDA, DFT was a fringe theory, mostly employed by solid-state physicists and relegated to a negligible role in computational chemistry. The situation changed significantly in the early eighties, when the first successful extensions to LDA were developed. This occurred by incorporating information about the gradient of the charge density in the density, giving the Generalised Gradient Approximation (GGA). This was done to account for the non-homogeneity of the true electron density. The GGA breakthrough led to the enhancement in the evaluation of the electronic structure and energies of molecules and to a large variety of functionals. Some of the more famous functionals include PBE[223] and BLYP.[224] Subsequently, meta-GGA DFT functionals[225,226] were developed to include the second derivative of the electron density (the Laplacian), including a dependence on the kinetic energy density.

The exact exchange contribution can be evaluated using the HF theory. The next step, taken by Becke, was to introduce semiempirical coefficients to determine the weights of the various components in the exchange-correlation term. The three empirical parameters (the 3 in the almost ubiquitous "B3LYP")[227] were chosen so that certain properties (atomisation and ionisation energies, proton affinities, total energies) of a selection of compounds were optimally reproduced. One should keep in mind that the selection bias used for the three parameters does not, *a priori*, guarantee similarly good performance in other scenarios. This class of functionals is called hybrid functionals, because they represent a hybrid between pure DFT exchange and exact Hartree-Fock exchange. In most functionals a fixed HF exchange percentage has been used, but some afford a more flexible parametrisation. A common example is the PBE0 functional, widely employed throughout this work.[228]

At long distances the HF exchange gives a good evaluation of the exchange potential. This prompted the development of long range corrected functionals,[229–231] comprising 100% HF exchange at long range while at short distances this exchange is small. More recent additions include double-hybrid functionals[232] (which combine the HF and the GGA exchange and the MP2 and the GGA correlation) and examples exist where self-interaction corrections, localized orbital scaling corrections, local hybrid functionals, real-space nondynamical correlation are implemented (summarised in Janesko's recent review).[233] A final, crucial ingredient to be added to the puzzle are the dispersion forces. This is rooted in its absence in DFT formalism. In some functionals, designed to deal with scenarios where dispersive forces are important, the dispersion parameters are built in. These forces are particularly important in bulky systems. Although several models exist,[234,235] the most frequently used is Grimme's D3 model, associated to the Becke-Johnson damping scheme.[236]

The natural assumption would be that the more sophisticated functional is likely to produce the better results. However, the performance of any given functional has to be tested and benchmarked in different scenarios to assess its suitability to compute a particular property.[237,238] Besides, the choice of the functional needs to reflect the balancing of different factors: the number of parameters inside the density functional, the computational cost (including size of the system and of the chosen basis sets), the calculated properties or the accuracy desired.

Lastly, as alluded to in the previous section, DFT computations might not be the best tool for a detailed characterisation of organolanthanide complexes. The main issue would probably most affect compounds where a very precise description of the electronic structure is required.[138,239] That said, there are numerous examples where DFT was sufficient to describe phenomena such as luminescence,[240,241] ligand conformation studies,[242] as well as the aforementioned examples of reactivity and mechanism studies.[213–215]

With that in mind, DFT calculations with lanthanides were performed all throughout this work at multiple levels of theory:

- **Geometry optimisations**: unless otherwise stated, all calculations were performed exclusively using ORCA at the PBE-D3 level of theory, with a scaled ZORA-MP Hamiltonian, in combination with segmented relativistically recontracted all-electron Gaussian TZVP basis sets and the corresponding auxiliary basis sets.[243–245] This level of theory shall henceforth be referred to as **ZORA1**. Frequencies were calculated (analytically for the precursors and numerically for the complexes containing lanthanides) to ensure these structures corresponded to energy minima on the potential energy surface.
  In the rare cases where convergence could not be achieved and in the heterometallic complexes presented in Section 3.4, equivalent SVP basis sets were used for the main group elements (C, H, O, N, Cl) – **ZORA2**.

- **Single point energy calculations**: all calculations were performed exclusively using ORCA on geometries obtained at the **ZORA1/2** level of theory, with a scaled ZORA-MP Hamiltonian, in combination with segmented relativistically recontracted all-electron Gaussian TZVP basis sets and the corresponding auxiliary basis sets. As a rule, these calculations were performed using the PBE, PBE0, TPSSh and ωB97X functionals, with the same dispersion corrections described above, but, unless otherwise stated, the orbitals and energies obtained with PBE0 will be presented as standard (**ZORA3**).

On a few specific occasions, both geometry optimisations and single point energy calculations were performed without the ZORA-MP Hamiltonian using Gaussian TVZP basis sets for the main elements. The Pd and Ln centres were described using the small-core relativistic effective core potential developed by the Stuttgart-Köln group, with their associated valence basis sets (**DFT-RECP**).

- **Transition state (TS) calculations**: calculations were performed at two, distinct levels of theory. Frequencies were calculated (analytically for all complexes when Gaussian 09 was used and numerically for the complexes containing lanthanides otherwise) to ensure these structures corresponded to energy minima. The TS was confirmed by a single imaginary frequency of high numerical value.

  Calculations were performed using the Gaussian 09 software[166] and the PBE functional. First and second row elements were described using the TZVP basis set for the C, H, N atoms. The Pd centre was described using the LanL2DZ effective core potential and its associated basis set.[246] Sm and Yb were described using the small-core relativistic effective core potential developed by the Stuttgart−Köln group,[194] associated with their optimised valence basis sets (**TS1**).
  Alternatively, calculations were performed using ORCA at the PBE-D3 level of theory, with a scaled ZORA-MP Hamiltonian, in combination with segmented relativistically recontracted all-electron Gaussian SVP basis sets for the main group elements and TZVP for the metal centres, along with the corresponding auxiliary basis sets (**TS2**).

VI.2.3. Other methods of evaluating chemical bonding.

Lastly, a series of tools based on DFT were sparsely used in order to get further information in the bonding patterns in some of the compounds that will be presented in this work.[247] The key concepts will, therefore, be briefly introduced.

One of the techniques most often employed is the Quantum Theory of Atoms in Molecules (QTAIM), introduced by Bader in the eighties.[248,249]. He argued that quantum subsystems within molecular structures are defined in real space by the boundary condition of electronic density. Since the maxima of charge distribution will be found at the nuclei (atoms), one can define a molecular structure, based on the gradient vector of the charge distribution. Specific mathematical conditions (which are not the primary focus of this work) have allowed the definition of so-called Critical Points (CPs), which can be used to define nuclei, bonds or rings.

By using the Laplacian of the electronic charge density, the physico-chemical properties of the system can be calculated and measured. For example, if the Laplacian is positive, the bonding is ionic; if the Laplacian is negative, the bonding is covalent. The numerical value of the density at the critical point can give information into the bonding itself – the stronger the value, the stronger the interaction.

Another computational tool which has received attention is the Electron Localisation Function (ELF).[250] This method evaluates the probability of finding an electron in the neighbourhood of another electron of the same spin, giving values from 0 (delocalised system) to 1 (localised system – core orbitals, lone pairs and strong bonds).[251] As is the case for QTAIM, values obtained via ELF can help quantify covalent interaction between two atoms.

In a molecule, the ELF function defines two types of "basins" – core basins, which surround the nuclei and valence basins. The valence basins are characterized by the number of atomic valence shells to which they participate. Monosynaptic basins correspond to the lone pairs of the Lewis model. For higher order basins, disynaptic correspond to two-centre bonds, trisynaptic to three-centre bonds and so forth for higher polysynaptic basins.

QTAIM and ELF have been applied (often in tandem) to RE complexes in numerous instances.[252–255]

The often large molecular structures of organolanthanide complexes often require a tailor-made approach to quantify dispersion interactions. A useful tool that can be applied is the Non-Covalent-Interaction (NCI) mapping, developed by the group of Wang.[256] This NCI method is calculated as the different points in which there are singularities for the reduced density gradient. At these points, the density is analysed using the gradient Laplacian. Three types of points can be found depending on Laplacian second component, which correspond to hydrogen bonds, repulsive forces and van der Waals interactions. This method has also found use in lanthanide chemistry.[159,257,258]

A fourth tool has been used to study the interactions between TM complexes and their ligand: Energy Decomposition Analysis (EDA). The theoretical background for this method was described in the seventies, but has found its use steadily increasing as computations became more available.[259,260]

This tool is effective and practical, as it allows quantifying a chemically intuitive description of the bond as the sum of the electrostatic interaction between two components, the Pauli repulsion and, lastly, the covalent interaction, which is issued from orbital mixing. The last contribution can be further broken down to distinguish between different types of interactions – σ, π, δ, dative interactions, back-bonding, etc. Although still tentative, the use of this method is gaining momentum in the lanthanide community.[159,261,262]

VII. Context, objectives and outline of this thesis.

The objective of this work is to synthesise heterometallic adducts comprising a divalent lanthanide fragment and a TM fragment, bridged by a RAL. The electron transfer originating from the Ln will be stored onto the RAL and the electronic contribution towards the TM fragment will be evaluated by spectroscopic and theoretical means. If possible, the reactivity of these species will be probed, with an eye towards novel applications.

Up to fall 2018, heterobimetallic complexes based on lanthanide-transition metal architectures had principally operated with neutral, symmetrical RAL, which could accommodate two metal centres.[157,159] In our laboratory, only group 10 metals in the TM^{2+} configuration had been used.[158] One of the main objectives set at the beginning was to diversify both the types of ligands that could be used and the nature of the TM fragments.

Chapter 1 will describe the syntheses of TM precursors based on two new ligand systems, with a variety of metal centres. The difficulties associated to their syntheses and reactivity will be discussed and several solutions will be proposed, with a view towards the continuity of the project. Their electronic structures will also be analysed, to assess their suitability as SET targets.

Once the procedures for the precursors are well established and repeatable, these will be put to the test in reactions where divalent organolanthanide fragments are added. This will be the focus of **Chapter 2**. The agreement between the electronic structure of any given complex, computed in

Chapter 1, and their behaviour upon electron transfer towards the RAL, will be tested and subsequently discussed.

Not all the additions of Ln fragments proceed in a predictable and controllable fashion. The formation and electronic structures of two such heterometallic complexes, isolated and described in **Chapter 2**, cannot be explained in a trivial way. An extensive experimental and theoretical study, whose objective is to help clarify the uncertainties associated with these complexes, will be pursued in **Chapter 3**. The agreement between spectroscopic evidence (when available) and theory will be assessed and the repercussions with respect to the chemical domain to which these complexes belong will be discussed.

Each of these chapters contain summaries and perspectives with respect to potential future developments on the subject at hand. An overall conclusion will close this manuscript, attempting to regroup each of the threads into a coherent global message and to delineate what might the evolution of this project portend.

References

(1) Wu, F.; Maier, J.; Yu, Y. *Chem. Soc. Rev.* 2020, *49* (5), 1569–1614. https://doi.org/10.1039/C7CS00863E.

(2) Caduff, M.; Huijbregts, M. A. J.; Althaus, H.-J.; Koehler, A.; Hellweg, S. *Environ. Sci. Technol.* 2012, *46* (9), 4725–4733. https://doi.org/10.1021/es204108n.

(3) Njiri, J. G.; Söffker, D. *Renew. Sustain. Energy Rev.* 2016, *60*, 377–393. https://doi.org/10.1016/j.rser.2016.01.110.

(4) Lee, C.; Lee, S.; Kim, G.-U.; Lee, W.; Kim, B. J. *Chem. Rev.* 2019, *119* (13), 8028–8086. https://doi.org/10.1021/acs.chemrev.9b00044.

(5) Saidi, K.; Omri, A. *Prog. Nucl. Energy* 2020, *126*, 103425. https://doi.org/10.1016/j.pnucene.2020.103425.

(6) Zhao, Y.; Pohl, O.; Bhatt, A. I.; Collis, G. E.; Mahon, P. J.; Rüther, T.; Hollenkamp, A. F. *Sustain. Chem.* 2021, *2* (1), 167–205. https://doi.org/10.3390/suschem2010011.

(7) Guillemard, L.; Kaplaneris, N.; Ackermann, L.; Johansson, M. J. *Nat. Rev. Chem.* 2021, *5* (8), 522–545. https://doi.org/10.1038/s41570-021-00300-6.

(8) Vitillo, J. G.; Smit, B.; Gagliardi, L. *Chem. Rev.* 2017, *117* (14), 9521–9523. https://doi.org/10.1021/acs.chemrev.7b00403.

(9) Mikkelsen, M.; Jørgensen, M.; Krebs, F. C. *Energy Env. Sci* 2010, *3* (1), 43–81. https://doi.org/10.1039/B912904A.

(10) Fu, H.-C.; You, F.; Li, H.-R.; He, L.-N. *Front. Chem.* 2019, *7*. https://doi.org/10.3389/fchem.2019.00525.

(11) Cook, A. K.; Schimler, S. D.; Matzger, A. J.; Sanford, M. S. *Science* 2016, *351* (6280), 1421–1424. https://doi.org/10.1126/science.aad9289.

(12) Nicolaou, K. C.; Bulger, P. G.; Sarlah, D. *Angew. Chem. Int. Ed.* 2005, *44* (29), 4442–4489. https://doi.org/10.1002/anie.200500368.

(13) Rogge, T.; Kaplaneris, N.; Chatani, N.; Kim, J.; Chang, S.; Punji, B.; Schafer, L. L.; Musaev, D. G.; Wencel-Delord, J.; Roberts, C. A.; Sarpong, R.; Wilson, Z. E.; Brimble, M. A.; Johansson, M. J.; Ackermann, L. *Nat. Rev. Methods Primer* 2021, *1* (1). https://doi.org/10.1038/s43586-021-00041-2.

(14) Jankins, T. C.; Martin-Montero, R.; Cooper, P.; Martin, R.; Engle, K. M. *J. Am. Chem. Soc.* 2021, *143* (37), 14981–14986. https://doi.org/10.1021/jacs.1c07162.

(15) Tortajada, A.; Börjesson, M.; Martin, R. *Acc. Chem. Res.* 2021, *54* (20), 3941–3952. https://doi.org/10.1021/acs.accounts.1c00480.

(16) Gandeepan, P.; Müller, T.; Zell, D.; Cera, G.; Warratz, S.; Ackermann, L. *Chem. Rev.* 2019, *119* (4), 2192–2452. https://doi.org/10.1021/acs.chemrev.8b00507.

(17) Curto, J. M.; Kozlowski, M. C. *J. Am. Chem. Soc.* 2015, *137* (1), 18–21. https://doi.org/10.1021/ja5093166.

(18) Sambiagio, C.; Schönbauer, D.; Blieck, R.; Dao-Huy, T.; Pototschnig, G.; Schaaf, P.; Wiesinger, T.; Zia, M. F.; Wencel-Delord, J.; Besset, T.; Maes, B. U. W.; Schnürch, M. *Chem. Soc. Rev.* 2018, *47* (17), 6603–6743. https://doi.org/10.1039/C8CS00201K.

(19) Chen, M. S.; White, M. C. *Science* 2007, *318* (5851), 783–787. https://doi.org/10.1126/science.1148597.

(20) Xue, X.-S.; Ji, P.; Zhou, B.; Cheng, J.-P. *Chem. Rev.* 2017, *117* (13), 8622–8648. https://doi.org/10.1021/acs.chemrev.6b00664.

(21) Gutekunst, W. R.; Baran, P. S. *Chem. Soc. Rev.* 2011, *40* (4), 1976. https://doi.org/10.1039/c0cs00182a.

(22) Vidal, C.; García-Álvarez, J.; Hernán-Gómez, A.; Kennedy, A. R.; Hevia, E. *Angew. Chem. Int. Ed.* 2014, *53* (23), 5969–5973. https://doi.org/10.1002/anie.201400889.

(23) Fairley, M.; Bole, L. J.; Mulks, F. F.; Main, L.; Kennedy, A. R.; O'Hara, C. T.; García-Alvarez, J.; Hevia, E. *Chem. Sci.* 2020, *11* (25), 6500–6509. https://doi.org/10.1039/D0SC01349H.
(24) Halpin, Y.; Pryce, M. T.; Rau, S.; Dini, D.; Vos, J. G. *Dalton Trans.* 2013, *42* (46), 16243. https://doi.org/10.1039/c3dt52319e.
(25) Melchionna, M.; Fornasiero, P. *ACS Catal.* 2020, *10* (10), 5493–5501. https://doi.org/10.1021/acscatal.0c01204.
(26) Martínez-Martínez, A. J.; Kennedy, A. R.; Mulvey, R. E.; O'Hara, C. T. *Science* 2014, *346* (6211), 834–837. https://doi.org/10.1126/science.1259662.
(27) Klatt, T.; Markiewicz, J. T.; Sämann, C.; Knochel, P. *J. Org. Chem.* 2014, *79* (10), 4253–4269. https://doi.org/10.1021/jo500297r.
(28) Magre, M.; Szewczyk, M.; Rueping, M. *Curr. Opin. Green Sustain. Chem.* 2021, *32*, 100526. https://doi.org/10.1016/j.cogsc.2021.100526.
(29) Gil-Negrete, J. M.; Hevia, E. *Chem. Sci.* 2021, *12* (6), 1982–1992. https://doi.org/10.1039/D0SC05116K.
(30) Toyao, T.; Maeno, Z.; Takakusagi, S.; Kamachi, T.; Takigawa, I.; Shimizu, K. *ACS Catal.* 2020, *10* (3), 2260–2297. https://doi.org/10.1021/acscatal.9b04186.
(31) Haxel, G. B.; Hendrick, J. B.; Orris, G. J. 2002. https://pubs.usgs.gov/fs/2002/fs087-02/ (Accessed 15th of January, 2022)
(32) Lang, P. F.; Smith, B. C. *J. Chem. Educ.* 2010, *87* (8), 875–881. https://doi.org/10.1021/ed100215q.
(33) Zhang, Q.; Hu, S.-X.; Qu, H.; Su, J.; Wang, G.; Lu, J.-B.; Chen, M.; Zhou, M.; Li, J. *Angew. Chem. Int. Ed.* 2016, *55* (24), 6896–6900. https://doi.org/10.1002/anie.201602196.
(34) Gompa, T. P.; Ramanathan, A.; Rice, N. T.; La Pierre, H. S. *Dalton Trans.* 2020, *49* (45), 15945–15987. https://doi.org/10.1039/D0DT01400A.
(35) Willauer, A. R.; Palumbo, C. T.; Scopelliti, R.; Zivkovic, I.; Douair, I.; Maron, L.; Mazzanti, M. *Angew. Chem. Int. Ed.* 2020, *59* (9), 3549–3553. https://doi.org/10.1002/anie.201914733.
(36) Willauer, A. R.; Palumbo, C. T.; Fadaei-Tirani, F.; Zivkovic, I.; Douair, I.; Maron, L.; Mazzanti, M. *J. Am. Chem. Soc.* 2020, *142* (12), 5538–5542. https://doi.org/10.1021/jacs.0c01204.
(37) Rice, N. T.; Popov, I. A.; Russo, D. R.; Bacsa, J.; Batista, E. R.; Yang, P.; Telser, J.; La Pierre, H. S. *J. Am. Chem. Soc.* 2019, *141* (33), 13222–13233. https://doi.org/10.1021/jacs.9b06622.
(38) Rice, N. T.; Popov, I. A.; Russo, D. R.; Gompa, T. P.; Ramanathan, A.; Bacsa, J.; Batista, E. R.; Yang, P.; La Pierre, H. S. *Chem. Sci.* 2020, *11* (24), 6149–6159. https://doi.org/10.1039/D0SC01414A.
(39) Fieser, M. E.; MacDonald, M. R.; Krull, B. T.; Bates, J. E.; Ziller, J. W.; Furche, F.; Evans, W. J. *J. Am. Chem. Soc.* 2015, *137* (1), 369–382. https://doi.org/10.1021/ja510831n.
(40) Nief, F. *Dalton Trans.* 2010, *39* (29), 6589. https://doi.org/10.1039/c001280g.
(41) Meyer, G. *Prog. Solid State Chem.* 1982, *14* (3), 141–219. https://doi.org/10.1016/0079-6786(82)90005-X.
(42) MacDonald, M. R.; Bates, J. E.; Ziller, J. W.; Furche, F.; Evans, W. J. *J. Am. Chem. Soc.* 2013, *135* (26), 9857–9868. https://doi.org/10.1021/ja403753j.
(43) Trinh, M. T.; Wedal, J. C.; Evans, W. J. *Dalton Trans.* 2021, *50* (40), 14384–14389. https://doi.org/10.1039/D1DT02427B.
(44) Kagan, H. B. *Tetrahedron* 2003, *59* (52), 10351–10372. https://doi.org/10.1016/j.tet.2003.09.101.
(45) Prasad, E.; Knettle, B. W.; Flowers, R. A. *Chem. - Eur. J.* 2005, *11* (10), 3105–3112. https://doi.org/10.1002/chem.200401163.
(46) Choquette, K. A.; Sadasivam, D. V.; Flowers, R. A. *J. Am. Chem. Soc.* 2010, *132* (49), 17396–17398. https://doi.org/10.1021/ja1088925.
(47) Fagin, A. A.; Balashova, T. V.; Kusyaev, D. M.; Kulikova, T. I.; Glukhova, T. A.; Makarenko, N. P.; Kurskii, Y. A.; Evans, W. J.; Bochkarev, M. N. *Polyhedron* 2006, *25* (5), 1105–1110. https://doi.org/10.1016/j.poly.2005.08.050.

(48) Szostak, M.; Procter, D. J. *Angew. Chem. Int. Ed.* 2012, *51* (37), 9238–9256. https://doi.org/10.1002/anie.201201065.
(49) Zhao, X.; Perrin, L.; Procter, D. J.; Maron, L. *Dalton Trans.* 2016, *45* (9), 3706–3710. https://doi.org/10.1039/C6DT00241B.
(50) Tilley, T. D.; Andersen, R. A.; Spencer, B.; Ruben, H.; Zalkin, A.; Templeton, D. H. *Inorg. Chem.* 1980, *19* (10), 2999–3003. https://doi.org/10.1021/ic50212a031.
(51) Evans, W. J.; Bloom, I.; Hunter, W. E.; Atwood, J. L. *J. Am. Chem. Soc.* 1981, *103* (21), 6507–6508. https://doi.org/10.1021/ja00411a046.
(52) Liu, J.-L.; Chen, Y.-C.; Tong, M.-L. *Chem. Soc. Rev.* 2018, *47* (7), 2431–2453. https://doi.org/10.1039/C7CS00266A.
(53) Day, B. M.; Guo, F.-S.; Layfield, R. A. *Acc. Chem. Res.* 2018, *51* (8), 1880–1889. https://doi.org/10.1021/acs.accounts.8b00270.
(54) Moore, E. G.; Samuel, A. P. S.; Raymond, K. N. *Acc. Chem. Res.* 2009, *42* (4), 542–552. https://doi.org/10.1021/ar800211j.
(55) Bünzli, J.-C. G.; Piguet, C. *Chem. Soc. Rev.* 2005, *34* (12), 1048. https://doi.org/10.1039/b406082m.
(56) Atwood, D. A., Ed.; EIBC books; John Wiley & Sons, Inc: Chichester, West Sussex, United Kingdom ; Hoboken, 2012.
(57) 1st ed.; Pöttgen, R., Jüstel, T., Strassert, C. A., Eds.; De Gruyter: Boston, 2020.
(58) Prasad, E.; Knettle, B. W.; Flowers, R. A. *J. Am. Chem. Soc.* 2004, *126* (22), 6891–6894. https://doi.org/10.1021/ja049161j.
(59) Binnemans, K. In *Handbook on the Physics and Chemistry of Rare Earths*; Elsevier, 2006; Vol. 36, pp 281–392. https://doi.org/10.1016/S0168-1273(06)36003-5.
(60) Broere, D. L. J.; Plessius, R.; van der Vlugt, J. I. *Chem. Soc. Rev.* 2015, *44* (19), 6886–6915. https://doi.org/10.1039/C5CS00161G.
(61) Chirila, A.; Das, B. G.; Kuijpers, P. F.; Sinha, V.; de Bruin, B. In *Non-Noble Metal Catalysis*; Klein Gebbink, R. J. M., Moret, M.-E., Eds.; Wiley-VCH Verlag GmbH & Co. KGaA: Weinheim, Germany, 2018; pp 1–31. https://doi.org/10.1002/9783527699087.ch1.
(62) Lyaskovskyy, V.; de Bruin, B. *ACS Catal.* 2012, *2* (2), 270–279. https://doi.org/10.1021/cs200660v.
(63) Taylor, J. W.; McSkimming, A.; Moret, M.-E.; Harman, W. H. *Angew. Chem. Int. Ed.* 2017, *56* (35), 10413–10417. https://doi.org/10.1002/anie.201703235.
(64) van de Watering, F. F.; Stroek, W.; Ivar van der Vlugt, J.; de Bruin, B.; Dzik, W. I.; Reek, J. N. H. *Eur. J. Inorg. Chem.* 2018, *2018* (11), 1254–1265. https://doi.org/10.1002/ejic.201701209.
(65) van der Vlugt, J. I. *Chem. - Eur. J.* 2019, *25* (11), 2651–2662. https://doi.org/10.1002/chem.201802606.
(66) Smith, A. L.; Clapp, L. A.; Hardcastle, K. I.; Soper, J. D. *Polyhedron* 2010, *29* (1), 164–169. https://doi.org/10.1016/j.poly.2009.06.046.
(67) Smith, A. L.; Hardcastle, K. I.; Soper, J. D. *J. Am. Chem. Soc.* 2010, *132* (41), 14358–14360. https://doi.org/10.1021/ja106212w.
(68) Chirik, P. J.; Wieghardt, K. *Science* 2010, *327* (5967), 794–795. https://doi.org/10.1126/science.1183281.
(69) Dzik, W. I.; van der Vlugt, J. I.; Reek, J. N. H.; de Bruin, B. *Angew. Chem. Int. Ed.* 2011, *50* (15), 3356–3358. https://doi.org/10.1002/anie.201006778.
(70) Chirik, P. J. *Inorg. Chem.* 2011, *50* (20), 9737–9740. https://doi.org/10.1021/ic201881k.
(71) Guo, L.; Li, S.; Ji, M.; Sun, W.; Liu, W.; Li, G.; Zhang, J.; Liu, Z.; Dai, S. *Organometallics* 2019, *38* (14), 2800–2806. https://doi.org/10.1021/acs.organomet.9b00325.
(72) Bianchini, C.; Giambastiani, G.; Luconi, L.; Meli, A. *Coord. Chem. Rev.* 2010, *254* (5–6), 431–455. https://doi.org/10.1016/j.ccr.2009.07.013.
(73) Römelt, C.; Weyhermüller, T.; Wieghardt, K. *Coord. Chem. Rev.* 2019, *380*, 287–317. https://doi.org/10.1016/j.ccr.2018.09.018.

(74) Panetier, J. A.; Letko, C. S.; Tilley, T. D.; Head-Gordon, M. *J. Chem. Theory Comput.* 2016, *12* (1), 223–230. https://doi.org/10.1021/acs.jctc.5b00968.
(75) Joannou, M. V.; Bezdek, M. J.; Albahily, K.; Korobkov, I.; Chirik, P. J. *Organometallics* 2018, *37* (20), 3389–3393. https://doi.org/10.1021/acs.organomet.8b00350.
(76) Lippert, C. A.; Riener, K.; Soper, J. D. *Eur. J. Inorg. Chem.* 2012, *2012* (3), 554–561. https://doi.org/10.1002/ejic.201101044.
(77) Moutet, J.; Philouze, C.; du Moulinet d'Hardemare, A.; Leconte, N.; Thomas, F. *Inorg. Chem.* 2017, *56* (11), 6380–6392. https://doi.org/10.1021/acs.inorgchem.7b00433.
(78) Ringenberg, M. R.; Kokatam, S. L.; Heiden, Z. M.; Rauchfuss, T. B. *J. Am. Chem. Soc.* 2008, *130* (3), 788–789. https://doi.org/10.1021/ja076801k.
(79) Blanchard, S.; Derat, E.; Desage-El Murr, M.; Fensterbank, L.; Malacria, M.; Mouriès-Mansuy, V. *Eur. J. Inorg. Chem.* 2012, *2012* (3), 376–389. https://doi.org/10.1002/ejic.201100985.
(80) Ma, X.; Suturina, E. A.; Rouzières, M.; Platunov, M.; Wilhelm, F.; Rogalev, A.; Clérac, R.; Dechambenoit, P. *J. Am. Chem. Soc.* 2019, *141* (19), 7721–7725. https://doi.org/10.1021/jacs.9b03044.
(81) Bagh, B.; Broere, D. L. J.; Siegler, M. A.; van der Vlugt, J. I. *Angew. Chem. Int. Ed.* 2016, *55* (29), 8381–8385. https://doi.org/10.1002/anie.201603659.
(82) Vreeken, V.; Siegler, M. A.; van der Vlugt, J. I. *Chem. - Eur. J.* 2017, *23* (23), 5585–5594. https://doi.org/10.1002/chem.201700360.
(83) Liberman-Martin, A. L.; Bergman, R. G.; Tilley, T. D. *J. Am. Chem. Soc.* 2013, *135* (26), 9612–9615. https://doi.org/10.1021/ja404339u.
(84) Liberman-Martin, A. L.; Levine, D. S.; Liu, W.; Bergman, R. G.; Tilley, T. D. *Organometallics* 2016, *35* (8), 1064–1069. https://doi.org/10.1021/acs.organomet.5b01003.
(85) Smith, A. L.; Clapp, L. A.; Hardcastle, K. I.; Soper, J. D. *Polyhedron* 2010, *29* (1), 164–169. https://doi.org/10.1016/j.poly.2009.06.046.
(86) Broere, D. L. J.; Metz, L. L.; de Bruin, B.; Reek, J. N. H.; Siegler, M. A.; van der Vlugt, J. I. *Angew. Chem. Int. Ed.* 2015, *54* (5), 1516–1520. https://doi.org/10.1002/anie.201410048.
(87) Smith, A. L.; Hardcastle, K. I.; Soper, J. D. *J. Am. Chem. Soc.* 2010, *132* (41), 14358–14360. https://doi.org/10.1021/ja106212w.
(88) Broere, D. L. J.; van Leest, N. P.; de Bruin, B.; Siegler, M. A.; van der Vlugt, J. I. *Inorg. Chem.* 2016, *55* (17), 8603–8611. https://doi.org/10.1021/acs.inorgchem.6b01192.
(89) Bagh, B.; Broere, D. L. J.; Sinha, V.; Kuijpers, P. F.; van Leest, N. P.; de Bruin, B.; Demeshko, S.; Siegler, M. A.; van der Vlugt, J. I. *J. Am. Chem. Soc.* 2017, *139* (14), 5117–5124. https://doi.org/10.1021/jacs.7b00270.
(90) Haddad, A. Z.; Cronin, S. P.; Mashuta, M. S.; Buchanan, R. M.; Grapperhaus, C. A. *Inorg. Chem.* 2017, *56* (18), 11254–11265. https://doi.org/10.1021/acs.inorgchem.7b01608.
(91) Jongbloed, L. S.; Vogt, N.; Sandleben, A.; de Bruin, B.; Klein, A.; van der Vlugt, J. I. *Eur. J. Inorg. Chem.* 2018, *2018* (20–21), 2408–2418. https://doi.org/10.1002/ejic.201800168.
(92) Arevalo, R.; Chirik, P. J. *J. Am. Chem. Soc.* 2019, *141* (23), 9106–9123. https://doi.org/10.1021/jacs.9b03337.
(93) Sikari, R.; Sinha, S.; Jash, U.; Das, S.; Brandão, P.; de Bruin, B.; Paul, N. D. *Inorg. Chem.* 2016, *55* (12), 6114–6123. https://doi.org/10.1021/acs.inorgchem.6b00646.
(94) Broere, D. L. J.; Modder, D. K.; Blokker, E.; Siegler, M. A.; van der Vlugt, J. I. *Angew. Chem. Int. Ed.* 2016, *55* (7), 2406–2410. https://doi.org/10.1002/anie.201509412.
(95) de Boer, S. Y.; Korstanje, T. J.; La Rooij, S. R.; Kox, R.; Reek, J. N. H.; van der Vlugt, J. I. *Organometallics* 2017, *36* (8), 1541–1549. https://doi.org/10.1021/acs.organomet.7b00111.
(96) Broere, D. L. J.; de Bruin, B.; Reek, J. N. H.; Lutz, M.; Dechert, S.; van der Vlugt, J. I. *J. Am. Chem. Soc.* 2014, *136* (33), 11574–11577. https://doi.org/10.1021/ja502164f.
(97) Bouwkamp, M. W.; Bowman, A. C.; Lobkovsky, E.; Chirik, P. J. *J. Am. Chem. Soc.* 2006, *128* (41), 13340–13341. https://doi.org/10.1021/ja064711u.

(98) Yang, X.; Gianetti, T. L.; Wörle, M. D.; van Leest, N. P.; de Bruin, B.; Grützmacher, H. *Chem. Sci.* 2019, *10* (4), 1117–1125. https://doi.org/10.1039/C8SC02864H.
(99) Trincado, M.; Sinha, V.; Rodriguez-Lugo, R. E.; Pribanic, B.; de Bruin, B.; Grützmacher, H. *Nat. Commun.* 2017, *8* (1). https://doi.org/10.1038/ncomms14990.
(100) Sinha, V.; Pribanic, B.; de Bruin, B.; Trincado, M.; Grützmacher, H. *Chem. - Eur. J.* 2018, *24* (21), 5513–5521. https://doi.org/10.1002/chem.201705957.
(101) Broere, D. L. J.; Plessius, R.; Tory, J.; Demeshko, S.; de Bruin, B.; Siegler, M. A.; Hartl, F.; van der Vlugt, J. I. *Chem. - Eur. J.* 2016, *22* (39), 13965–13975. https://doi.org/10.1002/chem.201601900.
(102) Rinehart, J. D.; Fang, M.; Evans, W. J.; Long, J. R. *Nat. Chem.* 2011, *3* (7), 538–542. https://doi.org/10.1038/nchem.1063.
(103) Rinehart, J. D.; Fang, M.; Evans, W. J.; Long, J. R. *J. Am. Chem. Soc.* 2011, *133* (36), 14236–14239. https://doi.org/10.1021/ja206286h.
(104) Cassani, M. C.; Duncalf, D. J.; Lappert, M. F. *J. Am. Chem. Soc.* 1998, *120* (49), 12958–12959. https://doi.org/10.1021/ja980377t.
(105) Huang, W.; Khan, S. I.; Diaconescu, P. L. *J. Am. Chem. Soc.* 2011, *133* (27), 10410–10413. https://doi.org/10.1021/ja204304f.
(106) Huang, W.; Le Roy, J. J.; Khan, S. I.; Ungur, L.; Murugesu, M.; Diaconescu, P. L. *Inorg. Chem.* 2015, *54* (5), 2374–2382. https://doi.org/10.1021/ic5029788.
(107) Guo, H.; Zhou, H.; Yao, Y.; Zhang, Y.; Shen, Q. *Dalton Trans.* 2007, No. 32, 3555. https://doi.org/10.1039/b705353c.
(108) Duan, L.; Jia, Y.-B.; Li, X.-G.; Li, Y.-M.; Hu, H.; Li, J.; Cui, C. *Eur. J. Inorg. Chem.* 2017, *2017* (15), 2231–2235. https://doi.org/10.1002/ejic.201601457.
(109) Trifonov, A. A.; Gudilenkov, I. D.; Fukin, G. K.; Cherkasov, A. V.; Larionova, J. *Organometallics* 2009, *28* (12), 3421–3425. https://doi.org/10.1021/om9001318.
(110) Lopez, N.; Zhao, H.; Prosvirin, A. V.; Wernsdorfer, W.; Dunbar, K. R. *Dalton Trans.* 2010, *39* (18), 4341. https://doi.org/10.1039/b922219g.
(111) Ballesteros-Rivas, M.; Zhao, H.; Prosvirin, A.; Reinheimer, E. W.; Toscano, R. A.; Valdés-Martínez, J.; Dunbar, K. R. *Angew. Chem. Int. Ed.* 2012, *51* (21), 5124–5128. https://doi.org/10.1002/anie.201107938.
(112) Isago, H.; Shimoda, M. *Chem. Lett.* 1992, No. 1, 147–150. https://doi.org/10.1246/cl.1992.147.
(113) Trojan, K. L.; Kendall, J. L.; Kepler, K. D.; Hatfield, W. E. *Inorganica Chim. Acta* 1992, *198–200*, 795–803. https://doi.org/10.1016/S0020-1693(00)92425-3.
(114) Morgan, I. S.; Mansikkamäki, A.; Rouzières, M.; Clérac, R.; Tuononen, H. M. *Dalton Trans.* 2017, *46* (38), 12790–12793. https://doi.org/10.1039/C7DT02766D.
(115) Tian, L.; Sun, Y.-Q.; Na, B.; Cheng, P. *Eur. J. Inorg. Chem.* 2013, *2013* (24), 4329–4335. https://doi.org/10.1002/ejic.201300524.
(116) Xiao, Z.-X.; Miao, H.; Shao, D.; Wei, H.-Y.; Zhang, Y.-Q.; Wang, X.-Y. *Chem. Commun.* 2018, *54* (70), 9726–9729. https://doi.org/10.1039/C8CC04739A.
(117) Hay, M. A.; Boskovic, C. *Chem. – Eur. J.* 2021, *27* (11), 3608–3637. https://doi.org/10.1002/chem.202003761.
(118) Trifonov, A. A.; Borovkov, I. A.; Fedorova, E. A.; Fukin, G. K.; Larionova, J.; Druzhkov, N. O.; Cherkasov, V. K. *Chem. - Eur. J.* 2007, *13* (17), 4981–4987. https://doi.org/10.1002/chem.200601481.
(119) Trifonov, A. A.; Shestakov, B. G.; Lyssenko, K. A.; Larionova, J.; Fukin, G. K.; Cherkasov, A. V. *Organometallics* 2011, *30* (18), 4882–4889. https://doi.org/10.1021/om200429h.
(120) Bogart, J. A.; Lewis, A. J.; Medling, S. A.; Piro, N. A.; Carroll, P. J.; Booth, C. H.; Schelter, E. J. *Inorg. Chem.* 2013, *52* (19), 11600–11607. https://doi.org/10.1021/ic401974t.
(121) Kim, J. E.; Carroll, P. J.; Schelter, E. J. *Chem. Commun.* 2015, *51* (81), 15047–15050. https://doi.org/10.1039/C5CC06052D.
(122) Kim, J. E.; Bogart, J. A.; Carroll, P. J.; Schelter, E. J. *Inorg. Chem.* 2016, *55* (2), 775–784. https://doi.org/10.1021/acs.inorgchem.5b02236.

(123) Bochkarev, M. N.; Fagin, A. A.; Druzhkov, N. O.; Cherkasov, V. K.; Katkova, M. A.; Fukin, G. K.; Kurskii, Y. A. *J. Organomet. Chem.* 2010, *695* (25–26), 2774–2780. https://doi.org/10.1016/j.jorganchem.2010.06.024.
(124) Klementyeva, S. V.; Lukoyanov, A. N.; Afonin, M. Yu.; Mörtel, M.; Smolentsev, A. I.; Abramov, P. A.; Starikova, A. A.; Khusniyarov, M. M.; Konchenko, S. N. *Dalton Trans.* 2019, *48* (10), 3338–3348. https://doi.org/10.1039/C8DT04849E.
(125) Fedushkin, I. L.; Maslova, O. V.; Baranov, E. V.; Shavyrin, A. S. *Inorg. Chem.* 2009, *48* (6), 2355–2357. https://doi.org/10.1021/ic900022s.
(126) Fedushkin, I. L.; Skatova, A. A.; Yambulatov, D. S.; Cherkasov, A. V.; Demeshko, S. V. *Russ. Chem. Bull.* 2015, *64* (1), 38–43. https://doi.org/10.1007/s11172-015-0817-6.
(127) Skatova, A. A.; Yambulatov, D. S.; Fedyushkin, I. L.; Baranov, E. V. *Russ. J. Coord. Chem.* 2018, *44* (6), 400–409. https://doi.org/10.1134/S1070328418060064.
(128) Fedushkin, I. L.; Maslova, O. V.; Morozov, A. G.; Dechert, S.; Demeshko, S.; Meyer, F. *Angew. Chem. Int. Ed.* 2012, *51* (42), 10584–10587. https://doi.org/10.1002/anie.201204452.
(129) Herzog, S.; Schuster, R. *Z. Für Chem.* 1967, *7* (1), 26–27. https://doi.org/10.1002/zfch.19670070125.
(130) Herzog, S.; Gustav, K. *Z. Für Anorg. Allg. Chem.* 1966, *346* (3–4), 162–165. https://doi.org/10.1002/zaac.19663460307.
(131) Bochkarev, M. N.; Petrov, B. I.; Fedyushkin, I. L.; Petrovskaya, T. V.; Nevodchikov, V. I.; Patrikeeva, N. B.; Zakharov, L. N.; Strucchkov, Yu. T. *Russ. Chem. Bull.* 1997, *46* (2), 371–373. https://doi.org/10.1007/BF02494383.
(132) Fedushkin, I. L.; Petrovskaya, T. V.; Girgsdies, F.; Nevodchikov, V. I.; Weimann, R.; Schumann, H.; Bochkarev, M. N. *Russ. Chem. Bull.* 2000, *49* (11), 1869–1876. https://doi.org/10.1007/BF02494926.
(133) Walter, M. D.; Schultz, M.; Andersen, R. A. *New J. Chem.* 2006, *30* (2), 238. https://doi.org/10.1039/b512865j.
(134) Halbach, R. L.; Nocton, G.; Amaro-Estrada, J. I.; Maron, L.; Booth, C. H.; Andersen, R. A. *Inorg. Chem.* 2019, *58* (18), 12083–12098. https://doi.org/10.1021/acs.inorgchem.9b01393.
(135) Schultz, M.; Boncella, J. M.; Berg, D. J.; Tilley, T. D.; Andersen, R. A. *Organometallics* 2002, *21* (3), 460–472. https://doi.org/10.1021/om010661k.
(136) Ruiz, D.; Yoo, J.; Hendrickson, D. N.; Guzei, I. A.; Rheingold, A. L. *Chem. Commun.* 1998, No. 19, 2089–2090. https://doi.org/10.1039/a802803f.
(137) Roux, C.; Adams, D. M.; Itié, J. P.; Polian, A.; Hendrickson, D. N.; Verdaguer, M. *Inorg. Chem.* 1996, *35* (10), 2846–2852. https://doi.org/10.1021/ic951080o.
(138) Booth, C. H.; Walter, M. D.; Kazhdan, D.; Hu, Y.-J.; Lukens, W. W.; Bauer, E. D.; Maron, L.; Eisenstein, O.; Andersen, R. A. *J. Am. Chem. Soc.* 2009, *131* (18), 6480–6491. https://doi.org/10.1021/ja809624w.
(139) Tricoire, M.; Mahieu, N.; Simler, T.; Nocton, G. *Chem. – Eur. J.* 2021. https://doi.org/10.1002/chem.202004735.
(140) Saleh, L. M. A.; Birjkumar, K. H.; Protchenko, A. V.; Schwarz, A. D.; Aldridge, S.; Jones, C.; Kaltsoyannis, N.; Mountford, P. *J. Am. Chem. Soc.* 2011, *133* (11), 3836–3839. https://doi.org/10.1021/ja2007092.
(141) Minasian, S. G.; Krinsky, J. L.; Arnold, J. *Chem. - Eur. J.* 2011, *17* (44), 12234–12245. https://doi.org/10.1002/chem.201101447.
(142) Denning, R. G.; Harmer, J.; Green, J. C.; Irwin, M. *J. Am. Chem. Soc.* 2011, *133* (50), 20644–20660. https://doi.org/10.1021/ja209311g.
(143) Labouille, S.; Clavaguéra, C.; Nief, F. *Organometallics* 2013, *32* (5), 1265–1271. https://doi.org/10.1021/om301018u.
(144) Neumann, C. S.; Fulde, P. *Z. Für Phys. B Condens. Matter* 1989, *74* (3), 277–278. https://doi.org/10.1007/BF01307872.

(145) Booth, C. H.; Walter, M. D.; Daniel, M.; Lukens, W. W.; Andersen, R. A. *Phys. Rev. Lett.* 2005, *95* (26). https://doi.org/10.1103/PhysRevLett.95.267202.
(146) Lukens, W. W.; Magnani, N.; Booth, C. H. *Inorg. Chem.* 2012, *51* (19), 10105–10110. https://doi.org/10.1021/ic300037q.
(147) Berg, D. J.; Boncella, J. M.; Andersen, R. A. *Organometallics* 2002, *21* (22), 4622–4631. https://doi.org/10.1021/om020477e.
(148) Kuehl, C. J.; Da Re, R. E.; Scott, B. L.; Morris, D. E.; John, K. D. *Chem Commun* 2003, No. 18, 2336–2337. https://doi.org/10.1039/B306484K.
(149) Carlson, C. N.; Kuehl, C. J.; Da Re, R. E.; Veauthier, J. M.; Schelter, E. J.; Milligan, A. E.; Scott, B. L.; Bauer, E. D.; Thompson, J. D.; Morris, D. E.; John, K. D. *J. Am. Chem. Soc.* 2006, *128* (22), 7230–7241. https://doi.org/10.1021/ja058667e.
(150) Carlson, C. N.; Kuehl, C. J.; Ogallo, L.; Shultz, D. A.; Thompson, J. D.; Kirk, M. L.; Martin, R. L.; John, K. D.; Morris, D. E. *Organometallics* 2007, *26* (17), 4234–4242. https://doi.org/10.1021/om061157o.
(151) Nocton, G.; Lukens, W. W.; Booth, C. H.; Rozenel, S. S.; Medling, S. A.; Maron, L.; Andersen, R. A. *J. Am. Chem. Soc.* 2014, *136* (24), 8626–8641. https://doi.org/10.1021/ja502271q.
(152) Nocton, G.; Booth, C. H.; Maron, L.; Ricard, L.; Andersen, R. A. *Organometallics* 2014, *33* (23), 6819–6829. https://doi.org/10.1021/om500843z.
(153) Demir, S.; Zadrozny, J. M.; Nippe, M.; Long, J. R. *J. Am. Chem. Soc.* 2012, *134* (45), 18546–18549. https://doi.org/10.1021/ja308945d.
(154) Gould, C. A.; Mu, E.; Vieru, V.; Darago, L. E.; Chakarawet, K.; Gonzalez, M. I.; Demir, S.; Long, J. R. *J. Am. Chem. Soc.* 2020, *142* (50), 21197–21209. https://doi.org/10.1021/jacs.0c10612.
(155) Demir, S.; Nippe, M.; Gonzalez, M. I.; Long, J. R. *Chem Sci* 2014, *5* (12), 4701–4711. https://doi.org/10.1039/C4SC02154A.
(156) Gould, C. A.; Darago, L. E.; Gonzalez, M. I.; Demir, S.; Long, J. R. *Angew. Chem. Int. Ed.* 2017, *56* (34), 10103–10107. https://doi.org/10.1002/anie.201612271.
(157) Goudy, V.; Jaoul, A.; Cordier, M.; Clavaguéra, C.; Nocton, G. *J. Am. Chem. Soc.* 2017, *139* (31), 10633–10636. https://doi.org/10.1021/jacs.7b05634.
(158) Wang; Moutet; Tricoire; Cordier; Nocton. *Inorganics* 2019, *7* (5), 58. https://doi.org/10.3390/inorganics7050058.
(159) Jaoul, A.; Tricoire, M.; Moutet, J.; Cordier, M.; Clavaguéra, C.; Nocton, G. *Chem. Squared* 2019, *3*. https://doi.org/10.28954/2019.csq.06.001.
(160) Hickson, J. R.; Horsewill, S. J.; Bamforth, C.; McGuire, J.; Wilson, C.; Sproules, S.; Farnaby, J. H. *Dalton Trans.* 2018, *47* (31), 10692–10701. https://doi.org/10.1039/C8DT01262H.
(161) Hickson, J. R.; Horsewill, S. J.; McGuire, J.; Wilson, C.; Sproules, S.; Farnaby, J. H. *Chem. Commun.* 2018, *54* (80), 11284–11287. https://doi.org/10.1039/C8CC05591B.
(162) McGuire, J.; Wilson, B.; McAllister, J.; Miras, H. N.; Wilson, C.; Sproules, S.; Farnaby, J. H. *Dalton Trans.* 2019, *48* (17), 5491–5495. https://doi.org/10.1039/C9DT00688E.
(163) Lotrich, V.; Flocke, N.; Ponton, M.; Yau, A. D.; Perera, A.; Deumens, E.; Bartlett, R. J. *J. Chem. Phys.* 2008, *128* (19), 194104. https://doi.org/10.1063/1.2920482.
(164) Saue, T.; Bast, R.; Gomes, A. S. P.; Jensen, H. J. Aa.; Visscher, L.; Aucar, I. A.; Di Remigio, R.; Dyall, K. G.; Eliav, E.; Fasshauer, E.; Fleig, T.; Halbert, L.; Hedegård, E. D.; Helmich-Paris, B.; Iliaš, M.; Jacob, C. R.; Knecht, S.; Laerdahl, J. K.; Vidal, M. L.; Nayak, M. K.; Olejniczak, M.; Olsen, J. M. H.; Pernpointner, M.; Senjean, B.; Shee, A.; Sunaga, A.; van Stralen, J. N. P. *J. Chem. Phys.* 2020, *152* (20), 204104. https://doi.org/10.1063/5.0004844.
(165) Guest, M. F.; Bush, I. J.; Van Dam, H. J. J.; Sherwood, P.; Thomas, J. M. H.; Van Lenthe, J. H.; Havenith, R. W. A.; Kendrick, J. *Mol. Phys.* 2005, *103* (6–8), 719–747. https://doi.org/10.1080/00268970512331340592.
(166) Frisch, M. J *et al*. Gaussian, Inc., Wallingford CT, 2013.
(167) Aquilante, F.; Autschbach, J.; Carlson, R. K.; Chibotaru, L. F.; Delcey, M. G.; De Vico, L.; Fdez. Galván, I.; Ferré, N.; Frutos, L. M.; Gagliardi, L.; Garavelli, M.; Giussani, A.; Hoyer, C. E.; Li Manni, G.;

Lischka, H.; Ma, D.; Malmqvist, P. Å.; Müller, T.; Nenov, A.; Olivucci, M.; Pedersen, T. B.; Peng, D.; Plasser, F.; Pritchard, B.; Reiher, M.; Rivalta, I.; Schapiro, I.; Segarra-Martí, J.; Stenrup, M.; Truhlar, D. G.; Ungur, L.; Valentini, A.; Vancoillie, S.; Veryazov, V.; Vysotskiy, V. P.; Weingart, O.; Zapata, F.; Lindh, R. *J. Comput. Chem.* 2016, *37* (5), 506–541. https://doi.org/10.1002/jcc.24221.
(168) Werner, H.-J.; Knowles, P. J.; Manby, F. R.; Black, J. A.; Doll, K.; Heßelmann, A.; Kats, D.; Köhn, A.; Korona, T.; Kreplin, D. A.; Ma, Q.; Miller, T. F.; Mitrushchenkov, A.; Peterson, K. A.; Polyak, I.; Rauhut, G.; Sibaev, M. *J. Chem. Phys.* 2020, *152* (14), 144107. https://doi.org/10.1063/5.0005081.
(169) Neese, F. *WIREs Comput. Mol. Sci.* 2012, *2* (1), 73–78. https://doi.org/10.1002/wcms.81.
(170) Balasubramani, S. G.; Chen, G. P.; Coriani, S.; Diedenhofen, M.; Frank, M. S.; Franzke, Y. J.; Furche, F.; Grotjahn, R.; Harding, M. E.; Hättig, C.; Hellweg, A.; Helmich-Paris, B.; Holzer, C.; Huniar, U.; Kaupp, M.; Marefat Khah, A.; Karbalaei Khani, S.; Müller, T.; Mack, F.; Nguyen, B. D.; Parker, S. M.; Perlt, E.; Rappoport, D.; Reiter, K.; Roy, S.; Rückert, M.; Schmitz, G.; Sierka, M.; Tapavicza, E.; Tew, D. P.; van Wüllen, C.; Voora, V. K.; Weigend, F.; Wodyński, A.; Yu, J. M. *J. Chem. Phys.* 2020, *152* (18), 184107. https://doi.org/10.1063/5.0004635.
(171) Hafner, J. *J. Comput. Chem.* 2008, *29* (13), 2044–2078. https://doi.org/10.1002/jcc.21057.
(172) Toli, I.; Zou, S. *Chem. Phys. Lett. X* 2019, *2*, 100021. https://doi.org/10.1016/j.cpletx.2019.100021.
(173) Born, M.; Oppenheimer, R. *Ann. Phys.* 1927, *389* (20), 457–484. https://doi.org/10.1002/andp.19273892002.
(174) Bubin, S.; Pavanello, M.; Tung, W.-C.; Sharkey, K. L.; Adamowicz, L. *Chem. Rev.* 2013, *113* (1), 36–79. https://doi.org/10.1021/cr200419d.
(175) Mátyus, E. *Mol. Phys.* 2019, *117* (5), 590–609. https://doi.org/10.1080/00268976.2018.1530461.
(176) In *Multiconfigurational Quantum Chemistry*; John Wiley & Sons, Inc.: Hoboken, NJ, USA, 2016; pp 23–41. https://doi.org/10.1002/9781119126171.ch3.
(177) Pyykko, P. *Chem. Rev.* 1988, *88* (3), 563–594. https://doi.org/10.1021/cr00085a006.
(178) Kerridge, A. In *Computational Methods in Lanthanide and Actinide Chemistry*; Dolg, M., Ed.; John Wiley & Sons Ltd: Chichester, UK, 2015; pp 121–146. https://doi.org/10.1002/9781118688304.ch5.
(179) van Lenthe, E.; Baerends, E. J.; Snijders, J. G. *J. Chem. Phys.* 1994, *101* (11), 9783–9792. https://doi.org/10.1063/1.467943.
(180) Filatov, M. *Chem. Phys. Lett.* 2002, *365* (3–4), 222–231. https://doi.org/10.1016/S0009-2614(02)01446-X.
(181) Filatov, M.; Cremer, D. *J. Chem. Phys.* 2003, *119* (22), 11526–11540. https://doi.org/10.1063/1.1623473.
(182) Filatov, M.; Cremer, D. *J. Chem. Phys.* 2005, *122* (4), 044104. https://doi.org/10.1063/1.1839856.
(183) van Wüllen, C. *J. Chem. Phys.* 1998, *109* (2), 392–399. https://doi.org/10.1063/1.476576.
(184) Reiher, M. *Theor. Chem. Acc.* 2006, *116* (1–3), 241–252. https://doi.org/10.1007/s00214-005-0003-2.
(185) Koch, H.; Sánchez de Merás, A.; Pedersen, T. B. *J. Chem. Phys.* 2003, *118* (21), 9481–9484. https://doi.org/10.1063/1.1578621.
(186) Aquilante, F.; Lindh, R.; Bondo Pedersen, T. *J. Chem. Phys.* 2007, *127* (11), 114107. https://doi.org/10.1063/1.2777146.
(187) Mintmire, J. W.; Dunlap, B. I. *Phys. Rev. A* 1982, *25* (1), 88–95. https://doi.org/10.1103/PhysRevA.25.88.
(188) Weigend, F.; Häser, M.; Patzelt, H.; Ahlrichs, R. *Chem. Phys. Lett.* 1998, *294* (1–3), 143–152. https://doi.org/10.1016/S0009-2614(98)00862-8.
(189) Neese, F.; Wennmohs, F.; Hansen, A.; Becker, U. *Chem. Phys.* 2009, *356* (1–3), 98–109. https://doi.org/10.1016/j.chemphys.2008.10.036.

(190) Merlot, P.; Kjaergaard, T.; Helgaker, T.; Lindh, R.; Aquilante, F.; Reine, S.; Pedersen, T. B. *J. Comput. Chem.* 2013, *34* (17), 1486–1496. https://doi.org/10.1002/jcc.23284.
(191) Rebolini, E.; Izsák, R.; Reine, S. S.; Helgaker, T.; Pedersen, T. B. *J. Chem. Theory Comput.* 2016, *12* (8), 3514–3522. https://doi.org/10.1021/acs.jctc.6b00074.
(192) Guidon, M.; Hutter, J.; VandeVondele, J. *J. Chem. Theory Comput.* 2010, *6* (8), 2348–2364. https://doi.org/10.1021/ct1002225.
(193) Dolg, M.; Cao, X. *Chem. Rev.* 2012, *112* (1), 403–480. https://doi.org/10.1021/cr2001383.
(194) Dolg, M.; Stoll, H.; Preuss, H. *J. Chem. Phys.* 1989, *90* (3), 1730–1734. https://doi.org/10.1063/1.456066.
(195) Dolg, M.; Stoll, H.; Savin, A.; Preuss, H. *Theor. Chim. Acta* 1989, *75* (3), 173–194. https://doi.org/10.1007/BF00528565.
(196) Kaltsoyannis, N. *Inorg. Chem.* 2013, *52* (7), 3407–3413. https://doi.org/10.1021/ic3006025.
(197) In *Multiconfigurational Quantum Chemistry*; John Wiley & Sons, Inc.: Hoboken, NJ, USA, 2016; pp 43–58. https://doi.org/10.1002/9781119126171.ch4.
(198) Chan, G. K.-L.; Dorando, J. J.; Ghosh, D.; Hachmann, J.; Neuscamman, E.; Wang, H.; Yanai, T. In *Frontiers in Quantum Systems in Chemistry and Physics*; Wilson, S., Grout, P. J., Maruani, J., Delgado-Barrio, G., Piecuch, P., Eds.; Springer Netherlands: Dordrecht, 2008; Vol. 18, pp 49–65. https://doi.org/10.1007/978-1-4020-8707-3_4.
(199) Lee, T. J.; Rendell, A. P.; Taylor, P. R. *J. Phys. Chem.* 1990, *94* (14), 5463–5468. https://doi.org/10.1021/j100377a008.
(200) Ma, D.; Li Manni, G.; Gagliardi, L. *J. Chem. Phys.* 2011, *135* (4), 044128. https://doi.org/10.1063/1.3611401.
(201) Møller, Chr.; Plesset, M. S. *Phys. Rev.* 1934, *46* (7), 618–622. https://doi.org/10.1103/PhysRev.46.618.
(202) Cremer, D. *Wiley Interdiscip. Rev. Comput. Mol. Sci.* 2011, *1* (4), 509–530. https://doi.org/10.1002/wcms.58.
(203) Noga, J.; Urban, M. *Theor. Chim. Acta* 1988, *73* (4), 291–306. https://doi.org/10.1007/BF00527416.
(204) Hättig, C.; Weigend, F. *J. Chem. Phys.* 2000, *113* (13), 5154. https://doi.org/10.1063/1.1290013.
(205) Angeli, C.; Cimiraglia, R.; Evangelisti, S.; Leininger, T.; Malrieu, J.-P. *J. Chem. Phys.* 2001, *114* (23), 10252–10264. https://doi.org/10.1063/1.1361246.
(206) Roos, B. O.; Taylor, P. R.; Sigbahn, P. E. M. *Chem. Phys.* 1980, *48* (2), 157–173. https://doi.org/10.1016/0301-0104(80)80045-0.
(207) Piela, L. In *Ideas of Quantum Chemistry*; Elsevier, 2014; pp 577–662. https://doi.org/10.1016/B978-0-444-59436-5.00010-6.
(208) Roos, B. O.; Lindh, R.; Malmqvist, P. Å.; Veryazov, V.; Widmark, P.-O. John Wiley & Sons, Inc.: Hoboken, NJ, USA, 2016. https://doi.org/10.1002/9781119126171.
(209) Booth, C. H.; Kazhdan, D.; Werkema, E. L.; Walter, M. D.; Lukens, W. W.; Bauer, E. D.; Hu, Y.-J.; Maron, L.; Eisenstein, O.; Head-Gordon, M.; Andersen, R. A. *J. Am. Chem. Soc.* 2010, *132* (49), 17537–17549. https://doi.org/10.1021/ja106902s.
(210) Pointillart, F.; Cador, O.; Le Guennic, B.; Ouahab, L. *Coord. Chem. Rev.* 2017, *346*, 150–175. https://doi.org/10.1016/j.ccr.2016.12.017.
(211) Atzori, M.; Dhbaibi, K.; Douib, H.; Grasser, M.; Dorcet, V.; Breslavetz, I.; Paillot, K.; Cador, O.; Rikken, G. L. J. A.; Le Guennic, B.; Crassous, J.; Pointillart, F.; Train, C. *J. Am. Chem. Soc.* 2021, *143* (7), 2671–2675. https://doi.org/10.1021/jacs.0c13180.
(212) Moutet, J.; Schleinitz, J.; La Droitte, L.; Tricoire, M.; Pointillart, F.; Gendron, F.; Simler, T.; Clavaguéra, C.; Le Guennic, B.; Cador, O.; Nocton, G. *Angew. Chem.* 2021, *133* (11), 6107–6111. https://doi.org/10.1002/ange.202015428.
(213) Shi, X.; Deng, P.; Rajeshkumar, T.; Zhao, L.; Maron, L.; Cheng, J. *Chem. Commun.* 2021, *57* (78), 10047–10050. https://doi.org/10.1039/D1CC04488E.

(214) Jaoul, A.; Yang, Y.; Casaretto, N.; Clavaguéra, C.; Maron, L.; Nocton, G. *Chem. Commun.* 2020, *56* (79), 11875–11878. https://doi.org/10.1039/D0CC05164K.
(215) Toniolo, D.; Willauer, A. R.; Andrez, J.; Yang, Y.; Scopelliti, R.; Maron, L.; Mazzanti, M. *Chem. – Eur. J.* 2019, *25* (33), 7831–7834. https://doi.org/10.1002/chem.201901321.
(216) Trifonov, A. A.; Mahrova, T. V.; Luconi, L.; Giambastiani, G.; Lyubov, D. M.; Cherkasov, A. V.; Sorace, L.; Louyriac, E.; Maron, L.; Lyssenko, K. A. *Dalton Trans.* 2018, *47* (5), 1566–1576. https://doi.org/10.1039/C7DT04299J.
(217) Goudy, V.; Xémard, M.; Karleskind, S.; Cordier, M.; Alvarez Lamsfus, C.; Maron, L.; Nocton, G. *Inorganics* 2018, *6* (3), 82. https://doi.org/10.3390/inorganics6030082.
(218) Roos, B. O.; Lindh, R.; Malmqvist, P.-Å.; Veryazov, V.; Widmark, P.-O.; Borin, A. C. *J. Phys. Chem. A* 2008, *112* (45), 11431–11435. https://doi.org/10.1021/jp803213j.
(219) Roos, B. O.; Lindh, R.; Malmqvist, P.-Å.; Veryazov, V.; Widmark, P.-O. *J. Phys. Chem. A* 2004, *108* (15), 2851–2858. https://doi.org/10.1021/jp031064+.
(220) Hohenberg, P.; Kohn, W. *Phys. Rev.* 1964, *136* (3B), B864–B871. https://doi.org/10.1103/PhysRev.136.B864.
(221) Kohn, W.; Sham, L. J. *Phys. Rev.* 1965, *140* (4A), A1133–A1138. https://doi.org/10.1103/PhysRev.140.A1133.
(222) Koch, W.; Holthausen, M. C. 1st ed.; Wiley, 2001. https://doi.org/10.1002/3527600043.
(223) Perdew, J. P.; Ernzerhof, M.; Burke, K. *J. Chem. Phys.* 1996, *105* (22), 9982–9985. https://doi.org/10.1063/1.472933.
(224) Lee, C.; Yang, W.; Parr, R. G. *Phys. Rev. B* 1988, *37* (2), 785–789. https://doi.org/10.1103/PhysRevB.37.785.
(225) Tao, J.; Perdew, J. P.; Staroverov, V. N.; Scuseria, G. E. *Phys. Rev. Lett.* 2003, *91* (14). https://doi.org/10.1103/PhysRevLett.91.146401.
(226) Zhao, Y.; Truhlar, D. G. *J. Chem. Phys.* 2006, *125* (19), 194101. https://doi.org/10.1063/1.2370993.
(227) Becke, A. D. *J. Chem. Phys.* 1993, *98* (7), 5648–5652. https://doi.org/10.1063/1.464913.
(228) Adamo, C.; Barone, V. *J. Chem. Phys.* 1999, *110* (13), 6158–6170. https://doi.org/10.1063/1.478522.
(229) Tsuneda, T.; Hirao, K. *Wiley Interdiscip. Rev. Comput. Mol. Sci.* 2014, *4* (4), 375–390. https://doi.org/10.1002/wcms.1178.
(230) Chai, J.-D.; Head-Gordon, M. *J. Chem. Phys.* 2008, *128* (8), 084106. https://doi.org/10.1063/1.2834918.
(231) Lin, Y.-S.; Li, G.-D.; Mao, S.-P.; Chai, J.-D. *J. Chem. Theory Comput.* 2013, *9* (1), 263–272. https://doi.org/10.1021/ct300715s.
(232) Goerigk, L.; Grimme, S. *Wiley Interdiscip. Rev. Comput. Mol. Sci.* 2014, *4* (6), 576–600. https://doi.org/10.1002/wcms.1193.
(233) Janesko, B. G. *Chem. Soc. Rev.* 2021, *50* (15), 8470–8495. https://doi.org/10.1039/D0CS01074J.
(234) Zhao, Y.; Truhlar, D. G. *Acc. Chem. Res.* 2008, *41* (2), 157–167. https://doi.org/10.1021/ar700111a.
(235) Mardirossian, N.; Head-Gordon, M. *J. Chem. Phys.* 2016, *144* (21), 214110. https://doi.org/10.1063/1.4952647.
(236) Grimme, S.; Ehrlich, S.; Goerigk, L. *J. Comput. Chem.* 2011, *32* (7), 1456–1465. https://doi.org/10.1002/jcc.21759.
(237) Jaoul, A.; Nocton, G.; Clavaguéra, C. *ChemPhysChem* 2017, *18* (19), 2688–2696. https://doi.org/10.1002/cphc.201700629.
(238) Liu, F.; Kulik, H. J. *J. Chem. Theory Comput.* 2020, *16* (1), 264–277. https://doi.org/10.1021/acs.jctc.9b00842.
(239) Janicki, R.; Kędziorski, A.; Mondry, A. *Phys. Chem. Chem. Phys.* 2016, *18* (40), 27808–27817. https://doi.org/10.1039/C6CP05284C.

(240) Wang, C.-X.; Li, Y.; Li, Z.-F.; Liu, Z.-J.; Valeev, E. F.; Moskaleva, L. V. *J. Phys. Chem. A* 2020, *124* (1), 82–89. https://doi.org/10.1021/acs.jpca.9b11089.
(241) Qiao, Y.; Sergentu, D.-C.; Yin, H.; Zabula, A. V.; Cheisson, T.; McSkimming, A.; Manor, B. C.; Carroll, P. J.; Anna, J. M.; Autschbach, J.; Schelter, E. J. *J. Am. Chem. Soc.* 2018, *140* (13), 4588–4595. https://doi.org/10.1021/jacs.7b13339.
(242) Hu, A.; MacMillan, S. N.; Wilson, J. J. *J. Am. Chem. Soc.* 2020, *142* (31), 13500–13506. https://doi.org/10.1021/jacs.0c05217.
(243) Pantazis, D. A.; Neese, F. *J. Chem. Theory Comput.* 2009, *5* (9), 2229–2238. https://doi.org/10.1021/ct900090f.
(244) Pantazis, D. A.; Neese, F. *Wiley Interdiscip. Rev. Comput. Mol. Sci.* 2014, *4* (4), 363–374. https://doi.org/10.1002/wcms.1177.
(245) Pantazis, D. A.; Chen, X.-Y.; Landis, C. R.; Neese, F. *J. Chem. Theory Comput.* 2008, *4* (6), 908–919. https://doi.org/10.1021/ct800047t.
(246) Hay, P. J.; Wadt, W. R. *J. Chem. Phys.* 1985, *82* (1), 270–283. https://doi.org/10.1063/1.448799.
(247) Frenking, G., Shaik, S., Eds.; Wiley-VCH Verlag GmbH & Co. KGaA: Weinheim, Germany, 2014. https://doi.org/10.1002/9783527664658.
(248) Bader, R. F. W. *Acc. Chem. Res.* 1985, *18* (1), 9–15. https://doi.org/10.1021/ar00109a003.
(249) Bader, R. F. W. *Chem. Rev.* 1991, *91* (5), 893–928. https://doi.org/10.1021/cr00005a013.
(250) Becke, A. D.; Edgecombe, K. E. *J. Chem. Phys.* 1990, *92* (9), 5397–5403. https://doi.org/10.1063/1.458517.
(251) Grin, Y.; Savin, A.; Silvi, B. In *The Chemical Bond*; Frenking, G., Shaik, S., Eds.; Wiley-VCH Verlag GmbH & Co. KGaA: Weinheim, Germany, 2014; pp 345–382. https://doi.org/10.1002/9783527664696.ch10.
(252) Kerridge, A. *Chem. Commun.* 2017, *53* (50), 6685–6695. https://doi.org/10.1039/C7CC00962C.
(253) Sadhu, B.; Mishra, V. *Dalton Trans.* 2018, *47* (46), 16603–16615. https://doi.org/10.1039/C8DT03262A.
(254) Wellington, J. P. W.; Kerridge, A.; Kaltsoyannis, N. *Polyhedron* 2016, *116*, 57–63. https://doi.org/10.1016/j.poly.2016.02.048.
(255) Kaltsoyannis, N.; Kerridge, A. In *The Chemical Bond*; Frenking, G., Shaik, S., Eds.; Wiley-VCH Verlag GmbH & Co. KGaA: Weinheim, Germany, 2014; pp 337–356. https://doi.org/10.1002/9783527664658.ch11.
(256) Contreras-García, J.; Johnson, E. R.; Keinan, S.; Chaudret, R.; Piquemal, J.-P.; Beratan, D. N.; Yang, W. *J. Chem. Theory Comput.* 2011, *7* (3), 625–632. https://doi.org/10.1021/ct100641a.
(257) Kumar, M.; Kariem, M.; Sheikh, H. N.; Frontera, A.; Seth, S. K.; Jassal, A. K. *Dalton Trans.* 2018, *47* (35), 12318–12336. https://doi.org/10.1039/C8DT02429D.
(258) Ashashi, N. A.; Kumar, M.; ul Nisa, Z.; Frontera, A.; Sahoo, S. C.; Sheikh, H. N. *J. Mol. Struct.* 2021, *1245*, 131094. https://doi.org/10.1016/j.molstruc.2021.131094.
(259) Morokuma, K. *J. Chem. Phys.* 1971, *55* (3), 1236–1244. https://doi.org/10.1063/1.1676210.
(260) Ziegler, T.; Rauk, A. *Theor. Chim. Acta* 1977, *46* (1), 1–10. https://doi.org/10.1007/BF00551648.
(261) Yang, X.; Burns, C. P.; Nippe, M.; Hall, M. B. *Inorg. Chem.* 2021, *60* (13), 9394–9401. https://doi.org/10.1021/acs.inorgchem.1c00285.
(262) Apostolidis, C.; Kovács, A.; Morgenstern, A.; Rebizant, J.; Walter, O. *Inorganics* 2021, *9* (6), 44. https://doi.org/10.3390/inorganics9060044.

Chapter One

Preparation of complexes based on conceptually different redox-active ligands

1.1. Introduction. Choice of ligands.

The results presented in the Introduction underlined the fact that the choice of the ligand in organolanthanide chemistry is of considerable importance. Some of the factors that are into play include the ligand reduction potential,[1] the symmetry of the frontier orbitals[2] or structural parameters that impact electron transfer (such as the torsion angle[3]).

Historically, the bipy ligand (Scheme 1.1A) provided an excellent framework for the theoretical study of the electron transfer in dual component lanthanide-ligand systems, owing to the ease of access of substituted versions. The phenanthroline-based family of ligands demonstrated a new type of behaviour for radical anionic ligands by forming a reversible C-C bond following electron transfer.[2,4]

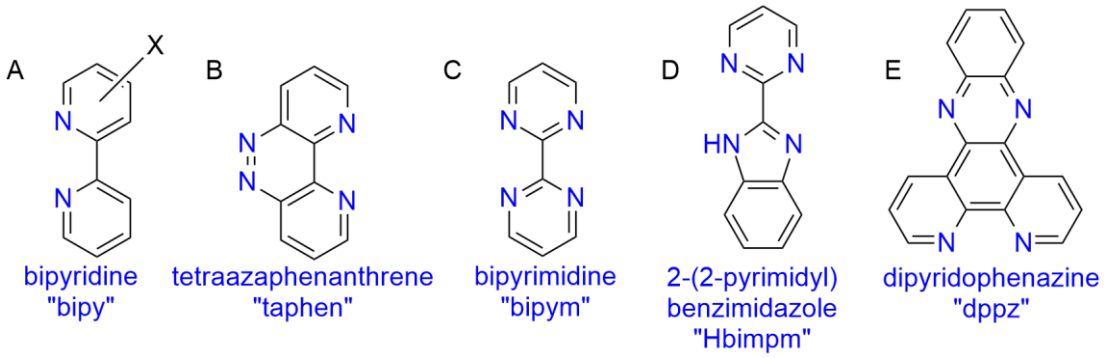

Scheme 1.1: Selection of RALs used in organolanthanide chemistry.

The evolution towards bimetallic systems naturally involved the presence of two coordination sites for the two metals. The bipyrimidine ligand (Scheme 1.1C; henceforth abbreviated to bipym) has found a widespread use as a bridging unit between two metals.[5–9] It has also been used in organolanthanide chemistry, principally as a radical bridging unit in order to measure the exchange coupling between the two metal centres (Scheme 12).[10,11]

Addition of ytterbocene,[‡] a divalent lanthanide complex, to the neutral bipym ligand leads to a coordination on both sides of the ligand by two equivalents of ytterbium, followed by double reduction of the ligand, regardless of the stoichiometry of the reaction.[1] Prior work in our group had obtained an analogous adduct when attempting to prepare heterobimetallic compounds with the

[‡] This term will be used all throughout this work in the interest of fluidity and will designate $Cp^*_2Yb(OEt_2)$. The same applies for "samarocene" and $Cp^*_2Sm(OEt_2)$.

tetraazaphenanthrene ligand (Scheme 1.2).[12] Given that the target complexes are heterobimetallic adducts, it was, therefore, concluded that the transition metal ought to be coordinated to the ligand before the addition of the organolanthanide fragment.

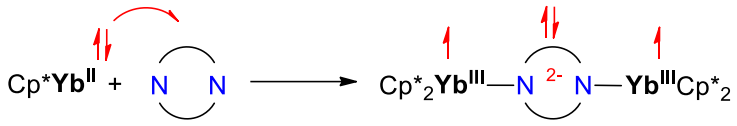

Scheme 1.2: Formation of doubly reduced bimetallic adducts with tetraazaphenanthrene and bipym.

At the beginning of this thesis, two conceptually different ligands were identified as promising scaffolds for synthesising heterometallic complexes: 2-(2-pyrimidyl)benzimidazole (**Hbimpym**) and dipyrido[3,2-a:2',3'-c]phenazine (**dppz**) (D and E in Scheme 1.1, respectively).

The use of the latter, following an initial report in 1984,[13] has blossomed in the '90s.[14] **dppz** (and its derivatives) has found application in biomedicine[15] as an anti-cancer agent[16,17] due to its ability to bind to DNA and other biomolecules.[18,19] Its extensive aromatic delocalisation makes it an excellent π-acceptor,[20] (which would qualify it for our purposes) a property that has been exploited in photophysical studies.[21–24] Furthermore, a very recent study deployed **dppz** as an anode in a rechargeable aqueous proton battery.[25] More pertinently, it has been used in tandem with lanthanides, in order to magnify their two most prominent intrinsic properties: luminescence[26,27] and magnetism.[28,29] The ligand, therefore, has a proven track record in organometallic chemistry. It was chosen as a target in order to provide a conceptual evolution of the ERC project. Up to this point, the architecture of our complexes always involved one organolanthanide fragment and one TM fragment bound to one RAL. The objective herein is to capitalise on its three coordination sites by coordinating two lanthanides on each monodentate site and one TM on the bidentate site (Scheme 1.3A). It is worth noting, however, that in all of the cited examples, the metal coordination occurs at the diimine site. To the best of our knowledge, no structures where metals are coordinated at one of the monodentate sites have been reported. This implies that one of the major synthetic challenges of this project will revolve around the stable coordination of the lanthanides.

In comparison, **Hbimpym** has found a relatively modest usage in organometallic compounds. The first such report described its use as a bridging ligand in ruthenium and osmium edifices, which allowed the observation of multiple reversible redox events in both cases.[30] More recently, the group of Yuan published two reports describing bimetallic Ir^{III}-bimpym-Ir^{III}, Ir^{III}-bimpym-Cu^{I} and Cu^{I}-bimpym-Cu^{I} (the Cu^{I} centre is coordinated in an unusual quasi-linear fashion) species.[31,32] These complexes have demonstrated interesting photophysical properties and the bimetallic Ir^{III} complex was shown to be a good phosphorescent probe for O_2. With respect to our project, **Hbimpym** differs from the previous ligands by virtue of presenting two dissimilar bidentate sites: L_2 and LX (following deprotonation), according to Green's classification.[33] In principle, this should afford flexibility in designing complexes, where it is possible to direct either the lanthanide or the transition metal fragments to a specific coordination site (Scheme 1.3B). The first results involving the bimpym ligand in lanthanide chemistry were published very recently during the PhD of Ding Wang.[34] Upon reduction, the bimpym ligand tends to form a C-C bond by coupling of the radical fragments formed. Depending on the reaction conditions, the $NiMe_2$ fragment could be maintained in the dimeric heterometallic complex or was expelled in favour of an Yb-Cp* fragment, prompting a trimetallic arrangement (Scheme 1.10).

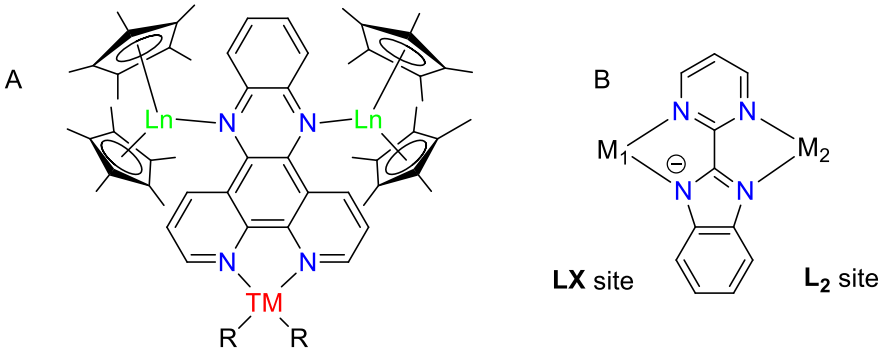

*Scheme 1.3: Proposed architectures for the **dppz** and **Hbimpym**-based complexes.*

The ligands **dppz**[35] and **Hbimpym**[30] were synthesised according to published procedures. The anionic site of **Hbimpym** was sought to be made more accessible by performing a simple deprotonation reaction to yield **Kbimpym** in a quantitative procedure (Scheme 1.5). The resulting beige solid was insoluble in all available solvents. After washing the solid with pentane and Et_2O, the quantitative conversion was confirmed by performing an ^1H NMR analysis that excluded the presence of either unreacted **Hbimpym** or KHMDS.

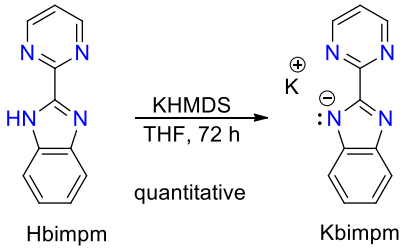

*Scheme 1.4: Synthesis of **Kbimpym**.*

The choice of the adequate transition metal precursor to be used in the complexation reactions with the ligand was guided by the anticipated subsequent reactivity with the divalent organolanthanide precursors. Functional groups susceptible to induce undesired reactivity are to be avoided. For example, acidic protons are known to readily hydrolyse the cyclopentadienyl moieties,[36] which are basic. Additionally, organolanthanide complexes (irrespective of oxidation state) are known to readily react with halides and activate C-X bonds.[37,38] Ideally, the precursor should be accessible synthetically and be sufficiently soluble to allow facile characterisation of the ensuing complex. The main precursors that have been selected are (tmeda)$PdMe_2$,[39] $[Me_2PtSMe_2]_2$,[40] $[Cp^*IrCl_2]_2$[41] and $[CODIrCl]_2$ and were either synthesised according to published procedures or bought from commercial suppliers.

1.2. dppz-based complexes.

1.2.1. Dimethylated transition metal complexes of dppz.

The series of (dppz)$TMMe_2$ complexes was synthesised starting from the available TM precursors. Their addition to **dppz** in THF produced very colourful black-purple (Ni – **1.1**), red (Pd – **1.2**), and orange (Pt – **1.3**) solids in high yields (Scheme 1.5). XRD-suitable crystals were grown from cooled saturated THF solutions (**1.1**) or by room temperature diffusions of Et_2O in saturated DCM solutions (**1.2** and **1.3**). Analyses showed isostructural, fully planar compounds.

The main structural features of the complexes are presented in Table 1.1. All TM are in a square planar coordination geometry, with deviations of less than 3.7° of the (NN)TM(Me_2) fragment with respect to the ligand plane. In contrast to the other structures, **1.1** presents asymmetrical distances for both the Ni-N and Ni-C_{Me} pair of bonds. The crystal structure of **1.2** was slightly disordered, hence the different Pd-C_{Me} distances (2.21 and 2.12 Å). This can be explained by the decomposition of the compounds, observed if they are left for extended periods of time in DCM – the solvent used for the

crystallisation procedures. It is assumed that the complex successively activates two C-Cl bonds in an oxidative addition, before immediately undergoing a reductive elimination, resulting in dppzPdCl$_2$. All three complexes decompose in solution if left for a few days in DCM. In all cases, the solution changes colour and the formation of black powder is attested.

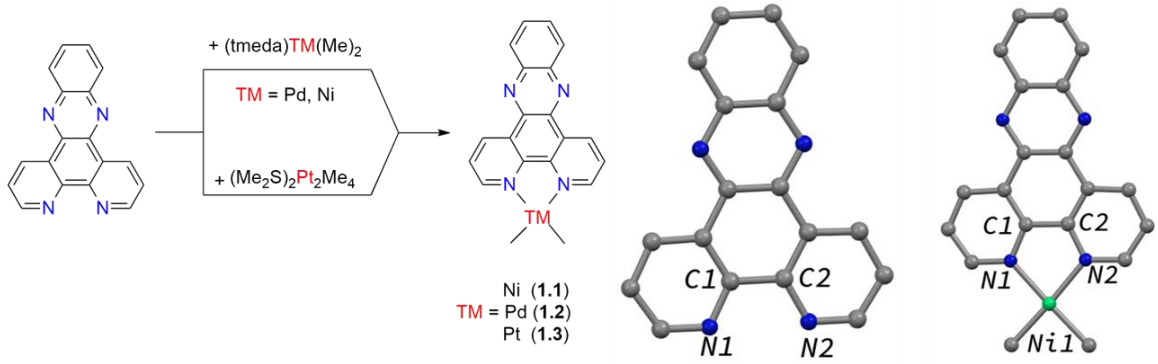

*Scheme 1.5: Synthesis of (dppz)TMMe$_2$ complexes **1.1-1.3** and ORTEP of **dppz**[42] and of dppzTMMe$_2$-type complexes (**1.1** shown here). The numbering scheme shown here is used throughout the chapter.*

	Av. Values (Å)			
Distances	**dppz**[42]	**1.1**	**1.2**	**1.3**
TM-N$_1$		1.967(2)	2.126(3)	2.095(6)
TM-N$_2$		1.975(2)	2.111(3)	2.095(6)
TM-Me (avg)		1.946(3)	2.168(7)	2.055(7)
C$_1$-C$_2$	1.464	1.449(3)	1.455(5)	1.429(4)

*Table 1.1: Main structural features of **dppz** and of compounds **1.1-1.3**.*

The C-C bond bridging the two pyridyl moieties is shortened upon coordination of the TM fragment, with a more pronounced effect in the case of **1.3**. The sets of ligand distances are in line with previously reported complexes of group 10 TM at the +2 oxidation state.[43–46] To have a better understanding of the electronic effect of the coordination, we turned to theoretical computations.

Free **dppz** was optimised at the **ZORA1** level of theory: the main distances are very well reproduced. The electronic structure, calculated at the **ZORA3** level, presented one orbital of interest (LUMO+2), with a bonding interaction between the bridging carbons (whose shape can be found at the LUMO+1 level of **1.3** in Figure 1.1). The coordination of the TM fragment is likely to entail electronic perturbation of the ligand: this orbital would be stabilised and explains the shortening of the C-C bond.

Complexes **1.1**-**1.3** were computed, with the main structural features largely well replicated, with almost all distances within 0.02 Å to the corresponding crystal structure differences (see Table 1.2). The asymmetry of the bonds involving the Ni in **1.1** is reproduced, while the other two computed complexes are highly symmetrical. The electronic structure is identical along the series: the occupied frontier orbitals are comprised of electrons from the d manifold, whereas the vacant orbitals are delocalised across the ligand (also shown in Figure 1.1 below). The coordination of the TM fragment stabilises the aforementioned LUMO+2 of **dppz**, lowering it to be the LUMO+1, and significantly reduces the HOMO-LUMO gap from 4.13 eV in free **dppz** to 2.05-2.47 eV for the series of compounds (according to calculations performed at the **ZORA3** level of theory).

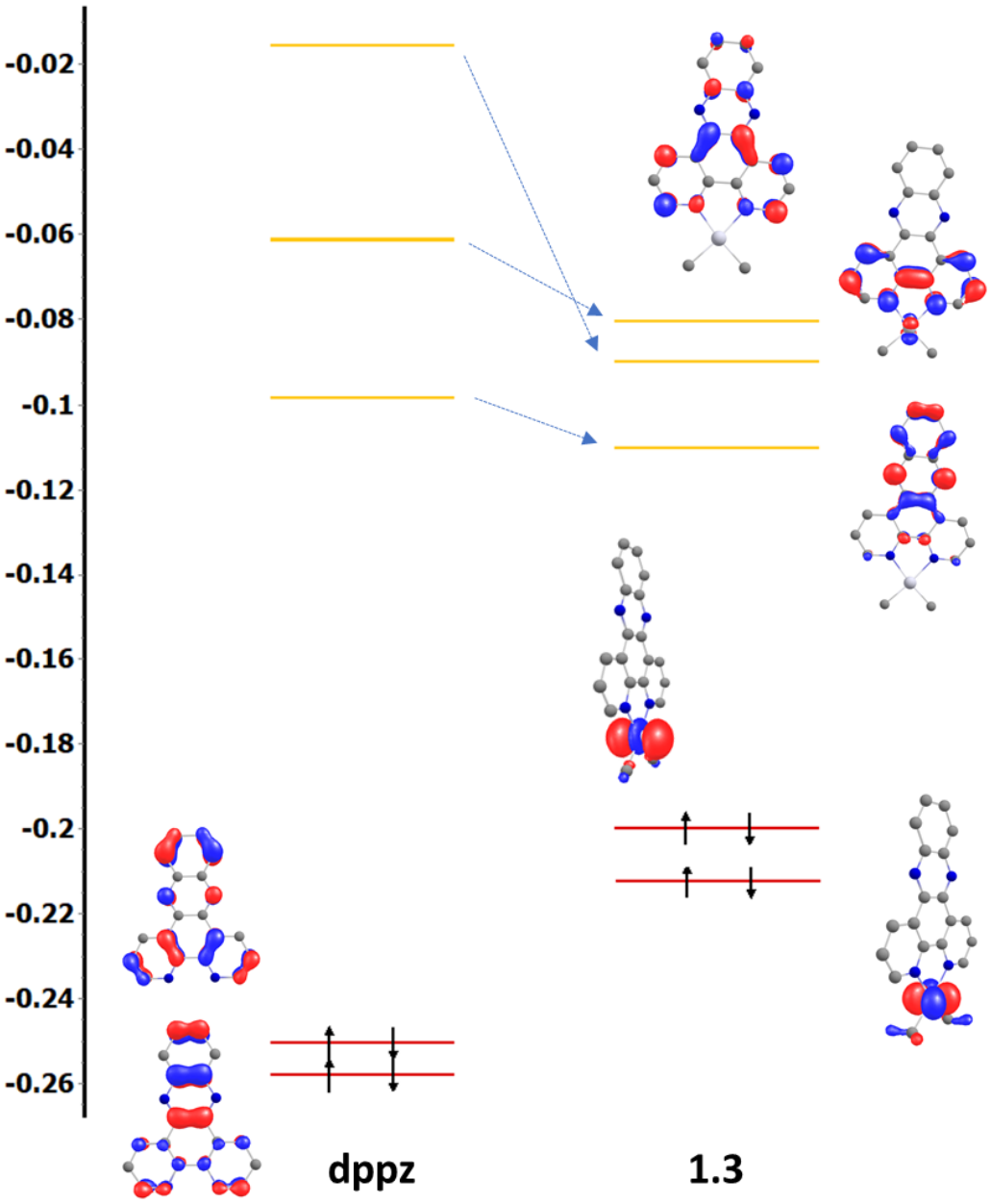

*Figure 1.1: MO diagram of **dppz** and of **1.3**, calculated at the **ZORA3** level of theory. The occupied orbitals are designated by the red dashes with arrows, whilst the vacant orbitals are represented by the yellow dashes. The LUMOs of **dppz** are identical in shape to the ones presented for **1.3** (excluding the TM fragment), but are not presented in the interest of clarity. The energies are given in Eh.*

	Av. Values (Å)		
Distances	**1.1**	**1.2**	**1.3**
TM-N_1	1.963	2.133	2.094
TM-N_2	1.972	2.133	2.094
TM-Me (avg)	1.944	**2.033**	2.039
C_1-C_2	1.445	1.450	1.444

Table 1.2: Main distances in the optimised geometries of the dppzTMMe_2 series of compounds. The distance in red and boldface indicates a significantly shorter difference with respect to the crystal structure.

Although the synthesis of these compounds is relatively straightforward, solution studies are hampered by very poor solubility in the solvents most commonly used in our laboratory. Only **1.2** afforded a satisfactory ^{1}H NMR spectrum, allowing its characterisation (Figure 1.2). Contrary to the slight asymmetry suggested by the crystallographic data, **1.2** is of C_2 symmetry in solution, judging by the number of signals and their integration.

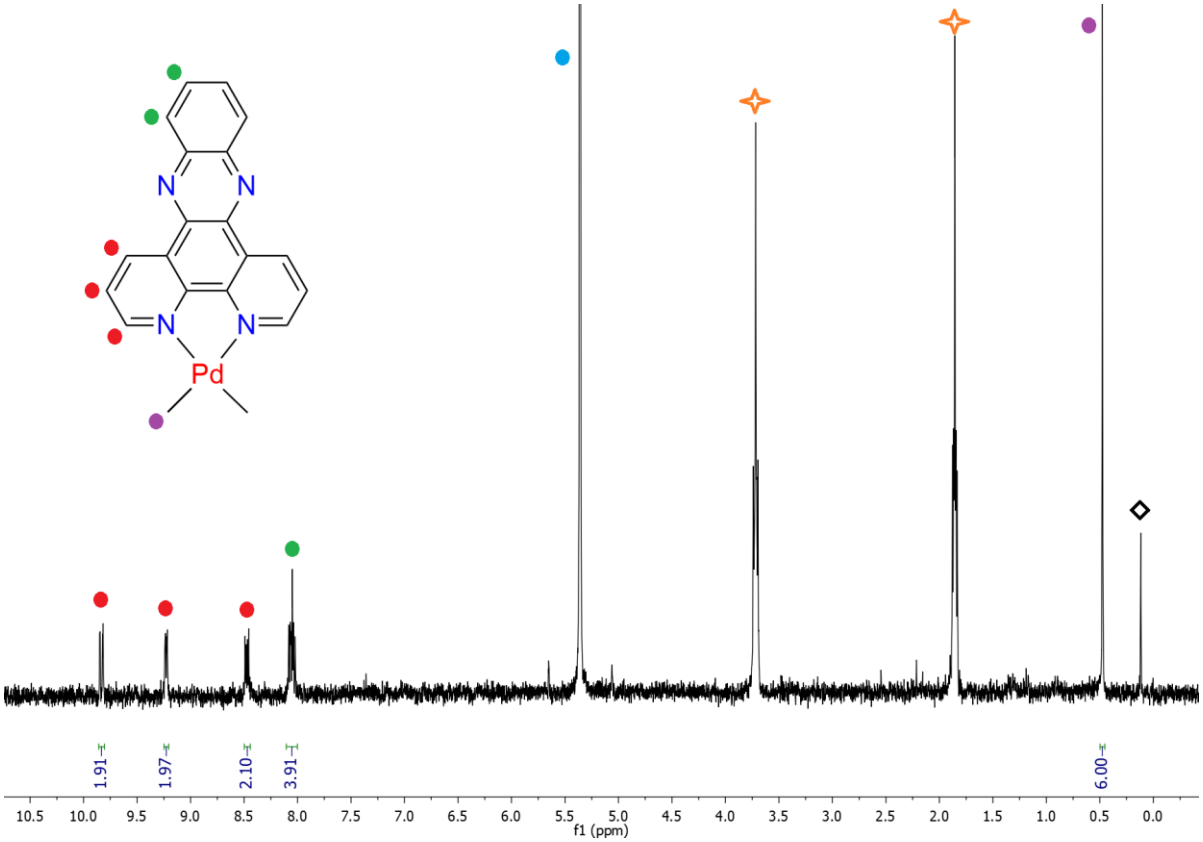

*Figure 1.2: ^{1}H NMR in CD_2Cl_2 of **1.2**. The blue dot indicates the solvent peak, the orange four-pointed star – residual THF, black lozenge – silicone grease.*

1.2.2. Iridium-based dppz complexes.

1.2.2.1. Synthesis and characterisation.

A group 9 metal – iridium – was envisaged as well as a building block for heterometallic complexes. There is some precedent in literature for organometallic complexes of Ir^{III} involving **dppz**, with biomedical and supramolecular applications.[47–51] **dppz** remains quite sought after for its photophysical properties and Ir is an excellent potential partner, due to its propensity for photocatalytic applications.

Initial trials have involved the more electron-rich Ir^{I} metal centre. The reaction between the cyclooctadiene iridium(I) chloride dimer and dppz in DCM resulted in a dark purple solution. Filtration, followed by room temperature crystallisation allowed the identification of the compound as an ion pair complex, **1.4** (Scheme 1.6). The breaking of the dimer resulted in a cation bearing the **dppz** coordinated to the Ir-COD moiety, whilst the anion is $[IrCODCl_2]^-$. Despite the presence of the lipophilic COD ligand, **1.4** remains poorly soluble, precluding further characterisation.

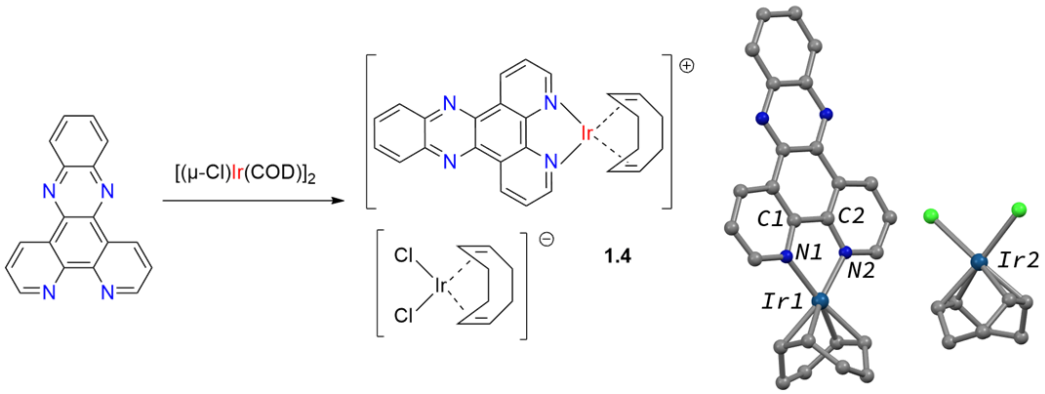

*Scheme 1.6: Synthesis of **1.4** and its ORTEP.*

1.2.2.2. Choice of counter-anion.

As mentioned in Chapter 1.1, the optimum design of the TM precursor requires the elimination of the chemical features that could impede reactivity with divalent lanthanides. Complex **1.4** has two very accessible Cl^- moieties on the anion. Given the overall affinity of lanthanides towards halides, it stands to reason to eliminate them to avoid undesired side-reactions.

A salt metathesis reaction was attempted with $NaBAr^F_4$ in DCM, leading to an immediate colour change to green. Leaving the solution at room temperature following filtration yielded XRD-suitable crystals, confirming the structure of **1.5** as $[(dppz)IrCOD]BAr^F_4$ (Scheme 1.7).

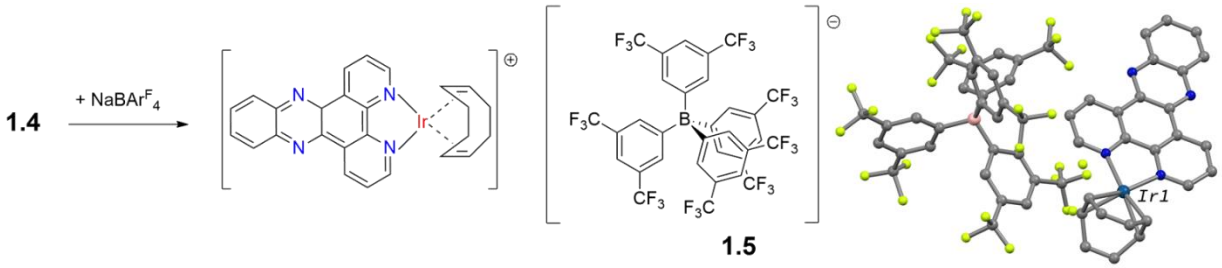

*Scheme 1.7: Synthesis and ORTEP of **1.5**.*

Analysis of the two structures reveals that the anion in **1.4** has a more perturbative effect on the coordination sphere of the Ir, as evidenced by the asymmetrical Ir-N bonds therein. The Ir-C_{COD} bonds are quite symmetrical, being within 0.006 Å of the average.

	Av. Values (Å)		
Distances	**1.4**	**1.4^+ (PBE-D3)**	**1.5**
Ir-N_1	2.069(5)	2.087	2.085(4)
Ir-N_2	2.100(5)	2.087	2.085(4)
Ir-C_{COD} (avg)	2.133(9)	2.140	2.125(9)
C_1-C_2	1.443(9)	1.441	1.441(8)

*Table 1.3: Main distances in the crystal structure of complexes **1.4** and **1.5**. **1.4^+** designates the cation of **1.4**, whose geometry was optimised at the **ZORA1** level of theory.*

On the other hand, **1.5** is perfectly symmetrical and crystallises in the I_{bam} space group. The BAr^F_4 anion does not seem to have an important effect on the geometry of the cation, despite it being relatively

close. The shortest C-H···F-C separation is 2.47 Å (the others are 2.68 Å or longer), which puts it slightly beyond the range for fluorine-based hydrogen bonding.[52]

Additionally, the Ir-dppz cation, designated as **1.4**$^{+}$, was computed separately at the **ZORA1** level of theory. The calculations were not performed on the full structure due to the associated computational cost and increased difficulty of convergence. The Ir-N bond distances are equal and are close to the lengths observed in **1.5** and to the average length in **1.4**. We can therefore assume that it represents a faithful reproduction of the electronic perturbation of the $[IrCOD]^{+}$ fragment on the **dppz** ligand. The frontier orbitals closely follow the pattern already established by **1.1**-**1.3**: the closest occupied orbitals are dominated by the Ir 5d electrons, whereas the LUMO+2 on the neutral **dppz** is also stabilised following coordination.

Although the procedure yielding **1.5** is straightforward, concerns remain whether the fluorine atoms in the BAr^{F}_{4} anion are sufficiently accessible to the lanthanide fragment. The same procedure can be applied with a vast number of other salts to yield more adequate compounds (*e.g.,* featuring the BPh_4 anion that lacks any carbon-halogen bond).

1.2.3. Addition of organolanthanide fragments.

Following the isolation of the desired precursors, the natural next step was the addition of divalent organolanthanide fragments to afford heterobimetallic complexes. Ytterbocene was chosen as the more adequate candidate, by virtue of the easier *in situ* tracking of the addition reactions, due to the enhanced paramagnetic effect inherent to Yb^{III} and, conversely, the diamagnetic character of Yb^{II} species.

The addition of $Cp^*_2Yb(OEt_2)$ to **1.1**-**1.3** was undertaken in a 2:1 stoichiometry. *In situ* ^{1}H NMR following of the reaction was in agreement with the coordination of Yb to the ligand and with the transfer of an electron, since several paramagnetically shifted signals appeared. In practice, though, the mixtures remain poorly soluble black suspensions. Nevertheless, crystals suitable for XRD studies could be grown following reactions of the Pd and Pt complexes by cooling saturated toluene solutions over a few days.

Unfortunately, the crystals obtained were of poor quality as a results of systematic twinning problems. Therefore, only XRD data of limited quality could be obtained. The resolutions leave little doubt as to the structure themselves – complexes of the formula $[Cp^*_2Yb^{III}]_2(dppz^{2-})TMMe_2$ (TM = Pd (**1.6**), Pt (**1.7**)) are obtained (Scheme 1.8), with two independent molecules in the unit cell of **1.6**. The metrics of these compounds, given in Table 1.4, are to be taken as qualitative hints of the electronic structure, rather than reliable, quantitative indications, due to the poor crystal quality.

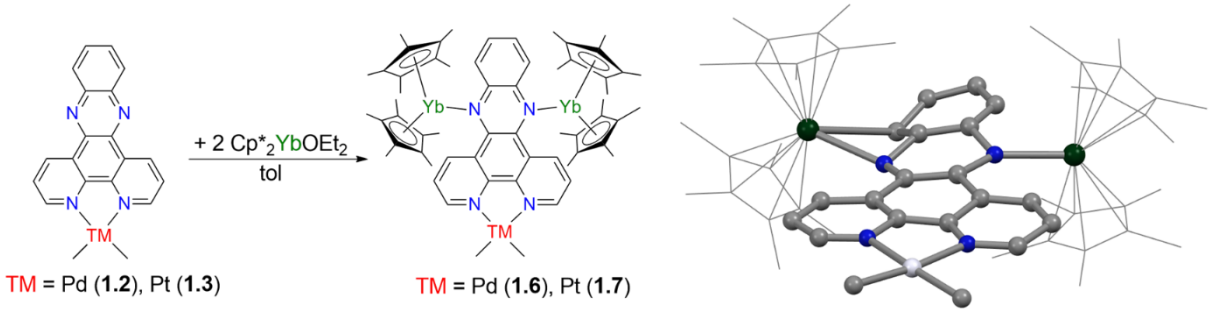

*Scheme 1.8: Synthesis of **1.6** and **1.7** and the ORTEP of **1.7**. The Cp* co-ligands are drawn in wireframe and the hydrogen atoms are omitted for clarity.*

One of the most glaring features is the fact that the ligand is twisted and no longer planar. This is consistent with a break of aromaticity – proof of electron transfer. This assertion is corroborated by the distance between the Yb metal centre and the centroid of the Cp*, which corresponds to previously tabulated values of Yb^{III} in the literature.[34,53,54] Indeed this Ln-Cp*(centroid) distance is highly sensitive to the oxidation state of the Ln metal centre. Another feature worth noting is that some of the ytterbium atoms – as is the case for one of the Yb centres in **1.7** and both Yb centres in one of the two molecules in **1.6** – seem to form an agostic interaction with the adjacent C-H bond (see ORTEP of **1.7**, Scheme 1.8). The length of these bonds (2.800 and 2.851 Å, respectively) are consistent with previously reported bonds between trivalent Yb and aromatic C-H bonds.[55]

	Av. Values (Å)	
Distances	**1.6**	**1.7**
Yb_1-N_3	2.274(9)	2.16(2)
Yb_2-N_4	2.271(10)	2.30(2)
Yb_1-Cp* (ctr)	2.300	2.311
Yb_2-Cp* (ctr)	2.330	2.310
TM-N_1	2.123(8)	2.149(18)
TM-N_2	2.107(10)	2.019(17)
TM-C_{Me} (avg)	2.031(12)	2.04(5)
C_1-C_2	1.44(2)	1.37(3)

*Table 1.4: Main distances in **1.6** and **1.7**. **1.6** crystallises as two independent, symmetrical molecules; the index in front of the Yb designates which centre coordinates the dppz ligand.*

Prior work on the subject performed in our laboratory described a solvent-dependent electron transfer,[12] a phenomenon that has rather limited described precedence.[56–58] The dissolution of **1.6** in polar solvents, such as THF, led to the crystallisation of $Cp^*_2Yb(THF)_2$ and **1.2**. Evaporating the solvent and redissolving the mixture in toluene resulted in the reformation of **1.6**. This highlights the relatively fragile coordination environment of the Yb – the crowded monodentate coordination site is not conducive to a strong stabilising interaction with the ligand. This conclusion can be seen in two different ways: on the one hand, it can be an advantage in potential catalytic applications, due to the facile mechanism for decoordination of the substrate (often a tricky step for obtaining the desired product). On the other, it could provide a pathway for possible side reactions involving the Yb^{II} metal centre, which could react (and transfer its electron) preferentially with the newly introduced compound, and not with **dppz**. More clues are to be gathered in order to have a firmer grasp on the behaviour of the complex in the presence of competing ligands or substrates.

The addition of ytterbocene to the nickel complex **1.1** and the Ir-based complexes **1.4** and **1.5** were also attempted. Highly shifted paramagnetic peaks were attested, which would imply electron transfer from the divalent ytterbium complex. However, since no crystals could be isolated, the definite outcome of these reactions is unclear.

1.2.4. Partial conclusion and perspectives.

A series of TM-based structures bearing the **dppz** ligand were synthesised and characterised in the solid state. Complexes **1.1**-**1.3** suffer from poor solubility, which complicates further characterisation. To compound the difficulty, the best solvent available – DCM – leads to decomposition of each of

these complexes after a few days. Correspondingly, ascertaining high purity of the substrate prior to the addition of divalent lanthanides is arduous.

Two **dppz** complexes of Ir^{I} were also synthesised. Although slightly more manoeuvrable synthetically due to the COD co-ligand (which confers higher solubility), challenges remain. Of note is the presence of accessible Cl^- ligands on the anion in **1.4**. An exploratory essay to change the counter anion was performed, yielding **1.5**, but its suitability with other non- or weakly coordinating anions remains to be confirmed. Perhaps further insurance against parasitic side reactions could be obtained by a more careful choice of counter-anion, such as BPh_4^-.

Addition of ytterbocene to **1.2** and **1.3** resulted in the formation of trinuclear complexes **1.6** and **1.7**. The deviation of the ligand from planarity, as well as the structural features of the Yb, were proof of double electron transfer, thus demonstrating the viability of the idea behind the choice of **dppz** as a ligand. Despite the presence of several highly soluble Cp* co-ligands, precise characterization of the final compounds was also inhibited by their quite poor solubility. This may be remedied by resorting to more lipophilic precursors. For example, using Cp^{ttt}_2Ln (Cp^{ttt} = 1,2,4-$(Me_3C)_3C_5H_2$) should afford better solubility in low-polar solvents, without any loss of reductive potential of the organolanthanide fragment. However, previous studies showed that the electron transfer depends on other factors, such as steric hindrance or symmetry, both of which might be compromised by these extra-bulky co-ligands.[59]

Seeing as how poor solubility is something of a leitmotif for **dppz** chemistry, one of the available solutions would be to improve the overall solubility of the TM precursors. Functionalising the **dppz** ligand is the most easily attainable modification, whilst keeping the same synthetic protocol. Substituted precursors are either commercially available or can be synthesised using previously described procedures.[60] The most easily obtainable precursors are modifications of the *o*-phenylenediamine (Scheme 1.9).[61]

Another concern is the coordination of the lanthanide fragment. As previously mentioned, the coordination of Yb can be easily displaced by a polar solvent. Having no precedent of the occupation of the monodentate site may be a telling sign as to the difficulty of this objective. The continuation of this project might require the modification of the ligand coordination site towards the lanthanides to afford bidentate chelating coordination pockets. Two similar ligands have previously been used: pyrazino[2',3':5,6]pyrazino-[2,3-f][1,10]phenanthroline (dpqp)[62] or dipyrido[3,2-f:2',3'-h]quinoxalino[2,3-b]quinoxaline (dpq-QX).[63] Whilst these targets are bound to improve the stability of the trimetallic edifices, the same solubility concerns are naturally applicable to these ligands. The strategies to ameliorate the solubility, discussed above, could be used for these ligands, as well. All the mentioned synthetic targets are illustrated in Scheme 1.9.

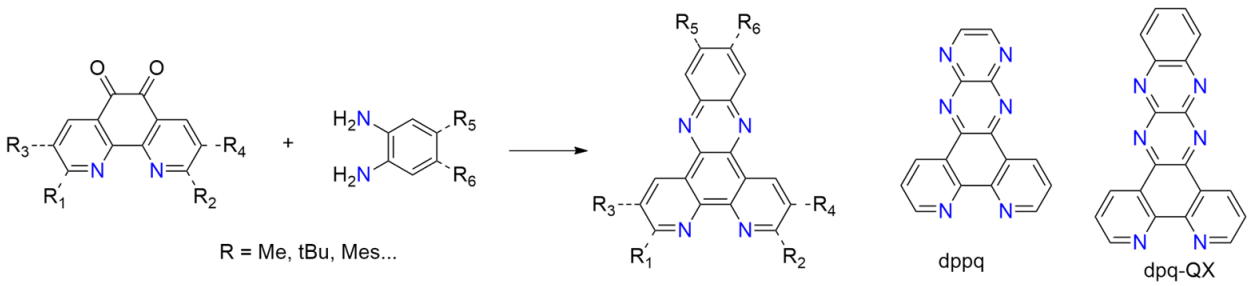

*Scheme 1.9: Proposed modifications or alternatives to the **dppz** ligands in order to enhance the solubility.*

1.3. Kbimpym-based complexes.

The rationale for the synthesis of **Kbimpym**-based compounds stems from two main reasons: the use of the potassium salt of the ligand in salt metathesis reactions, therefore exploiting the synthetic driving force of salt formation and the coordination of reactive, divalent organolanthanide fragments to an anionic LX site.

Both of these synthetic specificities have been put to good use in a recent publication of our group, describing the **K(bimpym)NiMe$_2$** complex.[34] The addition of ytterbocene results in an electron transfer, which is responsible for the formation of a C-C bond. In addition, formation of KCp* is invoked as a thermodynamic driving force, explaining the rearrangement of the system upon the coordination of the divalent lanthanide and the subsequent electron transfer when the reaction is performed at room temperature (Scheme 1.10).

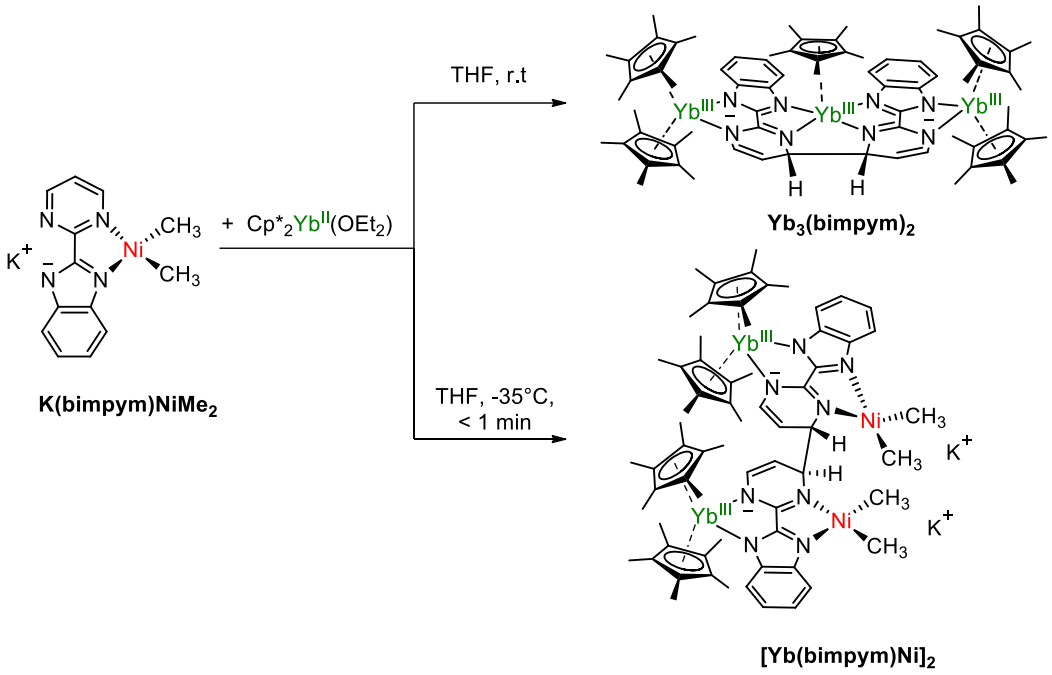

*Scheme 1.10: Reactivity of **K(bimpym)NiMe$_2$** with ytterbocene.*

As a mechanistic *thought experiment*, it could, perhaps, be posited on an electrostatic repulsion basis that the coordination of the lanthanide on the anionic site leads to the delocalisation of the negative charge across the ligand and the transition metal fragment, even prior to the electron transfer. The instability of the Ni fragment (which is bent by 31° with respect to the ligand plane in **[Yb(bimpym)Ni]$_2$**, prior to its expulsion from the complex) may stem from the accumulation of the negative charge in its coordination sphere and of spin density following the electron transfer on the metal centre. Naturally, this hypothesis is pure conjecture without any experimental evidence, but examining this reactivity and its dependency with the ligand and the TM centre constitutes a valuable objective.

1.3.1. Platinum complexes.

The synthesis of a complex where the platinum fragment is coordinated to the L$_2$ site of the bimpym ligand was undertaken. Two equivalents of **Kbimpym** were added to the [PtMe$_2$(SMe$_2$)] precursor in THF, leading to the formation of **1.8** (Scheme 1.11). Due to the insolubility of both **Kbimpym** and of

1.8, long reaction times and diluted conditions (*ca*. 1 mg product / mL of solvent), respectively, are necessary. The resulting blood red solution is subsequently filtered. Microcrystalline yellow-orange solid is formed directly during gentle evaporation of the solvent until the elimination of all volatiles. The complex **1.8** is formed with a 42% yield (based on crystals).

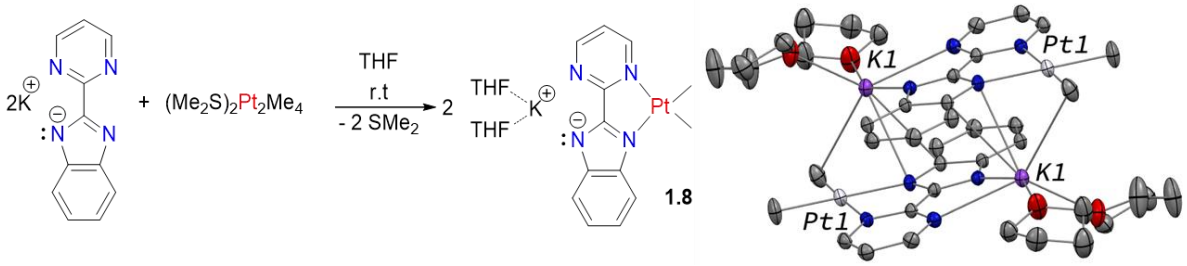

*Scheme 1.11: Synthesis and ORTEP of **1.8**. Hydrogen atoms have been hidden for clarity.*

The intense red coloration of the crude solution is due to an unknown impurity which can be removed by washing the crystals with THF. The complex can be recrystallised from THF – orange blocks are formed after a few days by leaving the pale orange solution at r.t. XRD analysis revealed a dimeric arrangement, where two molecules, inverted with respect to one another, form perfectly parallel planes. The K^+ cations are pulled out of plane (by 0.54 Å) by their interaction with both one of the Me moieties and a nitrogen on the benzimidazole moiety of the opposite molecule. The Pt atom is also slightly pulled out of plane (by 0.15 Å).

1.3.2. Palladium complexes.

The synthesis of the corresponding palladium complexes was pursued in an analogous fashion to the already published procedure with Ni (Scheme 1.12).[34] Addition of THF to the precursors results in a beige suspension, which gradually yields a golden supernatant after a few hours. Owing to its very poor solubility of the starting potassium salt, long reaction times and dilute conditions are necessary – similarly to the synthesis of **1.8**.

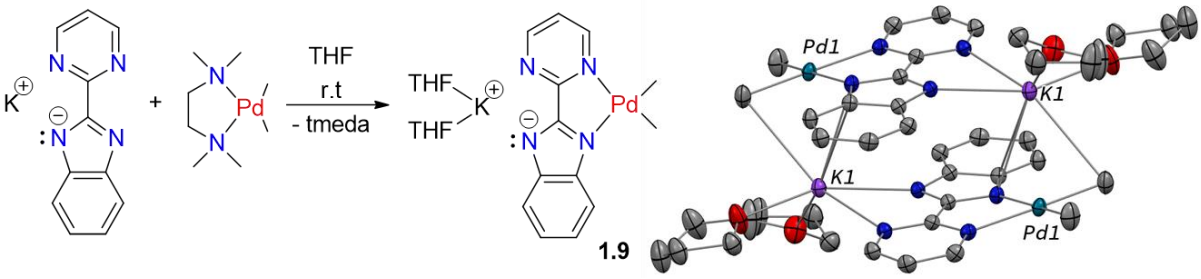

*Scheme 1.12: Synthesis and ORTEP of **1.9**. Hydrogen atoms have been hidden for clarity.*

Adequate crystals can be obtained by redissolving the microcrystalline solid in THF. Leaving the pale yellow solution at r.t for a few days yields yellow needles. XRD analysis allowed the elucidation of the structure of **1.9**, which is isostructural to **1.8**, in terms of the two inverted independent molecules and the presence of solvent in the coordination sphere of K^+.

If undertaken at a small scale (up to 25 mg of (tmeda)$PdMe_2$), the procedure and work-up is comparable to that of **1.8** – a 40% yield is attested (based on crystals). Analogously, the golden hue of the solution is due to an impurity, which can be removed by washing the solid with a minimum amount of THF.

Due to the time-consuming and sensitive nature of the process which requires highly diluted conditions, a larger scale synthesis was attempted. In contrast to the relatively straightforward procedure attested for the Ni complex, the reaction is fraught with difficulties. The insolubility of **Kbimpym** requires multiple days of reaction time for the ligand to be fully consumed. However, it would seem that longer reaction times also lead to the degradation of **1.9**, since, across multiple attempts, the same work-up procedure only produced very small, if any, quantities of **1.9** (yield < 5%) and an intractable mixture of side-products.

To verify this assertion, pure **1.9** was tested in order to ascertain its stability: it does not decompose in solution at room temperature for a week. Furthermore, raising the temperature to 60 °C for several hours produced no discernible evolution. However, the compound rapidly decomposed under UV-light, suggesting sensitivity to light. The same observations hold for **1.8**, as well. Given that the aforementioned trials at larger scale were protected against outdoor light anyway, it is unclear by which mechanism the product decomposes. It is, however, consistent with the difficulties encountered in our laboratory when using (tmeda)$PdMe_2$ in ligand exchange reactions in polar solvents. For example, the synthesis of bipym$PdMe_2$[54] was significantly improved by performing the reaction in toluene, leading to yields of >90%. This solution cannot be applied in this case, as no conversion to **1.9** was observed when the reaction was performed in non-polar solvents.

Based on the assertion that, indeed, the longer reaction times are responsible for the degradation of the product, a slight modification to the procedure was tested. After overnight stirring, the reaction mixture was left to settle (due to the presence of both **Kbimpym** and precipitated **1.9**), before the golden supernatant was transferred to another container via cannula filtration. The solvent was redistilled back into the initial vessel and the procedure was repeated until the supernatant therein was colourless. Unreacted (tmeda)$PdMe_2$ was extracted from the recovered crude product with Et_2O and was reintroduced into the reaction vessel as a THF solution and the reaction resumed. This procedure was repeated daily until no further **1.9** was produced. This modification did not, however, result in any improvement in the yield.

Another solution pursued was to increase the solubility of **Kbimpym** by trapping the K^+ ion with the adequate crown-ether chelating agent. In stark contrast to the aforementioned procedure, the **Kbimpym** suspension rapidly became a pale yellow solution upon the addition of the Pd precursor in the presence of 18-C-6. Following overnight stirring, the solution was filtered and the remaining product (**1.10**) was extracted with THF from the remaining solid to obtain **1.10** in a 68% yield (based on crystals).

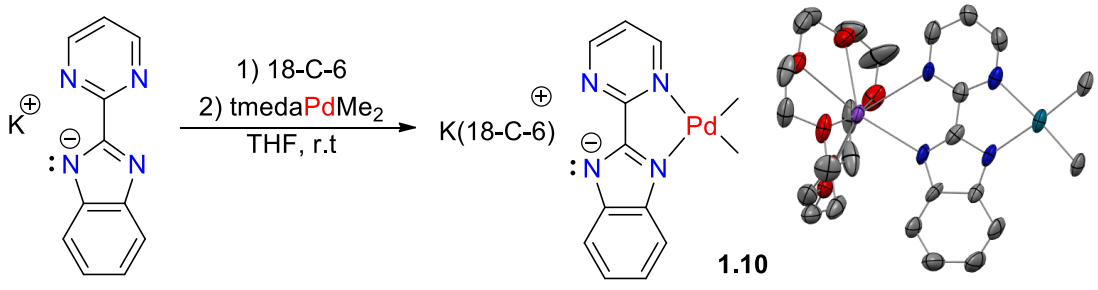

*Scheme 1.13: Synthesis and ORTEP of **1.10**. The hydrogen atoms and the solvent molecules have been omitted for clarity.*

Crystals of **1.10** suitable for XRD analysis were obtained by leaving a THF solution of the product at room temperature overnight. The encapsulation of the K^+ ion results in a slight elongation of the K-N bonds with the anionic system. It remains to be seen if having the K^+ ion entrapped affects the reactivity of the complex in subsequent trials.

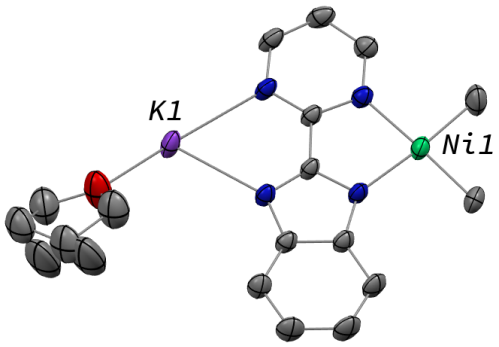

*Figure 1.3: ORTEP of **K(bimpym)NiMe$_2$**. Hydrogen atoms have been hidden for clarity. The THF molecule present in the crystal structure is disordered.*

1.3.3. Comparing the K(bimpym)TMMe$_2$ series of complexes.

1.3.3.1. Structural features.

After having synthesized the entire series of compounds with **Kbimpym** and group 10 transition metals, a comparison is warranted. The most salient structural features are collected in Table 1.5. The first and most glaring difference in the crystal structures is the number of THF molecules coordinated to the K^+ ion, which is one for the Ni complex (crystal structure shown in Figure 1.3) and two for the other two complexes. The supplementary steric crowding due to the extra molecule is most likely responsible for the larger deviation from the ligand plane of the K^+ ion in the case of **1.8** and **1.9**, as well as the longer distances with the nitrogen atoms on the ligand (which are almost identical between the two complexes).

As shown in Table 1.5, the TM(Me$_2$) fragments are pulled out of plane, due to the interaction between the K^+ ion and the opposite molecule (see crystal structures in Scheme 1.11 or Scheme 1.12). The mean deviation from the calculated (NN)TM(Me$_2$) plane by each of its atoms are 0.017 Å, 0.038 Å and 0.027 Å going from Ni to Pt. Therefore, the transition metal centres could all best be described as being tetracoordinated in the +2 oxidation state in a (more or less) distorted square planar geometry.

	Av. Values (Å or °)		
Atoms	**K(bimpym)NiMe$_2$**[34]	**1.9 (Pd)**	**1.8 (Pt)**
TM-N$_{pym}$	1.981(2)	2.1538(15)	2.1040(19)
TM-N$_{imid}$	1.969(2)	2.1551(13)	2.1115(17)
TM-Me (avg)	1.923(2)	2.0415(13)	2.034(2)
K-N$_{pym}$	2.775(2)	2.8812(16)	2.8745(19)
K-N$_{imid}$	2.770(2)	2.7930(18)	2.7781(19)
TM-K	3.1643(9)	3.3356(12)	3.3387(6)
C-C	1.451(3)	1.470(2)	1.452(3)
d(K-plane)	0.192	0.523	0.539
d(TM-plane)	0.012	0.243	0.154
d(plane$_1$-plane$_2$)	3.164	3.375	3.349
bimpym^TMMe$_2$	2	12.15	7.75

Table 1.5: Main distances and angles in the crystal structures of the KbimpymTMMe$_2$ complexes.

The nature of the interaction between the transition metal and the ligand can be inferred by the main structural features involving both partners. The differences in bond lengths are consistent with the differences of the crystal radii for the three metals in the +2 oxidation state and square planar geometry, which are 0.63 Å, 0.78 Å and 0.74 Å going from Ni to Pt.[64] However, the C-C bond length of the atoms bridging the pyrimidyl and benzimidazolate moieties is slightly different in **1.9** with respect to that in its congeners. As shown in numerous instances in organolanthanide chemistry (including the report of the Ni complexes),[34] the length of the bond linking two fragments of the ligand can be an important metric of the perturbation of the aromatic system, notably following an electron transfer.[54,65] Although an electron transfer is not in order in this instance, it may be indicative of how disruptive the coordination of the TM fragment is for the electronic structure of the ligand.

To ascertain the effect of coordination and of an eventual electron transfer in the case of the bimpym ligand, pertinent comparisons are necessary. Assessments of **Hbimpym** (previously crystallised by our group) and of some derived systems give rather different values for the C-C bond. The crystal structures of **Hbimpym**-based systems are shown in Figure 1.4. The two fragments of the ligand are not coplanar in the crystal structure of **Hbimpym**. This is not an unusual occurrence for N-heterocycles in the gas and liquid phase, due to the repulsion between the nitrogen lone pairs, but bicyclic aromatic systems tend to be planar in the solid state due to intermolecular packing forces.[66] The functionalised systems shall be referred to as **Hbimpym-ClBr** (centre) and **Hbimpym-Br** (right).

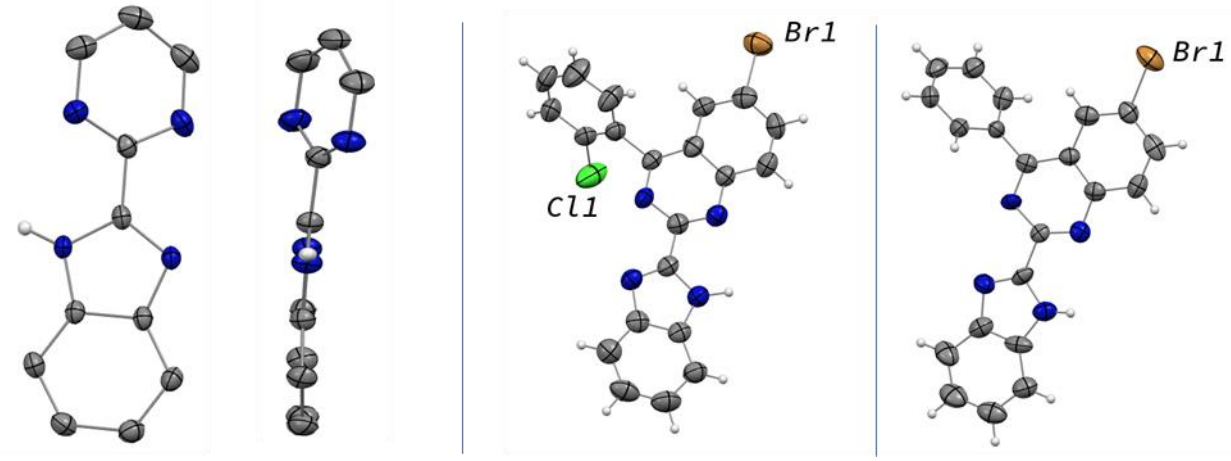

*Figure 1.4: Crystal structures of Hbimpym-based systems – **Hbimpym** (left), **Hbimpym-ClBr** (centre) and **Hbimpym-Br** (right). The derived structures were published in a private communication and are available on the CCDC database under the deposition numbers 993427 and 993428.*

Although a direct extrapolation is difficult, the evolution of the characteristic bonds of the ligand (given in Scheme 1.14) may provide an outline of how the perturbation of its electronic structure manifests itself in the structural features of the ligand. The fact that the pyrimidine and benzimidazole moieties are not coplanar (by 22.5°) in the crystal structure of **Hbimpym** has consequences on the conjugation between the two fragments, and therefore on the structural features therein. Most notably, it allows the two fragments to be treated as separate aromatic fragments (for example, all the symmetrical bonds defined along the C_2 symmetry axis on the pyrimidine moiety are almost perfectly equal to one another, which is not the case for the other protonated ligands in Table 1.6). Hence, the comparison between the uncoordinated ligands and the TM(Me_2) systems shall be made between the compounds where the ligand is planar, which is to say the derived systems.

In the uncoordinated, planar structures, it is evident that the presence of a negative charge on the LX site induces significant polarisation in the neighbouring bonds. As such, the bonds labelled as H are longer than I in the uncoordinated ligands. On the pyrimidine moiety, the opposite holds true – B is

shorter than G. The polarisation is also propagated across other pairs of bonds, but less so for bonds farther apart to the imidazolate moiety.

The perturbation due to the coordination of the TM(Me_2) fragments can be construed by comparing the structural features of these compounds to the aforementioned crystallised protonated ligands (Table 1.6). The most striking effect would be the inversion of the relative distances for the bonds H and I: H is significantly longer in the non-coordinated ligand and becomes shorter in the TM(Me_2) series. Whilst the polarisation of the bonds closest to the negative charge is still applicable (though lessened), the effect would seem to be additionally dampened for bonds farther apart.

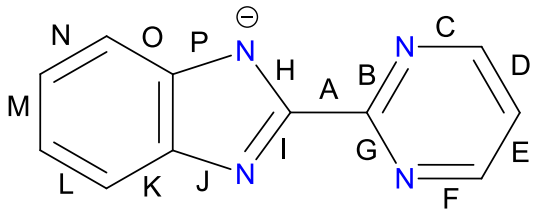

Scheme 1.14: Main bond labelling in bimpym-based ligands.

	Av. Values (Å or °)					
Bond	**K(bimpym)NiMe$_2$**	**1.9**	**1.8**	**Hbimpym**	**Hbimpym-ClBr**	**Hbimpym-Br**
A	1.451	1.470	1.452	1.474	1.465	1.498
B	1.331	1.345	1.337	1.334	1.302	1.315
G	1.355	1.360	1.356	1.337	1.364	1.363
H	1.336	1.349	1.337	1.357	1.369	1.342
I	1.356	1.367	1.360	1.323	1.309	1.312
P	1.376	1.379	1.371	1.374	1.369	1.379
J	1.378	1.383	1.373	1.388	1.394	1.397
C	1.339	1.343	1.337	1.335	1.366	1.381
F	1.337	1.348	1.346	1.336	1.314	1.328
D	1.368	1.396	1.385	1.379	1.404	1.391
E	1.381	1.387	1.376	1.375	1.427	1.428

Table 1.6: Main ligand bond lengths in the (bimpym)TM(Me_2) series and in the non-coordinated ligands.

1.3.3.2. Electronic structure and theoretical computations.

To obtain further insight into the electronic perturbation induced by coordination or electron transfer, theoretical computations were pursued. The structures of **Hbimpym** and **Kbimpym** were optimised at the **ZORA1** level of theory. In theory, the significantly stronger ionic character in the bond between the formal charge carriers in **Kbimpym** should manifest itself in the partial charges of the main atoms. Mulliken population analyses on both molecules are consistent with this interpretation (Table 1.7).

The examination of the frontier orbitals revealed that the more negative partial charges on the **Kbimpym** are reflected in larger orbital coefficients on the benzimidazolate fragment, at the expense of those on the pyrimidine moiety (Table 1.8), as well as more electronic density concentrated on the nitrogen atoms.

Atom	Hbimpym	Kbimpym
H^+/K^+	0.222	0.780
N_{imid}^-	-0.174	-0.498
N_{imid}	-0.143	-0.156
N_{pym}^-	-0.246	-0.362
N_{pym}	-0.135	-0.111
C_{imid}	0.189	0.323
C_{pym}	0.151	0.112

*Table 1.7: Mulliken atomic population analyses performed on **Hbimpym** and **Kbimpym**. "imid" designates the imidazolyl moiety on the ligand, "pym" the pyrimidine, "-" the side of the ligand where the negative charge is located.*

Orbital	Hbimpym	Kbimpym	bimpym$^-$
HOMO	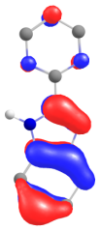	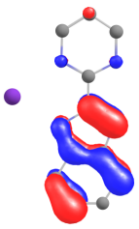	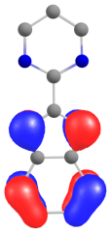
LUMO		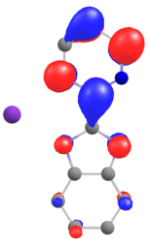	
LUMO+1	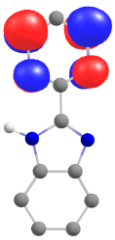	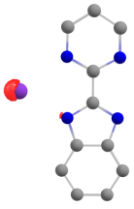	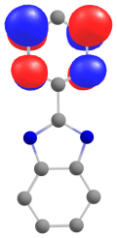
LUMO+2	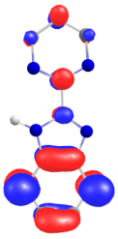	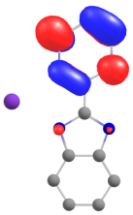	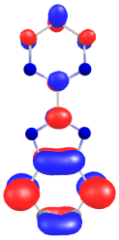

*Table 1.8: Main orbitals of **Hbimpym**, **Kbimpym** and **bimpym**$^-$ computed at the **ZORA3** level of theory.*

The role of the K^+ ion is all the more apparent when examining the electronic structure of the modelled **bimpym**$^-$ anion, which was also computed. The calculated geometry is consistent with a C_2 symmetry (the axis bisecting the ligand along the bridging C-C bond), indicative of a highly delocalised electronic density. All the frontier orbitals respect this symmetry, thus demonstrating subtle differences with **Hbimpym**, notably in the case of the HOMO and of the LUMO.

The electronic structure of all three computed species hint at the potential reactivity of the ligand upon the reduction by an organolanthanide fragment. Electronic density would be transferred mainly on the bridging C-C bond and on the pyrimidine moiety. If consistent with previously established effects following a lanthanide-driven reduction, the bond is expected to shorten upon electron

transfer to the LUMO of the ligand.[67] The coefficients on the carbon atoms on the meta positions to the bridging carbon are most susceptible to be altered by an electronic perturbation.

Computing the (bimpym)TM(Me_2) complexes was performed in various configurations. First, the full crystal structure of **1.9** was computed at the **ZORA1** level of theory (henceforth referred to as **1.9A**, Figure 1.5A). The resulting structure, by and large, closely follows the main structural features of the crystal structure, with the exception of the aforementioned deviation of the $PdMe_2$ fragment from the ligand plane, whose effect is significantly lessened by the computations. The deviations from the standard square planar geometry are smaller, as well.

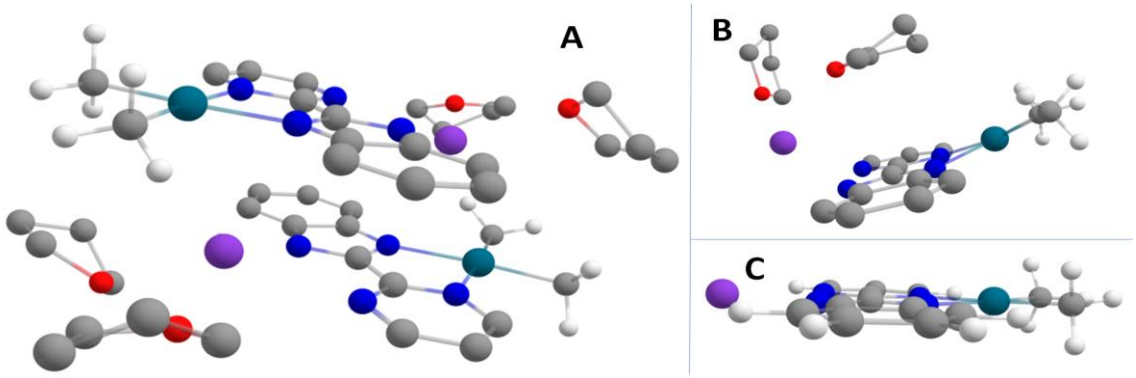

*Figure 1.5: Structure of **1.9**, computed in different configurations at the **ZORA1** level of theory.*

The second configuration was based on a single molecule, whilst keeping the solvent molecules of the crystal structure. Two such structures were computed – **K(bimpym)NiMe$_2$(B)** and **1.9B**. In both cases, the optimisation runs of the geometries (see Figure 1.5B for an illustrative example) shifted the solvent molecules above the ligand plane. The displacement of the K^+ ion is correspondingly exaggerated with respect to the crystal structure. As shown above, this is likely to entail modifications in both the polarisation of the main bonds, as well as in the orbital structure of the compounds.

The last configuration removed the solvent molecules, leading to a planar arrangement for all complexes, in good agreement with square planar geometries. The main structural features are given in Table 1.9.

	Av. Values (Å or °)		
Atoms	**K(bimpym)NiMe$_2$(C)**	**1.9C**	**1.8C**
TM-N_{pym}	1.952	2.138	2.090
TM-N_{imid}	1.960	2.144	2.109
TM-Me (avg)	1.917	2.035	2.039
K-N_{pym}	2.737	**2.747**	**2.742**
K-N_{imid}	**2.580**	**2.576**	**2.589**
C-C	1.439	1.447	1.449
d(K-plane)	**0.054**	**0.022**	**0.032**
d(TM -plane)	0.123	**0.045**	**0.009**
bimpym^$TMMe_2$	5.11	3.10	0.31

*Table 1.9: Main distances in the optimised geometries of the K(bimpym)$TMMe_2$ series of compounds, computed at the **ZORA1** level of theory. Variations in distances, with respect to the crystal structures, are colour-coded thusly: a difference of up to 0.03 Å is indicated by red if bond length is inferior to that of the crystal structure, green if superior, a difference superior to 0.03 Å is indicated by boldface.*

As could be expected, removing the solvent molecules from the vicinity of the K^+ strongly impacts its coordination environment, leading to significant discrepancies from the crystal structure. It should be noted, however, that the ligand and transition metal environments seem to be very well reproduced, regardless of the position of the K^+ ion.

The electronic structure does not change significantly along the Ni-Pt series, as the frontier orbitals are very similar to one another. In itself, the addition of the TM fragment does, however, modify the electronic density on the LUMO of the adducts. To better gauge the relative effect of the coordination of each metal, the **bimpymNiMe$_2^-$** adduct was computed. The relative contributions of the atoms on the pyrimidine moiety to the LUMOs – illustrated in Figure 1.6 – are meaningfully adjusted by the coordination of the TM fragment. The electronic density is "inverted" between the carbons on the *meta* position relative to the bridging carbon. The implication of this observation is that there would be substantial electronic density on this carbon atom in the event of an electron transfer, which was ultimately proven when reacting **K(bimpym)NiMe$_2$** with KC_8. A C-C coupling occurred on the opposite side to the nickel fragment.[34] It would seem that, contrary to the difference observed between **Kbimpym** and **bimpym$^-$**, the removal of the K^+ ion does not significantly affect the electronic structure of the adduct. This would suggest that its electronic impact is dwarfed by that of the TM.

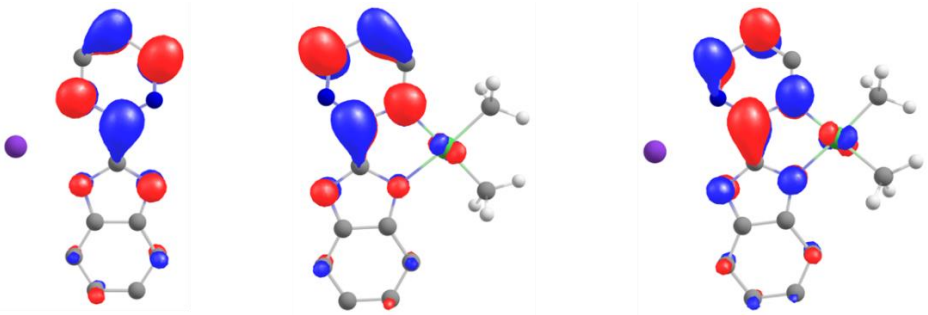

*Figure 1.6: The LUMOs of **Kbimpym**, **bimpymNiMe$_2^-$** and **KbimpymNiMe$_2$**, computed at the **ZORA3** level of theory.*

Another way to gauge the electronic structure along the series is by performing UV-visible spectroscopic analyses. An overlay of the spectra of **1.8-1.10** in THF is presented in Figure 1.7 and the results are collected in Table 1.10. The strong absorption band at λ=310-350 nm is assigned to a spin-permitted ligand-based π->π* transition, consistent with previous absorption data for complexes based on bimpym.[31] The transition is redshifted in the case of both **1.8** and **1.10** with respect to **1.9**. This implies that both minimising the perturbative effect of the K^+ ion or using a more electron-rich metal can have stabilising effects on the excited state of the complex. This is supported by the difference in the molar extinction coefficient, which is almost an order of magnitude higher in **1.8** than in **1.9**. A second band at around λ=486 nm is also present for **1.8** and can be assigned to a MLCT (metal-to-ligand charge transfer).

	1.8		**1.9**	**1.10**
λ (nm)	339	486	321	340
ε ($Lcm^{-1}mol^{-1}$)	21800	3000	3350	4100
Transition	π->π*	MLCT	π->π*	π->π*

*Table 1.10: UV-Visible data obtained for **1.8-1.10** in THF solutions.*

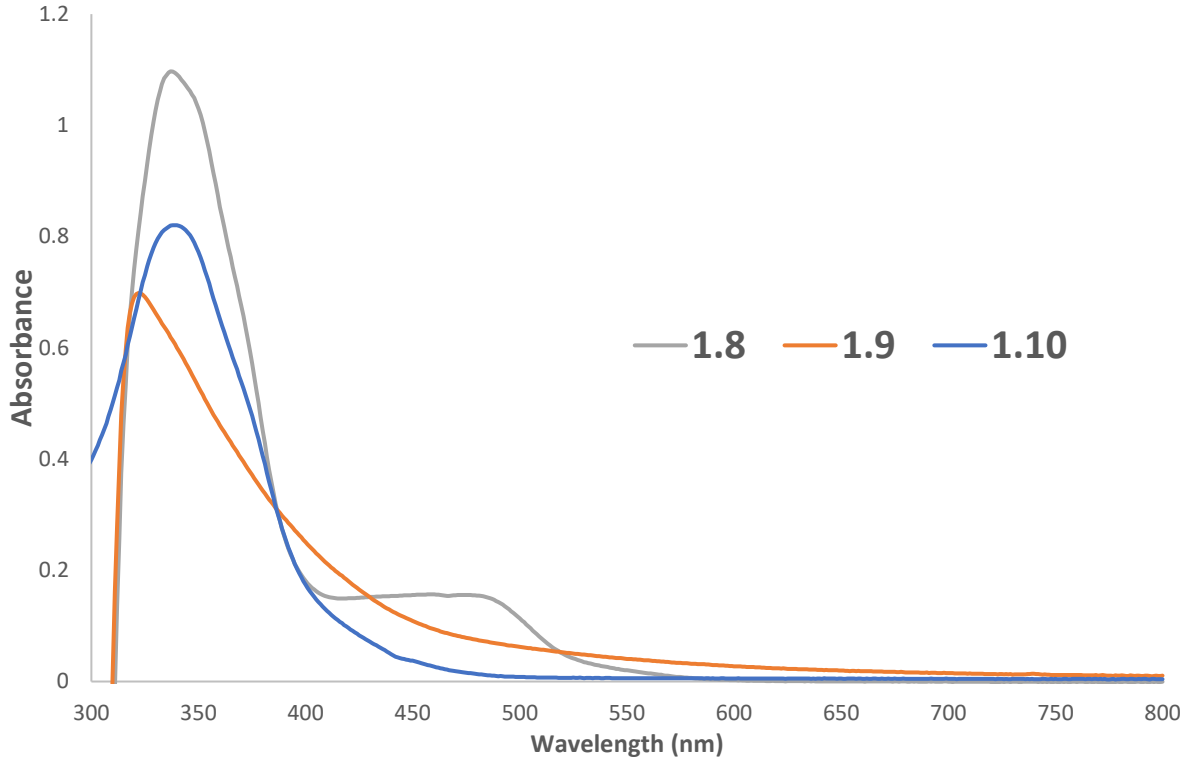

*Figure 1.7: UV-Visible spectrum of **Kbimpym**-based complexes in THF.*

1.3.4. Partial conclusion and perspectives.

The series of group 10 TM complexes with **Kbimpym** was completed following the synthesis of **1.8** and **1.9** (and its derivative **1.10**). Large-scale processes of the first two are rendered inefficient and complicated by what seems to be a degradative process.

The compounds, themselves, suffer from poor solubility, mainly due to the ligand itself. Improving its solubility would go a long way to simplifying the synthetic issues encountered for the complexes. This could be achieved by either reducing the size of the aromatic system[68] (thereby disfavouring π-stacking) or by introducing lipophilic substituents (Scheme 1.15). The latter strategy has the advantage of being based on functionalising commercially available reagents using previously described methods.[69,70]

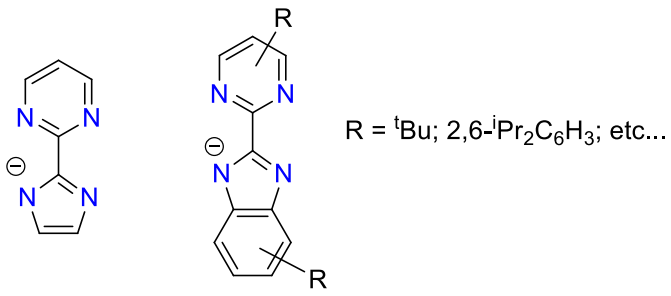

*Scheme 1.15: Target alternative options to **Hbimpym**.*

In other uses, **Kbimpym** systems may prove to be interesting, because it may allow a conceptual break with the ERC project. Rather than attempt to exploit electron-rich systems (TM centres stabilised and enhanced by the electron stored on the ligand), it could be used as a scaffold to build electron deficient

complexes, which have already found catalytic use.[71] This may be achieved by reacting **Kbimpym**-based systems with halide-bearing precursors of Ln^{III} (Scheme 1.16) – compounds familiar to our group.[72]

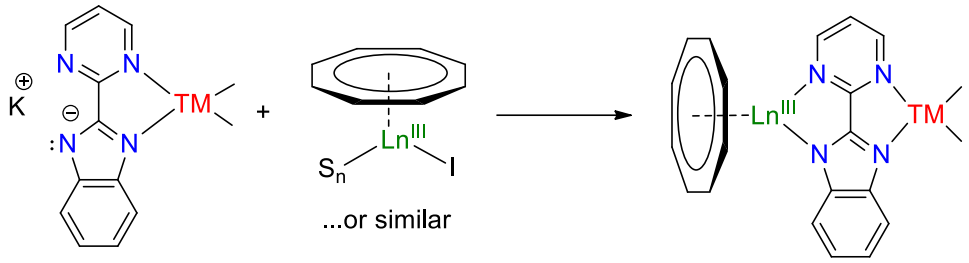

Scheme 1.16: Synthesis of novel heterobimetallic complexes.

Several preliminary *in situ* reactions were undertaken between either **1.8** or **1.9** and complexes of the formula (COT)LnI (COT = the cyclooctatetraenyl dianion). The major products were, in all cases, precipitates that were formed almost immediately, precluding further analysis. However, the supernatant, obtained following a reaction with (COT)LnI, crystallised after a few weeks, affording crystals suitable for XRD analysis. The resulting structure revealed a trimeric arrangement **1.11** of the formula $[COTSm(bimpym)]_3$, in which one ligand is lopsided with respect to its neighbours. As in the case of the **K(bimpym)NiMe$_2$** complex, the TM fragment is ejected following the coordination of the lanthanide. In contrast to the aforementioned example, no electron transfer took place, which leaves open the question of the mechanism of the expulsion of the TM fragment and of the nature of the ensuing species. Examples of metal expulsions are quite rare and usually involve a trigger – Sauvage described the removal of a ruthenium fragment from a macrocyclic complex after photochemical excitation.[73]

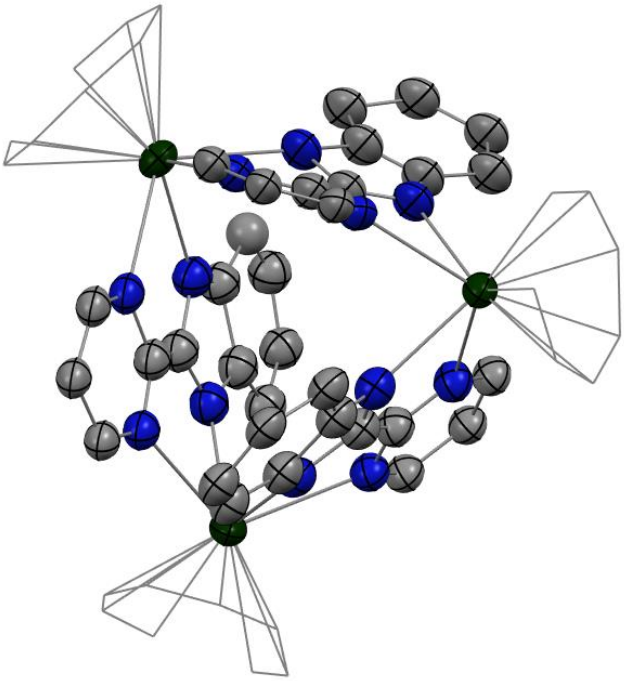

*Figure 1.8: ORTEP of **1.11**. The COT ligands are shown in wireframe to avoid clutter.*

As mentioned above, the poor solubility conferred by the ligand complicates, if not entirely prevents the characterisation of the newly-formed species. Solving this issue is crucial in order to enable future work in this regard.

1.4. bimpym-based complexes of palladium and platinum.

1.4.1. Synthesis of palladium and platinum complexes.

The synthesis of group 10 TM complexes with the bimpym ligand were undertaken, with the objective of coordinating them to the LX coordination site. Therefore, **Hbimpym** was the starting ligand. This implies, in turn, that the deprotonation of the ligand has to take place during the reaction.

Initial coordination trials were performed with (tmeda)$PdMe_2$ in coordinating solvents, such as acetonitrile or THF. Bright yellow solid was formed rapidly. ^{1}H NMR analysis only showed the signals characteristic of the unreacted ligand, as the solid formed was insoluble in the available solvents. Further characterisation of this product was hampered by the fact that the species could not be crystallised.

Dissolving this species in pyridine yielded a rich golden solution and led to an intense gaseous evolution. Diffusion of pentane in the pyridine solution at room temperature produced crystalline yellow blocks overnight. The XRD analysis allowed the identification of this product as (bimpym)PdPyrMe (**1.12**, see Scheme 1.17). The coordination of the Pd to the LX site is evident – one methyl group departs and is replaced by pyridine – an L-type ligand. The availability of the LX site presupposes deprotonation, which would, therefore, be consistent with the departure of methane during the formation of the complex.

The same product could be obtained by either adding a few drops of pyridine to the reaction mixture described above or by directly performing the reaction using pyridine as the solvent (Scheme 1.17). The latter procedure is the most efficient, as the product can be obtained in very high yields (up to 90%) by precipitating the product with pentane. Washing the solid with Et_2O is necessary to remove any excess of the (tmeda)$PdMe_2$ precursor.

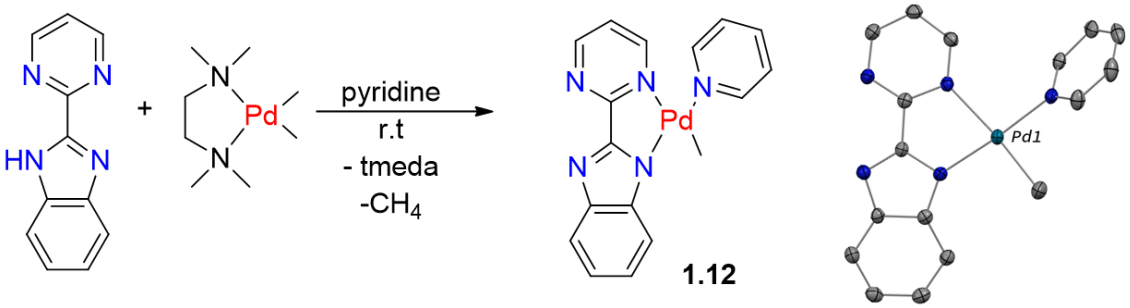

*Scheme 1.17: Synthesis and ORTEP of **1.12.***

Once crystallised or precipitated, the complex could only be redissolved in THF-d_8 in order to obtain ^{1}H NMR spectra. This procedure tended to be very slow. The main signals of the complex were very broad, but their integration was in good agreement with the isolated structure (Figure 1.9). A curious feature of this complex was that the pyridine signals, in contrast to the ligand ones, were very sharp. This hints towards a fluxional behaviour of the pyridine in solution. To test this assertion, the volatiles were evaporated for several hours, before being redissolved in the same solvent. The intensity of pyridine signals decreased significantly and could even be removed entirely upon prolonged exposure to reduced pressure. The nature of the resulting species is unknown, as it could not be crystallised.

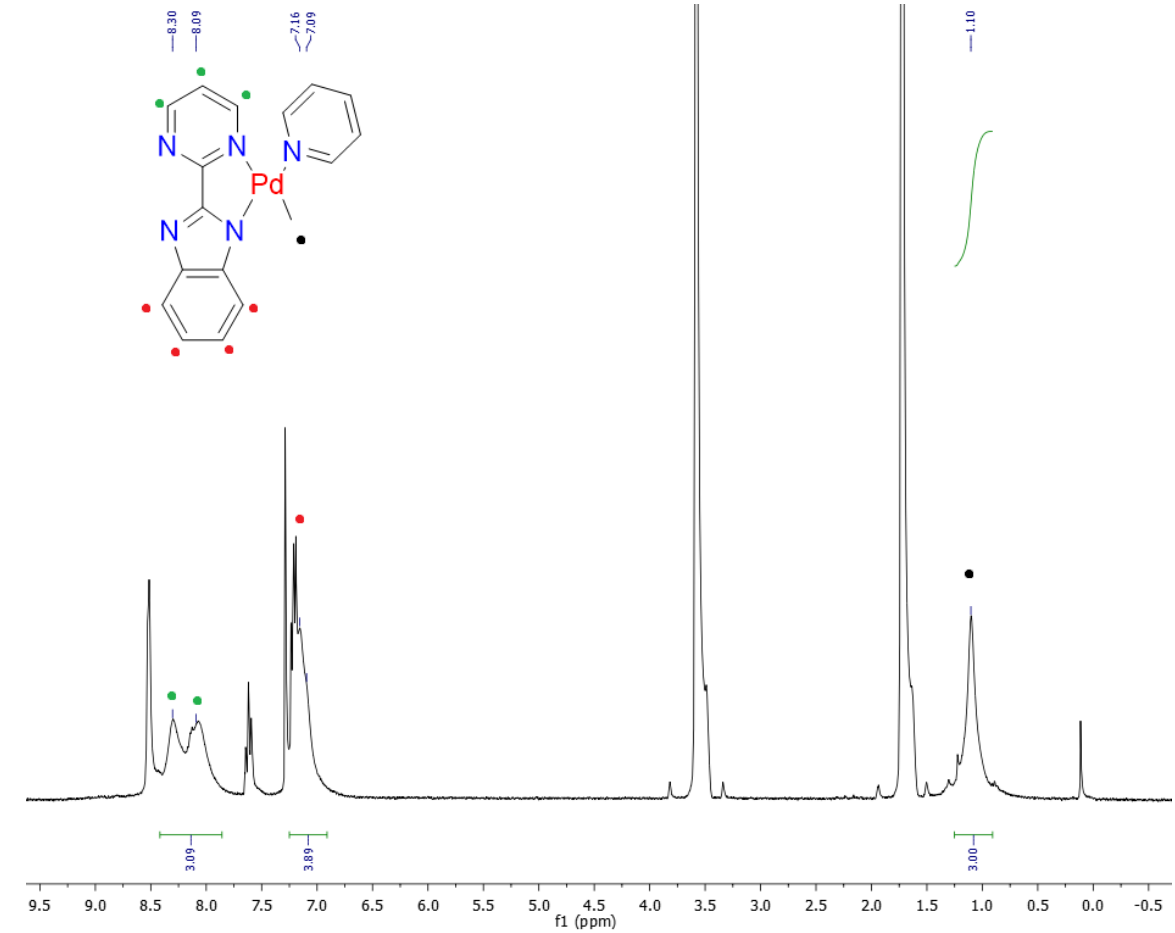

*Figure 1.9: ^{1}H NMR of complex **1.12** in THF-d_8 at 333 K.*

The reaction was also attempted in the presence of other weak bases, in order to facilitate the deprotonation of **Hbimpym**, but **1.12** was not obtained therefrom. Given that pyridine is necessary for the activation of the reaction mechanism, it is proposed that it plays the role of a prototropy-driving catalytic base that triggers the rearrangement leading to **1.12** (Scheme 1.18). Following deprotonation, the negative charge on the nitrogen is transferred to the opposite side (where the Pd is coordinated) due to the mesomeric effect.

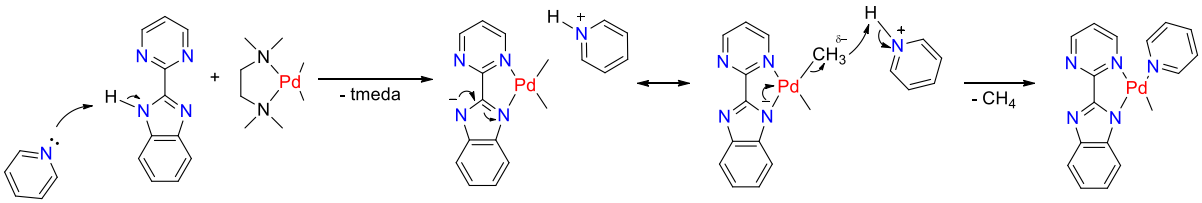

*Scheme 1.18: Proposition of the rearrangement mechanism leading to **1.12**.*

The corresponding syntheses with the Pt precursor presented a different evolution. The straightforward reaction in pyridine gave a yellow-orange solution that afforded the isostructural (bimpym)PtPyrMe compound (**1.13**, Scheme 1.19). The procedure is very similar to that described above, with the primary difference being that the gaseous evolution responsible for eliminating methane is not easily noticed. It would appear that the reaction is slower than in the case of **1.12**. Elseways, an identical work-up equally yields the pure complex in very high yields.

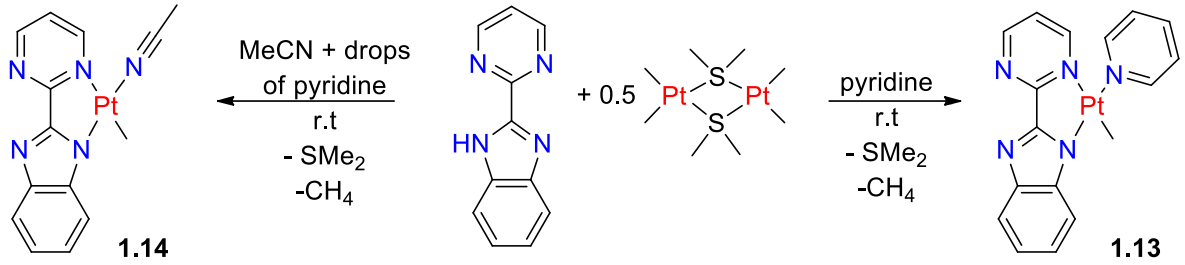

*Scheme 1.19: Synthesis of Pt-based bimpym complexes **1.13** and **1.14**.*

Conversely, performing the same reaction in acetonitrile with a few drops of pyridine gave a crimson solution. Following evaporation of the volatiles, diffusing pentane in a pyridine solution resulted in the growth of crystals of **1.14** (Figure 1.10). It would, therefore, appear that the reaction mechanism closely follows that of **1.12**, but acetonitrile is either preferentially coordinated (due to the large excess) or is able to replace pyridine in the coordination sphere of the complex. Both of these hypotheses are corroborated by the presence of an uncoordinated pyridine molecule in the crystal structure of **1.14**.

As can be evidenced by the main structural parameters in Table 1.11, the TM bond distances between the two coordinating nitrogen atoms on the bimpym ligand are dissymmetrical, a fact which can well be explained by the superior electrostatic interaction between the metal and the nitrogen of the imidazole site, due to the higher local charge concentrated at that atom. Otherwise, the small difference in the Pt-N_{pym} distances between **1.13** and **1.14** can be attributed to steric repulsion imposed by the pyridine moiety (as illustrated by the ~60° deviation with respect to the ligand plane).

	Av. Values (Å or °)		
Atoms	**1.12**	**1.13**	**1.14**
TM-N_{pym}	2.176(2)	2.152(4)	2.122(4)
TM-N_{imid}	2.034(2)	2.023(4)	2.001(3)
TM-N_L	2.040(2)	2.022(4)	1.961(3)
TM-Me	2.022(3)	2.033(6)	2.048(4)
bimpym^L	60.68	61.94	

Table 1.11: Main distances and angles in the crystal structures of the bimpym-based complexes of Pd and Pt. "L" designates the L-type ligand coordinating the TM centre.

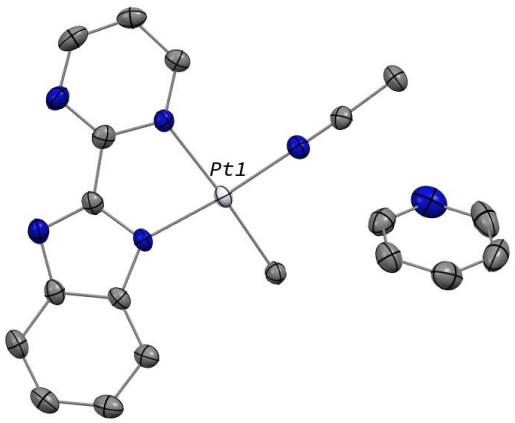

*Figure 1.10: ORTEP of **1.14**. The pyridine molecule co-crystallises with the complex. The hydrogen atoms are omitted for clarity.*

1.4.2. Electronic structure of the compounds. Analysis.

The occupation of the LX coordination site by the TM fragments of the complexes described in this section, as opposed to the L_2 site in Chapter 1.3, is assumed to entail variations in the electronic structure. The differences could provide a predictive platform as to the future reactivity with divalent lanthanides.

In order to answer this query, theoretical computations were performed on the three complexes described in this section. All three structures were optimised at the **ZORA1** level of theory. The main features of the crystal structure geometries are very well reproduced.

The examination of the electronic structure revealed virtually identical main orbitals for the isostructural **1.12** and **1.13**. The L-type ligand seems to have little influence on the occupied frontier orbitals, which mostly present antibonding interactions between the d-orbitals of the TM and the bimpym orbitals. Its main contribution is manifested in the form and the energies of the vacant orbitals (Table 1.12). In the case of **1.14**, the LUMO and LUMO+1 are quite similar to those seen in Chapter 1.3 – transferring an electron to this orbital would result in the similar accumulation of electronic density on the pyrimidine moiety. This type of orbital shall henceforth be shortened to **LUMO^{pym}**.

Orbital	1.12	1.14
HOMO	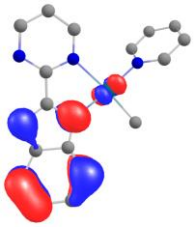	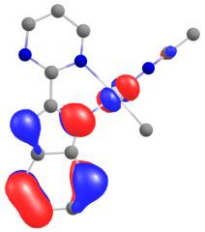
LUMO	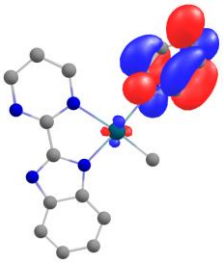	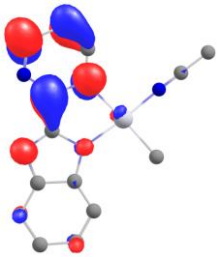
LUMO+1	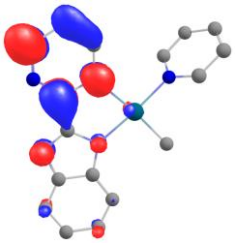	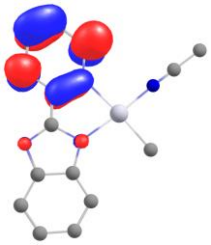
LUMO+2	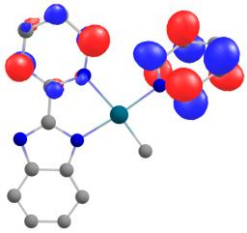	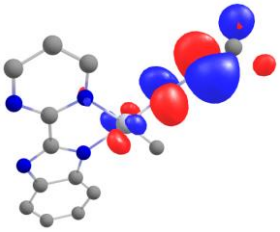

*Table 1.12: Preview of main orbitals of bimpym-based complexes of Pd and Pt, computed at the **ZORA3** level of theory.*

The corresponding orbitals in **1.12** and **1.13** is the LUMO+1, whilst LUMO+2 and LUMO+3 are both antibonding orbitals hybridised across the pyridine and the pyrimidine (**LUMO^{pym+L}**). Interestingly, the

LUMOs of these complexes are π* anti-bonding orbitals localised mainly on the pyridine moiety, with a minor contribution from the metals. This type of orbital shall from hereon in be shortened to **LUMO^{L}**.

The shape of the LUMO on the pyridine-based complexes is quite surprising. One would not necessarily expect reactivity to be promoted via a relatively labile L-type ligand. Displacement of such ligands in catalytic cycles is quite common.[74] In order to compare our findings with known examples, a brief survey of the literature was conducted.* In the case of a majority of matches, the ligands play spectator roles, with insignificant, if any contributions at all to the frontier orbitals.[75–79] The group of Sadler described photoactivatable ruthenium systems with pyridine-based L-ligands, that would decoordinate upon excitation with UVA or white light, generating reactive species.[80] One of the sole counter-examples arose from a description of [(bipy)Pd(R-py)]$^{2+}$ species, where the LUMO+1 and LUMO+2 were anti-bonding orbitals mainly delocalised on the L-ligand (with a small contribution from the Pd centre on the former).[81]

Another common feature to all of these complexes is an antibonding orbital involving the metal centre and all of the ligands in its coordination sphere – henceforth designated as **LUMO^{ab}**, illustrated in Figure 1.11. It is immediately above the pyridine-pyrimidine based orbitals in **1.12** and **1.13** (LUMO+4) and even farther away in the case of **1.14** (LUMO+6).

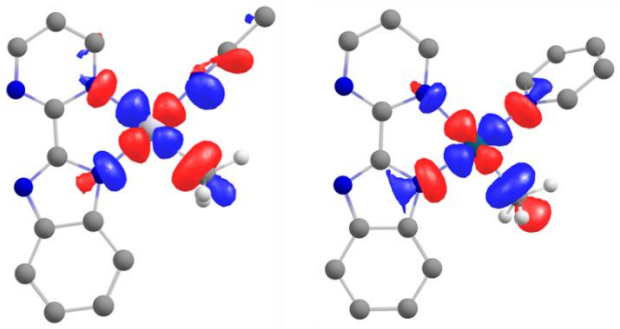

*Figure 1.11: Preview of **LUMO^{ab}** in **1.12** and **1.14**, computed at the **ZORA3** level of theory.*

Of even more pertinence is the energy gap between the HOMO and these respective orbitals. The main energy gaps are collected in Table 1.13. The main energy differences of the pyridine-bearing complexes follow each other closely – the LUMO-LUMO+1 gaps are very small and correspond to 0.44 and 0.34 eV for **1.12** and **1.13**, respectively. This would imply that two distinct reactivity pathways would be accessible upon electron transfer for both complexes. In the case of **1.14**, the energy gap between the HOMO and the pair of vacant orbitals mainly situated on the pyrimidine (its LUMO) is quite similar to the other two complexes (HOMO-LUMO+1 gap). Its LUMO+2 and LUMO+3 are anti-bonding orbitals of **LUMO^{L}**-type with more important contributions from the Pt centre. Its putative L-ligand-based reactivity pathway is much less energetically available, as the LUMO-LUMO+2 gap is 1.38 eV.

The significance of these observations remains to be seen. As shown in numerous instances, the coordination of divalent lanthanides is quite likely to alter the electronic structure of the ligand.[1,53]

* Due to the vague nature of this query, examples were collected by identifying TM complexes coordinated to redox-active (in most cases, N-heterocyclic compounds) bi- or tridentate ligands with simple accompanying co-ligands, such as pyridine or THF and their derivatives. The results (upwards of 150 complexes) were collected and the articles, as well as the citing literature, was filtered for inclusion of theoretical computations. A sample size of 20 articles was obtained. The quality of the data extracted was highly dependent on the available material in the articles.

Compound / Energy gap	**1.12**	**1.13**	**1.14**
HOMO-LUMO	3.34	3.34	3.70
LUMO-LUMO+1	0.44	0.34	0.29
LUMO-LUMO+2	0.54	0.56	1.38

*Table 1.13: Main orbital energies and energy gaps for the bimpym-based complexes of Pd and Pt. All energies are computed at the **ZORA3** level of theory. All energies are given in eV.*

To gauge whether this unusual influence of the L ligand on the electronic structure is correlated to the nature of the ligand itself, a series of complexes bearing various ligands, based on the **1.12** framework, were computed at the **ZORA1** level of theory (Table 1.14). The chosen co-ligands were meant to probe the influence of the HSAB character of the coordinating atom, of the ligand aromaticity and of steric hindrance.

The resulting compounds can be divided in 5 categories. Ligands that induce the same type of behaviour as pyridine predictably include its direct derivatives, such as phosphorine (analogous to pyridine, with a phosphorous atom instead of the nitrogen) and pyridazine, as well as the aromatic 5-membered ring thiophene (the sole caveat is that the **LUMO^{L}** therein contains non-negligible participation from the neighbouring atoms). Bipy is computed to coordinate in an η^1 fashion and the two rings are twisted due to the steric hindrance of the nearby hydrogens (Figure 1.12). Surprisingly, the LUMO of the acetone complex also prominently involves electronic density on the ligand. The common denominator of this group is the presence of a π system: the stabilisation due to the extension of the π system is a potential argument justifying the comparable behaviour.

The influence of the ligand on the electronic structure is inferred on the basis of the order of the orbitals. A second group – whose behaviour is similar to that of **1.14** – is therefore established. The electronic structure of **1.14** is reproduced with Pd, as is the case when the ligand is PPh_3.

The third group includes a number of different categories of ligands. L-type ligands based on double bonds – ethylene, COD (which, after geometry optimisation, is coordinated through a single double bond), heteroatom-based ligands (water, dihydrogen sulphide, phosphine, carbon monoxide) and one aromatic ligand – furan. All of these present at least one well-defined **LUMO^{L}** orbital, but it is even further away from the frontier orbitals than the previous complexes. The difference between the electronic influence of essentially isostructural ligands – furan and thiophene – can be explained using HSAB principles, given that Pd^{2+} is a soft acid, therefore more compatible with a softer donor atom. This situation holds, despite the fact that the thiophene plane is more twisted from the axis of the Pd-S bond than the corresponding Pd-O bond, which would limit orbital overlap (Figure 1.12).

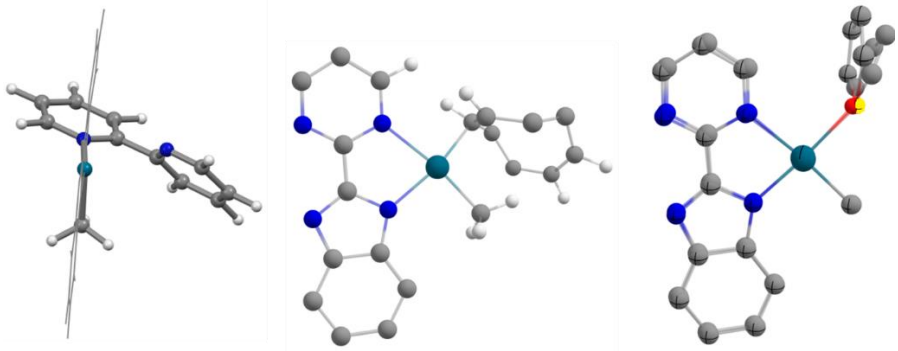

*Figure 1.12: Computed complexes analogous to **1.12** with bipy (left), COD (centre) and the overlay (right) between thiophene (the S atom is in yellow and the others are crossed) and furan (atoms not crossed). All complexes were computed at the **ZORA1** level of theory.*

The following group, comprising ammonia, as well as unconjugated O-bound systems, show no influence of the L ligand to the vacant frontier orbitals. The same HSAB rationale can be applied to the phosphine-ammonia pair to explain the difference in behaviour.

Lastly, two ligands were probed to study the behaviour of ligands that have either an electron hole (borane) or are strongly π-accepting (carbon dioxide). Electron transfer in these two complexes would first result in the population of bonding orbitals.

	Ligand	LUMO order	LUMO order	Ligand	
Pyridine-type	Acetone	L*, pym, ab	Pym, ab, L*	CO	Lesser influence
	bipy	L*, pym, L-pym, ab	Pym, ab, L*	COD	
	Phosphorine	L*, pym, L-pym, ab	Pym, ab, L*	$H_2C=CH_2$	
	Pyridazine	L*, pym, ab	Pym, ab, L*	Furan	
	Thiophene	L*, pym, ab, L*	Pym, ab, L*	H_2S	
MeCN-type	MeCN	Pym, L*, ab	Pym, ab, L*	PH_3	
	PPh_3	Pym, L*, pym, L*(3), ab	Pym, ab, L*	Water	
Acceptors	Borane	L, pym, ab	Pym, ab	Ammonia	No effect
			Pym, ab	Et_2O	
	CO_2	L, pym, ab, L*	Pym, ab	Me_2O	
			Pym, ab	THF	

*Table 1.14: Main characteristics of the frontier orbitals for the computed **(bimpym)Pd(L)Me** complexes, obtained at the **ZORA1** level of theory. "pym" designates the **LUMO^{pym}**-type orbitals, "L" the **LUMO^{L}**-type orbitals and "ab" the **LUMO^{ab}**-type orbitals, "Acc." stands for acceptors.*

A closer inspection at some of the complexes would imply that the finer features of the electronic structure can be tuned. Two of the more salient examples are chosen: bipy and pyridazine (Figure 1.13). The pyridazine ligand stabilises the complex more than its pyridine analogue, as evidenced by the smaller HOMO-LUMO gap (again, the magnitude varies between functionals, whilst respecting the trend). Moreover, the closest **LUMO^{pym}**-type orbital becomes less accessible, being substituted by another **LUMO^{L}** orbital. The **LUMO^{L}-LUMO^{pym}** gap becomes 1.08 eV, as opposed to circa 0.43 eV in **1.12**.

The same scenario occurs in the bipy analogue. However, due to the enhanced conjugation of this ligand, the subsequent orbitals are much closer in energy to each other. As such, the LUMO-LUMO+4 gap is only 0.94 eV. This could imply that a wider range of reactivity is available after a strong perturbative event (such as the coordination of a lanthanide and an electronic transfer).

Obtaining such complexes, however, is contingent on the possibility of either substituting the pyridine in the coordination sphere of the complexes **1.12** or **1.13**, or on the activation of the formation mechanism of the complexes in another way. The former was shown to be possible, following tests performed on **1.12**: dissolving the complex in THF-d_8, followed by evaporation of all the volatiles for several hours allowed removing the pyridine (as confirmed by ^{1}H NMR). No crystals could be obtained, precluding a full characterisation of the resulting compound.

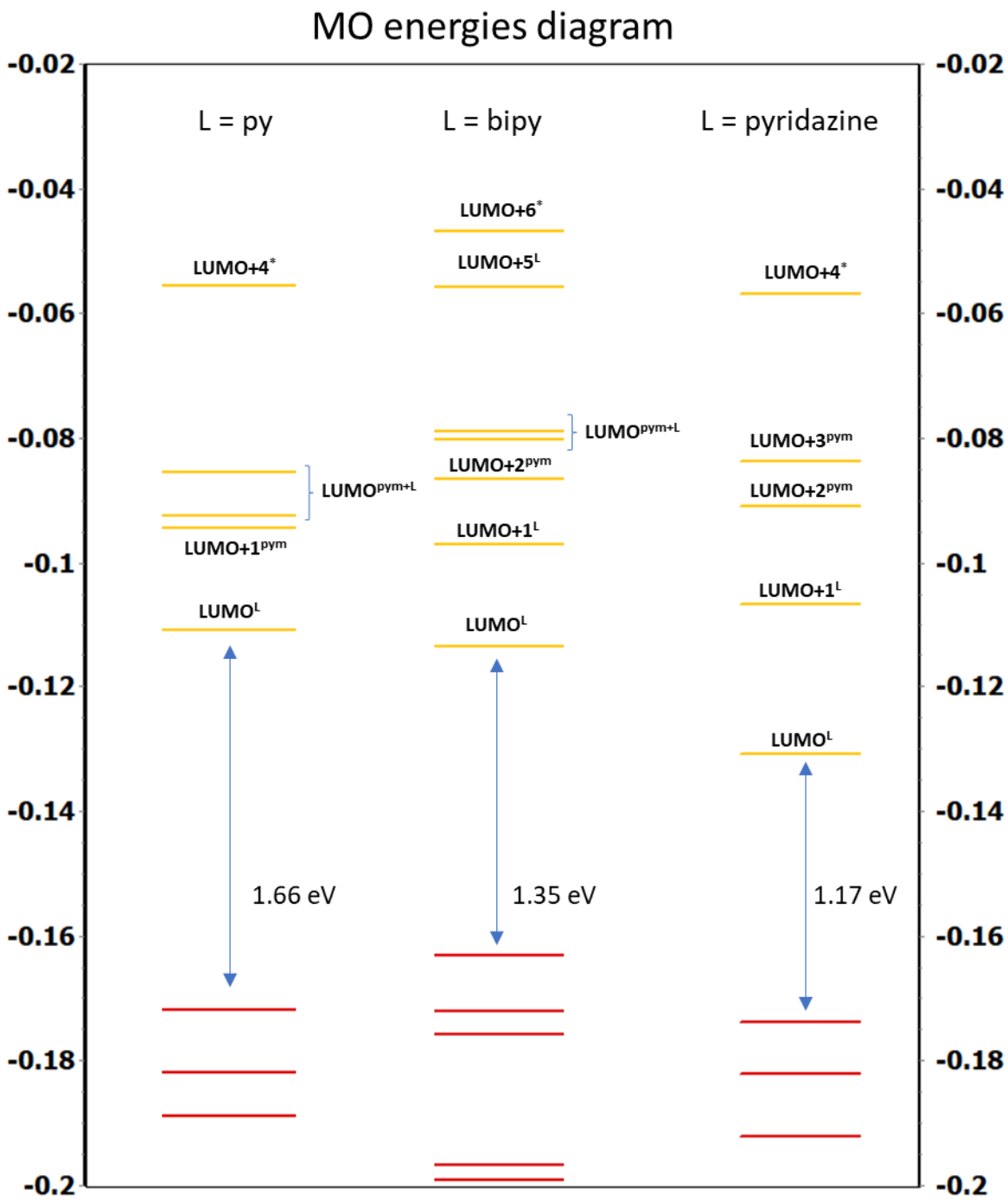

*Figure 1.13: MO energy diagram (in Eh) for **1.12** and the corresponding pyridazine and bipy analogues, computed at the **ZORA1** level of theory. The red and yellow dashes indicate occupied and vacant orbitals, respectively.*

1.4.3. Partial conclusion.

The synthesis of bimpym-based complexes of Pd^{2+} and Pt^{2+} aimed to explore the effect of coordinating the metal centres on the LX site of the bimpym ligand. Three such compounds were synthesised and characterised. The presence of the anionic ligand expels one of the methyl moieties, making room for a solvent molecule – an L-type ligand.

The examination of the electronic structure highlighted the unusual influence of the pyridine, which has the most significant contribution to the LUMOs of both **1.12** and **1.13**. Subsequent orbitals involve the pyrimidine moiety on the bimpym ligand. The marked contrast between the pyridine-based complexes and **1.14** is manifested in the different frontier orbitals. The significant energy gaps at play in the aforementioned complexes would suggest that, following the addition of organolanthanide fragments, different reactivity can be accessed.

A theoretical study seems to confirm the influence of the ligand in the modulation of electronic properties. Two extreme behaviours were observed. For several unconjugated ligands, no impact on the frontier orbitals was observed. This seems to be due to their inability to extend the low-lying π system of the organometallic system.

On the opposite end, highly conjugated, aromatic systems are able to mimic the behaviour of the pyridine. Ligand-based orbitals were found in all such cases. Moreover, it was shown that careful choice of the ligand permits a finer alteration of the electronic structure. Promising as they may be, the translation of these findings in real-life scenarios depends on the ability to replace the pyridine ligand in these complexes. So far, only the fluxional behaviour of pyridine was observed.

The obvious next steps, as shall be seen in the following chapters, is the addition of organolanthanide fragments to these complexes, which should provide the clearest indication of the behaviour or such species upon reduction.

1.5. bimpym-based Ir complexes.

Our choice of precursors in the form of the iridium(I) cyclooctadiene chloride dimer and the iridium(III) $[Cp^*IrCl_2]_2$ dimer provides an excellent platform to test the addition of both **Hbimpym** and **Kbimpym**. Due to the presence of the Cl^-, the reaction should be driven by virtue of the formation of KCl as a by-product. The COD and Cp* co-ligands should help with the previously experienced solubility issues of the bimpym ligand.

1.5.1. Single ligand complexes.

1.5.1.1. Syntheses and characterisation.

Each of the precursors was reacted with both **Hbimpym** and **Kbimpym**. The syntheses were initially carried out in THF. In the case of the crimson Ir^{I} dimer, dark purple and bright red suspensions were rapidly formed upon addition of **Hbimpym** and **Kbimpym**, respectively. In both cases, the product seemed to be very poorly soluble in THF. Evaporation of the crude fractions and redissolution in DCM greatly improved the solubility. Subsequent filtrations resulted in dark purple and red solutions.

The same outcomes were observed using the Ir^{III} dimer. The reaction in THF rapidly yielded pale yellow and golden suspensions after the respective additions of **Hbimpym** and **Kbimpym**. The subsequent redissolution in DCM similarly afforded significantly higher solubility. Further iterations of the syntheses were directly performed in DCM (Scheme 1.20). Both reactions involving **Kbimpym** resulted in the precipitation of insoluble white solid, consistent with the expected salt formation.

In all cases, the procedure that yielded the best single crystals involved storing the saturated DCM solutions for several days at room temperature. Crystals of excellent quality were grown in all cases, allowing the identification of the compounds as (Hbimpym)IrCODCl (**1.15**), (bimpym)IrCOD (**1.16**), [(Hbimpym)IrCp*Cl]Cl (**1.17**) and (bimpym)IrCp*Cl (**1.18**). The crystal structures are presented in

Figure 1.14. In the cases of the complexes with the protonated ligands, the data was of sufficient quality to allow the clear-cut identification of the proton.

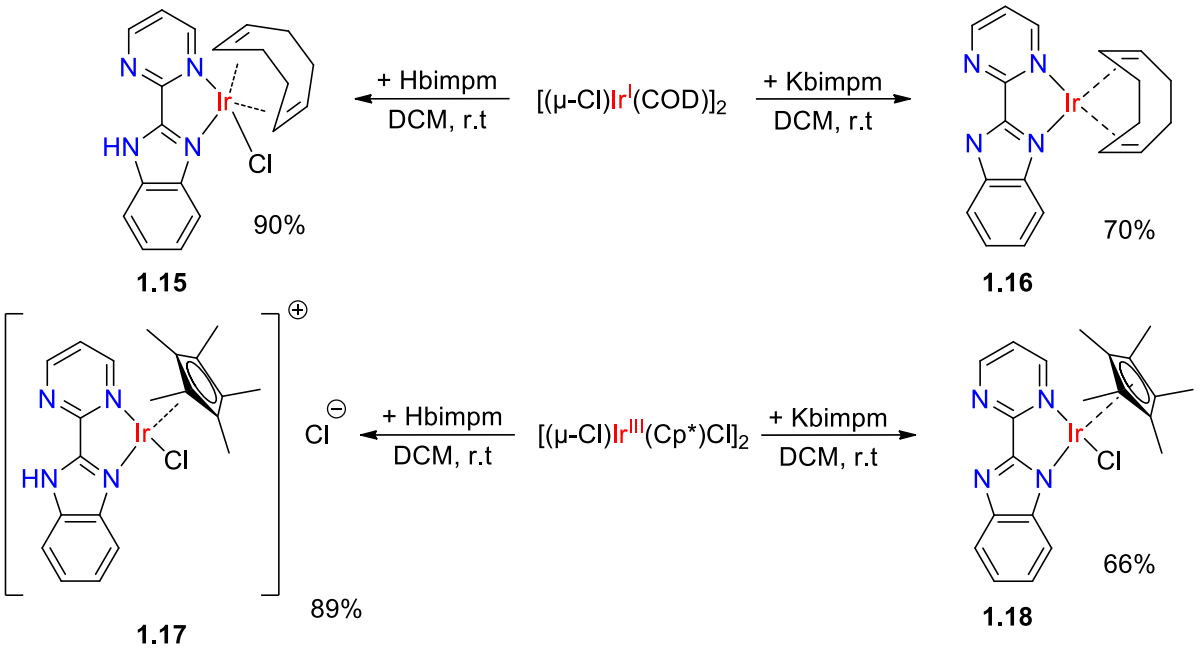

*Scheme 1.20: Synthesis of Ir-based bimpym complexes **1.15**-**1.18**.*

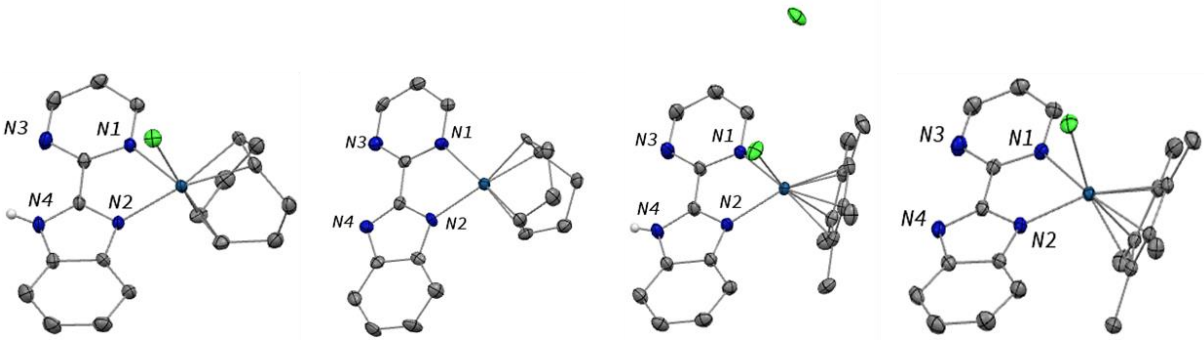

*Figure 1.14: ORTEP of complexes **1.15**-**1.18**. All the hydrogen atoms (except for the ligand proton in **1.15** and **1.17**) are omitted for clarity. The labelling on the nitrogen atoms is adopted for the rest of the section.*

For **1.16** and **1.18**, the formation of KCl was, in itself, a strong indication of the occupation of the LX site by the Ir centre. This was, naturally, confirmed, following the elucidation of the structures. This can also be observed by analysing the main structural features of the four complexes. A pertinent comparison should be pre-empted by highlighting the quite different coordination environments for all the complexes: **1.15** and **1.16** are classified as $[IrL_4X]$ and $[IrL_3X]$, whilst **1.17** and **1.18** are $[IrL_4X_2]$ and $[IrL_3X_3]$ – the Cp* co-ligand is classified as L_2X. The formal coordination numbers are 5 for **1.15**, 6 for **1.17** and **1.18**, whereas it is 4 for **1.16**. Lastly, the bulky Cp* ligand is likely to impose supplementary steric constraints with respect to the more flexible COD.

With that in mind, on the basis of inter-ligand distances, neither the oxidation state of the Ir, nor its co-ligands seem to make a significant difference to the ligand environment. The lengths of the C-C bond bridging the two moieties are within 0.015 Å of one another. In a similar vein to the study of the (Kbimpym)TM(Me_2) series in Chapter 1.3, the C-N bond lengths (numbering scheme shown in Figure 1.14) reflect the polarisation due to the accumulation of the negative charge on the ligand.

	Av. Values (Å or °)			
Atoms	**1.15**	**1.16**	**1.17**	**1.18**
C_1-C_2	1.453(5)	1.458(7)	1.452(3)	1.450(3)
Ir-N_1	2.212(3)	2.108(4)	2.1163(17)	2.0736(15)
Ir-N_2	2.054(3)	2.048(4)	2.1054(17)	2.1251(15)
C_1-N_1	1.355(4)	1.361(6)	1.356(3)	1.353(2)
C_1-N_3	1.323(5)	1.327(6)	1.327(3)	1.332(2)
C_2-N_2	1.323(4)	1.368(6)	1.327(3)	1.355(2)
C_2-N_4	1.347(5)	1.324(6)	1.342(3)	1.331(2)

*Table 1.15: Main distances in complexes **1.15**-**1.18**.*

The C_2-N bond corresponding to the nitrogen formally holding the negative charge is longer than the opposite one. On the pyrimidine side, however, the C_1-N_1 bond (the atom bonding the Ir) is always longer than C_1-N_3. As for the Ir-N bonds, there is no clear trend across the series. The relative difference in the bond lengths in the Ir^{I} complexes is more likely to be explained by the steric constraints imposed by the different coordination environments (square planar vs trigonal bipyramidal). Seeing as there are no other differences in the Ir coordination sphere, shifting between the L_2 and LX coordination sites in **1.17** and **1.18** explains the modifications in the Ir-N bond lengths, although the Cl^- counter-anion in **1.17** could play a role, as well.

As for the previously described precursors, theoretical computations were also performed on complexes **1.15**-**1.18**. For the most part, the calculations managed to reproduce the main features of the crystal structures. The sole exception is the coordination sphere of the Ir^{I} in **1.15**, which shifts to an η^1 coordination mode (on the imidazolyl moiety) with respect to the bimpym ligand. This is likely due to the higher stability conferred by a square planar geometry. This affects the electronic environment on the pyrimidine moiety.

The unfaithful computational reproduction of the geometry in the case of **1.15** renders moot any precise investigation into its electronic structure. There is some insight that can be gathered, though, as exemplified by a selection of orbitals. The chloride co-ligand affects the frontier orbitals by lowering the benzimidazolyl-based orbitals.

Orbital	**1.15**	**1.16**
HOMO	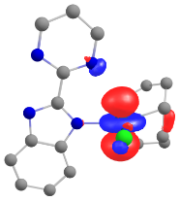	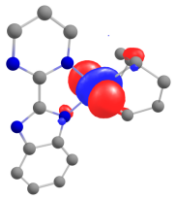
LUMO	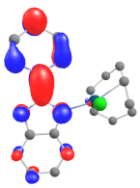	
LUMO+4	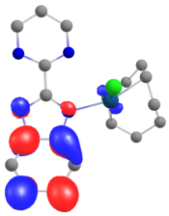	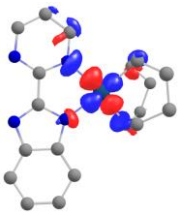

*Table 1.16: Main orbitals in complexes **1.15** and **1.16**, computed at the **ZORA3** level of theory.*

There are more ligand-based vacant orbitals available, which would be occupied in the event of an electron transfer (see LUMO+4, which would correspond to a **LUMO^{ab}**-type orbital in **1.16**). In a continuation of the observations of the effect of metal coordination, gathered in Chapter 1.3, the shape of the pyrimidine-based vacant orbitals is significantly impacted by the coordination of the Ir (see LUMO) – it is quite symmetrical in **1.15** (similar to **bimpym$^-$**, Table 1.8), but not in **1.16**.

The two differences between **1.17** and **1.18** revolve around the ligand coordination site and the presence of an outer-sphere Cl^- counter-ion. Surprisingly, it would seem that the latter also has an impact on both the symmetry and the position of the ligand-based orbitals. The first ligand-based orbital is the HOMO-6 in **1.17**, in stark contrast to **1.18**, where they compose the HOMO-HOMO-1. From the perspective of the vacant orbitals, it would appear that the Cl^- anion counteracts the impact of the coordination of the Ir, given how the LUMO and LUMO+1 (of **LUMO^{pym}** shape) differ between the two Ir^{III}-based complexes.

Orbital	1.17	1.18
HOMO	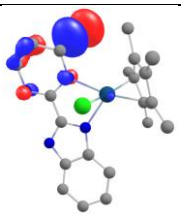	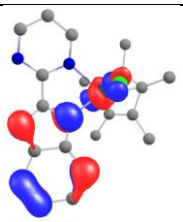
LUMO	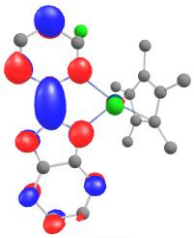	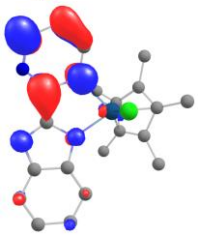
LUMO+1	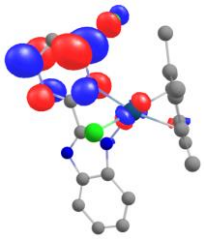	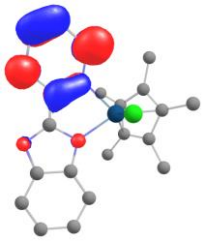

*Table 1.17: Main orbitals in complexes **1.17** and **1.18**, computed at the **ZORA3** level of theory.*

To further probe the impact of the coordination of the Ir fragments on the ligand environments, UV-Visible analyses were carried out. This comparison is particularly opportune, given that Ir^{I} and Ir^{III} are each coordinated to both the LX and L_2 sites on the ligand. Therefore, the impact on the electronic structure of the coordination on each site can be inferred. An overlay of the spectra of **1.15-1.18** in DCM is presented in Figure 1.15 and the results are collected in Table 1.18.

	1.15			1.16			1.17	1.18
λ (nm)	317	367	460	318	366	516	351	341
ε ($L\ cm^{-1}\ mol^{-1}$)	1200	340	150	6600	4400	360	3200	3400
Transition	π->π*	MLCT	MLCT	π->π*	MLCT	MLCT	π->π*	π->π*

*Table 1.18: UV-Visible data obtained from DCM solutions of **1.15-1.18**.*

The main absorption is attributed to a ligand-based π->π* transition in all cases. This transition is isoenergetic in the case of the Ir^{I} complexes. However, it is more than 5 times more intense in the case

of **1.16**, compared to **1.15**. This could be explained by the superior electrostatic interaction between metal and ligand (due to anionic LX site vs neutral L_2 site), which is reflected in a stronger electronic interaction between the two components. Curiously, this band is similar in both energy and intensity for the Ir^{III} complexes, which is in contrast to the situation described above. This may be due the counter-anion, which was shown to impact the molar absorption coefficients of a given transition.[82]

The most salient difference between the complexes is that two additional bands, ascribed to MLCT transitions, are only present in the case of Ir^{I} compounds. This is logical, since the electron-rich Ir^{I} is able to contribute electronic density much more effectively to the ligand than its Ir^{III} counterpart. As for the π->π* transition, these absorptions are much more intense in the case of **1.16**; this can be rationalised in the same manner as above.

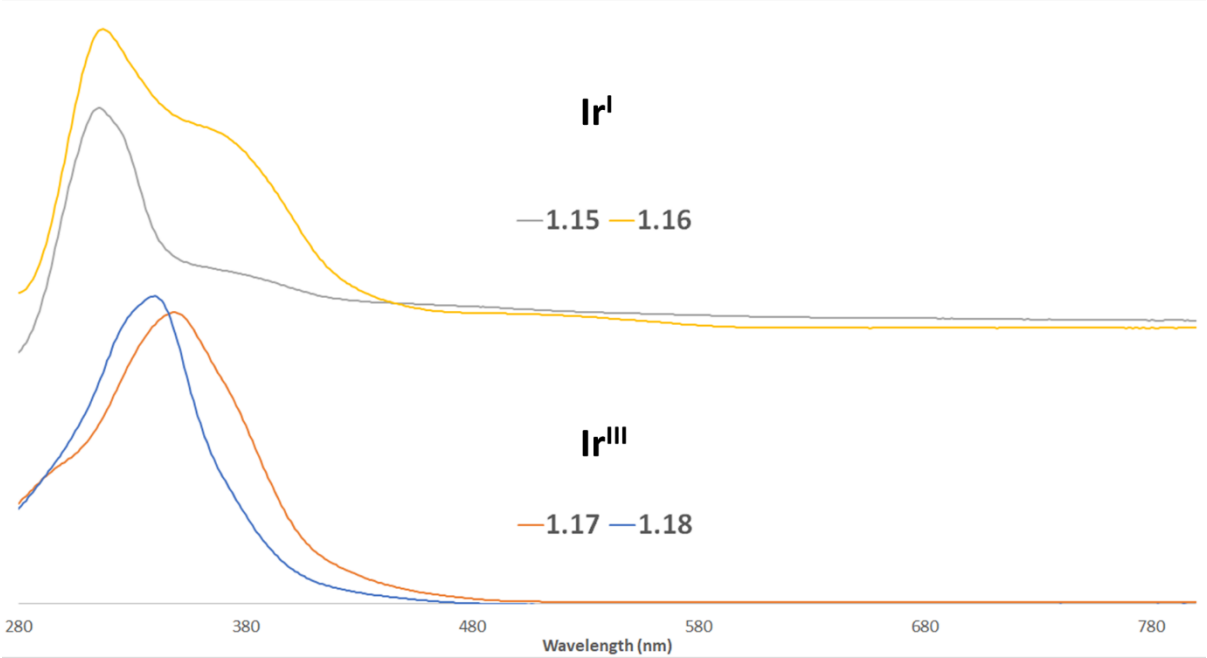

*Figure 1.15: Overlay of UV-Visible spectra of **1.15**-**1.18** in DCM.*

It was of interest whether the anionic site could be rendered more accessible for the coordination of lanthanide fragments in complexes **1.15** and **1.17**. The objective was to obtain complexes similar to the (Kbimpym)TM(Me)$_2$ series, whereby the subsequent organolanthanide fragment would target the anionic, LX site. Correspondingly, these complexes were reacted with excess KHMDS, in the hope of installing the K^+ as the counter-cation to the deprotonated LX site (Scheme 1.21). In both cases, however, the resulting complexes were **1.16** and **1.18**, respectively. In the first case, the most likely outcome is the reorganisation of the charge within the ligand via mesomeric effect, leading to the complex where elimination of KCl has occurred. Doing the reaction in the presence of the potassium trapping agent 18-C-6 did not change the outcome.

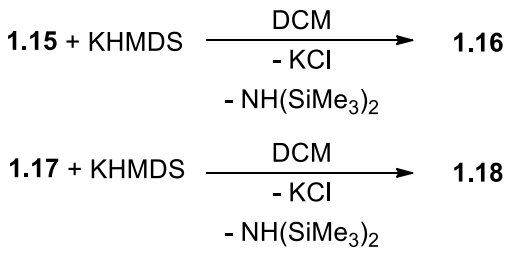

*Scheme 1.21: Deprotonation attempts of **Hbimpym**-based complexes.*

1.5.1.2. Perspectives. Preventing unwanted reactivity.

The reactivity of three of the synthesised complexes with organolanthanide fragments could be compromised by the presence of the acidic proton and/or the chloride anion. It would be worthwhile to adapt these complexes to ensure that no parasitic reactions occur.

However, given the propensity of **1.15** and **1.17** to reorganise following deprotonation discussed above, it is unclear how such a process could be prevented. Further trials with softer bases could be attempted, but are not a priority. In the case of the latter complex, the most pressing concern is eliminating the very accessible chloride anion in the outer sphere. This was achieved following salt metathesis, where [(Hbimpym)IrCp*Cl]BPh_4, bearing the innocent and weakly interacting BPh_4^- anion, was isolated (**1.19**, Scheme 1.22). In theory, the chloride in the coordination sphere of the Ir should be significantly less accessible for reactivity with a divalent lanthanide fragment. This assertion shall be tested in future chapters.

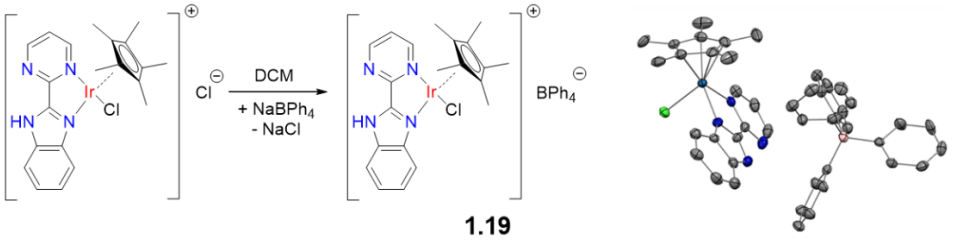

*Scheme 1.22: Synthesis and crystal structure of **1.19**.*

Another attempted solution involved reduction trials of complexes **1.15**-**1.18** with Na/Naphthalene, KC_8 and Cp^*_2Co, in the hope that the ligand could be reduced once, therefore eliminating the Cl^- ligand from the coordination sphere of the Ir centres. The rationale in the case of **1.16** was to probe whether the substrate could be reduced by complexes other than lanthanides, in a manner analogous to the one examined for the **(Kbimpym)NiMe$_2$** compound.[34] In all cases, *in situ* reactions followed by ^{1}H NMR revealed only intractable mixtures.

The remaining acidic proton is still potentially problematic. The most likely outcome after the addition of $Cp^*_2Ln(OEt_2)$ would be the protolysis of the Cp* co-ligand. Other synthetic solutions should be tested. However, significant efforts in this direction should be withheld until it is proven that the chloride in the coordination sphere of the Ir is either not harmful or can be controlled.

Conversely, maybe the presence of the acidic proton can be used to selectively trigger the departure of one Cp* co-ligand, resulting in an unsaturated coordination environment of the lanthanide. This type of configuration, where trivalent Ln metal centres were coordinated to only one Cp* group, was previously seen as a result of Sterically Induced Reductions and can result in bridging coordination patterns or inclusion of solvent in the coordination sphere.[83–85]

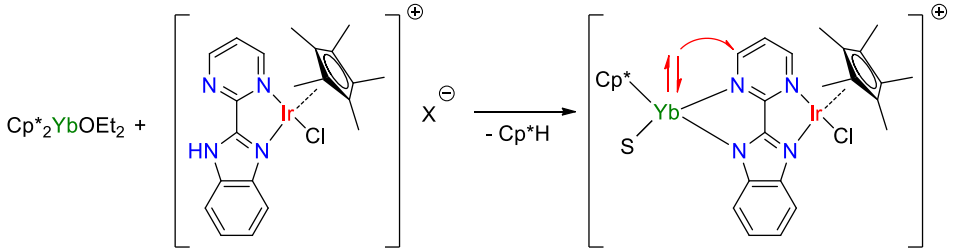

*Scheme 1.23: Proposition of reaction mechanism involving the acidic proton on structures such as **1.15**, **1.17** or **1.19**.*

Perhaps the safest bet for a frictionless reaction with divalent lanthanides would be to extract the chloride in the coordination sphere of **1.18** in favour of a non- or weakly-coordinating anion. This was attempted in a reaction with $NaBPh_4$, followed by ^1H NMR (Figure 1.16). Although no colour change was attested, the signals belonging to **1.18** were instantly shifted, indicating that a reaction had occurred. Despite our best efforts, no crystals could be grown that would confirm our assertions.

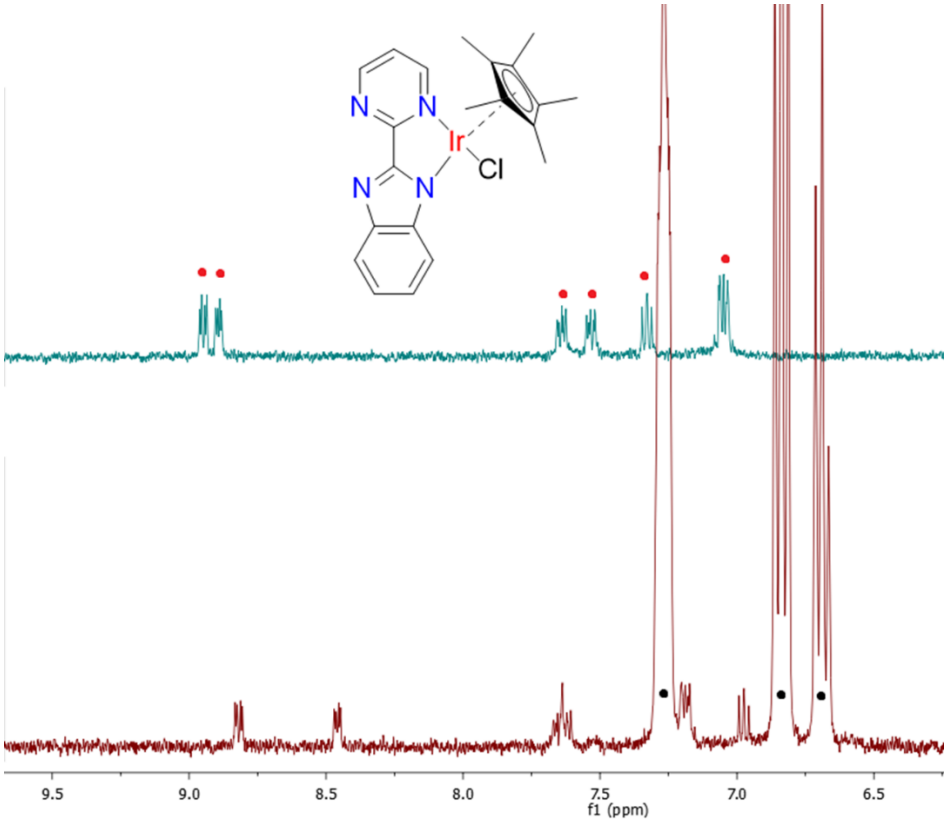

*Figure 1.16: ^1H NMR in THF-d_8 of **1.18** (above, red dots) and after reaction with $NaBPh_4$ (below, black dots indicate reagent signals) – aromatic region.*

1.5.2. Towards the preparation of iridium-based complexes bearing two RALs

1.5.2.1. Rationale.

There is both experimental[34] and theoretical proof (presented in Sections 1.4 and 1.5) for a coupling reaction on the bimpym ligand, following an electron transfer. The resulting species may be of interest, perhaps by presenting a bimetallic cavity that could be useful catalytically, but this premise is untested. The coupling reaction is not necessarily the optimum outcome, since the electronic density stored on the radical ligand is immediately used to form a C-C bond, rather than contribute to the environment of the TM.[54] As such, it may be of interest to try to prevent the coupling reaction.

One of the ways this could be achieved is by introducing substituents on the possible coupling positions. This solution should be carried out cautiously, since the simplest substituents – methyl groups – have previously proven to be a source of a different side-reaction altogether.[86]

Another perspective would be to try to reduce the transferred electronic density, concentrated in the coupling carbons, in the hope of avoiding the bond formation. This can be achieved by increasing the conjugation of the ligand's aromatic cycle by extending it. This solution would involve having a second

RAL in order to attempt to shift the electronic density, susceptible to accumulate in the C atoms on the pyrimidine moiety, towards this second ligand. As was shown in Chapter 1.4, the ligand field of (bimpym)PdPyMe (**1.12**) could quite effectively modulate the shape and nature of the frontier orbitals. The same rationale can be applied to Ir-based compounds. There is ample precedent of Ir-based edifices with multiple RALs. For example, there are 384 iridium complexes indexed in the CCDC database bearing three ligands based on the bipy architecture (most often the phenylpyridine in the interest of preserving charge neutrality).[87–89]

However, to the best of our knowledge, there is a relative paucity of similar configurations with Ir^{I}, mainly due to its preference of adopting a square planar geometry. Stabilising a species of the $Ln^{III}(bimpym^{\bullet-})Ir^{I}(L)$ configuration could be of considerable interest. Moreover, the appropriate choice of L could allow the coordination of a second equivalent of divalent lanthanide.

1.5.2.2. Preliminary studies of the electronic structure.

The abundance in Ir^{III} complexes with multiple ligands inspired an investigation into a similar compound. The **Ir(bimpym)$_3$** complex was computed. It features an octahedral geometry, with all the Ir-N_{pym} and Ir-N_{imid} bonds within 0.02 Å of each other. A series of closely packed orbitals, where the Ir 5d orbitals hybridise with the imidazole moieties of the ligands make up the occupied frontier orbitals. Each of these orbitals involve just one ligand, with minimal contributions from its vicinal ligands. Conversely, the first three vacant orbitals are of **LUMO^{pym}** shape, one for each bimpym ligand. Only LUMO+4 and LUMO+5 showed any delocalisation across more than one ligand.

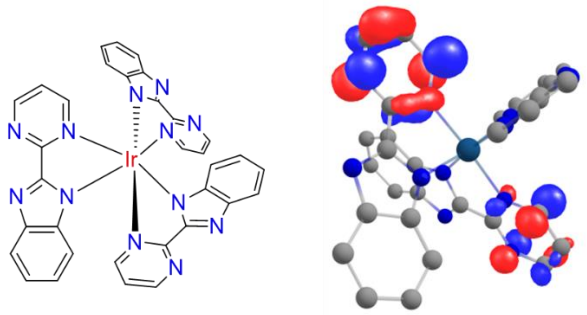

*Figure 1.17: Structure and hybridised vacant orbital of **Ir(bimpym)$_3$**.*

A series of putative Ir^{I} complexes were subsequently computed – **(bimpym)Ir(bipy)**, **(bimpym)Ir(bipym)** and **[(bimpym)$_2$Ir]$^-$**. In all cases, the geometries are best described as severely distorted square planar, due to the repulsion between the proximal hydrogen atoms on both ligands. It would appear that the two hydrogens on the pyrimidine moiety and its closest counterpart on the opposite ligand are crucial – they cannot be closer than 2 Å (Table 1.19). In all three cases, the angle formed between the two ligand planes exceeds 30° (shown in Figure 1.18). Furthermore, the two fragments of each ligand of the three complexes are slightly twisted with respect to one another (highlighted as "pym^imid" and "L distortion" in Table 1.19).

The main structural features are collected in Table 1.19. It is not surprising that the bipy and bipym complexes present nearly identical geometries. The only differences therein – C-C_{bimpym} bond length and the distortion between the two ligand fragments – are negligible. For **[(bimpym)$_2$Ir]$^-$**, the two bimpym ligands are nearly identical to one another.

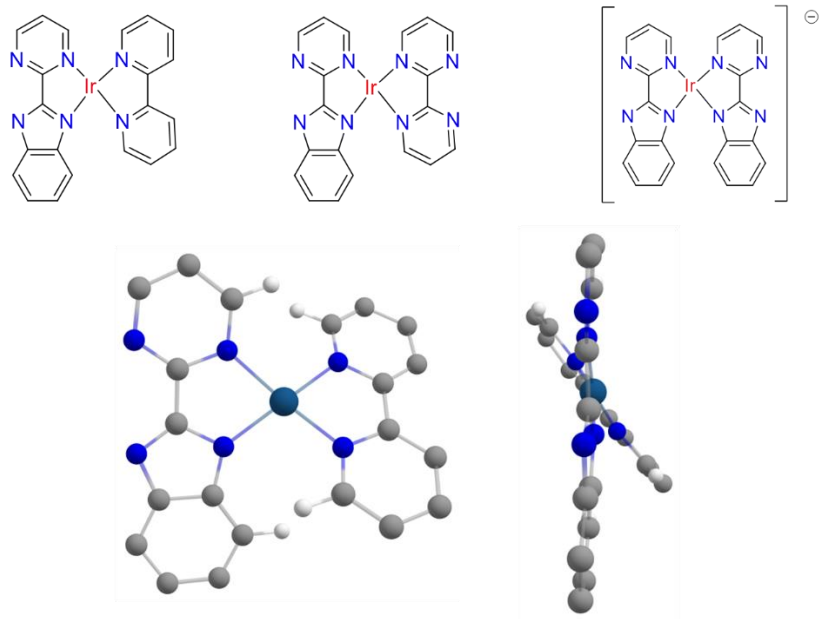

Figure 1.18: Structure of dual-ligand Ir^{I}-based complexes. Only the hydrogens on the bimpym and L that impose steric constraints are shown.

The significant steric strain observed in these three ligands is likely to affect the electronic interaction between the ligand and Ir by reducing the orbital overlap between the two components. This steric strain can be lessened with a more adequate ligand: the choice was made to deliberately build in the torsion angle by using the 3,3'-Me$_2$-bipy in the **(bimpym)Ir(3,3'-bipy)** complex, which was also computed. Previous reports containing crystal structures of this ligand had $\overline{\text{CCCC}}$ and $\overline{\text{NCCN}}$ torsion angles of around 30-40°.[3,90,91] The computed structure of **(bimpym)Ir(3,3'-bipy)** lowers the same angles to 13.5° and 25°, respectively. This accrued steric tension is counterbalanced by the fact that the torsion angle of the ligand results in the two closest hydrogens ("H_{pym}-H_L" in Table 1.19) of the opposite ligands being inherently kept apart. The angle between the two ligands is therefore less exaggerated in comparison to that of its peers.

	Av. Values (Å or °)			
Atoms	**(bimpym)Ir(bipy)**	**(bimpym)Ir(3,3'-bipy)**	**[(bimpym)$_2$Ir]$^-$**	**(bimpym)Ir(bipym)**
Ir-N_{pym}	2.036	2.048	1.999	2.038
Ir-N_{imid}	2.010	2.020	2.016	2.005
Ir-N^L_1	1.987	1.977	1.999	1.985
Ir-N^L_2	1.991	1.982	2.016	1.990
H_{pym}-H_L	2.031	2.032	2.032	2.034
H_{bim}-H_L	2.273	2.311	2.499	2.300
C-C_{bimpym}	1.442	1.441	1.441	1.454
C-C_L	1.446	1.454	1.441	1.442
pym^bim	7.22	6.18	6.56	7.25
L distortion	5.80	10.91	6.68	4.77
bimpym^L	34.59	17.28	33.11	31.95

*Table 1.19: Main angles and distances in the computed dual-ligand Ir^{I} complexes, computed at the **ZORA1** level of theory. "pym" and "bim" indicate the pyrimidyl and benzimidazolyl moieties on the bimpym, "L" indicates the ligand opposite bimpym.*

Further investigations into the electronic structure were carried out by performing computations at the **ZORA3** level of theory. The occupied orbitals are similar in nature and shape to their equivalents on other bimpym-based complexes and are not of primary interest. In all the cases, the presence of a second N-heteroaromatic ligand has a significant impact on the main vacant orbitals. The symmetry present in the **[(bimpym)$_2$Ir]$^-$** anion imposes equal contributions from each ligand for every orbital. The electron density on the individual carbon atoms, susceptible to couple, is diminished in comparison to the mono-bimpym complexes. This conclusion should be treated cautiously, as the coordination of an additional metal centre has a strong perturbative effect on the ligand orbitals. The behaviour resulting from the addition of divalent lanthanides to such a structure may or may not comply with the increased delocalisation imposed by the second ligand.

In the other three complexes, the electronic structure is modified in a different way. The vacant frontier orbitals involve dominant contributions from one of the ligands. In all cases, the LUMO is based on the other N-heterocycle ligand. The more pronounced orbital overlap due to the lesser inter-ligand angle in **(bimpym)Ir(3,3'-bipy)** may be most prominently manifested in the form of LUMO+2, which is delocalised across the two ligands, rather than concentrated on the bimpym in **(bimpym)Ir(bipy)**. The bipym seems to be more effective than its counterparts, as the vacant frontier orbitals have considerably smaller contributions from the bimpym ligand. Despite the impact of the increased conjugation on the vacant orbitals due to the second ligand, consequential contributions on the carbons susceptible to couple are present in all the computed compounds.

Orbital	(bimpym)Ir(bipy)	(bimpym)Ir(3,3'-bipy)	(bimpym)Ir(bipym)
LUMO	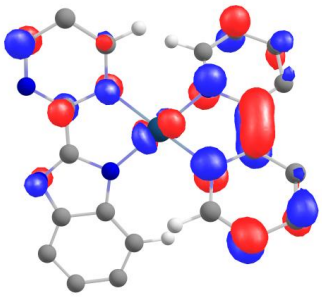	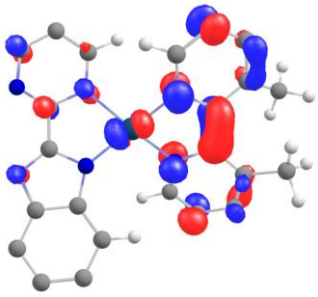	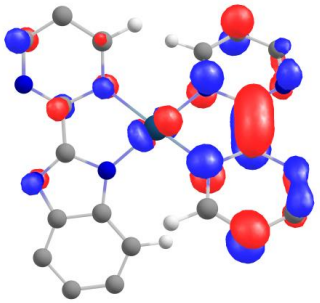
LUMO+1	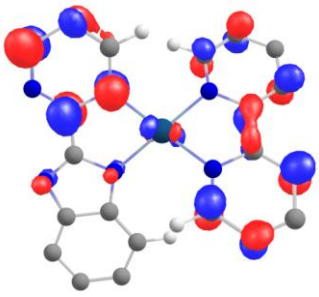	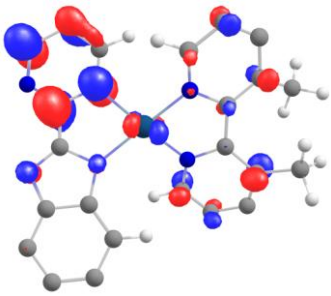	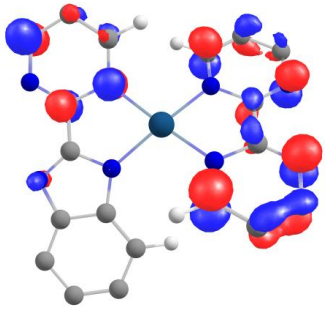
LUMO+2	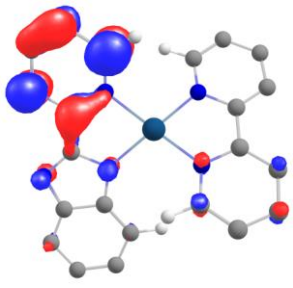	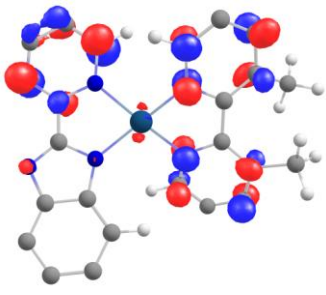	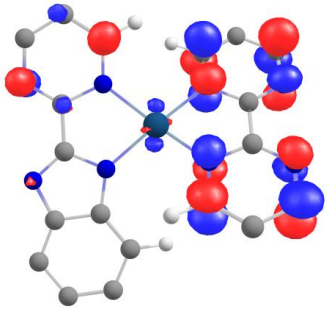

*Table 1.20: Main orbitals of the computed dual-ligand Ir^I complexes, computed at the **ZORA3** level of theory.*

The deviation of the optimised geometry of **1.15** with respect to its crystal structure, where the bimpym ligand was monocoordinated to ensure the square planar geometry of the Ir^{I} centre, was a point of reflection in the design of a second coordinating ligand. In order to try to "force" the trigonal bipyramidal geometry, the bulky, tridentate terpyridine (terpy) ligand was chosen. The resulting compound – **(bimpym)Ir(terpy)** – indeed presented a pentavalent Ir^{I} centre with two orthogonal ligands in the coordination sphere. The electronic structure presented a succession of bimpym- and terpy-based orbitals, with no hybridisation between them.

These findings provide a good guide for the conception and optimum architecture of such complexes.

1.5.2.3. Synthetic trials.

The promise of high electronic delocalisation borne by the computed adducts determined us to pursue various synthetic strategies to attempt their isolation. Reactions were carried out with the bimpym, bipy and bipym ligands. The first series involved reacting the isolated compounds **1.16** and **1.18** with the target second ligands, in hope of substituting the COD or Cp* co-ligands. This proposition was tenuous at best, given that Cp* is an anionic, η^5-coordinating ligand and COD is a good π-acceptor, in a good match with the electron-rich Ir^{I} centre. In all cases, no reactions occurred (Scheme 1.24).

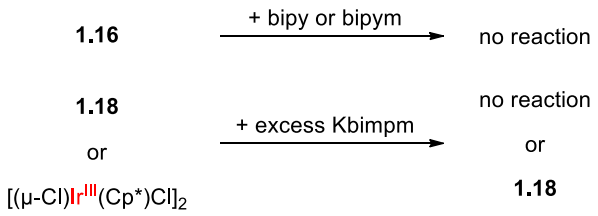

Scheme 1.24: Ligand substitution reactions with the previously isolated compounds.

A different synthetic strategy involved attempting to exploit the driving force of salt formation by the addition of **Kbimpym**. In order to do so, previously characterised complexes **(L)IrCODCl** and **[(L)IrCp*Cl]Cl** (L = bipy, bipym) were synthesised (Scheme 1.25).[92,93] The bipym-based compounds were previously obtained in our laboratory. The salt formation did, indeed, help the coordination of the bimpym ligand, but the Cp* and COD co-ligands could not be evicted from the coordination sphere of the Ir centres. On the contrary, the signals of free bipy and bipym ligands were detected in the *in situ* reaction mixtures, as well as those of **1.16** and **1.18**.

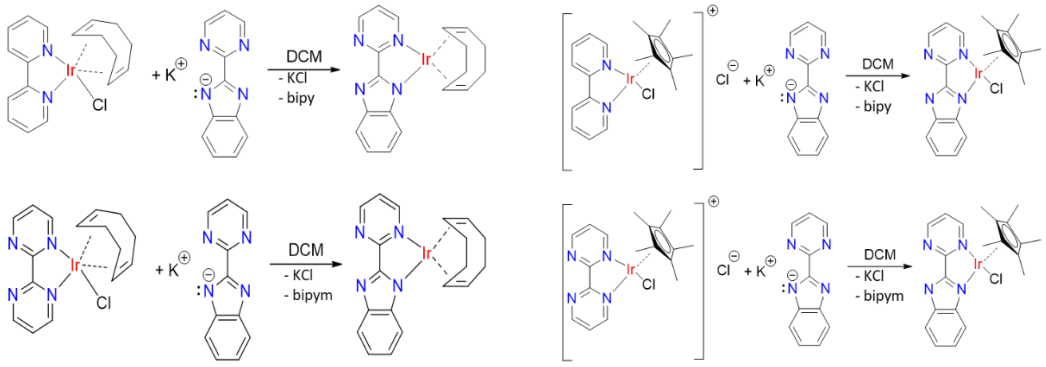

*Scheme 1.25: Ligand substitution reactions with **(L)IrCODCl** and **(L)IrCp*Cl₂** (L = bipy, bipym).*

The very favourable coordination of COD compelled us to explore different pathways. In this regard, the iridium(I) bis-cyclooctene chloride dimer $[Ir(COE)_2Cl]_2$ seemed promising, as the weaker

coordination via a single double bond has already been used to facilitate decoordination of the π-accepting ligand.[94]

The addition of bipy to $[Ir(COE)_2Cl]_2$ in THF immediately resulted in a red-brown mixture, which became entirely soluble within a few minutes of stirring. If left overnight at room temperature, a brown solid precipitates. ^1H NMR analysis of the mixture showed the release of free COE. The decoordination of the COE co-ligands is, therefore, responsible for the precipitation of the substrate overnight. The mixture is much more stable if stored at -30 °C. Diffusion of Et_2O in the saturated THF solution at -30 °C led to the growth of small brown prisms, which allowed the acquisition of XRD data. Due to the poor quality of the data, the resolution of the crystal structure could only allow the determination of the atom connectivity as $(bipy)Ir(COE)_2Cl$ (Scheme 1.26).

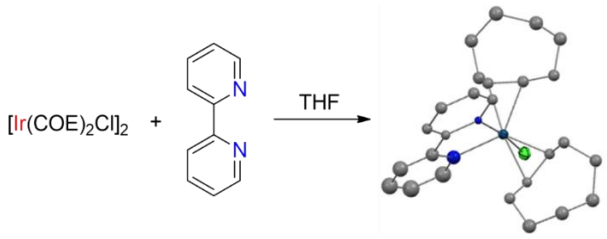

Scheme 1.26: Addition of bipy to $[Ir(COE)_2Cl]_2$ and the ORTEP of the resulting structure.

In situ tracking of the reaction performed in THF-d_8 shows the formation of 7 distinct signals, alongside those of free bipy. Careful integration of these signals indicate that an eighth signal is hidden in one of the bipy peaks (the largest triplet at 7.8 ppm integrating for 2.54 protons in Figure 1.19; another free bipy peak is integrated for scale at 8.51 ppm). Even after a short period of time, small side-products are noticed and their growth continues. Among these newly formed signals, several significantly shielded peaks appear between -16.8 ppm and -21.0 ppm within a few hours, before converging towards the signal at -21.0. These chemical shifts are in the characteristic zone of transition metal hydrides.[95] The fact that this signal integrates in a 1:1 ratio with the other signals being formed indicates that a hydride product is being formed.

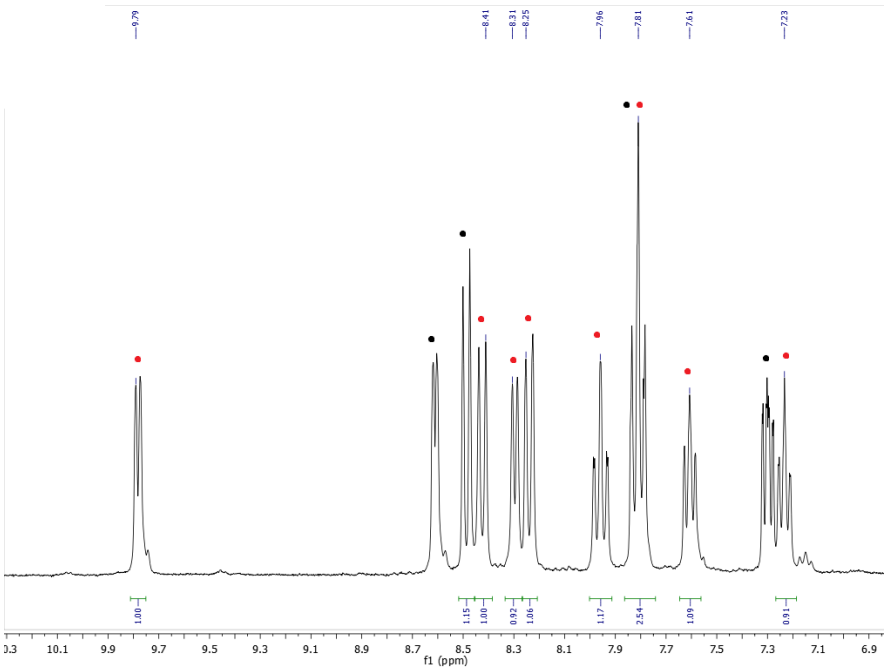

Figure 1.19: In situ *^1H NMR tracking of the addition of bipy to $[Ir(COE)_2Cl]_2$ – after 15 minutes. Red dots indicate the formed product, black – free bipy.*

The same reaction was performed in non-polar toluene to probe for the factors that triggered or influenced the evolution described above. The reaction was started and kept at -60 °C for 30 minutes, before the temperature was gradually increased to room temperature within two hours. The temperature bore no influence on the behaviour of the compound. The mixture showed no evolution of the primary product within the day. The only observable phenomenon was the precipitation of the product, as was observed with THF. We may therefore surmise that the evolution towards the hydride compound is solvent-dependent, whereas the precipitation due to the release of COE occurs naturally at room temperature in all circumstances. Further proof of the former conclusion was provided upon redissolution of the *in situ* reaction mixture in DMSO-d_6 – signals in the hydride region were noticed within a few hours of the redissolution.

Unfortunately, no crystals could be grown from the toluene reaction mixture. Therefore, on the basis of all the evidence presented above, the proposed mechanism is shown in Scheme 1.27. The initial product – (bipy)Ir(COE)$_2$Cl (**1.20**) – is formed initially, regardless of solvent or temperature. If **1.20** is left in a coordinating solvent, the intramolecular cross-coupling is performed, following the rotation of one of the pyridine moieties to yield (pyr)(py)IrH(COE)$_2$Cl (**1.21**). This interpretation is consistent with the crystal structure obtained. However, due to the poor quality of the data, no reliable distinction could be made between the nitrogen or the carbon coordinating the Ir centre. By extension, the unequivocal attribution of the hydride was impossible, due to the insufficiently precise data.

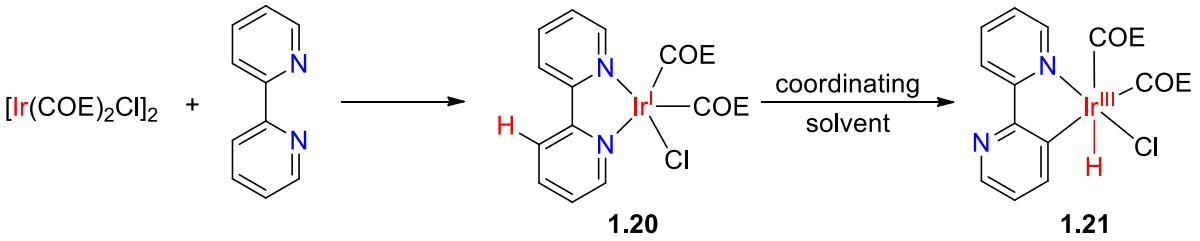

Scheme 1.27: Proposed mechanism for the reaction between bipy and [Ir(COE)$_2$Cl]$_2$.

Other attempts to coordinate multiple RAL were performed by reacting **Kbimpym** with [Ir(COE)$_2$Cl]$_2$ in THF. The insolubility of the initially formed pale beige suspension suggested long reaction times are necessary. However, after overnight stirring, the dominant product was a black powder that was insoluble in all of our available solvents. It is probable that the same mechanism of COE decoordination applies to this reaction, which would explain the lack of solubility observed.

A similar reaction with two equivalents of **Kbimpym** was performed by refluxing the mixture in THF for two days, resulting in a brown suspension. Red-brown solid was isolated after filtering the mixture (to try to remove the presumed KCl, poorly soluble in THF). The solid was washed to remove any free COE that could be present. If the expected product, **K[Ir(bimpym)$_2$]**, is taken as a reference, a 90% conversion was observed. The dissolution of the solid in DMSO-d_6 afforded a red-auburn solution with no visibly remaining residue.

^{1}H NMR analysis showed a very clean product, with the only impurities being THF and Et$_2$O – used for washing. The remaining four signals integrated cleanly, consistent with the presence of symmetric bimpym-based species (Figure 1.20). In principle, this would match the attribution of the species as **K[Ir(bimpym)$_2$]**, where the K$^+$ is expected to be an outer-sphere cation with no bearing on the solution symmetry.

On the other hand, the presence of only 4 signals would imply little influence from the Ir on the putative complex, which would be unusual. Furthermore, there was no change in either colour,

solubility or NMR signals after the addition of the potassium-trapping agent 18-C-6, which may point to the absence of potassium cation.

These contrasting arguments put into doubt the definitive interpretation of the product. Unfortunately, no crystals could be grown, therefore precluding the determination of the structure.

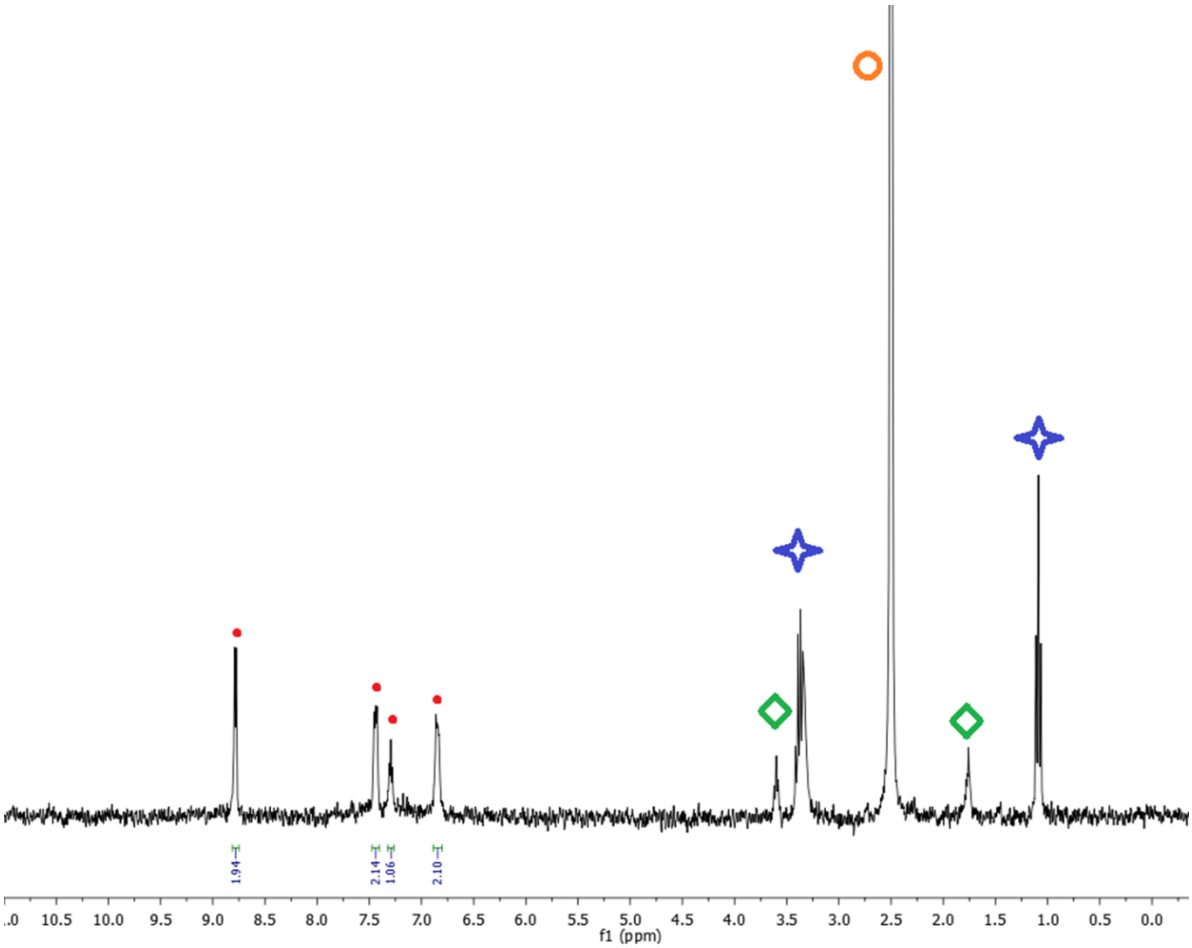

*Figure 1.20: ^{1}H NMR of the product of the addition of two equivalents of **Kbimpym** to $[Ir(COE)_2Cl]_2$ in DMSO-d_6. The product signals are designated by red dots, the solvent peak by the orange circle, THF – green lozenge and Et_2O – blue four-pointed star.*

Preliminary attempts to form **(bimpym)Ir(bipy)**-type species were hampered by the low solubility of the different adducts formed. Therefore, up to this point, no irrefutable proof of complexes coordinated to two RAL can be provided. The last option that was explored was the addition of divalent lanthanide fragments directly to the isolated products, namely the presumed **K[Ir(bimpym)$_2$]** and an *in situ* addition to compounds where the coordination of bimpym was possible. The rationale behind this decision was to exploit the enhanced solubility conferred by the very lipophilic Cp* co-ligands on the lanthanide. Ytterbocene was preferred, due to the easy and immediate indication of its oxidation state in ^{1}H NMR – paramagnetic signals are expected if there is any reduction of the ligands.

Indeed, paramagnetically shifted peaks were immediately observed in the black suspensions obtained when reacting the presumed **K[Ir(bimpym)$_2$]** with organolanthanide fragments, but these signals either subsided with time or led to intractable, ultimately unidentifiable mixtures.

1.5.2.4. Partial conclusion and perspectives.

Upon reduction, electron transfer to the bimpym ligand leads to a coupling reaction between two C atoms on the pyrimidine moiety.[34] This behaviour was also previously observed using divalent lanthanide adducts with the phenanthroline family of ligands.[2,4] With the help of theoretical computations, this coupling could be rationalised by the presence of vacant orbitals which are concentrated on the pyrimidine moiety (designated as **LUMO^{pym}** throughout this work). The most important features of this type of orbital are significant contributions from the carbon atoms in the *meta* position relative to the carbon bridging the pyrimidine with the benzimidazolyl moieties. It was shown in this chapter that the shape and individual contributions on the carbons can be modulated by the coordination of transition metal fragments. It stands to reason that a more significant electronic perturbation, in the form of the coordination of and reduction by an organolanthanide fragment is likely to also impact this type of orbital.

Therefore, the synthetic objective presented herein is in line with the principles of the ERC project – it would be beneficial to avoid the coupling reaction to maximise the electronic density stored on the ligand, which would then have a more prominent effect on the transition metal fragment. One of the proposed paths to achieve this involves trying to enhance the delocalisation across the π system by adding a second RAL to the coordination sphere.

Theoretical computations on a series of compounds were performed to construct a viable system, in order to achieve this effect. Ir^{III} complexes bearing multiple RAL are already widely known. The calculated example, **Ir(bimpym)$_3$**, however, did not show any conjugation between the ligands in its electronic structure. This could be due to the orthogonal orientation between the ligands. Regardless, such a complex is not the primary objective of this study.

A more promising target would be Ir^{I}-based complexes with two RAL, which are rare. The advantages of such structures – which would adopt square planar geometries – are inter-ligand arrangements close to co-planar, that would facilitate inter-ligand electronic communication, as well as better spatial availability for a potential substrate, that could be exploited catalytically. All the computed adducts, bar **(bimpym)Ir(terpy)**, largely conform to these geometrical requirements. The exception to the rule is due to the tridentate terpy ligand, which is perpendicular to the bimpym plane, therefore limiting conjugation.

The electronic structures of the remaining complexes – **(bimpym)Ir(bipy)**, **(bimpym)Ir(3,3'-bipy)**, **(bimpym)Ir(bipym)** and **[(bimpym)$_2$Ir]$^-$** – all show diminished electronic contributions on the carbon atoms susceptible to couple and vacant orbitals with the electronic density redistributed across the two ligands. These results justified a preliminary study into the synthetic feasibility of such complexes.

However, following the reactions was severely hamstrung by the very poor solubility of the adducts involved. As was mentioned in Section 1.3.3, using the **Kbimpym** ligand presupposes long reaction times and enormous difficulty in tracking reaction products. The decoordination of COE from **1.20** (and, presumably, **1.21**) entails an almost total loss of solubility. The synthetic issues made any further studies both fruitless and pointless.

The solutions proposed to counter these problems are in tune with those suggested in Sections 1.2.4 and 1.3.3. Introducing substituents on the ligands could attenuate the issues encountered tracking the evolution of the compounds. The options proposed in Section 1.3.3 naturally apply here, as well. Given the open choice of the second RAL, more derivatives can be proposed – 5,5'-di-*tert*-butyl-bipym[96] or the commercially available 4,4'-di-*tert*-butyl-bipy as just some of the examples. Using 3,3'-Me$_2$-bipy

(not yet attempted) or derivatives[97] could not only contribute to better solubility, but would block the cross-coupling reaction explaining the formation of **1.21**.

1.6. Conclusion.

This chapter presented the synthesis of a number of organometallic complexes based on two ligands – **dppz** and **Hbimpym**. Both of these were chosen with the goal of providing a conceptual evolution to the field of heterometallic complexes based on divalent lanthanides, which has heretofore only used symmetrical ligands with L_2 coordination sites.

dppz-based complexes present the advantage of a supplementary coordination site, which allows the planning of architectures with two organolanthanide fragments. This was, in fact, observed, with the heterometallic complexes **1.6** and **1.7**, where the structural features pointed to oxidised Yb centres. This implies that the ligand is twice reduced and is, therefore, dianionic. The monodentate sites undoubtedly offer a less stabilising coordination environment for the Ln. This fact is corroborated by the solvent-dependent electron transfer.

Although promising, these findings could not be explored further, since the poor solubility of the **dppz** ligand precludes solution studies, which are indispensable for reactivity trials. A series of synthetic solutions was proposed in Section 1.2.4, which would ameliorate the solubility of the ligand.

The second chosen ligand – **Hbimpym** – provides an anionic coordination site upon deprotonation. This affords the user a measure of synthetic control in the order of placing the transition metal fragments. As such, complexes were synthesised and characterised, where the TM fragment was coordinated to either the L_2 or the LX site.

In the former case, the precursors of the group 10 metals are now fully characterised. The reactivity of the Ni adduct towards the addition of divalent lanthanide precursors was already studied.[34] Upon the coordination of ytterbocene, an electron transfer occurs, triggering a coupling reaction on the bimpym ligand between two molecules. A tetrametallic complex is isolated, after which the Ni fragment is subsequently ejected. Theoretical computations show that the coupling reaction can be rationalised by the accumulation of significant electronic density on the C atoms in the *meta* position with respect to the bridging atom on the ligand.

This presents us with the opportunity to perform a comparative study, to investigate whether the TM has any influence on the behaviour of the complex. These findings shall be described in the following chapter.

Under different conditions, the same TM(II) precursors could be used to obtain adducts, where the metal has lost one of its X substituents, only to be replaced by a neutral solvent molecule (complexes **1.12**-**1.14**). Theoretical computations show that this neutral ligand is very influential in determining the electronic structure of these complexes. Indeed, when the ligand in question is pyridine, the LUMO is almost exclusively composed by the contribution from the pyridine.

These findings are promising on two levels. First, it could suggest a new pathway for the reactivity for the corresponding Pd and Pt-based adducts. This shall be explored at length in the subsequent chapters.

Second, this could open up new avenues in how the reactivity with divalent lanthanides can be tuned. This conclusion is yet to be proved, as efforts to isolate such complexes stand outside the scope of this work. Preliminary observations indicate that it should be possible, as the pyridine ligand demonstrates fluxional behaviour. However, the underlying difficulty is to actually replace the pyridine with the target L-type ligand.

Lastly, Ir-based complexes, where the metal is nestled in either of the two coordination sites, were synthesised and characterised. Although this situation may provide additional flexibility in tuning ensuing reactivity, there are a number of concerns regarding potential parasitic side reactions upon the addition of divalent lanthanides. This proposition will be put to the test in the next chapter.

References

(1) Berg, D. J.; Boncella, J. M.; Andersen, R. A. *Organometallics* 2002, *21* (22), 4622–4631. https://doi.org/10.1021/om020477e.

(2) Nocton, G.; Lukens, W. W.; Booth, C. H.; Rozenel, S. S.; Medling, S. A.; Maron, L.; Andersen, R. A. *J. Am. Chem. Soc.* 2014, *136* (24), 8626–8641. https://doi.org/10.1021/ja502271q.

(3) Nocton, G.; Booth, C. H.; Maron, L.; Andersen, R. A. *Organometallics* 2013, *32* (19), 5305–5312. https://doi.org/10.1021/om400528d.

(4) Nocton, G.; Ricard, L. *Chem. Commun.* 2015, *51* (17), 3578–3581. https://doi.org/10.1039/C5CC00289C.

(5) Hull, J. F.; Himeda, Y.; Wang, W.-H.; Hashiguchi, B.; Periana, R.; Szalda, D. J.; Muckerman, J. T.; Fujita, E. *Nat. Chem.* 2012, *4* (5), 383–388. https://doi.org/10.1038/nchem.1295.

(6) Marino, N.; Armentano, D.; De Munno, G.; Cano, J.; Lloret, F.; Julve, M. *Inorg. Chem.* 2012, *51* (7), 4323–4334. https://doi.org/10.1021/ic202740b.

(7) Brereton, K. R.; Pitman, C. L.; Cundari, T. R.; Miller, A. J. M. *Inorg. Chem.* 2016, *55* (22), 12042–12051. https://doi.org/10.1021/acs.inorgchem.6b02223.

(8) Liberman-Martin, A. L.; Levine, D. S.; Liu, W.; Bergman, R. G.; Tilley, T. D. *Organometallics* 2016, *35* (8), 1064–1069. https://doi.org/10.1021/acs.organomet.5b01003.

(9) Wang, Y.; Li, J.; Zhang, L.; Chen, C.; Feng, R.; Zhao, Y.; Zhang, Y.-Q.; Tan, G.; Song, Y.; Wang, X. *Dalton Trans.* 2018, *47* (48), 17211–17215. https://doi.org/10.1039/C8DT04157A.

(10) Demir, S.; Zadrozny, J. M.; Nippe, M.; Long, J. R. *J. Am. Chem. Soc.* 2012, *134* (45), 18546–18549. https://doi.org/10.1021/ja308945d.

(11) Gould, C. A.; Mu, E.; Vieru, V.; Darago, L. E.; Chakarawet, K.; Gonzalez, M. I.; Demir, S.; Long, J. R. *J. Am. Chem. Soc.* 2020, *142* (50), 21197–21209. https://doi.org/10.1021/jacs.0c10612.

(12) Arnaud Jaoul, PhD thesis, Université Paris-Saclay, Ecole Polytechnique, 2017.

(13) Ackermann, M. N.; Interrante, L. V. *Inorg. Chem.* 1984, *23* (24), 3904–3911. https://doi.org/10.1021/ic00192a014.

(14) Amouyal, E.; Homsi, A.; Chambron, J.-C.; Sauvage, J.-P. *J Chem Soc Dalton Trans* 1990, No. 6, 1841–1845. https://doi.org/10.1039/DT9900001841.

(15) Puckett, C. A.; Barton, J. K. *J. Am. Chem. Soc.* 2007, *129* (1), 46–47. https://doi.org/10.1021/ja0677564.

(16) Pierroz, V.; Joshi, T.; Leonidova, A.; Mari, C.; Schur, J.; Ott, I.; Spiccia, L.; Ferrari, S.; Gasser, G. *J. Am. Chem. Soc.* 2012, *134* (50), 20376–20387. https://doi.org/10.1021/ja307288s.

(17) Roy, N.; Sen, U.; Ray Chaudhuri, S.; Muthukumar, V.; Moharana, P.; Paira, P.; Bose, B.; Gauthaman, A.; Moorthy, A. *Dalton Trans.* 2021, *50* (6), 2268–2283. https://doi.org/10.1039/D0DT03586F.

(18) Saeed, H. K.; Sreedharan, S.; Jarman, P. J.; Archer, S. A.; Fairbanks, S. D.; Foxon, S. P.; Auty, A. J.; Chekulaev, D.; Keane, T.; Meijer, A. J. H. M.; Weinstein, J. A.; Smythe, C. G. W.; Bernardino de la Serna, J.; Thomas, J. A. *J. Am. Chem. Soc.* 2020, *142* (2), 1101–1111. https://doi.org/10.1021/jacs.9b12564.

(19) Kumar, P.; Butcher, R. J.; Patra, A. K. *Inorganica Chim. Acta* 2020, *506*, 119532. https://doi.org/10.1016/j.ica.2020.119532.

(20) Jia, C.; Liu, S.-X.; Tanner, C.; Leiggener, C.; Neels, A.; Sanguinet, L.; Levillain, E.; Leutwyler, S.; Hauser, A.; Decurtins, S. *Chem. - Eur. J.* 2007, *13* (13), 3804–3812. https://doi.org/10.1002/chem.200601561.

(21) Brennaman, M. K.; Meyer, T. J.; Papanikolas, J. M. *J. Phys. Chem. A* 2004, *108* (45), 9938–9944. https://doi.org/10.1021/jp0479670.

(22) Kurz, P.; Probst, B.; Spingler, B.; Alberto, R. *Eur. J. Inorg. Chem.* 2006, *2006* (15), 2966–2974. https://doi.org/10.1002/ejic.200600166.

(23) Kamecka, A.; Grochowska, O.; Kapturkiewicz, A. *Inorg. Chem. Commun.* 2019, *108*, 107547. https://doi.org/10.1016/j.inoche.2019.107547.
(24) Sun, L.-Z.; Kuang, X.-N.; Lin, S.; Zhao, L.; Yu, X.; Li, Z.-F.; Min-Liu; Xin, X.-L.; Yang, Y.-P.; Jin, Q.-H. *Polyhedron* 2020, *175*, 114177. https://doi.org/10.1016/j.poly.2019.114177.
(25) Qiao, J.; Qin, M.; Shen, Y.-M.; Cao, J.; Chen, Z.; Xu, J. *Chem. Commun.* 2021, *57* (35), 4307–4310. https://doi.org/10.1039/D1CC01486B.
(26) Sun, P.-P.; Duan, J.-P.; Shih, H.-T.; Cheng, C.-H. *Appl. Phys. Lett.* 2002, *81* (5), 792–794. https://doi.org/10.1063/1.1497714.
(27) Kozlov, M. I.; Aslandukov, A. N.; Vashchenko, A. A.; Medvedko, A. V.; Aleksandrov, A. E.; Grzibovskis, R.; Goloveshkin, A. S.; Lepnev, L. S.; Tameev, A. R.; Vembris, A.; Utochnikova, V. V. *Dalton Trans.* 2019, *48* (46), 17298–17309. https://doi.org/10.1039/C9DT03823J.
(28) Cen, P.; Liu, X.; Ferrando-Soria, J.; Zhang, Y.; Xie, G.; Chen, S.; Pardo, E. *Chem. – Eur. J.* 2019, *25* (15), 3884–3892. https://doi.org/10.1002/chem.201805608.
(29) Shen, N.; Liang, J.; Qu, X.; Liu, S.; Zhu, L.; Zhang, S.; Chen, L.; Zhang, J.; Hu, D.; Yin, B. *CrystEngComm* 2021, *23* (22), 4013–4027. https://doi.org/10.1039/D1CE00431J.
(30) Haga, M.; Ishizuya, M.; Kanesugi, T.; Yutaka, T.; Sakiyama, D., Feed, J.; Kuim, W. *IJC-A* 2003, *42A*, 2290-2299. http://nopr.niscair.res.in/handle/123456789/20737.
(31) Shi, C.; Li, Q.; Zou, L.; Lv, Z.; Yuan, A.; Zhao, Q. *Eur. J. Inorg. Chem.* 2018, *2018* (9), 1131–1136. https://doi.org/10.1002/ejic.201800004.
(32) Shi, C.; Huang, M.; Li, Q.; Xie, G.; Yang, C.; Yuan, A. *Dalton Trans.* 2018, *47* (48), 17299–17303. https://doi.org/10.1039/C8DT04007A.
(33) Green, M. L. H. *J. Organomet. Chem.* 1995, *500* (1–2), 127–148. https://doi.org/10.1016/0022-328X(95)00508-N.
(34) Wang, D.; Tricoire, M.; Cemortan, V.; Moutet, J.; Nocton, G. *Inorg. Chem. Front.* 2021. https://doi.org/10.1039/D0QI00952K.
(35) Dickeson, J.; Summers, L. *Aust. J. Chem.* 1970, *23* (5), 1023. https://doi.org/10.1071/CH9701023.
(36) Toney, J. H.; Marks, T. J. *J. Am. Chem. Soc.* 1985, *107* (4), 947–953. https://doi.org/10.1021/ja00290a033.
(37) Cole, M. L.; Deacon, G. B.; Junk, P. C.; Konstas, K. *Chem Commun* 2005, No. 12, 1581–1583. https://doi.org/10.1039/B419047E.
(38) Burns, C. J.; Anderson, R. A. *J Chem Soc Chem Commun* 1989, No. 2, 136–137. https://doi.org/10.1039/C39890000136.
(39) De Graaf, Wim.; Boersma, Jaap.; Smeets, W. J. J.; Spek, A. L.; Van Koten, Gerard. *Organometallics* 1989, *8* (12), 2907–2917. https://doi.org/10.1021/om00114a028.
(40) Hill, G. S.; Irwin, M. J.; Levy, C. J.; Rendina, L. M.; Puddephatt, R. J.; Andersen, R. A.; Mclean, L. In *Inorganic Syntheses*; Darensbourg, Marcetta. Y., Ed.; John Wiley & Sons, Inc.: Hoboken, NJ, USA, 2007; pp 149–153. https://doi.org/10.1002/9780470132630.ch25.
(41) Kang, J. W.; Moseley, K.; Maitlis, P. M. *J. Am. Chem. Soc.* 1969, *91* (22), 5970–5977. https://doi.org/10.1021/ja01050a008.
(42) Phillips, T.; Haq, I.; Meijer, A. J. H. M.; Adams, H.; Soutar, I.; Swanson, L.; Sykes, M. J.; Thomas, J. A. *Biochemistry* 2004, *43* (43), 13657–13665. https://doi.org/10.1021/bi049146r.
(43) Klein, A.; Scheiring, T.; Kaim, W. *Z. Für Anorg. Allg. Chem.* 1999, *625* (7), 1177–1180. https://doi.org/10.1002/(SICI)1521-3749(199907)625:7<1177::AID-ZAAC1177>3.0.CO;2-1.
(44) Bergman, S. D.; Goldberg, I.; Carfagna, C.; Mosca, L.; Kol, M.; Milani, B. *Organometallics* 2006, *25* (26), 6014–6018. https://doi.org/10.1021/om060624z.
(45) Wang, J.-T.; Xiao, X.; Zhang, Y.-Q.; Xue, S.-F.; Zhu, Q.-J. *Acta Crystallogr. Sect. E Struct. Rep. Online* 2009, *65* (4), m475–m475. https://doi.org/10.1107/S1600536809011441.
(46) Gao, C.-Y.; Ma, Z.-Y.; Zhang, Y.-P.; Li, S.-T.; Gu, W.; Liu, X.; Tian, J.-L.; Xu, J.-Y.; Zhao, J.-Z.; Yan, S.-P. *RSC Adv.* 2015, *5* (39), 30768–30779. https://doi.org/10.1039/C4RA16755D.

(47) Kokoschka, M.; Bangert, J.-A.; Stoll, R.; Sheldrick, W. S. *Eur. J. Inorg. Chem.* 2010, *2010* (10), 1507–1515. https://doi.org/10.1002/ejic.200901123.
(48) Pracharova, J.; Vigueras, G.; Novohradsky, V.; Cutillas, N.; Janiak, C.; Kostrhunova, H.; Kasparkova, J.; Ruiz, J.; Brabec, V. *Chem. – Eur. J.* 2018, *24* (18), 4607–4619. https://doi.org/10.1002/chem.201705362.
(49) Sreedharan, S.; Sinopoli, A.; Jarman, Paul. J.; Robinson, D.; Clemmet, C.; Scattergood, P. A.; Rice, C. R.; Smythe, Carl. G. W.; Thomas, J. A.; Elliott, P. I. P. *Dalton Trans.* 2018, *47* (14), 4931–4940. https://doi.org/10.1039/C8DT00046H.
(50) Zhang, H.-N.; Gao, W.-X.; Deng, Y.-X.; Lin, Y.-J.; Jin, G.-X. *Chem. Commun.* 2018, *54* (13), 1559–1562. https://doi.org/10.1039/C7CC09448E.
(51) Novohradsky, V.; Vigueras, G.; Pracharova, J.; Cutillas, N.; Janiak, C.; Kostrhunova, H.; Brabec, V.; Ruiz, J.; Kasparkova, J. *Inorg. Chem. Front.* 2019, *6* (9), 2500–2513. https://doi.org/10.1039/C9QI00811J.
(52) Howard, J. A. K.; Hoy, V. J.; O'Hagan, D.; Smith, G. T. *Tetrahedron* 1996, *52* (38), 12613–12622. https://doi.org/10.1016/0040-4020(96)00749-1.
(53) Schultz, M.; Boncella, J. M.; Berg, D. J.; Tilley, T. D.; Andersen, R. A. *Organometallics* 2002, *21* (3), 460–472. https://doi.org/10.1021/om010661k.
(54) Goudy, V.; Jaoul, A.; Cordier, M.; Clavaguéra, C.; Nocton, G. *J. Am. Chem. Soc.* 2017, *139* (31), 10633–10636. https://doi.org/10.1021/jacs.7b05634.
(55) Ying, H.; Gong, M.; Pi, C. *Dalton Trans.* 2019, *48* (8), 2722–2729. https://doi.org/10.1039/C8DT04768E.
(56) Jaoul, A.; Tricoire, M.; Moutet, J.; Cordier, M.; Clavaguéra, C.; Nocton, G. *Chem. Squared* 2019, *3*. https://doi.org/10.28954/2019.csq.06.001.
(57) Moore, J. A.; Cowley, A. H.; Gordon, J. C. *Organometallics* 2006, *25* (22), 5207–5209. https://doi.org/10.1021/om060793j.
(58) Trifonov, A. A.; Fedorova, E. A.; Ikorskii, V. N.; Dechert, S.; Schumann, H.; Bochkarev, M. N. *Eur. J. Inorg. Chem.* 2005, *2005* (14), 2812–2818. https://doi.org/10.1002/ejic.200401014.
(59) Nocton, G.; Ricard, L. *Dalton Trans* 2014, *43* (11), 4380–4387. https://doi.org/10.1039/C3DT52641K.
(60) Pellegrin, Y.; Sandroni, M.; Blart, E.; Planchat, A.; Evain, M.; Bera, N. C.; Kayanuma, M.; Sliwa, M.; Rebarz, M.; Poizat, O.; Daniel, C.; Odobel, F. *Inorg. Chem.* 2011, *50* (22), 11309–11322. https://doi.org/10.1021/ic2006343.
(61) Burgstahler, A. W.; Chien, P.-Lu.; Abdel-Rahman, M. O. *J. Am. Chem. Soc.* 1964, *86* (23), 5281–5290. https://doi.org/10.1021/ja01077a047.
(62) Sun, Y.; Collins, S. N.; Joyce, L. E.; Turro, C. *Inorg. Chem.* 2010, *49* (9), 4257–4262. https://doi.org/10.1021/ic9025365.
(63) da Silva Miranda, F.; Signori, A. M.; Vicente, J.; de Souza, B.; Priebe, J. P.; Szpoganicz, B.; Gonçalves, N. S.; Neves, A. *Tetrahedron* 2008, *64* (22), 5410–5415. https://doi.org/10.1016/j.tet.2008.02.097.
(64) Shannon, R. D. *Acta Crystallogr. Sect. A* 1976, *32* (5), 751–767. https://doi.org/10.1107/S0567739476001551.
(65) Demir, S.; Nippe, M.; Gonzalez, M. I.; Long, J. R. *Chem Sci* 2014, *5* (12), 4701–4711. https://doi.org/10.1039/C4SC02154A.
(66) Fernholt, L.; Rømming, C.; Samdal, S.; Näsäkkälä, E.; Wahlberg, O. *Acta Chem. Scand.* 1981, *35a*, 707–715. https://doi.org/10.3891/acta.chem.scand.35a-0707.
(67) Booth, C. H.; Kazhdan, D.; Werkema, E. L.; Walter, M. D.; Lukens, W. W.; Bauer, E. D.; Hu, Y.-J.; Maron, L.; Eisenstein, O.; Head-Gordon, M.; Andersen, R. A. *J. Am. Chem. Soc.* 2010, *132* (49), 17537–17549. https://doi.org/10.1021/ja106902s.
(68) Bibi, N.; de Arruda, E. G. R.; Domingo, A.; Oliveira, A. A.; Galuppo, C.; Phung, Q. M.; Orra, N. M.; Béron, F.; Paesano, A.; Pierloot, K.; Formiga, A. L. B. *Inorg. Chem.* 2018, *57* (23), 14603–14616. https://doi.org/10.1021/acs.inorgchem.8b02278.

(69) Hintermann, L.; Xiao, L.; Labonne, A. *Angew. Chem. Int. Ed.* 2008, *47* (43), 8246–8250. https://doi.org/10.1002/anie.200803312.
(70) Kim, H.-Y.; Shieh, W.-C.; Prashad, M. *Tetrahedron Lett.* 2014, *55* (36), 5055–5057. https://doi.org/10.1016/j.tetlet.2014.07.033.
(71) Wolters, L. P.; van Zeist, W.-J.; Bickelhaupt, F. M. *Chem. - Eur. J.* 2014, *20* (36), 11370–11381. https://doi.org/10.1002/chem.201403237.
(72) Tricoire, M.; Münzfeld, L.; Moutet, J.; Mahieu, N.; La Droitte, L.; Moreno-Pineda, E.; Gendron, F.; Hilgar, J. D.; Rinehart, J. D.; Ruben, M.; Cador, O.; Le Guennic, B.; Roesky, P. W.; Nocton, G. *Chem. – Eur. J.* 2021. https://doi.org/10.1002/chem.202101599.
(73) Laemmel, A.-C.; Collin, J.-P.; Sauvage, J.-P.; Accorsi, G.; Armaroli, N. *Eur. J. Inorg. Chem.* 2003, *2003* (3), 467–474. https://doi.org/10.1002/ejic.200390066.
(74) Swarts, A. J.; Zheng, F.; Smith, V. J.; Nordlander, E.; Mapolie, S. F. *Organometallics* 2014, *33* (9), 2247–2256. https://doi.org/10.1021/om5001293.
(75) Searles, K.; Das, A. K.; Buell, R. W.; Pink, M.; Chen, C.-H.; Pal, K.; Morgan, D. G.; Mindiola, D. J.; Caulton, K. G. *Inorg. Chem.* 2013, *52* (9), 5611–5619. https://doi.org/10.1021/ic400803e.
(76) Huang, W.; Abukhalil, P. M.; Khan, S. I.; Diaconescu, P. L. *Chem Commun* 2014, *50* (40), 5221–5223. https://doi.org/10.1039/C3CC47505K.
(77) Steel, H. L.; Allinson, S. L.; Andre, J.; Coogan, M. P.; Platts, J. A. *Chem. Commun.* 2015, *51* (57), 11441–11444. https://doi.org/10.1039/C5CC04003E.
(78) Ruggiero, E.; Garino, C.; Mareque-Rivas, J. C.; Habtemariam, A.; Salassa, L. *Chem. - Eur. J.* 2016, *22* (8), 2801–2811. https://doi.org/10.1002/chem.201503991.
(79) Hebenbrock, M.; Stegemann, L.; Kösters, J.; Doltsinis, N. L.; Müller, J.; Strassert, C. A. *Dalton Trans.* 2017, *46* (10), 3160–3169. https://doi.org/10.1039/C7DT00393E.
(80) Betanzos-Lara, S.; Salassa, L.; Habtemariam, A.; Novakova, O.; Pizarro, A. M.; Clarkson, G. J.; Liskova, B.; Brabec, V.; Sadler, P. J. *Organometallics* 2012, *31* (9), 3466–3479. https://doi.org/10.1021/om201177y.
(81) Rotondo, A.; Bruno, G.; Cusumano, M.; Rotondo, E. *Inorganica Chim. Acta* 2009, *362* (13), 4767–4773. https://doi.org/10.1016/j.ica.2009.06.047.
(82) Gayton, J.; Autry, S.; Fortenberry, R.; Hammer, N.; Delcamp, J. *Molecules* 2018, *23* (12), 3051. https://doi.org/10.3390/molecules23123051.
(83) Evans, W. J. *J. Organomet. Chem.* 2002, *647* (1–2), 2–11. https://doi.org/10.1016/S0022-328X(01)01462-0.
(84) Trifonov, A. A.; Fedorova, E. A.; Fukin, G. K.; Baranov, E. V.; Druzhkov, N. O.; Bochkarev, M. N. *Chem. - Eur. J.* 2006, *12* (10), 2752–2757. https://doi.org/10.1002/chem.200501181.
(85) Vasudevan, K.; Cowley, A. H. *Chem. Commun.* 2007, No. 33, 3464. https://doi.org/10.1039/b708758f.
(86) Nocton, G.; Booth, C. H.; Maron, L.; Ricard, L.; Andersen, R. A. *Organometallics* 2014, *33* (23), 6819–6829. https://doi.org/10.1021/om500843z.
(87) Morton, C. M.; Zhu, Q.; Ripberger, H.; Troian-Gautier, L.; Toa, Z. S. D.; Knowles, R. R.; Alexanian, E. J. *J. Am. Chem. Soc.* 2019, *141* (33), 13253–13260. https://doi.org/10.1021/jacs.9b06834.
(88) Sun, M.-J.; Zhong, Y.-W.; Yao, J. *Angew. Chem. Int. Ed.* 2018, *57* (26), 7820–7825. https://doi.org/10.1002/anie.201803546.
(89) He, L.; Tan, C.-P.; Ye, R.-R.; Zhao, Y.-Z.; Liu, Y.-H.; Zhao, Q.; Ji, L.-N.; Mao, Z.-W. *Angew. Chem. Int. Ed.* 2014, *53* (45), 12137–12141. https://doi.org/10.1002/anie.201407468.
(90) Chabolla, S. A.; Dellamary, E. A.; Machan, C. W.; Tezcan, F. A.; Kubiak, C. P. *Inorganica Chim. Acta* 2014, *422*, 109–113. https://doi.org/10.1016/j.ica.2014.07.007.
(91) Baxter, P. N. W.; Connor, J. A.; Wallis, J. D.; Povey, D. C.; Powell, A. K. *Polyhedron* 1992, *11* (14), 1771–1777. https://doi.org/10.1016/S0277-5387(00)83237-4.
(92) Youinou, M.-T.; Ziessel, R. *J. Organomet. Chem.* 1989, *363* (1–2), 197–208. https://doi.org/10.1016/0022-328X(89)88054-4.

(93) Seechurn, C. C. C. J.; Sivakumar, V.; Satoskar, D.; Colacot, T. J. *Organometallics* 2014, *33* (13), 3514–3522. https://doi.org/10.1021/om500420d.
(94) Danopoulos, A. A.; Pugh, D.; Wright, J. A. *Angew. Chem. Int. Ed.* 2008, *47* (50), 9765–9767. https://doi.org/10.1002/anie.200804573.
(95) Ruiz-Morales, Y.; Schreckenbach, G.; Ziegler, T. *Organometallics* 1996, *15* (19), 3920–3923. https://doi.org/10.1021/om960218n.
(96) Crossley, M.; Gorjian, S.; Sternhell, S.; Tansey, K. *Aust. J. Chem.* 1994, *47* (4), 723. https://doi.org/10.1071/CH9940723.
(97) Talele, H. R.; Koval, D.; Severa, L.; Reyes-Gutiérrez, P. E.; Císařová, I.; Sázelová, P.; Šaman, D.; Bednárová, L.; Kašička, V.; Teplý, F. *Chem. - Eur. J.* 2018, *24* (30), 7601–7604. https://doi.org/10.1002/chem.201800369.

Chapter Two

Preparation of bimpym-based bimetallic complexes.

The series of complexes based on the bimpym ligand, bearing TM fragments, was described in Chapter 1. This provides the opportunity to enlarge the study of heterobimetallic adducts in multiple ways and from different points of view.

For one, no group 9 TM were yet to be used in the ERC project. Therefore, the addition of divalent lanthanide fragments to the Ir-based complexes can help understand its behaviour in the event of an electron transfer. Furthermore, the various coordination spheres of both Ir^{I} and Ir^{III} complexes previously described provides the opportunity to study if and how potentially reactive groups (acidic proton or Cl^-) are tolerated by the organolanthanides.

The flexibility of the coordination environment of the bimpym ligand will then allow a comparative study into how the addition of an electron source to the neutral L_2 or the anionic LX sites may impact reactivity.

In this regard, the previous work on the **K(bimpym)NiMe$_2$** system is a good preview of what might be expected for complexes **1.8** and **1.9**. Nevertheless, it is of interest to scope out any potential differences in the reactivity of the homologous group 10 metal complexes.

2.1. Ir-based complexes

Complexes **1.15**-**1.18** were put to the test in organolanthanide addition reactions. The presence of the either acidic protons or available chloride functions in all but **1.16** was evoked in Section 1.5.1.2 as a potential source of unwanted reactivity.

Reactions between **1.15** or **1.17** and divalent lanthanide precursors led to immediate colour changes. All the in-situ reactions showed paramagnetically shifted ^{1}H NMR peaks. The only species that could be isolated was issued from the reaction with $Cp^*_2Sm(OEt_2)$. It was a poorly characterised cluster, tentatively identified as Sm_4Cl_6 (the number of Cp* co-ligands on each Sm could not be determined). On this basis, the precautions that were previously mentioned would seem to be justified.

On the other hand, the chloride in **1.18** should be less accessible than the one in **1.17**; plus, its lack of acidic proton, compared to **1.15** would make it a potentially more suitable target for reactivity with a divalent lanthanide. The *in situ* addition of **1.18** to ytterbocene in toluene revealed a number of paramagnetically shifted signals, which would be consistent with the reduction of the ligand, as well as a very broad signal at around 3 ppm. This could be construed to be the Cp* signal of a similar cluster to the one described above.

Consequently, it was hypothesised that the local excess of ytterbocene (due to its excellent solubility in toluene and **1.18**'s lack thereof) is responsible for activating the Ir-Cl bond. To test this assertion, a sub-stoichiometric quantity (0.7 eq) of ytterbocene was initially added, producing a relatively clean

spectrum (Figure 2.1). It should be noted, however that neither the number, nor the integration of the peaks was consistent with the presence of a single species (there are at least 5 signals that could correspond to Cp* co-ligands). Our best attempts at crystallising such mixtures only produced a small quantity of minuscule crystals, which were ultimately identified as the ion pair $[Cp^*_2YbCl_2]^+[Cp^*_2Ir]^-$ – a clear side-product.[1]

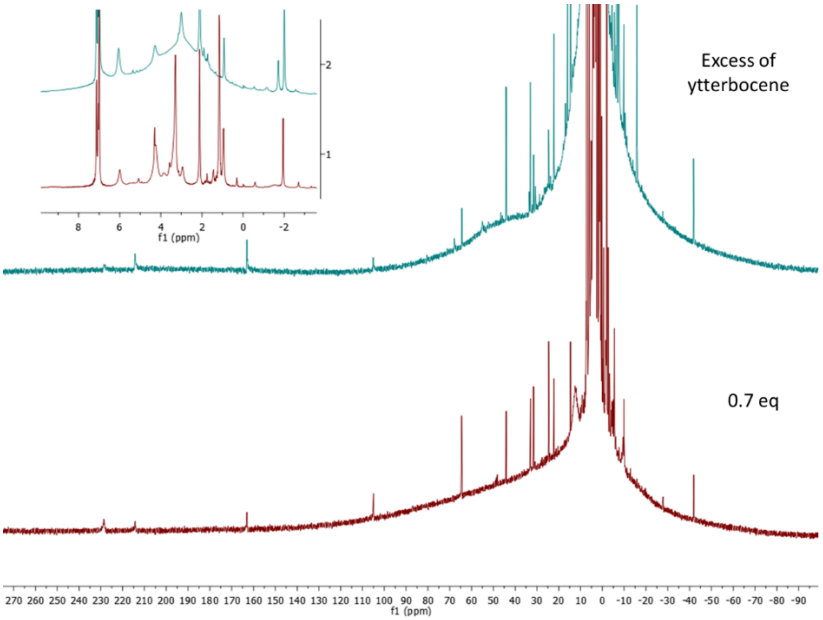

*Figure 2.1: In-situ addition of different quantities of ytterbocene to **1.18** in tol-d_8, followed by ^{1}H NMR.*

If further ytterbocene is added to these species, the signal attributed to the cluster grows in intensity, alongside a series of other signals in the paramagnetic region. No further characterisation was possible on any similar mixtures.

The same reactions with **1.16** were more straightforward. Upon the addition of a toluene solution of ytterbocene to crystals of **1.16**, a crimson solution was instantly obtained. Evaporation of the volatiles and washing the dark red powder with cold pentane yielded an analytically pure product in very high yield (>95%). This compound displayed excellent solubility in all available solvents, which actually hampered its crystallisation. There was a very fine margin between an unsaturated solution and one where the compound precipitated. XRD-suitable crystals were finally obtained by dissolving the compound in a minimal amount of pentane and storing the solution at -40 °C over a few days. Analyses allowed the identification of the complex as $[Cp^*_2Yb(bimpym)Ir(COD)]_2$ (**2.1**, Figure 2.2).

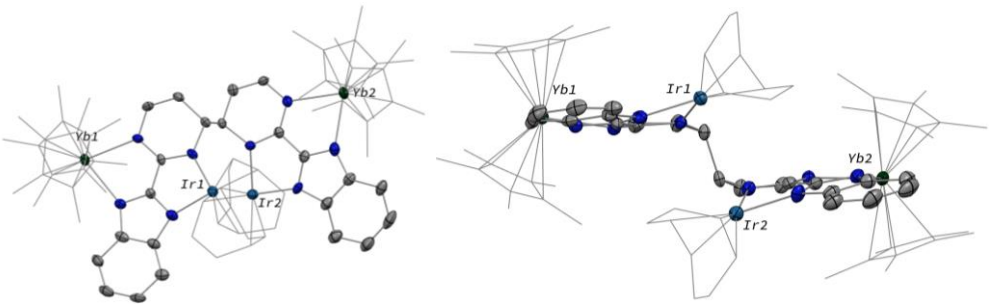

*Figure 2.2 : ORTEP of **2.1**. The Cp* co-ligands are displayed in wireframe to avoid clutter.*

The dimeric unit is consistent with an electron transfer from the divalent ytterbium to the ligand. The resulting ligand radical formed allows the accumulation of significant electronic density on the

coupling carbon, which therefore triggers the reaction. As a result, the pyrimidine moieties dearomatise and the coupling carbons are pulled out of plane. Both Ir centres are torqued out of plane by an average of 0.5 Å, presumably due to steric hindrance caused by the bulky COD ligands. The structural characteristics themselves are unremarkable: the Yb centres are trivalent (based on the distance to the centroid of the Cp*) and the ligand and Ir environments are not significantly altered by the electron transfer and the ensuing coupling reaction.

The relative conformation of the heterobimetallic fragments with respect to one another merits elaboration. The two fragments form what would be best described as two quasi-parallel planes, where the molecules are twisted with respect to the other. The torsion angle between the two fragments is ~63°, which is in contrast to 162° in the tetrametallic adduct **[Yb(bimpym)Ni]$_2$** and 178° in the homologous 18-C-6 capped adduct.[2] The conformation of the Ni-based coupling products is likely due to the presence of the counter-ions in the Ni-based complexes, which prevent proximity to the vicinal molecule.

Solution studies were then undertaken. The ^{1}H NMR spectrum shows highly paramagnetically shifted signals, consistent with the oxidation of the Yb centres to the trivalent state. The number of signals and their integration point to a species with a C_2 symmetry in solution.

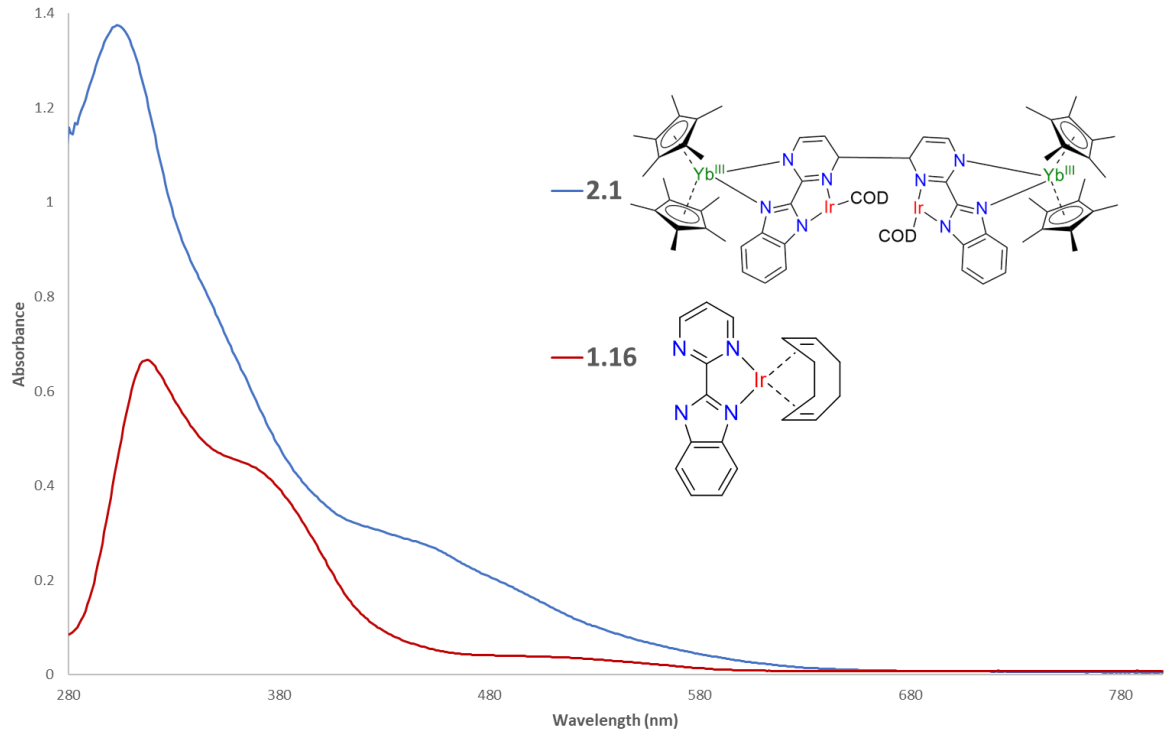

*Figure 2.3: UV-Visible spectra of the (bimpym)IrCOD complexes **1.16** and **2.1**.*

The most salient comparison for the UV-Visible data obtained for **2.1** is, clearly, the precursor **1.16**. Analogous transitions can be found in the complex bearing the additional Yb fragment on the ligand (Figure 2.3). In all cases, the transitions are both blue shifted and become more intense due to the presence of the Yb (Table 2.1). This can be explained by the increase in the overall electronic density following the coordination of Cp*$_2$Yb(OEt$_2$), whose probable repercussion is a better π-donating ability of the ligand. This raises the level of the empty ligand orbitals and makes the MLCT transition more demanding in energy.

	1.16			**2.1**		
λ (nm)	318	366	516	305	344	452
ε ($Lcm^{-1}mol^{-1}$)	6600	4440	365	13900	8570	2660
Transition	π->π*	MLCT	MLCT	π->π*	MLCT	MLCT

*Table 2.1: UV-Visible data obtained from the (bimpym)IrCOD complexes **1.16** and **2.1**.*

Complex **2.1** follows the same trend as the documented YbNi complexes cited above, as well as the theoretical observations outlined in Section 1.3.3.2. The reduction of the ligand is followed by a coupling reaction, seemingly irrespective of the TM environment. With potential catalytic applications in mind, this feature is undesirable, as the electronic density provided by the SET from the lanthanide is immediately channelled into the coupling reaction and not used to change the electronic properties of the transition metal.

That said, perhaps the spatial proximity between the two reactive Ir^{I} centres (3.84 Å) could lead to provide a reactive site for an in tandem catalytic activity. A preliminary trial sought to study the hydrogenation of alkenes using **2.1**, but no reactivity was observed. The encumbered coordination sphere of the Ir centres may explain this lack of reactivity.

Another attempt drew inspiration from the well-known Cativa catalytic cycle (Scheme 2.1), which also uses an Ir-based catalyst (Ir^{I} as an intermediate) to achieve methanol carbonylation.[3,4] However, this process is performed under high carbon monoxide overpressure and high temperature to ensure its efficiency. Naturally, **2.1** is not an adequate replacement for the active species in the Cativa cycle, as the Cp* co-ligands all but guarantee hydrolysis and decomposition in protic media. Therefore, efforts are underway to substitute them with iodides. As of yet, the addition of LnI_2 (Ln = Sm, Yb) to **1.16** has not allowed the isolation of any heterometallic complexes.

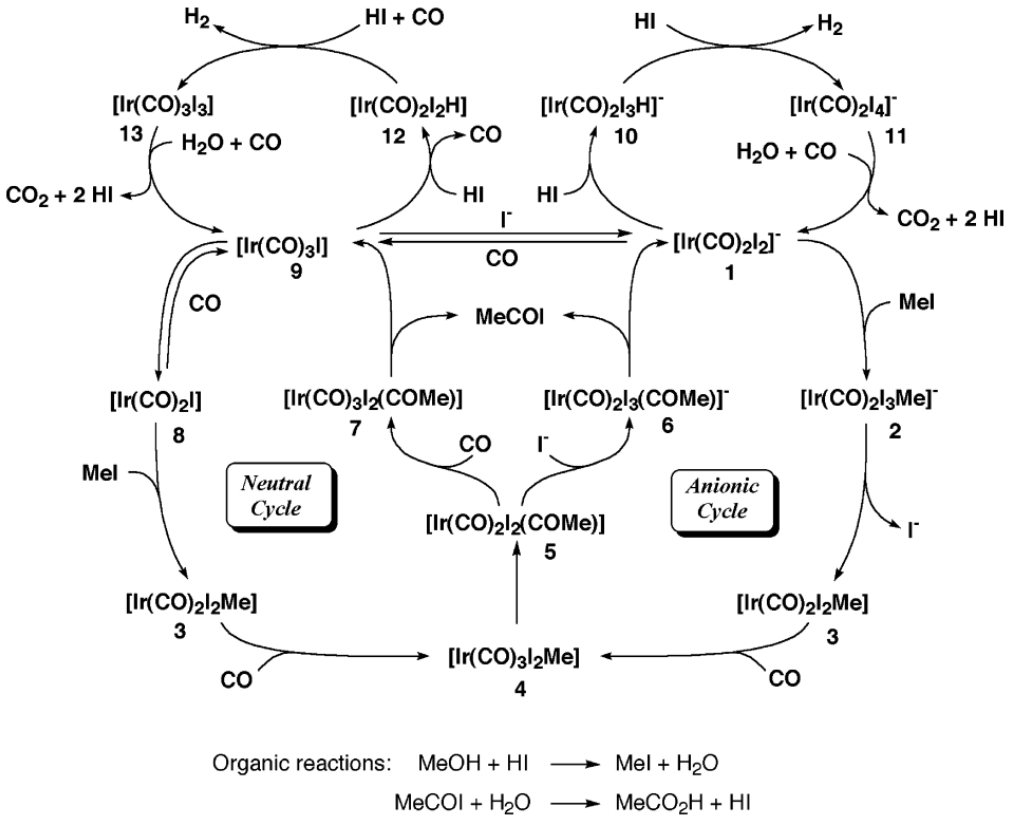

Scheme 2.1: Catalytic cycle of the Cativa process.[3]

2.2. Kbimpym-based complexes.

The addition of complexes **1.8**-**1.10** to the **K(bimpym)TMMe$_2$** family provided an opportunity to explore the reactivity of the other TM in group 10. The reactivity of **K(bimpym)NiMe$_2$**[2] was previously described during the PhD of Ding Wang.[5] The addition of divalent lanthanide precursors of Sm and Yb to **K(bimpym)NiMe$_2$** results in an initial electron transfer, leading to the coupled product of the formula [KCp*$_2$Ln(bimpym)NiMe$_2$]$_2$ in both cases. The reorganisation observed for the Yb complex – towards **Yb$_3$(bimpym)$_2$** – however, does not account for all the fragments in the tetrametallic adduct. The "missing pieces" are highlighted in Scheme 2.2 by considering 2 molecules of **[Yb(bimpym)Ni]$_2$**, after which one equivalent of **Yb$_3$(bimpym)$_2$** is obtained. All the Yb centres have already been oxidised, so it is assumed that no additional electron transfer occurs. Therefore, one equivalent of [Cp*$_2$Yb^{III}]$^+$ was ejected, along with all the Ni fragments (counting for 4 equivalents). Likewise, the fate of the second equivalent of bimpym$_2$, which presumably remains coupled and therefore a tetraanion, is unknown. The formation of one equivalent of KCp* (which co-crystallises with **[Yb(bimpym)Ni]$_2$**) is consistent with the Yb^{III} nestled in the middle of **Yb$_3$(bimpym)$_2$**, which only contains one Cp* co-ligand.

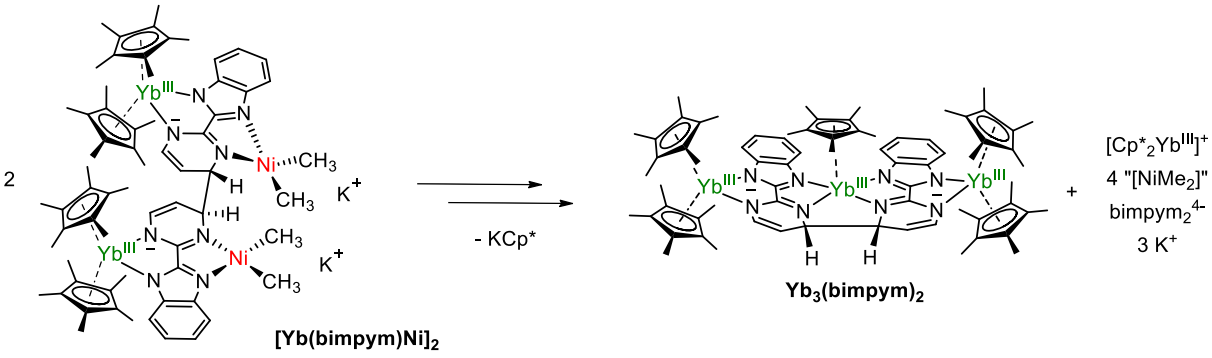

*Scheme 2.2: Full account of the main fragments of the reorganisation from **[Yb(bimpym)Ni]$_2$** to **Yb$_3$(bimpym)$_2$**.*

The objective in this chapter, therefore, will be to explore the corresponding reactivity with the aforementioned metal precursors.

2.2.1. Reactivity of the K[(bimpym)PtMe$_2$] complex.

The addition of ytterbocene to crystals of **1.8** in toluene resulted in the gradual darkening of the initial green suspension. The reaction was run until no further traces of the **1.8** could be distinctly observed: an overnight reaction was necessary. The filtration of the mixture resulted in a dark red solution. Cooling a saturated solution at -40 °C produced a small number of bright red crystals. Despite an outwardly excellent shape and adequate size, these crystals diffracted very poorly. It was impossible to obtain XRD data allowing us to characterise the compound.

Redissolution of the crystals in tol-d$_8$ resulted in a clean ^{1}H NMR spectrum, shown in Figure 2.4. The integration is telling: there are seven signals integrating for 1H each, two signals integrating for 3H and two signals with integrations close to the 15H of the Cp* co-ligands (obtaining a precise match is complicated by the dominant solvent signals on either side). This spectrum, containing highly paramagnetically shifted peaks, is a cogent indication of an asymmetric bimetallic species, whereby the ytterbocene has reduced the bimpymPtMe$_2$ fragment. Furthermore, it is a relatively close match to the spectrum of the **[Yb(bimpym)Ni]$_2$** species.[2] The presence of two separate methyl peaks

reproduces the behaviour of the Ni complex, which would imply a perturbative influence from the K^+ counter-cation that remains close to the complex. The main difference with regard to the **[Yb(bimpym)Ni]$_2$** complex, is that no bimpym signal was found between the two Cp* signals. Rather, the last signal shifts to 31.96 ppm, where the sole point of contention is that the integration does not entirely match the 1H of the other peaks attributed to the bimpym ligand.

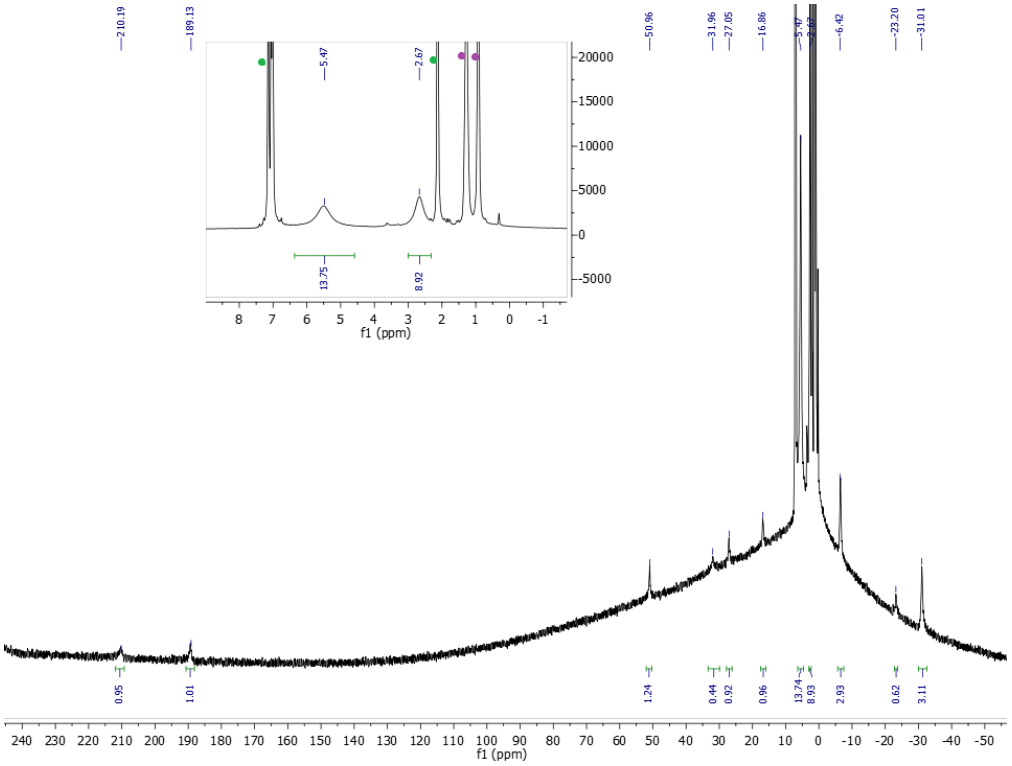

*Figure 2.4: ^{1}H NMR of the red crystals issued from the reaction between **1.8** and ytterbocene. The green dots in the inset correspond to solvent peaks; the purple ones to* n*-pentane.*

Nevertheless, the crystallised species – henceforth referred to as **Yb(bimpym)Pt** – is bound to be an adduct containing Cp*$_2$Yb, bimpym and $PtMe_2$ fragments. Given the ligand's propensity towards coupling reactions, it is more likely that **Yb(bimpym)Pt** is a dimeric species, as is **[Yb(bimpym)Ni]$_2$**, but this assertion could not be experimentally verified.

The poor yield of the crystallisation was interpreted to be an indication that **Yb(bimpym)Pt** is not the only species formed. Addition of pentane to the crystallisation solution resulted in the formation of a sandy brown precipitate. Upon its isolation and redissolution in tol-d_8, small traces of **Yb(bimpym)Pt** were found. The supernatant was also recovered. Its ^{1}H NMR analysis showed a near-perfect match with that of the previously described **Yb$_3$(bimpym)$_2$** species (Figure 2.5).

Based on the observations described above, it is within reason to presume that the reaction between ytterbocene and **1.8** behaves in a similar manner to that of the analogous K(bimpym)$NiMe_2$ species. To test this assertion, the same reaction was performed *in situ* in THF-d_8. The resulting purple solution was consistent with the formation of Cp*$_2$Yb(THF)$_2$,[6] but signals of **Yb(bimpym)Pt** were also found as a minority product. The fact that the reaction mixture did not evolve within the following week perhaps hints at the greater stability of the **Yb(bimpym)Pt** species with respect to the transformation towards **Yb$_3$(bimpym)$_2$**.

The same reaction was performed at larger scale under stirring in THF. Despite multiple attempts, the **Yb(bimpym)Pt** species could not be crystallised in a satisfactory manner, therefore impeding a definitive identification of the product.

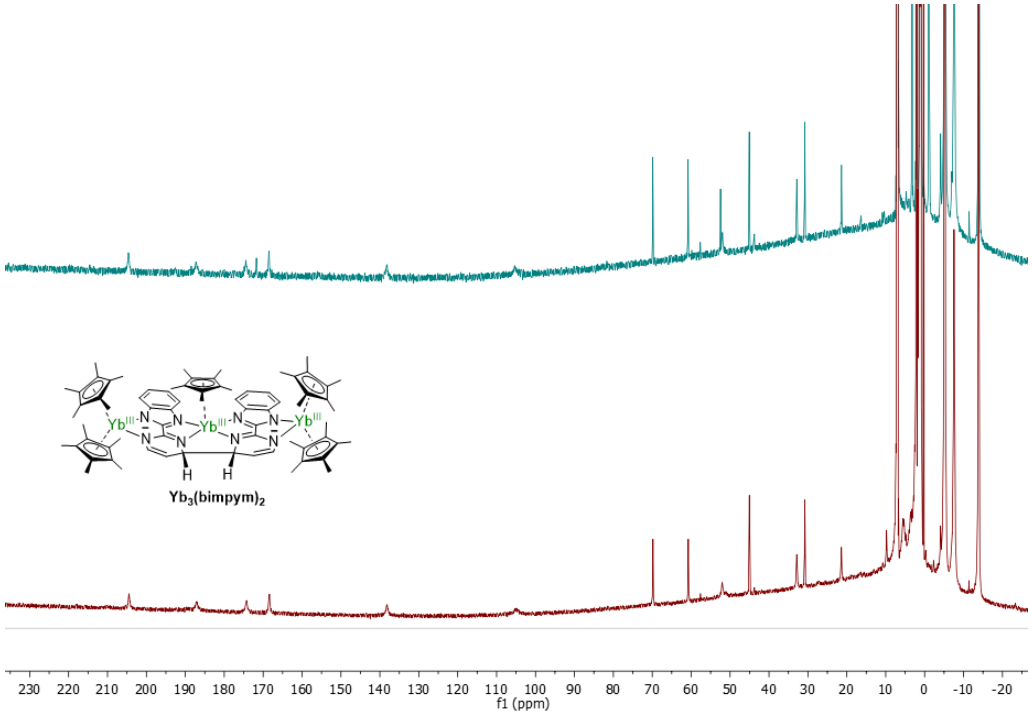

*Figure 2.5: Overlay of the spectra of **Yb_3(bimpym)$_2$** and of the second product of the reaction between **1.8** and ytterbocene.*

2.2.2. Reactivity of the K[(bimpym)PdMe$_2$] complex.

2.2.2.1. Synthesis and isolation and of the bimetallic dimethyl-bridged complex.

The same strategy was applied to **1.9**. The addition of ytterbocene to the Pd precursor in toluene was quicker than the corresponding reaction with **1.8** – all the crystals were dissolved within two hours to yield a black mixture with red hues. Letting the solution settle permitted the detection of very fine black powder. Careful filtration allowed obtaining a dark red solution and the separation of the black powder, which was insoluble in the available solvents. No ^{1}H NMR data could be obtained. This powder could presumably be Pd^0.

The supernatant was evaporated. Addition of pentane resulted in the formation of a black-red solution, with some remaining red solid. The red powder was determined to be the same **Yb_3(bimpym)$_2$** species obtained for the Ni and Pt adducts. The remaining solution was left at -40 °C. Pentane was an unsuitable crystallization solvent, as the resulting solid was not crystalline. Redissolution in toluene and storing the solution at -40 °C produced large black-brown crystals overnight. Acquisition of XRD data allowed the identification of the compound as Cp*$_2$Yb(μ-Me)$_2$PdCp* (**2.2**, Figure 2.6). These were the only isolated products from the reaction. It would appear that, contrary to the synthesis with **K(bimpym)NiMe$_2$**, no KCp* is produced.

The main distances of **2.2** are gathered in Table 2.2. The compound crystallises in the P2$_1$/n space group. The Yb-Cp* centroid distance is in line with that of other Yb^{III} species.[5,7] In consequence, on the basis of the ligands present, the other metal centre is Pd^{II}. The Pd-C_{Me} distances are longer than in the

parent **1.9** complex (2.123 Å vs 2.042 Å), which is consistent with both the partition of the negative charge with the Yb and the presence of another anionic ligand in the coordination sphere – the Cp*.

The presence of the latter is a rare occurrence, as there are only four other structurally authenticated complexes containing the same co-ligand.[8–11] Cp-based rings compounds with Pd^{II} in tandem with η^3-allyl co ligands are quite known[12] and are often used in chemical vapour deposition procedures.[13] The vast majority of organometallic compounds including a Cp-based ring coordinated to Pd involve the functionalisation of Cp sandwiches of other metals (mainly Fe[14], Co[15] and Ru[16]), which then coordinate the Pd.

Atoms	Av. Values (Å)
Yb-Pd	2.877(1)
Pd-Me (avg)	2.123(2)
Yb-Me (avg)	2.555(3)
Yb-H (avg)	2.206
Pd-Cp*$_{ctr}$	2.017
Yb-Cp*$_{ctr}$ (avg)	2.332

*Table 2.2: Main distances in complex **2.2**.*

The Pd-Cp* centroid distance is in the range of the other described complexes (1.926-2.060 Å). However, the more important feature in such cases are the individual Pd-C(Cp*) distances, as they would give a better idea of the hapticity of the Cp* co-ligand. The more pertinent comparisons would be with other Pd^{II} centres[8,11] described, as this configuration has a strong tendency to form square planar complexes. In such examples, the centroids are, indeed, very close to the one in **2.2** (1.98 Å and 2.00 Å), and the Pd-C(Cp*) bond lengths present a considerable spread (2.21-2.40 Å[8] and 2.28-2.36 Å[11]), compared to typical bond lengths in η^5-coordinated Cp*-metal centres. This is, indeed, the situation in **2.2**, as the two C atoms which best fit the square planar environment have shorter bonds than the other three (all the Pd-C bond lengths are shown in the central panel of Figure 2.6), with bond lengths ranging from 2.27 Å to 2.42 Å. As evidenced by the $\overline{RPdR'}$ angles, the square plane is slightly distorted.

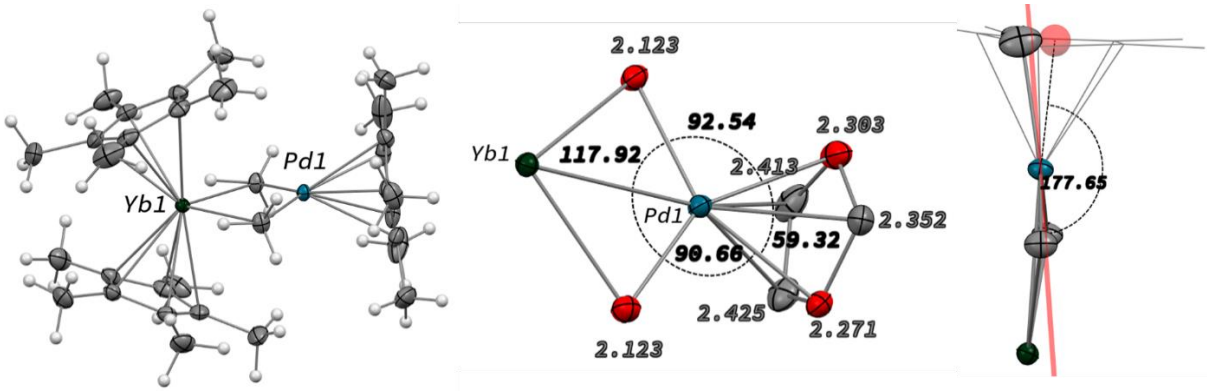

*Figure 2.6: Left: ORTEP of **2.2**. Centre: coordination environment of the Pd^{II}, including bond distances and angles between the four coordinating atoms defining the square plane (the composing atoms are shown in red). Right: perspective of the distorted square planar environment, along with the angle formed by Yb, Pd and the centroid of the Cp*.*

Another notable structural feature is the presence of two methyl moieties bridging the trivalent Yb and the Pd. The two distances are identical to one another. This motif has been some precedent. The first reports presenting such a pattern involved the salt metathesis between Cp_2YbCl and $Li[AlMe_4]$.[17]

Addition of an equivalent of Lewis base (pyridine) to this complex, as well as analogues with other lanthanides, lead to the Ln-Me_2-Ln (Ln = Y, Dy, Ho, Er, Tm, and Yb) compounds.[18] Similar strategies have since been employed to form similar bridging complexes with both trivalent[19,20] and divalent[19,21] Yb centres. The group of Anwander also described complexes with either two or three bridging motifs.[20,22] Addition of Pt^{II} complexes bearing hydrides and/or methyl moieties to ytterbocene results in Yb^{II}-Pt^{II} complexes.[23] Andersen found Yb-H interactions to be stronger than those in the Yb-CH_3 bond.

The compound also features a short Yb-Pd distance. Crystallographic evidence of other Ln-Pd short distances exist in the literature. Kempe was the first to publish such complexes, containing a Nd-Pd distance of ~3.04 Å.[24] Subsequent reports have since described numerous other complexes, often supported by acetate or carboxylate co-ligands.[25–28] The same distance in **2.2** is of around 2.88 Å, which qualifies it as among the shortest in the literature.

Furthermore, there is an almost perfectly linear arrangement (177.65°) between Yb, Pd and the Cp* centroid (Figure 2.6, right). If the square plane determined by the Pd coordination environment ($C_{Me}C_{Me}PdC_{Cp*}C_{Cp*}$) is slightly distorted (average deviation = 0.077 Å, with the two C_{Cp*} the most torqued out of the plane), the plane created by Yb, Pd, the two C_{Me} and the centroid of the Cp* contains all of its elements much more neatly (average deviation = 0.056 Å). The short Yb-Pd distance and the specific spatial arrangement described herein will be investigated further in the following sections.

The aforementioned crystals were washed with cold pentane to remove traces of **Yb_3(bimpym)$_2$** and redissolved in tol-d_8, resulting in a purple solution. The spectrum presents only 3 signatures, which is consistent with a symmetrical species in solution. It is worth noting that the methyl signal is significantly paramagnetically shifted, at 388 ppm, much more than other compounds in its class.[19,20] Likewise, the attribution of the PdCp* signal at -11.4 ppm is far from the typical range of the Cp family in diamagnetic compounds. For comparison, all the PdCp* peaks in the works cited above are in the 1.40-2.17 ppm range. This is indicative of a clear paramagnetic shift, as is characteristic for paramagnetic complexes of Ti^{III} or the commonly used cobaltocene family.[29,30]

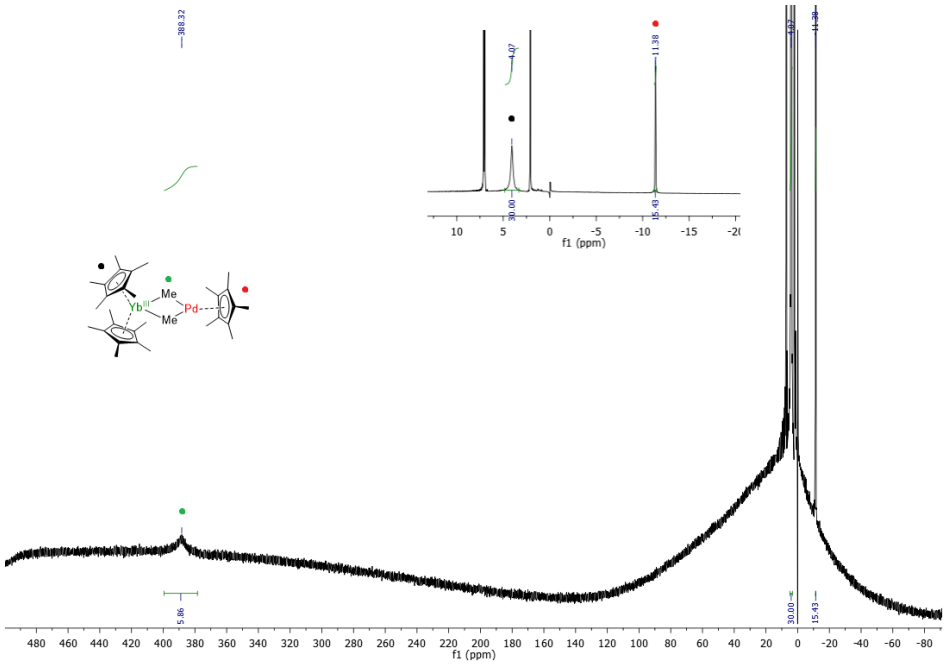

*Figure 2.7: ^{1}H NMR of **2.2** in tol-d_8.*

The most likely explanation is that the paramagnetic effect of the Yb^{III} is strong enough to engender this shift.[31] There is precedent for the shifting of Cp* peaks due to the substantial paramagnetic effect induced by several lanthanides. Comparable structures featuring Ln^{III} ions and TM-Cp* fragments exist, although the lanthanoids are predominantly the diamagnetic Y, La or Lu. Such complexes were described by the groups of Evans,[32] Anwander[33] and Hou.[34] Andersen described methyl-bridged mixed ytterbocene-titanocene complexes, where the Yb was diamagnetic – the paramagnetic effect came from Ti^{III}.[19] Pr^{III} and Nd^{III} have negligible effects on the Cp* signal.[35] Numerous recent works by the group of Roesky[36–38] and Hou[39–41] reported compounds that would fit the bill, but ^{1}H NMR information is not given (surprisingly, even in the cases with the milder Sm^{III} and Yb^{III}).

Alternatively, the paramagnetic effect would originate from the Pd^{II} centre. This would, indeed, be unexpected, as Pd^{II} is not typically paramagnetic in the square planar configuration, although a recent example of paramagnetism was observed in a polyoxopalladate, due to the presence of vicinal out-of-plane oxygen anions.[42] Substantiating such an assertion would be difficult and will be discussed in the following sections.

Further tests were performed to probe the effect of solvent on the reaction forming **2.2**. The addition of ytterbocene to **1.9** in THF results in a purple-red solution. ^{1}H NMR analyses of the crude reaction mixture showed the characteristic peaks of **Yb_3(bimpym)$_2$**, but not of **2.2**, implying that this solvent is not conducive to the reorganisation leading to its formation. It was, however, possible to deduce the presence of another species amidst all those present, which would be consistent with a $Cp^*_2Yb^{III}$(bimpym)$PdMe_2$ formulation (henceforth referred to as **Yb(bimpym)Pd**, Figure 2.8). This can be affirmed due to the similarity borne by the spectrum to the comparable Ni and Pt species. As in the case of **Yb(bimpym)Pt**, it is difficult to state with conviction whether or not this species is a dimer. No further studies on this species were performed, as it could not be isolated cleanly. It is also worth noting that this species was never observed when the reaction solvent was toluene.

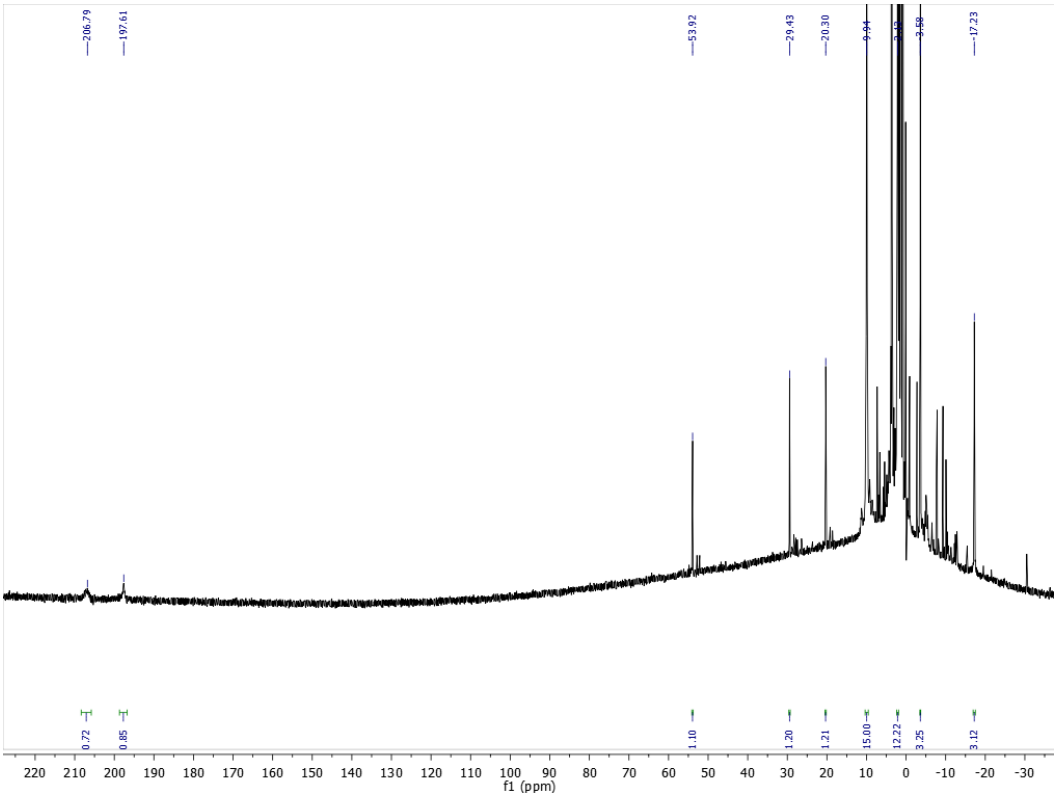

*Figure 2.8: ^{1}H NMR in THF-d_8 of the reaction mixture, following the addition of ytterbocene to **1.9** in THF.*

The use of toluene as the reaction solvent is, therefore, necessary to obtain **2.2**. Once the previously described crude mixture is obtained, however, isolating **2.2** from **Yb_3(bimpym)$_2$** is not a trivial matter. **2.2** is indeed the more soluble of the two in pentane or Et_2O. As a result, leaving a concentrated reaction mixture in either of these two solvents at -40 °C leads to the precipitation of a solid, where **Yb_3(bimpym)$_2$** is largely dominant**.** However, this procedure only works to a certain point, as, according to ^{1}H NMR, molar ratios of, at best, 5:1 in favour of **2.2** can be obtained in subsequent recrystallisation attempts (Figure 2.9). Given this impasse, pure **2.2** was isolated by leaving a very concentrated toluene solution of the mixture at -40 °C, as **2.2** crystallises preferentially. After removal of the supernatant, the crystals are rapidly washed with cold pentane a few times to remove the traces of **Yb_3(bimpym)$_2$** – this procedure was necessary to obtain a clean ^{1}H NMR spectrum, as shown in Figure 2.7.

The caveat of this protocol is the overall poor crystallisation yield of this mixture, which does not allow recuperating large quantities of **2.2**. Despite our best efforts, isolating enough pure **2.2** in order to obtain solid-state magnetic data and an elemental analysis report was not possible. To compound this, the difficulty in obtaining the pure precursor **1.9**, documented in Section 1.3.2, makes the overall procedure very inefficient.

The more facile isolation of **1.10** offered a potentially more promising approach. The *in situ* addition of ytterbocene to the capped complex revealed a virtually superimposable spectrum to the one of the crude mixture following the same reaction with **1.9**. Although auspicious, this method confronts the same product separation issues described above.

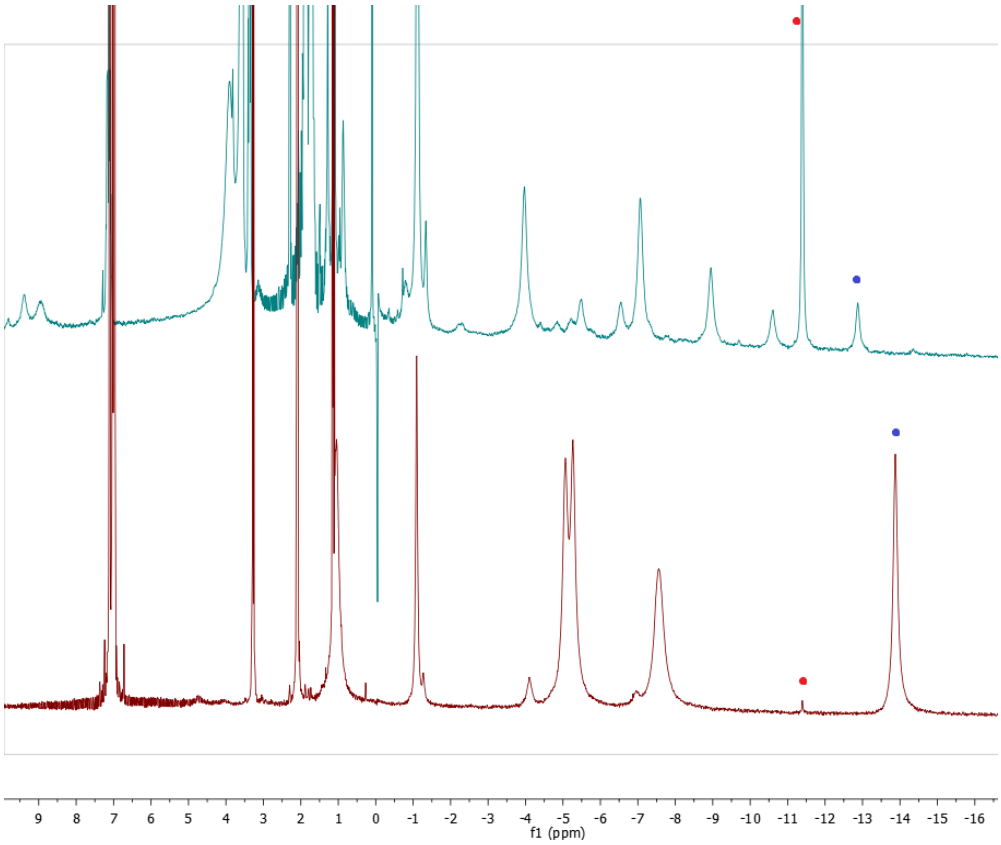

*Figure 2.9: Work-up of the reaction leading to the formation of **2.2**. The red dots indicate **2.2**, while the blue ones indicate **Yb_3(bimpym)$_2$**. The ^{1}H NMR of the solid after the first recrystallisation in Et_2O – in tol-d_8 – is shown below. The ^{1}H NMR of the solid formed in subsequent recrystallisation reactions – in THF-d_8 – is shown above.*

2.2.2.2. Reactivity with samarocene.

The surprising structure of **2.2** led to the pursuit of the homologous Sm adduct. The addition of samarocene ($Cp^*_2Sm(OEt_2)$)to **1.9** resulted in a yellow-brown suspension, which gave a yellow solution after filtration. No adequate crystals could be obtained from cooling a saturated toluene solution. Redissolution in THF afforded adequate yellow crystals, which were XRD-suitable and allowed the identification of the compound as $[Cp^*_2Sm(bimpym)]_2Sm(THF)Cp^*$ (**2.3**, Figure 2.10). The main structural features confirmed that it is isostructural to **Yb_3(bimpym)$_2$**.

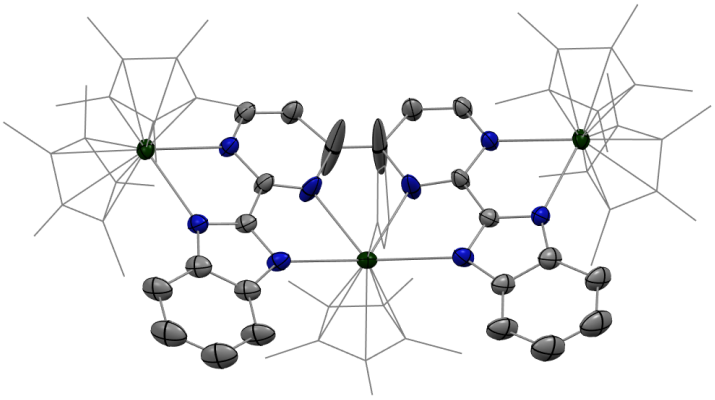

*Figure 2.10: ORTEP of **2.3**. The Cp* co-ligands and the THF coordinated to the central Sm are set in wireframe for clarity.*

Employing the same work-up procedure described for **2.2** in the case of Sm adduct allows the separation of **2.3** from another compound. The integration of the signals of the latter is not immediately suggestive – a 30:4:4:1:1 ratio is obtained for the peaks attributed to this compound. This species could not be isolated, precluding further characterisation.

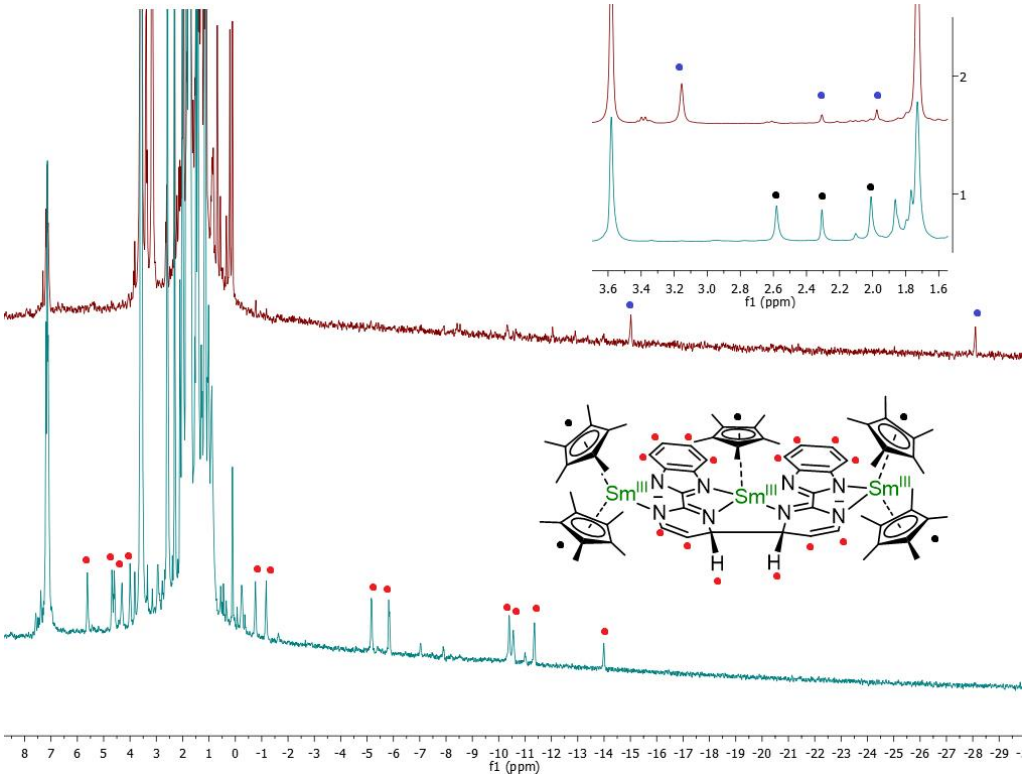

*Figure 2.11: ^{1}H NMR of **2.3** (below) and of the product following recrystallisation of **2.3** (blue dots, above) in Et_2O.*

2.2.2.3. Understanding the formation.

The exact stoichiometry of this reaction was not known, as the ratio between **Yb_3(bimpym)$_2$** and **2.2** could not be reliably established on a large scale. To probe this, two *in situ* reactions were carried out in tol-d_8, with one and two equivalents of $Cp^*_2Yb(OEt_2)$, respectively. This choice of solvent is not ideal, because the signals of the precursor **1.9** cannot be tracked. As mentioned above, THF-d_8 could not be used, as **2.2** would not be generated under these conditions.

Both *in situ* reactions produced black-dark red mixtures instantly upon the addition of the solvent. Signals of both compounds are immediately observed and the evolution is quite clean all throughout the duration of the study. In the 1:1 reaction, the two products are initially in an equimolar ratio, whereas **2.2** accounts for almost 60% when using more ytterbium. In both cases, the proportion of **2.2** declines over time (Figure 2.12). It was not possible to determine visually if this was due to its precipitation/crystallisation or if **Yb_3(bimpym)$_2$** is formed preferentially over longer periods of time. In both cases, the conversion of the precursor **1.9** could not be reliably quantified *in situ* over the course of the reaction, either. Curiously, free ytterbocene is consumed faster when 2 equivalents are used, as its signal was no longer observed in the spectrum acquired 21 hours after the beginning of the reaction, whereas there were still traces thereof after two days in the 1:1 reaction. This would imply that both the outcome and the kinetics of the reaction are influenced by the local concentration in ytterbocene.

Unattributed, but well-defined signals were found in both reactions (highly shifted, at -121 and -215 ppm). This suggests that a supplementary product is likely to be formed. It was, however, impossible, to identify and characterise this product.

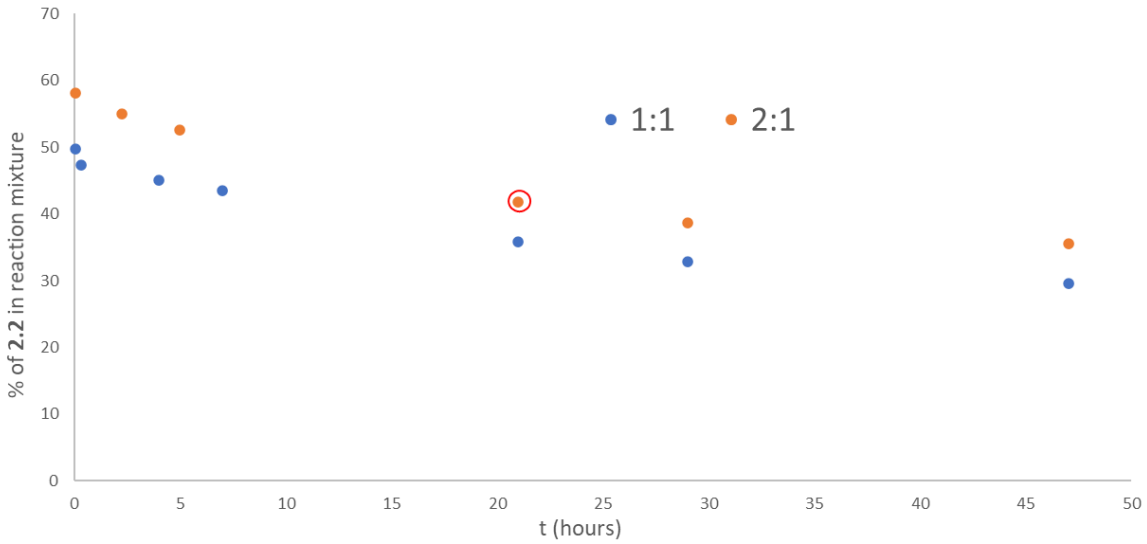

*Figure 2.12: Evolution of the proportion of **2.2** with respect to **Yb_3(bimpym)$_2$** in the reaction mixture over time, following in situ reactions with one and two equivalents of ytterbocene. No more ytterbocene could be distinctly identified after 21h (circled in red) in the case of the 2:1 reaction.*

There are several missing pieces to the puzzle necessary for a fuller understanding of the reaction mechanism, the most glaring of which is the lack of a transient species. We assume a similar evolution to the one postulated for the reactivity of the **K(bimpym)NiMe$_2$** precursor: a very unstable heterometallic species is formed after the addition of ytterbocene. *A priori*, **Yb(bimpym)Pd** would fit the bill.

We propose two likely outcomes for the following steps (shown in Scheme 2.3). In the first case, this species degrades into **Yb_3(bimpym)$_2$** and **2.2**. This assumption is supported by the fact that, contrary to the Ni species, no KCp* was detected throughout our work, which would enable the coordination of the Cp^{*-} co-ligand to the Pd^{II} centre. This hypothesis is imperfect, as it does not explain the varying ratios between **2.2** and **Yb_3(bimpym)$_2$** observed throughout the reaction.

The second possibility is that more than one equivalent of ytterbocene per molecule of **1.9** is necessary in order to form **2.2**. Given that **1.9** is insoluble in toluene, the coordination of Yb to the bimpym ligand, leading to an intermediate species, is most likely a heterogeneous procedure. Any intermediate species (**Yb(bimpym)Pd** or others) are bound to be more soluble, due to the presence of the lipophilic Cp* co-ligands on the Yb centre. The next step of the transformation would be the reaction with a second molecule of ytterbocene, which would trigger the reorganisation towards the final products. This mechanism is more consistent with the observed dependence of the concentration of ytterbocene.

In such a case, the reaction with the 2:1 stoichiometry proceeding faster is logical – more ytterbium is necessary after the intermediate species is formed to trigger the rearrangement towards **Yb_3(bimpym)$_2$**. Therefore, the local concentration of ytterbocene would be very influential in both generating the intermediate species, as well as for triggering the reorganisation leading to **Yb_3(bimpym)$_2$** and **2.2**. Lastly, this scenario would also explain the observed black powder as zero-valent Pd formed after reduction by the ytterbocene, thus accounting for the equivalent of Pd proposed in.

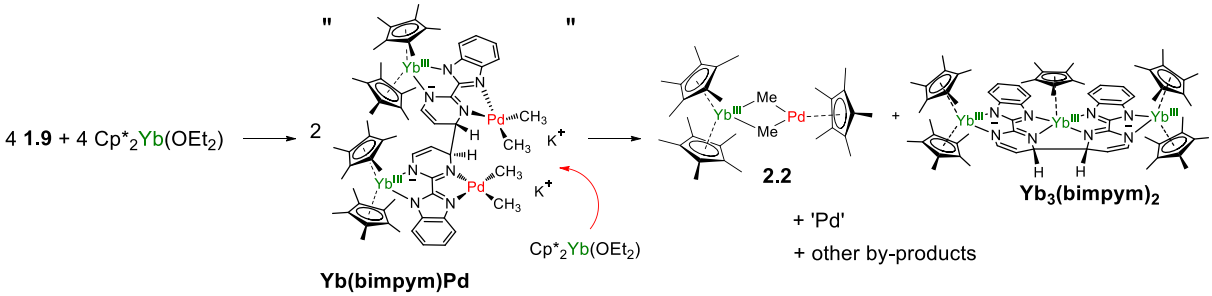

Scheme 2.3: Two propositions for the reaction mechanism. The second one, which involves the interaction with another ytterbocene molecule, is shown with the red arrow.

2.2.2.4. Spectroscopic studies.

The unusual structure of **2.2** might hint at an interaction between the two metal centres. The close proximity between two metals in similar adducts has been previously invoked to justify such interactions.[43–45] It should be noted that, from an orbital perspective, all of these interactions were shown to be dative interactions, highly dominated by the contributions of a single metal, usually the non-rare earth metal centre.

The first concern was establishing the behaviour of the Yb centre. The ^{1}H NMR spectrum at r.t clearly shows a consequential paramagnetic effect, which is a sure-fire indication of the Yb^{III} configuration. In conventional complexes with RAL, the electron transfer was shown to be reversible. If, indeed, there is an interaction with the Pd centre, then perhaps it is temperature-dependent. The easiest way to probe this is by acquiring solid-state magnetic data. Unfortunately, a sufficient quantity of pure **2.2** could not be collected for a SQUID analysis.

The closest alternative found was to perform variable temperature ^{1}H NMR acquisitions. Over the studied temperature range (-70 °C to 60 °C), this analysis would indicate whether the evolution of the paramagnetic shift follows the Curie law. Any deviation from this behaviour could be indicative of a multiconfigurational state.[46] As it were, no such deviation was observed, as the evolution of the displacement over the inverse of the temperature was perfectly linear (R^2>99.5%) across the entire range (Figure 2.13).

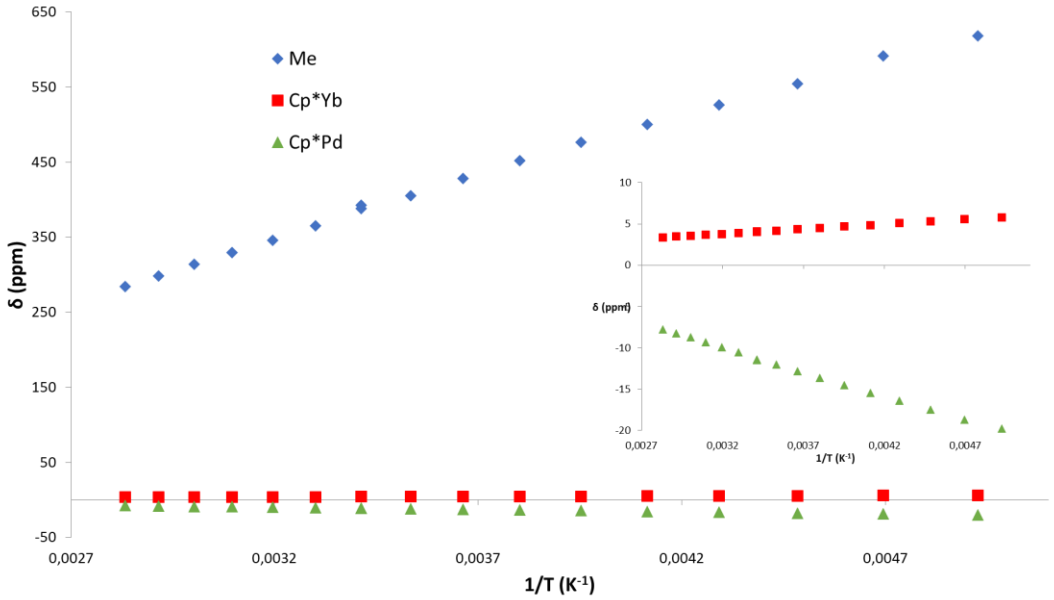

*Figure 2.13: Variable temperature ^{1}H NMR of **2.2** – δ over 1/T. The evolution of the signals near 0 ppm is shown in the inset.*

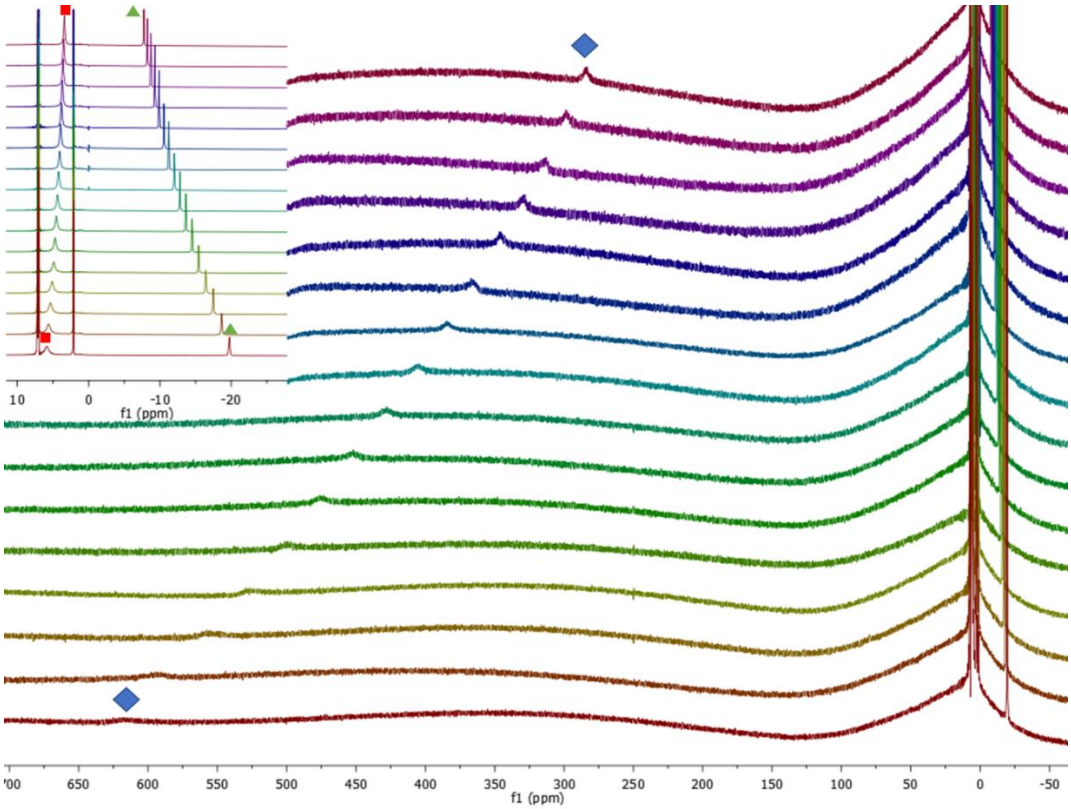

*Figure 2.14: Variable temperature ^{1}H NMR acquisitions for **2.2**. The blue lozenge designates the methyl peak, the red square the YbCp* and the green triangle the PdCp*.*

Due to the low availability of clean, isolated compound, the IR spectrum was recorded by letting a drop of concentrated solution dry on the detector. Satisfactory data was obtained. The only features that would be expected involve the Cp^{*-} anion and the methyl bridging groups. The signature bands of a alkyl C-H stretching (2853-2960 cm^{-1}) and bending (1446 cm^{-1}) are observed and are consistent with previous reports of comparable products.[19,20]

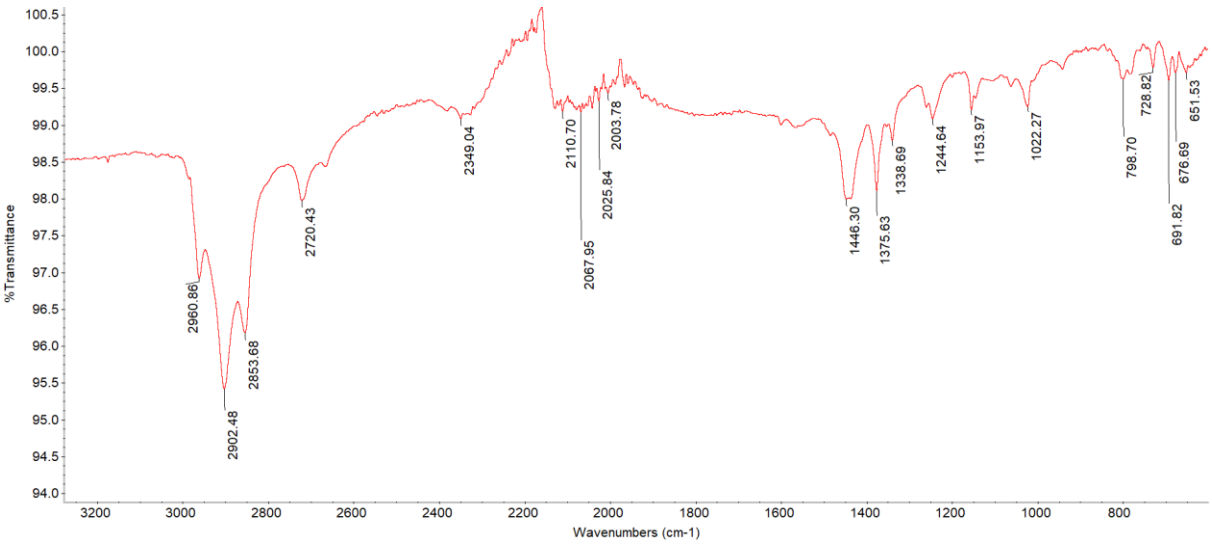

*Figure 2.15: IR spectrum of **2.2**. The main bands are indexed.*

2.2.2.5. Reactivity.

The difficulty associated with obtaining **2.2** in high yield has limited the scope of reactivity that could be attempted. The main objectives were probing the stability of the bridged Yb-Pd bond and whether it could be shortened further.

Reduction of the complex was attempted with KC_8 in pursuit of the former objective. Performing an *in situ* reaction in tol-d_8 only led to the gradual discolouring of the purple solution, which was corroborated by the extinction of the product signals over the course of 24 h. The ensuing black powder could not be dissolved in the other attempted solvents, therefore precluding its chemical characterisation.

A second trial involved a low-pressure addition of H_2. This method has previously been used to produce lanthanide hydride complexes starting from alkyl of η^3-allyl moieties.[47,48] No evolution was noticed across multiple days of reaction time.

It would appear that the compound is unreactive when submitted to some of the classical transformations in organometallic chemistry. That said, this conclusion should not be interpreted to be definitive. The addition of dihydrogen, although theoretically favourable, was performed at a low overpressure (0.2 bar). Further trials could involve higher pressures and perhaps higher temperatures.

Additionally, perhaps the reduction trials would yield better results if the reaction were performed with a soluble partner, as potassium graphite has a heterogenous reduction mechanism. The reaction with freshly prepared NaNaphtalene solutions should be considered for further information.

2.2.3. Partial conclusion.

The reactivity of **1.8** and **1.9** towards reductive divalent lanthanide complexes was explored in this section. This was motivated by the desire to probe whether the complexes of the group 10 metals, Pd and Pt, were to behave in a similar fashion to the previously established template of the **K(bimpym)NiMe$_2$** complex.

The answer is not entirely straightforward, since the three complexes share aspects of their reactivity and differ substantially in others. The first steps of the reaction are common to all three – formation of **Yb(bimpym)TM**-type species indicates that the coordination of Cp*$_2$Yb(OEt$_2$) has occurred and is accompanied by an electron transfer. Although not proven definitively for the Pd and Pt adducts, there are strong reasons to believe that these compounds are very similar to [**Yb(bimpym)Ni**]$_2$ in that a coupling reaction has occurred.

The formation of the trimetallic adduct **Yb$_3$(bimpym)$_2$** in all three cases also indicates that the reactivity shares notable elements with respect to the final products.

It is what goes on between the beginning and the end of the reaction that the three reactivities diverge. [**Yb(bimpym)Ni**]$_2$ is an unstable adduct and always evolves towards **Yb$_3$(bimpym)$_2$**. The formation of KCp* is cited as a thermodynamic driving force that helps the reaction evolve towards the final compounds.

Yb(bimpym)Pt is perfectly stable at room temperature and shows no tendency to evolve in THF. When the reaction is performed in toluene, it seems to remain stable in a separate fraction to its end point, **Yb$_3$(bimpym)$_2$**. These conclusions are subject to evolution, as this reaction was not studied as thoroughly, due to the synthetic difficulties in obtaining pure **1.8**.

The Pd reactivity is definitively the most interesting. When the addition of ytterbocene to 1.9 is performed in THF, both the heterometallic adduct **Yb(bimpym)Pd** and **Yb$_3$(bimpym)$_2$** are detected. When the solvent is toluene, an unusual bimetallic adduct, bearing a short Yb-Pd distance is isolated, in addition to **Yb$_3$(bimpym)$_2$**. It would appear that the driving forces behind the final products are different to those in the Ni adduct, as no KCp* was detected. Rather, the Cp* group, presumably eliminated by the central Yb atom in the trimetallic complex, coordinates to the PdMe$_2$ fragment.

The two main products are both formed almost immediately after the beginning of the reaction, although the proportion of **2.2** decreases over time. There are still some question marks hanging over some specific details regarding the formation mechanism of this compound. Alas, due to the lack of solubility of **1.9** in toluene, its evolution cannot be tracked. Other solvents will be trialled to see if more information can be gathered.

There are several important synthetic difficulties that are yet to be resolved, hindering attempts for a more rigorous spectroscopic characterisation of this adduct and of its reactivity. This is compounded by the difficulty in obtaining the precursor in an efficient manner. Considerable efforts shall be invested in this direction.

Also intriguing in this regard is the analogous reactivity with samarocene. Although the equivalent of **Yb$_3$(bimpym)$_2$** was isolated (**2.3**), no isostructural complex to **2.2** was obtained. The presence of a second product issued from this reaction is likely, but could not be confirmed. A potential explanation that would justify such a difference with regards to the reactivity of ytterbocene will be provided in Chapter 3.

2.3. Pd(bimpym)-based complexes.

The next precursor whose reactivity was examined was **1.12**. It was of interest to see whether the energetical proximity of the two closest vacant orbitals – centred on the pyridine (LUMO) or on the ligand (LUMO+1) – would afford the opportunity for different reactivity.

2.3.1. Reactivity with divalent lanthanides.

2.3.1.1. Isolation of the coupling products

The addition of ytterbocene to **1.12** in toluene immediately results in a brown-black suspension. Filtration of the mixture, followed by storing a concentrated solution at -40 °C allows the isolation of satisfactory crystals. XRD analysis allowed the identification of the compound as $[Cp^*_2Yb(bimpym)Pd(py)(Me)]_2$ (**2.4**). As was observed in previous bimpym-based complexes, the addition of divalent lanthanides leads to an electron transfer, which prompts a coupling reaction. It would appear that the coordination of the lanthanide lowers the **LUMO^{pym}** below the **LUMO^{L}** (Table 1.12), activating the ligand-based pathway.

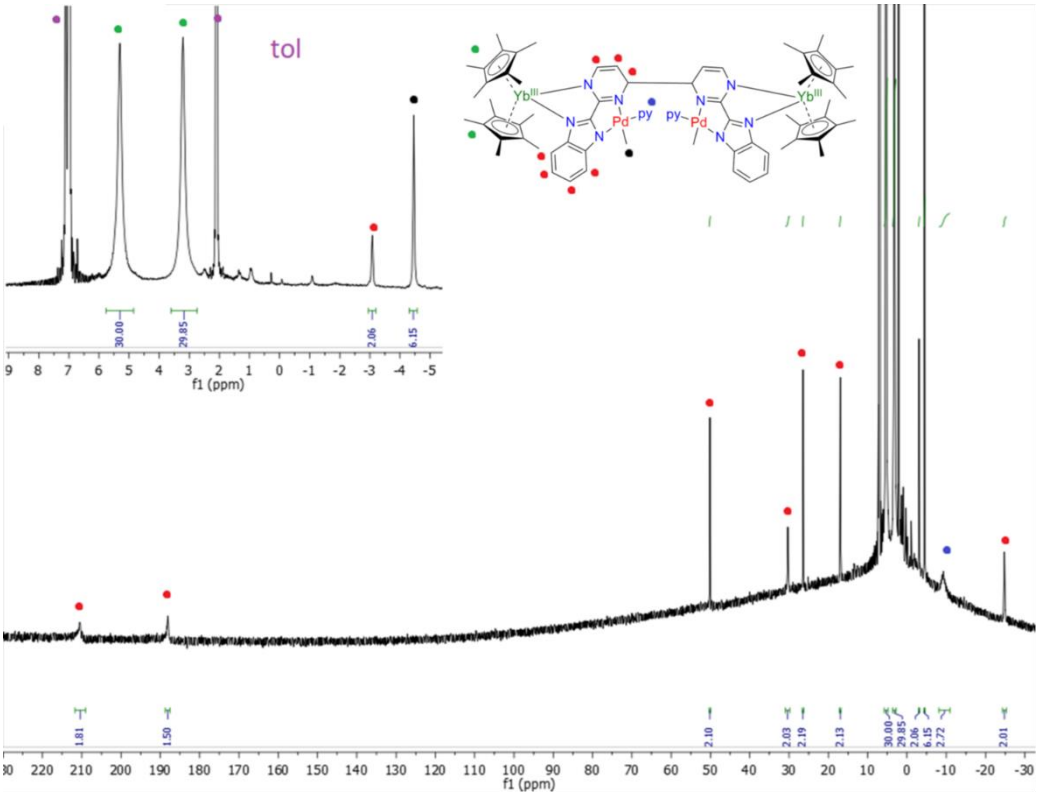

*Figure 2.16: ^{1}H NMR of **2.4** in tol-d_8 at r.t.*

^{1}H NMR studies revealed a symmetrical species in solution (Figure 2.16), as evidenced by the 7 signals corresponding to the protons on the bimpym ligand, 2 signals for the Cp* co-ligands and the single peak accounting for the methyl moiety. The pyridine signals could not be reliably identified at r.t, indicating a fluxional behaviour. Lowering the temperature to -70 °C slows the pyridine exchange in solution to the NMR timescale, allowing the definitive attribution of its signals.

Curiously, if left at room temperature, the characteristic peaks of **2.4** slowly evolve cleanly (Figure 2.17 and Scheme 2.4). A new set of signals, having the same symmetry and integration, replaces the ones

of **2.4** within 10 days (can be shortened to less than 3 days under stirring). This product is less soluble in toluene, but careful dilution and storage in the freezer allowed the growth of crystals of sufficient quality. XRD analysis allowed the structural characterisation of the species as $[Cp^*_2Yb(bimpym)Pd(Me)(py)]_2$ (**2.5**). The evolution observed by NMR is, therefore, the isomerisation of the species, whereby the pyridine and methyl moieties switch places.

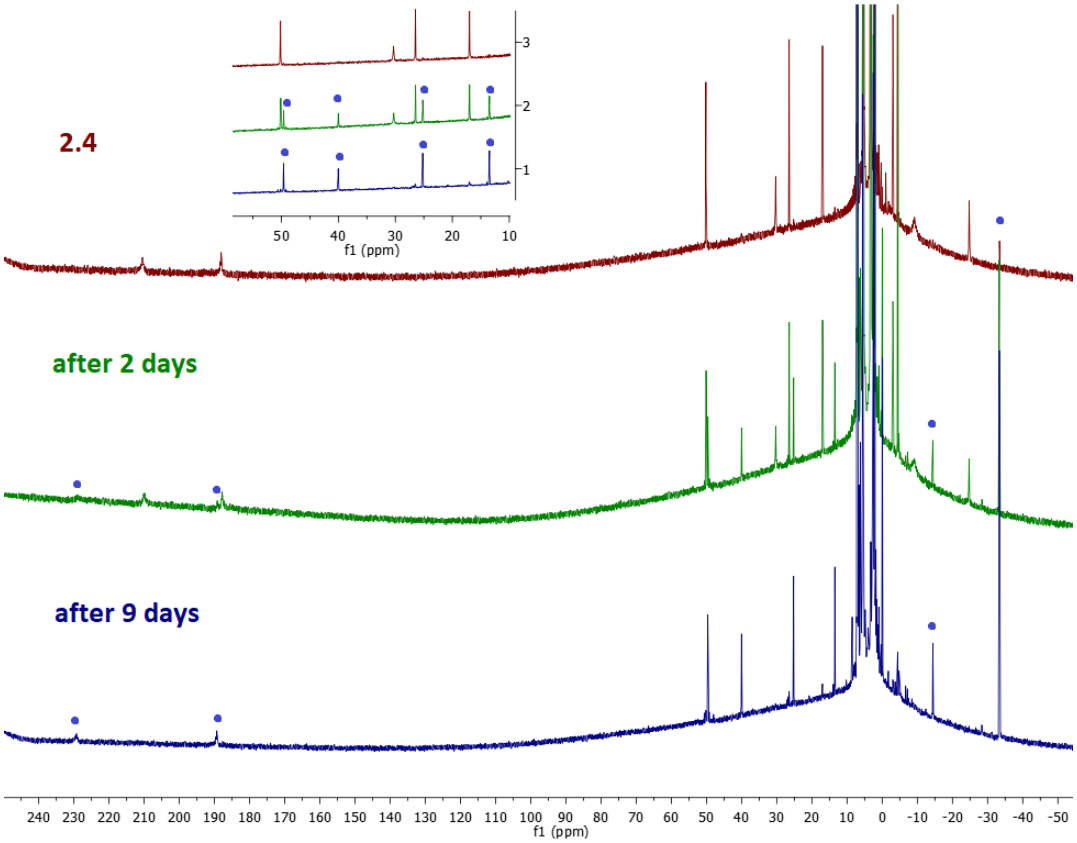

*Figure 2.17: Evolution of **2.4** to **2.5** (blue dots), studied by ^1H NMR in tol-d_8.*

Due to this isomerisation process, the synthesis of **2.4** calls for a careful approach. Optimal conditions require very short reaction times (less than one minute stirring) and a slight excess in **1.12** (1.2 eq) to prevent the decomposition of **2.4**, presumably by reacting with a second molecule of $Cp^*_2Yb(OEt_2)$ (Figure 2.18). A flurry of unknown signals appears very rapidly after the beginning of the reaction. Among these, a dominant peak (at 9.1 ppm) progressively grows. Higher concentrations or excess of ytterbocene leads to the more rapid decomposition of **2.4**'s characteristic signals.

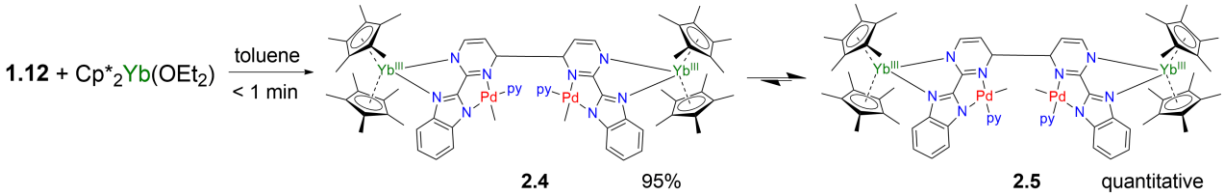

*Scheme 2.4: Addition of ytterbocene to **1.12** and the subsequent isomerisation to form **2.5**.*

The use of a coordinating solvent, such as THF, results in the formation of an adduct with ytterbocene and blocks any subsequent reactivity.

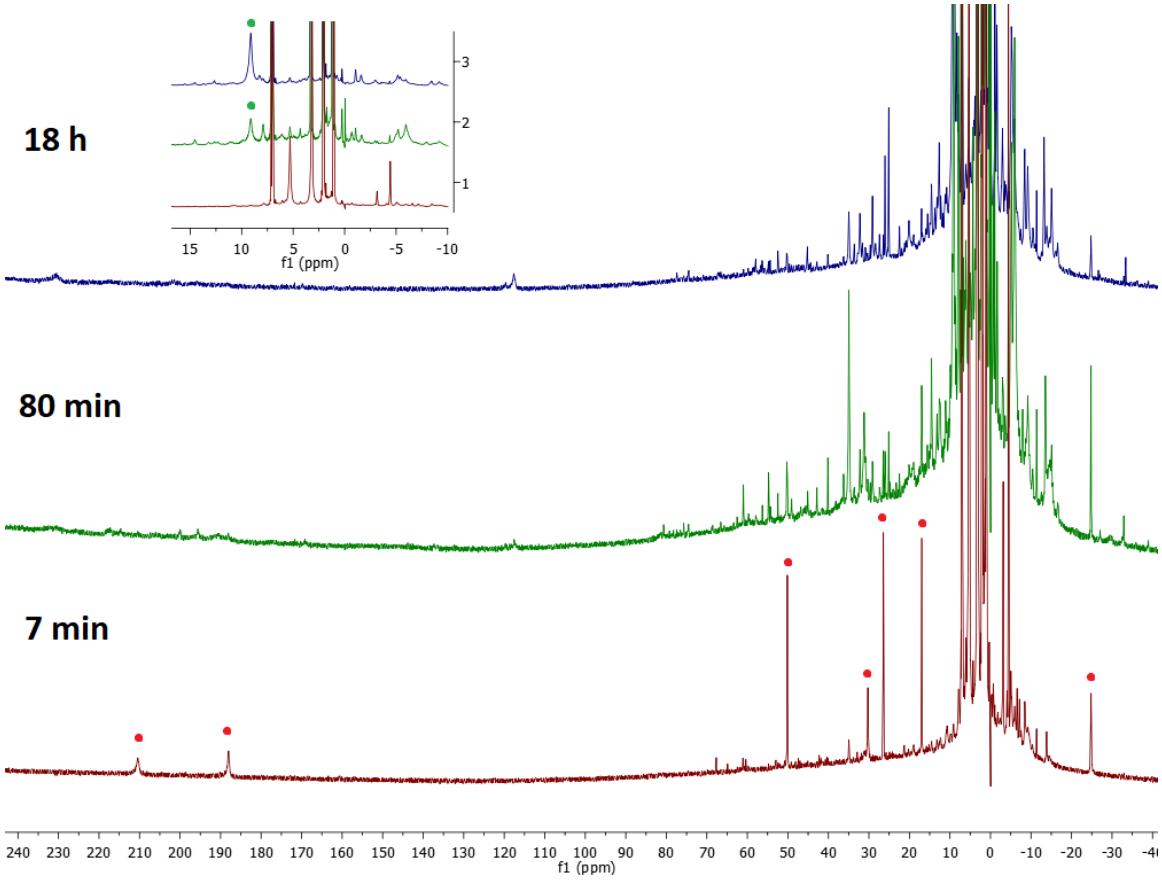

*Figure 2.18: ^{1}H NMR of the in-situ addition of an equivalent of $Cp^*_2Yb(OEt_2)$ to **1.12**. **2.4** is designated by the red dots. The dominant product formed by the decomposition is designated by the green dot.*

The most efficient purification method consists of evaporating the volatiles after filtration, followed by a rapid washing with cold pentane. Due to the accelerated isomerisation under stirring, the evaporation of toluene has to be performed without stirring, preferably at cold. Optimal conditions ensure a very high yield (up to 95%) and excellent purity (<1% of **2.5**).

2.3.1.2. Characterisation of the coupled products

In both cases, structural analyses reveal a similar situation to the one in **2.1** – the coupling occurs in the same position on the pyrimidine, forming two fragments that are twisted with respect to one another (Figure 2.19). The bond lengths on the two fragments on both **2.4** and **2.5** are not symmetrical with respect to the other. The pattern of Pd-N distances is inverted upon the isomerisation. The Pd-N_{imid} distance is shorter than Pd-N_{pym} in **1.12** and **2.4**, but the opposite holds in the case of **2.5**. This could likely be explained by the trans effect of the methyl group. The main difference between the two structures, however, is that the torsion angle is much larger in **2.4** than in **2.5** ($NCCN_{tor}$ in Table 2.3).

This would suggest that the main reason for the isomerisation is the steric strain within the structure. The most probable source is the pyridine moiety, which is twisted by ~60° from the square plane in **1.12**, due to the repulsion between its proton on the α position and that of the pyrimidine. The pyridines point towards the opposite molecule in **2.4** and outwards in **2.5** (and are almost parallel to one another; Figure 2.19). It would seem that, once this strain is released, the molecule relaxes and the two fragments can get closer, maximising the attractive dispersion forces.

	Av. Values (Å or °)	
Atoms	**2.4**	**2.5**
Yb-N_{pym}	2.333(6)	2.324(14)
Yb-N_{imid}	2.320(6)	2.343(12)
Yb – Cp^*_{ctr}	2.327	2.335
C-$C_{coupling}$	1.578(8)	1.556(15)
Pd-N_{pym}	2.163(6)	2.042(12)
Pd-N_{imid}	2.031(6)	2.188(13)
Pd-N_{py}	2.052(6)	2.021(13)
Pd-C_{Me}	2.027(9)	2.006(15)
Pd-Pd	4.176	3.321
d(Pd-plane)	0.412	0.369
$NCCN_{tor}$	95.50	68.69
$(py\text{-}plane)_{tw}$	57.08	52.51

*Table 2.3: Main average distances and angles in **2.4** and **2.5**. The metrics which are dissymmetrical by more than 0.02 Å / 10° between the two fragments in the dimer are highlighted in red. $NCCN_{tor}$ designates the inter-fragment torsion angle, and $(py\text{-}plane)_{tw}$ the average angle between the pyridine plane and the square plane of the Pd coordination sphere.*

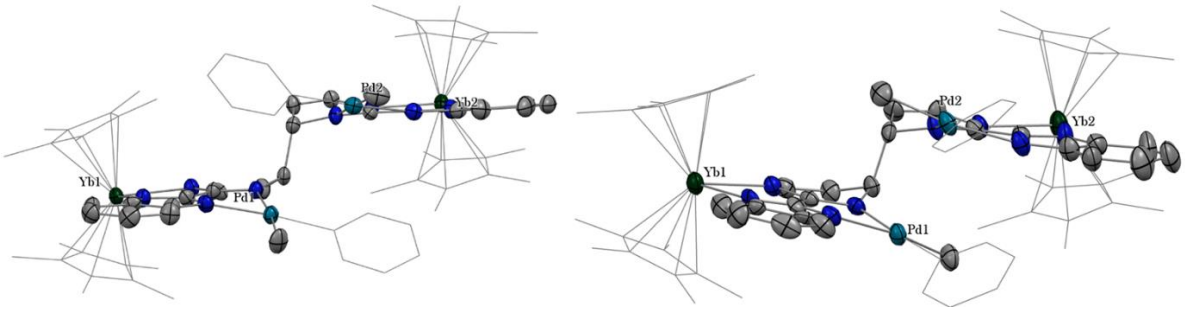

*Figure 2.19: ORTEPs of **2.4** and **2.5**. The Cp* co-ligands and the pyridine moieties are set in wireframe to avoid clutter.*

To try to get a better idea of the relative energy between the two isomers, we performed theoretical computations. The calculations were saddled with difficulties. The optimisation run of **2.5** resulted in the breaking of the C-C bond formed during the coupling reaction and the re-aromatisation of the bimpym ligand. To counter this, geometrical restraints related to the distance between the atoms were imposed to prevent the bond breaking. However, due to the enormous size of the structures (178 atoms), the geometry optimisations could not provide reliable results. The most problematic parts of the molecules are the Cp* co-ligands, whose methyl functions have the tendency to oscillate, precluding the convergence.

In order to overturn these issues, simplifications of the molecules were undertaken to better understand the electronic structure of these coupled products (Figure 2.20). The rationale behind them is that the steric constraints imposed by the bulky Cp* can be built in with geometrical restraints and that their contribution to the overall electronic structure is negligible. The first set of simplifications replaced the Cp* ligands with Cl^- (**2.4**$_{Cl}$ and **2.5**$_{Cl}$); these structures were computed as neutral triplets. The second pair of calculations removed the organolanthanide fragments entirely, yielding dianionic singlets (**2.4**$_{dian}$ and **2.5**$_{dian}$).

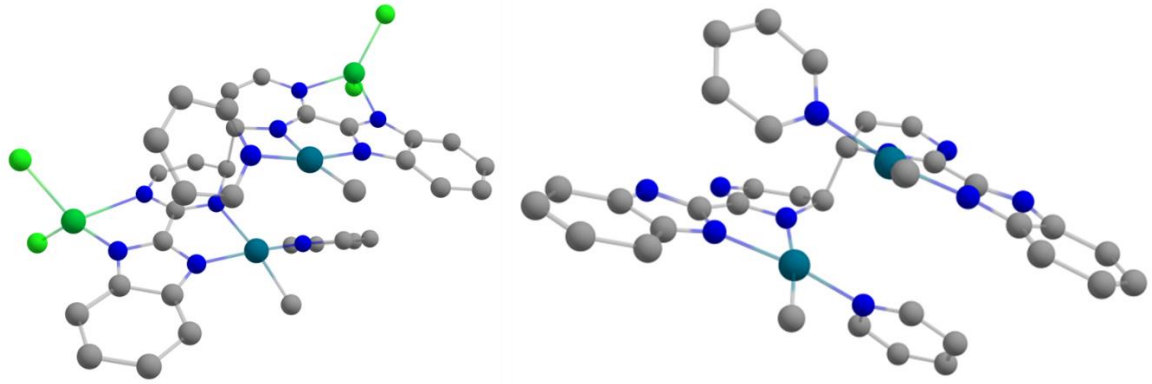

Figure 2.20: Proposed simplified structures, where the Cp co-ligands are replaced by Cl^- (left and where the lanthanide is removed entirely (right).*

The dianionic structures have matching orbital structures. The main orbitals are gathered in Table 2.4. The close proximity between the Pd centres yields orbitals that would suggest a δ bond with a dominant contribution from the $4dz^2$ orbital, followed by the corresponding anti-bonding orbital between them. The HOMO of the system is on both pyrimidine moieties, with a strong contribution coming from the newly generated C-C bond. The formation of this bond is proof that the coordination of the lanthanide to the ligand lowers the **LUMO^{pym}**-type orbital below the **LUMO^{L}**. The first two vacant orbitals are mainly concentrated on the pyridine moieties and thus remain of **LUMO^{L}** shape.

The complexes with the Cl^- co-ligands mirror the electronic structure above quite closely. The LUMO is mainly situated on the C-C bond bridging the pyrimidine and the benzimidazole moieties, which was not previously observed. The subsequent vacant orbitals are principally of **LUMO^{L}** shape. Between them, the two compounds sometimes differ in terms of order of the ligands (several LUMOs), but no significant changes between them are observed.

The LUMOs on **2.4$_{Cl}$** and **2.5$_{Cl}$** would suggest that a second electron transfer towards the ligand is plausible and would, at least, impact the bridging bond and probably dearomatise the ligand. The pertinence of these results will be examined shortly when exploring the reactivity of these coupled products, especially towards reductive substrates.

Orbitals	Dianionic	Cl^-	Orbitals
HOMO-9	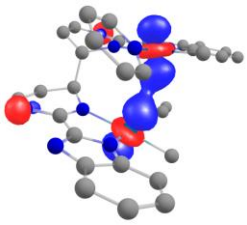	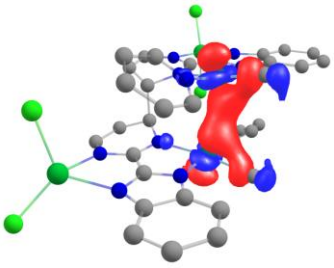	SOMO-9
HOMO-2	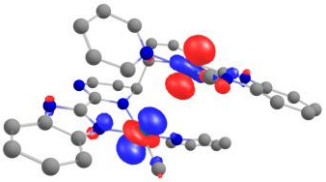	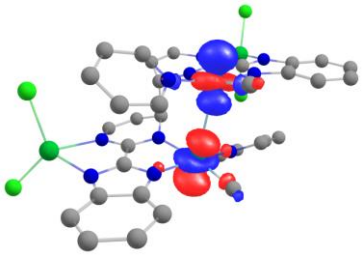	SOMO-1

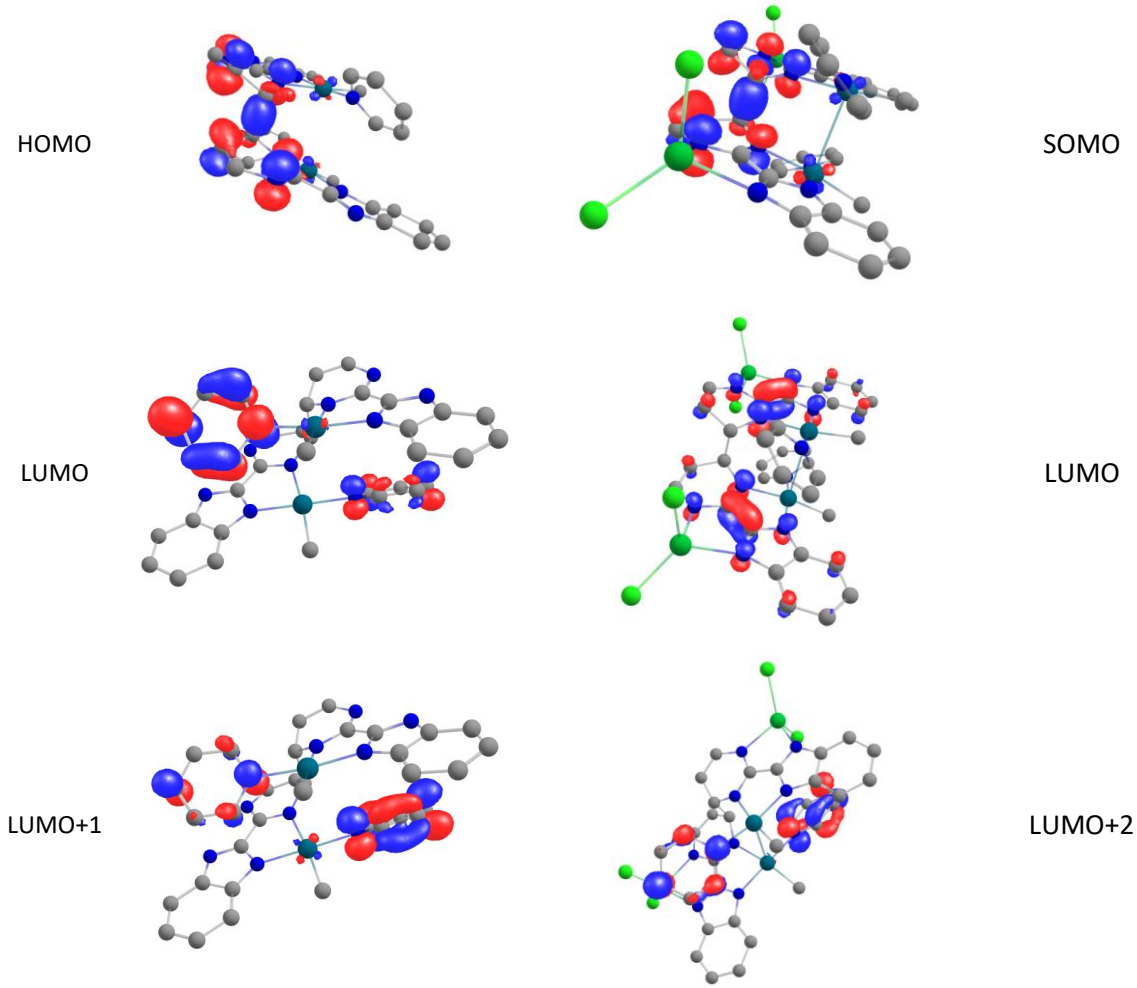

*Table 2.4: Main orbitals in the simplified structures of **2.4** and **2.5**.*

To probe whether the coupling reaction was reversible, VT ^{1}H NMR analyses were carried out on **2.4** in the (-70 °C, 80 °C) range. No indication of a monomeric species could be found at lower temperature. However, upon raising the temperature past 60 °C, new signals were gradually being formed at the expense of those of **2.4**. Returning to r.t did not lead to the disappearance of the new compound, indicating that an irreversible transformation has occurred. Closer study showed that **2.5** and another, new compound, were being formed. This observation is consistent with a faster isomerisation of **2.4**. If kept at 80 °C, an almost full conversion to the unknown compound is completed (Figure 2.21). The new complex has the same symmetry and integration patterns as both its parent complexes, suggesting that it is another isomer.

Heating up a sample of **2.5** lead to the same evolution. This implies that the transformation is only activated at higher temperatures, as **2.5** was kept at in solution at r.t for several weeks with no sign of degradation. Despite our best efforts, this unknown compound could not be crystallised, precluding its structural authentication.

The UV-Visible spectra of the two coupled products were recorded in toluene. The corresponding spectrum of the precursor, **1.12**, is also presented in Figure 2.22 for the sake of comparison. The perturbation due to the presence of the Yb fragment is similar to the one seen for **2.1** (see Figure 2.3). The main absorption band, assumed to be the ligand π->π*, is common to all three complexes, but it is blue-shifted in the coupled products (Figure 2.22). Furthermore, the extinction coefficients more

than double upon the addition of the lanthanide. As for the difference between **2.4** and **2.5**, it would appear to be insignificant, if not even within experimental error.

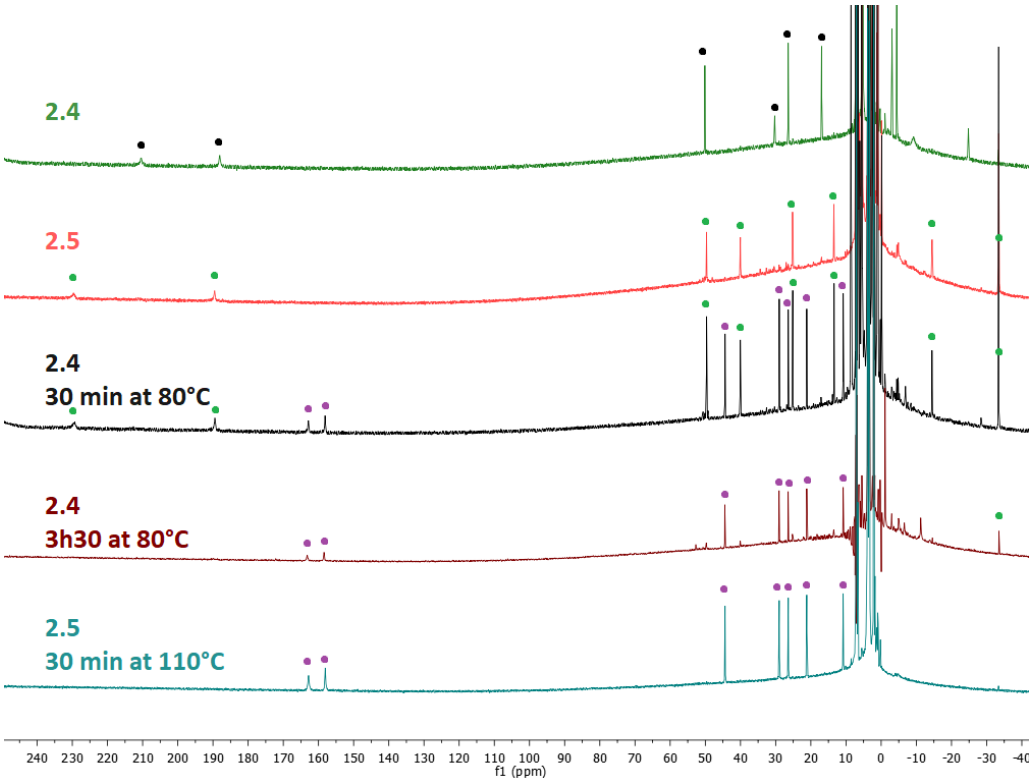

*Figure 2.21: High temperature induced evolution of **2.4** and **2.5** towards an unknown compound. Black dots indicate **2.4**, green dots – **2.5** and purple dots – the unknown complex.*

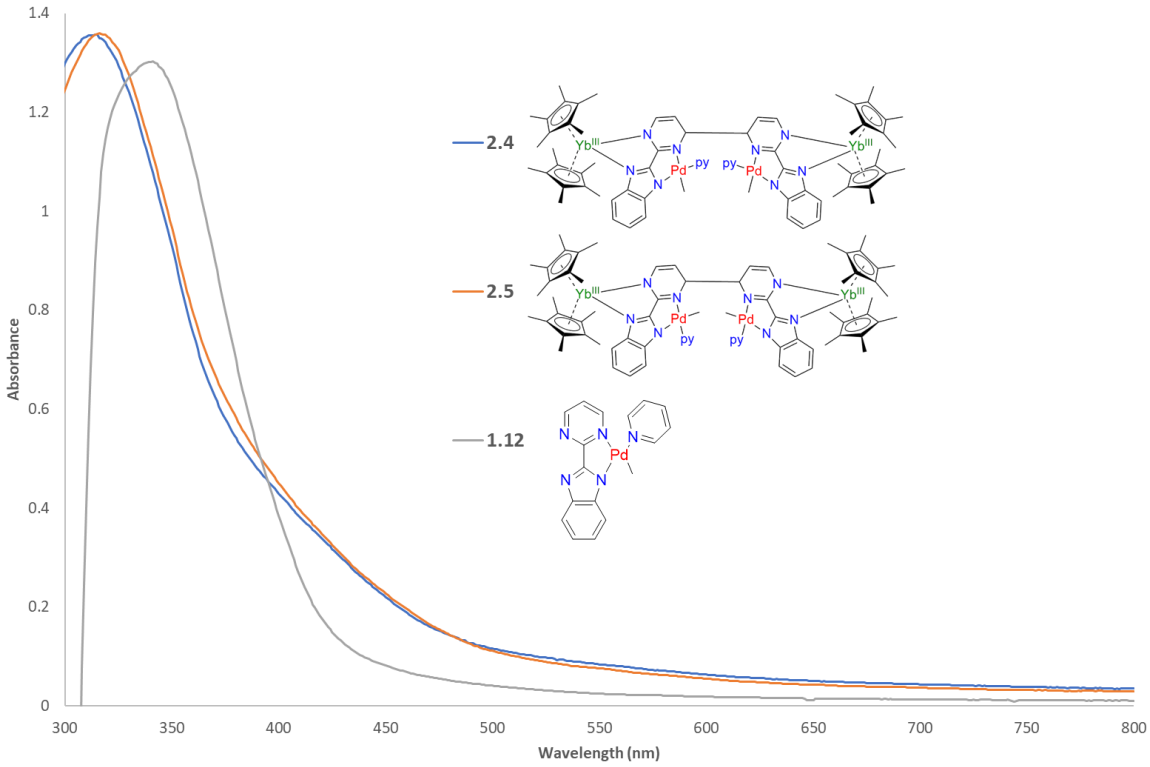

*Figure 2.22: UV-Visible spectra of the Pd-pyridine complexes **1.12**, **2.4** and **2.5**.*

2.3.1.3. Trials with divalent europium.

The reactivity observed when producing **2.4** and **2.5** prompted an investigation as to whether the weaker reductant europium homologue of the ytterbocene could trigger the same coupling behaviour.

Addition of $Cp^*_2Eu(OEt_2)$ to **1.12** in an *in situ* reaction resulted in a pronounced colour change to brown. Due to the significant paramagnetic effect of Eu, ^1H NMR analysis did not provide any useful insight as to the evolution of the substrates. A red powder was formed inside the tube. The soluble fraction was siphoned away and left to crystallise at -40° C. The solid, though, could be solubilised in THF-d_8 – only one distinctive peak could be identified (-14.76 ppm), but no further information could be extracted.

The reddish-brown solution yielded a limited amount of small crystals. Acquisition of XRD data allowed the identification of this product as $Cp^*_2Eu(pyr)$. A second molecule is generated by the symmetry afforded by the P-1 space group. This reveals what would appear to be an agostic bond with one of the methyls of the vicinal Cp* groups (Figure 2.23). The Eu-C_{Me} distance is of 3.09 Å. Despite this, the structural features of this complex would point rather to an unchanged Eu^{II} centre, as the distance to the Cp* centroid is 2.538 Å. In principle, this value is closer to the ones tabulated for Eu^{III} complexes (~2.45 Å), rather than other divalent Eu^{II} species.[49] However, a more informative comparison is with other Eu^{II} adducts containing a weak base in its coordination sphere: the same average distance in $Cp^*_2Eu(OEt_2)$ is 2.52 Å.[50]

To eliminate the possibility of this compound being due to trace amounts of free pyridine, **1.12** was vigorously dried beforehand. The same complex was obtained. At the very least, this result underlines the lability of the pyridine motif in precursor.

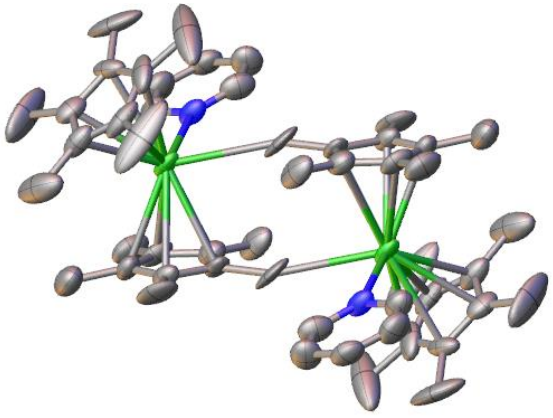

Figure 2.23: ORTEP of the $Cp^*_2Eu(pyr)$ complex and its symmetry-generated interaction with a second molecule.

Other attempts performed at larger scale and under stirring, only lead to the eventual recrystallisation of the divalent europium precursor. It would appear that its lower reduction potential is insufficient to trigger the electron transfer towards **1.12**.

2.3.2. Isolation of trimetallic complexes.

2.3.2.1. Formation and isolation of trimetallic complexes.

The rapid formation of decomposition products following the addition of ytterbocene to **1.12** piqued our interest (Figure 2.18). As such, this evolution was allowed to continue. Stirring the mixture for two

hours allowed a gradual darkening of the brown-black solution to black. A gaseous evolution was also observed, particularly at the beginning of the reaction. Filtration was necessary to separate the solution from black powder, formed during the reaction. Overnight settling of the saturated solution led to the growth of large brown crystals. Acquisition of XRD data revealed the unexpected formation of a trimetallic adduct of the formula $[(Cp^*_2Yb)_2(\mu\text{-}Pd(pyr)_2)]$ (**2.6**, pyr = pyridyl).

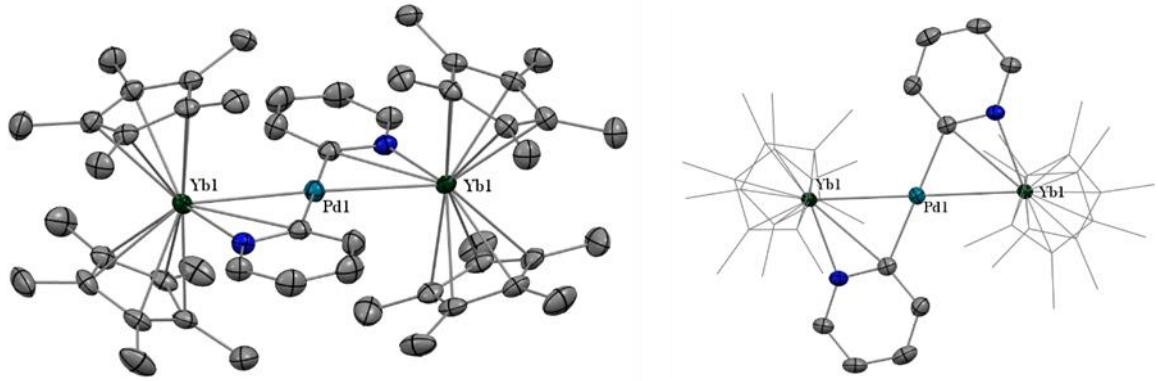

*Figure 2.24: ORTEP of **2.6** from two perspectives. The hydrogens are not shown and the Cp* groups are shown in wireframe in the second perspective in the interest of clarity.*

The structure is striking for several reasons. The bimpym ligand has departed the parent compound. The Pd centre is coordinated to two pyridyl moieties in an almost perfectly linear fashion. This is the result of a C-H activation in the α position of the pyridine. The departure of a proton is also consistent with the release of the methyl moiety that was present in **1.12**, **2.4** or **2.5**. The release of methane is the most likely explanation. Lastly, this complex is another example of a short Yb-Pd distance.

The complex bears some structural similarity to some mixed-metallic adducts of Sm and either Ga or In, described by Zeckert in 2013.[51] These complexes are also formed following electron transfer by a divalent Sm precursor. There, too, the transition metal fragment is coordinated to two pyridyl groups. The resemblances stop here, as the arrangement in these Ga or In fragments is, however, far from the linearity observed in **2.6**. This impacts the distance between the Sm and the other metal, which are around 3.8 Å. The two pyridyl groups (vs one in the case of **2.6**) equally coordinate the Sm^{III} centre via the N atom. Furthermore, the coordination sphere of the other metal has two further ethyl co-ligands, whereas the Pd centre is only directly coordinated to the pyridyls.

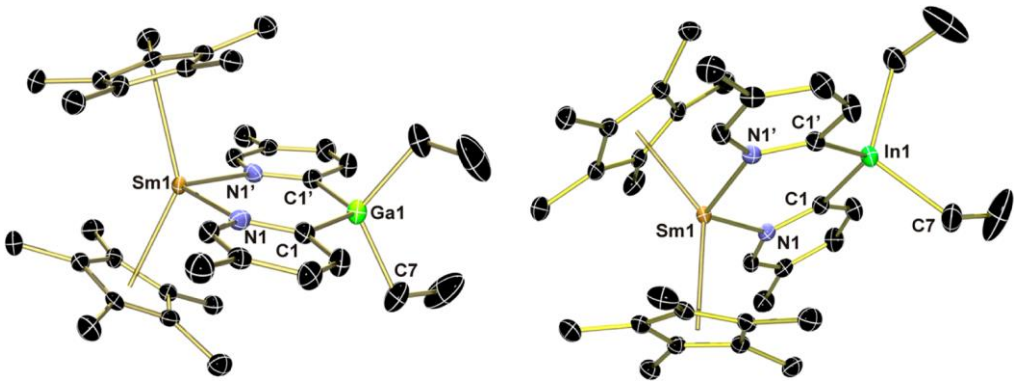

Figure 2.25: ORTEP of a structurally similar Ln^{III}-TM(pyr) complex, reprinted from the given reference.[51]

Faced with this unusual development, the corresponding reactivity with the more reducing samarium was investigated. Stirring a mixture of **1.12** and samarocene in toluene immediately results in a black solution with yellow hues, as well as in a similar gaseous evolution to the one observed during the

formation of **2.6**. The same treatment methods applied for **2.6** were also used in this case, yielding large yellow blocks that were suitable for XRD analysis. Resolution of the acquired data allowed the identification of $[(Cp^*_2Sm)_2(\mu\text{-}Pd(pyr)_2)]$ (**2.7**), an isostructural homologue to **2.6**.

Obtaining identical complexes would point to a similar formation mechanism. This would imply passing through the homologous coupling products, as was the case for the ytterbium compounds. To this effect, the straightforward in situ addition of one equivalent of samarocene to **1.12** was undertaken. We were unable to observe the related coupling products. If it is indeed formed, then it would appear that it is entirely consumed in the time span necessary for launching the reaction and registering the ^{1}H NMR spectrum (generally, 5-7 minutes). Precautions were taken in order to attempt to slow down the reaction. Alas, neither condensing tol-d_8 at cold (resulting in it thawing slowly in the NMR spectrometer), nor performing the reaction with an excess of **1.12** permitted the observation of an intermediate product. It would appear that the reaction with samarocene is significantly faster. This could be explained by the higher reducing potential of samarocene, with respect to its ytterbium counterpart.

What is common to both complexes is that a poor yield is obtained in a 1:1 reaction between the organolanthanide and **1.12**. Crystals are typically isolated in less than 10% yields. On the basis of stoichiometry, more than one equivalent of lanthanides is required. The best yields for these reactions involved large excesses of $Cp^*_2Ln(OEt_2)$: if 4 eq are used, yields of 35-40% can be reached.

The unusual chemical features of the two trimetallic complexes raise a series of questions. What is the electronic configuration of the two metal centres? In a related manner, what is the charge distribution within? Is there an interaction between the Ln and the Pd that modulates this charge distribution? Is it plausible to have a multiconfigurational ground state? To address these questions, a thorough spectroscopic characterisation was undertaken.

2.3.2.2. Characterisation and analysis.

The isolation of isostructural compounds makes a comparison between the two particularly pertinent. The analysis of the main distances and angles in the two complexes is instructive. Both distances between the lanthanide and the Cp* centroid are consistent with Ln^{III} configuration.[46,52] The presence of four Cp* groups and two pyridyl moieties are the only sources of negative charge. Together, they account for six negative charges. If the structural features are an accurate reflection of the oxidation state, it would imply that only the two Ln^{III} centres contribute any positive charge.

Therefore, the most accurate description of the remaining metal centre is Pd^0. The Pd-C(pyridyl) distances are longer than the relevant reported Pd^{II}-α-pyridyl fragments, which are found in the 1.95-2.01 Å range.[53–55] This corroborates our hypothesis of a lower palladium oxidation state.

The most conspicuous feature of these complexes is that the Ln-Pd distance is shorter in the case of the Sm adduct. This is contrary to the expected trend of the lanthanide contraction.[56] All things being equal in matters of electronic structure and geometry, one would expect a difference of circa 0.11 Å for equivalent features in favour of the Sm adduct. This is nicely reflected in the Ln- $N_{pyridyl}$ bonds, as well as the average distances from the Ln to the centroids of the Cp* co-ligands. In both cases, the Sm bond is superior in length by about the expected difference.

	Av. Values (Å or °)	
Atoms	**2.6**	**2.7**
Ln-Pd	2.924(1)	2.908(1)
Ln-$N_{pyridyl}$	2.275(3)	2.386(3)
Ln-$C_{pyridyl}$	2.773(4)	2.861(4)
Ln – Cp^*_{ctr}	2.342	2.449
Pd-$C_{pyridyl}$	2.078(4)	2.081(4)
<($C_{pyriyl1}$-Pd-$C_{pyridyl2}$)	178.87°	179.72°
<(Ln-Pd-$C_{pyridyl}$)	64.76(1)	67.67(1)
<($Cp^*_{1\ ctr}$ -Ln- $Cp^*_{2\ ctr}$)	134.70°	134.52°

Table 2.5: Main distances and angles in the trimetallic complexes.

Given that these complexes are isostructural, the difference in Ln-Pd bonds can evidently not be ascribed to different coordination environments or steric strains. There are a number of hypotheses that can be proposed to explain this behaviour.

In the event of an interaction between the Pd and the Ln centres, the length of the bond could be contingent on the strength of the interaction. In this case, the smaller Sm-Pd distance could be explained by a stronger interaction than in the case of **2.6**.

A second possibility would involve a multiconfigurational nature of one of the compounds. *A priori*, it is easier to assume this being the case for the Yb, where there is ample precedent.[7,57] This would imply admixture of Yb^{II} character into the wave-function of the Yb^{III} complex. Due to the considerable difference in the ionic radii of the two configurations (about 0.16 Å), this would result in a longer bond length in the case of **2.6**. Again, the underlying assumption in this case would be a reversible redox process in the form of an electron transfer to/from the lanthanide centres. The only possible substrates adequate would be the pyridyl group or the Pd. Therefore, the intermediate valence would rely on the Yb^{III}/Yb^{II} and $pyr/pyr^{-\bullet}$ couples or, alternatively, Yb^{III}/Yb^{II} and Pd^{0}/Pd^{II}.

Either scenario relies on subtle and complicated physico-chemical descriptions of systems. The second case is arguably more complicated, as 4f elements interactions with other metals are still a subject of some controversy[58] and the common description of these interactions are of predominantly electrostatic character, with small covalent contributions.

Regardless, a comprehensive spectroscopic characterisation is a *sine qua non* ingredient in understanding the electronic structure of these complexes.

For both of these compounds, ^1H NMR spectra were obtained by isolating the crystals and washing them rapidly with cold pentane 3-5 times. The resulting spectra contained slight impurities, integrating for less than 1% of the main Cp* signals. These impurities could not be separated from the trimetallic complexes, presumably on account of their very similar solubility in the available solvents. The presence of highly paramagnetically shifted peaks for **2.6** is a sure-fire indication of the trivalent state of the Yb centres, at least at r.t.

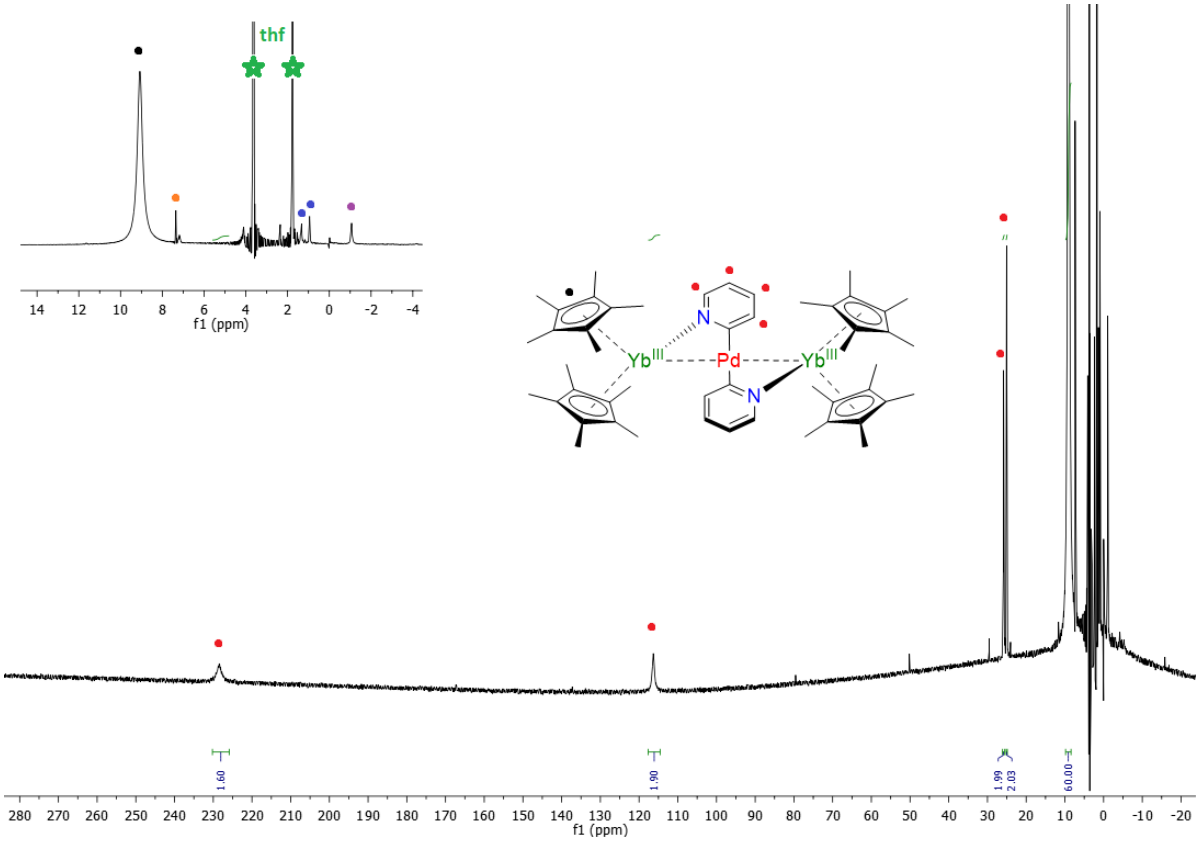

*Figure 2.26: ^{1}H NMR of complex **2.6** in THF-d_8 at 293 K. Red and black dots indicate the pyridyl peaks and the Cp* peak. The trace impurities have the following colours: blue – H grease, orange – residual toluene and purple – unknown impurity.*

The presence of impurities may complicate the definitive attribution of the signals to the pyridyl protons. As such, a solution was devised, allowing an unequivocal identification of the target protons. To this effect, py-d_5 was used as a substitute in the synthesis of **1.12** to obtain **1.12-py-d_5** (Scheme 2.5). The same purification method as for the regular complex was applied here and this complex was then used without further characterisation. Addition of samarocene to **1.12-py-d_5** gave a satisfactory batch of crystals, which was then used to obtain a high-quality spectrum of **2.7-pyr-d_4**. Unfortunately, this procedure was not successful with ytterbocene.

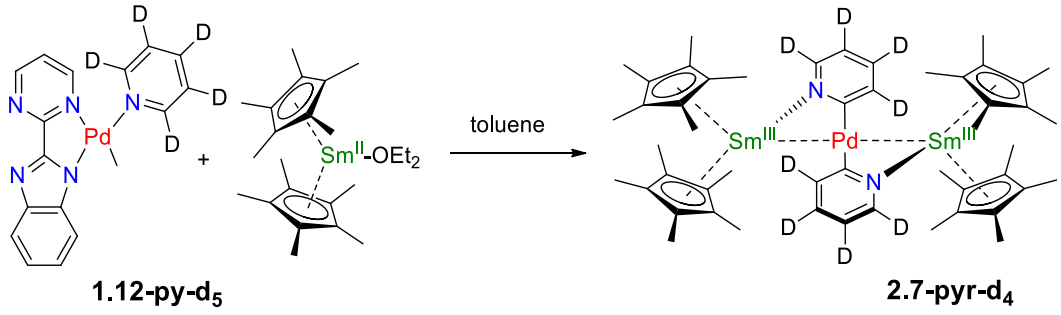

*Scheme 2.5: Synthesis of the deuterated pyridyl analogue of **2.7**.*

The questions raised in Section 2.3.2.1 pertaining to the electronic configurations of the metals could be further probed in solution studies. VT NMR studies were undertaken for both trimetallic edifices. The spectra are presented in Figure 2.28. The temperature-induced variations of the signal shifts are significant, but their evolution is consistent with the Curie law. The same observations were made for **2.7**. Consequently, we may conclude that both lanthanides are in the Ln^{III} configuration in the available temperature range.

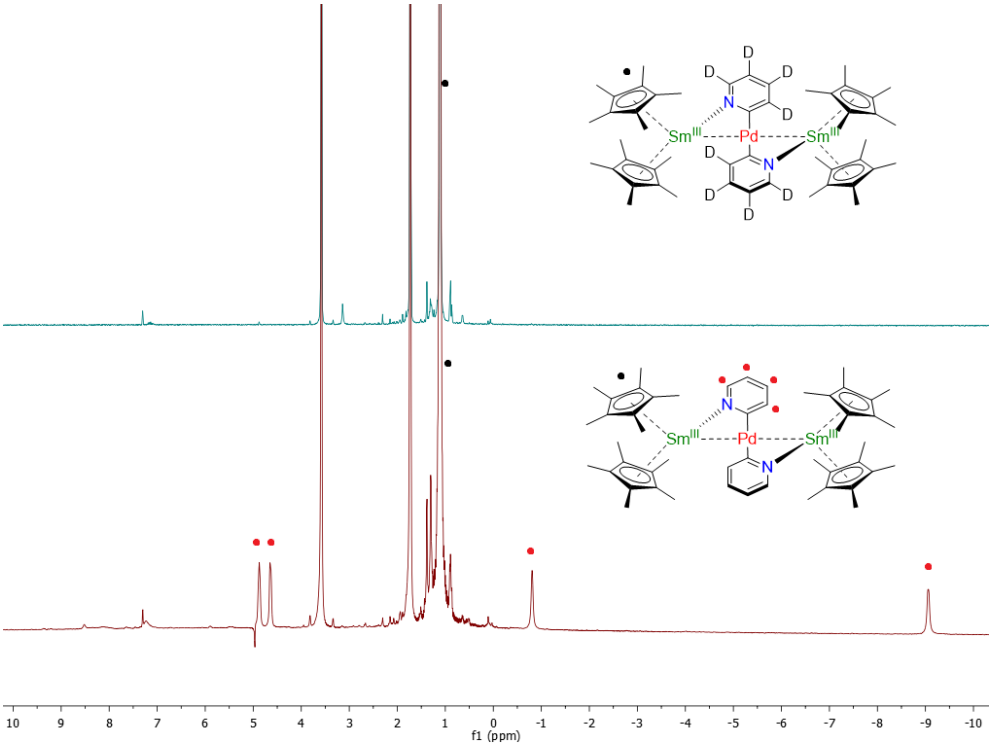

*Figure 2.27: ^{1}H NMR of **2.7** and **2.7-pyr-d$_4$** in THF-d$_8$.*

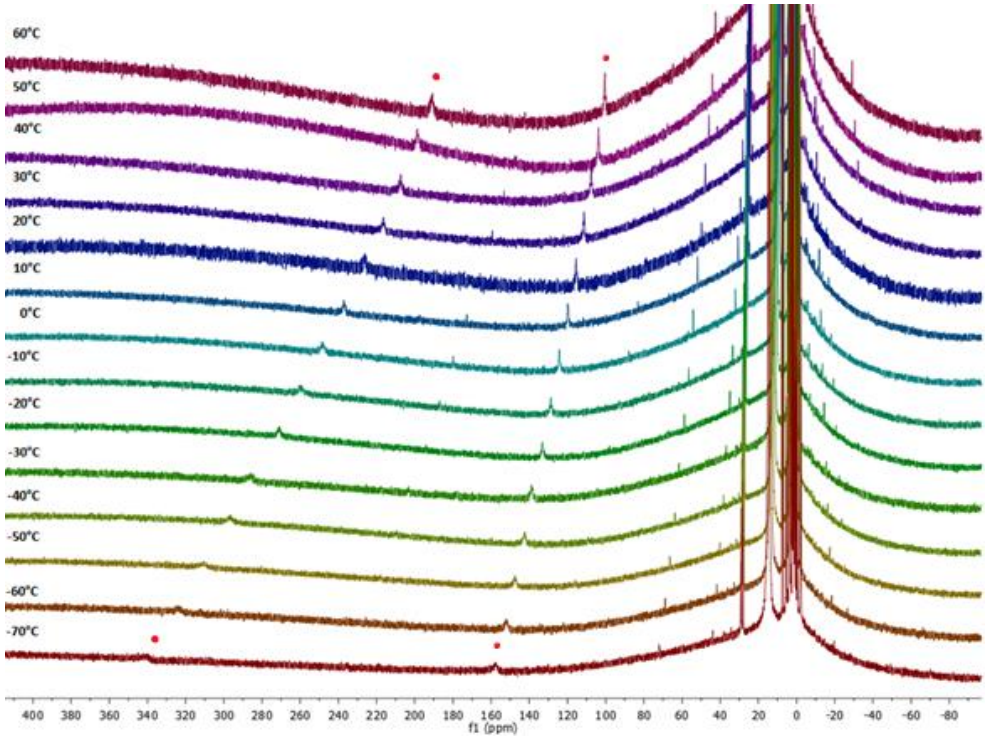

*Figure 2.28: Variable temperature ^{1}H NMR of **2.6** in THF-d$_8$. Red dots correspond to the pyridyl.*

Definitive proof of this assertion was provided by solid-state magnetic data, acquired in the 0-300 K temperature range. The data for the Yb adduct is shown in Figure 2.29 (the data for **2.7** is given in Figure S2). In **2.6**, the χT value monotonously decreases upon lowering the temperature to 4.09 cm^3.K.mol^{-1} at 15 K and then drops to 2.08 cm^3.K.mol^{-1} at 4 K. This behaviour is typical for Yb^{III} complexes and is attributed to the depopulation of the crystal field states. There is, thus no deviation

from the expected behaviour of two independent Yb^{III} centres all throughout the investigated temperature range. The same conclusion applies to **2.7**.

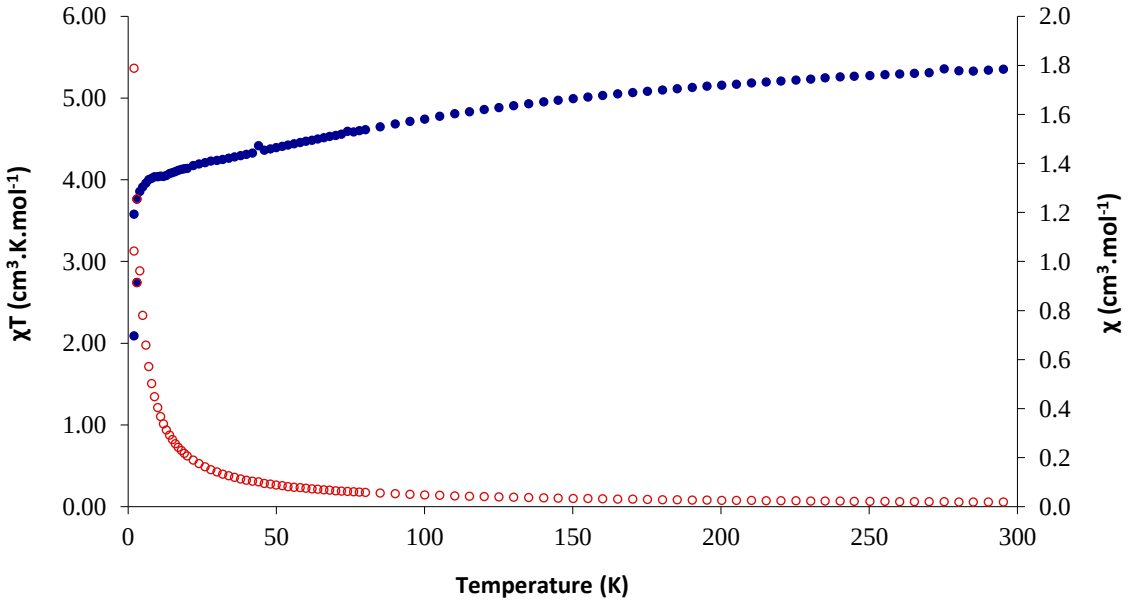

*Figure 2.29: Magnetic susceptibility (unfilled red dots) and the χT product (filled blue dots) for **2.6**.*

This allows us to unequivocally state that there is no Yb^{II} admixture into the trivalent Yb state to be found in **2.6**, since the presence of its diamagnetic character would make a marked alteration in solid-state magnetic data.

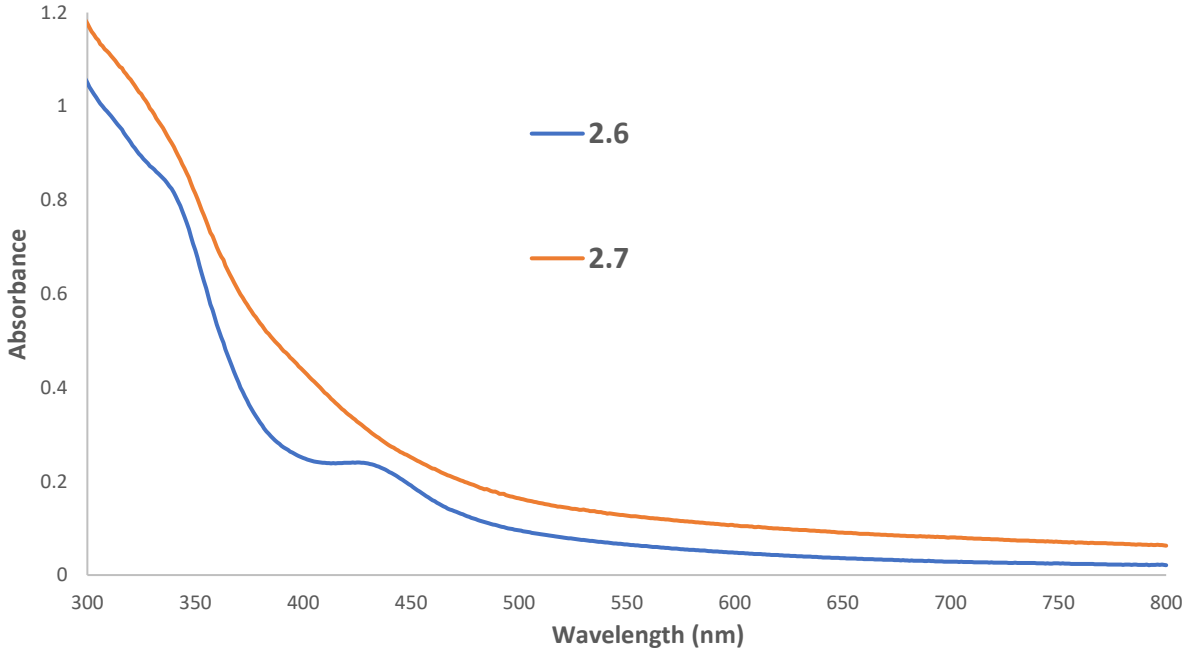

*Figure 2.30: UV-Visible data for the trimetallic complexes **2.6** and **2.7**.*

The UV-Visible data was acquired for both complexes. The main absorption band at around 290 nm is consistent with the features of other documented α-pyridyl transition metal complexes.[59] This is attributed to a π->π* transition. It is slightly surprising to see at least two further transitions distinctly outlined in the case of **2.6**, but not of **2.7**. Both of these are presumably MLCT transitions, although

the donating metal cannot be determined. This peculiarity of the Yb complex can be interpreted as a sign of a stronger interaction of the metal centres with the ligand, although no further inference can be made pertaining to the precise electronic structures.

2.3.2.3. Reactivity.

The unusual trimeric complexes were probed for any promising reactivity. The structural peculiarities, particularly of the Pd centre, could be conducive for a size-selective insertion of a small substrate in the space defined by the Pd and the Cp* co-ligands.

To this effect, the reactivity with gases was attempted. The low-pressure addition (0.2 bar of overpressure) of CH_4, CO and H_2 did not result in evolution of the trimers. There was no difference in behaviour between tol-d_8 and THF-d_8. The ^1H NMR spectra only showed the gradual decrease of the complex signals, but this could be ascribed to crystallisation. Likewise, the attempted catalytic hydrogenation of allyl-benzene using **2.7** resulted in the immediate precipitation of the complex itself.

The obscure formation mechanism of the two trimetallic adducts permit the hypothesis of an electron transfer from the lanthanide. To this effect, the addition of coordinating solvents, such as pyridine and acetonitrile was attempted to probe whether such a possibility is reversible. The complexes were shown, however, to permanently decompose when exposed to such a perturbative event.

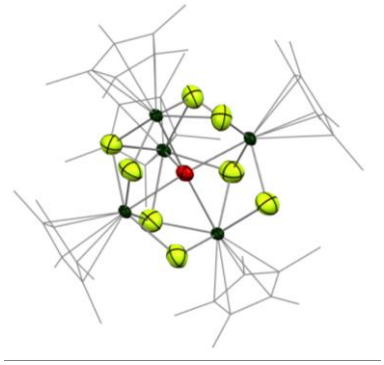

*Figure 2.31: ORTEP of a side-product following the addition of pentafluoropyridine to **2.7**.*

When pentafluoropyridine was added to **2.7**, two types of crystals could be grown in a concentrated solution – red prisms (that did not diffract) and yellow plaques, of acceptable quality for XRD studies. Analysis revealed a $(Cp^*Sm)_5F_8O$ cluster, in which the central O is coordinated to all five Sm centres (Figure 2.31). This reactivity reflects the strong affinity for halogens, characteristic to the Ln series.

It would, therefore, appear that the trimetallic edifices are not reactive towards the target substrates.

2.3.3. Trials with pyridine analogues.

The unexpected C-H activation in α the position of the pyridine prompted our interest in exploring the limit of this reactivity. A series of pyridine analogues (Scheme 2.6) were chosen to explore the effect of diverse steric environments, as well as bonds in the α position of a different chemical nature.

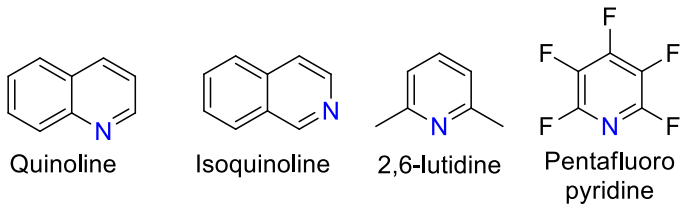

Scheme 2.6: Selected pyridine analogues.

For the first objective, the position of the coordinating N atom was varied, to examine if the decomposition giving the trimetallic adducts can be reproduced. In the second case, activating the C-F bond could be expected, given the inclination of lanthanides to coordinate halides, but this opens the possibility of more than one activation. In the case of the 2,6-lutidine (shortened hereafter to "lutidine"), an equivalent C-C_{Me} activation is expected to be significantly more demanding and difficult.

2.3.3.1. Preparing the requisite precursors.

The preparation of the desired precursors, analogues to **1.12**, was undertaken. The same synthetic protocols used to the pyridine complex were applied in these cases, but were fraught with difficulties. When the additional ligand was added in MeCN, the mixtures evolved to yellow-golden solutions. The same results were obtained when employing the pyridine analogue as the reaction solvent. In contrast to the procedure for **1.12**, no intense bubbling was noticed. The solutions were filtered to prevent recovering the unreacted ligand precursor.

At this point, numerous strategies were attempted to crystallise the products. Saturated solutions did not crystallise, at various temperatures and irrespective of the solvent used. The gas-gas diffusion of pentane, Et_2O or toluene produced non-crystalline solid.

Precipitating the complexes with the appropriate solvent (pentane or Et_2O), followed by washing (to remove any excess of the tmedaPdMe_2 precursor) led to the isolation of seemingly analytically pure yellow solids.

The ^{1}H NMR analysis of these compounds revealed the characteristic peaks of the bimpym ligand and the methyl group, with the adequate integrations. This would imply that a similar behaviour to that of the parent compound is observed. Indeed, *in situ* reactions confirmed the conversion of the reactants.

These complexes could only be solubilised in THF. The observations during the solution studies for **1.12** suggested that the pyridine has a fluxional behaviour. The most eloquent example would be the reactivity with $Cp^*_2Eu(OEt_2)$, outlined in Section 2.3.1.3. The fact that $Cp^*_2Eu(py)$ was obtained without any obvious external source of pyridine is most likely explained by the fact that the pyridine in **1.12** decoordinates just enough to allow it to react with europocene.

Therefore, the interpretation of the spectra shown in Figure 2.32 could be ambiguous. The presence of pyridine analogue peaks does not guarantee that the species in question actually contains the desired analogue.

Given that no structural authentication of these complexes was actually possible, the additions of divalent lanthanide precursors were performed on the basis of observing similar behaviour to the one of **1.12**.

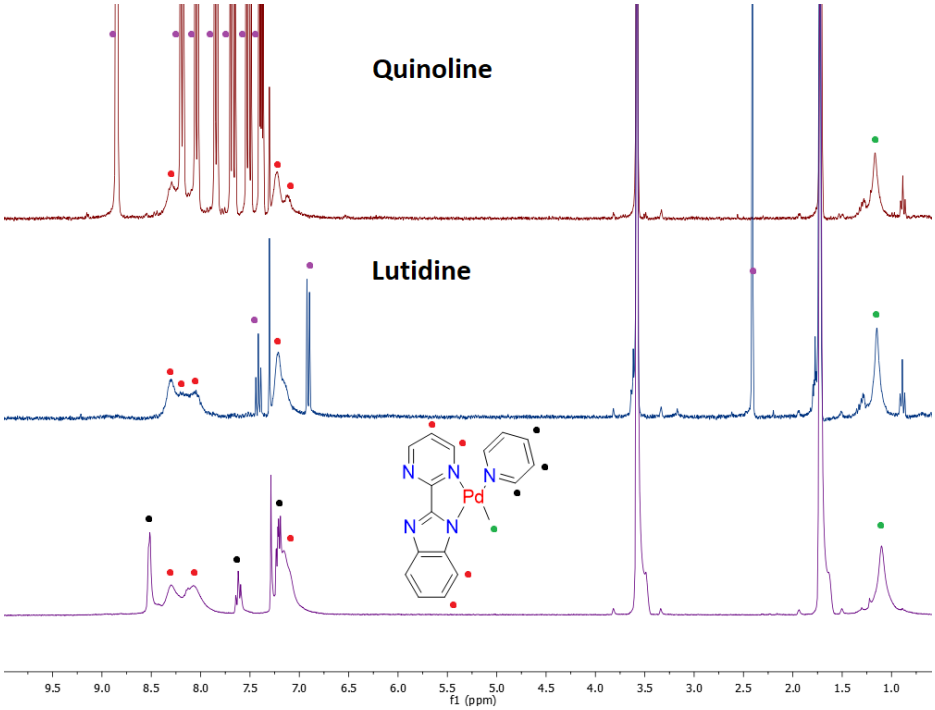

*Figure 2.32: ^{1}H NMR of **1.12** and the lutidine and quinoline precursors in THF-d_8. The red dots indicate the bimpym peaks, black dots – pyridine, green – methyl and purple – pyridine analogue peaks.*

2.3.3.2. Reactivity with divalent lanthanides.

The first synthetic trials of the addition of (bimpym)Pd precursors containing pyridine analogues involved the addition of a divalent lanthanide precursor in toluene. The evolutions observed were similar to those of the parent compound, **1.12**. In all cases, a dark mixture was rapidly produced. The solutions were filtered, before attempting the crystallisation of concentrated solutions at -40 °C. At best, this resulted in very low quantities of small crystals of poor quality. No structure could be obtained through this protocol.

These mixtures were then analysed by ^{1}H NMR. The spectra abounded in a great number of paramagnetically shifted signals. Unfortunately, no cogent conclusion could be reached, due to the vast number of unattributable signals. At best, careful washing of the solid with cold pentane and Et_2O allowed the clearing the majority of the unknown peaks to reveal a dominant complex (*Figure 2.33*). Alas, no structural authentication could be obtained in these cases.

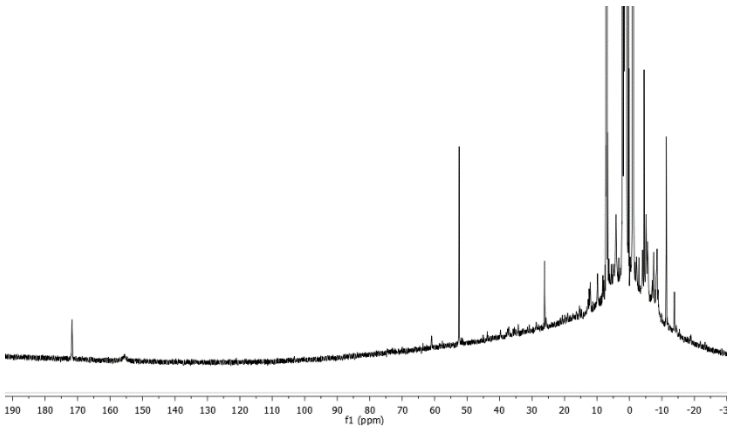

Figure 2.33: ^{1}H NMR of the reaction between ytterbocene and a Pd(bimpym) precursor that contains lutidine.

The uncertainty surrounding the effective coordination of the pyridine analogue on its Pd coordination site inspired a different strategy. The fluxional behaviour of the pyridine itself in **1.12** could be exploited by attempting to displace it with a slight excess of the desired analogue. This option holds the additional advantage of synthetic simplicity, due to the facile procedure affording **1.12**.

In an initial attempt, 5 eq of lutidine were added shortly after the beginning of the reaction between **1.12** and ytterbocene in toluene under stirring. The resulting black solution was filtered, before being concentrated to saturation. Storing this solution at cold produced small red needles, alongside a dark grey precipitate. XRD data was in agreement with the structure of **2.5**. The poor quality of the crystals could not allow the accurate attribution of the density peaks near the C atoms in the α position of the N atom on the lutidine.

Due to the inconclusive nature of the XRD analysis, ^{1}H NMR spectra were sought. Following evaporation of the volatiles, the solid was washed with cold pentane. Curiously, the washing solution had faint green hues, which may indicate unreacted ytterbocene. The remaining solid was dissolved in THF-d_8, where the dominant product was a match for the signals observed for **2.5** (Figure 2.34). The identity of the unknown signals could not be established.

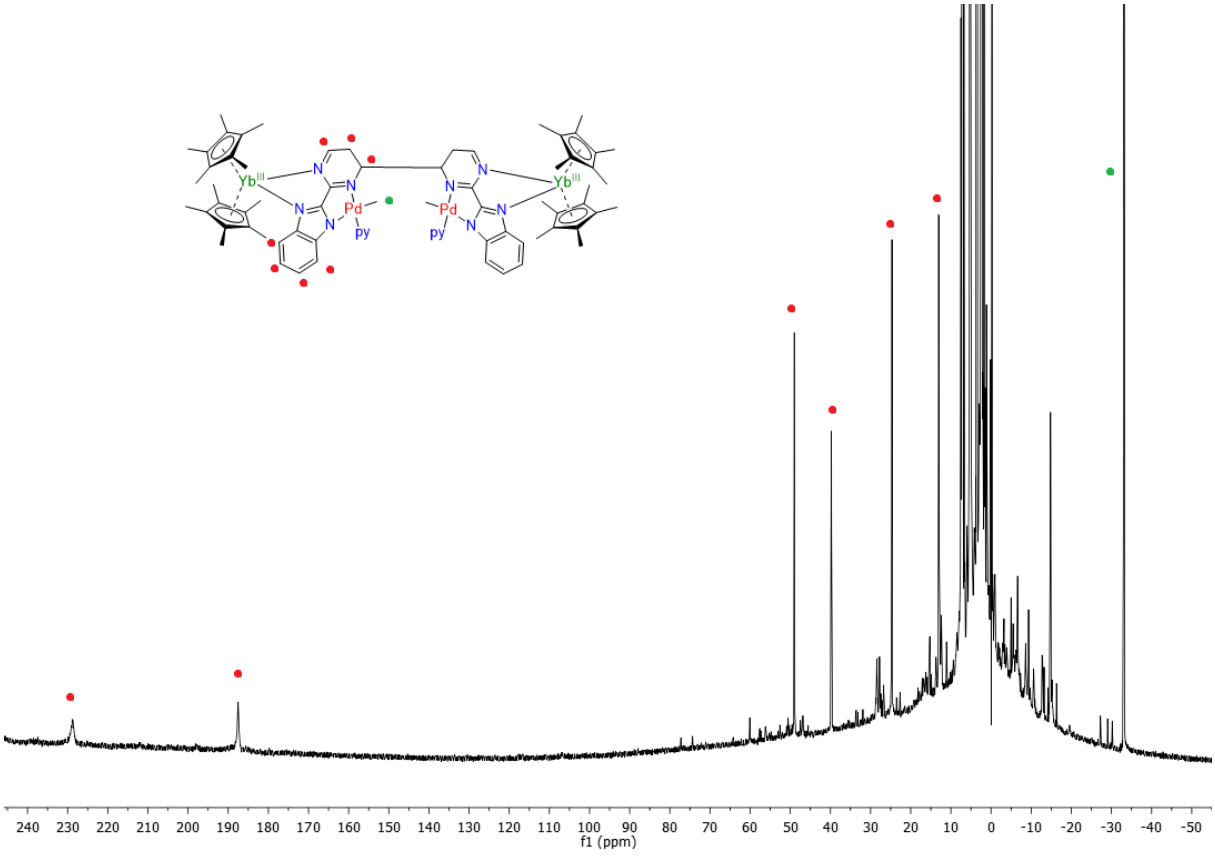

*Figure 2.34: ^{1}H NMR of the main product following the addition of ytterbocene to **1.12** in the presence of an excess of lutidine.*

Performing the same reaction with samarocene, followed by the same work-up procedure, resulted in the crystallisation of **2.7**. Overall, it could be concluded that the attempted substitution of pyridine with lutidine after the addition of the lanthanide was not efficient.

Given the rapidity of the formation of **2.4** (and, by subsequent isomerisation, **2.5**), the timing of the addition of the excess lutidine is bound to be important. Therefore, two variations of this reaction were attempted: either by adding the lutidine to solid **1.12** or by attempting to pre-substitute the pyridine by stirring a toluene suspension. A toluene ytterbocene solution was subsequently added in

both cases. A yellow solution is formed almost instantly, alongside black and yellow solids (Figure 2.35).

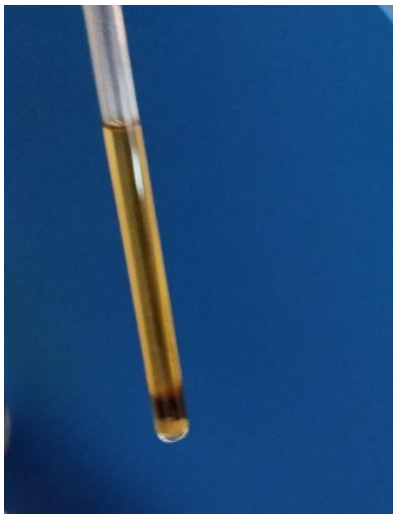

*Figure 2.35: Formation of the three phases in the reaction mixture of **1.12**, lutidine and ytterbocene.*

If performed *in situ*, tracking the reaction by ^{1}H NMR becomes complicated and inconclusive, due to the heterogenous medium. The yellow solution is recovered, the mixture is dried thoroughly, before redissolving the remaining solids in THF-d_8. Signals characteristic of (bimpym)Pd species are found, suggesting that the organometallic fragment remains unreacted.

This raises the possibility of a parasitic reaction between ytterbocene and the excess free lutidine. As is the case for other N-heterocycles or for THF, the coordination to the ytterbium is very thermodynamically favourable and further reactivity is stopped. As an example, the formation of $Cp^*_2Yb(py)_2$ starting from the diethyl ether adduct is instantaneous; crystals are formed within minutes.

This hypothesis was checked in two ways by forcefully drying **1.12** to attempt to remove the pyridine traces altogether. The disappearance of the corresponding peaks was monitored by ^{1}H NMR in THF-d_8. Although no structural proof can be provided, we assume a bridging arrangement between the methyl groups of two "**(bimpym)PdMe**"-type molecules in order to saturate the coordination environment of the Pd^{II} centre. The addition of ytterbocene to this adduct did, indeed, proceed quite differently to the reactivity of **1.12**. Slow conversion to an unknown product was observed. The integration of the unknown product is not immediately suggestive as to the chemical nature of this compound. If free lutidine is added to this mixture, the same three phases described above are almost instantly formed. However, the signals observed for the reaction without lutidine do not disappear; new peaks are formed, without seemingly perturbing the previous products.

Following the same logic, trying to add free lutidine to **2.4** only lead to the gradual decomposition of the substrate. This is, thus, not a viable route to obtain the complexes with the pyridine analogues.

The addition of samarocene in presence of **1.12** and of excess lutidine also results in the three phases described above. However, as opposed to ytterbium's case, the yellow solution appears to give a better indication of the compound that's formed. Based on the integration of the signals, it is not unreasonable to assume that a coupled product with lutidine, analogous to **2.4** or **2.5**, is formed (Figure 2.36). These solutions did not yield crystals, precluding further characterisation. As is the case for ytterbium, dissolving the solids in THF-d_8 reveals the characteristic broad (bimpym)Pd signals.

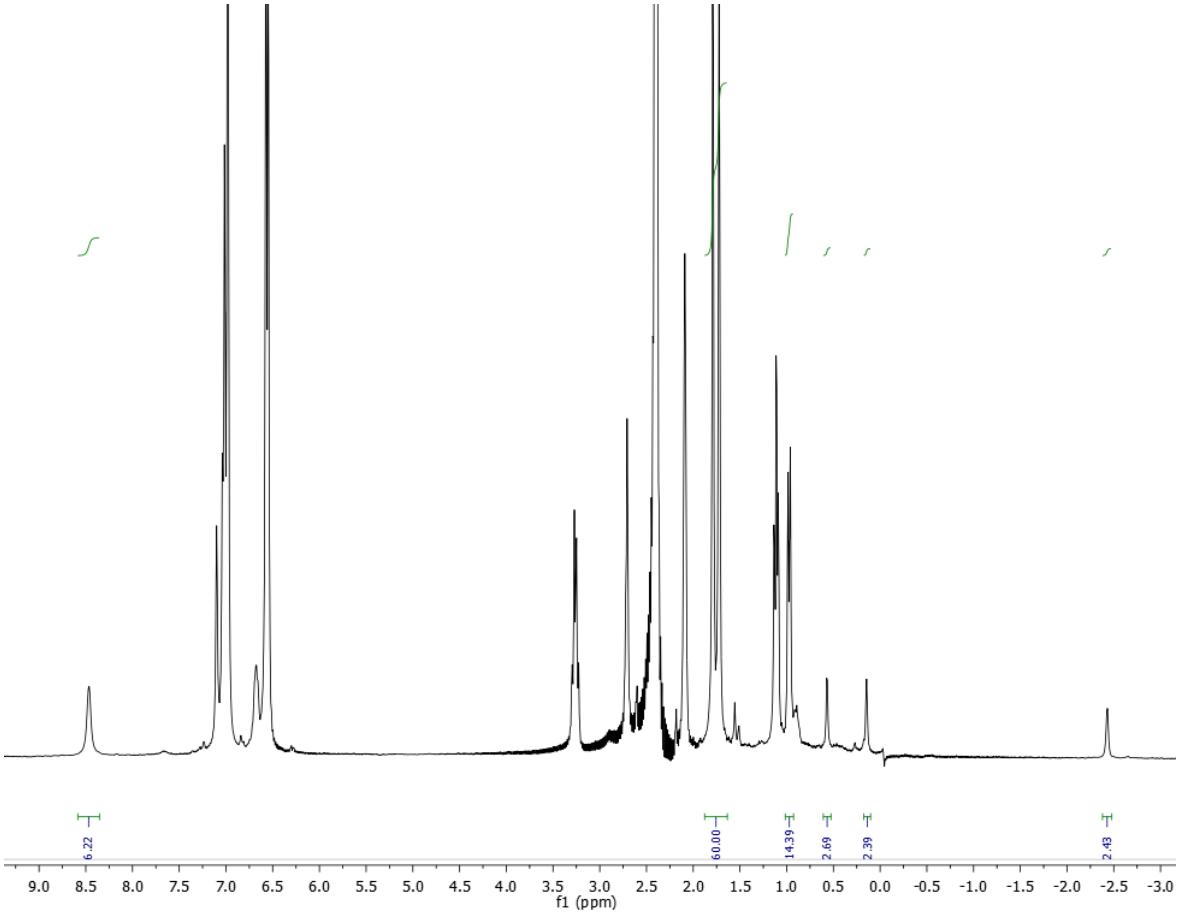

*Figure 2.36: ^{1}H NMR spectrum in tol-d_8 of the formed product after the addition of samarocene to **1.12** and free lutidine.*

The attempts of substituting the pyridine during the reaction were more fruitful with the other analogues, in tandem with samarocene. Addition of the organolanthanide precursor to **1.12** and excess free ligand (even a very large excess – up to a few drops – is tolerated!) permitted the isolation of the analogous trimetallic compounds with quinoline (**2.8**) and pentafluoropyridine (**2.9**) (Figure 2.37). The equivalent reactivity with ytterbocene produced no such complexes.

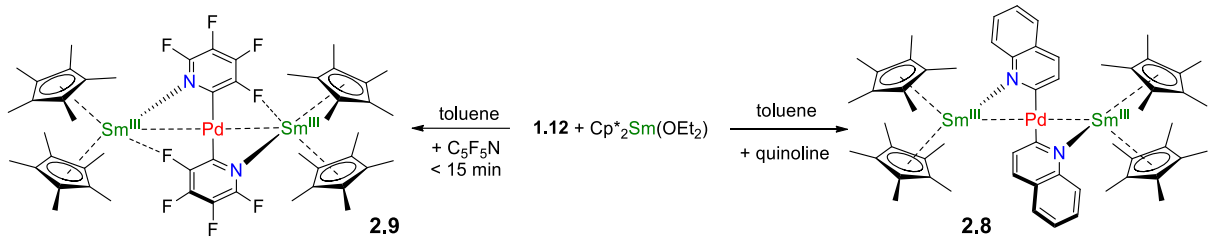

Scheme 2.7: Preparation of trimetallic edifices with pyridine analogues.

In the case of the quinoline, the addition of the excess ligand did not change the outward appearance of the reaction – the same black solution with golden hues was obtained. Afterwards, the same work-up procedure that was used for **2.6** or **2.7** was sufficient for obtaining adequate crystals that permitted the structural authentication of the quinoline motif. Irrespective of the crystallisation method, all of the measured crystals were quite significantly twinned. The resolution of the XRD data showed some moderate disorder in the phenyl ring (that is present in quinolyl, but not on the pyridyl in **2.7**). Perhaps this is an indication of an incomplete substitution of the pyridine by the quinoline.

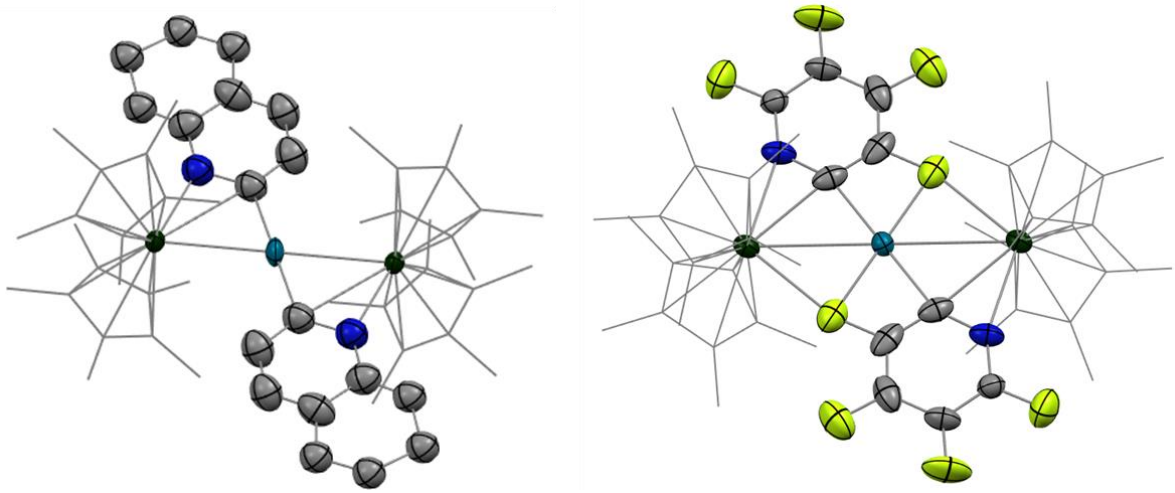

*Figure 2.37: ORTEP of **2.8** and **2.9**. The H atoms are hidden and the Cp* co-ligands are shown in wireframe for clarity.*

The case of **2.9** merits further comment, however. The addition of the drop of pentafluoropyridine resulted in an instantaneous colour change to bright red. The reaction was stirred for 15 minutes, before filtering the solution and storing it at -40 °C after adequate concentration. Very large red crystals were grown overnight. The XRD analysis showed two distinct molecules. The electronic density associated to the central atom was not equal in both adducts and was significantly inferior to that of Pd. Consequently, the best-fitting model for this system involved a partial occupation of the Pd sites, giving the formula $[(Cp^*_2Sm)_2(\mu\text{-}Pd_x(C_5F_4N)_2]$, where x = 0.133 and 0.268.

The main distances and angles in these complexes are given in Table 2.6. The structural features evolve when changing the coordinating ligand. This is most notable in **2.9**, since there is an attractive interaction between Sm and the neighbouring fluoride on the pentafluoropyridine. This induces a deviation in the relative arrangement between the organolanthanide and the Pd-pyridyl fragments. The angle formed by the Sm-Pd-Sm axis and the C-Pd-C axis is around 67° in all the trimetallic adducts, except for **2.9**, where this angle is around 55°. This percolates across the other features, such as the Sm-Pd and Sm-N distances.

	Av. Values (Å or °)			
Atoms	**2.7**	**2.8**	**2.9 (x=0.133)**	**2.9 (x=0.268)**
Sm-Pd	2.908(1)	2.918(2)	3.068(1)	3.066(1)
Sm-N	2.386(3)	2.425(11)	2.445(3)	2.457(3)
Sm-F			2.584(2)	2.583(2)
$Sm - Cp^*_{ctr}$	2.449	2.447	2.424	2.429
Pd-C	2.081(4)	2.090(15)	2.027(2)	2.035(3)
$<(C_{pyriyl1}\text{-}Pd\text{-}C_{pyridyl2})$	179.72°	180.0(5)	180.00	180.00
$<(Sm\text{-}Pd\text{-}C_{pyridyl})$	67.67(1)	68.1(4)	54.27(8)	55.12(13)
$<(Cp^*_{1\,ctr}\text{ -Ln- }Cp^*_{2\,ctr})$	134.52°	134.60	136.82	136.50

Table 2.6: Main distances and angles in the trimetallic edifices with pyridine analogues.

The proportions of Pd in **2.9** were not repeatable across other similar synthetic trials. This can provide two conclusions: the partial occupation may depend on the duration of the reaction and it should be feasible to form a similar compound, without the central Pd atom.

The first assertion was tested by stirring the mixture for longer periods of time. Although the bright red solution is indeed always immediately formed, the colour changes to dark brown after around 2h, accompanied by the troubling of the reaction mixture. However, no crystal structure could be obtained to help elucidate matters.

As for the second conclusion, tests were performed by performing a simple addition of pentafluoropyridine in a toluene solution of samarocene. The solution immediately became pink-red and, upon concentration, yellow blocks and red needles formed, which were later structurally authenticated as $[Cp^*_2Sm(\eta^2\text{-}C_5F_4N)]_2$ (**2.10**) and $[Cp^*_2Sm(\mu\text{-}F)(\mu\text{-}C_5F_3N)SmCp^*_2]_2$ (**2.11**), respectively (Figure 2.38). The poor crystal quality of the latter, however, imposes a tentative qualification of its chemical formula. For example, the fourth fluoride atom in the tetrafluoropyridyl could not be definitively identified. In both cases, it is clear that C-F activations took place. The structure of **2.10** is eerily reminiscent of that the pentafluorophenyl analogue described by Tilley in 2001.[60] In this case, however, the Sm^{III} centre is coordinated by the nitrogen on one molecule and the fluoride on the other, instead of two fluorides. There are no close matches for **2.11** in the literature, due to the unusual nature of the bridging pyridyl ligand, although there are numerous other examples of multimetallic edifices bridged by fluorides.[61,62]

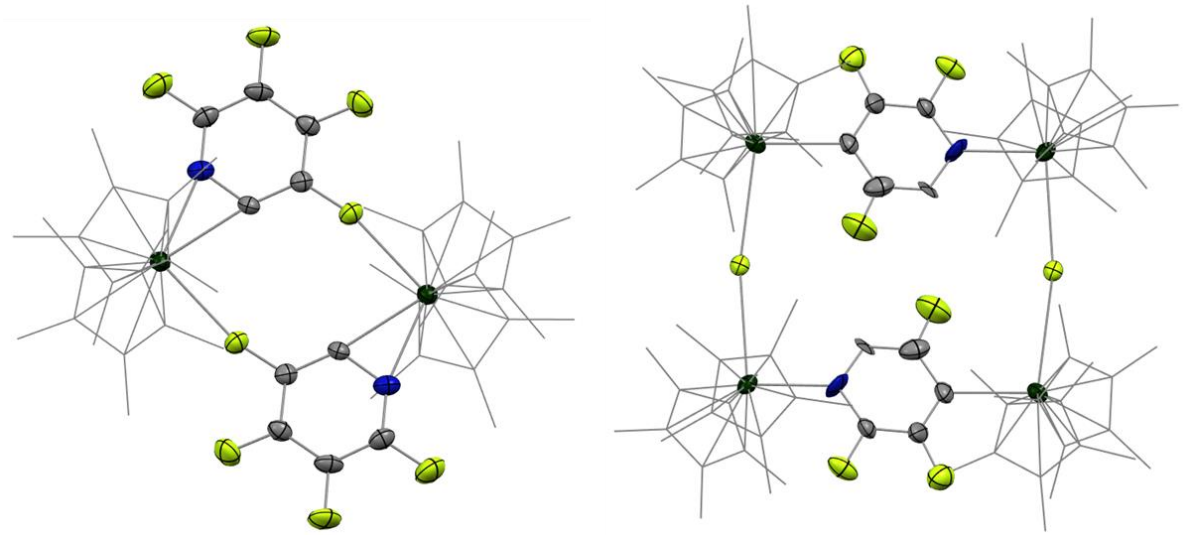

*Figure 2.38: ORTEP of C-F activation-induced multimetallic complexes based on pentafluoropyridine **2.10** and **2.11**.*

The corresponding reaction with ytterbocene resulted in a purple-pink solution, from which red-pink needles could be grown. Resolution of the XRD data indicated the formation of another multimetallic framework of the formula $Cp^*_6Yb_4(\mu\text{-}F)_6$ (**2.12**). This arrangement is very similar to a tetra-fluoride cluster described by Andersen.[63] The two Yb centres bearing two Cp* co-ligands only bond with two fluorides, whereas the ones with a single Cp* are coordinated to four.

The participation of the pentafluoropyridine in this complex is rather curious, as it appears that two separate C-F activations have taken place in the α positions of the nitrogen. In one of the sites of the activation, a coupling reaction to a methyl on the Cp* occurs, whilst the other seems to have been protonated by the prototropy of one of the H atoms on the coupling methyl. Lastly, the N atom is correctly positioned to form a bond with the Yb centre (Figure 2.39). In the cited article, Andersen argued for a mixed-valence $Yb^{II}_2Yb^{III}_2$ compound on the basis the magnetic properties and of the different Yb-C_{Cp^*} bond lengths. Indeed, there is a marked difference in the distance between the Yb centres and the centroids of the Cp*. Based on the same metric, only the Yb centre close to the

trifluoropyridyl would be in better agreement with an Yb^{II} configuration in our example (2.412 Å), whilst the other three would be more adequately described as Yb^{III} (2.341-2.360 Å).

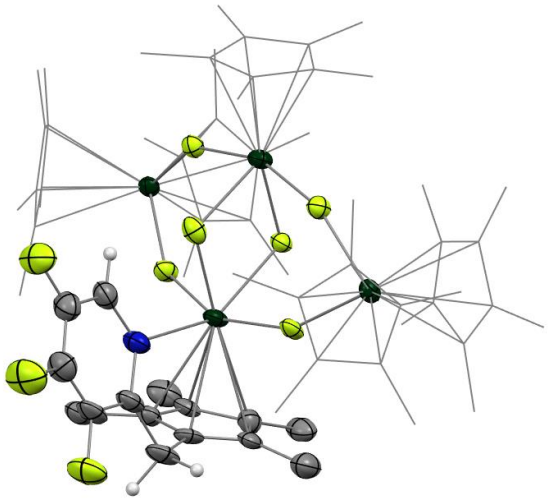

*Figure 2.39: ORTEP of **2.12**. The Cp* co-ligands are set in wireframe in the interest of clarity.*

2.3.4. Partial conclusion.

This section described the formation of heterometallic species, based on the (bimpym)Pd precursor, where the metal is coordinated on the LX site of the ligand.

The formation of the coupling products **2.4** and **2.5** is consistent with the previously observed behaviour of the bimpym ligand, even in the case of the conceptually similar Ir-based complex **2.1**. The coupling reaction, given the main vacant orbitals of the precursor **1.12**, would imply that the LUMO+1, with the significant participation of the coupling carbon, is stabilised below the LUMO upon the addition of the organolanthanide fragment (first step in Scheme 2.8). It is then populated by an electron transfer from the Yb^{II} centre, leading to the coupling of two fragments (therefore creating a doubly occupied orbital). The irreversible isomerisation reaction of the coupling products can be justified by the release of the steric strain associated with having the two pyridine molecules point in opposite directions. The configuration in **2.5** allows for a more relaxed geometrical structure, where the two adjoined fragments can get closer to one another, maximising attractive dispersive forces.

The third product that is obtained when heating up either of the coupling products has the same in-solution symmetry of the ^{1}H NMR signals alludes to a compound with a very similar chemical nature. Efforts are invested into trying to isolate this complex.

Following on the orbital analysis begun above, the formation of the trimetallic complex **2.6** from the coupling product is coherent with the activation of the pyridine-based reaction pathway implied by the LUMO in **1.12**. This is justified by the fact that this formation is promoted by the C-H activation of the pyridine in the α position. It is important to note that **2.6** is not formed as a result of the decomposition of the initial coupling product **2.4**. The latter is relatively stable and only evolves towards its isomer, **2.5**.

This decomposition pathway (as seen in Figure 2.18) is triggered when the reaction between **1.12** and ytterbocene is let to run its course. The most likely explanation for this behaviour is that not all the organolanthanide precursor is consumed before a large in-solution concentration of **2.4** is reached.

The remaining ytterbocene can then further react with the newly formed coupling product, presumably by a second electron transfer, thus activating the **LUMO**^{L}-type pathway (last step in Scheme 2.8). This hypothesis is substantiated by the fact that the synthetic protocol that assures the highest yield of pure **2.4** relies on both very rapid reaction times (less than a minute) and a slight excess of **1.12**.

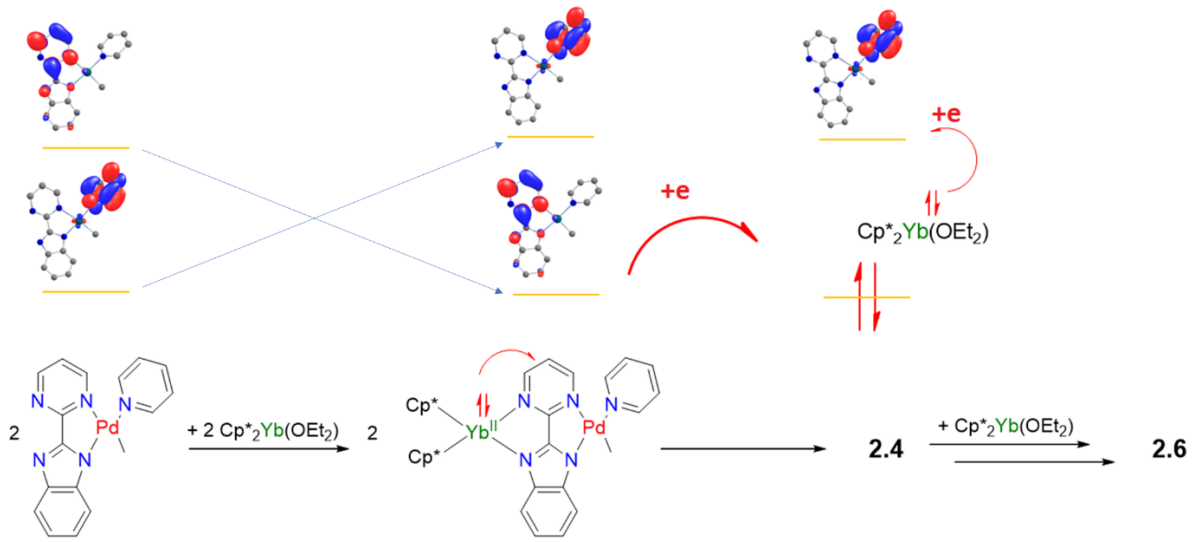

*Scheme 2.8: Schematic representation of the electronic perturbation and subsequent population of the main vacant orbitals of **1.12** upon the addition of ytterbocene. The orbitals of **1.12** are used as visual references in the heterobimetallic adducts.*

The fact that an isostructural coupling product could not be obtained after the reaction with samarocene is ascribed to the difference in redox potential between the two divalent metals. Nevertheless, the reaction with **1.12** evolves to the isostructural trimetallic complex **2.7**. The comparison of the main distances in the two complexes reveals an apparent break in the lanthanide contraction, as the Sm-Pd distance is shorter than that of the equivalent Yb-Pd.

Spectroscopic analyses would indicate the same electronic configuration of the lanthanide centres for the two adducts. Indeed, there is no indication at any point that the lanthanides are anything other than Ln^{III}. Based on precedence in the pertinent literature, it would be tempting to ascribe this difference to a stronger Pd-Ln interaction in the case of the Sm, but such an assertion must be investigated and proven cautiously to be validated.

An extensive theoretical study, aimed at elucidating this question, will be reported in Chapter 3.

The unusual C-H activation of the pyridine prompted a study into the possibility of enabling similar behaviour with pyridine analogues. Rather surprisingly, given the chemical similarity between the proposed ligands, the desired Pd precursors could not be isolated.

It would appear, based on the trials with lutidine, that subsequent reactions with organolanthanide fragments must proceed very cautiously, as excess lutidine invariably resulted in an undescriptive yellow solution, accompanied by undissolved solid, which bore the characteristic ^{1}H NMR signals of (bimpym)Pd-type species. It is very likely that ytterbocene reacts very rapidly with free lutidine, forming a stable complex, which engages in no further reactivity. Reducing the quantity of the available lutidine seemed to alleviate this issue, but the ensuing reactivity did not help clarify the chemical behaviour of these species. The case of samarocene is less conclusive, as the ^{1}H NMR

spectrum is not very dissimilar in symmetry and integration to the coupling products **2.4** and **2.5**, but no solid structural proof of the formed adduct could be gathered.

In that respect, the formation of complexes **2.8**-**2.10**, based on pyridine analogues, raises a number of questions regarding the reaction mechanism that results in the stabilisation of the trimetallic adducts **2.6** and **2.7**. In all cases, the structures were obtained without having had precursors with a confirmed coordination of the desired L ligand. Although the fluxionality of the pyridine in **1.12**, **2.4** and **2.5** was previously proven, its exchange with a desired target was not. This would seem to render a definitive analysis of the mechanism leading to the formation of the homologous quinolyl and tetrafluoropyridyl adducts **2.8** and **2.9** tenuous at best.

There are reasons to doubt that the ligand exchange between the pyridine and its analogue occurs efficiently in solution. The twinned nature of the crystals and the subsequently resolved structure of **2.8** would suggest that only a partial substitution of the pyridine has taken place.

The partial occupation of the Pd site in **2.9** definitively hints at the fact that the substitution of the pyridine is incomplete. That Pd is present is beyond reasonable doubt. Whilst the unit cells of **2.9** and of the Pd-less **2.10** are, indeed, the same, these complexes are different: the former is a bright red crystal, whereas the latter is golden yellow. The different colouring of the crystals is akin to the strong effect of minute quantities of impurities in minerals. Moreover, the Sm-C_{pyr} bond lengths are different (2.502 Å in **2.10** vs 2.531 Å in the molecule with the larger Pd occupation in **2.9**), suggesting the fact that the negative charge on the C is more equitably distributed when Pd is present.

It is worth noting that the addition of pyridine to samarocene leads to an electron transfer, followed by a coupling reaction.[64] If we are to compare pyridine and pentafluoropyridine, obtaining **2.10** as a stand-alone complex with its specific configuration, can be qualified as logical, for two reasons. The affinity of lanthanides for halides probably renders the C-F activation more advantageous than an electron transfer (and, presumably, the ensuing coupling reaction). Furthermore, the coordination environment offered to the Sm^{III} centre in the case of the putative pyridyl analogue of **2.10** is significantly less favourable. The very stabilising Sm-F interaction, originating from the opposite tetrafluoropyridyl molecule, undoubtably helps maintain this structure, as well. Such an interaction does not exist for the hypothetical pyridyl analogue of **2.10**.

Therefore, it seems reasonable to affirm that Pd^0 plays the role of a template agent in the formation of **2.6** and **2.7**. The formation of **2.9** and **2.10** help provide another piece of the puzzle, from a different perspective. The order in which the building blocks of these trimetallic structures are formed and assembled is unclear.

Each of the fragments – $[Pd^0(pyr)_2]^{2-}$ and $[Cp^*_2Ln]^+$ – are evidently very unstable and reactive species, that could not exist independently in solution for a long time. Is the $[Pd^0(pyr)_2]^{2-}$ formed first by expulsion of the bimpym ligand from the Pd coordination sphere and stabilised by the two $[Cp^*_2Ln]^+$ fragments? Or is an adduct of the type $[Cp^*_2Ln][Pd^0(pyr)]$ assembled first, before the second C-H activation takes place? These remain open questions and a more thorough mechanistic examination will be provided in Chapter 3.

2.4.Pt(bimpym)-based complexes.

The promising results obtained for the Pd-based complexes prompted the natural logical evolution in exploring the similar reactivity with the isostructural Pt-based precursor, **1.13**. After all, the two

complexes are quasi-identical in both their chemical behaviour and in the computed electronic structure (Table 1.12).

2.4.1. Synthesis of Pt(bimpym)-based complexes.

The addition of ytterbocene to **1.13** was performed in toluene under stirring. A dark red-brown mixture is rapidly formed. There is no further evolution in the mixture if the reaction is run for longer periods of time. Filtering the mixture gave a bright red solution, which, if left overnight, yields red needles. THF was found to be a better crystallising solvent for the complex. XRD analysis allowed the identification of the complex as $[Cp^*_2Yb(bimpym)Pt(py)(Me)]_2$ (**2.13**) – isostructural to the Pd homologue, **2.4**.

Given the brisk reactivity of **2.4** in the presence or organolanthanides, the initial work-up involved the same careful preparation and washing with cold non-polar solvents. This was proven not to be necessary, as **2.13** was stable at r.t in both the solid state and in solution. The synthetic yield was, however, slightly lower than in the Pd analogue, as roughly 70% molar equivalent of the initial quantity of **1.13** was recovered as crystalline material.

The same reaction was attempted with samarocene. In this case, a brown-yellow solution was formed. Filtration resulted in a brighter shade of yellow. Storing a saturated solution at cold produced suitable yellow needles. Acquisition of XRD data confirmed the attribution of the compound as the isostructural Sm-based coupling product, **2.14** (Figure 2.40). Contrary to the reactivity of **1.12**, the coupling product with Sm could be isolated and characterised. **2.14** could also be isolated as pure crystalline material in roughly 70% yield.

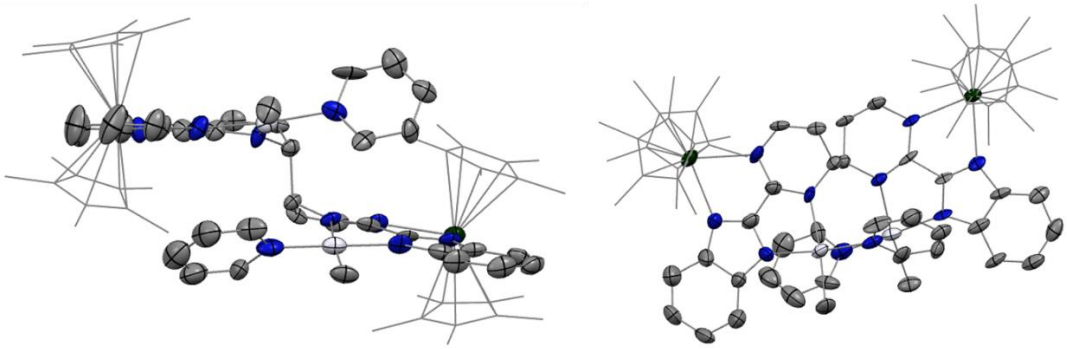

*Figure 2.40: ORTEP of **2.14**. The hydrogen atoms are not shown and the Cp* co-ligands are set in wireframe for clarity.*

The ubiquity of the coupling reaction in bimpym-based species motivated the inquiry into modifying the accessibility of the electron transfer. To this effect, the bulkier divalent lanthanide substrate $Cp^{ttt}_2Yb(OEt_2)$ was used (Cp^{ttt}=1,2,4-tri(tert-butyl)-cyclopentadienyl), since it had been previously shown that the steric constraints imposed by the co-ligand impacted the electron transfer.[65]

The reaction proceeded in a similar fashion to the ones described above. A brown solution was formed rapidly after the addition of toluene to the solids. The three ^{t}Bu groups confer excellent solubility to the resulting complex. Crystallisation could be achieved by leaving a very concentrated THF solution at -40 °C for a few days. Increasing the concentration also resulted in the precipitation of secondary products, which could not be adequately separated from the crystals. Acquisition and resolution of the XRD data demonstrated that the electron transfer did, however, still occur, as the corresponding coupling product **2.15** was identified.

The similarities end here, though. The steric repulsion presumably does not allow a similar conformation to all of the coupling products described in this chapter, as the two bimpym ligands are best described as being both opposite and orthogonal to one another (Figure 2.41).

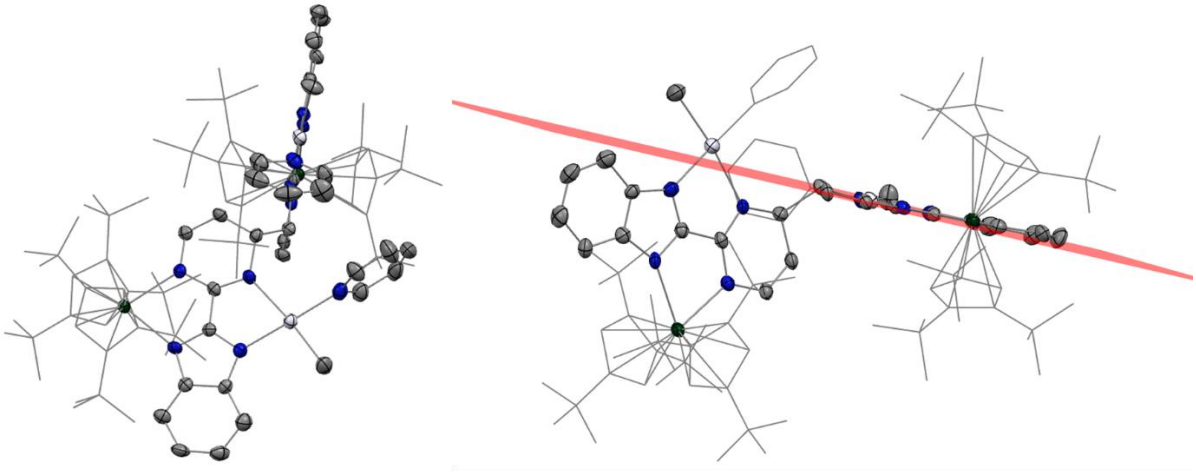

*Figure 2.41: ORTEP of **2.15**. The hydrogen atoms are hidden and the Cp^{ttt} groups are set in wireframe for clarity. The lack of deviation from planarity on the pyrimidine moiety is demonstrated by the neat arrangement within the plane formed by its composing atoms.*

2.4.2. Characterisation of the Pt(bimpym)-based complexes.

The expansion of the family of coupling products by three new members warrants a structural comparison of the adducts. The main distances and angles are collected in Table 2.7. The two Cp*-based complexes are practically identical for every metric, except the distances corresponding to the Ln centre, which follow the lanthanide contraction. In these two compounds, the two coupled ligands are virtually parallel to one another (with a circa 10° deviation of the two planes) and the torsion angle formed by the two coupled moieties is in the range of the previous examples. The latter angle is practically identical to that in **2.4**.

The Ln-Cp* centroid distances are in agreement with Ln^{III} centres. In these two complexes, the coupling C atom is pulled slightly out of the ligand plane, consistent with the dearomatisation of the pyrimidine moiety. On the basis of the structural features, the Pt centre is not perturbed by the redox event and the ensuing coupling reaction. All the bond lengths are comparable to those in the precursor **1.13**. As is the case for **2.4**, the two pyridine ligands point in opposite directions. Contrary to the Pd analogue, **2.13** and **2.14** do not isomerise in neither ambient conditions, nor when heated up. Keeping either complex at 70 °C for extended periods of time only results in their gradual decomposition.

2.15 does not respect the same trend regarding the relative orientation of the two bimpym ligands. Instead of being shifted by about 90° from one another ($NCCN_{tor}$ in Table 2.7), the two coupled moieties adopt a conformation reminiscent of that of **[Yb(bimpym)Ni]$_2$**-type species, where the torsion angles approach 180°.[2] Moreover, far from being close to parallel, as is the case in **2.13** and **2.14**, the two ligand planes are almost perfectly orthogonal.

This arrangement is almost certainly caused by the steric constraints imposed by the very bulky Cp^{ttt} co-ligand. Nevertheless, on the evidence of the coupling reaction, the electron transfer is not prevented. There are some peculiarities in the structural features that would seem to contradict this conclusion. For one, the pyrimidine remains planar (as shown in Figure 2.41), which is unique amongst its class of compounds. Second, the Yb-Cp^{ttt} centroid distance is unusually large, at 2.413 Å. Previously

tabulated values give 2.27-2.36 Å for the Yb^{III} configuration[66] and 2.38-2.47 Å for the Yb^{II} configuration.[67] The lower value for the divalent state is less pertinent, since it concerns the base-free Cp^{ttt}_2Yb adduct.

The first argument can be countered by the unique orthogonal orientation of the two ligands, as well as by the steric constraints imposed by the surroundings, which would limit the outwards extension of the coupling C atoms toward one another. Furthermore, the distances on the pyrimidine moiety in **2.15** are almost identical to the ones in the complexes where the aromaticity is broken, hinting that the same behaviour is observed here, bar the deviation from planarity.

The comparison of the Yb-Cp^{ttt} centroid distance with previously reported complexes is less appropriate, as there are only six examples in the literature – not enough to properly assess the impact of how different coordination environments can elongate the distance with the Cp^{ttt} ring. None of the reported examples feature a larger, multidentate ligand on the Yb, as is the case in **2.15**.

	Av. Values (Å or °)		
Atoms	**2.13**	**2.14**	**2.15**
Ln-N_{pym}	2.339(9)	2.459(9)	2.297(8)
Ln-N_{imid}	2.368(10)	2.454(9)	2.319(8)
Ln – Cp'_{ctr}	2.322	2.434	2.413
C-$C_{coupling}$	1.588(14)	1.601(14)	1.578(18)
Pt-N_{pym}	2.132(8)	2.140(9)	2.184(8)
Pt-N_{imid}	2.003(9)	2.034(10)	2.018(8)
Pt-N_{py}	2.009(9)	2.045(10)	2.011(9)
Pt-C_{Me}	2.043(11)	2.061(11)	2.053(10)
Pt-Pt	4.168	4.199	6.489
d(Pt-plane)	0.363	0.375	0.053
$NCCN_{tor}$	95.17	96.91	170.05
(L_1-L_2)	9.41	10.35	85.20
$(py\text{-}plane)_{tw}$	49.87	51.94	88.27

*Table 2.7: Main average distances and angles in **2.13-2.15**. The metrics which are dissymmetrical by more than 10° between the two fragments in the dimer are highlighted in red. $NCCN_{tor}$ designates the inter-fragment torsion angle, (L_1-L_2) the angle between the ligand planes of the first and second bimpym molecule and $(py\text{-}plane)_{tw}$ the average angle between the pyridine plane and the square plane of the Pd coordination sphere.*

Dissolution of the crystalline solid of the Cp*-based complex was informative. The ^{1}H NMR spectrum of **2.13** was, unsurprisingly, very similar to that of its Pd analogue, **2.4**. Given that there are only 7 signals corresponding to the bimpym ligand, this species has at least C_2 symmetry in solution. The pyridine signals were recovered at -30 °C, hinting at the same fluxional behaviour at r.t as is observed for **2.4**.

The conclusions for **2.14** were similar. The corresponding spectrum of the Sm-based complex is given in Figure 2.42. Six of the expected seven signals of the bimpym ligand are cleanly identified, with the last one presumably hidden in the shoulder of the residual tol-d_8 signals.

The ^{1}H NMR spectrum of **2.15** could not be cleanly isolated. The separation of this adduct from its accompanying impurity could not be reliably performed, as their solubility in all the tested solvents

were seemingly identical. The presence of highly paramagnetically shifted peaks is a reliable indication of the Yb^{III} configuration observed in this complex.

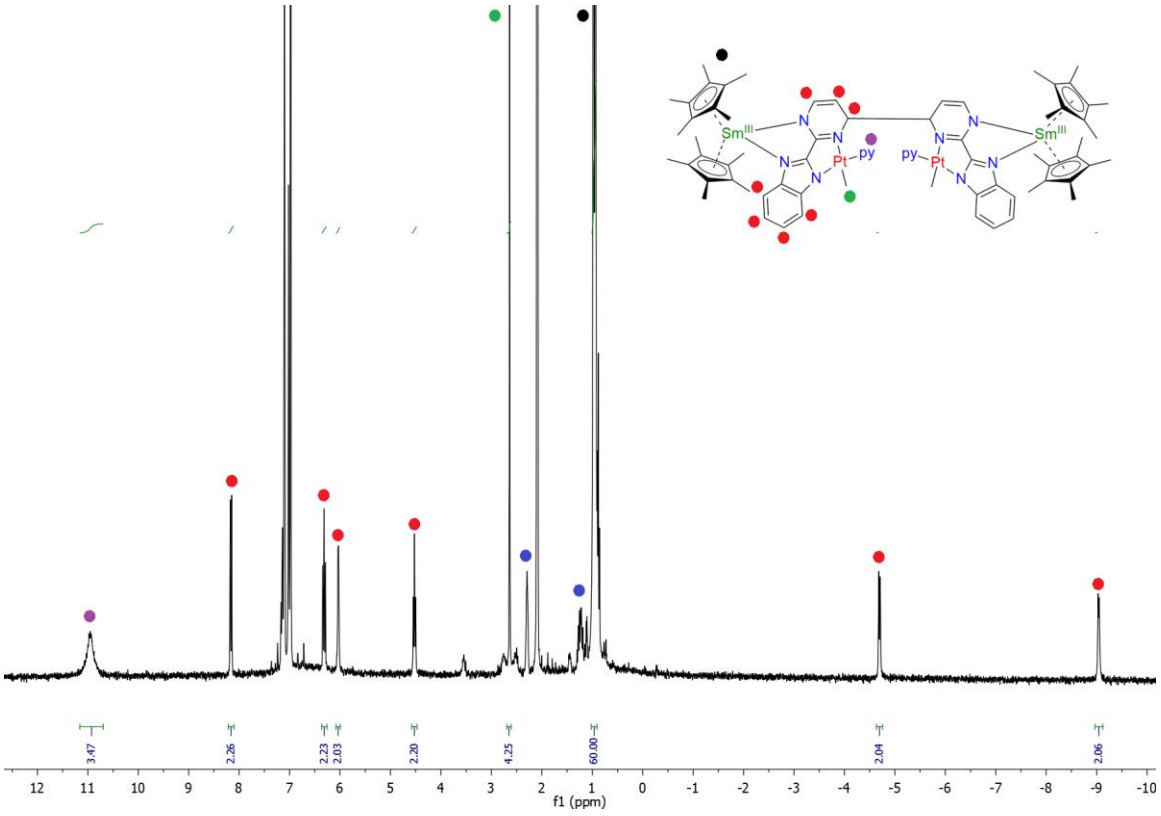

*Figure 2.42: ^{1}H NMR of **2.14** in tol-d_8. Residual solvent peaks of toluene and pentane are designated by the blue dots.*

The UV-Vis spectra were recorded for **2.13** and **2.14**. The chief difference between the two is an extra absorption for the Yb-based complex at 333 nm. The same contrast was observed in the UV-Vis spectra of the Pd-based trimetallic complexes **2.6** and **2.7** (Figure 2.30). The main absorption band (at 301 and 332 nm for **2.13** and **2.14**, respectively) is attributed to the ligand-based π->π* transition, whereas the others are ascribed to MLCT transitions.

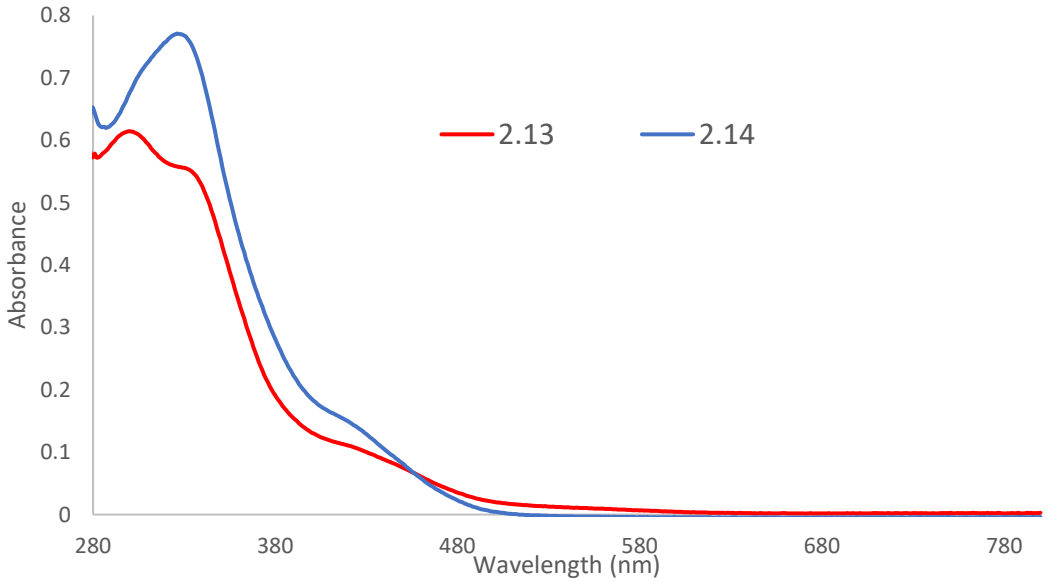

*Figure 2.43: UV-Visible spectra of **2.13** and **2.14**.*

The comparison between **2.4** and its Pt analogue is informative. There is only one neatly resolved absorption in the spectrum of the former (Figure 2.22), while there are more than one in the Pt-based complexes. This can be attributed to the more electron-rich nature of the Pt^{II} centre, which is more capable in engaging in MLCT transitions than its Pd^{II} counterpart. The same variation was observed in the **K(bimpym)TMMe$_2$** species – the Pt complex **1.8** was the only one to feature more than one absorption band (Figure 1.7).

2.4.3. Addition of an excess of organolanthanide precursors.

The presence of excess organolanthanide precursors in toluene solutions of **2.4** led to further reactivity, which ultimately results in the trimetallic adduct **2.6**. Although this pathway is not explicitly observed when using samarocene, it would appear logical that this is also the case.

On the basis of the very similar electronic structures of the precursors **1.12** and **1.13**, it is expected that they result in comparable reactivity. The isolation of the coupling products **2.13** and **2.14** is testament of this. Therefore, the addition of further organolanthanide precursors was pursued to investigate whether the subsequent step can be mimicked with Pt-based complexes.

An *in situ* reaction involving the addition of an excess of ytterbocene to **1.13** in tol-d_8 was performed. The formation of **2.13** is immediately attested. The supplementary ytterbocene did not react further. A higher concentration thereof was tested, but did not have any impact on proceedings. The solution was then heated up at 70 °C in an attempt to induce further reactivity (Figure 2.44). Although some evolution is indeed observed after 4h, this could not be effectively correlated with the decrease in the concentration of $Cp^*_2Yb(OEt_2)$. After 18 hours, the mixture presents a series of unidentified signals. No product could be isolated and characterised thereafter. It's worth noting, though, that the evolution of **2.13** when heated up in the presence of ytterbocene is different to that when only the complex is kept at 70 °C. In the latter case, only the decomposition of the substrate was observed.

If any evolution similar to that of **2.4** is to occur, heating clearly is insufficient to reach the reaction activation barrier. A different solution was tested. **2.13** and **2.14** were dissolved in tol-d_8 in the presence of their corresponding divalent organolanthanide precursor. The mixtures were then placed under a UV light. The evolution of the substrates was followed by ^{1}H NMR. In the case of **2.14**, it would appear that exciting the complex only results in its gradual decomposition, as the intensity of the characteristic product signals decline over time. The evolution of **2.13** was somewhat different. Although the compound peaks also gradually abate, new signals are formed (Figure 2.45). Among them, a dominant peak at 9.24 ppm closely resembles the Cp* signal in the trimetallic adduct **2.6**. No complex could, however, be isolated from this small-scale trial.

Encouraged by these findings, similar up-scaled reactions were carried out. Due to the limitations of the set-up of the UV lamp, the mixtures were added in 10 mL vials with stopcocks. This option does, in principle, offer sufficient protection against the infiltration of atmospheric oxygen and humidity in the short term. To isolate our samples further, the stopcocks were sealed off with parafilm. The mixtures were stirred for 4h under UV light before being re-entered in the glovebox. In both cases, the solutions darkened after this procedure.

Filtration, followed by storing the solutions at cold, resulted in the precipitation of red and yellow powder from the reaction mixtures of **2.13** and **2.14**, respectively. The volatiles were removed under reduced pressure and the ensuing powders were extracted with pentane and, separately, with Et_2O. The remaining solids were red and yellow-brown, respectively. All of the extraction fractions ultimately recrystallised as the parent compounds **2.13** or **2.14**.

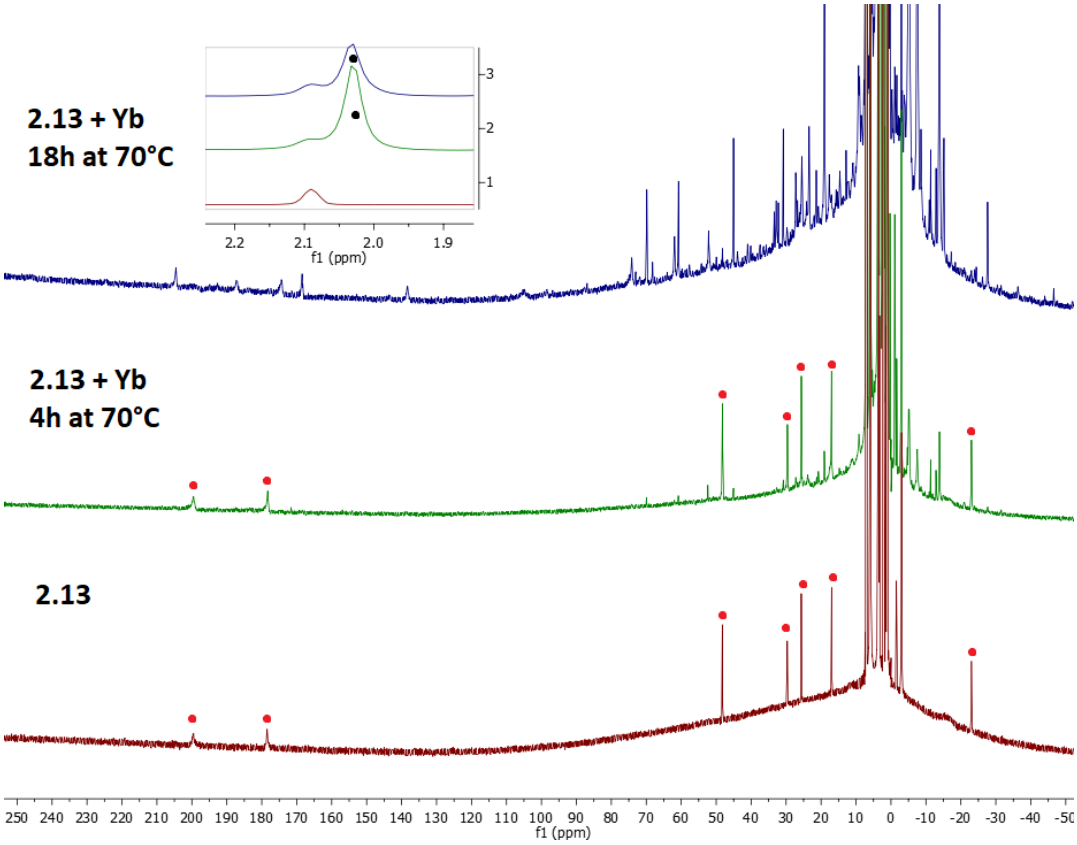

*Figure 2.44: ^{1}H NMR of **2.13** in tol-d_8 and the evolution when excess ytterbocene is added and the mixture is kept at 70 °C. The red dots indicate the bimpym peaks of the product, the black dot indicates the Cp* signal of ytterbocene.*

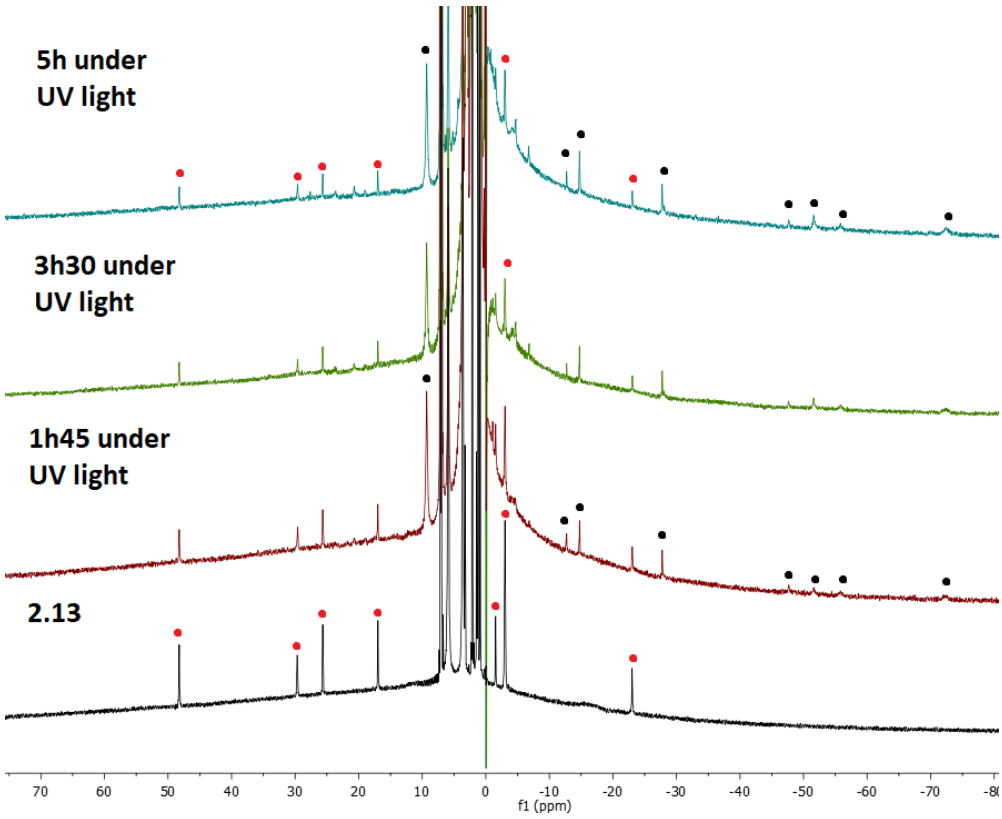

*Figure 2.45: Evolution of the mixture containing **2.13** and ytterbocene under UV light after different periods of time. The peaks of **2.13** are designated by the red dots, whilst the new signals are designated by the black dots.*

The remaining solid after the extraction in the case of the Yb product resulted in a bright red solution when dissolved in THF. Crystals of excellent quality were grown from a saturated solution. Acquisition of the XRD data allowed the identification of this complex as $[(Cp^*_2Yb)_2(\mu\text{-}O)]$. The probable source of the oxygen atom is unknown. The infiltration of the ambient atmosphere in the reaction vial is unlikely, as no starting compound could then have been isolated.

2.5. Conclusion and perspectives.

This chapter summarises the reactivity of some of the transition metal precursors, described in Chapter 1, towards divalent lanthanides.

Based on the relationship between the metal and the bimpym ligand, the complexes can be classified into two groups: those where the TM is coordinated on the L_2 site (K(bimpym)-based) and those where the TM is nestled in the anionic LX site ((bimpym)-based).

The reactivity of **K(bimpym)NiMe$_2$** was described during the PhD of Ding Wang.[5] It comes as no surprise that the other group 10 metals exhibit much of the same reactivity. There are strong arguments to suggest that the addition of divalent lanthanides can result in the formation of heterobimetallic complexes, where the lanthanide reduces the bimpym ligand. Complexes very similar to the isolated **[Yb(bimpym)Ni]$_2$** are found by ^{1}H NMR. These compounds are referred to as **Yb(bimpym)Pd** and **Yb(bimpym)Pt**. Although no definitive proof can be provided, there is nothing to suggest that these species are not also the result of coupling reactions, as the latter is a *leitmotif* for the bimpym-based complexes.

The shared reactivity does not stop here, as the final product of this sequence – the trimetallic compound **Yb$_3$(bimpym)$_2$** with two coupled ligand molecules – is also observed for the Pd and Pt analogues of the Ni complex.

What was shown to be rather remarkable in the case of the Pd precursor is its circumstantial evolution to the highly unusual species, **2.2**. Not only does this complex present a very rare Pd-Cp* bond, but it also features a very short Yb-Pd distance. From a formation mechanism perspective, **2.2** is different from the equivalent Ni chemistry, because the Cp* co-ligand released by the central Yb^{III} centre in **Yb$_3$(bimpym)$_2$** does not result in the formation of KCp*, which was attested for Ni.[2]

Instead, the Cp* anion presumably coordinates to the evicted $PdMe_2$ fragment. This is believed to be due to the stability of a transient species that precedes the reorganisation towards **2.2**. At this juncture, it is not clear what specific trait of Pd^{II} allows this stabilisation and does not in the other two cases. This statement is conditional on no breakthroughs in the reactivity of the Pt precursor, of which there were significantly fewer synthetic attempts. Perhaps altering the reaction conditions by way of increased temperature or reaction times could allow isolating the corresponding analogue.

The implications of these findings are, as of yet, unclear, mainly due to the synthetic difficulties associated with obtaining **2.2** in high quantities. At the time of writing, solid-state magnetic data for this complex was not obtained. This piece of the puzzle is crucial, as it could give insight into the nature of this interaction. It is unknown whether there is any shared electronic density between the two metals and, particularly, how this translates into the electronic configuration of the Yb centre. If, for example, it is not entirely trivalent at lower temperatures, then the magnetic susceptibility would be a dead give-away.

For these reasons alone, it is an absolute priority to obtain this data. Based on the findings, further studies, such as EPR, XMCD or XAS techniques could be required to better understand the electronic structure of this complex.

This would require improving the presently inefficient synthesis and purification procedures. The issues encountered in the synthesis of the precursor (**1.9**), detailed in Chapter 1, may be alleviated by the use of the equivalent capped complex (**1.10**). Afterwards, separating **2.2** from its counterpart, **Yb_3(bimpym)$_2$**, remains extremely tricky.

The other class of compounds studied in this Chapter – bimpym-based adducts – also share large parts of their reactivity. Addition of divalent lanthanide precursors, either in the form of the Cp*-based or the more sterically hindered $Cp^{ttt}_2Yb(OEt_2)$ precursor, invariably result in an electron transfer, followed by the coupling reaction. The ligand dearomatises and becomes negatively charged, therefore satisfying the electrostatic requirements of the newly trivalent lanthanide centre. Owing to this fact, no drastic reorganisation of the substrates is observed, contrary to the K(bimpym)-based adducts, where the Ln initially coordinates to an anionic site. For these complexes, the same dearomatisation and accumulation of negative charge probably constitute the cause of elimination of the TM fragment.

The formation of these coupled adducts can be rationalised by the shape of the dominant vacant orbital on these bimpym-based precursors. In the case of the Pd and Pt-based precursors **1.12** and **1.13**, this orbital is the LUMO+1, close in energy to the L-ligand-based LUMO, but it is presumably stabilised more by the coordination of the divalent lanthanide. When an electron is transferred to this orbital, significant electronic density is accumulated on the coupling C atom, resulting in an anionic radical. The coupling of two such molecules produces an overall doubly occupied orbital.

All of the bimpym-based adducts seem to be remarkably stable in their assumed configurations. The isomerisation of **2.4** towards **2.5** is an exception, but the final product merely relaxes its geometry for better stability. None of **2.1**, **2.4**, **2.5**, **2.13**, **2.14** or **2.15** demonstrate any degradation at r.t and are quite sturdy even in the face of higher temperatures. The reactivity trials of these complexes showed that they are stable when reacted with other substrates, even further divalent lanthanide precursors.

Except for – again – the Pd-based precursors **2.4** and **2.5**, rather intriguingly. These adducts exhibit very unusual reactivity when in the presence of divalent lanthanides. Following on the orbital rationale above, the second reaction with lanthanides presumably populates the pyridine-based vacant orbital, resulting in a C-H activation (Scheme 2.8). The final products of this pathway are the very curious trimetallic adducts **2.6** and **2.7**. Some of the structural features are themselves unique: a linear $Pd(pyr)_2$ arrangement is observed, as well as a collinear arrangement between two lanthanides, with a transition metal sandwiched in between.

The spectroscopic characterisations revealed that the Ln centres in both complexes are in the +3 oxidation state all throughout the 0-300 K temperature range. This implies that the Pd is in the zerovalent configuration. What this means for the electronic configuration of these complexes is unclear and shall be explored in detail in the following Chapter.

The formation mechanism is yet to be fully understood. The population of the pyridine-based vacant orbital is probably the starting point of a complex reorganisation/decomposition process, from which the trimetallic adducts are formed and are sufficiently stable to allow characterisation.

Further work on explaining the formation of the trimetallic adducts shall be presented in the following chapter.

Given the considerable similarity in the electronic structures of **1.12** and **1.13**, and the isostructural nature of the coupling adducts **2.4** and **2.5** on one hand and **2.13** and **2.14** on the other, it could be expected that the Pt-based compounds follow an analogous reactivity pathway. Alas, despite our best efforts, **2.13** and **2.14** could not be cajoled into reorganisation/degradation, leading to similar compounds to **2.6** and **2.7**. This is quite surprising, as the Pt-based adducts are nigh-identical from a structural perspective to **2.4**, which easily reacts with excess ytterbocene.

This seemingly element-specific difference observed for both classes of compound presented in this chapter could be the goal of an intriguing comparative theoretical study.

References

(1) Zhang, Y.; Hou, Z.; Wakatsuki, Y. Bull. Chem. Soc. Jpn. 1998, 71 (6), 1381–1384. https://doi.org/10.1246/bcsj.71.1381.

(2) Wang, D.; Tricoire, M.; Cemortan, V.; Moutet, J.; Nocton, G. Inorg. Chem. Front. 2021, 8 (3), 647–657. https://doi.org/10.1039/D0QI00952K.

(3) Haynes, A.; Maitlis, P. M.; Morris, G. E.; Sunley, G. J.; Adams, H.; Badger, P. W.; Bowers, C. M.; Cook, D. B.; Elliott, P. I. P.; Ghaffar, T.; Green, H.; Griffin, T. R.; Payne, M.; Pearson, J. M.; Taylor, M. J.; Vickers, P. W.; Watt, R. J. J. Am. Chem. Soc. 2004, 126 (9), 2847–2861. https://doi.org/10.1021/ja039464y.

(4) Sunley, G. J.; Watson, D. J. Catal. Today 2000, 58 (4), 293–307. https://doi.org/10.1016/S0920-5861(00)00263-7.

(5) Ding Wang, PhD thesis, Institut Polytechnique de Paris, Ecole Polytechnique, 2020.

(6) Tilley, T. D.; Andersen, R. A.; Spencer, B.; Ruben, H.; Zalkin, A.; Templeton, D. H. Inorg. Chem. 1980, 19 (10), 2999–3003. https://doi.org/10.1021/ic50212a031.

(7) Goudy, V.; Jaoul, A.; Cordier, M.; Clavaguéra, C.; Nocton, G. J. Am. Chem. Soc. 2017, 139 (31), 10633–10636. https://doi.org/10.1021/jacs.7b05634.

(8) Kraus, H.-J.; Werner, H.; Krüger, C. Z. Für Naturforschung B 1983, 38 (6), 733–737. https://doi.org/10.1515/znb-1983-0614.

(9) Boag, N. M.; Boucher, D.; Davies, J. A.; Miller, R. W.; Pinkerton, A. A.; Syed, R. Organometallics 1988, 7 (3), 791–792. https://doi.org/10.1021/om00093a041.

(10) Suginome, M.; Kato, Y.; Takeda, N.; Oike, H.; Ito, Y. Organometallics 1998, 17 (4), 495–497. https://doi.org/10.1021/om9710778.

(11) Bollermann, T.; Freitag, K.; Gemel, C.; Seidel, R. W.; Fischer, R. A. Organometallics 2011, 30 (15), 4123–4127. https://doi.org/10.1021/om200430t.

(12) Tatsuno, Y.; Yoshida, T.; Seiotsuka; Al-Salem, N.; Shaw, B. L. In Inorganic Syntheses; Shriver, D. F., Ed.; John Wiley & Sons, Inc.: Hoboken, NJ, USA, 2007; pp 220–223. https://doi.org/10.1002/9780470132500.ch51.

(13) Rajalingam, K.; Strunskus, T.; Terfort, A.; Fischer, R. A.; Wöll, C. Langmuir 2008, 24 (15), 7986–7994. https://doi.org/10.1021/la8008927.

(14) Martínez, J.; Mariño, M.; Caamaño, M.; Pereira, M. T.; Ortigueira, J. M.; Gayoso, E.; López-Torres, M.; Vila, J. M. J. Organomet. Chem. 2013, 740, 92–97. https://doi.org/10.1016/j.jorganchem.2013.05.007.

(15) Cassar, D. J.; Roghzai, H.; Villemin, D.; Horton, P. N.; Coles, S. J.; Richards, C. J. Organometallics 2015, 34 (12), 2953–2961. https://doi.org/10.1021/acs.organomet.5b00282.

(16) Safronov, S. V.; Gutsul, E. I.; Golub, I. E.; Dolgushin, F. M.; Nelubina, Y. V.; Filippov, O. A.; Epstein, L. M.; Peregudov, A. S.; Belkova, N. V.; Shubina, E. S. Dalton Trans. 2019, 48 (33), 12720–12729. https://doi.org/10.1039/C9DT02176K.

(17) Holton, J.; Lappert, M. F.; Ballard, D. G. H.; Pearce, R.; Atwood, J. L.; Hunter, W. E. J Chem Soc Dalton Trans 1979, No. 1, 45–53. https://doi.org/10.1039/DT9790000045.

(18) Holton, J.; Lappert, M. F.; Ballard, D. G. H.; Pearce, R.; Atwood, J. L.; Hunter, W. E. J Chem Soc Dalton Trans 1979, No. 1, 54–61. https://doi.org/10.1039/DT9790000054.

(19) Walter, M. D.; Matsunaga, P. T.; Burns, C. J.; Maron, L.; Andersen, R. A. Organometallics 2017, 36 (23), 4564–4578. https://doi.org/10.1021/acs.organomet.7b00384.

(20) Bienfait, A. M.; Wolf, B. M.; Törnroos, K. W.; Anwander, R. Organometallics 2015, 34 (24), 5734–5744. https://doi.org/10.1021/acs.organomet.5b00837.

(21) Burns, C. J.; Andersen, R. A. J. Am. Chem. Soc. 1987, 109 (19), 5853–5855. https://doi.org/10.1021/ja00253a049.

(22) Occhipinti, G.; Meermann, C.; Dietrich, H. M.; Litlabø, R.; Auras, F.; Törnroos, K. W.; Maichle-Mössmer, C.; Jensen, V. R.; Anwander, R. J. Am. Chem. Soc. 2011, 133 (16), 6323–6337. https://doi.org/10.1021/ja2001049.
(23) Schwartz, D. J.; Ball, G. E.; Andersen, R. A. J. Am. Chem. Soc. 1995, 117 (22), 6027–6040. https://doi.org/10.1021/ja00127a016.
(24) Spannenberg, A.; Oberthür, M.; Noss, H.; Tillack, A.; Arndt, P.; Kempe, R. Angew. Chem. Int. Ed Engl. 1998, 37 (15), 2079–2082. https://doi.org/10.1002/(SICI)1521-3773(19980817)37:15<2079::AID-ANIE2079>3.0.CO;2-Y.
(25) Nefedov, S. E.; Kozitsyna, N. Yu.; Vargaftik, M. N.; Moiseev, I. I. Polyhedron 2009, 28 (1), 172–180. https://doi.org/10.1016/j.poly.2008.10.006.
(26) Nefedov, S. E.; Kozitsyna, N. Yu.; Akhmadullina, N. S.; Cherkashina, N. V.; Vargaftik, M. N.; Moiseev, I. I. Inorg. Chem. Commun. 2011, 14 (4), 554–557. https://doi.org/10.1016/j.inoche.2011.01.023.
(27) Izuogu, D. C.; Yoshida, T.; Zhang, H.; Cosquer, G.; Katoh, K.; Ogata, S.; Hasegawa, M.; Nojiri, H.; Damjanović, M.; Wernsdorfer, W.; Uruga, T.; Ina, T.; Breedlove, B. K.; Yamashita, M. Chem. – Eur. J. 2018, 24 (37), 9285–9294. https://doi.org/10.1002/chem.201800699.
(28) Lang, Z.; Yang, P.; Lin, Z.; Yan, L.; Li, M.-X.; Carbó, J. J.; Kortz, U.; Poblet, J. M. Chem Sci 2017, 8 (11), 7862–7872. https://doi.org/10.1039/C7SC03441E.
(29) Luinstra, G. A.; Ten Cate, L. C.; Heeres, H. J.; Pattiasina, J. W.; Meetsma, A.; Teuben, J. H. Organometallics 1991, 10 (9), 3227–3237. https://doi.org/10.1021/om00055a046.
(30) Kemmitt, R. D. W.; Russell, D. R. In Comprehensive Organometallic Chemistry; Elsevier, 1982; pp 1–276. https://doi.org/10.1016/B978-008046518-0.00063-5.
(31) Allen, K. J. H.; Nicholls-Allison, E. C.; Johnson, K. R. D.; Nirwan, R. S.; Berg, D. J.; Wester, D.; Twamley, B. Inorg. Chem. 2012, 51 (22), 12436–12443. https://doi.org/10.1021/ic301830u.
(32) Evans, W. J.; Montalvo, E.; Champagne, T. M.; Ziller, J. W.; DiPasquale, A. G.; Rheingold, A. L. Organometallics 2009, 28 (9), 2897–2903. https://doi.org/10.1021/om8012103.
(33) Dietrich, H. M.; Törnroos, K. W.; Anwander, R. Angew. Chem. Int. Ed. 2011, 50 (50), 12089–12093. https://doi.org/10.1002/anie.201105251.
(34) Kawai, D.; Shima, T.; Nishiura, M.; Hou, Z. J. Organomet. Chem. 2017, 847, 74–81. https://doi.org/10.1016/j.jorganchem.2017.02.042.
(35) Pevec, A.; Mrak, M.; Demšar, A.; Petricek, S.; Roesky, H. W. Polyhedron 2003, 22 (4), 575–579. https://doi.org/10.1016/S0277-5387(02)01419-5.
(36) Schoo, C.; Bestgen, S.; Schmidt, M.; Konchenko, S. N.; Scheer, M.; Roesky, P. W. Chem. Commun. 2016, 52 (90), 13217–13220. https://doi.org/10.1039/C6CC07367K.
(37) Arleth, N.; Gamer, M. T.; Köppe, R.; Pushkarevsky, N. A.; Konchenko, S. N.; Fleischmann, M.; Bodensteiner, M.; Scheer, M.; Roesky, P. W. Chem. Sci. 2015, 6 (12), 7179–7184. https://doi.org/10.1039/C5SC02252E.
(38) Li, T.; Gamer, M. T.; Scheer, M.; Konchenko, S. N.; Roesky, P. W. Chem. Commun. 2013, 49 (22), 2183. https://doi.org/10.1039/c3cc38841g.
(39) Takenaka, Y.; Hou, Z. Organometallics 2009, 28 (17), 5196–5203. https://doi.org/10.1021/om900453j.
(40) O, W. W. N.; Kang, X.; Luo, Y.; Hou, Z. Organometallics 2014, 33 (4), 1030–1043. https://doi.org/10.1021/om401216v.
(41) Shima, T.; Luo, Y.; Stewart, T.; Bau, R.; McIntyre, G. J.; Mason, S. A.; Hou, Z. Nat. Chem. 2011, 3 (10), 814–820. https://doi.org/10.1038/nchem.1147.
(42) Smekhova, A.; Schmitz, D.; Izarova, N. V.; Stuckart, M.; Shams, S. F.; Siemensmeyer, K.; de Groot, F. M. F.; Kögerler, P.; Schmitz-Antoniak, C. Commun. Chem. 2020, 3 (1). https://doi.org/10.1038/s42004-020-0327-9.
(43) Ramirez, B. L.; Sharma, P.; Eisenhart, R. J.; Gagliardi, L.; Lu, C. C. Chem. Sci. 2019, 10 (11), 3375–3384. https://doi.org/10.1039/C8SC04712J.

(44) Hu, S.-X.; Lu, E.; Liddle, S. T. Dalton Trans. 2019, 48 (34), 12867–12879. https://doi.org/10.1039/C9DT03086G.
(45) Burns, C. P.; Yang, X.; Wofford, J. D.; Bhuvanesh, N. S.; Hall, M. B.; Nippe, M. Angew. Chem. 2018, 130 (27), 8276–8280. https://doi.org/10.1002/ange.201803761.
(46) Schultz, M.; Boncella, J. M.; Berg, D. J.; Tilley, T. D.; Andersen, R. A. Organometallics 2002, 21 (3), 460–472. https://doi.org/10.1021/om010661k.
(47) Evans, W. J.; Perotti, J. M.; Ziller, J. W. J. Am. Chem. Soc. 2005, 127 (11), 3894–3909. https://doi.org/10.1021/ja045064e.
(48) Liu, S.-S.; Gao, S.; Ziller, J. W.; Evans, W. J. Dalton Trans 2014, 43 (41), 15526–15531. https://doi.org/10.1039/C4DT02194K.
(49) Vasudevan, K.; Cowley, A. H. Chem. Commun. 2007, No. 33, 3464. https://doi.org/10.1039/b708758f.
(50) Moore, J. A.; Cowley, A. H.; Gordon, J. C. Organometallics 2006, 25 (22), 5207–5209. https://doi.org/10.1021/om060793j.
(51) Zeckert, K. Organometallics 2013, 32 (5), 1387–1393. https://doi.org/10.1021/om301032x.
(52) Evans, W. J.; Grate, J. W.; Levan, K. R.; Bloom, I.; Peterson, T. T.; Doedens, R. J.; Zhang, H.; Atwood, J. L. Inorg. Chem. 1986, 25 (20), 3614–3619. https://doi.org/10.1021/ic00240a017.
(53) Newkome, G. R.; Evans, D. W.; Fronczek, F. R. Inorg. Chem. 1987, 26 (21), 3500–3506. https://doi.org/10.1021/ic00268a018.
(54) Poulain, A.; Neels, A.; Albrecht, M. Eur. J. Inorg. Chem. 2009, 2009 (13), 1871–1881. https://doi.org/10.1002/ejic.200801155.
(55) Stander-Grobler, E.; Schuster, O.; Heydenrych, G.; Cronje, S.; Tosh, E.; Albrecht, M.; Frenking, G.; Raubenheimer, H. G. Organometallics 2010, 29 (22), 5821–5833. https://doi.org/10.1021/om100431u.
(56) Seitz, M.; Oliver, A. G.; Raymond, K. N. J. Am. Chem. Soc. 2007, 129 (36), 11153–11160. https://doi.org/10.1021/ja072750f.
(57) Booth, C. H.; Walter, M. D.; Kazhdan, D.; Hu, Y.-J.; Lukens, W. W.; Bauer, E. D.; Maron, L.; Eisenstein, O.; Andersen, R. A. J. Am. Chem. Soc. 2009, 131 (18), 6480–6491. https://doi.org/10.1021/ja809624w.
(58) Oelkers, B.; Kempe, R. In Molecular Metal-Metal Bonds; Liddle, S. T., Ed.; Wiley-VCH Verlag GmbH & Co. KGaA: Weinheim, Germany, 2015; pp 47–71. https://doi.org/10.1002/9783527673353.ch3.
(59) Nubel, P. O.; Wilson, S.; Brown, T. L. Organometallics 1983, 2 (4), 515–525. https://doi.org/10.1021/om00076a007.
(60) Castillo, I.; Tilley, T. D. J. Am. Chem. Soc. 2001, 123 (43), 10526–10534. https://doi.org/10.1021/ja011472w.
(61) Schumann, H.; Keitsch, M. R.; Winterfeld, J.; Demtschuk, J. J. Organomet. Chem. 1996, 525 (1–2), 279–281. https://doi.org/10.1016/S0022-328X(96)06511-4.
(62) Deacon, G. B.; Meyer, G.; Stellfeldt, D. Eur. J. Inorg. Chem. 2000, 2000 (5), 1061–1071. https://doi.org/10.1002/(SICI)1099-0682(200005)2000:5<1061::AID-EJIC1061>3.0.CO;2-7.
(63) Burns, C. J.; Berg, D. J.; Andersen, R. A. J Chem Soc Chem Commun 1987, No. 4, 272–273. https://doi.org/10.1039/C39870000272.
(64) Labouille, S.; Nief, F.; Le Goff, X.-F.; Maron, L.; Kindra, D. R.; Houghton, H. L.; Ziller, J. W.; Evans, W. J. Organometallics 2012, 31 (14), 5196–5203. https://doi.org/10.1021/om300573z.
(65) Nocton, G.; Ricard, L. Dalton Trans 2014, 43 (11), 4380–4387. https://doi.org/10.1039/C3DT52641K.
(66) Goodwin, C. A. P.; Reta, D.; Ortu, F.; Chilton, N. F.; Mills, D. P. J. Am. Chem. Soc. 2017, 139 (51), 18714–18724. https://doi.org/10.1021/jacs.7b11535.
(67) Weber, F.; Sitzmann, H.; Schultz, M.; Sofield, C. D.; Andersen, R. A. Organometallics 2002, 21 (15), 3139–3146. https://doi.org/10.1021/om0108705.

Chapter Three

In-depth study of the trimetallic palladium complexes.

3.1. Context and objectives.

The serendipitous isolation of the unusual heterometallic adducts **2.2**, **2.6** and **2.7** requires a more detailed study. Two main features are of particular interest: the short Ln-Pd distances, common to all, and the C-H activation in the α position of the pyridine, specific to the trimetallic complexes.

A brief survey of the literature will be presented, after which the specificities inherent to both issues will be discussed. Lastly, a series of objectives, based on the observations described herein, will be established in the last part of this section and explored throughout this chapter.

3.1.1. Heterometallic complexes bearing short Ln-TM distances.

Complexes containing multiple close metal centres, broadly classified as intermetallics, have been an object of some interest in the scientific community, most notably for the interaction between the two metals. There is a rich breadth of examples all across the periodic table.[1] Depending on the element involved, different types of electrons participate, as examples of complexes with s, d and f electrons all exist, either in homometallic or heterometallic structures. In some cases, this allows us to speak of chemical bonds in the classical sense, where there is an exchange of electrons between the participating metals.

As a rule, intermetallics follow the same chemical considerations common to basic covalent interactions. Some of the necessary factors that enable interactions include the orbital symmetry, efficient overlap and a good matching of the energy levels of the pertinent orbitals. In this regard, determining which orbitals participate depends significantly on the radial extension of each sub-shell.[2] Examples of the radial extension profiles specific to some elements are given in Figure 3.1. The *n*s and *n*p manifolds tend to be the most extended in both main group elements and in transition metals. The *n*f shells, as previously evoked, are contracted and practically behave as core electrons.[3] This behaviour is more subtle once the two 6s electrons are removed, as the 4f electrons are more involved in bonding.[4]

The higher the principal quantum number, the more the *n*s and *n*p shells tend to be diffuse. This directly impacts the interaction strength. For example, the BDE (Bond Dissociation Energy) in group 1 diatomics was determined to be 101.9 kcal/mol for Li_2,[5] whilst for Fr_2 it was computed to be less than half of that, at circa 42.1 kcal/mol.[6] That said, the same rationale applied to main group chemistry is valid in intermetallics: the higher the bond order, the stronger the bond will be.

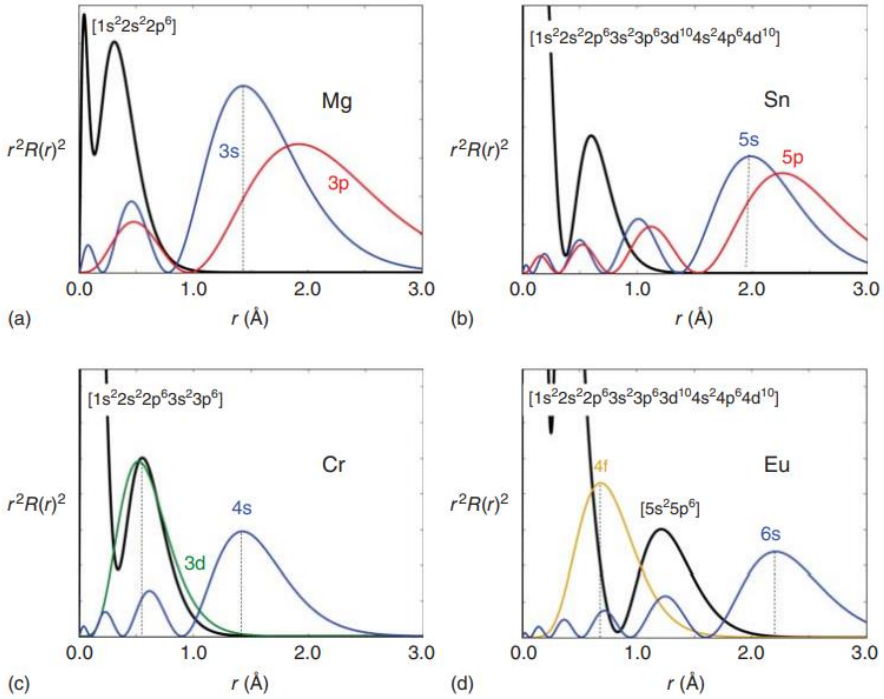

Figure 3.1: Radial distribution functions of the valence orbitals in the (a) s-(Mg), (b) p-(Sn), (c) d-(Cr), and (d) f-(Eu) blocks of the periodic table. Black lines correspond to the core density. Reprinted from ref 2.

In this respect, the pioneering work of Frank Albert Cotton has expanded our knowledge of the synthetic procedures that give intermetallics and the understanding of the nature of the bonds that are created. One of the most seminal examples is the $[Re_2Cl_8]^{2-}$ architecture, published more than 50 years ago, where a quadruple bond was established.[7] Ever since, examples with higher-order bonds between metals have abounded.

The difficulty in accurately modelling the electronic structures of these compounds has precluded the generalisation of a model to assess the bonding scheme in intermetallics. This is particularly true when heavier adducts are involved, where orbital overlap tends to be issued from complex hybridisations between orbitals involving electrons where the relativistic effect is significant. This implies that a careful assessment of the orbital energy level is necessary. In addition, the electron correlation is likely to play a significant part. Ensuring both of these factors are accurately computed is challenging. Since these systems tend to be large, the computational cost also needs to be considered. Given the above, the predominant use of DFT as the method of choice for determining electronic structures is particularly dubious, as it does not accurately treat multireference configurations.

Cotton's complex is an eloquent demonstration of this, as the electronic structure he proposed for the four bonding interactions is a complex linear combination of the participating $5d_{z^2}$, $5d_{xz}$, $5d_{yz}$, and $5d_{xy}$ orbitals (Figure 3.2).[8] The resulting ground-state configuration is $\sigma^2\pi^4\delta^2$, where the HOMO-LUMO gap (between the δ-δ* orbitals) is accessible, due to the weak orbital overlap involved for this set of orbitals. Multireference calculations at the CASSCF level have demonstrated that the ground state accounts for 63% of the total wavefunction, and that the occupation of the frontier orbitals is best described as $\delta^{1.5}\delta^{*0.5}$. These conclusions could not be reproduced by DFT-based methods, as they exhibited a persistent symmetry breaking in the computed structure. Again, multireference computations were necessary to properly reproduce the main geometric features of this complex.[9]

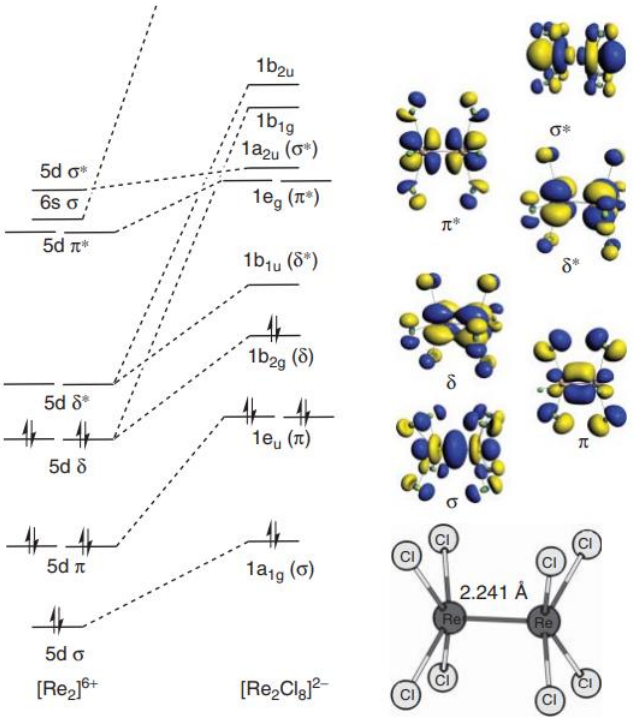

Figure 3.2: Adaptation of Cotton's proposed[8] electronic structure of the $[Re_2Cl_8]^{2-}$ architecture.[2]

Contrary to the tendency of the low angular momentum sub-shells *n*s and *n*p, going down in the same group for transition metals allows the respective *n*d manifold to extend outside the core orbitals, increasing overlap with the vicinal metal. Diatomic complexes of group 6 metals are a good example of this: the effective bond orders for Cr_2, Mo_2 and W_2 are 4.52, 5.2 and 5.2.[10]

Diatomic metal edifices in the f elements are restricted to the matrix isolation of H_2U-UH_2 hydrides[11] and the U_2 molecule. The bonding patterns of the latter has been the source of debate in the computational community, as bond orders of five[12] and four[13] have been postulated on the basis of multireference calculations. The very recent experimental proof of U_2^- corroborates a quintuple bond for the neutral adduct and a quadruple one for the anion.[14]

3.1.1.1. Previous synthetic strategies.

Heterometallic structures featuring rare earths are quite known in the literature. Those involving actinides are not the focus of this work, but a pertinent reference is provided for the curious reader.[15]

Following the first report by Beletskaya in the early 90s (Scheme 3.1, first line),[16] intermetallics involving lanthanides have steadily increased in both number and depth of description, resulting in some very impressive structures. Patterns of synthetic strategies have subsequently emerged.

One of the most effective avenues involves salt metathesis reactions, where the very favourable formation of simple salts is exploited (Scheme 3.1).[17] This method often requires the use of polar solvents, which sometimes compromises the stability of the formed intermetallics.

The presence of a leaving group was retained as a prolific strategy, although its nature was changed in subsequent examples, primarily described by the group of Kempe.[19–21] Protonolysis of alkyl complexes of a variety of lanthanides by Cp_2ReH resulted in the departure of alkanes and the formation of remarkable bi- and tetra-metallic edifices (Scheme 3.2).

Lastly, elegant and simple adduct formations were reported by the groups of Roesky and Arnold (Scheme 3.3).[22–25] This requires careful matching of the Lewis acidity inherent of most lanthanides with good organometallic fragments of neutral nucleophiles, which act as σ donors. The Nd-Ga adduct (bottom line) was only observed by VT ^{1}H NMR studies and not isolated and described structurally.

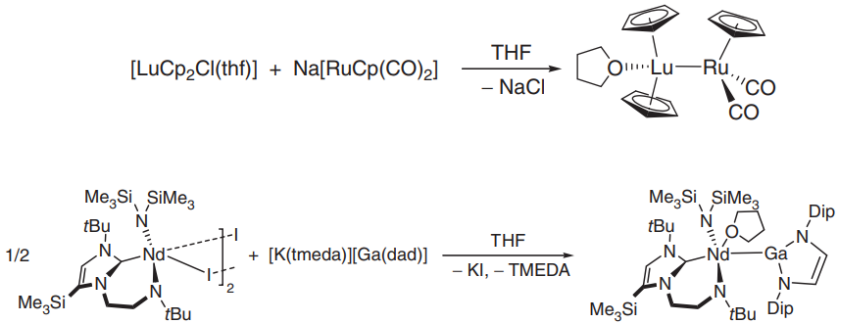

Scheme 3.1: Formation of complexes with Ln-M bonds by salt metathesis. Adapted from ref 18.[18]

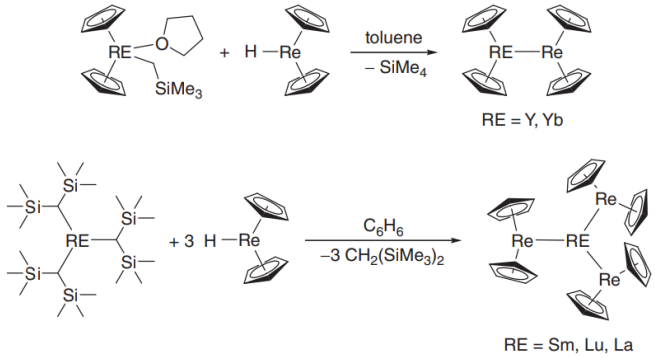

Scheme 3.2: Formation of complexes with Ln-M bonds by protonolysis, resulting in the elimination of alkanes. Adapted from ref 18.

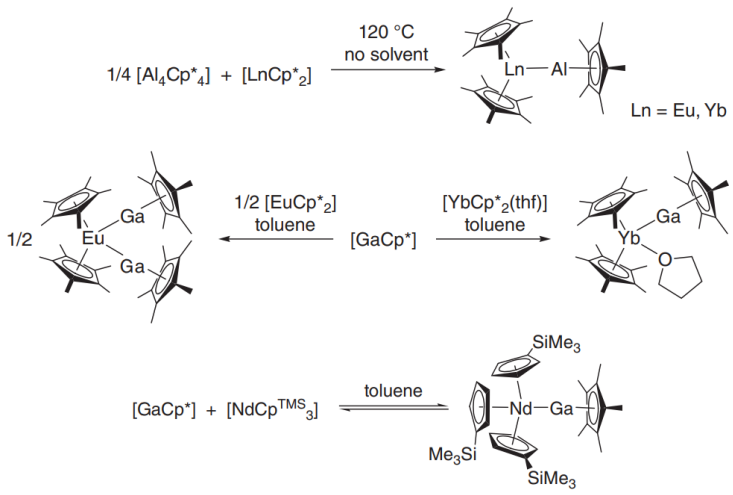

Scheme 3.3: Ln-M complexes formed by adduct formation. Adapted from ref 18.

What distinguishes the heterometallic adducts reported in this work from its peers is that they are not the result of a consciously planned synthetic strategy. Rather, they are issued from structural reorganisations, from which the most stabilised by-products that are ultimately favoured are the unusual complexes **2.2**, **2.6** and **2.7**. To the best of our knowledge, such occurrences are unique in lanthanide chemistry, perhaps with the exception of Zeckert's heterometallic Sm-Ga and Sm-In adducts, which, incidentally, also feature bis-pyridyl arrangements (Scheme 3.4).[26] Their formation is

accompanied by the deposition of zerovalent tin in the reaction mixture, alongside the departure of one of the ethyl groups on the partnering metal. Nevertheless, the chemical environment does not shift quite so dramatically than in the case of the complexes presented in this work.

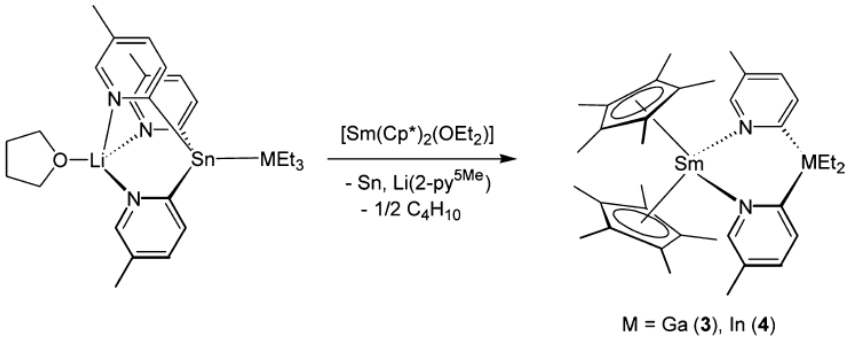

Scheme 3.4: Synthesis of heterometallic Sm-Ga and Sm-In complexes. Reprinted from ref 26.

The likely involvement of phenomena such as electron transfers, reactivity with more equivalents of divalent lanthanide precursors and the elimination of the TM fragment from the bidentate coordination site in the bimpym ligand strongly suggest a much more intricate formation mechanism than the ones cited above.

Due to the absence of predominantly covalent interactions in between the 4f metal and its partner, the structural features are regularly assumed to be due to the steric constraints imposed by the ligand environment. This would be naturally applicable to the short Ln-M distances in the complexes presented above. In some cases, the molecular architecture is the result of deliberate and careful tailoring of the coordinating ligands in order to approach the two metal centres to one another.

Some of the recent developments in the field, based on P-N ligands which coordinate both metals, are relevant, as they concern the group 10 metals in their zerovalent states. The group of Roesky described Pd^0-Ln^{III} complexes, obtained by the reduction of the Pd^{II} precursor.[27] The comparison in this case is particularly pertinent: the authors reported a Lu-Pd distance of 2.903 Å in the neutral adduct (as shown in Scheme 3.5, left). Although the comparison is imperfect (due to the contraction between Yb and Lu and the different coordination environments), this metric is very similar to that observed for **2.6**, where the Yb-Pd distance is 2.924 Å. Subsequent work isolated isostructural Pt^0 complexes.[28] The impact of specific structural features was eloquently demonstrated by a series of Lu-Ni complexes, where the intermetallic distance could be varied by up to 0.51 Å by altering the coordination number or the ligand platform (Scheme 3.5, centre).[29] Lastly, similar Sc-based complexes with all of the group 10 metals were isolated (Scheme 3.5, right).[30] In this case, significant evolutions of the Sc-TM metals were observed due to the presence (or not) of a substituent in the apical position on the TM.

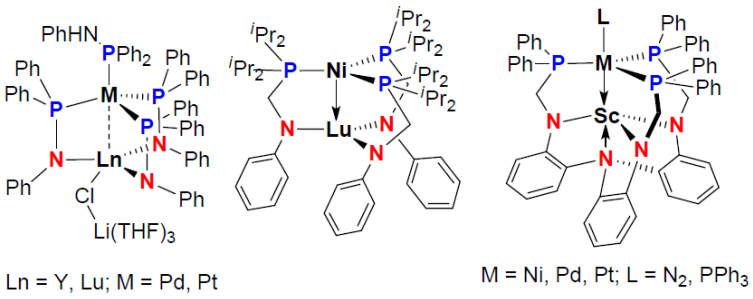

Scheme 3.5: Heterometallic complexes, where the ligand environment imposes short distances between the Ln and the group 10 metals. Scheme extracted and adapted from ref 30.

3.1.1.2. Interaction between the two metallic centres?

From a computational perspective, the contracted nature of the 4f electrons of the lanthanides limits possibilities to engage in covalent bonding. For example, calculations performed on some of the complexes of the series presented in Scheme 3.5 classified the Ln-TM interaction as weak (Mayer bond orders inferior to 0.5) and of a dative nature. The relative contributions in the orbitals involving both metals are significantly skewed towards one of the two metals (usually >85%).

In contrast, recent computational studies by the group of Liddle showed significantly more interaction with the actinide series. The structurally authenticated trimetallic $U^{IV}Rh^{I}_2$ complex is analysed as having a double U=Rh bond of a dative character.[31] A second publication reported a series of computed complexes of transition metals (Cr, Mn, Fe), based on strongly chelating trianionic $\{N(o\text{-}[NCH_2P(CH_3)_2]C_6H_4)_3\}^{3-}$ ligand (Figure 3.3). The difference between the actinides (U, Np, Pu) and Nd was first illustrated by the shorter RE-M bonds in the optimised structures. This was justified by the presence of strong interactions between the two metals. The electronic structures, computed at the CASSCF/CASPT2 level corroborated this: actinides were shown to promote significant interactions with the vicinal metals, which was not the case with Nd. Computed Mayer bond orders for the 9 actinide-based complexes were between 1.44-2.66.

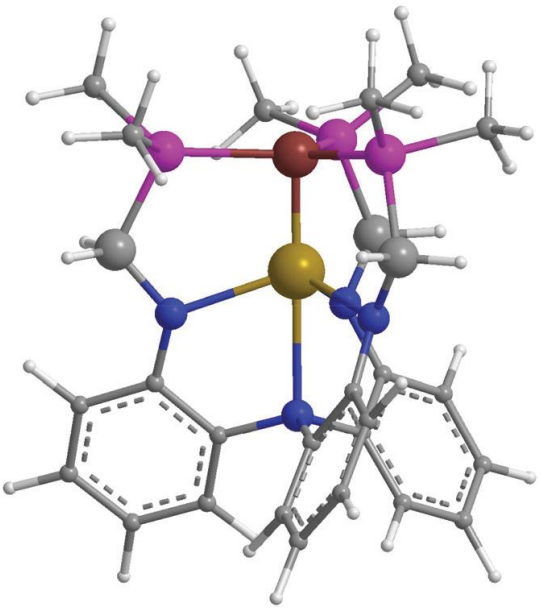

Figure 3.3: Representation of the $\{N(o\text{-}[NCH_2P(CH_3)_2]C_6H_4)_3\}^{3-}$ ligand in a heterobimetallic adduct.[32] Colour code: P – purple, N – blue, TM – red, RE – yellow, C – grey, H – white.

It is, thus, within this framework that the heterometallic complexes **2.2**, **2.6** and **2.7** will be discussed. An extensive computational study aimed at determining and explaining their electronic structures will be presented in this chapter.

3.1.2. C-H activation on the α position of the pyridine.

The second feature that merits further discussion is the C-H activation that occurs during the formation of 2.6 and 2.7. The presence of this phenomenon in the structures of these complexes can be looked at from two points of view: the C-H activation on the α position itself and the fact that the Pd^0 is subsequently coordinated by the two anionic pyridyl moieties.

Pyridine cycles are important heterocyclic units, featuring heavily in pharmaceutical and bioactive natural products.[33] However, they are usually quite chemically inert toward C-H activation due to the reduced electron density on the aromatic ring.[34] To this end, efforts have often been focused towards even more electronically impoverished analogues, such as pyridine-N-oxides, which increase the acidity of the protons on the ring.[35] Alternatively, highly electron-rich substrates are necessary to enable back-donation towards the coordinated pyridine, therefore enhancing reactivity.[36,37] Pyridine and its analogues can be catalytically activated with diverse target compounds,[38–40] including with rare-earth-based organometallic complexes.[41–43]

From an organometallic perspective, isolating complexes where the pyridine remains coordinated after the C-H activation appears to be more difficult. As an indication, there are only 192 complexes indexed in the CCDC database where unsubstituted pyridines are coordinated to metals (over 800 are available, if substituted rings are included). Of these, 117 require the cooperative effect of a second metal, which is coordinated by the N atom on the pyridine, underlining the difficulty in performing a C-H activation.[44,45] Some examples of the isolated complexes are presented in Figure 3.4.

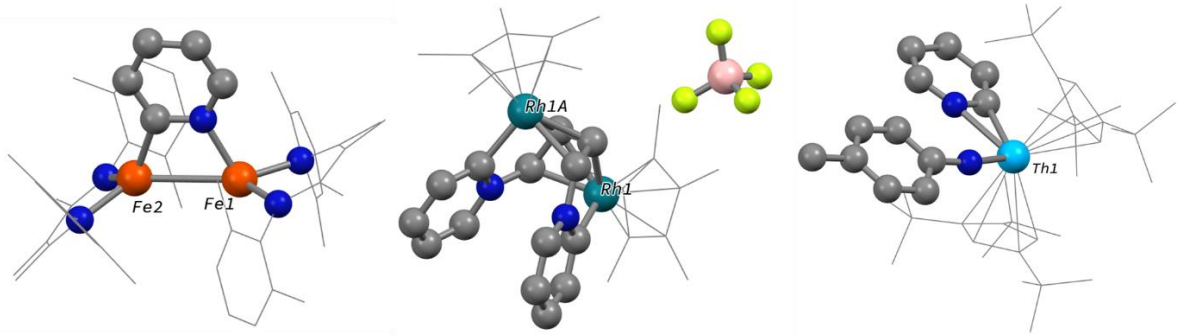

Figure 3.4: Ball and stick representations of some of the examples of organometallic complexes where pyridyl moieties are coordinated. The majority of hydrocarbons are set in wireframe and the hydrogens are not shown for clarity. Colour code for the non-labelled atoms: N – blue, B – pink, F – bright yellow.

In a more straightforward comparison with the complexes 2.6 and 2.7, the group of Kawaguchi described pyridines activated in all three positions – *ortho*, *meta* and *para* – by Pd^{II} species in 1980,[46,47] although only one pyridyl moiety is present in such complexes. There are also a number of examples of pyridines activated by rare-earths.[48] The report of the Walter group in 2015 is particularly pertinent, as the addition of pyridine to a Th complex with a terminal imido moiety resulted in the η^2-coordination of the ligand. The proton in the α position was displaced to the formerly imido moiety, which becomes an amido ligand (Scheme 3.6).

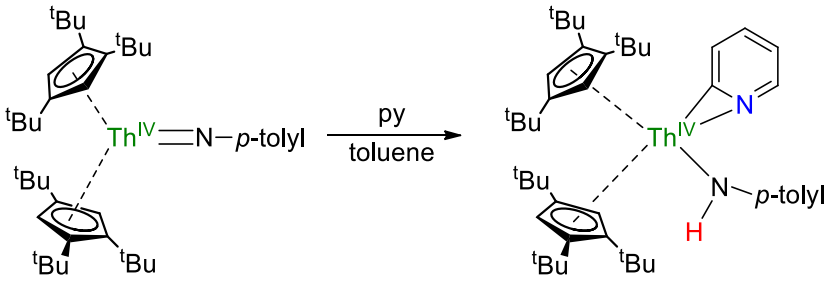

Scheme 3.6: C-H activation of pyridine by a Th imido complex.[49]

Similar activations were observed with other Th metallocene substrates.[49,50] The comparison is significant, due to the presence of the pyridine in the coordination sphere of the Th, as it is assumed at this conjecture that the reorganisation from 2.4 to 2.6 is triggered by the presence (*ergo*, likely

coordination) of excess ytterbocene. However, it should be noted that the reactivity of the Th complexes does not depend on electron transfer, which is likely to be the case for the compounds described in this work.

Structurally speaking, the second peculiar aspect of the trimetallic complexes is the stabilisation of a linear bis-pyridyl arrangement (in our case, coordinated to the Pd^0 centre). This situation is exceedingly rare. There are a few isolated complexes based on group 11 centres, where bis-*p*-tetrafluoropyridyl architectures are found.[51,52] To the best of our knowledge, the only structurally authenticated unsubstituted bis-pyridyls motifs are in mercury-supported adducts, where the pyridyls are coordinated in the *para* position.[53,54] The synthesis of such systems relies on the reaction between the Hg^{II} acetate precursor and boronic acids.

3.1.3. Objectives of the study.

Henceforth, this chapter will focus on two main objectives: determining whether there is any electronic interaction between the metal centres in the complexes **2.2**, **2.6** and **2.7** and gathering more clues into the mechanism of the formation of the trimetallic adducts.

There are some obvious differences between, on one hand, **2.2**, where the coordination sphere of the Pd^{II} is more orientated towards the Yb centre and, on the other, the $[Pd^0(pyr)_2]^{2-}$ fragment, which is slanted with respect to the surrounding Ln^{III} fragments. To begin with, the electronic structures of the trimetallic adducts will be studied at multiple levels of theory. The intermetallic interaction (if there is one) will be examined in order to determine its nature. Further descriptors of chemical bonding will aim to quantify the contribution of each type of interactions (electrostatic, orbital, dispersive) in maintaining these unusual edifices.

The second major objective concerns the formation mechanism for the trimetallic complexes **2.6** and **2.7**. Some aspects of this transformation appear to be clear: excess lanthanide precursor is necessary in order to trigger the decomposition of the coupled product **2.4**, leading to the trimetallic adducts. It is also coherent that this transformation involves a further electron transfer, which would lead to the population of the pyridine-based LUMO, also observed for the precursor **1.12** and in the electronic structure of the computed simplified adducts (Table 2.4).

However, these assertions provide no specific information as to how the reactivity actually occurs. In order to delve further in this area, a mixed experimental and theoretical study will be undertaken to provide further clues as to this transformation.

Some of the aspects that merit further discussion are the fate of the bimpym ligand and the exact origin of the second pyridine molecule, which accounts for the second pyridyl in the trimetallic adducts. It is, presumably, this double C-H activation which ultimately results in these unusual structures.

As established above, the paucity of examples of such linear structures highlights the difficulty in forming and stabilising them. In this respect, **2.6** and **2.7** are stabilised by the supplementary coordination of the Ln to the N of the pyridyl groups, in addition to the bonding with the Pd centre. The specific activation in the *ortho* position is curious. Not only are there no equivalent structures in the literature, but, in terms of the C-H activation, the isolation of equivalent complexes with *meta* or *para* arrangements should be feasible (Scheme 3.7), but their potential stability is unknown.

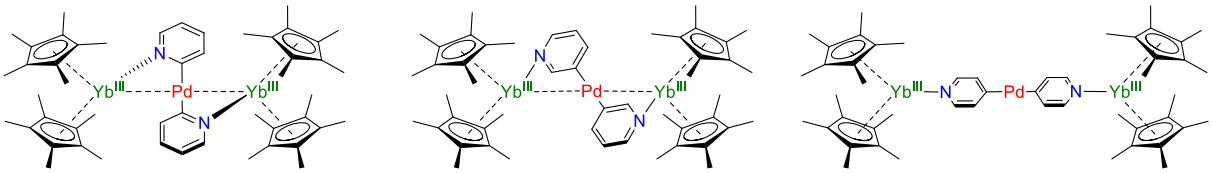

*Scheme 3.7: Complex **2.6** and putative homologues, where the C-H activation occur in the meta or para positions.*

This chapter will, therefore, tackle the issues delineated in this section, before proposing a series of cogent explanations for the phenomena observed in these heterometallic adducts.

3.2. Study of the formation of the trimeric complexes.

This section will contain a mixed and symbiotic experimental and theoretical examination of the most important features leading to the formation of the trimetallic structures **2.6** and **2.7**. To recap, it is presently known that the reorganisation towards **2.6** occurs after the rapid formation of the coupled product **2.4**, in the presence of unreacted ytterbocene. In between, there are some elements that need further clarification, such as the plethora of unattributed signals that are formed in the reaction mixture when ytterbocene is added to **1.12** or the role of **2.5** – the isomer of **2.4** – in the transformation.

3.2.1. Understanding the mechanism of the C-H activation.

The elimination of the methyl moiety, as well as the C-H activation on the α position of the pyridine in **1.12** or the coupled products, give us some important clues as to one of the key steps in the reorganisation of the Pd^{II} scaffold following the addition of further divalent lanthanide precursor to the coupled products. The fact that a gaseous evolution is also detected is a strong indication that the elimination of the C-H activation and the departure of the methyl group occur concurrently in the form of methane formation.

Due to the fluxional behaviour of the pyridine, observed for **1.12**, **2.4** and **2.5**, the specific order of the aforementioned events is not yet understood. Is this ligand coordinated to the Pd centre when the C-H activation occurs? Or is a looser interaction between the two necessary in order to enable this step? Answering these open questions shall be the focus of the following section.

3.2.1.1. 2D scan of the precursor by varying the Pd-pyridine distance.

The first objective of this study is to establish what are the prerequisite conditions of the C-H activation, from the perspective of the interaction between the Pd and the pyridine. It is unclear whether this is dependent on the distance between the two or if it is feasible that the process occurs when the pyridine is released from the coordination sphere of the metal.

Experimentally, there are reasons to suggest that the coordination of the pyridine is fluxional, but no proof of a potential C-H activation occurring on this L ligand in **1.12** could be obtained. Samples of the precursor were subjected to harsher conditions to probe whether any chemical evolution could be triggered.

Heating the THF solution of **1.12** up to refluxing conditions (no more than 100 °C) for several hours produced no quantifiable evolution of its ^{1}H NMR spectrum. Alternatively, exposing the compound to a UV light excitation resulted in the gradual formation of a black coating in the NMR tube. This is interpreted to be due to the decomposition of the product. No further information could be gathered from this procedure. The bottom line would appear to be that this complex does not react – certainly not in any way similar to the evolution resulting in the trimetallic adducts – in absence of divalent lanthanide precursors.

In this respect, the starting point of the theoretical study was axed on the fluxional behaviour of the pyridine. To obtain further insight into the coordination/decoordination mechanism, a relaxed surface scan was performed at the **ZORA1** level of theory. In this case, the scan involved varying the distance between the Pd and the N_{py} between two fixed values. A first iteration explored the 2.0-6.0 Å interval in 20 steps (Table 3.1). The two extremes are meant to reproduce the optimised structure of **1.12** and the release of pyridine from the coordination environment.

Several key observations emerge. At long range, the two fragments do not interact at all. Upon the reduction of the distance, the pyridine approaches via the proton on the α of the N atom. An agostic interaction is established even at a larger Pd-N distance of 3.89 Å and is maintained up to a corresponding distance of *ca.* 2.65 Å. The C-H bond (1.09 Å in both free pyridine and when the pyridine is fully coordinated) is lengthened slightly by this approach, as it varies between 1.13 and 1.16 Å in between the examined steps.

In between these two points, the pyridine approaches the Pd fragment, whilst being almost perpendicular to the plane formed by the molecule (snapshots at 3.05 Å and 2.62 Å in Table 3.1). The coordination mode changes brusquely at 2.60 Å, whereby the pyridine bonds with the Pd centre via its N atom, as in the optimised structure of **1.12**. To get further insight into the interval where the shift occurs, a second set of scans focused on the 2.60-3.05 Å range, in 0.025 Å increments.

Pd-N_{pyr} distance	6 Å	4.31 Å	3.89 Å
	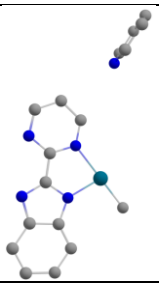	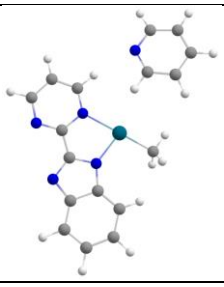	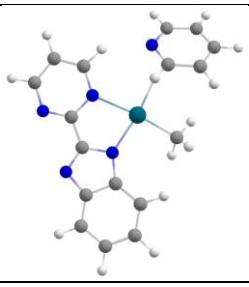
Pd-N_{pyr} distance	3.05 Å	2.62 Å	2.60 Å
	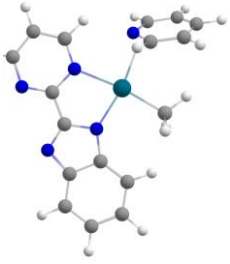	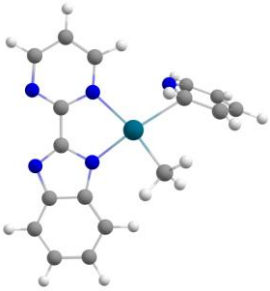	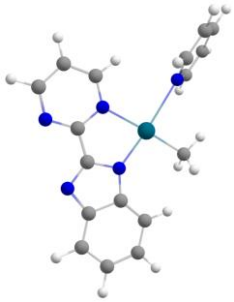

Table 3.1: Snapshots of the relaxed surface scan of the Pd-N_{py} distance. Some of the images are cropped for visibility.

The increased rapprochement between the two fragments imposes steric strain onto the rest of the molecule. This is eloquently illustrated in the evolution of the computed energies for each configuration, shown in Figure 3.5. The shortening of the bond from 3.05 Å to 2.90 Å is very slightly favourable energetically. The subsequent evolution, up to 2.62 Å, is increasingly costly, especially due to the steric strain incurred by the methyl moiety, which is pushed away from the plane of the molecule. This configuration is noteworthy, as it presents a seemingly η^2 coordination mode of the pyridine by both the N atom and the closest C atom (Figure 3.6, left).

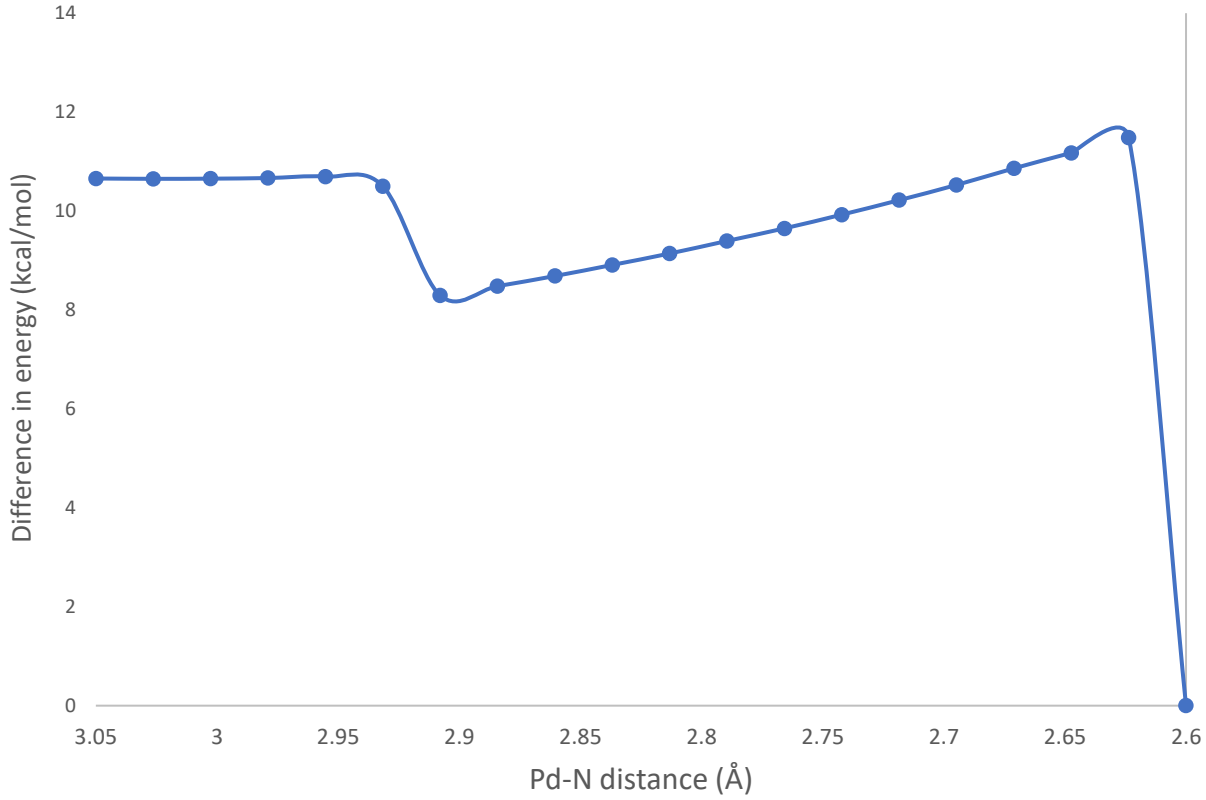

Figure 3.5: Evolution of the relative energy of the configurations examined throughout the second relaxed surface scan, in the 2.60-3.05 Å range. The configuration at d(Pd-N) = 2.60 Å is the most stable and is taken as the reference (E=0). The line serves merely as a visual guide.

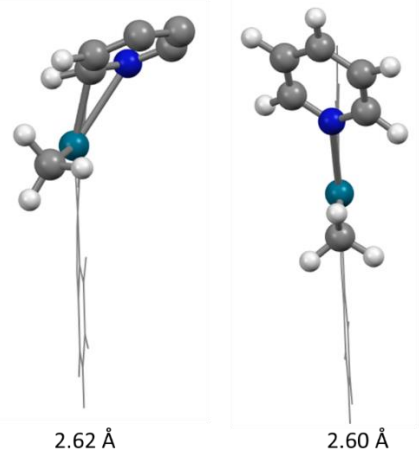

Figure 3.6: The evolution of the optimised geometries upon the reduction of the Pd-N_{py} distance, when the coordination mode of the pyridine switches towards coordination by the N atom. The bimpym ligand is shown in wireframe and only the most significant hydrogen atoms are shown.

The last step, where the distance is reduced to 2.60 Å, results in the coordination of the pyridine by the N atom and the immediate rearrangement of the substituents within a regular square planar environment (Figure 3.6, right). This step alone leads to the stabilisation by more than 11 kcal/mol due to the release of the steric strain.

3.2.1.2. Searching for the transition state. Optimisation.

The findings above would strongly suggest that the C-H activation of the pyridine and the subsequent coordination of the Pd centre by the C atom in the trimetallic adducts is not likely to occur while the pyridine still acts as a regular L ligand with respect to the Pd, at the distance of the ground state. The configuration where the Pd-N_{py} distance is 2.62 Å, shown in Figure 3.6, will be used as basis for the computation of a transition state that could rationalise the C-H activation.

The identification of the transition state (TS) is guided by the conditions at the end of the transformation: the proton in the α position has departed, leading to the coordination of the Pd to the corresponding C atom, and methane is most likely formed. The TS should reflect that. However, the considerable steric strain imposed by the relative position of the pyridine with respect to the bimpym ligand, as shown in Figure 3.6, left, is unlikely to be a conducive configuration.

Nevertheless, this was chosen to be the starting geometry for the TS calculation, performed at the **TS1** level of theory.

The computed TS (Figure 3.7) presented the following evolutions: the pyridyl moiety was angled away from the plane formed by the bimpym ligand and the Pd centre, similar to the geometry of the ground state configuration. The proton, formerly bonded to the C, is now placed midway between the two C atoms. The frequency calculation produced a single imaginary frequency of very high numeric value (*ca.* -1000 cm^{-1}). This frequency corresponds to an oscillatory motion of this proton between the two carbons. The methyl also displays bending motions of the three H atoms, in order to adopt a geometry closer to tetrahedral, characteristic of free methane.

All of this is in agreement with the description of this geometry as a TS of a C-H activation and of the transfer of the proton towards the vicinal methyl moiety in order to form a free methane molecule. It shall henceforth be referred to as **1.12-TS**.

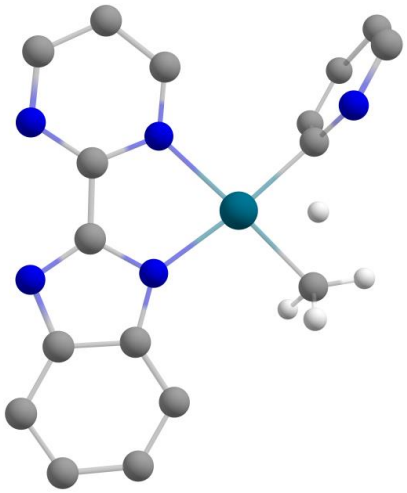

*Figure 3.7: Structure of **1.12-TS**, computed at the TS1 level of theory.*

An energetical comparison between the **1.12** (GS) and **1.12-TS** is necessary to ensure the feasibility of this transformation. Both the difference in enthalpy (ΔH) and in the Gibbs free energy (ΔG) are computed. These show that the **TS** is higher in energy by approximately 29.5-36 kcal/mol (depending on the density functional). In this particular case, there is a negligible (less than 0.5 kcal/mol) difference between ΔH and ΔG. This implies that the variation of entropy in this transformation is not significant. Unless explicitly stated otherwise, all future energy comparisons mentioned throughout this chapter will refer to ΔG between two states. A discussion as to the more pertinent metric shall be provided whenever relevant.

Multiple starting geometries were tested to probe whether there are other TS available on the potential energy surface. Across these trials, only one configuration led to a different structure. The pyridine was rearranged to mime the η^2 coordination mode shown in Figure 3.8 and the proton was already placed much closer to the carbon of the methyl. As a result, the computation resulted in a second geometry, where the pyridyl is fully coordinated to the C in the α position and the N acts as a proton shuttle. The methyl is rearranged in an intermediate configuration between that of the GS and that of free methane. Frequency calculations resulted, again, in a single imaginary frequency (-1488 cm^{-1}), which is consistent with a second possible TS.

The main structural features of the two TS are presented in Table 3.2. The coordination of the Pd metal centre to the bimpym ligand is not significantly perturbed, as the Pd-N distances remain close to the values for the GS. The same cannot be said about the fragments directly involved in the TS – the Pd-C_{Me} elongates, particularly for **1.12-TS2**; the angles formed between the pyridyl and the ligand plane change rather drastically.

	Av. Values (Å or °)		
Distance	**1.12** (PBE)	**1.12-TS**	**1.12-TS2**
Pd-C_{Me}	2.035	2.176	2.224
Pd-N_{pyr}	2.041		
Pd-C_{pyr}		2.120	2.043
Pd-H_{α}		1.661	1.975
C_{α}-H_{α}	1.089	1.428	2.130
C_{Me}-H_{α}	2.945	1.526	1.428
N_{py}-H_{α}			1.282
Pd-N_{pym}	2.162	2.137	2.137
Pd-N_{imid}	2.020	2.082	2.070
bimpym^py	56.92	88.97	30.25

*Table 3.2: Main distances and angles in **1.12** and the computed TS.*

In **TS**, the pyridyl is perpendicular to the ligand plane. This is presumably in the interest of minimising repulsive steric interactions with the protons from the bimpym ligand. In **TS2**, the role of the N atom as a proton shuttle, plus the necessary proximity of the activated proton to the methyl, forces a much more co-planar arrangement between the two fragments.

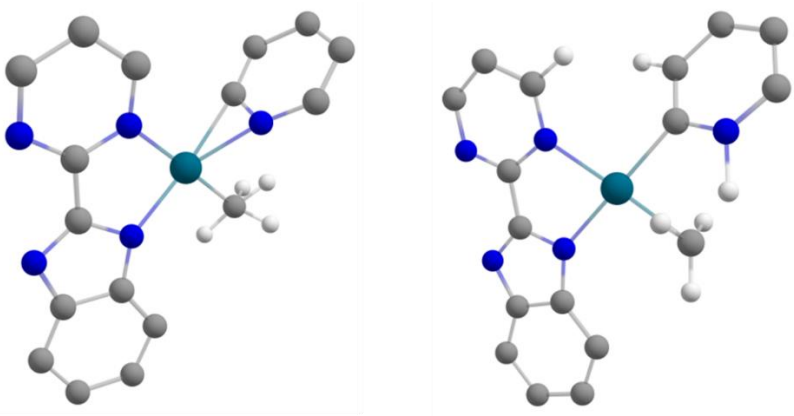

*Figure 3.8: Starting geometry (left) and optimised geometry (right) of **1.12-TS2**. The majority of the H atoms were hidden for clarity. On the TS, the H that are left indicate the steric hindrance between the pyridyl moiety and the bimpym ligand.*

The steric repulsion that is inherent to the second TS configuration exerts a cost from an energetic standpoint, as calculations performed at the **TS1** level show it to be approximately 12-20 kcal/mol higher in energy than **1.12-TS**, depending on the density functional that was used. Overall, it is around 45-50 kcal/mol higher in energy than the GS. This energy barrier is very large and unfeasible for a transformation in ambient conditions. Because of this difference, **1.12-TS2** is not considered in further computations.

3.2.1.3. Computing the departure of the methyl.

The next step, consistent with the expected reorganisation leading to the structures of the trimetallic edifices, would be the departure of the methyl moiety as methane. To this effect, it was removed and the structure was reoptimised at the **ZORA1** level of theory, starting from **1.12-TS**.

The reduction of the number of substituents in the coordination sphere of the Pd metal centre results in an η^2-coordination mode, where the pyridyl is coordinated by both the N atom and the activated vicinal C atom. This configuration shall henceforth be referred to as **1.12-η²** (Figure 3.9).

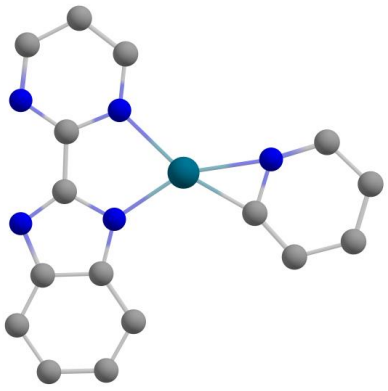

*Figure 3.9: Structure of **1.12-η²**, computed at the **ZORA1** level of theory.*

The main bond lengths show no major perturbation in the coordination of the Pd^{II} centre towards the bimpym. On the other hand, the two atoms on the pyridyl are almost equidistant with respect to the Pd. The Pd-N_{pyr} distance is slightly longer than for the GS (2.07 Å vs 2.04 Å), whilst Pd-C_{pyr} is significantly shorter than for the computed TS (1.94 Å vs 2.12 Å (**TS**) or 2.04 Å (**TS2**)).

The validity of this structure with respect to the reorganisation mechanism leading to the trimetallic complexes **2.6** and **2.7** depends on the energy difference with respect to the GS. Given that this configuration was not experimentally observed, it is logical that it is not stable. From an energy standpoint, this can be explained thusly: the η^2 state should be higher in energy than the GS, therefore the evolution from the TS towards this configuration leads to a metastable configuration and further reorganisation occurs. A schematic representation of the energy profile of the transformation is given in Figure 3.10.

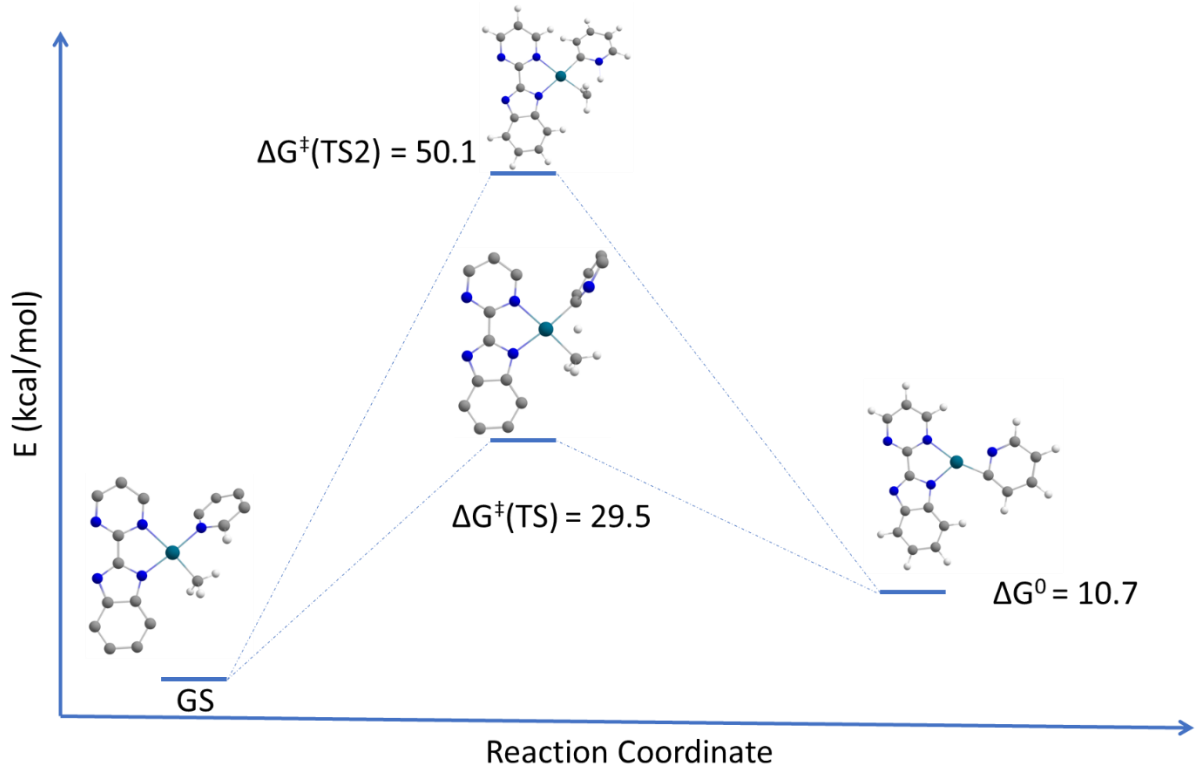

Figure 3.10: Schematic representation of the two computed TS with respect to the energy of the transformation. The relative energies of the computed states are not up to scale.

Computations at the **TS1** level of theory have been performed by adding a methane molecule to the η^2 configuration and found that it is higher in energy than the GS. The difference is not large, irrespective of the functional that was used (from 0.35 to 6.52 kcal/mol). For this transformation, the number of molecules increases, which would mean that it is entropically favourable. The figures for ΔH are, therefore, less ambiguous (they range from 4.92 to 11.18 kcal/mol) and would designate this configuration as metastable.

Since the computations agree that the η^2 configuration is less stable than the GS, this would imply that a subsequent reorganisation is necessary. However, this simplistic description of the evolution of the system is based solely on the precursor **1.12**, which is not representative of the behaviour of the system in presence of lanthanides. The experimental conditions that were probed, mentioned at the beginning of this section, showed that this species is unreactive.

As computations with lanthanides tend to be quite costly, a better understanding of the reaction mechanism is necessary before attempting to extrapolate the finding in this section for lanthanide-based systems. At this point, it is assumed that the transformation resulting in the trimetallic adducts begins from the coupled product **2.4**. However, as proven in Section 2.3.1.2, performing calculations

on these structures is highly unrealistic. Adding a further degree of complexity by including a further organolanthanide fragment renders such pursuits even more unfeasible.

The objective in the following sections will be to provide further experimental clues as to how the reaction yielding complexes **2.6** and **2.7** proceeds. A particular mention is reserved for the numerous unattributed signals that are observed in the reaction mixture, during which **2.6** is formed. Given that the isolation of these unknown species was shown to be implausible (Figure 2.18), more educated guesses as to the order and nature of the likely transformations and individual configurations will be required in order to perform further computations.

3.2.2. *In situ* NMR studies.

This section aims to answer several precise questions regarding the evolution from the coupled product **2.4** towards the trimetallic adduct **2.6**. The previous chapter presented the almost instantaneous formation of **2.4** following the *in situ* addition of ytterbocene to the precursor **1.12**. The presence of free ytterbocene in the opening stages is presumably responsible for the transformation that yields **2.6**.

However, at this point, it is not fully known what exactly triggers the subsequent reactivity. Is it the electron transfer or the coordination of $Cp^*_2Yb(OEt_2)$ *per se*? To that effect, trials involving other reductive substrates will be described.

The chemical nature and role in the reaction of the species responsible for the numerous unattributed signals are unknown. Although the transformation giving **2.4** seems to be very rapid, it cannot be excluded at this moment that the unattributed peaks are due to a by-product following the reaction between ytterbocene and **1.12**. A more thorough examination of the behaviour of these unknown species is necessary.

The short-lived nature of some of the species precludes identification and integration into the overall transformation. The missing elements will restrict us to approximations, which may be subsequently modelled *via* theoretical computations.

Throughout this section, the results and data will be gradually interpreted to provide insight into the key steps of the transformations. These will be summarised in order to form a cogent conclusion.

3.2.2.1. Addition of other non-lanthanide reductants.

One of the key hypotheses that rationalises the evolution from **2.4** to **2.6** is the electron transfer towards the pyridine-based **LUMO^L**-type orbital (see Scheme 2.8). Therefore, a good starting point for the objectives set for this Section is establishing whether the mere population of this orbital is enough to prompt the reactivity.

Three reductants were chosen: Cp^*_2Co, Na/Naphthalene mixture and KC_8. Their respective redox potentials, compared to that of ytterbocene, are given in Table 3.3.[55–57] These substrates should, on the basis of the redox potential alone, be equally capable of reducing the target compound. However, this premise may be misleading, as the coordination of reducing substrates is known to enhance their capabilities.[58,59] The behaviour of **2.4** towards reductants with an outer-sphere electron transfer mechanism is, therefore, of particular interest.

Reductant	$E_{1/2}$ (V) vs Fc^+/Fc
Cp^*_2Yb	-1.78
Cp^*_2Co	-1.94
Na/Naphthalene	-3.10
KC_8	-2.87

Table 3.3: Redox potentials of the other reductants used during this study.

Complex **2.4** was reacted with Cp^*_2Co in tol-d_8, with the reactions monitored by ^1H NMR. No new signals appeared. Rather, only the decrease of the intensity of the substrate peaks was attested, until they disappeared entirely after several days. Only the characteristic signals of free pyridine could be identified at the end of the reaction. This was accompanied by the deposition of black powder. Redissolving it in THF-d_8 revealed no supplementary signals. This is consistent with the formation of zerovalent metal, most likely Pd^0.

To probe whether this decomposition can be avoided, the same reaction setup was performed under intense stirring and with shorter timescales (2-3 h). Alas, only **2.5** could be isolated, as a result of the accelerated isomerisation under stirring. This evolution was found to be invariant upon changing the solvent. The same reaction was tried using **2.5** as a starting product, with no tangible difference.

Alternatively, the precursor **1.12** was also reacted with decamethylcobaltocene, to examine how a reduction would influence its behaviour. This was inspired by the coupling reaction of the **K(bimpym)NiMe$_2$** that occurred on a different position, that was triggered by the addition of KC_8. A black slurry was rapidly formed, but no product could be isolated and characterised.

The same synthetic protocols were employed for **1.12**, **2.4** and **2.5** using the other two reductants. Two solvents were used: toluene and THF. The only combination that yielded any product was the reaction between **2.4** and KC_8 in THF. A very small number of crystals could be isolated, of sufficient quality to permit the identification of the structure as $(Cp^*_2Yb(bimpym))_2$ (**3.1**, Figure 3.11)

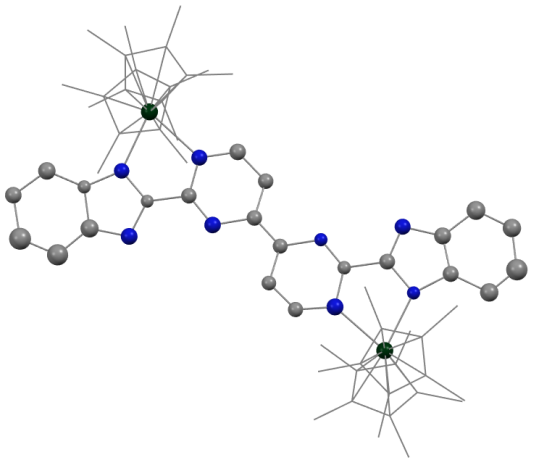

*Figure 3.11: ORTEP of **3.1**. The Cp* co-ligands are displayed in wireframe and the hydrogen atoms are omitted.*

The feeble quantity of **3.1** that was isolated raises doubts as to whether it can reliably be considered a major product of the reaction. If an electron transfer occurred, it would appear that the Pd fragment was the likely recipient, causing its departure from the bimpym coordination environment.

These trials unquestionably suggest that simply transferring an electron towards either of the coupled products is insufficient to instigate the rearrangement that results in the formation of the trimetallic adduct **2.6**. The fact that all of the chosen reductants operate via an outer-sphere mechanism points that, at the very least, the coordination of the molecular trigger of the rearrangement is necessary.

3.2.2.2. Addition of divalent lanthanides to the coupled products

It was established in Chapter 2 that the coupled products **2.4** and **2.5** do not spontaneously decompose towards **2.6**. Therefore, the presence of free ytterbocene in solution is necessary to trigger this transformation. Consequently, the first tests that were carried out involved an *in situ* study of the reactivity of the coupled products with ytterbocene in tol-d_8.

The isomer formed initially – **2.4** – was tried first. Adding approximately one equivalent of each adduct resulted in the gradual diminution of the intensity of the characteristic signals of the coupled product. Concurrently, the same unattributed peaks (as in Figure 2.18) of very low intensity developed within a few minutes. **2.4** was consumed rapidly – there were usually no clear-cut signals that could be attributed to this complex within, on average, 80-100 minutes. The intensity of the Cp* peak of **2.6** progressively increased, even beyond the point when **2.4** was no longer visible. Presumably due to the presence of an excess of ytterbocene in the initial mixture, its characteristic signal could be found more than two days after the beginning of the reaction. It can, therefore, be concluded, that the reaction between ytterbocene and **2.4** is quite rapid. The exact mixture of the products formed is unclear at this point.

The signals corresponding to the unattributed species abate after extended reaction times (Figure 3.12, top). This allows for a much cleaner reaction mixture. The supplementary signals, not belonging to **2.6**, can be attributed to two further products: **2.2** and **Yb_3(bimpym)$_2$**. The final molar ratio of these complexes is approximately 5/3/5. There do appear to be several key differences between this procedure and the straightforward reaction between **1.12** and multiple equivalents of Cp^*_2Yb. The comparison with a similar reaction, where two equivalents of ytterbocene were added to **1.12** (Figure 3.12, bottom), is telling.

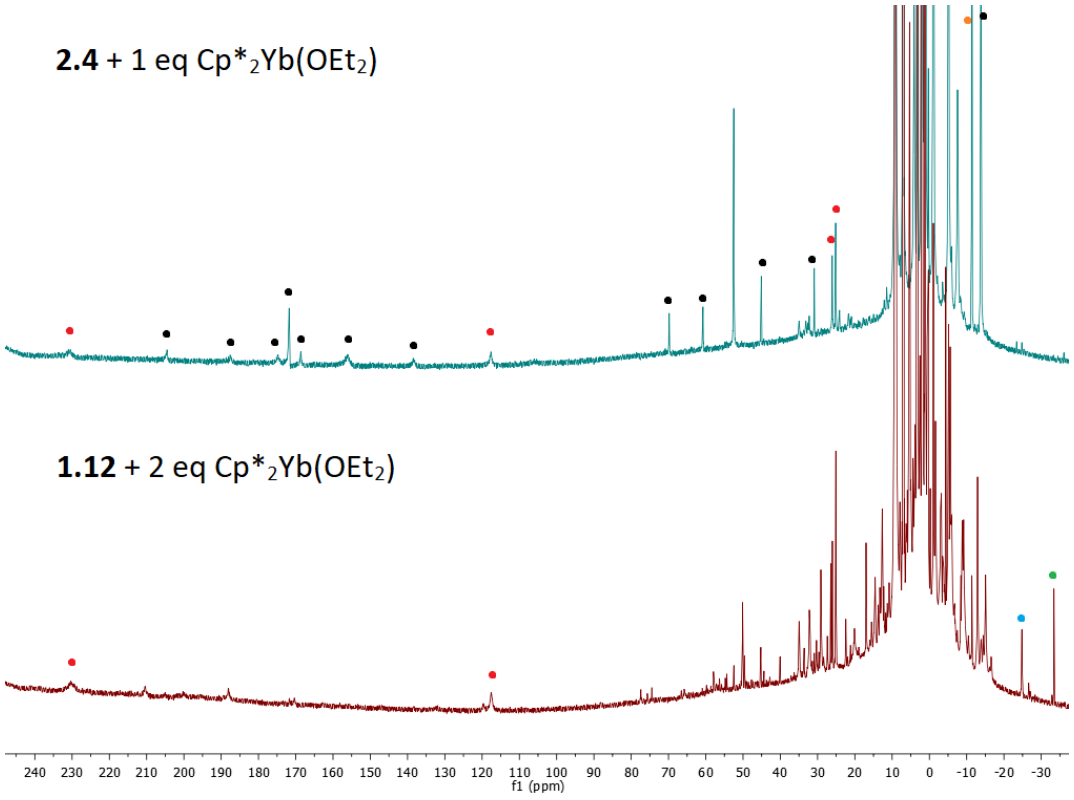

*Figure 3.12: Comparison between the in situ reactions of **2.4** and **1.12** with ytterbocene after approximately 18h. Colour code: red – **2.6**; black – **Yb_3(bimpym)$_2$**; orange – **2.2**; blue – **2.4**; green – **2.5**.*

In the second case, although the signals corresponding to **2.6** are identifiable, they do not constitute an outrightly dominant product. Furthermore, despite the entirety of free ytterbocene being consumed within less than 3 h (not shown in Figure 3.12), the reaction is visibly incomplete: the signals belonging to both the coupled products **2.4** and **2.5** are clearly present, alongside the numerous unattributable peaks.

It would appear that two equivalents of ytterbocene are insufficient to complete the conversion from **1.12** to **2.6**. To probe this assertion, another reaction, where three equivalents of $Cp^*_2Yb(OEt_2)$ were used, was undertaken. The final reaction mixture very closely resembled that following the direct addition of the divalent organolanthanide to **2.4**, as the signals of the unknown species were also consumed. In this case, the final ratio between **2.6**/**2.2**/**Yb_3(bimpym)$_2$** was 6/2/3. 18 h after the reaction began, free ytterbocene was still present in solution.

It seems logical that the formation and subsequent disappearance of the signals belonging to unknown species following the reactions involving **1.12** or **2.4** are subordinate to the presence of ytterbocene in solution. The increase in the intensity of the main products (primarily **2.6**) even after no further coupled product precursor can be distinguished can be rationalised as the result of the reaction between ytterbocene and the unknown species, which are also formed rapidly.

In situ kinetic study of the reaction between ytterbocene and 2.4.

To get a better idea of the dynamics of the formation of the three main products, a kinetic study of the reaction between **2.4** (at around 9mM concentration) and an excess of ytterbocene (*ca.* 1.7 eq or 15 mM) was performed (Figure 3.13). A lower concentration was deliberately chosen to ensure optimum solubility of all species. The objective was to establish the reaction dynamics, as well as the prevalence of each of the consumed/formed species over time. To this end, a sample of **2.4** containing approximately 10% of **2.5** (following the rapid isomerisation during the formation reaction) was chosen (Scheme 3.8). It was thus hoped that information regarding the competitive processes of the reaction of **2.4** with ytterbocene and the isomerisation towards **2.5** could be extracted.

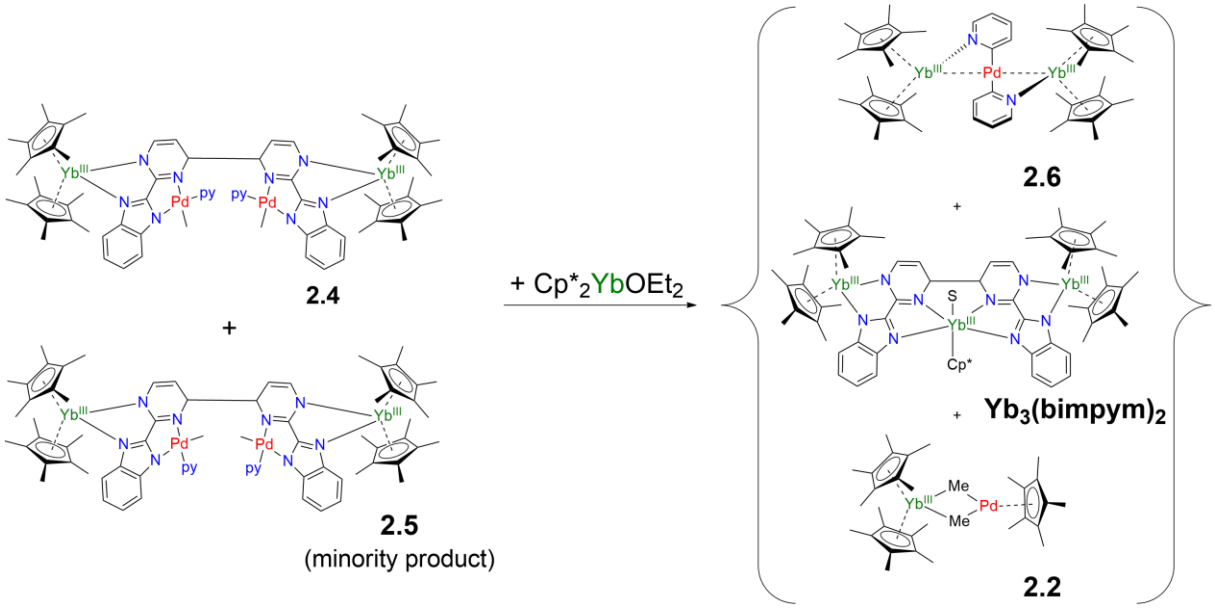

*Scheme 3.8: Reaction scheme of the kinetic study between **2.4** (with ca. 10% **2.5**) and ytterbocene.*

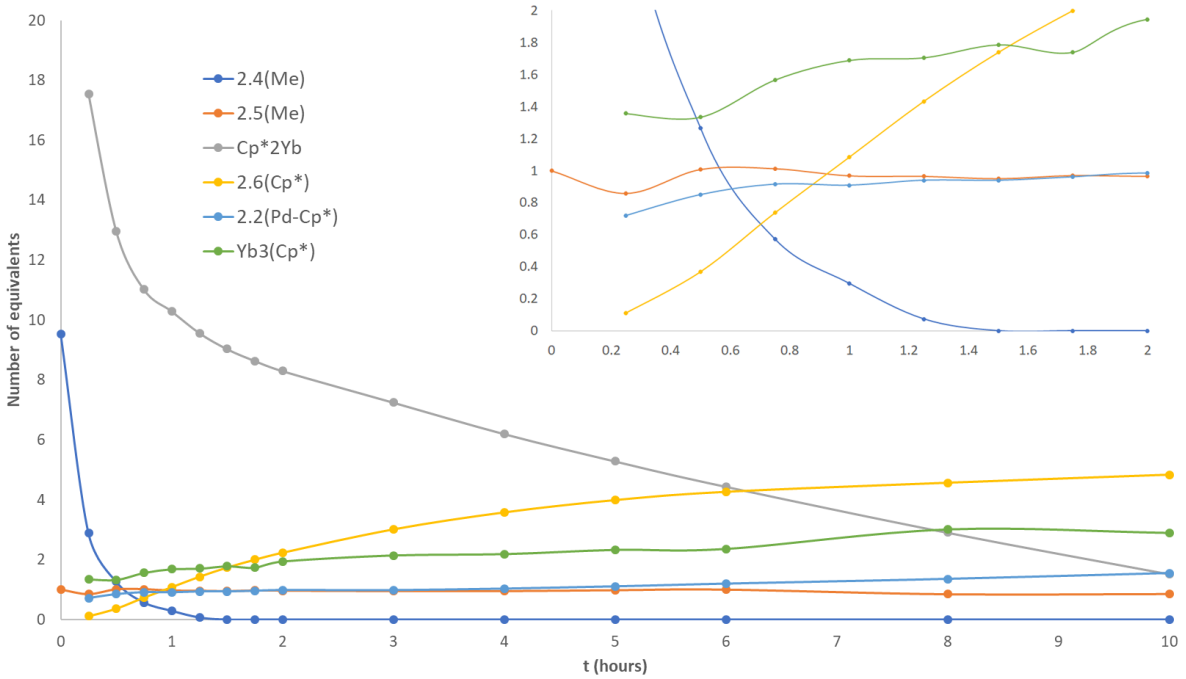

*Figure 3.13: Kinetic study of the reaction between **2.4** and an excess of ytterbocene in tol-d_8. t_0 is the scan prior to the addition of ytterbocene, included to show the relative proportions of **2.4** and **2.5** in the initial mixture. The inset shows the evolution of the formed species within the first 2 hours of the reaction. **$Yb_3(bimpym)_2$** was shortened to "Yb3" in the interest of clarity.*

The proportion of each species was calculated by careful integration of the most easily identifiable signal (written in parentheses in the graph) and subsequent renormalisation with respect to an internal standard. Whenever possible, the integration interval for each peak was kept identical for all the spectra for consistency. However, across the acquisition of the spectra, slight deviations of the paramagnetic shift were attested, forcing manual integrations in such cases. This method of calculating the integrations is evidently imperfect, due to occasional overlap between signals (particularly those of free ytterbocene and the Cp* of **2.6**), operator bias and the aforementioned occasional slight deviation of individual signals. Consequently, the analyses that follow should be taken to be qualitative. Any quantitative comparison hereafter is associated with a non-negligible error.

As previously evoked, the reaction between **2.4** and ytterbocene is rapid, as evidenced by the fact that the former seems to be entirely consumed within 90 minutes. Based on the evolution of the number of equivalents, a smaller quantity of ytterbocene than of **2.4** is consumed within this timeframe (8.5 eq vs 9.5 eq in Figure 3.13). This can be interpreted to be due to the competitive isomerisation reaction, also involving **2.4**. The evolution of **2.5** in the first 90 minutes (inset of Figure 3.13) can be split into several parts – the decrease between t = 0 and t = 15 minutes is due to the change of reference in between the blank scan and the first one, where the reaction has begun. The slight increase in concentration between t = 15 min and t = 45 min (where the concentration of **2.5** reaches its maximum) is, therefore, due to accumulation of **2.5**, following the isomerisation of **2.4**.

After 90 minutes, when no further **2.4** is attested, the rate of consumption of ytterbocene slows dramatically, but does not stop entirely (Table 3.4). This can be explained by the reaction with the transient species, mentioned above. This is corroborated by the fact that the intensity of these peaks also declines over time, as previously observed. However, they are noticeably more prominent than following the reactions of pure **2.4** with ytterbocene after the equivalent intervals of time.

	t = 0	t = 90 minutes	t = 10 hours
2.4	9.52	0	0
2.5	1	0.95	0.85
$Cp^*_2Yb(OEt_2)$	16.18	9.03	1.51
2.6	0	1.73	4.83
2.2	0	0.94	1.54
$Yb_3(bimpym)_2$	0	1.79	2.89

Table 3.4: Estimation of the number of equivalents (with respect to the internal standard) of each of the main compounds at various points during the kinetic study.

This can be explained by the following observations: the concentration of **2.5** remains stable (within the margin of error) through 5 hours, but starts decreasing steadily and slowly (Table 3.4). The only plausible explanation is that **2.5** also reacts with ytterbocene (Scheme 3.9). A comparison of the spectra following the consumption of **2.4** and one showing the transient species during the reaction of pure **2.4** would point to the fact that the reaction of either of the coupled products generates the same species, to whom the unattributed signals belong. At the very least, the two products share some of transient species that are formed following the reaction with $Cp^*_2Yb(OEt_2)$.

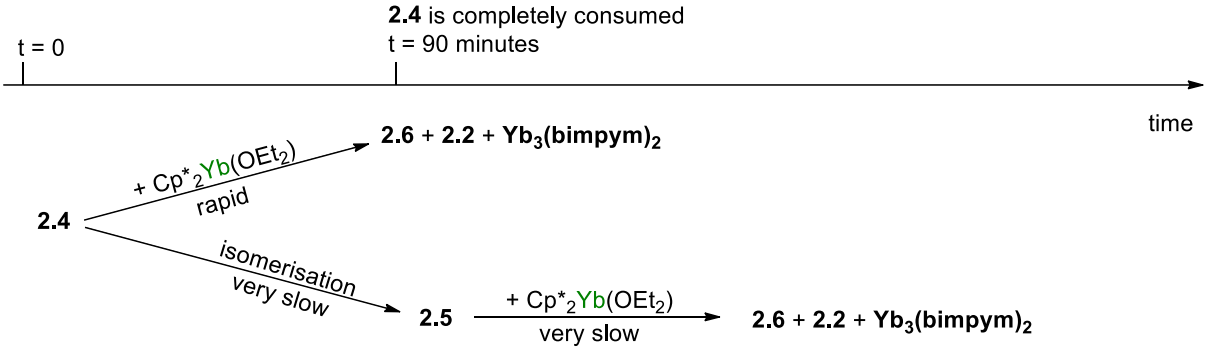

*Scheme 3.9: Schematic representation of the timeline of the reaction. The reactivity of the initial quantity of **2.5** is neglected.*

The evolution of the three identified formed products – **2.6**, **2.2** and **$Yb_3(bimpym)_2$** – is also interesting. The gradual increase in the concentration of **2.6** corroborates the hypothesis of its formation (mentioned above) following two key steps: the reaction between the coupled products and ytterbocene, which generates the transient species and the subsequent reaction between the transient species and further ytterbocene. In contrast, the pair of **2.2** and **$Yb_3(bimpym)_2$**, whose symbiotic formation was described in Section 2.2.2.3, is observed in a fair amount almost instantly. The ratio between the two is, within experimental error, maintained at *ca.* 0.53-0.54 throughout the reaction. Overall, the final ratio of the products seems consistent across several reiterations of the reaction.

What does this mean with respect to the reaction mechanism?

In itself, the formation of both **2.2** and **$Yb_3(bimpym)_2$** is quite surprising, especially the former. On the one hand, forming the latter (in a relatively high concentration) neatly explains the fate of the bimpym ligand throughout the transformation. On the other, although it may be intuitive that from two Pd(py)Me fragments in the coupled products one obtains one each of $Pd(pyr)_2$ (in **2.6**) and $PdMe_2$ (in **2.2**), the exact mechanism that leads to these species is far from evident. From a bottom-line perspective, it would appear that a ligand exchange of some sorts occurs.

An optimal Yb-triggered ligand exchange would provide a simple explanation as to the whereabouts of each important fragment of **2.4** (Scheme 3.10). An ideal reaction pathway would give a 1/1/1 ratio between the three main components. Based on the observed ratios, this is clearly not the case. If a ligand exchange between the two Pd centres does occur, then the mechanism is neither simple, nor efficient. The ramifications of this observation with regards to how the trimetallic adducts are formed will be discussed in larger detail below.

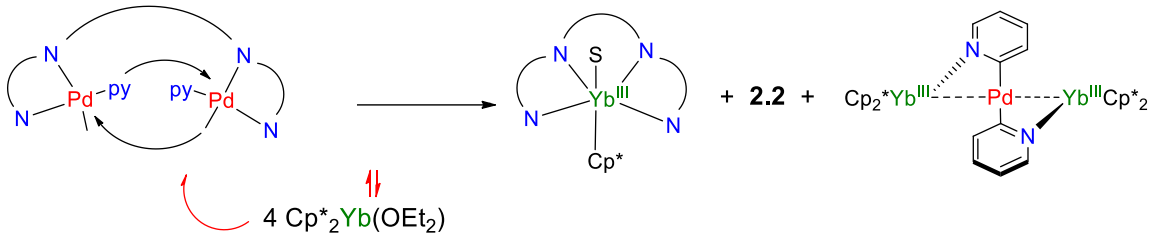

*Scheme 3.10: Idealised reaction between **2.4** and ytterbocene, involving a ligand exchange between the two Pd centres.*

The fact that **2.2** and **Yb_3(bimpym)$_2$** are detected almost instantaneously after the beginning of the reaction (see inset of Figure 3.13) suggests that their formation mechanisms are much simpler and more straightforward than that of **2.6**. Moreover, it would necessarily imply that the transfer of the second methyl moiety towards a single Pd centre occurs quite readily. Whether or not this passes through a ligand exchange-type mechanism is not clear at this point.

If the procedure were quantitative, the isolation of **2.2** would run counter to the previously posited explanation of the formation of methane following the C-H activation on the pyridine. Judging by the conversion of **2.4** to **2.2** in Figure 3.13, it would appear that only 15% of the methyl fragment is preserved and found in the bridging bis methyl moiety in **2.2**.

It is assumed that a good proportion of the rest is eliminated as methane. This possibility is corroborated by the gaseous evolution that was observed when the reaction is performed. Additionally, the ^{1}H NMR study of the reactions of ytterbocene with both **1.12** and **2.4** showed signals very close to the tabulated value in tol-d_8 (at 0.22 ppm and 0.17 ppm for the reference, respectively). The other possibilities are the release of ethane and dihydrogen, none of which were attested spectroscopically in the reaction media. It should be stated, though, that both of the characteristic signals for these gases (at 0.81 and 4.50 ppm, respectively) are likely to be overlapped by other signals in those regions, hampering their detection.

The formation of methane reposes on the assumption that the C-H activation occurs on a Pd fragment which holds both the pyridine and the methyl substituents, as was proposed in Section 3.2.1. Therefore, it seems evident that this scenario cannot take place at the same time as the proposed ligand exchange reaction. It then appears likely that both pathways are activated to different degrees during the reaction between **1.12** or **2.4** and ytterbocene.

In situ kinetic study of the reaction between ytterbocene and 2.5.

The same reaction was undertaken with the isomer, **2.5**. The evolution was significantly slower than that of its counterpart (Figure 3.14). Even after two weeks, the reaction was not complete (73% conversion, not shown). More pertinently, the ratio between the complexes is significantly altered with respect to that of the reaction of **2.4**. All three complexes are produced in similar proportions – **Yb_3(bimpym)$_2$** is the most abundant and **2.2** the least, but the former's concentration after 2 weeks is only 12.5% higher.

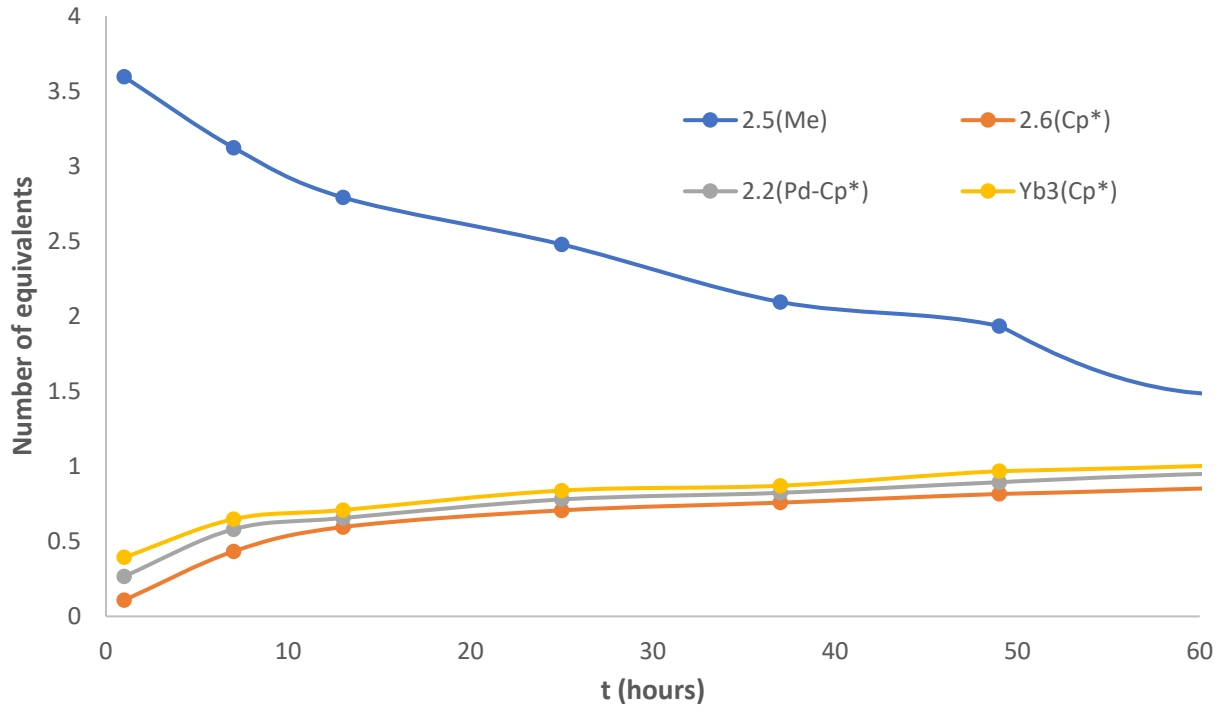

*Figure 3.14: Kinetic study of the reaction between **2.5** and an excess of ytterbocene in tol-d_8. The number of equivalents of each species was calculated with respect to an internal reference. $Cp^*_2Yb(OEt_2)$ could not be reliably integrated at all times and is not included. **$Yb_3(bimpym)_2$** was shortened to "Yb3" in the interest of clarity.*

At the NMR reaction scale, no gaseous evolution was observed, contrary to the previously described attempts with **1.12** or **2.4**. Equally, the signal at 0.22, interpreted to be the released methane following the reaction, is significantly less prominent than in the reaction utilising **2.4**. The C-H activation pathway, leading to the methane elimination, would seem to be less favoured when **2.5** is involved than in the case of its isomer. This shall be further discussed below.

Based on the integrations of the kinetic study, the reactivity of **2.5** with ytterbocene is much closer to the putative ligand exchange mechanism, as one equivalent of **2.5** gives close to one equivalent of each of the three products (Table 3.5; it should be noted that the conversion estimation does not take into account the transient species, which are still present in the mixture after two weeks). The reaction could not be followed until full conversion due to the decomposition of the substrates.

	t = 0	t = 60 hours	t = 360 hours	Conversion
2.5	3.60	1.48	0.96	73%
2.6	0	0.85	1.96	74%
2.2	0	0.95	1.91	72%
$Yb_3(bimpym)_2$	0	1.00	2.15	81%

*Table 3.5: Estimation of the number of equivalents for each species at various points during the kinetic study and the respective conversion of **2.5** towards the three main products. The conversion of **2.5** is calculated based on the integration at t_0, those of the three products are calculated based on the consumed quantity of **2.5**.*

There are other persistent signals that remain after both of these reactions, but none of these products could be reliably identified. A few by-products were crystallised as a very limited number of small crystals, precluding the identification of their solution signatures. These could be isolated following the reaction between **1.12** and either of the divalent lanthanide precursors as isostructural complexes of the formula $[(Cp^*_2Ln)_2(bimpym)]_2$ (Ln = Yb (**3.2**) and Sm (**3.3**), Figure 3.15).

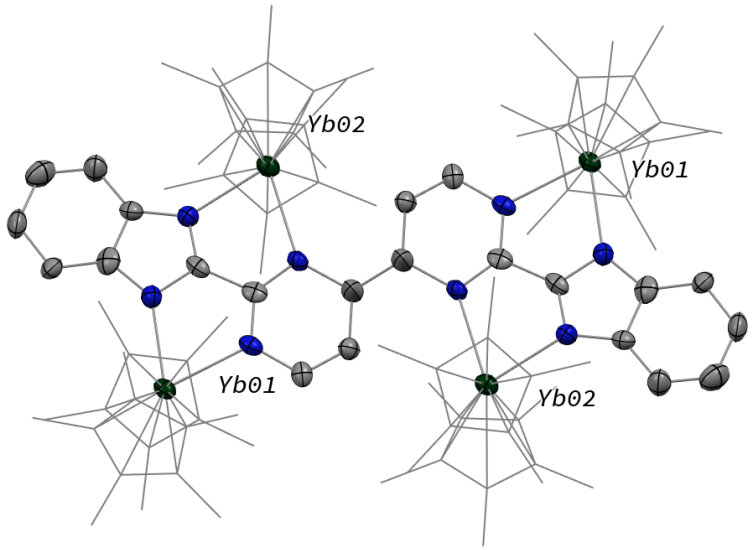

*Figure 3.15: ORTEP of **3.2**, isolated in the later crystallisation fractions after the addition of ytterbocene to **1.12**.*

These are clearly minor by-products of the reaction.

Overall reaction.

These findings allow us to present the overall reaction scheme for these species, shown in Scheme 3.11.

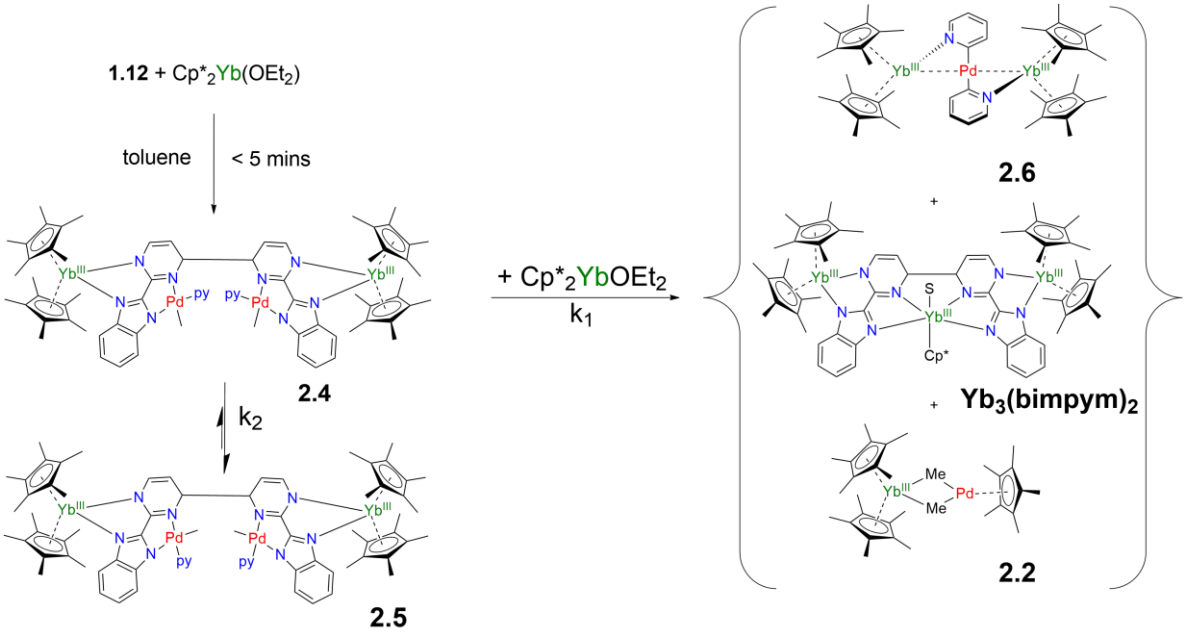

Scheme 3.11: Complete reaction scheme involving the (bimpym)Pd(py) species.

Given their structural similarities, it is not particularly surprising that adding ytterbocene to either **2.4** or **2.5** results in the same identified complexes. However, the two reactions are far from identical. First of all, there is a clear distinction in the reaction rates. On the basis of experimental observations, they could be summarised as follows:

$$k_1 >> k_2 \approx k_3$$

This is supported by the approximate half-times of the respective reactions, which are approximately 15 minutes and 50-60 hours for the last two, respectively.

The second major difference revolves around the relative proportion of the three main products. This raises the question as to why the two coupled products react differently. Given that the presence of free ytterbium is an indispensable condition for triggering further reactivity, a good starting point would be understanding how it would interact with the coupled edifices. The main assumption is that the lanthanide would coordinate on potential coordination sites on either of the coupled products. However, one has to take into account the enormous steric obstacles hampering such an event. It is unclear from which side the Yb could approach the molecules.

To the best of our knowledge, there are no structurally authenticated complexes in the literature that provide a satisfactory comparison with the coupled products. However, two examples may offer a clue as to how $Cp^*_2Yb(OEt_2)$ might react: a Yb^{II}-Pt^{II} adduct described by Andersen[60] and one recent example from our group.[61] In both cases, the lanthanide approaches and coordinates to the two methyl moieties. In the latter case, the Yb coordinates at an angle with respect to the TM square planar coordination environment (Figure 3.16), but the authors reported magnetic data consistent with a second electron transfer towards the ligand. In our case, the reduction of the Pd^{II} centre in the coupled products to the Pd^0 found in the trimetallic adducts would suggest that, at some point in the mechanism, two electrons have been transferred to the Pd.

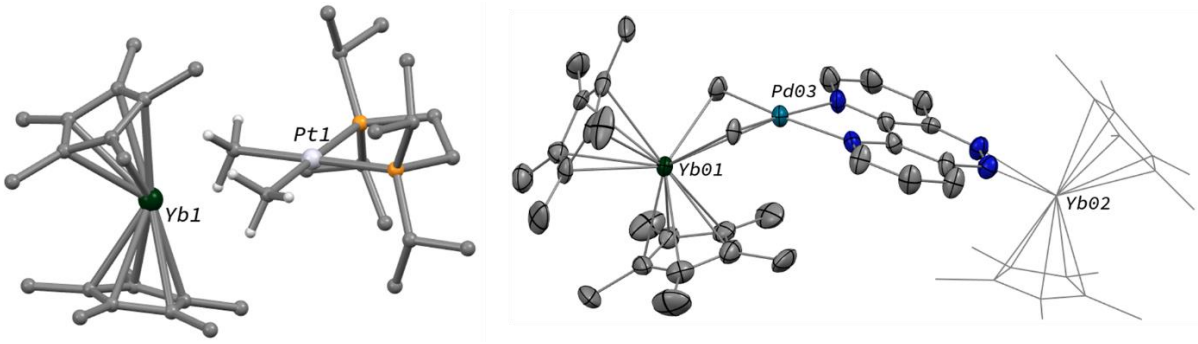

Figure 3.16: ORTEP of two complexes where Cp^*_2Yb fragments coordinate methyl moieties.[60,61]

With respect to our complexes, the comparison is not fully representative, though, as the second substituent is the pyridine. Either way, free ytterbocene has more space to approach close to these substituents than if it were to do so closer to the Yb fragments or to the space between the bimpym ligand and the Pd metal centre. It is assumed that the more favourable configuration would be the nestling of ytterbocene in between the pyridine and the methyl, in order to maximise the number of substituents.

A closer look at the geometrical arrangement of the coordination environment of the two Pd centres may provide part of the answer, rationalising the different ratios of the major reaction products. The structural differences between the two complexes revolve around the switching of the relative positions of the two substituents of the Pd and the significantly smaller torsion angle between the two identical molecular fragments in the case of **2.5** (68.69° vs 95.50°). There are two observations that stand out and have major implications regarding the C-H activation that ensues and which results in the formation of the trimetallic adducts.

First of all, the two Pd→pyridine bond axes point in opposite directions in **2.4**, mimicking the arrangement in **2.6**, whilst we can approximate this to be the case (due to the non-straight dihedral angle) for the methyl moieties in **2.5** (Figure 3.17, top). The second and more important observation

relates to the relative orientations of the cone angles formed by the methyls and pyridines of each Pd centre. In the case of **2.4**, there is a sizeable intersection between the two overtures, whereas for **2.5** they practically point in opposite directions (Figure 3.17, bottom).

Taken in tandem, the information gathered above allows us to propose several simple and logical hypotheses and to summarise the observations pertaining to the reaction mechanism:

- the "preorganisation" of the two pyridine moieties in the same configuration as the one in the final compound accelerates the subsequent rearrangement from **2.4** towards **2.6**;
- two molecules of free ytterbocene are necessary per equivalent of coupled product to trigger the formation of **2.6**; the same is probably true in order to evict the Pd centres in order to form **Yb_3(bimpym)$_2$**; it is unclear if the first and the second set of $Cp^*_2Yb(OEt_2)$ are the same;
- the mechanism(s) leading to the formation of the three main products is (are) facilitated by the greater proximity afforded by the closer coordination sites (see Figure 3.17, bottom) in **2.4**. This allows a more efficient cooperative interaction with **2.4** and explains the vastly different reaction rates between the two coupled products;
- the formation of one $Pd(pyr)_2$ and one $PdMe_2$ fragment could suggest that a ligand exchange between the two Pd centres on the coupling products occurs;
    - **2.2** (quasi-immediate formation) and **2.6** (gradual increase in concentration) are formed at different rates, following the reaction with **2.4**. It is likely that the second pyridine is not immediately coordinated to the Pd(py) or Pd(pyr) fragment, slowing down the formation of the trimetallic adducts;

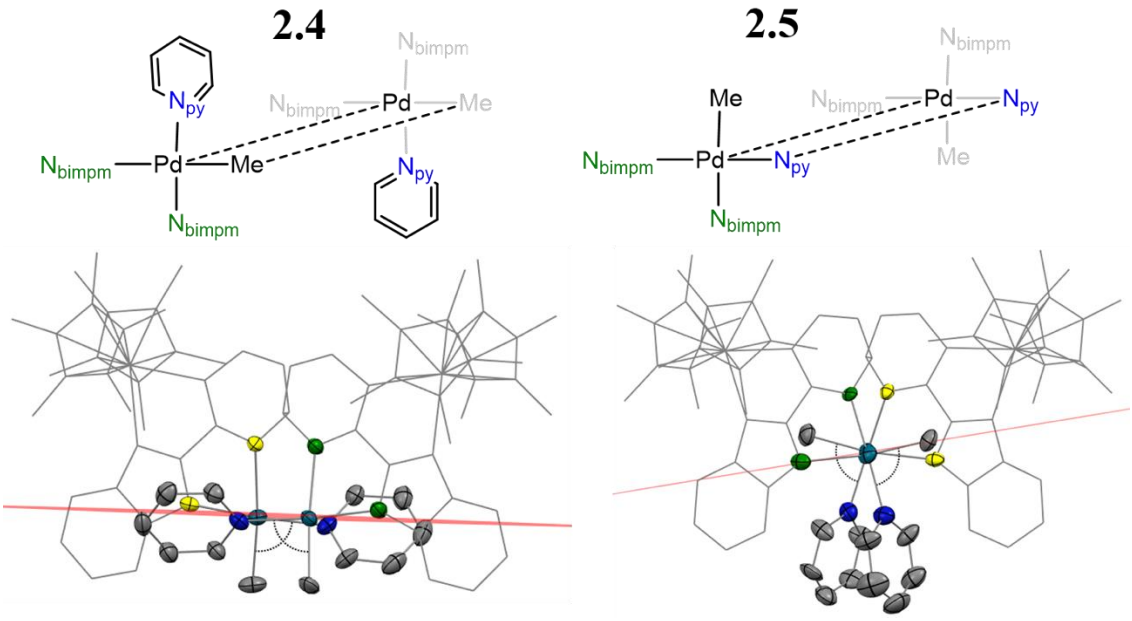

*Figure 3.17: Schematic representation and the corresponding simplified ORTEPs of the relative orientations of the pyridine and methyl moieties in the two Pd coordination spheres on **2.4** and **2.5**, viewed from above. Planes were calculated based on the substituents of the Pd centre. In both cases, the maximum available space for an ytterbocene approach would be from below the plane shown in the figure. The angle formed between these two substituents is shown for emphasis. The N atoms of the bimpym ligands closer to the viewer's perspective are shown in green, the ones farther in yellow.*

- the vastly different reaction rates between ytterbocene and **2.4** or **2.5** indicate that the activation barrier is higher in the case of **2.5**;
    - it is not known if **2.5** is reactive in its described configuration or if its conformation must change to allow the reaction;

  - it is unclear why the three main products are formed in almost equal measure following the addition of ytterbocene to **2.5**;
  - if these products are also formed by a ligand exchange of the Pd centres, the almost equal proportion between **2.2** and **2.6** would imply that it is more efficient (see Scheme 3.10 for a possible mechanism);
- the elimination of methane during the reaction between **2.4** and ytterbocene is very probable, as it was observed experimentally and via ^{1}H NMR;
  - if methane is formed *via* a C-H activation and a structure similar to **1.12-TS**, the ligand exchange mechanism proposed cannot occur concurrently;
  - the conversion of the methyl moiety to **2.2** is probably a good gauge to indicate the prevalence of each of the two pathways;

These findings and the proposed interpretation provide an adequate guideline for further assessment of the reaction mechanism.

3.2.2.3. Reactivity with samarocene.

Although no homologue of the coupled products **2.4** and **2.5** could be isolated following the reaction between **1.12** and samarocene, it would seem very likely that the reaction proceeds in a similar fashion. The *in situ* reactions in toluene resulted in the formation of **2.7**, irrespective of the stoichiometry. No other product could be reliably identified.

Nevertheless, the conclusions formulated in Section 3.2.2.2 provide a useful opportunity to slightly tweak the reaction conditions. As such, the reaction between **2.4** and samarocene was performed and followed by ^{1}H NMR (Figure 3.18). The evolution was relatively clean and the number of signals is coherent with the 14H of the expected [Cp*$_2$Yb(bimpym)$_2$]Cp*$_2$Sm(S) adduct. There were 4 signals that were more paramagnetically shifted than those illustrated in Figure 3.18, at 276.66, 241.67, 60.05 and 28.25 ppm. The attribution of the corresponding Cp* signals is more difficult, since there is significant overlap with the peaks of samarocene and of the residual solvent.

Curiously, there was one signal (designated by the black dot in the figure below), at -11.14 ppm, that was also instantly observed. This shift is eerily similar to that of the Pd-Cp* in **2.2**, which is at -11.34 ppm. The integration of this signal most certainly dispels the hypothesis of the formation of the analogue of **2.2**, a complex of the formula Cp*$_2$Sm(μ-Me)$_2$PdCp*. Its integration corresponds to approximately 30 H, if the average signal, assigned to the protons on the bimpym ligands, is set to 1H. No signal, potentially belonging to the Cp*$_2$Sm, can be found. Therefore, this signal, at -11.14 ppm, is very likely a Cp* signal of the supposed [Cp*$_2$Yb(bimpym)$_2$]Cp*$_2$Sm(S) product.

Crucially, the characteristic Cp* peak of **2.7** was observed within *ca.* 7 min of the beginning of the reaction. This corroborates the previous observations of a very rapid formation. The equivalent signals of **2.6** were never attested. The mixtures were left to crystallise at cold and XRD studies confirmed that the formed products were **2.7**. No other products could be isolated.

The implication herein supports a rather intuitive conclusion: starting from the coupled product **2.4**, the ensuing Ln$_3$(bimpym)$_2$ compound that is formed is issued from the [Ln(bimpym)]$_2$ scaffold of **2.4**. This confirms the assertion that the free divalent lanthanide precursor kicks out the Pd fragments to form the Ln$_3$(bimpym)$_2$-type adduct, and then further divalent lanthanide molecules reacts with the evicted Pd fragments to form the trimetallic adducts **2.6** or **2.7**. The same is likely to be true for **2.5**.

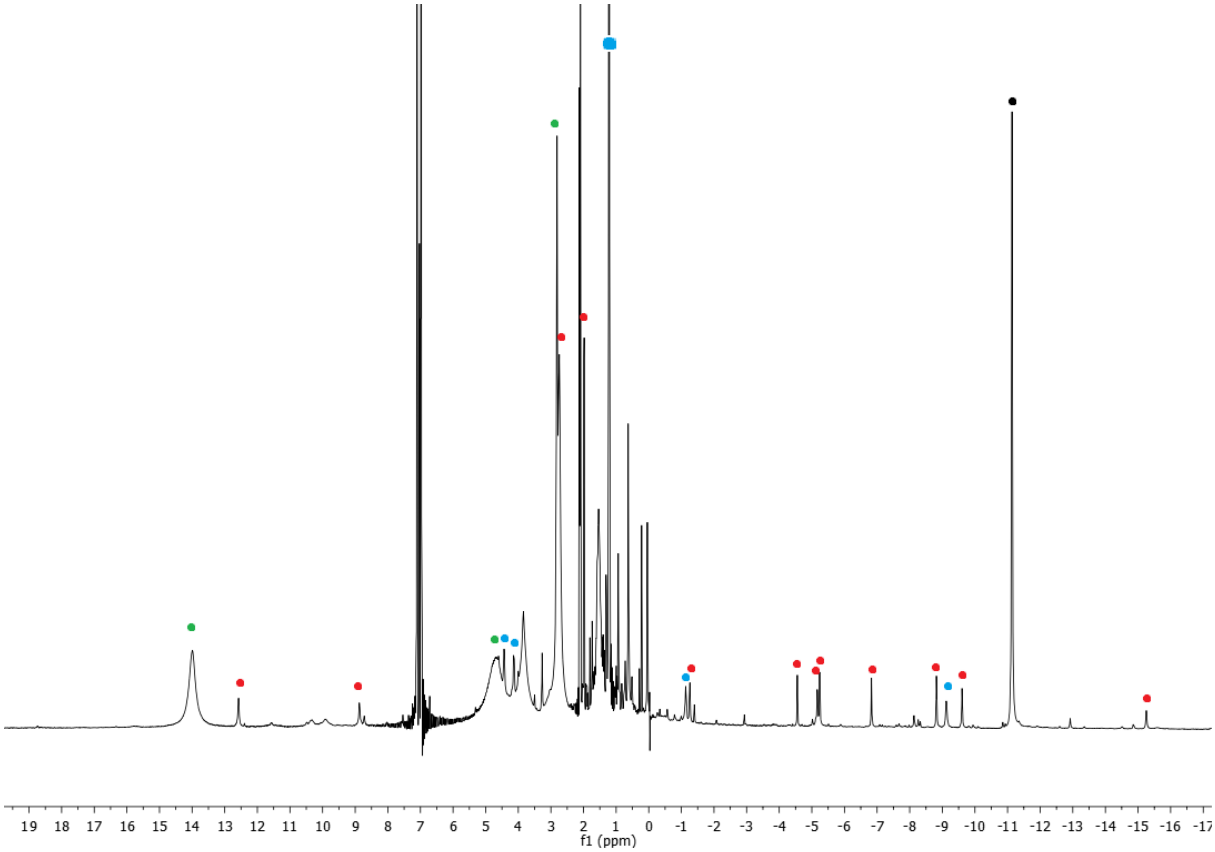

*Figure 3.18: ^{1}H NMR of the reaction between **2.4** and samarocene. The signals of **2.7** are designated by blue dots, free samarocene – green, assumed H_{bimpym} – red. The black dot designates the signal very close to that of the Pd-Cp* of **2.2**.*

Reactions with samarocene can also help obtain further clues as to the difference between the proportions of **2.6** formed after the reaction of the two coupled products. To that effect, the quinoline equivalent of the Sm-based trimetallic adduct (**2.8**) described in Section 2.3.3.2, is re-examined.

Analysis of the quinolyl adduct.

To recall, this complex was formed by the reaction between **1.12** and samarocene in presence of free quinoline in solution. There are, however, reasons to doubt that the ligand exchange between the pyridine and its analogue occurs efficiently in solution prior to the reaction with the divalent lanthanide. The twinned nature of the crystals was the cause of an average agreement with the initial model, which suggested that only a partial substitution of the pyridine had taken place.

In fact, there are several crystallographically plausible outcomes regarding this complex. **2.8** is initially resolved in the P-1 space group (which possesses an inversion centre). The asymmetric unit contains half of the entire molecule – $Cp^*_2SmPd(quin)$ (quin = quinolyl) – with the other generated by symmetry. If the 4 carbon atoms defining the supplementary benzene cycle inherent to quinoline (shown in dashed lines in Scheme 3.12, first structure) are allowed to have partial occupation, a better fit to the model is obtained and a statistical disorder ensues.

From a quantitative standpoint, the model suggests that the ligands coordinating the metal centres are 50% pyridyl and 50% quinolyl. This would mean, chemically, that there are three possible distinct molecules: quin-quin, pyr-pyr (**2.7**) and quin-pyr (Scheme 3.12). Following this model to its logical conclusion, it is impossible to find out the exact proportion of each species. Therefore, this

interpretation gives us no further information as to the reaction mechanism. The pyridine-quinoline exchange could take place at any moment, apparently in a random manner.

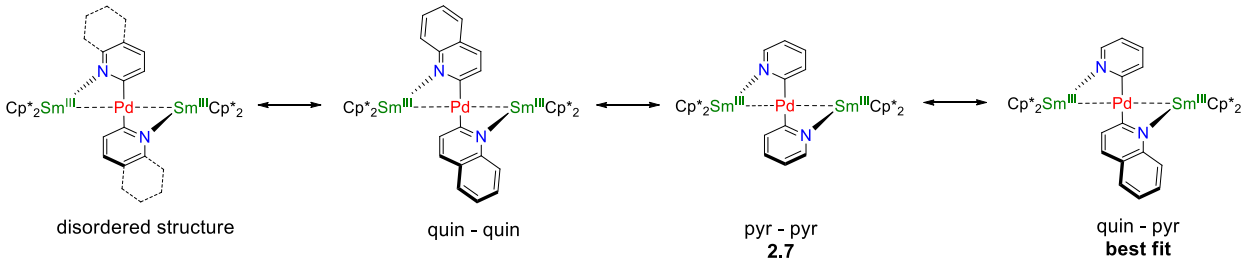

*Scheme 3.12: All the potential structures of **2.8**, based on the interpretation and resolution of the structural disorder.*

An alternative solution is revealed if the crystallographic data is resolved in a non-symmetric space group – P1. The statistical disorder is entirely eliminated and the proposed solution is the quin-pyr configuration. This solution is robust: if the same 4 carbon atoms are assigned partial occupation, the statistical agreement with the data worsens. Despite the overall improvement of this solution, the overall data is still not of good quality, which means that the conclusions are not irrefutable. At this conjecture, it is unclear if these defects are inherent to the crystals or if there are other possibilities that were not considered. Other crystal batches were analysed and presented the same issues.

If, however, this solution is chemically accurate – 100% of the complex is of the quin-pyr configuration – specific assertions can be made regarding the reaction mechanism. The presence of one pyridyl group would most logically be interpreted as originating from the parent compound – **1.12**. The addition of samarocene would trigger the first C-H activation, resulting in the pyridyl group being formed and coordinated to the Pd. The second C-H activation would therefore originate from the quinoline, of which there is an excess in the reaction media. This would suggest that the second C-H activation – which, presumably, leads to the stabilisation of the trimetallic adducts **2.6** and **2.7** – is due to free ligand that is close to the reaction site. In this case, the quinoline would be preferred due to its abundance to any potential free pyridine that may have been released due to its fluxional behaviour.

The two C-H activations occurring separately would also be consistent with the formation of the transient species, attested for the reaction resulting in **2.6**. From this perspective, the unattributed peaks include (among others, probably) species of the formula [$Cp^*_2Yb^{III}$(pyr)Pd(R)], which ultimately become the trimetallic adduct upon further reactivity.

3.2.3. Theoretical studies.

The previous section helped provide a significant number of clues as to how the divalent lanthanide helps trigger the evolution from **1.12** until the trimetallic adducts **2.6** and **2.7**.

Even so, there are certain minute steps or transformations at the molecular level that are far beyond the capacity of the available spectroscopic tools. To this end, theoretical computations are a very useful tool to provide further insight.

In this respect, the TS and the subsequent reorganisation of the precursor **1.12**, computed in Section 3.2.1, provide useful information to understand the mechanism of the C-H activation from a conceptual standpoint, but its precision in representing the chemical picture once divalent lanthanides are included is, as of yet, unclear. This section will add such fragments whenever pertinent and computationally plausible.

Other than C-H activation of the pyridine, the formation of **2.2** and **Yb_3(bimpym)$_2$**, in addition to **2.6**, suggests that a ligand exchange of some sorts occurs between the two halves of the coupled products **2.4** or **2.5**. This would explain the formation of the bridging [$PdMe_2$] or [$Pd(pyr)_2$] motifs from the initial Pd(py)Me arrangement. If this is true, this mechanism is undoubtedly complex and is beyond the scope of this work. The objective of this study will be restricted only to the C-H activation.

Given the significant role of the steric hindrance in deciding the approach vector of the divalent lanthanide to **2.4**, it is important that the computations represent a loyal representation of the molecular environment.

However, the modelling of these ponderous structures was shown to be very complicated, as detailed in Section 2.3.1.2. An eloquent example of this is the need for imposing geometrical restraints in the optimisation runs of **2.5**, as the coupling C-C bond was severed. This size of system – close to 180 atoms, with multiple metal centres – would appear to be the computational limit of our study.

3.2.3.1. Computing heterobimetallic adducts.

The computational ceiling of the heterometallic adducts prompts the need to examine the pertinence of substitutes, which would be based on approximations. For example, the symmetrical structure of the coupled products should indicate that there is no difference in the electronic structure of the two identical fragments. The question in this case is whether having both fragments generates any additional interactions that would register in terms of electronic structures. Previous studies have shown, for example, that spatial separation allowed isolating separate electron transfers in complexes featuring two ytterbocene groups by distancing them *via* extension of the aromatic system.[62]

The very rapid formation of **2.4** (and the other coupling products) indicates that the electron transfer is favourable from an energetic standpoint. To probe this computationally, heterobimetallic adducts, accounting for half of **2.4**, were considered.

These complexes will be referred to as **1.12-Yb** and **1.12-Sm** (Figure 3.19) and were optimised at the **ZORA1** level of theory as triplets and septuplets, respectively. The multiplicities aim to reproduce the electron transfer, which is to say the ($4f^{13}$-(bimpym)$^{\bullet-}$) and ($4f^{5}$-(bimpym)$^{\bullet-}$) configurations. The geometrical features proposed by both calculations reliably describe Ln^{III} states, as evidenced by the distance to the centroid of the Cp* co-ligand. As is the case for **2.4**, the Pd centre is unaffected by the addition of another metal centre, as none of its main distances vary to any meaningful extent.

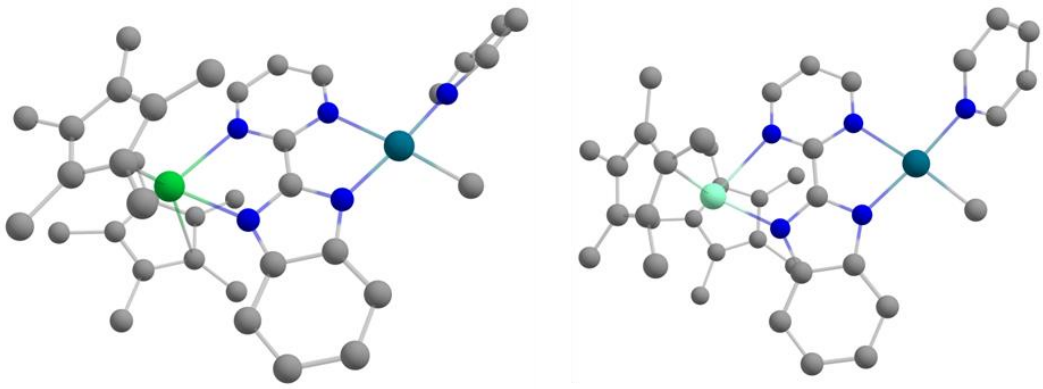

*Figure 3.19: Structures of **1.12-Yb** and **1.12-Sm**, obtained at the **ZORA1** level of theory.*

However, a deeper look into their electronic structures (at the **ZORA3** level of theory) highlights that the putative Yb complex does not reflect the anticipated electron transfer. The SOMO on **1.12-Yb**

shows only contributions from the ligand, but none from the Yb centre. This is in contrast to that of its counterpart, where there is an important participation from the Sm^{III} centre. However, the LUMOs of these structures were invariably the same pyridine-based, **LUMO^{L}**-type orbitals. This complex is a good approximation of how the radical anion on the pyrimidine would behave, as significant electronic density is concentrated on the coupling carbon. Multiple functionals were probed to verify these conclusions, but the electronic structure was invariant in all cases.

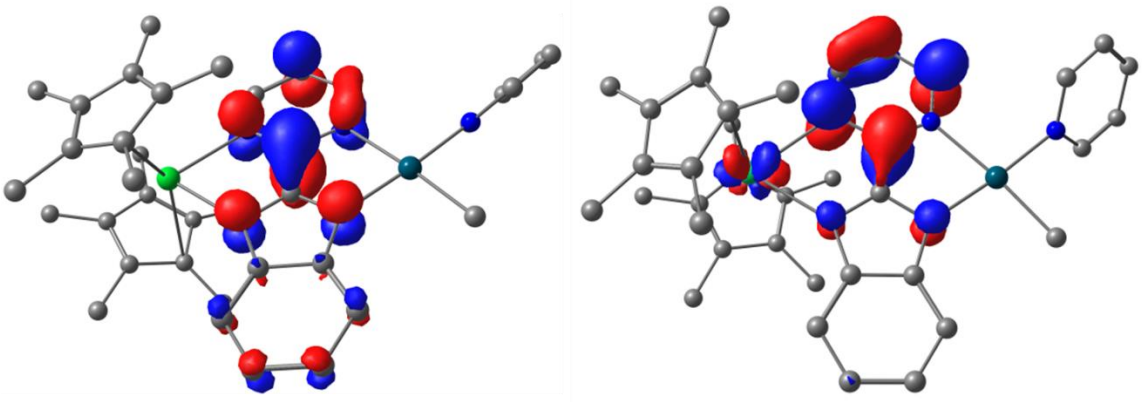

*Figure 3.20: Alpha SOMO on the computed heterobimetallic adducts **1.12-Yb** (left) and **1.12-Sm** (right).*

These findings would point to the fact that DFT is not capable of reproducing all the finer electronic features expected of this structure. Quite tellingly, the SOMO on the homologous **1.12-Eu**, computed for comparison, is identical to that of **1.12-Sm**, despite there not being any experimental evidence that Eu^{II} is capable of reducing **1.12**.

The heterobimetallic compounds were used as basis for TS calculations at the **TS1** level of theory. As was done for **1.12-TS**, the GS geometry was biased so that it would resemble the expected TS. The resulting structures did, indeed, faithfully reproduce the same TS as for the Pd-based precursor – the H issued from the pyridine is positioned midway between the pyridyl and the methyl moieties. These complexes will be referred to as **Yb-TS** and **Sm-TS**, respectively (an overlay between the two is given in Figure 3.21). There is no noticeable difference in between the coordination environment of the Pd centres in these two complexes, which does not evolve in between the GS and the TS configurations.

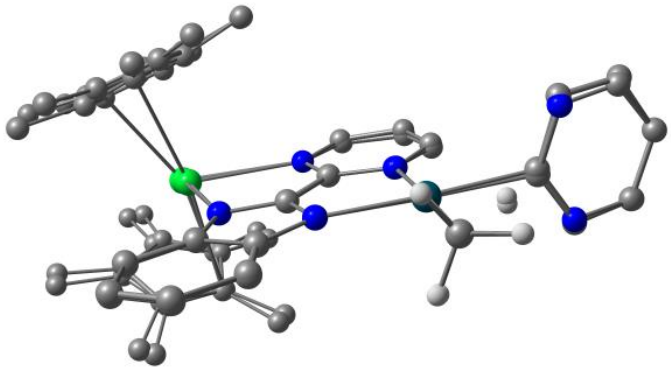

*Figure 3.21: Overlay of **Yb-TS** and **Sm-TS**. The majority of H atoms are hidden in the interest of clarity.*

The same considerations hold for the next step, following the departure of methyl moiety. The analogous structures to **1.12-η^2** are computed using the same methodology and will be referred to as **Yb-η^2** and **Sm-η^2**. As for the TS, the coordination of the lanthanide fragments does not induce any consequential changes with respect to **1.12-η^2**.

The comparison of the relative energies (computed at the **TS1** level of theory) of the GS, TS and η^2 configurations for each of these series of complexes is presented in Figure 3.22. The coordination of the divalent lanthanide fragments seems to bear a sizeable influence on the activation barrier for the C-H activation. **1.12-TS** is roughly 30 kcal/mol above the GS, making it unreachable at r.t. This is consistent with the fact that **1.12** does not engage in any reactivity.

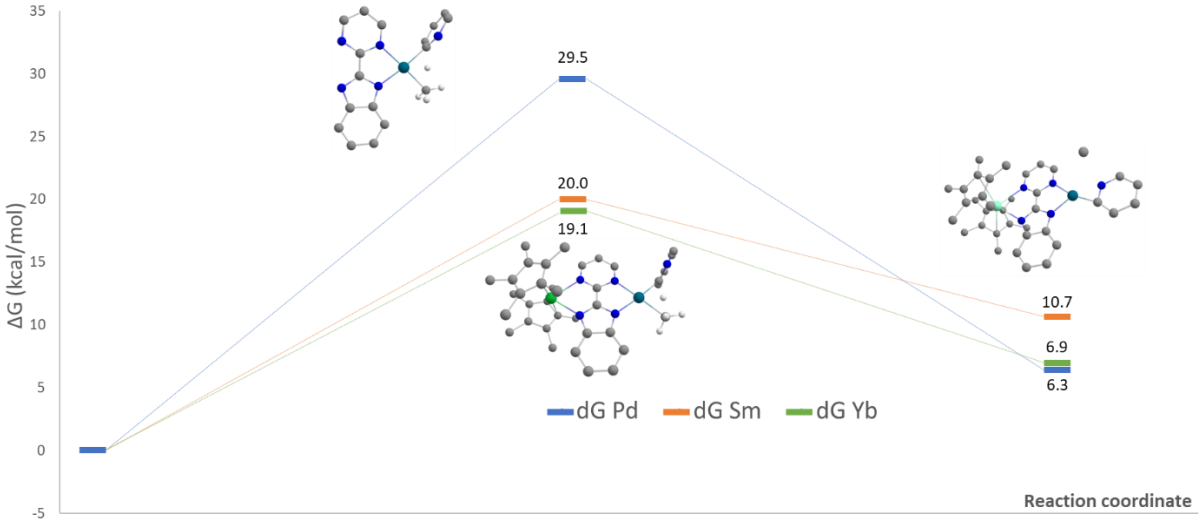

*Figure 3.22: Computed Gibbs Free Energy profile, at the **TS1** level of theory, of the C-H activation on **1.12**-based structures.*

In the case of the heterobimetallic complexes, this barrier is reduced by approximately 10 kcal/mol with respect to the Pd-based precursor. The same functional-dependent variation, seen in Section 3.2.1.2, is applicable for these compounds. The η^2 configurations follow the same trend, as they are higher in energy than the GS. Just as was proposed for the precursor, the C-H activation would generate a metastable species, which would subsequently undergo further transformation. This is in agreement with the assumed experimental behaviour.

These findings are not coherent with the fact that the C-H activation does not occur in the coupled products. It was shown that it is the addition of ytterbocene that allows the subsequent transformation from the coupled products towards the trimetallic complex **2.6**. That **Yb-TS** and **Sm-TS** are 20-25 kcal/mol (depending on the density functional that was used) higher in energy than their respective GS would imply that these transformations are attainable at r.t, which is clearly not the case in experimental conditions. With that in mind, it is legitimate to interrogate both the model and the methodology.

These observations do possess a caveat: the bimetallic adducts are meant to model the coupled products. It is not known what a comparable TS on the full-size complexes would behave.

3.2.3.2. Analysis of the results. Influence of the method.

The energetical considerations presented above point to an unrealistic replication of experimental observations. This prompts a closer look into the computed energies. As referenced in the discussion about the relative energies of **1.12** and the subsequent configurations, the differences in energy can be expressed by comparing the enthalpies and the Gibbs free energies. The latter also includes the variation of the entropy throughout the transformation.

$$\Delta G = \Delta H - T\Delta S$$

This difference was found to be negligible for the Pd-based precursor. It is not the case for the heterobimetallic adducts (Table 3.6).

Δ(TS-GS) (kcal/mol)	**1.12-Yb**	**1.12-Sm**
ΔH	28.09	30.35
ΔG	19.05	19.97

Table 3.6: Computed enthalpies and Gibbs free energies for the heterobimetallic complexes.

This difference is substantial and warrants further examination. Its origins could feasibly be traced to:

- the deficiencies implicit to DFT in the calculation of entropy[63]
- the significant entropy variation due to molecular changes when going from **1.12** to **1.12-Ln**
- the poorly adapted choice of some of the elements of the computational method (basis set or use of the relativistic Hamiltonian)
- the method by which the thermal corrections are calculated

These factors will be analysed individually. If the DFT-specific issues in entropy calculation are the root of the observed discrepancy, then it would affect all complexes equally. The main differences between the monometallic and bimetallic adducts are related to the size of the system and the number of heavy elements. If these are responsible for the propagation of the error of the estimation of entropy for individual displacements, then it makes sense to analyse it more thoroughly through a molecular perspective.

The most obvious disparity between the Pd-based structure and the heterobimetallic ones, which would contribute to the entropy calculations, is the presence of the bulky Cp* co-ligands. In the absolute sense, it is logical that there is a superior entropic contribution to the energy when adding these ligands. The key to this analysis is, therefore, understanding what causes the variation of entropy for the same geometry.

The total entropy of the system, S_{tot}, can be broken down into several components:

$$S_{tot} = S_t + S_r + S_v + S_e$$

Where S_t – translational; S_r – rotational; S_v – vibrational and S_e – electronic. For all of the complexes, only S_v varies at all between GS and TS. This is logical, since the TS is, by definition, an excited vibrational state. The net value of this variation is not the same in between **1.12** and the heterobimetallic complexes: less than 4 $cal.mol^{-1}K^{-1}$ for the former and approximately 30 $cal.mol^{-1}K^{-1}$ for the lanthanide-based structures. It is precisely in this regard that the Cp* co-ligands contribute significantly, as they account for a multitude of vibrations, which are populated at r.t. As they contribute to a greater overall vibrational entropy, it stands to reason that an excited vibrational state will incur a proportionate, more significant variation of the energies associated with the vibration.

Although this explanation is satisfactory from a qualitative standpoint, it is unclear if the numerical values of the described variation are accurate.

In terms of methodology, all of the TS calculations described in this chapter were performed at the **TS1** level of theory. One of the drawbacks of the method is the choice of the ECP for the Pd centre. It was described using the LanL2DZ ECP, with its associated basis set. A more adequate choice for future studies would be the ECP of the Stuttgart-Köln group, which were used for the Ln centres. An important ingredient which is missing is the correction for the dispersive forces. Given the more

sterically encumbered structures of the heterobimetallic complexes, it is pertinent to query their importance in obtaining a meaningful energetical comparison.

To this effect, consistency was sought by computing some of the structures presented in this Section at the **TS2** level of theory (rightmost in Table 3.7). This framework was found to be more forgiving and allowed the examination of a variety of factors, to probe their influence in the energy calculations.

Therefore, the computations examined the role of the inclusion of a relativistic Hamiltonian, of the basis set (relativistically recontracted or not), of the use of RECP on the metals, of the inclusion of corrections for dispersive forces, and of the functional. Alas, for the last term, neither geometry optimisations, nor frequency calculations could be converged for PBE0 and TPSSh. In these cases, the ΔG were obtained by adding the thermal corrections obtained using the PBE density functional.

None of the parameters bore any significant influence on **1.12**. This simpler structure affords greater tolerance for the more exact parametrisation of the dispersive forces – of which there are fewer than in the case of the heterobimetallic analogues – or of the basis sets employed for describing the composing atoms. For this reason, the corresponding computations were not pursued with other functionals, as the differences would more likely be associated with the change in functional, rather than being due to the approximations.

The metric that was used for this study is ΔG. A close examination of the ORCA results showed that there was negligible difference between the enthalpy and the Gibbs free energy for the computed series, contrary to the findings at the **TS1** level of theory.

	Gaussian (**TS1**)	ORCA (**TS2**)						
Complex/method	RECP, no D3	RECP, no D3			RECP, D3			ZORA, AE, D3
Functional	PBE	PBE	PBE0	TPSSh	PBE	PBE0	TPSSh	PBE
1.12 (singlet)	29.59	29.32			29.18			29.70
1.12-Yb (triplet)	19.06	29.52	30.82	33.11	26.50	24.44	29.41	30.60

*Table 3.7: Computed ΔG for the complexes **1.12** and **1.12-Yb**, accounting for changes in the methodology. "ZORA" signifies the use of a relativistic Hamiltonian and of the corresponding relativistically recontracted basis sets. "D3" – Grimme's D3 model, associated to the Becke-Johnson damping scheme. "RECP"/"AE" – relativistic effective core potential / all-electron. The blacked-out fields indicate that the computations were not performed.*

The data presented in Table 3.7 allow us to form the following conclusions:

- adding corrections for dispersive forces lowers the energy barrier for the proposed C-H activation, but not significantly: the transformation does not become achievable at r.t by including them
- changing the density functional also induces some measure of numerical variation of the energy barrier
- the inclusion of a relativistic Hamiltonian, coupled to all-electron relativistically recontracted basis sets, renders this transformation less accessible

Another factor worth examining is related to how the thermal corrections, which are added to the total electronic energy of the system in question (ε_0), are computed in either case.

In Gaussian, only an analytical calculation of the frequencies is offered for DFT computations. When complicated systems are at play, the numerical calculation of frequencies is preferred in ORCA to facilitate convergence. Despite our best efforts, the equivalent computations involving analytical

frequencies could not be completed. This discrepancy in methods is responsible for the different computed outcomes.

In all of the cases studied, $\Delta\varepsilon_0$ (the difference between ε_0 for the GS and TS) is higher than ΔG. The difference in the thermal corrections to the total inner energy (ΔU_{corr}; not shown) and to enthalpy ΔH_{corr} (which include the former) do not significantly contribute to the reduction of the energy barrier and are quite similar in between the two methods. The same cannot be said when it comes to the thermal corrections to the Gibbs free energy, which have a more marked impact the energy barrier. Even more importantly, this metric is significantly different between the two methods.

	$\Delta\varepsilon_0$	ΔH_{corr}	ΔH	ΔG_{corr}	ΔG
Numerical frequencies	34.49	-3.13	31.36	-4.97	29.52
Analytical frequencies	30.32	-2.23	28.09	-11.26	19.06

Table 3.8: Comparison between the main energies of the two methods, in this case following computations performed with RECP and no dispersion corrections. "G_{corr}" is the thermal correction to the Gibbs free energy. All energies are expressed in kcal/mol.

Given that ΔG is dependent on the aforementioned calculation of the entropy, this disparity contributes to the overall difference. In this scenario, where the viability of the C-H activation is gauged, the more reliable comparison would seem to be ΔH, whose numerical values are more consistent with the experimental observation that there is no C-H activation which occurs on the coupled products **2.4** or **2.5**.

Similar trends to the ones presented above were noticed when attempting to model the electron transfer into the pyridine-based LUMO by adding an electron to **1.12-Yb** and **1.12-Sm** at the **TS1** and **TS2** levels of theory. At the **TS1** level, although ΔG would suggest that the energy barriers of the transformations were attainable at r.t, ΔH precluded them, also showing that the entropy calculations over-corrected the activation barrier. Results at the **TS2** level consistently showed that the computed TS were inaccessible.

These findings are consistent with the conclusions of Section 3.2.2.1 – the mere reduction of the coupled complexes is not sufficient to trigger the reactivity resulting in the trimetallic complexes. They also serve as a cautionary tale in the interpretation and framing of the computational results in complicated cases. None of the approximations considered here are adequate for modelling the molecular reorganisation from the coupled products towards the trimetallic adducts **2.6** or **2.7**.

3.2.3.3. Adding a further organolanthanide precursor.

The inadequacy of the results in the previous section demonstrates that the beginning of the reorganisation mechanism from the coupled products towards **2.6** or **2.7** cannot be correctly modelled without considering an explicit involvement of another lanthanide fragment. This is consistent with the available experimental data, which suggests that neither submitting the substrates to harsher conditions of temperature or UV excitation, nor reacting them with other reductants is sufficient.

A faithful reproduction of the environment is impossible from the perspective of the computational cost, due to the tremendous size of the full systems. Naturally, the next logical step is attempting the addition of another organolanthanide fragment to the existing half-molecule edifices, **1.12-Yb** and **1.12-Sm**. These were computed at the **ZORA1** level of theory by placing a Cp^*_2Ln molecule close to the most likely coordination site, in between the methyl and the pyridine. These complexes will be

referred to as **1.12-Yb$_2$** (computed as a triplet, assuming the oxidation of each Yb centre and an antiferromagnetic coupling between the transferred electrons) and **1.12-Sm$_2$** (computed assuming non-interacting Sm^{III} centres (S = 10/2) and an antiferromagnetic coupling between the transferred electrons).

The compounds are shown in Figure 3.23. The geometry optimisations settled on the coordination of these second lanthanide fragments with the bond axes formed at an angle with respect to the coordination environment of the Pd centre. This is reminiscent of the trimetallic edifices based on the taphen ligand, illustrated in Figure 3.16.

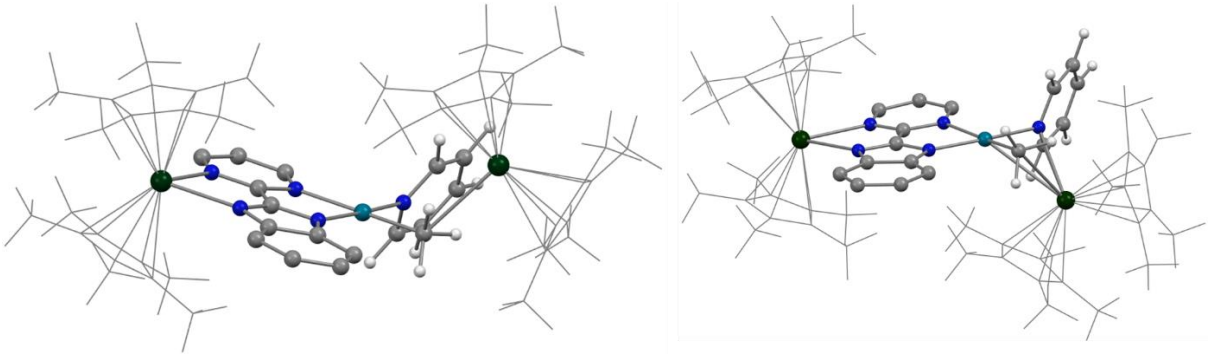

*Figure 3.23: Optimised structures of **1.12-Yb$_2$** and **1.12-Sm$_2$**. The Cp* co-ligands are shown in wireframe and the majority of H atoms are hidden for clarity.*

The main interest in this study is to examine the plausible coordination patterns of the second lanthanide fragment. The structural features give a good indication of how this might perturb the existing system (Table 3.9). Neither case shows any measure of influence over the coordination environment of the first lanthanide centre. The same could be said with respect to the Pd-bimpym interaction, since the main distances are shifted negligibly (not included in Table 3.9).

	Av. Values (Å or °)			
Atoms	**1.12-Sm**	**1.12-Yb**	**1.12-Sm$_2$**	**1.12-Yb$_2$**
Pd-N_{py}	2.032	2.031	2.083	2.046
Ln_2-H_α			2.816	2.672
Ln_2-H_{1Me}			2.531	2.338
Ln_2-H_{2Me}			2.680	2.400
Ln_2-C_{Me}			2.796	2.762
Ln_2-N_{py}			2.720	3.916
Ln_2-C_{py}			3.017	3.322
Ligand plane^py	59.50°	58.74°	70.89°	72.80°
Ln_2-ligand plane			~55°	~51°
(Pyr plane)^(Pd-N_{pyr} bond)			148.17°	178.20°

*Table 3.9: Main bond lengths and angles in the computed Ln-bearing derivatives of **1.12**. "H_α" designates the proton on the α position of the pyridine; "H_{1Me}" and "H_{2Me}" designate the closest and second closest H atoms on the methyl moiety.*

It is worth noting that the lanthanides approach the molecule from different sides. Assuming a plane formed by the bimpym and the coordination sphere of the Pd, the second ytterbocene is placed above this plane, whilst the second samarocene is under it. Both complexes show an interaction with the

methyl and pyridine moieties, although this applies to a lesser extent to **1.12-Yb$_2$**. **1.12-Sm$_2$** is much closer to the pyridine and it interacts quite strongly with the N and the C atoms in the α position.

This discrepancy can be rationalised by the size of the organolanthanide fragment. All of the Ln centres are in the +3 oxidation state and the distance between the centroid of the Cp* to the Ln follows the lanthanidic contraction. Seeing as how the axis formed by the Ln and the centroid of the Cp* co-ligands points away from the molecule, the space between the two Cp* is heavily influenced by the distance between the Ln and the Cp* (Figure 3.24). The second Cp*$_2$Sm fragment has more space to accommodate closer contact between the Sm and the pyridine.

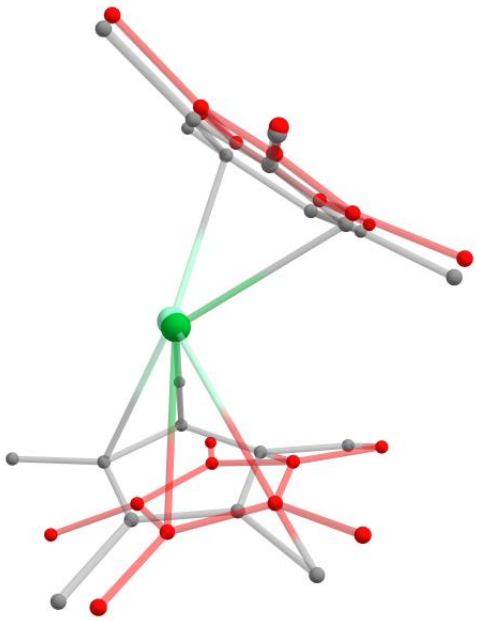

*Figure 3.24: Overlay between the second organolanthanide fragment in **1.12-Yb$_2$** and **1.12-Sm$_2$**. The C atoms of **1.12-Sm$_2$** are shown in red.*

In return, the coordination of the pyridine towards the Pd in **1.12-Sm$_2$** is altered, as the ligand is pushed closer to the bimpym ligand. This is illustrated by the angle formed between the pyridine plane and the Pd-N$_{py}$ bond axis ((Pyr plane)^(Pd-N$_{pyr}$ bond) in Table 3.9). In the case of the Yb adduct, the coordination is unperturbed, whilst this metric is deviated by more than 30° in **1.12-Sm$_2$**.

The different positioning of the second organolanthanide fragment with respect to the ligand plane was intriguing. To this end, the geometry of **1.12-Sm$_2$** was used as a basis for another calculation at the **ZORA1** level. The Sm atoms were replaced by Yb. The optimisation run repositioned the lanthanide fragment in a different pocket of space. This time, it is nestled in between the methyl and the benzimidazole moieties, with short distances to the C$_{imid}$ and the two nearest H atoms. This structure will be referred to as **1.12-Yb$_2$'**. The structural features surrounding the Pd centre were virtually unchanged with respect to those of **1.12-Yb**.

These three structures provide a preview of how the initial coordination of an additional divalent lanthanide molecule would coordinate to the coupled products **2.4** or **2.5**. It goes without saying that in real-time scenarios, the interactions between the coupled products and the supplementary lanthanide fragment are bound to be different, due to the presence of the other half of the molecule. What seems clear, even from the way this molecule arranges itself with respect to the putative bimetallic adduct, is that the steric hindrance intrinsic to the chemical environment (be it the space

between the pyridine and the methyl, or between the methyl and the benzimidazole) is the key factor that governs the approach between the two.

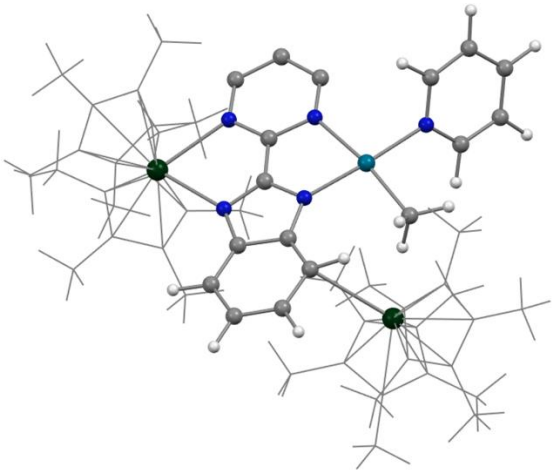

*Figure 3.25: Structure of **1.12-Yb$_2$'**, computed at the **ZORA1** level of theory. The Cp* are set in wireframe and most of the H atoms are hidden for clarity.*

3.2.3.4. Partial conclusions.

This theoretical study was aimed at elucidating the finer details in the mechanism of the C-H activation. The TS found for the precursor, **1.12-TS**, was the starting point, since it consisted a plausible approximation of the evolution of the pyridine and methyl moieties, if they are taken in isolation and if the evolution of the rest of the molecule is neglected. It is assumed that this is the transformation that gives the pyridyl and free methane following the reorganisation yielding the trimetallic adducts **2.6** and **2.7**.

It is perfectly clear that such behaviour occurring whilst there is only the Pd metal centre is not a faithful representation of reality, as **1.12** displays no tendencies to such evolutions. The calculations support this: the activation barrier for such a TS is far beyond what is attainable at the observed experimental conditions.

The obvious solutions in this regard are following the experimental observations step by step, to mime the coordination of the lanthanides and the ensuing electron transfer. In this regard, the calculations attempted on the coupled products **2.4** and **2.5** seem to set an upper limit on the size of the computable system. Simply put, performing additions of divalent lanthanide precursors on such structures and beyond is unrealistic.

It is in this vein that further approximations were carried out in order to find a reliable proxy of a system whose reactivity would credibly imitate that of **2.4** or **2.5**. The computed heterobimetallic adducts, **1.12-Yb** and **1.12-Sm**, represent half of the observed or putative coupled complex. The equivalent TS that were found for these structures are identical to that of **1.12-TS**, showing the H_α in transition from the pyridine to the methyl moieties. The corresponding vibration consisted of the see-saw motion from the two extremes, accompanied by the reorganisation of either host due to the imminent bond formation. It's worth remembering that the coupled products do not degrade by themselves *via* a C-H activation pathway.

This transformation was, therefore, screened from a methodological standpoint, as the variation of the computational parameters did not have a drastic effect on the transformation. A closer

examination of the energy barrier indicated that the Gibbs free energy was not the adequate metric to evaluate the transformation energy. This is attributed to an imprecise evaluation of the entropy by the computation. Although the increase of the entropy and of its TS→GS variation when going from the precursor **1.12** to hetero(bi)metallic species is consistent from a thermodynamic point of view, there was nevertheless an overcorrection at the **TS1** level of theory.

The careful reappraisal of this energy barrier placed it at around 30 kcal/mol above the GS, which would indicate that it would not be populated at r.t. It also shows that the addition of the lanthanide does not significantly affect feasibility of the C-H activation, as the two energy barriers are comparable. Further computations, which attempted to mimic the addition of a further electron to the edifice, point to the same conclusion.

This shows that the heterobimetallic complexes **1.12-Yb** and **1.12-Sm**, in themselves, cannot be used as accurate approximations of the reactivity of the coupled products with divalent lanthanides. However, **1.12-Yb** and **1.12-Sm** seem to be faithful representations of the coupled product themselves, as evidenced by both the TS computations and elements of their electronic structures.

The next step involved the addition of a second organolanthanide fragment to these heterobimetallic complexes, yielding **1.12-Yb$_2$** and **1.12-Sm$_2$**. These can help provide a glimpse into how the coordination of the second lanthanide is likely to occur. Due to the highly sterically encumbered environment of both of the coupled products, this matter is far from trivial. In both cases, the second lanthanide is coordinated at an angle with respect to the ligand and Pd plane. These solutions are plausible and, to an extent, pertinent even when extrapolated to the full, coupled product. Based on the computations, it would appear that the overall size of the Cp*$_2$Ln edifice is likely to be an important consideration, as the more compact Yb adduct is restricted in how close it can approach the pyridine and methyl moieties. The implications as to how this affects the beginning of the reorganisation towards the trimetallic complexes are currently under study.

3.2.4. Conclusion. Mechanistic summary.

The heterometallic Ln-Pd complexes described in this work are interesting additions to the budding field of intermetallics. The main difference with respect to its peers is the way by which the complexes **2.2**, **2.6** and **2.7** (as well as its pyridine analogue counterparts) are formed. In stark contrast to the straightforward reactions with known and controllable driving forces, as is the norm for the previously described compounds, the mechanism for these complexes is intricate, with interwoven dependencies and probabilities for the proposed individual steps. This section attempts to untie the Gordian knot and deduce some of the key features of this transformation.

The formation of **2.6** as a result of the interaction between **1.12** and divalent Yb was assumed to be due to the reaction between the rapidly formed coupled product **2.4** and free ytterbocene. This was corroborated by the fact that pure **2.4** does not evolve towards **2.6**, but isomerises towards **2.5**. The reactions with other reductants demonstrated that an electron transfer is not enough to trigger the rearrangement. Afterwards, the *in situ* reactions between **2.4** and ytterbocene, plus the kinetic study described in this section ultimately proved that the initial hypothesis was correct.

Regardless of whether the starting product is **1.12** or **2.4**, the addition of ytterbocene results in the formation of a significant number of unknown signals, which are common to both reactions. These transient species are evidently of the same parentage and, at longer reaction times, are consumed as long as divalent Yb is still present in the reaction media, resulting in a relatively clean final reaction mixture. The fact that the concentration of **2.6** increases even after **2.4** is no longer identifiable,

coupled with the abating intensity of the transient signal peaks, is a sign that these transient species are the last step prior to the final reorganisation towards the trimetallic adduct **2.6**.

Surprisingly, **2.6** is not the sole product formed during these reactions, as it is accompanied by **2.2** and **Yb_3(bimpym)$_2$**. This observation clarifies and obscures the reaction mechanism at the same time.[§] On the one hand, it adeptly explains the fate of the coupled bimpym ligands (they are present in **Yb_3(bimpym)$_2$**) and gives a logical alternative (the bridging bis-methyl fragment of **2.2**) to the formation of methane (following the C-H activation of the pyridine), which is not unequivocally proven.

On the other hand, if **2.2** is formed, bearing two methyl moieties, then the previously favoured C-H activation pathway cannot occur in parallel, as it reposes on a configuration where both the pyridine and the methyl are coordinated to the Pd centre. To rationalise the formation of **2.2**, a rapid ligand exchange of the Pd centres is proposed.

This has the advantage of a simple accounting of the three main ingredients: two of each of Pd, Me and pyridine reorganise to form one $PdMe_2$ fragment and one $Pd(pyr)_2$ fragment. In principle, one equivalent of the coupled products should give one equivalent of each of the main three products. This is very close to the ratio obtained following the reaction between ytterbocene and **2.5** (Table 3.5). Therefore, a ligand exchange-based mechanism is a very good fit for this reaction. Yet, this is far from the observed ratios following the same reaction with **2.4**, as, for example, **Yb_3(bimpym)$_2$** is always around twice as abundant as **2.2** and comparable in concentration to **2.6**.

The fact that **2.6** is accumulated in higher concentration and at a drastically different rate to the other products points to the fact that the ligand exchange hypothesis is either incomplete (it does not explain the C-H activation on the pyridine), or that, in this case, there is a competing mechanism.[**]

Another shortcoming of the ligand exchange hypothesis is that it cannot neatly account for the unmistakeable gaseous evolution that is observed when **1.12** or **2.4** is reacted with ytterbocene, and even more visibly, when the former is reacted with samarocene. The best fit for this release would be that of methane, but its slightly shifted attribution with respect to the reference leaves room for ambiguity.

Nevertheless, the formation of methane in tandem with the C-H activation on the pyridine is a good candidate for the aforementioned competing mechanism. The prevalence of each of the supposed pathways can be estimated by the conversion of **2.4** to **2.2**, which is the least abundant complex of the three formed. In this case, the conversion of the soluble methyls in **2.4** to those in **2.2** is around 15%.

Computations performed throughout this section propose a TS that competently renders the evolution of the activated proton and the methyl group. The energy profiles obtained from these computations show that this TS is not populated in the experimental conditions to which **1.12** or the coupled products were submitted. The caveat of this TS is that it does not account for the interaction with a divalent lanthanide fragment, which was shown to actually trigger the molecular rearrangement.

It was proposed that the difference in reactivity – both in terms of rate and of the ratio of the three products – of the two coupled products is due to their structural features. For example, it makes sense that the relative orientations of the Pd-py bonds in **2.4**, identical to that in the $Pd(pyr)_2$ fragment in

[§] …forcing the reader in a tortuous, hard to follow circular logical circuit that starts here.
[**] …and temporarily stops here.

2.6, favours the formation of the latter. This is supported by the fact that **2.6** is the dominant product in the reaction between **2.4** and ytterbocene, but is formed in almost equimolar quantity with **2.2** and **Yb_3(bimpym)$_2$** when **2.5** is used.

It is also possible that the difference in the relative configurations of the two coupled products is responsible for the drastically slower reaction rate observed for **2.5**. The working assumption was that the most likely coordination modes of the incoming ytterbocene were the spaces between the methyl and the pyridine groups, due to the considerable steric strain inherent to the coupled products. This hypothesis was challenged by the computed adducts **1.12-Yb_2** and **1.12-Sm_2**, which showed that multiple coordination modes were foreseeable.

In fact, only Cp^*_2Sm could nestle in between the methyl and pyridine groups. This was ascribed to the larger opening in between the Cp* groups afforded by the larger Sm^{III} ion (Figure 3.24), which allows a closer contact with the more encumbered pyridine group. Although these computed adducts are only approximations of the full-size coupled products, their coordination at an angle to the ligand plane should be compatible with the increased strain of the entire structure.

These findings are curious, because they suggest that samarocene and ytterbocene may interact differently with the bimpym-Pd fragment. This raises the obvious question: is it legitimate to assume that the formation of **2.7** goes through an analogous coupled product pathway? After all, no such compound could ever be inferred when **1.12** was reacted with samarocene. The closest hint that this mechanism is viable is a ^{1}H NMR spectrum following the reaction between **1.12** and the divalent lanthanide in the presence of lutidine (Figure 2.36). Even so, this product was not isolated.

Another indirect proof is provided by the best-fitting model of the resolution of the XRD data of **2.8**. This complex was initially ascribed to a [$Cp^*_2Sm(\mu\text{-quin})_2Pd$] formula, but further analysis pointed to the presence of precisely one quinolyl and one pyridyl group coordinated to the metals. Given that this species was obtained by reacting **1.12** and samarocene in the presence of free quinoline, this allows us to make a more educated guess as to the reaction mechanism.

This reaction, as is always the case when Cp^*_2Sm was involved, was nearly instantaneous. It would be logical that the initial C-H activation occurs on the pyridine of **1.12**, which could not have been substituted in the structure of the precursor, since it is not soluble in the reaction solvent (toluene). The second C-H activation would occur on a quinoline molecule, which is present in higher concentration in the reaction mixture and is most likely not coordinated to any Pd centre. Can this finding be extrapolated to imply that the source of the second C-H activation when forming **2.7** must be free pyridine, released in the environment from **1.12**?

This interpretation is compelling, since it is consistent with the experimental evidence that **2.6** is formed after the transient species, responsible for the numerous unknown ^{1}H NMR signals, react with free ytterbocene. The putative [$Cp^*_2Sm(\mu\text{-pyr})Pd$]-type adduct could very well have the same behaviour as the transient species in the case of the Yb-based trimetallic adduct. With this in mind, we may cautiously conclude that **2.6** and **2.7** are formed in a very similar manner.

The overall conclusion of the mechanistic study can be simply stated by carrying on the analogy of the Gordian knot. The complexity of the mechanism resulting in the trimetallic complexes was evident even prior to the undertaking of this series of analyses. Ultimately, we are not chemical Alexanders, cutting the knot in one fell swoop, since the mechanism cannot be explained in an uncomplicated manner. With the help of both experimental and theoretical tools, this chapter rationalises several distinctive elements of the reactivity of both coupled products in a plausible way and proposes a

number of hypotheses concerning the aspects that are inaccessible to the methods at our disposal. In other words, the knot was simplified.

3.3. Electronic structure of the heterometallic complexes.

The second major question revolving around the heterometallic complexes concerns their electronic structures. In all of them, short Pd-Ln distances are present. The primary objective is establishing whether there is any orbital interaction between the two complexes. Therefore, the adducts will be computationally reoptimised in the gas phase before a detailed examination of the electronic structure will ensue at the DFT and CASSCF levels of theory.

3.3.1. Trimetallic complexes.

The spectroscopic characterisation of the adducts, described in Section 2.3.2.2 leave no doubt as to the configuration of the metal centres. Therefore, the computations were run considering non-interacting Ln^{III} metal centres. This implies a triplet (S=1) for **2.6** and 10 unpaired spins (S=5) for **2.7**. The optimisation runs of the complexes were performed at the **ZORA2** level of theory. The main distances and angles are presented in Table 3.10.

Overall, the computations do an excellent job in reproducing the main features of the trimetallic adducts. Of particular interest is the relative distance between the Yb and Sm adducts. The XRD structures (within experimental error) point to a shorter Sm-Pd bond, which goes counter to the expected lanthanidic contraction. While the computations do not reproduce this phenomenon, the difference between the two distances is still much shorter than what would be expected, based on the ionic radii. Therefore, whilst the computations do not offer a perfect match for this specific metric with respect to the crystal structures, the data still point to an apparent deviation in the lanthanidic contraction, on the basis of the Ln-Pd distances.

	2.6		**2.7**	
Distance	XRD structure	**ZORA2**	**ZORA2**	XRD structure
Ln_1-Pd	2.924(1)	2.902	2.925	2.908(1)
Ln_2-Pd	2.924(1)	2.902	2.927	2.908(1)
Pd-C_{pyr}	2.078(4)	2.077	2.082	2.081(4)
Ln-N_{pyr}	2.275(3)	2.320	2.411	2.386(3)
Ln-C_{pyr}	2.773(4)	2.844	2.926	2.861(4)
Ln – Cp* ctr	2.342	2.370	2.470	2.449
<(C_{pyr1}-Pd-C_{pyr2})	178.88(18)	176.44°	176.43°	179.8(2)
<(Ln-Pd-C_{pyr})	64.76(1)	67.33	69.15	67.67(1)
<(Cp^*_1 ctr -Ln-Cp^*_2 ctr)	134.70	131.92°	135.64°	134.52

Table 3.10: Average lengths (in Å) and angles (in °) in the crystal and the computed structures of the trimetallic complexes. The values in red indicate a slight asymmetry (>0.1 Å) in the distances.

The electronic structure at the **ZORA3** level of theory was screened for orbitals with contributions from the Ln 4f electrons and the Pd 4d. These sub-levels were quite low-lying in energy – the 4f electrons were approximately 6.07 and 4.33 eV below the SOMO in **2.6** and **2.7**, respectively. There

were no definitive signs of orbital interaction in either case. The only orbitals that would fit the description were primarily ligand-dominated and presented only very feeble contributions from both metals (shown in the case of **2.7** in Figure 3.26).

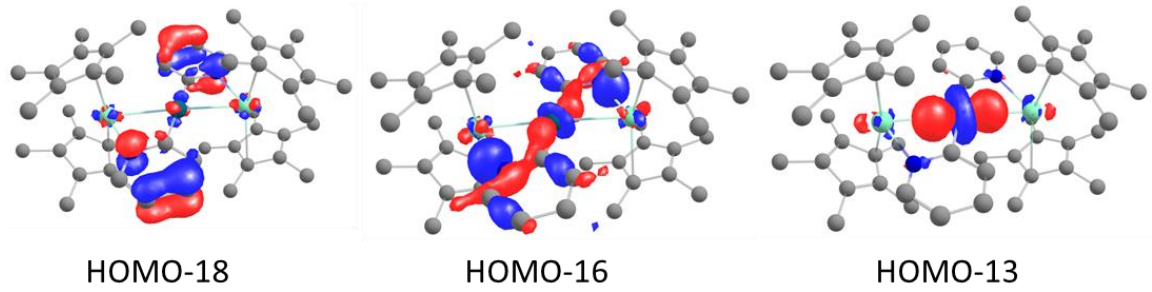

*Figure 3.26: Selection of orbitals of **2.7**, computed at the **ZORA3** level, containing contributions from both metals.*

Of note is the HOMO-13, in which a Pd 4dz^2 is pointed towards the two Sm^{III} centres (the same orbital can be found for **2.6**). It would appear that, at least, the Pd orbitals have the adequate symmetry to interact with the Ln^{III} centres. Despite this, the contributions from the Ln remain overwhelmingly small.

Further analyses were carried out at the CASSCF level, using the DFT-optimised geometries. For **2.6**, initial trials were performed with an initial (6,12) active space, but featured no contributions from the metal orbitals. In order to attempt to mix in the Yb 4f electrons and Pd 4d electrons in the active space, it was progressively increased up to the (12,16) configuration. This did not produce any measurable change in the electronic structure, though.

The active space on this species is occupied by a combination of bonding orbitals of the Cp* and pyridyl groups, and a pair of bonding and anti-bonding orbitals between the Pd and the pyridyl groups, with contributions from the Pd 4p and 4d electrons (Figure 3.27). The vacant orbitals included further Pd-pyridyl anti-bonding orbitals, as well as pyridyl-based orbitals of the same nature.

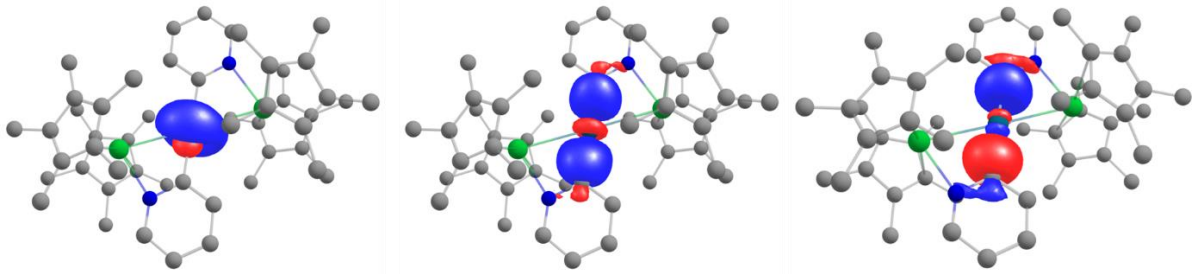

*Figure 3.27: Occupied CASSCF orbitals of the active space for **2.6**.*

In terms of orbitals of interest, there were a series of low-lying orbitals containing contributions from both the Pd and the Yb centres. These orbitals do not hint at a strong interaction between the two metals, as the metallic contributions are either not the main features of their respective orbitals, or they are highly polarised. Both of these scenarios are shown in Figure 3.28. For example, the Pd 4d contribution to the orbital shown on the right is around 4%, which qualifies it as an almost pure Yb 4f orbital. Slightly above these types of orbitals in energy are a series of pure Yb 4f electrons.

For the computations on **2.7**, the active space was also gradually increased, reaching a description of 18 electrons in 18 orbitals. In this case, the description of the electronic structure was much more straightforward. There were no signs of any intermetallic interaction at any level. The active space was

entirely composed of the Sm 4d and 4f electrons, whilst the vacant orbitals featured orbitals with predominant Sm 5f contributions.

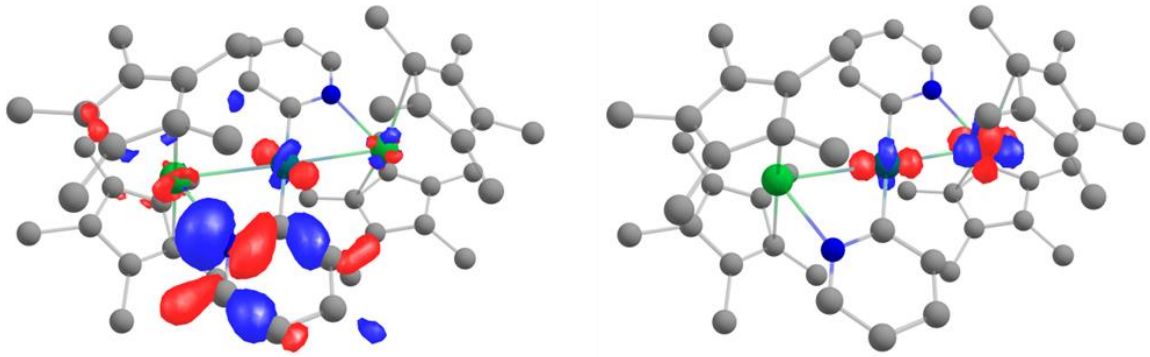

*Figure 3.28: CASSCF-generated orbitals of **2.6**, which contain contributions from both the Pd and the Yb metal centres.*

These conclusions indicate that the energy levels of the subshells of the two metals do not match and this is likely to be the cause of the poor or non-existing interactions between the Pd and the Ln. This assertion was tested by performing orbital permutations (a schematic representation is given in Figure 3.29). In the case of **2.6**, two types of such permutations were attempted: promoting either pure Yb 4f electrons or the orbitals bearing interactions between the metals into the active space at the expense of some of the Cp*-based orbitals. Only the shifting of Pd 4d orbitals into the active space was attempted in the case of **2.7**.

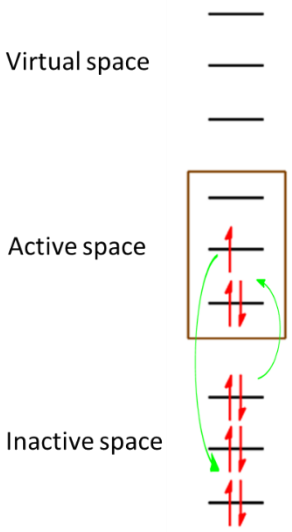

Figure 3.29: Principle of orbital permutations at the CASSCF level.

Regardless of the manoeuvre performed, the permutations did not succeed, since none of the attempted operations resulted in any interaction between the electrons already present in the active space and those that were promoted. There were no notable changes in the electronic structures, implying that such permutations were not realistic or plausible from an energetical point of view.

3.3.2. The methyl-bridged Yb-Pd complex.

The unusual structure of **2.2** raises several questions about the electronic interactions within the molecule. Is there an interaction between the Yb and the Pd metal centres, due to their close proximity? What is its magnetic configuration? The ^{1}H NMR data collected in a relatively narrow

temperature range would point to a doublet, on account of the paramagnetically shifted signals, presumably due to the $4f^{13}$ configuration of the Yb^{III} (Figure 2.13). However, a recent report described a mixed-metallic Gd-Pd complex (d(Gd-Pd) = 3.20 Å), where a large split in the peaks was observed in the EPR spectra, suggesting an axial perturbation by the Pd centre. This was indicative of electron density donation towards the lanthanide centre.[64] Perhaps the shorter distance in **2.2** could be conducive to an exchange coupling between the two metals.

In the absence of more experimental evidence that could substantiate these claims, we turned to theoretical computations. The geometry optimisations were carried out at the **ZORA2** level for three configurations – doublet, quadruplet and sextuplet. Clearly, the doublet is the most probable state and the latter two would require unlikely scenarios, such as an open-shell on the Pd centre and a considerable excitation to promote an electron to an unoccupied shell on either metal.

	Av. Values (Å or °)			
Distances	XRD structure	doublet	quadruplet	sextuplet
Yb-Pd	2.877(1)	2.922	2.852	2.960
Pd-Me_1	2.123(2)	2.116	2.226	2.157
Pd-Me_2	2.123(2)	2.120	2.209	2.155
Yb-H_{Me1}	2.179	2.196	2.307	2.408
Yb-H_{Me2}	2.233	2.205	2.310	2.383
Yb-C_{Me1}	2.552(2)	2.602	2.582	2.966
Yb-C_{Me2}	2.559(2)	2.602	2.586	2.941
Pd – Cp*ctr	2.017	2.036	2.163	2.316
Yb – Cp*ctr (avg)	2.332	2.359	2.376	2.317
Me-Pd-Me	117.92	118.71	119.16	135.87
Me-Yb-Me	90.78	88.91	95.47	85.17
Yb-Pd-Cp* ctr	177.65	179.31	176.94	178.33

*Table 3.11: Main distances and angles in the crystal structure of **2.2** and the computed structures, at different multiplicities.*

On the basis of the geometrical features, the sextuplet results in the worst reproduction of the crystal structure, as evidenced by the considerable deviations in the Yb-C_{Me} bond and the Pd-Cp* environment. Between the doublet and the quadruplet, the former does a better job, on average, although the distance between the Yb and the Pd is not in perfect agreement with the solid-state data. The doublet reproduces the finer features of the crystal structure better: the linear arrangement between Yb, Pd and the centroid of the Cp* and the way the latter isn't contained in the plane formed by the atoms of the Pd coordination environment (Figure 2.6). The geometry optimisation homogenises the Pd-C_{Cp*} bonds, as they are all contained in a smaller spread than in the crystal structure (2.332-2.407 Å).

The DFT calculations would place the doublet as the most stable state, with the quadruplet and the sextuplet being 28.20 kcal/mol and 100.82 kcal/mol above in energy, respectively. Due to the limitations inherent to the method, notably due not reproducing the relative energies of the 4f orbitals accurately, calculations were also performed at the CASSCF level (9,12). The geometries obtained at the DFT level were used as basis for the CASSCF calculations. All of these resulted in systems which were predominantly mono-configurational (>93% weight of the dominant configuration). The implications of these results will be discussed in larger detail below. At the CASSCF level, the order of

the three configurations remains unchanged, but the energy gaps now grow to 108.40 kcal/mol and 233.10 kcal/mol for the quadruplet and sextuplet, respectively.

Subsequently, the question regarding the interaction between the two metals was investigated at both levels of theory.

The electronic structure, computed for the doublet state at the **ZORA3** level, would not suggest any interaction between the two metal centres near the frontier orbitals. The most striking feature would be that the Pd 4dz^2 orbital is pointed towards the Yb (HOMO-8 in Figure 3.30), which would create the spatial conditions for an orbital interaction. The only orbital presenting any hints of participation from both metals is the HOMO-47, where both contributions are meagre. This Pd 4dz^2 does not participate in the bonding Pd-Cp* interactions. The Yb 4f orbitals are also quite low-lying in terms of energy, regardless of the methodology chosen.

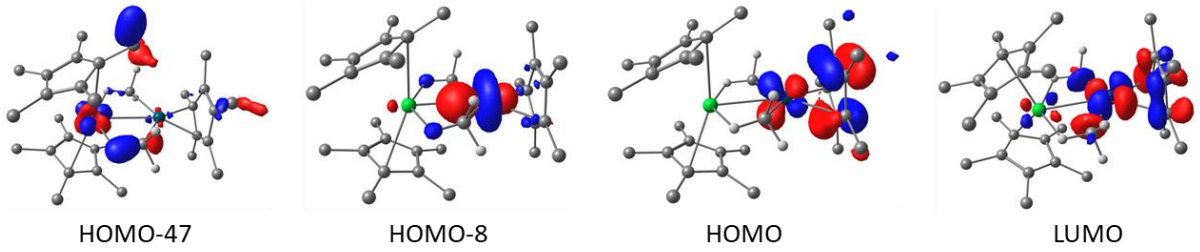

*Figure 3.30: Main orbitals at the DFT level for **2.2** in the doublet configuration.*

The electronic structure at the CASSCF (9,12) level is significantly different. The active space was chosen in order to include the 4f and 4d orbitals and a number of the corresponding electrons. The size of the active space was varied to monitor the evolution of the electronic structure. **2.2** was therefore calculated as a doublet at the (5,8) and (23,15) configurations. Increasing the active space lowers the weight of the dominant configuration, but has no impact on the orbitals themselves.

In the active space, the 9 electrons populate only Cp*-based antibonding orbitals, whilst the vacant orbitals involve similar interactions. Therefore, examining the relative occupations of the orbitals therein does not seem chemically pertinent, as they would play spectator roles in reactivity. The non-dominant configurations are not very influential, either, as they contribute to a variation of no more than 0.07 electrons in the occupancy of the orbitals in the active space.

The active space comprised of 9 electrons in 12 orbitals does not include the desired Yb 4f and Pd 4d electrons. Only in the (23,15) configurations are there Pd 4d electrons present. Below the active space, regardless of the active space, the Pd 4d electrons are involved in bonding interactions with the Cp* and methyl groups (sometimes with marginal contributions; Figure 3.31).

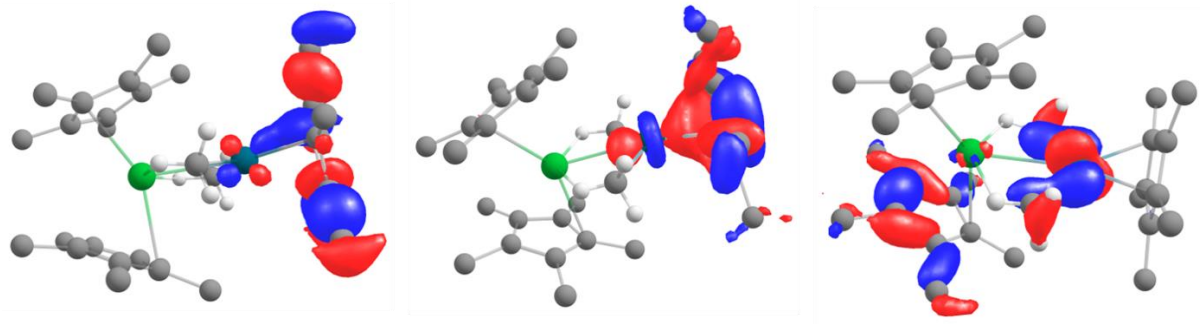

Figure 3.31: Involvement of Pd 4d electrons in bonding interactions, below the active space.

The remarkable feature of this compound is found within a series of closely packed (all within 1.1 eV) orbitals below the active space, containing significant participation from both the Pd 4d and Yb 4f shells. Some of the orbitals involve an interaction over the bridging methyl groups (Figure 3.32, right). There is some variation in the precise shape of these orbitals in between the computed multiplicities, but the conclusion is the same. Overall, these orbitals amount to 3 pairs of bonding and anti-bonding orbitals. This suggests a global bond order of zero between Yb and Pd. It is worth noting that, contrary to the DFT calculation, the Pd $4dz^2$ is involved in both bonding orbitals with the Yb and with the Cp*. This would be consistent with the observation mentioned above, that this orbital is pointed towards the Yb and this orientation may be related to the coordination environment of the Pd. Perhaps due to the difference in the description of the relative energy of the lanthanide 4f orbitals between CASSCF and DFT, the interaction with the Pd orbital is now enabled. This discrepancy will be examined in broader detail further on.

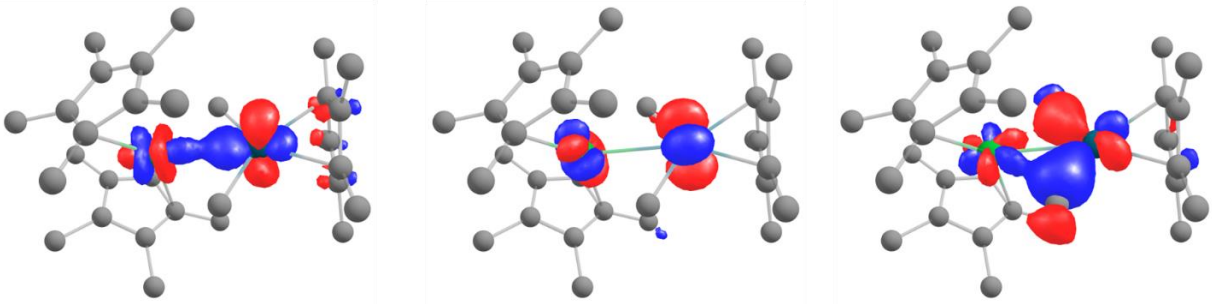

*Figure 3.32: Preview of some of the CASSCF orbitals of **2.2** that contain contributions from both metal centres.*

Previous examples of heterometallic complexes where wave-function methods were used found an interaction placed the contribution of the lanthanide at less than 10%, a figure which is clearly exceeded in this case.[29] The bonds in the cited example are qualified as dative. The analysis of the orbitals shown in the left and the centre of Figure 3.32 show Yb/Pd orbital contribution ratios of 63/37 and 60/40, figures which are unheard of in the literature. Given the controversy[65] surrounding the interpretation of Ln-TM "bonds", a knee-jerk assimilation of these results as evidence of covalent interactions is imprudent and would require extensive experimental and theoretical validation before a definitive attribution of its nature.

The most conspicuous void in the available data is the solid-state magnetic data, which would, at least, confirm the oxidation state of the Yb throughout the usual temperature range. Any deviation from the expected behaviour of Yb^{III} species[58,66] would be an invitation to examine further spectroscopic techniques for more insight.[3]

3.3.3. Further descriptors to analyse the interactions.

It would appear that, contrary to **2.2**, no important covalent interactions are present in the trimetallic adducts. This raises the question as to which forces help stabilise the unusual arrangements in complexes **2.6** and **2.7**. To this effect, further analyses on all three complexes were performed.

A quantitative appreciation of the main bonds in these complexes was sought. Some of the more frequently computed bond indices, used to gauge the strength of the interaction between two metals, were calculated. The Wiberg bond order (WBO)[67–69] and the Formal Shortness Ratio (FSR)[31,70] were both used in several influential works related to intermetallic distances. The latter is calculated as the ratio between the intermetallic distance and the sum of the covalent radii of the two metals. In this case, the references for the radii will be the values tabulated by Pyykkö.[71]

	2.6	**2.7**	**2.2**
WBO	0.62	0.77	0.53
FSR	1.01	0.99	0.99

Table 3.12: Bond indices computed for the Ln-Pd bond in the heterometallic complexes. "WBO" – Wiberg bond order; "FSR" – formal shortness ratio.

In both metrics, whilst not necessarily excelling, the complexes presented in this work are competitive with the references in the field. To the best of our knowledge, the highest WBO computed for Ln-M complexes is 0.83 for a Nd-Ga adduct.[17] The previously cited $U^{IV}Rh^{I}_2$ complex, described by the group of Liddle as having a double dative bond, presented a WBO of 1.30 and a head-in-class FSR of 0.87.[31] For further comparison, FSR_{LuNi} =0.90[29] and FSR_{LuPd} =1.03[27] in some of the more pertinent Ln-based heterometallic adducts. On this basis alone, it could be inferred that there are non-negligible intermetallic interactions in the three complexes.

QTAIM analyses were therefore pursued. The results for the main Bond Critical Points (BCP) are presented in Table 3.13.

	Property	ρ(BCP)	∇^2(ρ(BCP))	H(BCP)	DI
2.6	Yb-N_{pyr}	0.06	0.217	-0.008	0.339
	Yb-Pd	0.03	0.058	-0.007	0.267
	Pd-C_{pyr}	0.11	0.313	-0.033	0.860
2.7	Sm-N_{pyr}	0.06	0.183	-0.007	0.346
	Sm-Pd	0.04	0.083	-0.008	0.354
	Pd-C_{pyr}	0.11	0.305	-0.032	0.847
2.2	Yb-C_{Me}	0.04	0.129	-0.002	0.192
	Yb-Pd	0.04	0.064	-0.007	0.200

Table 3.13: QTAIM analysis of the trimetallic adducts. Nomenclature: ρ(BCP) – electron density at the BCP; ∇^2(ρ(BCP)) – Laplacian of the density; H(BCP) – energy density at the BCP; DI – delocalisation index.

There are several trends that stand out. In the classical interpretation of AIM theory, the value of the Laplacian ∇^2(ρ(BCP)) is an indication of the type of interactions, which is to be paired with the value of the total energy density H(BCP). The absolute values are related to the strength of the interactions. For example, a covalent bond is described by large negative values for both metrics, whilst positive ones correspond to ionic interactions. In our case, the values correspond to weak dative interactions.[72] Further, the delocalisation index (DI) is a measure of the quantitative sharing of electrons between the two considered atoms, but, according to Bader, is not equivalent to a bond order.[73]

In the trimetallic adducts, all the values are, overall, low, but are highest for the Pd-C_{pyr} bond, indicating that it is the strongest interaction among those that are more important to the binding of the molecular fragments to each other. There is not a significant difference between the same values for **2.6** and for **2.7**. This can be interpreted as follows: the previously used separation of the molecule into the $[Cp^*_2Ln^{III}]^+$ and $[Pd^0(pyr)_2]^{2-}$ is pertinent. In each fragment stronger interactions are present, that maintain each of the fragments together (notably the Pd-C_{pyr}) bond, but the attractive forces between the fragments themselves are not particularly strong (relatively weak Ln-N_{pyr} and Ln-Pd interactions).

As for **2.2**, QTAIM analyses would suggest that the strength of the interaction between Yb^{III} and Pd^{II} is very similar to those of the trimetallic complexes.

These conclusions for **2.6** and **2.7** are corroborated by ELF analyses. Valence basins, integrating for a larger number of electrons, are found for the Pd-C_{pyr} and Yb-N_{pyr} for both complexes (Figure 3.33, left and centre). Two valence basins were also found for Yb-Pd (no equivalent basin was found for **2.7**),

accounting for approximately 2 electrons, with a strong localisation index. This indicates that the electronic density is principally concentrated on the Yb^{III} centre, with low participation from the Pd.

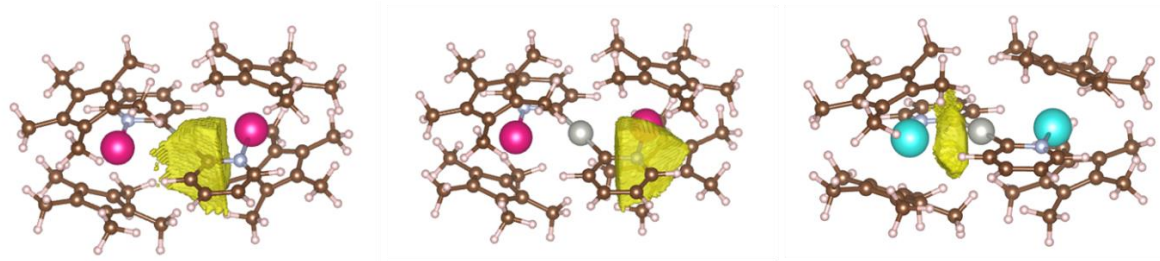

*Figure 3.33: Main ELF valence basins found for the trimetallic complexes, illustrating the Pd-C_{pyr} bond (left), Ln-N_{pyr} (centre, both computed for **2.7**) and the Yb-Pd interaction (right, only found for **2.6**).*

The same ELF analysis was performed for **2.2**. A valence basin between the Yb and Pd centres was located, with nearly identical metrics and conclusions to the ones presented above.

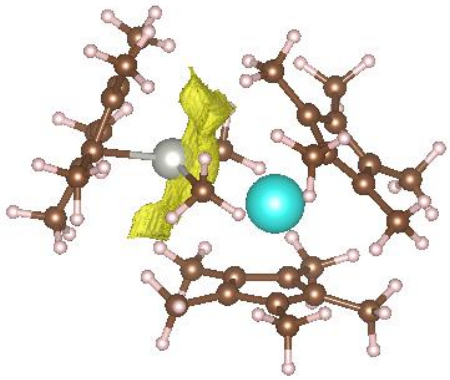

*Figure 3.34: ELF valence basin interposed between the Yb and the Pd centres, found for **2.2**.*

The forces that ensure that the atypical structures of the trimetallic complexes are kept in place therefore include a number of interactions that could be considered covalent. Another component that may contribute is the stabilising effect of dispersive forces. To that end, the Non-Covalent Interaction (NCI) mapping was performed. The NCI plots are ostensibly identical for both complexes (that of **2.7** is shown in Figure 3.35).

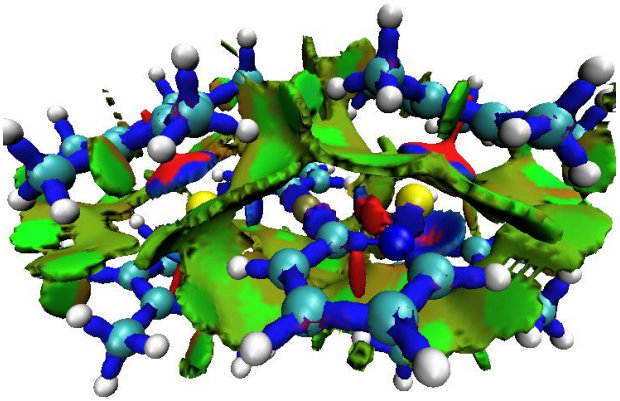

*Figure 3.35: NCI plot of **2.7**. Colour-code: repulsive forces – red, covalent interaction – blue, non-covalent interaction – green.*

Besides the expected and aforementioned covalent interactions, it is interesting to note that the $[Pd(pyr)_2]^{2-}$ fragment is englobed by a significant amount of non-covalent interactions with the Cp*

co-ligands on the Ln centres. Stabilising interactions are also found between the Cp* groups on the same and on opposite metal centres. Therefore, dispersive forces play an important role in stabilising these edifices. This is not surprising, as the large and relatively encumbered structures are conducive for these types of interactions.

To better quantify the contributions of each type of forces at play in the trimetallic adducts, Energy Decomposition Analyses (EDA) were carried out. Two different ways of splitting the complexes were envisaged (Scheme 3.13). First, one $[Cp^*_2Ln^{III}]^+$ fragment was split from the trimetallic complexes, leaving one $[Cp^*_2Ln(pyr)Pd]^-$ adduct. The second, describing the aforementioned partitioning into two $[Cp^*_2Ln^{III}]^+$ and one $[Pd^0(pyr)_2]^{2-}$ fragments was proposed. The former was inspired by the findings, presented in Section 3.2.2, inferred from the formation rates of **2.6**, after the reaction between ytterbocene and **2.4**.

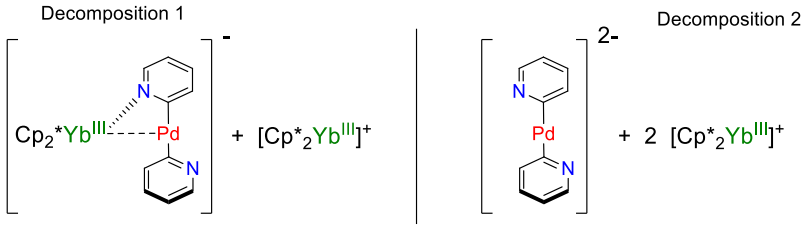

Scheme 3.13: The two proposed decomposition schemes for the EDA analyses.

Following on the methodology described by the group of Hall in a recent work,[65] the fragments were to be computed as either charged or neutral fragments. This allows a more nuanced interpretation of the electrostatic interactions between the chosen fragments. As is intuitive, the relative contributions from such interactions are enhanced if charged fragments are considered. However, due to the significant computational cost of such calculations, only the decompositions based on neutral fragments were performed. The breakdown into each energy component for the two decomposition schemes is shown in Table 3.14. The EDA analyses were sensibly identical between the two complexes, therefore only the data for **2.6** is presented.

	Decomposition 1	**Decomposition 2**
Pauli repulsion (steric)	227.55 (62.07)	466.59 (42.44)
Electrostatic	-165.47	-404.15
Orbital	-160.41	-203.61
Dispersion	-22.59	-32.69
Bonding Energy	-120.92	-193.87
Orbital %	*46*	*32*

*Table 3.14: EDA results for complex **2.6**, following the two proposed decomposition schemes. All energies are given in kcal/mol.*

It is not very surprising that the electrostatic contributions and the Pauli repulsions in Decomposition 2 are roughly two times larger than that of its counterpart, as it twice considers the interaction between the Ln and the Pd fragments. However, not all of the components vary in the same proportionate way. Most notably, the orbital contributions from the two decomposition schemes are within 20% of each other. This difference could be rationalised by an underestimation of the covalent forces that come into play for the two separate interactions in Decomposition 2. Nevertheless, this comes to show that there is a good measure of stabilising orbital interactions that help keep the structure in place.

The same analyses could be carried out for both charged and neutral fragments configuration for **2.2**. In this case, the decomposition separated the same $[Cp^*_2Yb^{III}]^+$ fragment as for the trimetallic adducts and a $(Cp^*PdMe_2)^-$ fragment.

Computing the fragments as charged fragments increases the overall bonding energy by more than 55 kcal/mol. This is due to the Pauli repulsion, which is decreased fourfold. Curiously, the attractive electrostatic interactions are within 5 kcal/mol of each other in both cases. When the fragments are computed as neutral species, the orbital interactions play the dominant role in the overall bonding energy.

	Neutral fragments	**Charged fragments**
Pauli repulsion (steric)	424.94 (261.15)	102.54 (-65.62)
Electrostatic	-163.79	-168.16
Orbital	-354.5	-83.75
Dispersion	-17.94	-17.94
Bonding Energy	-111.29	-167.31
Orb%	*66*	*31*

*Table 3.15: EDA results for complex **2.2**, computed as either neutral and charged fragments. All energies are given in kcal/mol.*

3.3.4. Partial conclusion.

The short distances between the Pd and the Ln centres in the three heterometallic complexes described in this work could have suggested intermetallic communication between the metal centres. This assertion prompted a theoretical study into their electronic structure.

The topological analyses undertaken so far support the assertion that there is no significant covalent interaction between the Pd and the Ln centres in **2.6** or **2.7**. A weak, dative interaction can be inferred. This would indicate that the short intermetallic distance is not sufficient to enable a stronger interaction between them. This conclusion is slightly antithetical to some of the more intuitive chemical considerations, related to the extrapolations between bond length and the strength of the interaction.

The computed data validates the premise of a lack of any electron sharing in the case of the trimetallic adducts. There is no evidence for any electron transfer between the Ln and the Pd, since the solid-state magnetic data unequivocally point to Ln^{III} centres across the entire studied temperature range. Therefore, the Pd is zerovalent. Arguably, the electron transfer from ytterbocene to the coupled products **2.4** or **2.5** is the triggering step for the genesis of these trimetallic complexes, but the experimental data does not support any strong interaction between the metals once the complex is formed. Further analyses, such as EPR or XAS, could be carried out for a finer understanding of the configurations of the major components – Ln, Pd, pyridyl groups – of the complexes **2.6** and **2.7**.

It should be noted, however, that these bond orders are extrapolated on the basis of covalent radii, which, themselves, are empirically created averages for each element. Without experimental and theoretical support, the bonding schemes they infer should be interpreted cautiously. Their predictive powers could be poorly adapted to the minute variations due to the specificities of various chemical parameters, such as choice of ligands or the steric constraints of the environment. Moreover, the continuous evolution of the theoretical bases of the organometallic chemistry of lanthanides would suggest that there is much yet to learn as to their behaviour in complex situations, such as their redox

chemistry or of multiconfigurational ground states.[74,75] This would, logically, also apply to a field so dependent on subtle chemical considerations, such as lanthanide-based intermetallics.

This may explain some small inconsistencies in the data for the trimetallic adducts. Both of them have roughly the same FSR, but differ in the WBO. The one with the highest apparent bond order – **2.7** – offers no sign of any orbital interaction in the electronic structure and its ELF data shows no valence basin corresponding to the Sm-Pd interaction.

On the other hand, the complex with the lowest WBO – **2.2** – has a very intriguing set of orbitals, showing a strong participation from both metals – a unique situation in lanthanide-based intermetallics. Despite this apparent sharing of electrons, it is important to remember that the bonding and anti-bonding orbitals in **2.2** even each other out (3 each). Therefore, the electronic structure at the CASSCF level is consistent with the overall low bond order between the two metals, that is suggested by the topological analyses.

The EDA analyses for this complex offer an eloquent demonstration as to why the methodology chosen has a significant impact on the result. Computing the fragments as either neutral or charged species drastically alters the relative weight of either the electrostatic or the orbital contributions. In this respect, the work of the group of Hall is, once again, pertinent.[65] The EDA analyses carried out in the cited work resulted in comparable differences in the relative contribution of the attractive electrostatic energy, depending on the charge of the fragments.

Specifically, for computed La-Fe or Lu-Fe compounds, the percentage of the electrostatic energy was circa 74% and 41 or 56% when the fragments were computed as charged and neutral species, respectively. The percentage of electrostatic contribution was compared to EDA results for other typically ionic bonds, such as Ln-X (where X is a halide) bonds, finding the same overall percentage. In contrast, for a Zn-Fe interaction, of a significantly more covalent nature, the electrostatic interaction accounted for 64.6% in this case. The authors concluded that the EDA analyses pointed to a strong ionic bonding character in the Ln-based intermetallic interaction.

In our study of **2.2**, this percentage is 69% – an intermediate figure between a presumed ionic interaction and a covalent one. This would, in theory, support the observations issued from the orbitals at the CASSCF level of theory (Figure 3.32), where there are multiple orbitals with significant participation from both metals.

Contrary to the case of the trimetallic adducts, it was not possible to obtain, at least, the solid-state magnetic data required to arbitrate the contradiction between the electronic structure and topological analyses. *Ab initio* calculations of magnetic properties could prove to be a competent substitute, due to their proven track record in giving a very good estimation of the magnetic properties of organometallic complexes.[76–78] Efforts are currently invested in this direction.

In the absence of such data, further theoretical work was carried out to delve into the origins of the Yb-Pd orbital interactions.

3.4. Theoretical computations on the $Cp^*_2REMe_2TMCp^*$ structure.

As shown in Figure 3.32, there is an unusual amount of orbital interaction between the two metal centres in **2.2**. This situation is atypical for 4f-TM compounds, as it is assumed that the f-electrons of the lanthanide series have insufficient radial extension to reliably form orbital interactions. It seems reasonable to assume that these bonding orbitals contribute to the stabilisation of the complex.

Furthermore, the presence of a number of methyl-mediated orbitals would suggest their key role in favouring such a close interaction.

As such, it was unknown at this conjecture what factor is responsible for the unusual orbital interaction at the CASSCF level between the Yb and the Pd. One of the crucial questions to be answered *via* spectroscopic analyses is whether the orbital interaction is actually manifested in an experimentally verifiable exchange of electrons. Additionally, an obvious question to be examined relates to the difference between **2.2** and **2.6**, where no comparable interactions were observed, which is an agreement with some of the experimental data (most notably, solid-state magnetism). Clearly, there are several important distinctions between the two complexes, related to the oxidation state of the Pd, its chemical environment and the bridging units between the two metals (methyls vs pyridyls).

In absence of experimental data, we turned to theoretical computations. A series of complexes was computed in order to probe the influence of all of the potential elements in this structure. All the complexes in this Section were optimised at the **ZORA2** level of theory. Since the bonding orbitals were obtained at the CASSCF level of theory, our efforts were focused on this method, permitting a pertinent comparison with the data obtained for **2.2**.

3.4.1. Dependency on the Pd coordination environment.

It is plausible that the Pd coordination sphere helps spatially block the Pd in close proximity to the Yb and therefore orientate its 4d orbitals towards the Yb 4f electrons. But this, in itself, might not be enough to enable an interaction. As there are other examples in the literature of relatively short Pd-Ln distances, it is pertinent to wonder if there is a minimal required distance that would enable an electronic interaction. Within this discussion, it is opportune to also query whether the relative orientation of the plane formed by the coordination sphere of the Pd centre with respect to the lanthanide is also a requisite condition for an interaction. Indeed, a good matching of the orbital symmetries is required for a good overlap and the angle of the aforementioned coordination sphere of the Pd is likely to be an influential metric. The computed compounds in this section will probe both factors.

Furthermore, the chemical nature of both the bridging methyls and the Cp* will be changed to test their impact on the orbitals featuring the contributions of both metals. Unless stated otherwise, all complexes herein have been characterised at the CASSCF level with a (9,12) active space.

As all the computed complexes that will be considered in this Section are bound to alter the calculated Yb-Pd distance, it is useful to examine, all other things being equal, the range within which we can find the specific orbital interactions discussed in the previous section. To this regard, a series of homologues of **2.2** were computed, where the Yb-Pd distance was fixed at given values.

The Yb-Pd distance was varied from 3.00 Å to 3.20 Å in 0.05 Å increments. Helpfully, in all cases, these different distances did not lead to significantly altered geometrical environments. The molecular scaffold is invariable – the Yb-Pd-Cp* ctr angle is contained in the (179.31°-179.91°) range throughout the study. This should imply that any divergence in the electronic structure is exclusively due to the evolution of this specific metric.

The only changes observed – decrease in the Me-M-Me angles and lengthening of the Yb-C_{Me} bond length – are inherent to the stretching of the structure. It's worth remarking that the Pd-C_{Me} and Yb-H_{Me} bond lengths are almost constant throughout the studied range. Conversely, the distances with

respect to the centroids of the Cp* co-ligands decrease for both metals (by about 0.2 Å in both cases). We attribute this to a greater electrostatic interaction between the Cp* groups and the metals.

The gradual increase of this distance did not lead to a dramatic change in the computed orbitals. The characteristic orbitals, bearing contributions from both metal centres, are still present. The key difference is that the relative participations become increasingly one-sided. Case in point: the orbital bearing an interaction between the Pd $4dz^2$ and the Yb 4f orbitals shown in Figure 3.32 evolves upon the lengthening of the bond: the direct overlap disappears at 3.00 Å and the contribution of the Pd initially increases (not shown in Figure 3.36), before diminishing dramatically. In the case of the methyl-bridged orbital, the evolution is two-fold: the contribution of the Yb increases during all the range at the expense of Pd one. The methyl contribution steadily decreases, up to the point (at 3.15 Å), where it disappears almost entirely. These conclusions ought to be measured prudently, as the electronic structure is not entirely invariant upon the lengthening of the distance. The orbitals shown in Figure 3.36 are simply the best fit for their peers observed at a shorter distance.

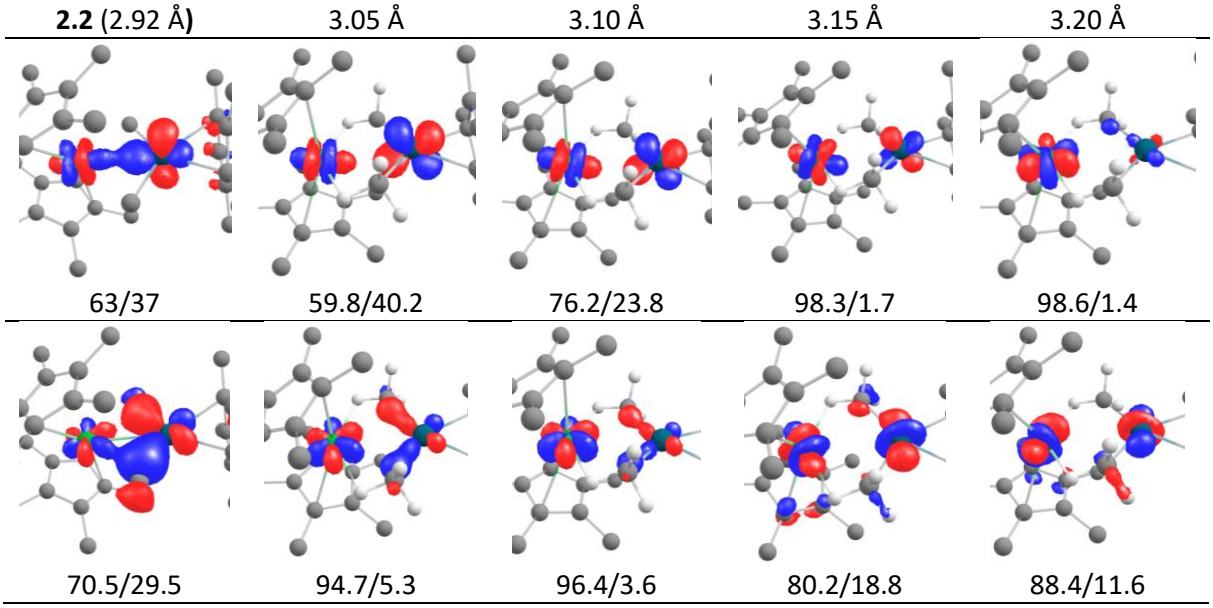

Figure 3.36: Evolution of two CASSCF orbitals across the lengthening of the bond and their relative Yb/Pd contributions (in %). The upper line shows the orbital bearing an interaction between the Pd $4dz^2$ and the Yb 4f orbitals and the bottom line shows the methyl-bridged orbital. The Cp co-ligands are cropped and the complex where d(Yb-Pd) = 3.00 Å is not shown for clarity.*

In this sense, it becomes apparent that the orbitals of **2.2** showing a hybridisation of both metals are the result of significant electronic perturbation of the Yb 4f orbitals by the Pd 4d electrons. The farther the Pd is, the less capable it is of affecting its partner. It is remarkable, though, that a non-negligible effect remains even at 3.10 Å.

The next effect that was probed was the ligand environment of the Pd centre. The objective is to investigate the relation between, on one hand, the chemical nature of the coordination sphere and, on the other, the symmetry that is imposed by it. Of particular importance is the relative orientation of the square plane defining the Pd towards the Cp^*_2Yb fragment.

In that respect, the first step was to study whether the bridging function plays any role as an electron relay from the Pd towards the Yb. The complex that was computed replaced the bridging methyl moieties with hydrides – **YbH_2Pd**. In principle, this substitution should preclude any hyperconjugation that would be afforded by the carbon atom.

The structural features of **YbH$_2$Pd** present no surprises. The smaller bridging moiety imposes shorter distances all around (M-Cp* centroids), as well as more acute angles. The Yb-Pd distance is slightly larger than in the computed structure of **2.2** (2.945 Å vs 2.922 Å). From an electronic standpoint, there is no significant difference with respect to the methyl-bridged complex. There are even a number of orbitals involving the hydrides, along with the two metal centres (Figure 3.37).

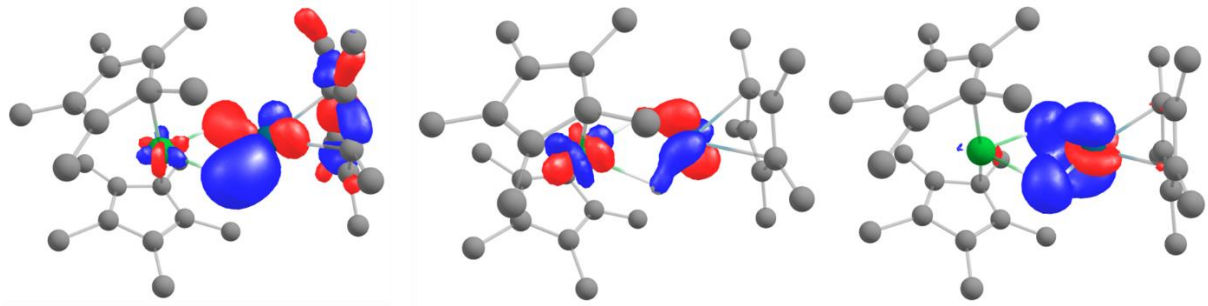

*Figure 3.37: Main CASSCF orbitals of **YbH$_2$Pd**, highlighting the orbitals involving the bridging hydrides.*

Subsequently, the role of the Cp* co-ligand on the Pd was examined.

The Cp* was replaced in two complexes by cyclononatetraenyl (Cnt) – a larger equivalent of Cp*, used in our laboratory[79] (**YbPdCnt**) – or 2-pyrimidine-(1H-imidazol-2-yl) (a smaller equivalent of the bimpym ligand – **YbPd(impym)**). The rationale behind these choices was to also explore whether introducing ring slippage (owing to the much larger size) or replacing the highly σ-donating Cp* with a π-acceptor, respectively, would engender any noticeable changes in the electronic structure of the complex.

Lastly, a third complex was computed, where the anionic ligand was put in the outer sphere. To that effect, two MeCN were introduced in the coordination sphere of the Pd, with the bulky tetraphenylborate anion completing the outer sphere (**YbPdBPh$_4$**).

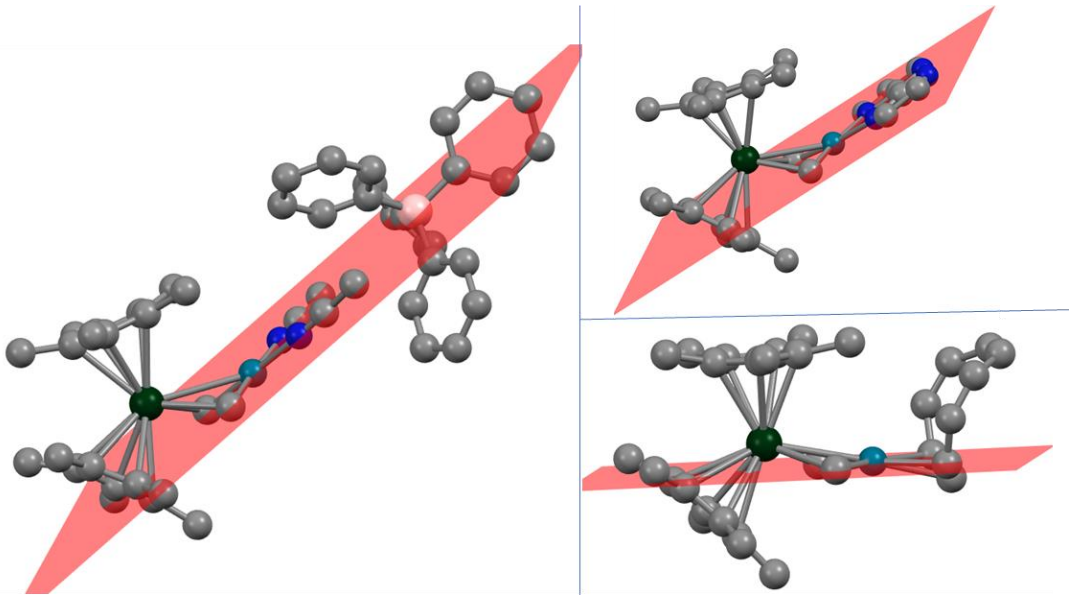

*Figure 3.38: Computed structures of **YbPdL**, where L is the anion replacing Cp*. The plane determined by the Pd substituents is calculated (shown in red) to highlight the relative orientation with respect to the Yb centre. Left: **YbPdBPh$_4$**; top right: **YbPd(impym)**; bottom right: **YbPdCnt**.*

All three complexes are shown in Figure 3.38. With regards to the Pd centre, **YbPdBPh$_4$** and **YbPd(impym)** are both square planar complexes. A square plane can be identified in the case of **YbPdCnt**, as well (as shown in the calculated plane in Figure 3.38), but the Cnt is η^3-coordinated, and

all three Pd-C_{Cnt} bonds are almost equal in length (2.25-2.27 Å). The rest of the ring dearomatizes and thus is deformed, as the Cnt ligand is wont to do when smaller metals coordinate it.[80] It is evident that all three complexes induce deviations from the geometry of **2.2**. This effect is less significant in **YbPdCnt** – the angle formed between the square plane of the Pd coordination sphere and the one formed by the Yb and the two methyls is 23.92°, whilst this value is 42.45° in **YbPd(impym)** and 47.65° in **YbPdBPh$_4$**. For reference, the same angle in the optimised structure of **2.2** is 13.94°. The Yb-Pd distances are, in the same order of the complexes, 3.064 Å, 3.090 Å and 3.197 Å.

The electronic structures of these three compounds show, as a rule, fewer pure Yb 4f - Pd 4d orbitals than in the case of **2.2**. Pure 4f-4d orbitals designate those which contain little orbital participation from the other fragments of the molecule, notably the Cp* groups. There are more orbitals where there are non-negligible contributions from either the Cp* bound to the Yb or from the anionic ligand (Figure 3.39). This effect is again less pronounced in the case of **YbPdCnt**, compared to the other two structures – the contribution of the two metals to the orbital exceeds 94% in some of the concerned orbitals, whereas none could be found where this proportion reaches 80% in the other two. In the second type of orbitals, the relative contributions of the Yb and of the Pd may seem to also be quite equitable, but the orbital involvement of the other groups skews this perception. Therefore, these orbitals are not the best reference for a comparison with the electronic structure of **2.2**.

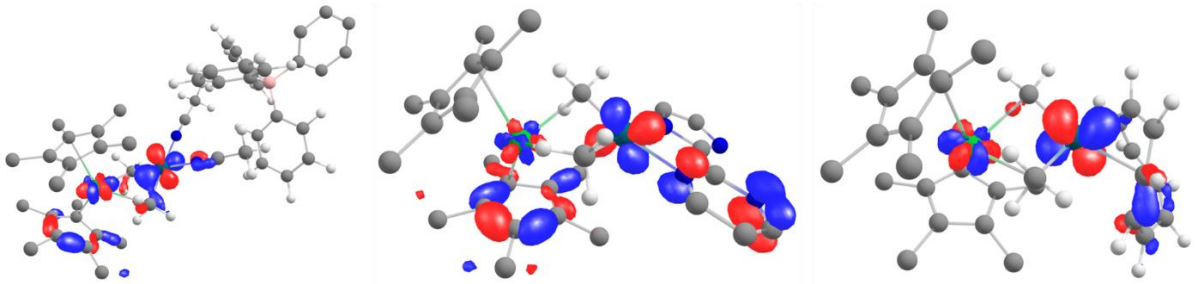

*Figure 3.39: Examples of CASSCF orbitals of the **YbPdL** series, presenting involvement of other fragments of the molecules, other than the metal centres.*

In the pure Yb-Pd bonding orbitals, however, the relative contributions of each metal tend to be significantly more one-sided (where participation from the secondary metal plateaus around 14%) than in the parent complex. This, again, affects, **YbPdCnt** the least of the three (where this figure can reach 17.6%). The contributions become more balanced in the anti-bonding orbitals, with the added caveat that such orbitals also involve considerable participation from other atoms.

Given the dependency on the Yb-Pd distance discussed above, it could be argued that the lesser inter-metallic interaction is due to the increased distance, which is no longer propitious for orbital overlap.

To probe this effect, all three complexes were reoptimized by fixing the Yb-Pd distance to that in the parent complex, **2.2** (2.92 Å). The shorter distances imposed changes in the geometries of the complexes, but these mostly affect the aforementioned angles between the coordination sphere planes (Table 3.16). Even so, these shifts are not consequential enough to invalidate the comparison of the effect of the three anions.

It would appear that in the case of **YbPdCnt** the interaction between the metals becomes even more favourable, as the pure Yb-Pd orbitals show up to a 76/24 split (compared to 17.6% in the unrestricted geometry). This amelioration is most likely due to a mix of the closer distance and the more acute angle, both of which should favour the orbital overlap between the two components.

	Relaxed geometry	Fixed Yb-Pd distance (2.92 Å)
YbPdCnt	23.92	18.90
YbPd(impym)	42.45	45.60
$YbPdBPh_4$	47.65	57.75

Table 3.16: Angles formed between the planes of the coordination spheres of the Yb and of the Pd. All values are in °.

In the other two complexes, there is not a significant evolution of the relative contributions from each metal in the pure Yb-Pd bonding orbitals. The comparison is particularly salient in **YbPd(impym)**, as the angular variation between the relaxed geometry and the one with the fixed Yb-Pd distance is small. Since the relative contributions of each metal do not vary in a meaningful way between the two geometries of **YbPd(impym)** (Figure 3.40), the implication herein is that the orientation between the metals is a more significant metric than the distance between them.

	YbPd(impym) (3.09 Å)	**YbPd(impym)** (2.92 Å)
Total contribution to orbital from metals	77.2%	84.0%
Orbital	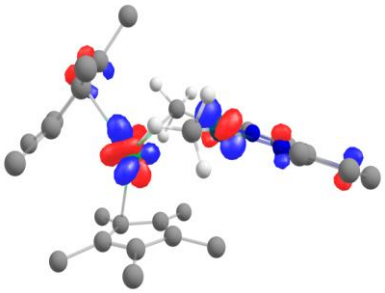	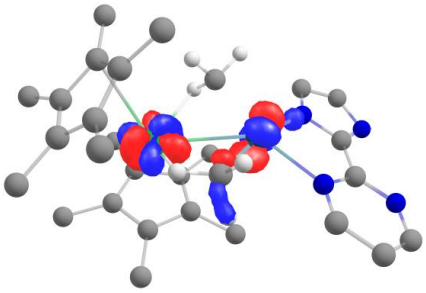
Yb/Pd	86.6/13.4	87.2/12.8

*Figure 3.40: Evolution of a CASSCF orbital computed for the two configurations of the **YbPd(impym)** complexes: unrestrained (3.09 Å) and restrained Yb-Pd distance (2.92 Å). The relative Yb/Pd contributions (in %) are given in the bottom line. Due to variation in the shape of the orbitals upon the changing of the distance, the presented orbital is the best available fit.*

3.4.2. Dependency on the transition metal.

Our synthetic trials performed by changing both the Pd and Yb reactants with homologous Pt and Sm compounds, respectively, have heretofore failed to yield isostructural $Cp^*_2LnMe_2TMCp^*$ complexes.

The presumed reaction mechanism, predicated on the reorganisation of the putative **Yb(bimpym)Pd** complex towards **Yb_3(bimpym)$_2$**, may be highly dependent on the stabilisation of transient species. It is unknown why the Pd^{II} fragment is capable of maintaining the structure, whereas the homologous Ni and Pt species cannot. Based on the observations of the **K(bimpym)TMMe$_2$** family, the sole argument that springs to mind is related to the ion size – Pd^{II} is slightly larger than its congeners. Therefore, perhaps similar species could be obtained with larger divalent metals, such as Ca^{2+} or Mg^{2+}.

All the compounds calculated from hereon in shall be shortened to the **LnTM** nomenclature, with Ln indicating the metal substituting Yb and TM – the Pd centre. The TM will be metals in the +2 oxidation state. In all cases, geometry optimisations were carried out at first at the DFT level. Frequency calculations confirmed that the optimised structures corresponded to minima. The cases where this was not possible will be discussed individually in the subsequent sections.

The first set of computations were carried out in order to examine whether **2.2** being formed was uniquely due to specific interactions with the Pd. The most obvious candidates for an initial study are Pd's group 10 stablemates. Consequently, **YbPt** and **YbNi** were calculated as doublets.

	Av. Values (Å or °)		
Distances	**YbNi**	**2.2**	**YbPt**
Yb-TM	2.964	2.922	2.911
TM-Me	1.991	2.118	2.101
Yb-H_{Me}	2.138	2.200	2.173
Yb-C_{Me}	2.582	2.602	2.618
TM – Cp*ctr	1.787	2.036	2.010
Me-TM-Me	117.42	118.71	120.90
Me-Yb-Me	82.50	88.91	88.57
Yb-Pd-Cp* ctr	179.12	179.31	177.53

Table 3.17: Main distances and angles in the computed YbTM series, where TM are the group 10 metals.

These structures kept the overall geometries of **2.2** – all three compounds keep the distorted square planar configuration of the TM. The Ni^{II}-Cp* centroid distance is in the range of previous referenced complexes in the literature (1.75-1.83 Å).[81,82] Pt-Cp* complexes, as for Pd, are quite rare species (only 13 structurally authenticated compounds), and the computed Pt-centroid distance is slightly longer than the other Pt^{II} examples.[83–85]

On the basis of the geometrical features, the interaction with the organolanthanide fragment is different in the case of **YbNi**. The intermetallic distance is lengthened. In comparison with the other structures, the Me-M-Me angle remains identical for Ni, but is reduced for Yb. This may have to do with the steric constraint associated with approaching the Cp* groups to one another.

Perhaps owing to the larger Yb-Ni distance, the electronic structure of **YbNi** presents some differences to **2.2**. There are still some orbitals with contributions from both metals, but they are both fewer (3 vs 10) than in the case of **2.2** and these interactions seem less clear-cut. For example, in the orbital shown in the centre of Figure 3.41, the contributions from Yb and Ni account for 9.4% and 6.3% respectively. For the orbital shown on the right, those figures are 3.8% and 8.8%. Furthermore, it would appear that the Ni $3dz^2$ is oriented perpendicular to the Yb-Ni axis (Figure 3.41, left). This is unusual, since there are no obvious reasons why the orbital interaction with the Cp* would be forbidden. The orientation of the dz^2 orbital was speculated to be one of the conditions enabling the Yb-Pd interaction in **2.2**. At this stage, it is unclear precisely which factor is responsible for the divergence of the two electronic structures.

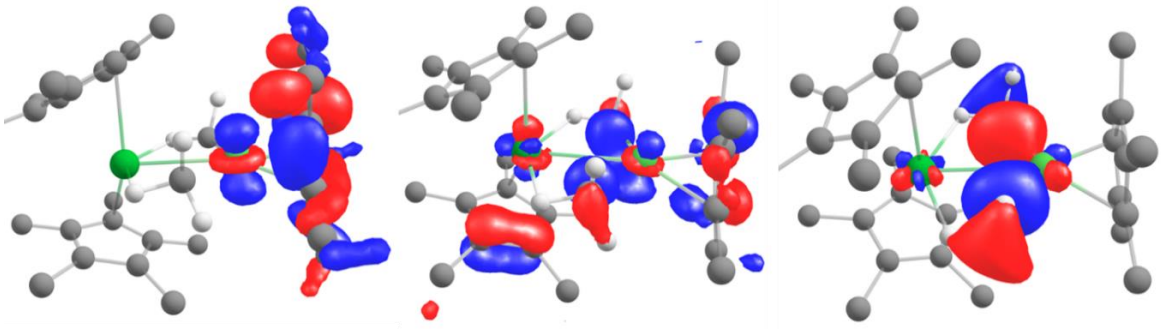

*Figure 3.41: Preview of some of the more salient CASSCF orbitals of **YbNi**.*

Conversely, **YbPt** effectively mirrors **2.2**'s behaviour. The same Pt 5d-Yb 4f orbitals are present.

In order to try to narrow down the list of factors contributing to the Yb-Pd bond, several other metals were screened. Due to the higher simplicity of calculating neutral species, metals having a stable +2 oxidation state were favoured. Unless otherwise stated, all complexes were computed assuming low-spin states on the TM, therefore a global doublet state. The active space for the CASSCF calculations was kept to 9 electrons in 12 orbitals.

The presence of *n*d electrons in the valence shell proved to be necessary, as the alkaline earth metals showed no sign of interaction. Their large ionic radii imposed deviations from the geometry of **2.2**, notably in the orientation of the methyl functions, but this was shown not to be essential in the previous sections.

In the case of group 8 metals, the findings were slightly surprising. Although neither **YbFe**, nor **YbRu** presented any significant interaction with the Yb centre, as is the case of **2.2**, there were more orbitals involving both the 4f and 3d shells in the case of Fe than there were 4f-4d for Ru. Perhaps this difference can be rationalised by the structural features of the two complexes. Contrary to the Ni-Pd pair, the Yb-Fe distance is much shorter than the Yb-Ru distance.

In a first approximation, the group 9 and 11 adducts were calculated to be isoelectronic to their peers in the group 10. A similar principle was applied in a study of the activation barriers towards C-H activation of methane, carried out by the group of Bickelhaupt.[86] Therefore, the group 9 complexes are calculated as anionic doublets, whereas group 11 are computed as cationic doublets. A simplistic summary of the interactions of these **YbTM** complexes is presented in Table 3.18.

Alkaline	Transition metals			
Mg	Fe	Co^-	Ni	Cu^+
Ca	Ru	Rh^-	Pd	Ag^+
Ba		Ir^-	Pt	Au^+

*Table 3.18: Computed **YbM** complexes. "+" indicates that the complexes were computed as cations, "-" as anions. The green filling for each respective metal indicates the presence of Yb-M interactions. The relative strength is colour-coded: very pale green indicates weak interaction, green indicates pure 4f – nd orbitals with dominant contributions from one metal and dark green indicates more equal contributions from said orbitals.*

The availability of all the redox states from +1 to +3 for the group 9 and 11 metals is a good opportunity to also investigate the correlation between the Yb-TM interaction and the charge of the TM. Specifically, the objective of this study is to gauge the influence of the energy levels of the d sub-shell of the TM. Therefore, all the complexes were reoptimised in the respective configuration. All the charged compounds maintained the same active space, whereas the neutral adducts were computed as singlets at the (10,12) level.

Co^+	Co	Co^-	Cu^+	Cu	Cu^-
Rh^+	Rh	Rh^-	Ag^+	Ag	Ag^-
Ir^+	Ir	Ir^-	Au^+	Au	Au^-

Table 3.19: Evolution of the Yb-TM interaction for the three possible oxidation states of the group 9 and 11 metals. Elements written in red designate geometries that deviate significantly from that of the parent compound.

There is no clean-cut pattern that emerges. Elements such as Ag and Co show little interaction in all the configurations. The fact that their respective Yb-TM distances also fluctuate rather significantly (Figure 3.43) would seem to indicate that there is no dependency on either of the varying parameters: bond length or charge. The **YbCo** (neutral) adduct, for example, has the shortest intermetallic distance among the computed configurations, yet it shows the least interaction with Yb. The **YbAg** complexes are invariant in both scenarios. Furthermore, the complexes where there are strong interactions with

the Yb – **YbRh**$^{+}$, **YbRh**$^{-}$, **YbIr**$^{+}$ – are not the ones with the shortest distance in their respective series. The case of **YbAu**$^{-}$ should be taken with a pinch of salt, as it deviates from the geometry of **2.2** (Figure 3.42).

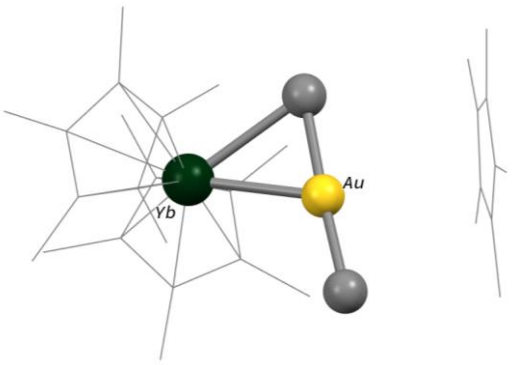

*Figure 3.42: Computed geometry of **YbAu**$^{-}$, which deviate from **2.2**'s structure.*

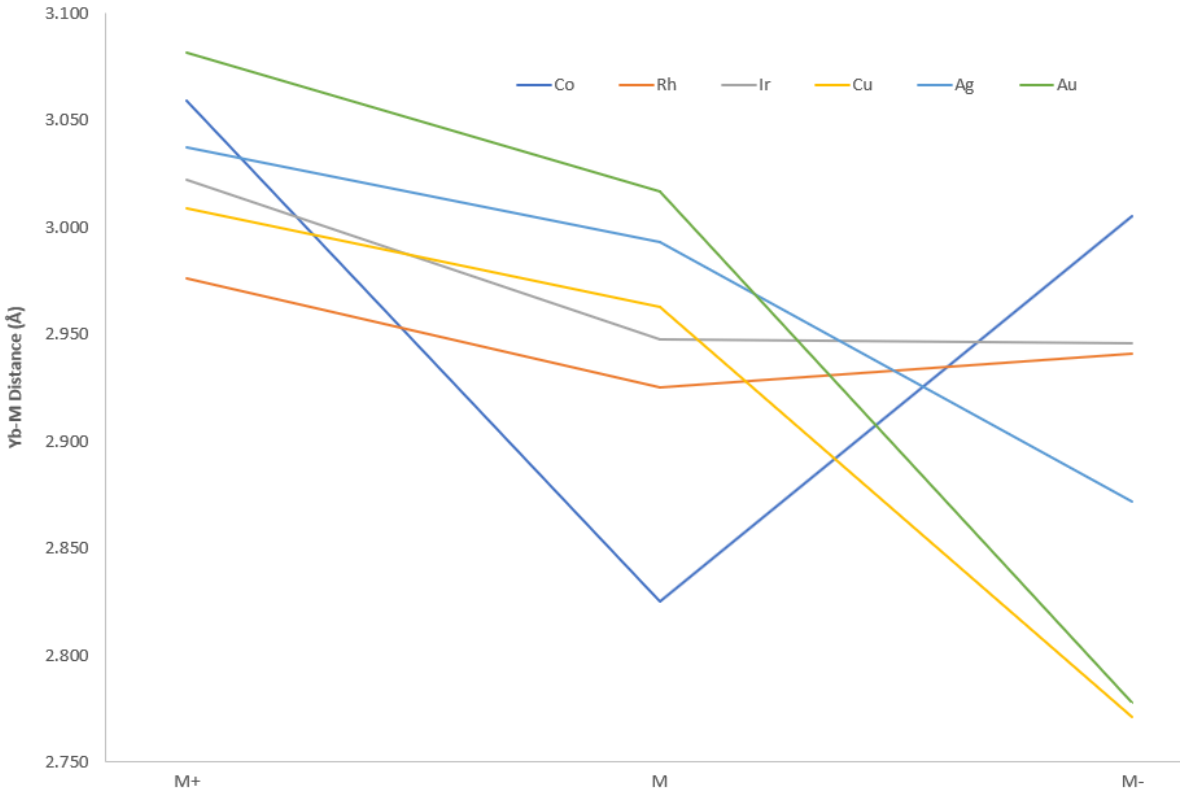

Figure 3.43: Evolution of the Yb-TM distance as a function of the metal charge.

3.4.3. Dependency on the lanthanide.

The entire lanthanide series was computed, as well as the group 3 metals – Y, Sc and La, in tandem with the Me_2PdCp^* fragment. The last three are not expected to contribute in the same way as the Yb, given that there are no *n*f electrons to speak of. They were computed in order to probe whether interactions of a different nature could be found. In all cases, these compounds were computed assuming the highest possible spin configuration for the Ln and no free spin for the Pd (i.e., m_S=7/2 for **GdPd**, 3/2 for **NdPd** and **ErPd**, etc.).

The computed structures can be divided into two general categories: symmetrical and asymmetrical species. The first category of complexes are quasi-identical to **2.2**, in the sense that the two bridging methyls are almost equidistant with respect to each metal centre and that one H atom on each side is in the plane formed by $LnC_{Me}C_{Me}Pd$. This geometry can be seen in both the crystal and computed structures of **2.2** (see Figure 2.6 or Table 2.2 for examples). In the second case, one of the methyls respects this configuration, whilst the other has two H atoms pointing towards the Ln (Figure 3.44). The asymmetrical structures are seen for **PrPd** and **NdPd**. This asymmetrisation is propagated across the Ln-C_{Me} and Pd-C_{Me} distances.

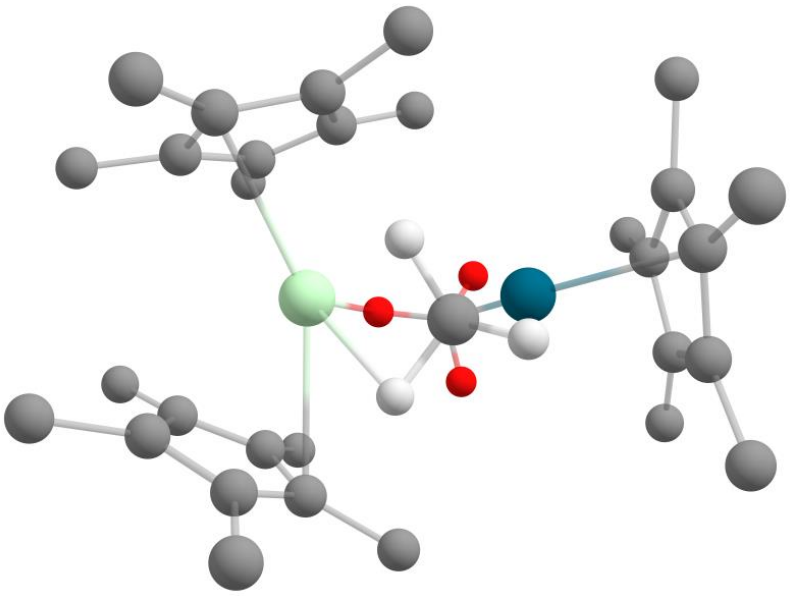

*Figure 3.44: Structure of **NdPd**, oriented in a Newman-like projection. The H atoms belonging to the masked C atom are shown in red.*

For the most part, the geometry optimisations ran smoothly and frequency calculations confirmed the structures corresponded to minima. The only exceptions were the Pm, Gd and Er complexes, where the usual convergence criteria (Tight) could not be achieved. For these specific examples, a lower criterion was accepted (Loose). This was considered an acceptable solution, as the majority of the optimisations that were run did not show any significant difference between the two convergence criteria (Figure 3.45).

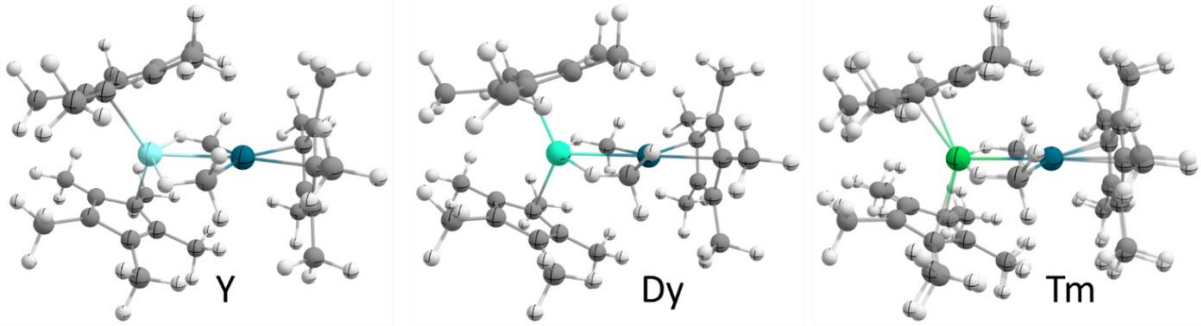

Figure 3.45: Examples of the overlay of the geometries obtained using Loose and Tight convergence criteria.

As a measure of the good convergence for the symmetrical species, all the main distances and angles on the Pd fragment are very well reproduced. For example, all the Pd-C_{Me} and Pd-Cp* centroid distances are contained within the 2.103-2.127 Å and 2.041-2.081 Å intervals. The only exceptions are

GdPd and **ErPd**, where both distances are larger than the average by about 0.1 Å. These deviations could be rationalised by the fact that the Cp* bound to the Pd is not in the same position than in the other compounds. Whilst the Ln-Pd axis is almost perfectly perpendicular to the Cp* plane, this is not the case for **GdPd** and **ErPd**. Whether this is due to a poor convergence of the geometry optimisations or to a specificity of these two complexes is unclear at this stage.

CASSCF calculations were subsequently performed, using the computed geometries. The primary objective of this study is to investigate the role of all of the potential attributes specific to the Ln centre in the formation of a Ln-Pd interaction, as was shown for **2.2**.

The most immediately accessible factor to study is the population of the 4f sub-shell. None of the group 3 metals in the +3 oxidation state possess any electrons in the f manifold. It is curious that, although all these complexes were computed as singlets, these complexes were not monoconfigurational. The dominant closed-shell configuration accounted for 84-88% of the wavefunction. In all of the cases, there were small contributions from open-shell singlet configurations.

No trace of Ln-Pd interaction was found in the group 3 complexes. In the very few orbitals which registered participation from both metals, the Ln contribution was ~1%, a threshold that may qualify such contributions as artefacts from the computation. Moreover, these contributions were issued from trace populations of electrons excited into the unoccupied orbitals (4p and 3d for Sc, 5p and 4d for Y, 5d for La) or from core orbitals (5s and 5p for La). The active space in **ScPd** and **YPd** presented some orbitals with contributions from both centres, although these orbitals were barely occupied (less than 0.005 electrons; Figure 3.46, right).

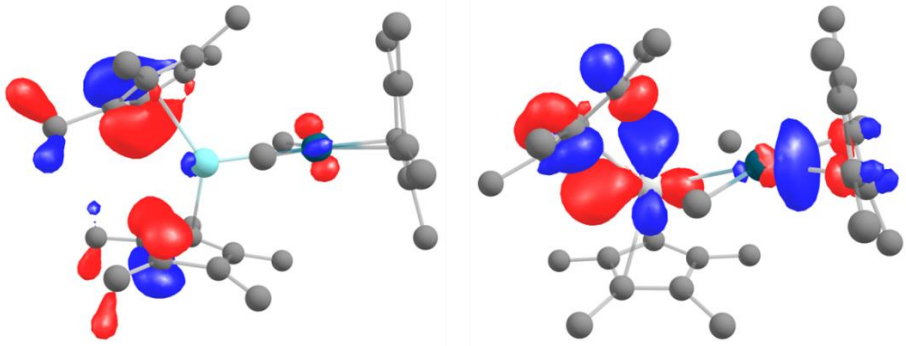

Figure 3.46: Examples of CASSCF orbitals of group 3 complexes, showing Pd-dominated interactions with the bridging methyls and an orbital in the active space with contributions from unoccupied orbitals of the Sc centre.

The next computed complexes involve the early lanthanides (Ce-Sm), where the 4f manifold is starting to fill up. Perhaps slightly surprisingly, no significant interactions with the Pd are observed. The only hints of such are the same orbitals with fleeting contributions from the excited unoccupied orbitals of the metals.

To test whether this conclusion was specific to lanthanides, the model actinide system **UPd** was computed. Given the higher propensity of the actinides to engage in covalent bonding,[3,32] the comparison with its neighbour (Nd) could prove to be informative. The computed structure, as is the case for **NdPd**, was also asymmetrical. As it were, the situation is rather similar to the complexes discussed above, except for one orbital, which presents a more evident bonding interaction with the methyls (Figure 3.47). The methyls are in anti-phase with the Pd 4d orbitals, implying that there is no attractive interaction between the two metals. However, there is no participation from the U 5f scaffold in this orbital, which is consistent with what occurs with the lanthanides.

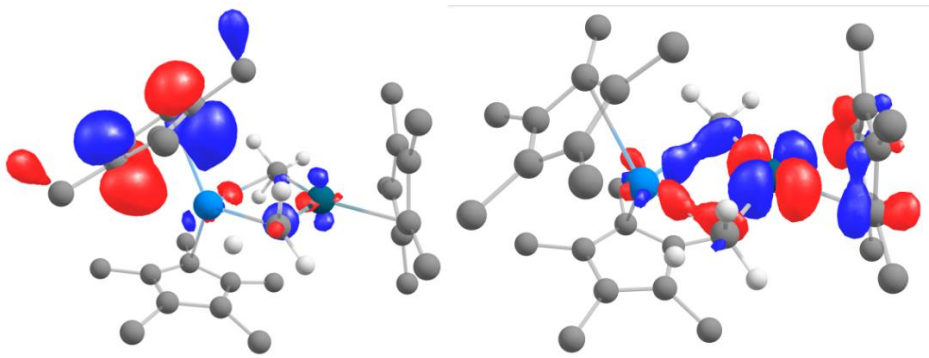

*Figure 3.47: Preview of the CASSCF orbitals of **UPd**, where both metals participate.*

The rest of the lanthanide series presented a mixed bag. There were strong interactions present in **EuPd** and **TmPd** and some weaker ones in **HoPd**, and none for the remaining complexes. Incidentally, the latter is the only complex where such an orbital was found in the active space. Not only were there fewer bonding Ho-Pd orbitals, but they featured disproportionate contributions from each metal centre. The Ho/Pd ratio in the orbitals in question are 6.2/93.8% and 97.7/2.3%, which would seem to indicate that they are more one-sided dative bonds, in line with previous reports.[29] Only **TmPd**, however, presented the orbital where the Pd $4dz^2$ orbital spatially extends towards the 4f manifold, as is seen in the left panel of Figure 3.32.

In order to quantify the effect of the Ln-Pd interaction, an analysis of the structural features of these complexes is pursued. Counter-intuitively, the Ln compounds containing an interaction all present an upward tick in the Ln-Pd distance, breaking the expected evolution with respect to the lanthanide contraction (Figure 3.48). One explanation that could rationalise this behaviour is that the electron donation from the Pd centre reduces the partial charge on the Ln, contributing to a more significant divalent character. On average, the ionic radii for the divalent metals is larger than the trivalent one by 0.16 Å, whereas the difference between Pd^{II} and Pd^{III} (the corollary of electron donation to the Ln) is smaller (0.12 Å).[87]

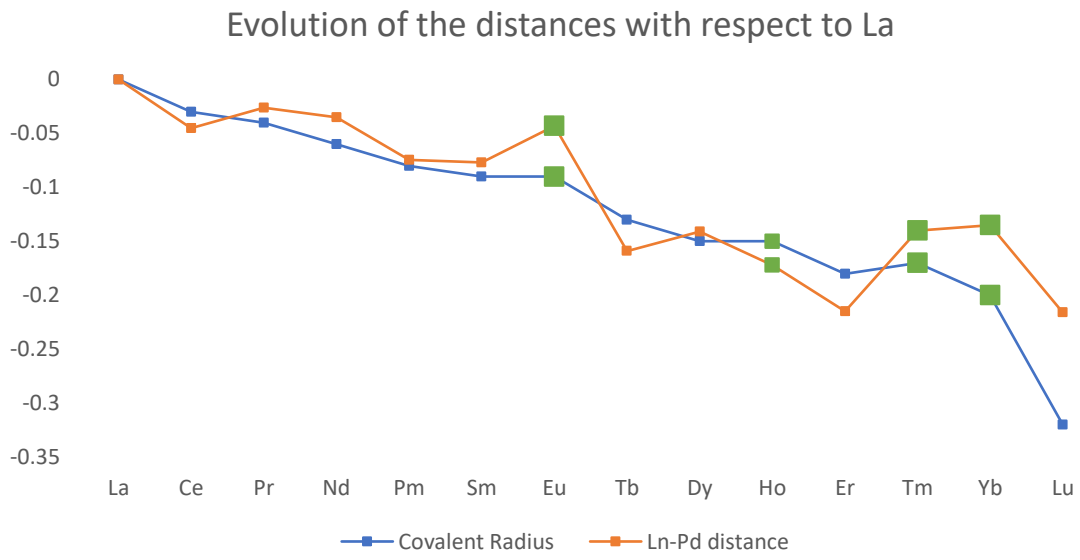

Figure 3.48: Evolution of the Ln-Pd distances, compared to the covalent radii of the lanthanide series.[88]. Gd was excluded, due to the dubious optimisation. The complexes where there were 4f-Pd 4d interactions were found are designated by the green squares. The size of the square gives a measure of the strength of the interaction.

It would, therefore, perhaps be no coincidence that the Ln for which these interactions are observed are the most readily available divalent lanthanides in the series. The sole point of contention in this conclusion is the lack of an effect seen for the **SmPd** complex. In this case, a possible explanation is that the fewer number of electrons available in the 4f shell does not allow all the required hybridisations of the 4f orbitals in order to achieve the necessary symmetry of the orbitals, so that a proper interaction with the Pd 4d electrons can occur.

To test this assertion, the **CePd**$^{+}$ complex was also computed. The reasoning is as follows: all the Ln in the series are considered to be trivalent. The electronic configuration of Ce^{III} is $4f^{1}$. This is very well illustrated in **CePd**, which is predominantly monoconfigurational (94.3% weight of the dominant configuration) and the sole 4f electron is located in a single, pure 4f orbital. By removing an electron, the logical configuration would be Ce^{IV}-Pd^{II}. If the Pd centre does, indeed, contribute electronic density towards its partnering metal, Ce^{IV} would be a good target, as the Ce^{IV}/Ce^{III} couple is relatively accessible.[89]. This species was computed as a singlet cation.

The evolution of the structural features with respect to the neutral adduct is consistent with enhanced electrostatic interaction between the oppositely charged fragments, owing to the global positive charge. The Ce-Pd distance is shortened by about 0.12 Å with respect to **CePd,** to 2.892 Å. The distances between the centroids of the Cp* co-ligands and their metals are reduced by circa 0.045 Å. The corresponding Ce-Cp*(ctr) distance in the neutral adduct (2.501 Å) was already shorter than the previously described equivalents (2.534-2.578 Å).[90–92] Unfortunately, there are no structurally authenticated Ce^{IV}-Cp* compounds, so a direct comparison cannot be made. Given that the M-C_{Me} bonds are shortened in the case of Ce, but not of Pd, it is reasonable to affirm that the Ce^{IV} configuration is more likely, on the basis of the computed geometry.

The interpretation becomes more convoluted upon examining the electronic structure of **CePd**$^{+}$, computed at the CASSCF (8,10) level. In stark contrast to the neutral adduct, a pair of singly occupied orbitals are found in the active space, presenting bonding and anti-bonding interactions between the Ce 4f and the Pd 4d electrons (Figure 3.49).

Orbital	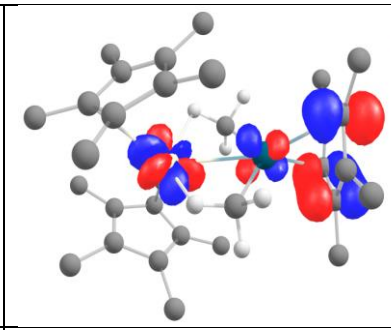	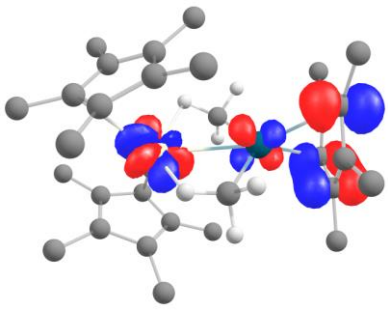
Ce/Pd electron contribution	0.48/0.09	0.51/0.10

*Figure 3.49: Singly occupied CASSCF orbitals in **CePd**$^{+}$, showing Ce-Pd interaction and each metal's contribution to the orbital.*

It is difficult to rationalise these observations. The presence of precisely one 4f electron in **CePd**$^{+}$ is quite puzzling, as it would imply that Ce is trivalent in this complex. There are two possibilities that can explain this behaviour.

In the first case, it would appear, based on the atomic population analyses[††], that the calculation failed to adequately attribute the loss of one electron vis-à-vis **CePd** to the presence of a Ce^{IV} centre. Rather,

[††]Calculated using the LoProp formalism.[93] Population analyses are not used as an absolute indication, due to their relative controversy.[94] Rather, what's being investigated is the evolution when going from **CePd** to **CePd**$^{+}$. In this case, the variation in the local population of the Ce and Pd atoms is negligible (less than 0.02 electrons!).

the positive charge is spread evenly throughout the molecule. The more polarised environment would explain the shorter bonds with the Cp* co-ligands observed for both metals.

Nevertheless, there is a distinct Ce-Pd interaction in **CePd**$^{+}$, but not in **CePd**. The underlying explanation therein is that the interaction in **CePd**$^{+}$ is enabled by the shorter distance between the two metals (as observed in Section 3.4.1). To eliminate this possibility, the neutral adduct was recomputed using the geometry of the cationic structure (specifically, where d(Ce-Pd) = 2.89 Å). The electronic structure of this species is identical to that of the optimised structure of **CePd** – no inter-metallic interaction is found. Clearly, the ambiguity surrounding these results precludes a simple analysis.

The second possibility is that the calculations would compute the Ce centre as trivalent (or very close to it), under the assumption that its surroundings would instigate a reduction of a putative Ce^{IV}. The most obvious source of a supplementary electron in this case would be the Pd^{II}. The alternatives would be Cp*, which are known to be oxidised and subsequently expelled from the coordination sphere of its binding metal.[95–97] This hypothesis can be discounted, since one of the Cp* ligands would have decoordinated had it been oxidised. The implication of the second scenario is that the population analyses are unreliable and not a good indication of the electronic structure of the compound.

The configuration of the Ce centre in **CePd**$^{+}$ was further explored by allowing multiple roots (10) within the CI (Configuration Interaction) formalism. The state interaction reshuffled the Ce 4f orbitals: there are now three orbitals with the 4f electron participation in the active space – one pure 4f orbital and two bearing interactions between the metals. Overall, the sum of the electronic contributions from the Ce 4f electrons in the ground state rounds up to one electron. It is only in the excited states that the complex showed a non-integer population (0.70 electrons) of the Ce 4f manifold. The first such state was 56.48 kcal/mol above the ground state.

A *leitmotif* of all these complexes is the orbital centred on the 4d electrons of the Pd, which involves the bridging methyl groups (Figure 3.50), which was also observed for **2.2**. What is most conspicuous is the absence of the participation from the pairing Ln in all but the aforementioned complexes. The crux of the problem is to determine what factor enables the Ln 4f-Pd 4d interaction in some cases, but not in others.

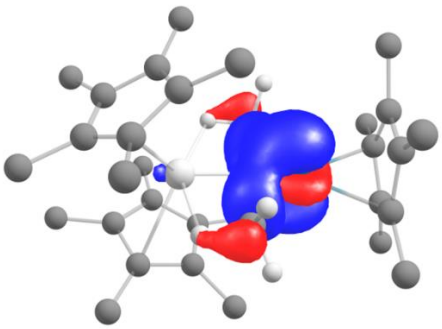

Figure 3.50: Pd 4d-dominated orbital found in all the complexes of the computed REPd series.

3.4.4. Partial conclusion.

3.4.4.1. Finding patterns.

This section has sought to investigate some of the conditions necessary for enabling and enhancing the unusually strong Yb-Pd interaction that was calculated for the complex **2.2**. Some of the factors are intuitive and straightforward, whilst others require a more subtle and careful examination.

It was shown, for example, that the nearly equitable contribution from both the Yb 4f and the Pd 4d manifolds in a number of orbitals – a situation that has no precedent – is sensitive to the intermetallic distance. This concept is relatively unambiguous, as sufficient proximity is required for an efficient orbital overlap.

On the other hand, the evolution of the methyl-bridged orbitals upon the gradual lengthening of the Yb-Pd distance (bottom line in Figure 3.36) raises a good question concerning the role of the methyl moieties. At closer range, the bridging groups contribute significantly to the bonding orbital, in a symbiotic relationship involving bonding interactions with each of the metals. Past a certain "bond" length, the methyls no longer contribute to the orbital and the metal orbitals hybridise differently, entirely changing their shape, whilst still maintaining the relative orientations required for bonding interactions. By which mechanism does this occur? Is there spin density transferred towards the Me? The answer to this question is unclear and requires further experimental and theoretical data.

The other structural ingredient which was tested was the co-ligand on the Pd. The main objective was to investigate how the anion influences the geometry adopted by the Pd fragment with respect to the organolanthanide. Our attempts, across three complexes, differed mainly by the angle formed between the two metals' coordination spheres (where the methyls are common to both). This angle is quite small in **2.2** – 12.65° in the crystal structure, 13.94° in the computed structure and no larger than 15.84° when the Yb-Pd distance was varied. In this regard, the three complexes can thus be classified as having a small deviation (**YbPdCnt** – 18.90-23.92°, depending on the Yb-Pd distance) or more perturbative ones (for **YbPd(impym)** and **YbPdBPh$_4$** – where the values ranged from 42.45° to 57.75°).

It would appear that it is this metric that is most meaningful when it comes to governing the strength of the Yb-Pd interaction, since specific symmetry requirements must be met in order to maximise the orbital overlap between the Yb 4f orbitals and the Pd 4d ones. As was shown in the electronic structure at all levels of theory, the Pd 4dz^2 is pointed towards the Yb, no doubt under the influence of the Cp* co-ligand, with which it also heavily interacts. It is in this respect that the angle between the planes determined by the metals' coordination spheres plays its most crucial role. If the deviation were large, then the Pd orbital would be poorly orientated, which would remove or severely hamper the necessary conditions for the interaction with the Yb.

Once the structural requirements are established, the role of each metal was investigated. The first set of calculations exchanged the Pd for other metals. The first observation pertains to the absence of d electrons, which precludes any interaction with the neighbouring Yb.

The rest of the series would seem to exhibit no observable dependency on Yb-TM distance or overall charge. The isoelectronic **YbRh$^-$** and **YbPt** – the homologue from the following period – manifest the same strong interaction with the Yb, suggesting that electronic similarity to the Pd enables the interaction. This does not, however, explain why **YbRh$^+$** and **YbIr$^+$** are alike.

Exchanging Yb for the entire lanthanide series also produced mixed results. **EuPd** was the first complex where strong interactions were present, to be joined by **TmPd** and **2.2**. The cases of **HoPd** and **UPd** deserve special mention, as the interactions within are weak or do not originate from f electrons, respectively.

The observation that the complexes where interactions were observed are the most accessible divalent lanthanides set the tune for a tentative conclusion: the interaction with the Pd is sufficiently donating to induce the divalent character of the Ln. This, in turn, would lengthen the bond, explaining the uptick in the Ln-Pd distance observed with respect to the lanthanide contraction (Figure 3.48).

The absence of **SmPd** – more readily available in the divalent state than Tm – among the complexes bearing an interaction is surprising, given that it has only one 4f electron fewer than **EuPd**, where the characteristic orbitals are found. It can be argued that more electrons occupying the 4f orbitals are necessary to enable the hybridisation that is vital for an adequate match with the opposing 4d orbitals. This explanation is not particularly convincing, as the CASSCF computations shows the involvement of all 7 of the 4f orbitals for the occupied pure Sm 4f orbitals. These orbitals are found in the active space, alongside significant contributions from the Pd 4d electrons, yet they do not interact. Recomputing this complex with multiple roots (10) did not reveal excited states, where such interactions are enabled.

CePd^{+} was computed to test the theory of the contribution of the electronic density from the Pd. In principle, it would imply that the electronic configuration of this adduct would be $Ce^{IV}Pd^{II}$. In contrast to the neutral homologue **CePd**, a pair of the characteristic Ln-Pd orbitals were, indeed, found for the cationic compound. It was suspicious, however, that there was exactly one 4f electron belonging to Ce. This can mean one of two things.

The electronic configuration may have been poorly computed – the metals would be in the $Ce^{III}Pd^{II}$ state and the positive charge is spread evenly across the molecule. This conclusion is corroborated by the population analyses, which show no significant modification of the metal environments. It also seems plausible from a structural perspective, since the distances to the centroids of the Cp* decrease for both metals, but the evolution of the other bond lengths seem to impact the Ce centre more. However, this hypothesis is undercut by the fact that population analyses are famously unreliable and do not give a faithful indication of the oxidation states – in this case – of the metal centres.

The other possibility is that the *ab initio* calculation assumes the Ce^{IV} configuration is not the most energetically favourable, due to the donating interaction with the Pd. Enabling the configuration interaction with 10 roots would seem to substantiate this claim. The first state, where there isn't roughly one electron in the Ce 4f manifold, is more than 50 kcal/mol above the ground state.

In a sense, the computations on **CePd** may be construed to be similar to how interactions between the metal centres were found in the **YbM** series. What could explain the fact that there are orbitals with strong and comparable contributions from both metals in **YbRh**$^{+}$ and **YbRh**$^{-}$, but not in **YbRh**, for example?

There isn't an obvious common denominator among the factors that were examined in this section that explains the observations for both the **YbM** and the **LnPd** series. The closest resemblance to a trend is that the closest peers of **2.2** were the isoelectronic **YbRh**$^{-}$ and neighbouring **YbPt**, on one hand, and the other Ln with the most accessible divalent states, on the other.

This points to the fact that, other than intermetallic distance or symmetry, the matching of the energies of the main interacting orbitals also plays a significant role in determining if or how strong an

interaction can be. This observation would not be new: Andersen, for example, persuasively argued that the prevalence of the monomeric or dimeric forms of $Cp^*_2Yb(phen)$-type complexes (phen = phenanthroline) depends on the orbital matching between, on one hand, the Yb 4f and 5d levels and, on the other, the ligand orbitals, bearing specific symmetries.[98]

What constitutes an evolution in this study is applying the same principles commonly reserved for covalent orbital interactions to intermetallic species, based on lanthanides. It is somewhat ironic to frame this discussion in this way, given the commonly held belief that the 4f elements do not engage in a great deal of covalency.[3] After all, there are numerous examples in the literature of short-contact heterometallic complexes, where no such strong interactions were computed.[99,100] In fact, some of them even bear a striking resemblance to **2.2**.[23,24]

Perhaps the requirements for the intermetallic interaction dictate which of these putative complexes can be isolated. The best bet for a homologous complex would be **YbPt**, which was not isolated in real-life conditions, although not many attempts were made and its chemistry is still to be fully understood. Further trials constitute a synthetic priority for the future.

3.4.4.2. Limits of the methods.

The hypothesis pertaining to the interaction enabled by the proper matching of the orbitals presents one potentially glaring flaw: it may be dependent on the level of theory of the computation. The significant difference seen between the intermetallic interactions within **2.2** at the CASSCF and **ZORA3** levels of theory may be an illustrative example. There is quite likely an important difference in the way the two computations evaluate the energy of the Yb 4f electrons. The electronic structure of **2.2**, if computed at the **DFT-RECP** level, shows several pairs of bonding-antibonding orbitals in between the two metals, similar to those computed at the CASSCF level of theory. The same result could be reached following a test at the Hartree-Fock level.

How is this development to be interpreted? There are two main differences between the **ZORA3** and the **DFT-RECP** levels of theory: the basis sets and the use of a relativistic Hamiltonian. It is unclear if the difference in the electronic structures originates from these two factors. Is the use of a relativistic Hamiltonian indispensable to enable the interaction? Or does the use of the pseudopotentials result in a more accurate assessment of the Yb 4f orbitals?

To test this, a series of computations were performed on place-holder systems at both DFT levels, as well as SA-CASSCF (State Averaged CASSCF), where the first 20 roots were taken into account. For simplicity, the free ions Pd^{II} and Yb^{III} were chosen. The objective herein is to approximate how the energies of the two main sub-shells are calculated. The results of these calculations are presented in Figure 3.51.

As it were, the difference in the energy of the orbitals (taken, in this case, to be between the SOMO of the Yb^{III} and the lowest occupied 4d orbital of the Pd^{II}) between the two methods is very small at the DFT level (less than 0.5 eV, for a total value of *ca.* 8.7 eV). The same metric is twice as large at the SA-CASSCF (13,7) level.

Both of these observations strain the applicability of the method. The quasi-identical energy gap found for the DFT methods is not consistent with the differing intermetallic interactions. The only difference in the methodology that might explain this is the relativistic Hamiltonian and the adapted relativistically recontracted basis sets, which would need to be sufficiently perturbative to induce consequential variation of the metal orbital levels following the interaction with their respective

coordination spheres. This hypothesis is dubious, especially with respect to the Pd centre. Whilst there are minor differences in how the Yb 4f orbitals are computed between the **DFT-RECP** and **ZORA3** methods, the Pd 4d orbitals are identical within a few wave numbers. This is to be expected, since Pd is far less affected by relativistic effects than Yb.

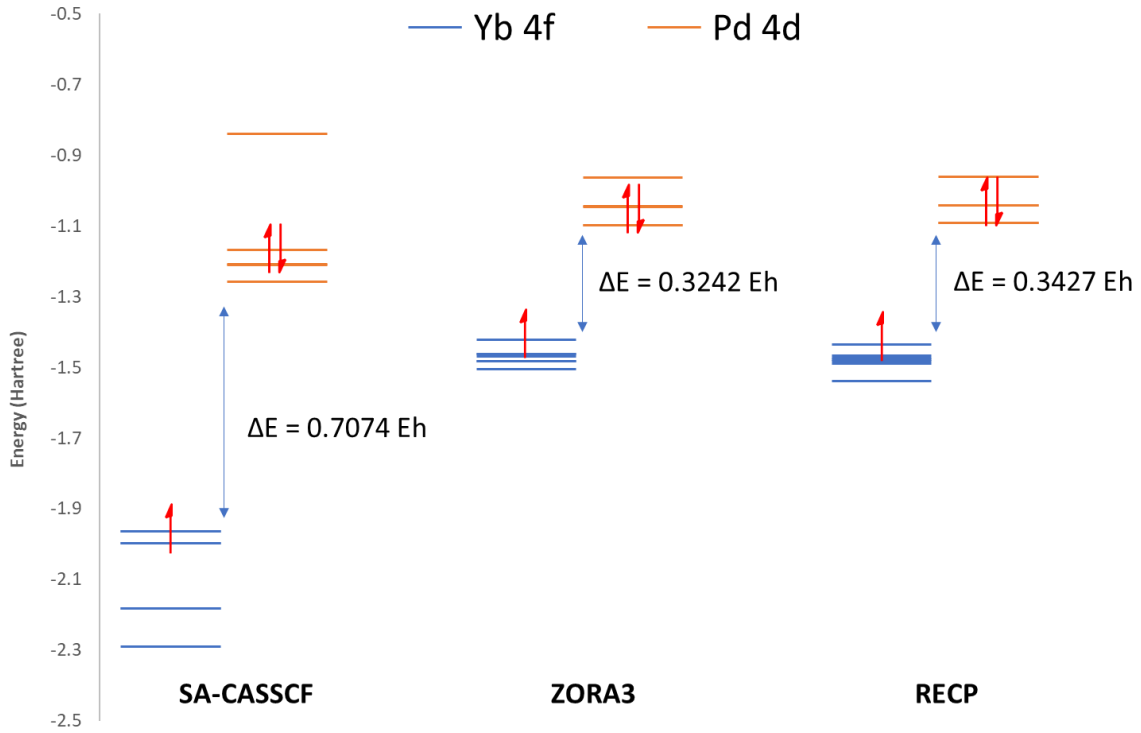

Figure 3.51: Energy levels of the Yb^{III} 4f (blue) and Pd^{II} 4d orbitals, computed at multiple levels of theory. In the interest of clarity, only the electrons of the SOMO/HOMO are shown.

These findings cannot, then, cleanly explain why different types of computations produce different interactions. To better understand the implications of this conclusion, it is important to return to the initial premise, that motivated the extensive computational study presented in this section. All other factors being equal, there were two vastly different intermetallic interactions in the electronic structures computed for two complexes with short Yb-Pd distances – **2.2** and **2.6** – using the same methodology (CASSCF). The lack of quantifiable interaction in the latter is substantiated by preliminary spectroscopic investigations, as both of the concerned metal centres are in the Ln^{III} configuration. The contrast observed for **2.2** is a very promising object of study in itself, although the absence of equivalent magnetic data limits the confidence margin in the conclusions presented in this work. Simply put, one cannot confirm the data for **2.2** since the CASSCF methodology was validated in the case of a similar complex.

3.5. Conclusion.

Contrary to the majority of characterised intermetallics, which are formed following deliberate synthetic planning, all three Ln-Pd complexes presented in this work are obtained after complicated molecular rearrangements. It was worth investigating the mechanism which leads to their formation, in order to establish the necessary ingredients to trigger the rearrangement starting from the coupled products **2.4** or **2.5**.

The use of other reductive substrates confirmed that simply transferring an electron onto either the starting precursor **1.12** or the coupled products is not enough to activate the transformation pathway. An argument that could explain this relates to the fact that none of the other reductants coordinate to the substrate, presumably changing the target orbital where the electron is dispatched. Similar observations were made for the **K(bimpym)NiMe$_2$** system, since the use of ytterbocene and of KC_8 both resulted in coupling reactions, but not in the same positions.[101] The influence of coordination of metals to RAL edifices can be seen *via* theoretical computations (Figure 1.6).

Therefore, the use of **2.4** as a test subject for a further reaction with divalent lanthanide precursors sought to obtain further clues as to the evolutions that lead to the trimetallic complexes. Three simultaneous events take place when **2.4** is used: the reactivity with ytterbocene, the isomerisation towards **2.5**, and the latter's own reactivity with ytterbocene.

What emerges from the reaction between **2.4** and ytterbocene is an intricate mechanism, from which three products are isolated: **2.2**, **2.6** and **Yb$_3$(bimpym)$_2$**. The same complexes are obtained when the isomer, **2.5**, is used, but the reaction rate and the final ratio between them depends heavily on the nature of the coupled product. These two differences can be attributed to the main structural features within the two coupled complexes, namely in the relative arrangements of the two Pd coordination spheres, where free ytterbocene is expected to react.

All the experimental observations collected in Section 3.2.2.2 pertain to the formation of the Yb-based trimetallic adduct, as none could be collected following the direct reaction between samarocene and **1.12**. Although it seems logical that the mechanism leading to **2.7** would be identical to that of **2.6**, this could not be experimentally verified. It is possible that some important clues can be gathered in the synthetic attempts performed in the presence of the pyridine analogues, quinoline (leading to **2.8**).

In this respect, the theoretical computations may offer an explanation as to why the two divalent lanthanides perform differently. The larger samarocene would offer lesser steric constraints when approaching the (bimpym)Pd fragment, allowing it easier access to the methyl and pyridine groups. This should favour the subsequent reactivity of the degradation and reorganisation of the precursor scaffold.

The second major objective of this chapter revolved around analysing these short Ln-Pd distances from a quantum chemical computational perspective. Indeed, it is natural to assume that having "bond" lengths close to the sum of covalent radii necessarily implies the presence of interactions between two atoms, but the specificities of the radial extension of the 4f sub-shell in lanthanides warrants scepticism.

Since lanthanides do not engage in covalent bonding to any significant extent,[3] strong (non-ionic) interactions with its coordination sphere tend to leave subtler clues. This is manifested in phenomena such as redox isomerism[102] or multiconfigurational ground states.[75] The advantage of these occurrences is that they tend to have very strong perturbative effects on the Ln[103] and they leave spectroscopic signatures. Take, for example, the magnetic properties of ytterbocene-based charge transfer complexes.[66] The characteristic evolution of an Yb^{III} ion (green dots in Figure 3.52) is in immediate contrast with those of its multiconfigurational peers.

In that sense, the lack of strong electronic interaction between the Pd and the Ln in the trimetallic adducts could have been foreshadowed by the magnetic data, reported in Section 2.2.3.2 (Figure 2.29 and Figure S2). In the solid state, **2.6** and **2.7** are nothing other than $Ln^{III}_2Pd^0$ adducts all throughout the 0-300 K range. This means that the proximity to the Pd centre is not sufficiently perturbative in

order to induce a deviation from the expected magnetic evolution. Therefore, there is no electron transferred between the two metals in the final compound (although, arguably, several electrons exchange hands during the formation mechanism).

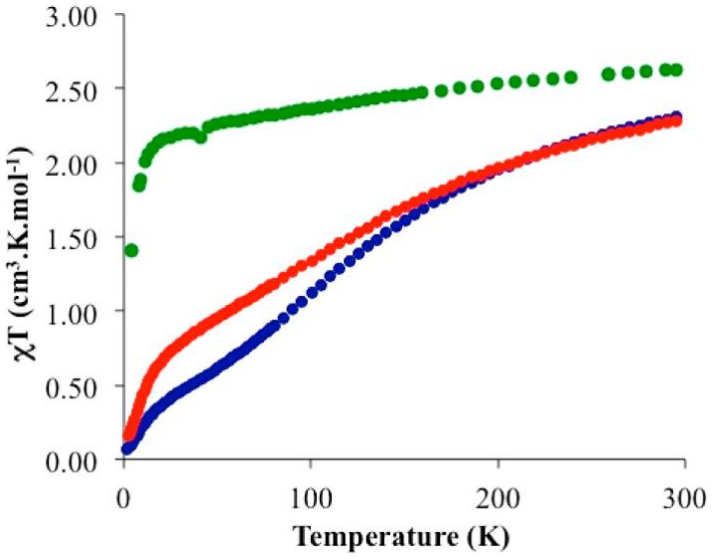

Figure 3.52: Evolution of χT over T(K) for a series of $Cp^*_2Yb(RAL)PdMe_2$-type complexes. Figure reprinted from ref 65.

Therefore, the electronic structures of the trimetallic complexes were in good agreement with the magnetic data. The few computed orbitals where both metals contribute showcase negligible participation from the junior partner, indicative of, at best, a dative bond between the metals. This is corroborated by the analyses of the interactions within these structures, which show a weak interaction between the Ln and the Pd centres. The main attractive interaction within these complexes is undoubtedly electrostatic, legitimising their description as two $[Cp^*_2Ln^{III}]^+$ fragments that interact with one $Pd^0(pyr)_2^{2-}$ species. This is complemented by orbital interactions due to the Pd-C_{pyr} and Ln-N_{pyr} bonds, as well as by dispersive forces.

The electronic structure of the bimetallic **2.2** was computed at different levels of theory. A unanimous conclusion is the fact that the Pd $4dz^2$ orbital points to the Yb centre (incidentally, the same observations are valid for **2.6** and **2.7**). For reasons that may be related to the treatment of the Yb 4f electrons in all-electron DFT calculations, the theoretical conclusions offered by DFT and wave-function-based methods diverge somewhat. The CASSCF computations reveal a series of orbitals with unusually equitable Yb-Pd contributions, suggesting covalent interactions between the two metals, although the number of bonding and anti-bonding orbitals even out, leaving a bond order close or equal to zero.

Inspired by the intriguing electronic structure of **2.2**, an extensive theoretical study focused on determining the contributing factors to the Yb-Pd interaction was carried out. The structure of **2.2** is a very good basis for such an exploration, since it has a much more workable size than its heterometallic fellows, **2.6** and **2.7**. This work explored the role of the structural features and the participation of each metal centre. The findings paint a complex picture, where there is not one reigning factor that explicitly enables this interaction. However, significant deviation from the optimal parameters – be they structural (distance, angle) or due to chemical nature (choice of either metal) – either reduces the strength of the interaction or eliminates it entirely.

The isolation of **2.2** – which seems to satisfy each and every computed criterion – does seem to be the organometallic equivalent of finding the needle in the proverbial haystack. As previously mentioned,

the Pd 4d orbitals point towards the Yb 4f manifold by virtue of being locked in this geometry by the Cp* and the bridging methyl ligands, ensuring a short intermetallic distance along the way.

Furthermore, changing either of the participating metals results in only a handful of combinations which keep the same potent inter-metallic interactions. The resulting implication would seem to heavily borrow from chemical canon that is usually reserved for covalent orbital interactions, a domain that is quite unfamiliar to the lanthanide series. It seems very likely that the intermetallic interactions are activated for systems which maintain a very good match in the specific energy levels of the participating orbitals between the two metals.

This would explain why, on one hand, **YbPt** and **YbRh**$^-$ are capable of facilitating the same strong interactions. Both of the valence orbitals should be energetically comparable to those of the Pd. On the other hand, the common feature of **EuPd**, **TmPd** and **2.2** is the fact that all have accessible divalent states for the lanthanide. This is slightly different conceptually to the considerations for the TM, but still rely on the similarity of energetic features, in this case, the energy required to transfer an electron onto the lanthanide.

These exciting findings could provide the impetus for attempts to obtain such complexes. Efforts should be dedicated to exploring different synthetic avenues, as the mechanism resulting in **2.2** is probably too specific to the Pd centre.

In the interests of caution, however, these preliminary conclusions ought to be grounded in scepticism. The electronic structure of **2.2** is so enticing, precisely because it is in contrast with those of **2.6** and **2.7**. Yet, simply because they were all computed using the same methods, one cannot simply extrapolate the findings and promote these computational conclusions to the level of real-life experimental evidence. That the presence of these interactions seems to be dependent on the methodology used add a further layer of uncertainty. Further studies corroborated the overall electronic structure of this adduct, though, as the topological analyses would be consistent with a weak interaction between the two metals, although the EDA results point to a more significant covalent character in the attractive energy breakdowns (although it should be noted that other covalent interactions contribute to this figure).

The evolution of this project is evident. Experimental data must be gathered in order to better understand the nature of the interactions within this architecture. This sets the stage for an alluring *denouement*: if the orbital interactions present in this structure are not corroborated by spectroscopic analyses, then it's worth questioning the methods that bore these results. If solid proof of electron sharing between Yb and Pd is provided, then these findings would constitute a meaningful addition to the understanding of Ln-based intermetallics.

References

(1) Liddle, S. T., Ed.; Wiley-VCH Verlag GmbH & Co. KGaA: Weinheim, Germany, 2015. https://doi.org/10.1002/9783527673353.

(2) McGrady, J. E. In *Molecular Metal-Metal Bonds*; Liddle, S. T., Ed.; Wiley-VCH Verlag GmbH & Co. KGaA: Weinheim, Germany, 2015; pp 1–22. https://doi.org/10.1002/9783527673353.ch1.

(3) Neidig, M. L.; Clark, D. L.; Martin, R. L. *Coord. Chem. Rev.* 2013, *257* (2), 394–406. https://doi.org/10.1016/j.ccr.2012.04.029.

(4) Labouille, S.; Clavaguéra, C.; Nief, F. *Organometallics* 2013, *32* (5), 1265–1271. https://doi.org/10.1021/om301018u.

(5) Coxon, J. A.; Melville, T. C. *J. Mol. Spectrosc.* 2006, *235* (2), 235–247. https://doi.org/10.1016/j.jms.2005.11.009.

(6) Pershina, V.; Borschevsky, A.; Anton, J. *Chem. Phys.* 2012, *395*, 87–94. https://doi.org/10.1016/j.chemphys.2011.04.017.

(7) Cotton, F. A.; Harris, C. B. *Inorg. Chem.* 1965, *4* (3), 330–333. https://doi.org/10.1021/ic50025a015.

(8) Cotton, F. A. *Inorg. Chem.* 1965, *4* (3), 334–336. https://doi.org/10.1021/ic50025a016.

(9) Gagliardi, L.; Roos, B. O. *Inorg. Chem.* 2003, *42* (5), 1599–1603. https://doi.org/10.1021/ic0261068.

(10) Roos, B. O.; Borin, A. C.; Gagliardi, L. *Angew. Chem. Int. Ed.* 2007, *46* (9), 1469–1472. https://doi.org/10.1002/anie.200603600.

(11) Souter, P. F.; Kushto, G. P.; Andrews, L.; Neurock, M. *J. Am. Chem. Soc.* 1997, *119* (7), 1682–1687. https://doi.org/10.1021/ja9630809.

(12) Gagliardi, L.; Roos, B. O. *Nature* 2005, *433* (7028), 848–851. https://doi.org/10.1038/nature03249.

(13) Knecht, S.; Jensen, H. J. Aa.; Saue, T. *Nat. Chem.* 2019, *11* (1), 40–44. https://doi.org/10.1038/s41557-018-0158-9.

(14) Ciborowski, S. M.; Mitra, A.; Harris, R. M.; Liu, G.; Sharma, P.; Khetrapal, N.; Blankenhorn, M.; Gagliardi, L.; Bowen, K. H. *J. Am. Chem. Soc.* 2021, *143* (41), 17023–17028. https://doi.org/10.1021/jacs.1c06417.

(15) Minasian, S. G.; Krinsky, J. L.; Arnold, J. *Chem. - Eur. J.* 2011, *17* (44), 12234–12245. https://doi.org/10.1002/chem.201101447.

(16) Beletskaya, I. P.; Voskoboynikov, A. Z.; Chuklanova, E. B.; Kirillova, N. I.; Shestakova, A. K.; Parshina, I. N.; Gusev, A. I.; Magomedov, G. K. I. *J. Am. Chem. Soc.* 1993, *115* (8), 3156–3166. https://doi.org/10.1021/ja00061a015.

(17) Arnold, P. L.; Liddle, S. T.; McMaster, J.; Jones, C.; Mills, D. P. *J. Am. Chem. Soc.* 2007, *129* (17), 5360–5361. https://doi.org/10.1021/ja0710858.

(18) Oelkers, B.; Kempe, R. In *Molecular Metal-Metal Bonds*; Liddle, S. T., Ed.; Wiley-VCH Verlag GmbH & Co. KGaA: Weinheim, Germany, 2015; pp 47–71. https://doi.org/10.1002/9783527673353.ch3.

(19) Butovskii, M. V.; Tok, O. L.; Wagner, F. R.; Kempe, R. *Angew. Chem. Int. Ed.* 2008, *47* (34), 6469–6472. https://doi.org/10.1002/anie.200800407.

(20) Butovskii, M. V.; Döring, C.; Bezugly, V.; Wagner, F. R.; Grin, Y.; Kempe, R. *Nat. Chem.* 2010, *2* (9), 741–744. https://doi.org/10.1038/nchem.718.

(21) Butovskii, M. V.; Oelkers, B.; Bauer, T.; Bakker, J. M.; Bezugly, V.; Wagner, F. R.; Kempe, R. *Chem. - Eur. J.* 2014, *20* (10), 2804–2811. https://doi.org/10.1002/chem.201304125.

(22) Roesky, P. W. *Dalton Trans.* 2009, No. 11, 1887. https://doi.org/10.1039/b816377d.

(23) Gamer, M. T.; Roesky, P. W.; Konchenko, S. N.; Nava, P.; Ahlrichs, R. *Angew. Chem. Int. Ed.* 2006, *45* (27), 4447–4451. https://doi.org/10.1002/anie.200600423.

(24) Wiecko, M.; Roesky, P. W. *Organometallics* 2007, *26* (19), 4846–4848. https://doi.org/10.1021/om7005672.
(25) Minasian, S. G.; Krinsky, J. L.; Rinehart, J. D.; Copping, R.; Tyliszczak, T.; Janousch, M.; Shuh, D. K.; Arnold, J. *J. Am. Chem. Soc.* 2009, *131* (38), 13767–13783. https://doi.org/10.1021/ja904565j.
(26) Zeckert, K. *Organometallics* 2013, *32* (5), 1387–1393. https://doi.org/10.1021/om301032x.
(27) Völcker, F.; Mück, F. M.; Vogiatzis, K. D.; Fink, K.; Roesky, P. W. *Chem. Commun.* 2015, *51* (59), 11761–11764. https://doi.org/10.1039/C5CC03944D.
(28) Völcker, F.; Roesky, P. W. *Dalton Trans.* 2016, *45* (23), 9429–9435. https://doi.org/10.1039/C6DT00417B.
(29) Ramirez, B. L.; Sharma, P.; Eisenhart, R. J.; Gagliardi, L.; Lu, C. C. *Chem. Sci.* 2019, *10* (11), 3375–3384. https://doi.org/10.1039/C8SC04712J.
(30) Cui, P.; Xiong, C.; Du, J.; Huang, Z.; Xie, S.; Wang, H.; Zhou, S.; Fang, H.; Wang, S. *Dalton Trans.* 2020, *49* (1), 124–130. https://doi.org/10.1039/C9DT04369A.
(31) Lu, E.; Wooles, A. J.; Gregson, M.; Cobb, P. J.; Liddle, S. T. *Angew. Chem. Int. Ed.* 2018, *57* (22), 6587–6591. https://doi.org/10.1002/anie.201803493.
(32) Hu, S.-X.; Lu, E.; Liddle, S. T. *Dalton Trans.* 2019, *48* (34), 12867–12879. https://doi.org/10.1039/C9DT03086G.
(33) Zhang, W.-B.; Yang, X.-T.; Ma, J.-B.; Su, Z.-M.; Shi, S.-L. *J. Am. Chem. Soc.* 2019, *141* (14), 5628–5634. https://doi.org/10.1021/jacs.9b00931.
(34) Ye, M.; Gao, G.-L.; Yu, J.-Q. *J. Am. Chem. Soc.* 2011, *133* (18), 6964–6967. https://doi.org/10.1021/ja2021075.
(35) Nakao, Y.; Kanyiva, K. S.; Hiyama, T. *J. Am. Chem. Soc.* 2008, *130* (8), 2448–2449. https://doi.org/10.1021/ja710766j.
(36) Takao, T.; Kawashima, T.; Kanda, H.; Okamura, R.; Suzuki, H. *Organometallics* 2012, *31* (13), 4817–4831. https://doi.org/10.1021/om300379d.
(37) Shih, W.-C.; Ozerov, O. V. *J. Am. Chem. Soc.* 2017, *139* (48), 17297–17300. https://doi.org/10.1021/jacs.7b10570.
(38) Li, Y.; Deng, G.; Zeng, X. *Organometallics* 2016, *35* (5), 747–750. https://doi.org/10.1021/acs.organomet.5b01021.
(39) Tobisu, M.; Hyodo, I.; Chatani, N. *J. Am. Chem. Soc.* 2009, *131* (34), 12070–12071. https://doi.org/10.1021/ja9053509.
(40) Nagae, H.; Shibata, Y.; Tsurugi, H.; Mashima, K. *J. Am. Chem. Soc.* 2015, *137* (2), 640–643. https://doi.org/10.1021/ja511964k.
(41) Guan, B.-T.; Hou, Z. *J. Am. Chem. Soc.* 2011, *133* (45), 18086–18089. https://doi.org/10.1021/ja208129t.
(42) Song, G.; Wang, B.; Nishiura, M.; Hou, Z. *Chem. - Eur. J.* 2015, *21* (23), 8394–8398. https://doi.org/10.1002/chem.201501121.
(43) Song, G.; O, W. W. N.; Hou, Z. *J. Am. Chem. Soc.* 2014, *136* (35), 12209–12212. https://doi.org/10.1021/ja504995f.
(44) MacLeod, K. C.; Lewis, R. A.; DeRosha, D. E.; Mercado, B. Q.; Holland, P. L. *Angew. Chem. Int. Ed.* 2017, *56* (4), 1069–1072. https://doi.org/10.1002/anie.201610679.
(45) Hayashi, A.; Olmstead, M. M.; Attar, S.; Balch, A. L. *J. Am. Chem. Soc.* 2002, *124* (20), 5791–5795. https://doi.org/10.1021/ja012416y.
(46) Isobe, K.; Kai, E.; Nakamura, Y.; Nishimoto, K.; Miwa, T.; Kawaguchi, S.; Kinoshita, K.; Nakatsu, K. *J. Am. Chem. Soc.* 1980, *102* (7), 2475–2476. https://doi.org/10.1021/ja00527a065.
(47) Nakatsu, K.; Kinoshita, K.; Kanda, H.; Isobe, K.; Nakamura, Y.; Kawaguchi, S. *Chem. Lett.* 1980, *9* (8), 913–914. https://doi.org/10.1246/cl.1980.913.
(48) Jantunen, K. C.; Scott, B. L.; Gordon, J. C.; Kiplinger, J. L. *Organometallics* 2007, *26* (10), 2777–2781. https://doi.org/10.1021/om0702330.
(49) Zhou, E.; Ren, W.; Hou, G.; Zi, G.; Fang, D.-C.; Walter, M. D. *Organometallics* 2015, *34* (14), 3637–3647. https://doi.org/10.1021/acs.organomet.5b00454.

(50) Fang, B.; Zhang, L.; Hou, G.; Zi, G.; Fang, D.-C.; Walter, M. D. *Chem. Sci.* 2015, *6* (8), 4897–4906. https://doi.org/10.1039/C5SC01684C.
(51) Ferrer, M.; Gutiérrez, A.; Mounir, M.; Rodríguez, L.; Rossell, O.; Font-Bardia, M.; Gómez-Sal, P.; Martín, A.; Solans, X. *Organometallics* 2011, *30* (12), 3419–3429. https://doi.org/10.1021/om200318c.
(52) Tyrra, W.; Aboulkacem, S.; Pantenburg, I. *J. Organomet. Chem.* 2006, *691* (3), 514–522. https://doi.org/10.1016/j.jorganchem.2005.09.017.
(53) Mocanu, T.; Kiss, L.; Sava, A.; Shova, S.; Silvestru, C.; Andruh, M. *Polyhedron* 2019, *166*, 7–16. https://doi.org/10.1016/j.poly.2019.03.020.
(54) Partyka, D. V.; Gray, T. G. *J. Organomet. Chem.* 2009, *694* (2), 213–218. https://doi.org/10.1016/j.jorganchem.2008.10.024.
(55) Connelly, N. G.; Geiger, W. E. *Chem. Rev.* 1996, *96* (2), 877–910. https://doi.org/10.1021/cr940053x.
(56) Pavlishchuk, V. V.; Addison, A. W. *Inorganica Chim. Acta* 2000, *298* (1), 97–102. https://doi.org/10.1016/S0020-1693(99)00407-7.
(57) Hodge, S. A.; Tay, H. H.; Anthony, D. B.; Menzel, R.; Buckley, D. J.; Cullen, P. L.; Skipper, N. T.; Howard, C. A.; Shaffer, M. S. P. *Faraday Discuss* 2014, *172*, 311–325. https://doi.org/10.1039/C4FD00043A.
(58) Schultz, M.; Boncella, J. M.; Berg, D. J.; Tilley, T. D.; Andersen, R. A. *Organometallics* 2002, *21* (3), 460–472. https://doi.org/10.1021/om010661k.
(59) Berg, D. J.; Boncella, J. M.; Andersen, R. A. *Organometallics* 2002, *21* (22), 4622–4631. https://doi.org/10.1021/om020477e.
(60) Schwartz, D. J.; Ball, G. E.; Andersen, R. A. *J. Am. Chem. Soc.* 1995, *117* (22), 6027–6040. https://doi.org/10.1021/ja00127a016.
(61) Jaoul, A.; Tricoire, M.; Moutet, J.; Cordier, M.; Clavaguéra, C.; Nocton, G. *Chem. Squared* 2019, *3*. https://doi.org/10.28954/2019.csq.06.001.
(62) Carlson, C. N.; Kuehl, C. J.; Da Re, R. E.; Veauthier, J. M.; Schelter, E. J.; Milligan, A. E.; Scott, B. L.; Bauer, E. D.; Thompson, J. D.; Morris, D. E.; John, K. D. *J. Am. Chem. Soc.* 2006, *128* (22), 7230–7241. https://doi.org/10.1021/ja058667e.
(63) Yokogawa, D.; Ikegami, T. *J. Chem. Phys.* 2009, *131* (22), 221101. https://doi.org/10.1063/1.3272029.
(64) Izuogu, D. C.; Yoshida, T.; Zhang, H.; Cosquer, G.; Katoh, K.; Ogata, S.; Hasegawa, M.; Nojiri, H.; Damjanović, M.; Wernsdorfer, W.; Uruga, T.; Ina, T.; Breedlove, B. K.; Yamashita, M. *Chem. – Eur. J.* 2018, *24* (37), 9285–9294. https://doi.org/10.1002/chem.201800699.
(65) Yang, X.; Burns, C. P.; Nippe, M.; Hall, M. B. *Inorg. Chem.* 2021, *60* (13), 9394–9401. https://doi.org/10.1021/acs.inorgchem.1c00285.
(66) Goudy, V.; Jaoul, A.; Cordier, M.; Clavaguéra, C.; Nocton, G. *J. Am. Chem. Soc.* 2017, *139* (31), 10633–10636. https://doi.org/10.1021/jacs.7b05634.
(67) Arnold, P. L.; McMaster, J.; Liddle, S. T. *Chem Commun* 2009, No. 7, 818–820. https://doi.org/10.1039/B819072K.
(68) Liddle, S. T.; Mills, D. P.; Gardner, B. M.; McMaster, J.; Jones, C.; Woodul, W. D. *Inorg. Chem.* 2009, *48* (8), 3520–3522. https://doi.org/10.1021/ic900278t.
(69) Feng, G.; McCabe, K. N.; Wang, S.; Maron, L.; Zhu, C. *Chem. Sci.* 2020, *11* (29), 7585–7592. https://doi.org/10.1039/D0SC00389A.
(70) Feng, G.; Zhang, M.; Wang, P.; Wang, S.; Maron, L.; Zhu, C. *Proc. Natl. Acad. Sci.* 2019, *116* (36), 17654–17658. https://doi.org/10.1073/pnas.1904895116.
(71) Pyykkö, P. *J. Phys. Chem. A* 2015, *119* (11), 2326–2337. https://doi.org/10.1021/jp5065819.
(72) Gardner, B. M.; Patel, D.; Cornish, A. D.; McMaster, J.; Lewis, W.; Blake, A. J.; Liddle, S. T. *Chem. - Eur. J.* 2011, *17* (40), 11266–11273. https://doi.org/10.1002/chem.201101394.
(73) Fradera, X.; Austen, M. A.; Bader, R. F. W. *J. Phys. Chem. A* 1999, *103* (2), 304–314. https://doi.org/10.1021/jp983362q.

(74) Booth, C. H.; Walter, M. D.; Kazhdan, D.; Hu, Y.-J.; Lukens, W. W.; Bauer, E. D.; Maron, L.; Eisenstein, O.; Andersen, R. A. *J. Am. Chem. Soc.* 2009, *131* (18), 6480–6491. https://doi.org/10.1021/ja809624w.
(75) Tricoire, M.; Mahieu, N.; Simler, T.; Nocton, G. *Chem. – Eur. J.* 2021, *27* (23), 6860–6879. https://doi.org/10.1002/chem.202004735.
(76) Liu, J.; Chen, Y.-C.; Liu, J.-L.; Vieru, V.; Ungur, L.; Jia, J.-H.; Chibotaru, L. F.; Lan, Y.; Wernsdorfer, W.; Gao, S.; Chen, X.-M.; Tong, M.-L. *J. Am. Chem. Soc.* 2016, *138* (16), 5441–5450. https://doi.org/10.1021/jacs.6b02638.
(77) Ungur, L.; Chibotaru, L. F. *Chem. - Eur. J.* 2017, *23* (15), 3708–3718. https://doi.org/10.1002/chem.201605102.
(78) Vieru, V.; Ungur, L.; Cemortan, V.; Sukhanov, A.; Baniodeh, A.; Anson, C. E.; Powell, A. K.; Voronkova, V.; Chibotaru, L. F. *Chem. - Eur. J.* 2018, *24* (62), 16652–16661. https://doi.org/10.1002/chem.201803821.
(79) Xémard, M.; Zimmer, S.; Cordier, M.; Goudy, V.; Ricard, L.; Clavaguéra, C.; Nocton, G. *J. Am. Chem. Soc.* 2018, *140* (43), 14433–14439. https://doi.org/10.1021/jacs.8b09081.
(80) Tricoire, M.; Münzfeld, L.; Moutet, J.; Mahieu, N.; La Droitte, L.; Moreno-Pineda, E.; Gendron, F.; Hilgar, J. D.; Rinehart, J. D.; Ruben, M.; Cador, O.; Le Guennic, B.; Roesky, P. W.; Nocton, G. *Chem. – Eur. J.* 2021. https://doi.org/10.1002/chem.202101599.
(81) Holland, P. L.; Smith, M. E.; Andersen, R. A.; Bergman, R. G. *J. Am. Chem. Soc.* 1997, *119* (52), 12815–12823. https://doi.org/10.1021/ja971830o.
(82) Burney, C.; Carmichael, D.; Forissier, K.; Green, J. C.; Mathey, F.; Ricard, L. *Chem. - Eur. J.* 2005, *11* (18), 5381–5390. https://doi.org/10.1002/chem.200401293.
(83) O'Hare, Dermot. *Organometallics* 1987, *6* (8), 1766–1772. https://doi.org/10.1021/om00151a024.
(84) Landorf, C. W.; Jacob, V.; Weakley, T. J. R.; Haley, M. M. *Organometallics* 2004, *23* (6), 1174–1176. https://doi.org/10.1021/om034371a.
(85) Jacob, V.; Landorf, C. W.; Zakharov, L. N.; Weakley, T. J. R.; Haley, M. M. *Organometallics* 2009, *28* (17), 5183–5190. https://doi.org/10.1021/om900439z.
(86) Wolters, L. P.; van Zeist, W.-J.; Bickelhaupt, F. M. *Chem. - Eur. J.* 2014, *20* (36), 11370–11381. https://doi.org/10.1002/chem.201403237.
(87) Shannon, R. D. *Acta Crystallogr. Sect. A* 1976, *32* (5), 751–767. https://doi.org/10.1107/S0567739476001551.
(88) Cordero, B.; Gómez, V.; Platero-Prats, A. E.; Revés, M.; Echeverría, J.; Cremades, E.; Barragán, F.; Alvarez, S. *Dalton Trans.* 2008, No. 21, 2832. https://doi.org/10.1039/b801115j.
(89) Schmickler, W.; Nazmutdinov, R. R.; Wang, Q.; Daoud, W. A. *Electrochimica Acta* 2021, *368*, 137601. https://doi.org/10.1016/j.electacta.2020.137601.
(90) Mehdoui, T.; Berthet, J.-C.; Thuéry, P.; Salmon, L.; Rivière, E.; Ephritikhine, M. *Chem. - Eur. J.* 2005, *11* (23), 6994–7006. https://doi.org/10.1002/chem.200500479.
(91) Mehdoui, T.; Berthet, J.-C.; Thuéry, P.; Ephritikhine, M. *Chem. Commun.* 2005, No. 22, 2860. https://doi.org/10.1039/b503526k.
(92) Evans, W. J.; Rego, D. B.; Ziller, J. W. *Inorg. Chem.* 2006, *45* (26), 10790–10798. https://doi.org/10.1021/ic061485g.
(93) Gagliardi, L.; Lindh, R.; Karlström, G. *J. Chem. Phys.* 2004, *121* (10), 4494–4500. https://doi.org/10.1063/1.1778131.
(94) Cho, M.; Sylvetsky, N.; Eshafi, S.; Santra, G.; Efremenko, I.; Martin, J. M. L. *ChemPhysChem* 2020, *21* (8), 688–696. https://doi.org/10.1002/cphc.202000040.
(95) Trifonov, A. A.; Fedorova, E. A.; Fukin, G. K.; Baranov, E. V.; Druzhkov, N. O.; Bochkarev, M. N. *Chem. - Eur. J.* 2006, *12* (10), 2752–2757. https://doi.org/10.1002/chem.200501181.
(96) Vasudevan, K.; Cowley, A. H. *Chem. Commun.* 2007, No. 33, 3464. https://doi.org/10.1039/b708758f.

(97) Evans, W. J. *J. Organomet. Chem.* 2002, *647* (1–2), 2–11. https://doi.org/10.1016/S0022-328X(01)01462-0.
(98) Nocton, G.; Lukens, W. W.; Booth, C. H.; Rozenel, S. S.; Medling, S. A.; Maron, L.; Andersen, R. A. *J. Am. Chem. Soc.* 2014, *136* (24), 8626–8641. https://doi.org/10.1021/ja502271q.
(99) Liddle, S. T.; Mills, D. P. *Dalton Trans.* 2009, No. 29, 5592. https://doi.org/10.1039/b904318g.
(100) Butovskii, M. V.; Kempe, R. *New J. Chem.* 2015, *39* (10), 7544–7558. https://doi.org/10.1039/C5NJ00802F.
(101) Wang, D.; Tricoire, M.; Cemortan, V.; Moutet, J.; Nocton, G. *Inorg. Chem. Front.* 2021, *8* (3), 647–657. https://doi.org/10.1039/D0QI00952K.
(102) Fedushkin, I. L.; Maslova, O. V.; Morozov, A. G.; Dechert, S.; Demeshko, S.; Meyer, F. *Angew. Chem. Int. Ed.* 2012, *51* (42), 10584–10587. https://doi.org/10.1002/anie.201204452.
(103) Lukens, W. W.; Magnani, N.; Booth, C. H. *Inorg. Chem.* 2012, *51* (19), 10105–10110. https://doi.org/10.1021/ic300037q.

General conclusion and perspectives.

The synthesis, characterisation and exploitation of heterometallic complexes based on (divalent) lanthanides and transition metals, bridged by redox-active ligands have been one of the main axes of research in our group. This architecture is promising, since the potential stabilisation of reactive redox states on the TM is likely to be conducive for new reactivity. Recent results in our group have shown the benefit of this strategy[1–3] and are part of the growing interest in the field of the cooperative action inherent to some multimetallic edifices.

Within this context, this PhD sought to expand the categories of RAL that could be used. Up to this point, the complexes always comprised one organolanthanide fragment and one TM fragment bound to one symmetrical, neutral RAL. Two different types of ligands were envisaged to break this pattern: the **dppz** and the **Hbimpym** (also used during the PhD of Ding Wang[4]).

dppz presents three coordination sites. The desired complexes would include two lanthanides on each monodentate site and one TM on the bidentate site. Almost all the synthesised TM precursors suffer from poor solubility, which complicates further characterisation and the *in situ* study of subsequent reactivity. Nevertheless, trinuclear Pd and Pt-based complexes were obtained (**1.6** and **1.7**). The deviation of the ligand from planarity, as well as the structural features of the Yb, were proof of double electron transfer, thus demonstrating the viability of the idea behind the choice of **dppz** as a ligand.

The continuation of this project depends on improving the solubility of the TM precursors. This was seen in the Ir-based complexes, **1.4** and **1.5**, which were more amenable to characterisation, due to the presence of the lipophilic COD group. Otherwise, functionalising the **dppz** ligand is the most easily attainable modification, whilst keeping the same synthetic protocol (Scheme 1.9). Another aspect to be considered is the fragile coordination of the lanthanides, which could be displaced by a coordinating solvent. It could be necessary to modify the destined coordination site for the lanthanides to afford bidentate chelating coordination pockets.

Hbimpym can be obtained in either its protonated form, or as a deprotonated salt (**Kbimpym**). It offers two different coordination sites: L_2 and LX. This increases the synthetic options for adding a TM fragment on a precise coordination site. This was nicely illustrated in the Ir-based complexes **1.15**-**1.19**, where the metal can be deliberately placed in either of the two coordination sites. Although this situation may provide additional flexibility in tuning ensuing reactivity, the presence of the acidic proton or of chloride atoms are a very probable vector for potentially parasitic side reactions upon the addition of divalent lanthanides. This was, in fact, illustrated by the synthetic trials, where only one precursor could engage in reactivity with ytterbocene without the formation of a side product.

Kbimpym may prove to be very useful, since the presence of the K^+ ion as an anion abstractor would favour the formation of simple salts, providing the driving forces for new synthetic avenues. Rather than attempt to exploit electron-rich systems, where divalent lanthanides transfer an electron towards the ligand and, ultimately, the TM centres, it could be used as a scaffold to build electron deficient complexes (Scheme 1.16). Trivalent lanthanides could be coordinated to the ligand *via* salt metathesis. However, the formation of **1.11**, instead of the expected bimetallic system, would indicate that the bimpym ligand may be an inadequate scaffold for the coordination of two metals simultaneously.

The series of group 10 complexes of the formula **K(bimpym)TMMe$_2$** was completed following the synthesis of **1.8** and **1.9** (and its derivative **1.10**). In all of these, the TM is coordinated to the L_2 site. The low solubility of the ligand renders syntheses inefficient and any large-scale attempts are complicated by what seems to be a degradative process. Improving the solubility of **Kbimpym** would help alleviate the synthetic issues encountered for the complexes. As for **dppz**, this could be achieved by either reducing the size of the aromatic system (thereby disfavouring π-stacking) or by introducing lipophilic substituents (Scheme 1.15).

The full family of group 10 **K(bimpym)TMMe$_2$** complexes paved the way for a comparative study in their reactivity towards divalent organolanthanides. The work performed on the Ni complex served as a good guide for what could be expected.[5] Given that there are minimal differences in the structural features between the three, one could have anticipated nigh-identical reactivities. Reactions with ytterbocene proved this assertion to be both correct and false at the same time, since the three reactions share a number of important features. At the beginning of the reaction, a heterometallic **Yb(bimpym)TM**-type adduct, where ytterbocene has transferred an electron towards the ligand, is formed. **Yb(bimpym)Pd** could only be observed when the reaction was performed in THF, however.

Depending on the TM metal, this complex is more or less stable towards the subsequent decomposition towards the homotrimetallic **Yb$_3$(bimpym)$_2$**, following the ejection of the TM fragment. What is unique to the Pd reactivity is the isolation of a heterometallic Yb-Pd complex, **2.2**. It would seem that only in this case the $TMMe_2$ fragment is stabilised and can undergo reactivity, in order to incorporate a Ln^{III} fragment, resulting in a short Yb-Pd distance. This conclusion may be subject to change, as the analogous Pt reactivity was not thoroughly analysed, due to the aforementioned synthetic difficulties associated to the precursor, **1.8**.

As an evolution of this project, more efforts could be dedicated to, at first, improving the synthetic procedure of the formation of the precursors. Capping the K^+ is a promising avenue – the yield obtained for **1.10** is much higher and the procedure is much more rapid. A second issue is related to the difficult separation of **2.2** and **Yb$_3$(bimpym)$_2$**, which severely hampers the isolation of high quantities of the former. This is a crucial requirement for an exhaustive characterisation of this unusual complex.

On the other hand, **Hbimpym** was used as the starting ligand for the synthesis of complexes, where Pd^{2+} and Pt^{2+} fragments were coordinated to the LX site of the bimpym ligand. Three such compounds were synthesised and characterised – **1.12**-**1.14**. The localised negative charge on the ligand expels one of the methyl moieties, making room for a solvent molecule – an L-type ligand.

From a computational perspective, the work carried out throughout this thesis explored the electronic structures of these complexes, to accompany the experimental observations in a symbiotic fashion. The peculiarity of bimpym is that a coupling reaction occurs when an electron is transferred onto the ligand. This could be deduced from the computed electronic structure, performed in numerous configurations. It was established that the coordinating metal has an influence on the position of the coupling reaction, but it is the nature of the metal that bears more weight. For example, there is little difference in the electronic structures of **(bimpym)NiMe$_2^-$** and **K(bimpym)NiMe$_2$**, demonstrating that the presence of the K^+ does not meaningfully affect the frontier orbitals. On the basis of the LUMOs of these complexes, the coupling reaction should take place on the C atom on the opposite side of the coordination site of the TM (Figure 1.6). Similar assertions can be made regarding the complexes **1.12**-**1.14**. When lanthanide fragments were added (for example, in **1.12-Yb** or **1.12-Sm**), it is the C atom

on the TM side that has the largest contribution in the relevant vacant orbitals. This is ultimately consistent with the subsequent experimental observations. We can therefore conclude that DFT can competently describe and potentially predict the behaviour of such species.

The tendency of the bimpym-based precursors to couple when divalent lanthanide fragments are added demanded a solution as to how this reactivity might be prevented. One of the hypotheses that was proposed was that the presence of a second RAL in the coordination sphere of the TM might result in a more significant delocalisation of the transferred electron. Although this could not be verified experimentally, owing to the poor solubility of the bimpym ligand, the theoretical studies could prove to be valuable in other synthetic conditions.

Likewise, the shape of the LUMO of the complexes where pyridine was the coordinated L ligand (**1.12** and **1.13**) was relatively unusual. The fact that it was almost entirely composed of the contributions of the pyridine suggested that it could be involved in subsequent reactivity – an assertion that was finally proven to be correct in the case of the Pd-based complex. The ensuing theoretical study sought to replace the pyridine by other comparable ligands to examine the orbital interplay between the Pd centre and the ligand. The results of the computations suggest that this interaction can be effectively modulated – either the ligand's tendency to interfere in the electron transfer can be enhanced (**(bimpym)Pd(bipy)Me**) or, conversely, using an electron deficient substrate can promote the population of bonding orbitals. It remains to be seen if these putative complexes are experimentally feasible, since, at this point, only the fluxional character of the pyridine was proven, and not the capacity of other substrates to coordinate in its place.

One point of contention in the accord between theory and synthesis is the different behaviour of the isostructural (bimpym)TM(py)Me complexes, since both present the same electronic structure. Upon the addition of divalent lanthanides, they both form coupled products (**2.4**, **2.5**, **2.13**, **2.14** (the sole heterometallic complex containing the bimpym ligand, issued from a reaction with samarocene) and **2.15**). The subsequent reactivity observed for the Pd-based complexes could not be matched by its Pt-based homologues, no matter the reaction conditions. This is intriguing, since, on the basis of the computations, there is a minimal difference (less than 0.43 eV) in the energy gap between the LUMO (pyridine pathway) and LUMO+1 (coupling pathway) for the two complexes. Since the electronic structure of the coupled products was inaccessible due to their considerable size, simplified versions of the Pd systems were computed. They, too, suggested that a pyridine-based reactivity would follow the transfer of another electron. An equivalent study into the electronic structure of the Pt complexes could be of interest in order to justify this discrepancy.

The addition of further divalent ytterbocene to the coupled products **2.4** and **2.5** results in a complex decomposition mechanism, from which three main complexes emerge: the heterometallic Pd-Yb adducts **2.2** (mentioned above) and **2.6** and the homotrimetallic **Yb_3(bimpym)$_2$**. The formation of the heterometallic adducts was unexpected and pushed this work into the domain of Ln-based intermetallics, which arguably became the focal point of the doctoral project. It rapidly became clear that the intricate formation mechanism of the heterometallics was exceedingly rare, if not unique, among its peers, as the majority of Ln-based intermetallics are obtained via relatively simple routes, following deliberate synthetic planning. This prompted a combined experimental and theoretical study into the behaviour of the coupled products after ytterbocene addition.

What was established beyond reasonable doubt is that the addition of the divalent organolanthanide kicks out the Pd fragments, in order to form **Ln_3(bimpym)$_2$**. This accounts for the whereabouts of the bimpym ligand and confirms that the Yb^{III} centres already coordinated to the scaffold do not engage in further reactivity.

As for the other components, the evolution is undoubtedly much more complicated. The bottom line is straightforward: two complexes are formed, one with a $Pd^{II}Me_2$ pattern (**2.2**) and one with a $Pd^0(pyr)_2$ (**2.6**) pattern. The efficiency of the conversion towards either of the motifs is not fully clear and depends on the coupled product that was used. In the case of **2.4**, the kinetic studies would indicate that a non-negligible portion of the Pd is not efficiently converted, which would explain the black powder observed after the reaction is performed at a larger scale. It would appear, however, that the process is more efficient in the case of **2.5**, as, based on the kinetic data, consuming one equivalent of **2.5** results in almost the same amount of each of the three complexes.

There is a significant difference in both the reaction rates and the ratio of the final compounds between the two coupled products, **2.4** and **2.5**. This is ascribed to the different arrangement of the two Pd fragments with respect to one another. These discrepancies could point to the presence of more than one reaction mechanism. Two such options stand out: one initiated by the C-H activation of the pyridine group, which was modelled computationally, and one based on a ligand exchange-type mechanism. Criteria such as the aforementioned ratios between the products or the formation of gas during the reaction can be more consistent with either of the proposed evolutions.

The unusual Yb-based trimetallic complex prompted the examination of the same reactivity with samarocene. Although no analogous coupled products can be isolated in this case, the isostructural trimetallic complex is obtained (**2.7**). The natural conclusion in this case would be to assume that the two adducts are formed following the same reaction mechanism. There are some indirect proofs which suggest that this is the case, notably the careful resolution of the XRD data of the quinolyl-based equivalent of **2.7**.

The analysis of the structural features indicated that the Sm-Pd distances are shorter than the equivalent Yb-Pd ones in **2.6**, which is contrary to the expected lanthanidic contraction. This unusual phenomenon prompted a thorough investigation. All the spectroscopic characterisations pointed to Ln^{III} configurations on both complexes, throughout the entire 0-300 K range.

It could be of interest to attempt the synthesis of analogous Ln-Pd-Ln arrangements with other lanthanide synthons. However, reproducing the same approximate reaction conditions – addition of divalent lanthanide precursors as a coordinating electron source – could prove to be problematic in the case of the non-classical divalent lanthanides, which tend to be less stable in solution.

Further analyses were performed *via* theoretical computations to study whether an orbital interaction between the two metals could justify this break in the lanthanidic contraction. No definitive proof of such interactions could be found, at either the DFT or CASSCF levels. Topological analyses were in agreement with the classification of the Ln-Pd interactions as weak dative.

On the other hand, the electronic structure of **2.2** at the CASSCF and **DFT-RECP** levels of theory showed a series of orbitals with seemingly strong participations of the Pd and Yb metal centres. Moreover, the relative contributions of the two were significantly more equitable than those of the previously reported Ln-based intermetallics. Nevertheless, this seemingly covalent interaction does not mean there is a strong bond between the two metals, as the overall bond order is zero. This interpretation is corroborated by the topological (weak dative bond) and EDA (high contribution from attractive covalent interactions in the overall interaction energy between the two fragments) analyses. With regards to the latter, the contribution from the Yb-Pd interaction cannot be decorrelated from the overall energy, so specific assertions in that regard cannot be made. Future work, related to decoupling the intermetallic interaction from the rest, could be of some interest.

These observations set the stage for an extended theoretical study, aimed at determining which factors were important in enabling the aforementioned intermetallic interaction. It was found that the structural features – distance between the metals and the relative positioning of one metal fragment with respect to the other – play a key role in mediating the strength of the orbital interaction. This forms the basis of a straightforward conclusion: if the two metals are not close enough and/or do not have matching symmetries for an efficient overlap, the interaction will not occur.

The substitution of either the TM (**YbM** series) or the Ln (**LnPd** series) within this architecture resulted in the interaction being maintained only for a select few complexes. The common feature of these was electronic proximity to the metal that had been replaced. For example, **YbRh**$^{-}$ and **YbPt** – isoelectronic to **2.2** and the homologue to Pd from the following period, respectively – manifest the same strong interaction with the Yb. Why **YbNi** does not is worthy of a closer investigation, as are the reasons why there are considerable orbital interactions in **YbRh**$^{+}$ and **YbIr**$^{+}$, since it is not clear in what way they are similar to **2.2**.

As for the lanthanides, the only complexes similar to the parent compound were those where the divalent state is most accessible. The implication therein is that, within the structure, the Pd^{II} centre would transfer a significant amount of electronic density towards the Ln. This is corroborated by the fact that the Ln-Pd distances in these adducts deviated from the expected lanthanidic contraction within the series: there was a marked uptick for each of them, which would be consistent with a stronger divalent character on the Ln.

This hypothesis was tested on another relatively accessible redox couple – Ce^{IV}/Ce^{III}. The electronic structure of **CePd**$^{+}$ shows one pair of orbitals with Ce-Pd interactions, where the former contributes with one electron. In a certain sense, this result epitomises the difficulty associated with analysing these results. The presence of the 4f electron is inconsistent with the intended computation and the population analyses (admittedly, not the most reliable metric) do not indicate any change from **CePd** for either metal. Only an excited state (more than 50 kcal/mol higher in energy), computed within the CI formalism, indicates a non-integer population of the 4f sub-shell, which would point to a multi-configurational nature.

In the absence of experimental data for **2.2**, which would substantiate (or not) the theoretical results, the methodology cannot be reliably validated. All the computational findings highlight the difficulties in accurately assessing Ln-based intermetallics, starting from the terminology and the metrics that are usually employed. Intermetallic “bonds” are often inferred on the basis of short distances, yet this assertion is not informative as to the nature of the interaction between the two metals. After all, a number of such complexes naturally produce short distances, due to the positioning of the coordination sites – the metals are “forced” to be close to each other. Based on the results presented in this work, it is clear that the intermetallic interactions are globally quite weak. Are the computational means at our disposal adequate in order to gauge these interactions up to chemical accuracy? More theoretical work in this area is required, both in terms of assessing the commonly used methods and in eventually developing new methods fit for the purpose.

Furthermore, there has yet to be unifying breakthrough in the theoretical framework of Ln-based intermetallics, that would explain by which mechanism the two metals would interact by anything other than pure electrostatic forces. In a number of the cited examples (Scheme 3.1 and Scheme 3.2, for example), the reaction yielding the intermetallics is deliberately planned as to put together positively and negatively charged fragments. Can Ln 4f electrons interact with other metal’s orbitals? In principle, their low radial extension would preclude an efficient overlap with other orbitals. Yet, the significant progress of the past few decades has challenged the long held belief that lanthanides are

restricted to ionic bonding. There are now more mechanisms known by which the lanthanide series can interact with other compounds, although these mechanisms are far from trivial.

For the sake of comparison, there was longstanding disagreement in the organometallic lanthanide community about the electronic structure of cerocene ($Ce(C_8H_8)_2$),[6,7] but meticulous spectroscopic analyses turned inconsistencies into a theoretical framework that could account for the presence of the signatures of both Ce^{IV} and Ce^{III}. Anecdotally, Richard A. Andersen refused to publish the findings on his seminal $Cp^*_2Yb(bipy)$ complex[8] for years before understanding the then-aberrant magnetic behaviour. What followed was a series of highly influential reports that set the foundation for describing and assessing multiconfigurational ground states and the fine details of the electronic configurations that explain how divalent Yb transfers an electron towards RAL.[9–12]

At present, the situation with respect to the ambiguous electronic structure of **2.2** is delicately poised. The presence of a number of orbitals featuring significant contributions from both Yb 4f electrons and Pd 4d electrons is a unique situation in Ln-based intermetallics. Does this necessarily imply covalent interactions? If so, a spectroscopic characterisation of this interaction would require advanced tools, such as EPR and XANES. Proof of any orbital interaction would both validate the CASSCF methodology and would mean that the computational study in Section 3.4 could be an adequate guide as to how to activate intermetallic interactions featuring lanthanides.

If, however, no covalent interactions can be found, how can these orbitals be explained? Is it possible that a simple orbital matching of the energy of the electrons results in contributions from both in the orbitals, without further interactions? Is it possible that the CASSCF methodology – often very accurate in describing complicated phenomena – produced inaccurate descriptions of the interactions between the metals?

In order to answer these questions, more thorough experimental data is an absolute prerequisite. Depending on the outcome, a careful calibration of the pertinence and applicability of each of the utilised analytical tools is called for.

This outlines the priorities for this project very clearly. Spectroscopic characterisation of **2.2** – pending improvement of the work-up procedure – should clarify the most immediate questions and inconsistencies. For this, the acquisition of solid-state magnetic data is an imperative first step. The synthesis of analogues, such as **YbPt**, **YbNi** or **SmPd**, could be pursued for further validation.

References

(1) Goudy, V.; Jaoul, A.; Cordier, M.; Clavaguéra, C.; Nocton, G. *J. Am. Chem. Soc.* 2017, *139* (31), 10633–10636. https://doi.org/10.1021/jacs.7b05634.

(2) Jaoul, A.; Tricoire, M.; Moutet, J.; Cordier, M.; Clavaguéra, C.; Nocton, G. *Chem. Squared* 2019, *3*. https://doi.org/10.28954/2019.csq.06.001.

(3) Wang, D.; Moutet, J.; Tricoire, M.; Cordier, M.; Nocton, G. *Inorganics* 2019, *7* (5), 58. https://doi.org/10.3390/inorganics7050058.

(4) Ding Wang, PhD thesis, Institut Polytechnique de Paris, Ecole Polytechnique, 2020.

(5) Wang, D.; Tricoire, M.; Cemortan, V.; Moutet, J.; Nocton, G. *Inorg. Chem. Front.* 2021, *8* (3), 647–657. https://doi.org/10.1039/D0QI00952K.

(6) Neumann, C. S.; Fulde, P. *Z. Für Phys. B Condens. Matter* 1989, *74* (3), 277–278. https://doi.org/10.1007/BF01307872.

(7) Smiles, D. E.; Batista, E. R.; Booth, C. H.; Clark, D. L.; Keith, J. M.; Kozimor, S. A.; Martin, R. L.; Minasian, S. G.; Shuh, D. K.; Stieber, S. C. E.; Tyliszczak, T. *Chem. Sci.* 2020, *11* (10), 2796–2809. https://doi.org/10.1039/C9SC06114B.

(8) Schultz, M.; Boncella, J. M.; Berg, D. J.; Tilley, T. D.; Andersen, R. A. *Organometallics* 2002, *21* (3), 460–472. https://doi.org/10.1021/om010661k.

(9) Booth, C. H.; Walter, M. D.; Daniel, M.; Lukens, W. W.; Andersen, R. A. *Phys. Rev. Lett.* 2005, *95* (26). https://doi.org/10.1103/PhysRevLett.95.267202.

(10) Booth, C. H.; Walter, M. D.; Kazhdan, D.; Hu, Y.-J.; Lukens, W. W.; Bauer, E. D.; Maron, L.; Eisenstein, O.; Andersen, R. A. *J. Am. Chem. Soc.* 2009, *131* (18), 6480–6491. https://doi.org/10.1021/ja809624w.

(11) Booth, C. H.; Kazhdan, D.; Werkema, E. L.; Walter, M. D.; Lukens, W. W.; Bauer, E. D.; Hu, Y.-J.; Maron, L.; Eisenstein, O.; Head-Gordon, M.; Andersen, R. A. *J. Am. Chem. Soc.* 2010, *132* (49), 17537–17549. https://doi.org/10.1021/ja106902s.

(12) Nocton, G.; Lukens, W. W.; Booth, C. H.; Rozenel, S. S.; Medling, S. A.; Maron, L.; Andersen, R. A. *J. Am. Chem. Soc.* 2014, *136* (24), 8626–8641. https://doi.org/10.1021/ja502271q.

Appendices

Experimental section

General considerations

All reactions were performed using standard Schlenk-line techniques or in nitrogen-filled gloveboxes (MBraun, Garching, Germany). All glassware was dried at 140 °C for at least 12 h prior to use.

Tetrahydrofuran (THF), THF-d_8, toluene, and toluene-d_8 were dried over sodium, degassed, and transferred under reduced pressure in a cold flask. Acetonitrile (MeCN), MeCN-d_3, pyridine (py), py-d_5 were dried over CaH_2, distilled and degassed prior to use.

Gas addition studies were conducted in 5 mm NMR tubes adapted with a J. Young valve by adding the gasses directly to a degassed frozen solution and letting it react at room temperature.

^{1}H NMR spectra were recorded in 5-mm tubes adapted with a J. Young valve on Bruker AVANCE II or III-300 MHz (Bruker, Billerica, MA, USA) spectrometers. ^{1}H chemical shifts were expressed relative to TMS (tetramethylsilane) in ppm.

Temperature dependent magnetic susceptibility measurements were made with a SQUID in sealed quartz tube on a SQUID at 0.5 and 2 T. Diamagnetic corrections were made using Pascal's constants.

UV-visible spectra were recorded in 300-800 nm range at room temperature on an Agilent Cary 60 Spectrometer in 2 or 10 mm quartz cuvettes with solvent background correction.

Single crystals were mounted on a Kapton loop using a Paratone N oil. An APEX III CCD BRUKER detector and a graphite Mo-Kα monochromator were used for the data acquisition. All measurements were done at 150 K and a refinement method was used for solving the structure. The structure resolution was accomplished using the SHELXS-97 and SHELXT[1] programs, and the refinement was done with the SHELXL program.[2,3] The structure solution and the refinement were achieved with the and Olex2[4] software. Pictures of the compound structure were obtained using the MERCURY software. During the refinement steps, all atoms except hydrogen atoms were refined anisotropically. The position of the hydrogen atoms was determined using residual electronic densities. Finally, in order to obtain a complete refinement, a weighting step followed by multiple loops of refinement was done.

Elemental analyses were obtained from Mikroanalytisches Labor Pascher (Remagen, Germany).

dypridophenazine (dppz),[5] 2-(benzimidazol-2-yl)pyrimidine (Hbimpym),[6] tmedaPdMe_2,[7] tmedaNiMe_2, $(Me_2SPtMe_2)_2$,[8] [Cp*IrCl_2],[9] $[(COE)2IrCl]_2$,[10] Cp*$_2$Sm(OEt_2)[11], Cp*$_2$Eu(OEt_2)[11] and Cp*$_2$Yb(OEt_2)[12] were synthetized according to described procedures. $(CODIrCl)_2$, 18-C-6, bipyrimidine, bipyridine, quinoline, isoquinoline, pentafluoropyridine and 2,6-lutidine were bought from commercial suppliers. Quinoline and 2,6-lutidine were purified by fractional distillation before use.

Chapter 1

(dppz)$NiMe_2$ (**1.1**):

(tmeda)$NiMe_2$ (221.8 mg, 1.08 mmol, 1.0 eq.) and dppz (305.5 mg, 1.08 mmol, 1.0 eq.) were dissolved and suspended, respectively, in cold THF (-35 °C, 10 mL each). Transferring the greenish yellow Ni solution dropwise into the beige dppz suspension at room temperature gave a dark coloured mixture after stirring for several minutes. The mixture was stirred overnight and was filtered through a fritted funnel. The dark powder was collected, dried, solubilised into THF, filtered and the dark blue solution collected was stored at -35 °C. Dark blue needles, suitable for XRD diffraction, were obtained after 1 week.

(dppz)$PdMe_2$ (**1.2**):

(tmeda)$PdMe_2$ (425.5 mg, 1.68 mmol, 1.0 eq.) and dppz (474.8 mg, 1.68 mmol, 1.0 eq.) were respectively dissolved and suspended in THF (10 mL each). Transferring the beige dppz suspension onto the grey Pd solution dropwise at room temperature resulted in the formation of a red blood-coloured suspension after stirring. The mixture was stirred overnight and was filtered through fritted funnel. Analytically pure red powder was dried and collected in 88 % yield (617.4 mg, 1.47 mmol).

A few milligrams of red powder were solubilized into DCM, filtered and the solution was crystallised by pentane vapor diffusion. Dark red plates of a statistical mixture of desired product and (dppz)$PdCl_2$, suitable for XRD diffraction, were obtained after 3 weeks.

^{1}H NMR (300 MHz, 293.15K, CD_2Cl_2): δ (ppm) = 9.80 (m, 2H, dppz), 9.19 (m, 2H, dppz), 8.43 (m, 2H, dppz) , 8.01 (m, 4H, dppz), 0.47 (s, 6H, Pd-Me).

(dppz)$PtMe_2$ (**1.3**):

$[Me_2PtSMe_2]_2$ (56.3 mg, 0.098 mmol, 1.0 eq.) and dppz (54.8 mg, 0.194 mmol, 1.0 eq.), were respectively suspended in 4 mL and 3 mL of DCM. Transferring the white/grey Pt suspension dropwise into the beige dppz suspension at room temperature gave an orange/red-colored mixture after stirring for two hours. The orange-red supernatant was removed. The remaining red powder was washed twice with DCM and dried, yielding 75% (75.2 mg, 0.146 mmol).

A few milligrams of red powder were solubilized into DCM, filtered and the solution was crystallised by pentane vapor diffusion. Clear reddish orange plates of the desired product, suitable for XRD diffraction, were obtained after 2 weeks.

^{1}H NMR (300 MHz, $CDCl_3$) δ 9.67 (m, 2H, dppz), 9.29 (m, 2H, dppz), 8.37 (m, 2H, dppz), 7.96 (m, 2H, dppz), 7.84 (m, 2H, dppz), 1.54 (s, 6H, Pd-Me).

$[(Cl)_2Ir]^-[Ir(COD)(dppz)]^+$ (**1.4**):

$[(\mu\text{-}Cl)Ir(COD)]_2$ (50.0 mg, 0.074 mmol, 1.0 eq.) and dppz (45.7 mg, 0.162 mmol, 2.2 eq.) were dissolved and suspended, respectively, in 3 mL and 4 mL of DCM. Transferring the white/beige dppz suspension dropwise into the red/orange solution at room temperature turned dark purple after stirring for several minutes. The poorly soluble mixture was stirred overnight and was filtered through a fritted funnel. The dark powder was collected and solubilised in DCM, filtered and the dark purple solution was crystallised by gas diffusion (DCM/pentane). Black-purple plates were obtained after two days.

[IrCODdppz]BAr^F_4 (**1.5**):

[Ir(COD)(dppz)][$Ir(Cl)_2$] (12.9 mg, 0.014 mmol, 1.0 eq.) and sodium tetrakis[3,5-bis(trifluoromethyl)phenyl]borate ($NaBAr^F_4$, 22.1 mg, 0.025 mmol, 1.8 eq.), were partially dissolved and suspended in DCM, respectively (3 mL each). Transferring the white $NaBAr^F_4$ suspension dropwise into the dark purple solution at room temperature instantly gave a green coloured mixture. The mixture was stirred over the week-end and was filtered through a fritted funnel. The dark green powder was collected and was solubilized in DCM, filtered and the dark green solution was crystallised by gaz diffusion (DCM/pentane). Dark green blocks were obtained after two days.

^{1}H NMR (300 MHz, CD_2Cl_2) δ 10.04 (m, 2H, dppz), 8.56 (m, 2H, dppz), 8.47 (m, 2H, dppz), 8.14 (m, 4H, dppz), 7.72 (m, 12H, BAr^F_4), 7.55 (m, 4H, COD), 4.65 (m, 4H, COD), 2.48 (m, 4H, COD).

$(Cp^*_2Yb)_2$dppzPdMe_2 (**1.6**):

(dppz)$PdMe_2$ (7.0 mg, 0.017 mmol, 1 eq.) and $Cp^*_2Yb(OEt_2)$ (17.7 mg, 0.034 mmol, 2 eq.) were suspended in 3 mL and dissolved in 4-5 mL of toluene, respectively. Transferring the green Yb solution dropwise into the red dppzPdMe_2 suspension gave a dark mixture. The mixture was stirred overnight. The supernatant was filtered and the dark solution was stored at -35 °C to crystallise. Dark black blocks, suitable for XRD analysis, were obtained after a few days.

$(Cp^*_2Yb)_2$dppzPtMe_2 (**1.7**):

(dppz)$PtMe_2$ (74.2 mg, 0.146 mmol, 1.0 eq.) and $YbCp^*_2(OEt_2)$ (151.7 mg, 0.293 mmol, 1.0 eq.) were suspended in 3 mL and dissolved in 4-5 mL of cold toluene, respectively. Transferring the green Yb solution dropwise into the red dppzPtMe_2 suspension gave a dark mixture. The mixture was stirred overnight. The supernatant was filtered and the dark solution was stored at -35 °C to crystallise. Dark black blocks, suitable for XRD analysis, were obtained after a few days.

$(THF)_2$K(bimpym)PtMe_2 (**1.8**):

An off-white suspension of K(bimpym) (25 mg, 0.11 mmol, 1.1 eq.) and a grey solution of $[Me_2PtSMe_2]_2$ (28 mg, 0.05 mmol, 1.0 eq.), both in THF (4 mL each), were mixed. The mixture gradually turned into a red suspension under stirring. The solution was stirred overnight. The supernatant was filtered; THF was added and the supernatant was filtered until there was no more product left. The rejoined solutions are evaporated under reduced pressure. The orange solid is washed with a minimum amount of THF until the washing solutions are no longer bright red, yielding analytically pure orange solid (40%, 18 mg).

The orange solid was dissolved in THF and the orange solution was left in the freezer at -40 °C. Orange blocks were formed overnight.

^{1}H NMR (300 MHz, THF) δ 8.94 (m, 1H, bimpym), 8.39 (m, 1H, bimpym), 7.95 (m, 1H, bimpym), 7.34 (m, 1H, bimpym), 6.93 (m, 2H, bimpym), 6.78 (m, 1H, bimpym), 1.37 (s, 3H, Me), 0.70 (s, 3H, Me).

$(THF)_2$K(bimpym)PdMe_2 (**1.9**):

An off-white suspension of K(bimpym) (23 mg, 0.10 mmol, 1 eq) and a grey solution of tmedaPdMe_2 (28 mg, 0.11 mmol, 1.1 eq), both in THF (4 mL each), were mixed. The mixture gradually turned into a golden suspension under stirring. The solution was stirred overnight. The supernatant was filtered; THF was added and the supernatant was filtered until there was no more product left. The rejoined

solutions are evaporated under reduced pressure. The pale yellow solid is washed with a minimum amount of THF until the washing solutions are no longer golden, yielding analytically pure pale yellow solid (42%, 27 mg).

The yellow solid was dissolved in THF and the pale yellow solution was left in the freezer at -40 °C. Yellow blocks were formed overnight.

^{1}H NMR (300 MHz, THF) δ 8.51 (m, 1H, bimpym), 8.31 (m, 1H, bimpym), 7.79 (m, 1H, bimpym), 7.30 (m, 1H, bimpym), 6.89 (m, 3H, bimpym), 0.52 (s, 3H, Me), 0.01 (s, 3H, Me).

[K(18-C-6)][(bimpym)PdMe$_2$] (**1.10**):

An off-white THF (10 mL) suspension of K(bimpym) (83 mg, 0.35 mmol, 1 eq) was stirred in the presence of 18-C-6 (90 mg, 0.34 mmol, 1 eq) before tmedaPdMe$_2$ (100 mg, 0.34 mmol, 1 eq) was added. The mixture almost instantly turned into a golden solution under stirring. The supernatant was filtered; THF was added and the supernatant was filtered until there was no more product left. The rejoined solutions are left to crystallise. Yellow blocks were formed overnight (68%, 150 mg).

The yellow solid was dissolved in THF and the pale yellow solution was left in the freezer at -40 °C.

^{1}H NMR (300 MHz, THF) δ 8.73 (m, 2H, bimpym), 7.83 (m, 1H, bimpym), 7.56 (m, 1H, bimpym), 7.15 (m, 1H, bimpym), 6.84 (m, 2H, bimpym), 3.51 (s, 24H, 18-C-6), 0.51 (s, 3H, Me), -0.03 (s, 3H, Me).

(bimpym)Pd(pyr)(Me) (**1.12**):

Hbimpym (390 mg, 2.0 mmol, 1 eq) and (tmeda)Pd(Me)$_2$ (520 mg, 2.05 mmol, 1.03 eq) were dissolved in pyridine (25 mL). The initially colourless suspension gradually turned to a golden solution within 30 minutes. An intense gaseous evolution was concurrently observed. The mixture was stirred for an hour. Adding pentane to the solution precipitated the product as a beige solid. The solid was recovered by filtering the mixture. Further washing with pentane and diethyl ether yielded analytically pure (bimpym)Pd(py)(Me), 1.12 (700 mg, 1.77 mmol, 88 % yield). Crystals suitable for XRD studies were obtained by dissolving the compound in pyridine (golden solution), filtering it through a MF-Millipore membrane filter and performing a low vapour diffusion of pentane in the pyridine solution at room temperature.

^{1}H NMR (300 MHz, THF-d$_8$, 60 °C): δ (ppm): 8.51 (2H, pyridine), 8.30 (1H, pyrimidine), 8.07 (2H, pyrimidine), 7.62 (1H, py), 7.20 (2H, py), 7.15 (4H, benzimidazole), 1.10 (3H, CH_3) Anal. calculated for $C_{17}H_{15}N_5Pd$: C, 51.59; H, 3.82; N, 17.70; Pd, 26.89. Found: C 45.87, H 3.89, N 11.4.

(bimpym)Pd(py-d$_5$)(Me) (**1.12-py-d$_5$**):

8 mL of acetonitrile were poured over Hbimpym (80 mg, 0.4 mmol, 1 eq) and (tmeda)Pd(Me)$_2$ (110 mg, 0.43 mmol, 1.06 eq) under stirring, yielding a beige suspension. A few drops of pyr-d$_5$ were then added to the mixture. Within 30 minutes, the suspension acquired a rich golden hue. The mixture was stirred for 4 h. A gaseous evolution was concurrently observed. At the end of the reaction, all the volatiles were evaporated, after which a yellow powder was obtained. Further washing with pentane and diethyl ether yielded (bimpym)Pd(py-d$_5$)(Me) (150 mg, 0.36 mmol, 91 % yield).

(bimpym)Pt(pyr)(Me) (**1.14**):

Hbimpym (77 mg, 0.4 mmol, 1 eq) and $[Me_2PtSMe_2]_2$ (115 mg, 0.2 mmol, 1.03 eq) were dissolved in pyridine (10 mL). The initially colourless suspension gradually turned to a orange-golden solution within 30 minutes. A gaseous evolution was concurrently observed. The mixture was stirred for an hour. Adding pentane to the solution precipitated the product as a beige solid. The solid was recovered by filtering the mixture. Further washing with pentane and diethyl ether yielded analytically pure (bimpym)Pt(py)(Me), 1.14 (80 mg, 0.16 mmol, 40 % yield). Crystals suitable for XRD studies were obtained by dissolving the compound in pyridine (golden solution), filtering it and performing a low vapour diffusion of pentane in the pyridine solution at room temperature.

(Hbimpym)IrCODCl (**1.15**):

102 mg $[IrCODCl]_2$ (0.15 mM) and 63 mg Hbimpym (0.3 mM) are dissolved in DCM (8 mL). A purple suspension is quickly formed. After one night of stirring, the product is dried under vacuum and washed with acetonitrile and diethylether. 113 mg of a purple solid is obtained, giving a yield of 90%.

^{1}H NMR (300 MHz, DMSO-D6) δ 9.13 (d, J = 4.96 Hz, 2H), 7.74 (m, J = 27.98 Hz, 3H), 7.48 (m, J = 53.99 Hz, 2H), 4.22 (m, J = 41.02 Hz, 2H), 2.28 (m, J = 12.13 Hz 2H), 1.75 (m, J = 14.12 Hz, 2H). Anal. calculated: C, 42.86; H, 3.79; N, 10.53. Found: C, 40.86; H, 3.62; N, 9.76.

(bimpym)IrCOD (**1.16**):

25 mg of $[IrCODCl]_2$ (0.05 mM) and 43 mg of Kbimpym (0.1 mM) are dissolved in DCM (5 mL). A red suspension is formed. Some KCl precipitates. The solution is stirred for two hours. After filtration and drying, 32 mg of a red solid is obtained, giving a yield of 70%.

^{1}H NMR (300 MHz, CD_2Cl_2) δ 8.96 (m, J = 6.14 Hz, 1H), 8.10 (d, J = 5,57 Hz, 1H), 7.74 (m, J = 8,91 Hz, 1H), 7.33 (t, J = 10.73 Hz, 1H), 7.19 (m, J = 24,86 Hz, 3H), 3.73 (s, 2H), 2.38 (s, 4H), 1.98 (m, J = 12,79 Hz, 2H), 1.79 (d, J = 13,49 Hz, 2H). Anal. calculated: C, 46.05; H, 3.86; N, 11.30. Found: C, 46.30; H, 3.73; N, 11.2.

$[(Hbimpym)IrCp^*Cl]^+Cl^-$ (**1.17**):

81 mg of $[IrCp^*Cl_2]_2$ (0.1 mM) and 41 mg of Hbimpym (0.2 mM) are dissolved in DCM (8 mL). An orange solution forms quickly and turns yellow within a few minutes. A yellow solid is gradually formed. After one night of stirring, the supernatant is filtered, evaporated and washed with diethyl ether. The same yellow solid is then formed. This solid and the solid remaining in the first fraction are dried. This gives 105 mg of product, and a yield of 89%.

^{1}H NMR (300 MHz, CD_2Cl_2) δ 9.26 (dd, J = 6.90 Hz, 1H), 9.01 (dd, J = 7.84 Hz, 1H), 8.30 (d, J = 7.93 Hz, 1H), 7.74 (m, J = 25.20 Hz, 2H), 7.55 (m, J = 33.86 Hz, 2H), 1.81 (s, 15H, Cp* peak). Anal. calculated: C, 42.42; H, 3.90; N, 9.42. Found: C, 41.09; H, 3.69; N, 9.09.

(bimpym)IrCp*Cl (**1.18**):

125 mg of $[IrCp^*Cl_2]_2$ (0.15 mM) and 75 mg of Kbimpym (0.3 mM) are dissolved in DCM (15 mL). An orange solution is formed. After a few minutes, a yellow solid precipitates. Some KCl also precipitates. After one night of stirring, the supernatant is filtered, evaporated, washed with diethyl ether. The same yellow solid is then formed. This solid and the solid remaining in the first fraction are dried. This gives 115 mg of product, and a yield of 66%.

^{1}H NMR (300 MHz, CD_2Cl_2) δ 8.94 (q, J = 6.90 Hz, 1H), 8.83 (dd, J = 5.86 Hz, 1H), 7.78 (m, J = 9.30 Hz, 1H), 7.56 (m, J = 9.67 Hz, 1H), 7.33 (m, J = 10.14 Hz, 1H), 7.21 (m, J = 18.30 Hz, 2H), 1.74 (s, 15H, Cp* peak). Anal. calculated: C, 44.79; H, 4.83; N, 9.95. Found: C, 38.97; H, 3.40; N, 7.81.

Chapter 2

$((bimpym)IrCODYbCp^*_2)_2$ (**2.1**):

$Cp^*_2Yb(OEt_2)$ (20 mg, 38 µmol) and 1.16 (23 mg, 41 µmol) are dissolved in toluene (5 mL), resulting in an immediate dark red colour solution. After two hours, the solution is filtered, evaporated under reduced pressure and rapidly washed with cold pentane. 42 mg of analytically pure solid was isolated. Red crystals were grown from saturated pentane solutions after a week at -35 °C.

^{1}H NMR (300 MHz, Tol-d_8) δ 222.82 (s, 1H), 179.27 (s, 1H), 47.17 (s, 1H), 43.97 (s, 1H), 23.78 (s, 1H), 13.15 (s, 1H), 6.06 (s, 15H, Cp* peak), 4.58 (s, 4H), 3.01 (s, 15H, Cp* peak), 1.76 (d, J = 23 Hz, 1H), 1.25 (m, 4H), 0.92 (m, 4H), 0.14 (m, 1H), - 0.54 (s, 2H), - 1.05 (s, 1H), - 1.32 (s, 2H), - 5.30 (s, 2H), -6.09 (s, 2H), - 9.45 (s, 1H), - 10.63 (s,2H), - 11.05 (s, 1H), -12.04 (s, 2H), -16.70 (d, J = 13,79 Hz, 1H), - 20,21 (s, 1H), -23.66 (s, 1H), -37,93 (s, 1H). EA Calculated: C, 49.88; H, 5.56; N, 5.97. Found: C, 51.17; H, 5.38; N, 5.44.

$Cp^*_2Yb(\mu\text{-}Me)_2PdCp^*$ (**2.2**):

The addition of ytterbocene to $(THF)_2K(bimpym)PdMe_2$ (**1.9**) in toluene (5 mL) results in a black mixture with red hues under stirring. Within two hours, all the crystals of **1.9** are consumed. The mixture is filtered to yield a dark red solution. The supernatant was evaporated. Redissolution in pentane resulted in the formation of a black-red solution. Storing the solution at cold results in the precipitation of red solid overnight. The remaining solution was extracted and evaporated under reduced pressure. Redissolution in toluene and storing the concentrated solution at -40 °C produced large black-brown crystals overnight.

^{1}H NMR (300 MHz, Tol-d_8) δ 388.32 (s, 6H), 4.07 (s, 30H, Yb-Cp*), -11.38 (s, 15H, Pd-Cp*).

$[Cp^*_2Yb(bimpym)Pd(py)(Me)]_2$ (**2.4**):

5 mL of toluene were added to a mixture of (bimpym)Pd(Pyr)(Me), 1.12, (54 mg, 0.14 mmol, 1.4 eq) and $Cp^*_2Yb(OEt_2)$ (52 mg, 0.1 mmol, 1 eq). The resulting black suspension was stirred for approximately 30 s before the supernatant was filtered. The black solution was evaporated under vacuum without stirring. The black-brown powder was washed thrice with cold pentane. Evaporating the volatiles yielded $[Cp^*_2Yb(bimpym)Pd(py)(Me)]_2$ as a brown powder (91 mg, 0.054 mmol, 95%

yield). Crystals suitable for XRD analysis were grown by dissolving the powder in toluene. Adequate plates were formed after a few days by storing the solution at -40 °C. The product is thermally sensitive above 70 °C.

^{1}H NMR (300 MHz, Tol-d_8): δ (ppm): ^{1}H NMR (300 MHz, Tol) δ 210.62 (s, 2H), 188.21 (s, 2H), 50.12 (s, 2H), 30.29 (s, 2H), 26.43 (s, 2H), 16.95 (s, 2H), 5.31 (s, Cp*, 30H), 3.21 (s, Cp*, 30H), -3.08 (s, 2H), -4.46 (s, Me, 6H), -9.29 (s, 2H), -24.80 (s, 2H).

[Cp*$_2$Yb(bimpym)Pd(Me)(py)]$_2$ (**2.5**):

5 mL of toluene were added to 30 mg of **2.4**. The dark red-brown solution was stirred at room temperature for 3 days, during which the solution acquired a darker hue. The solution was evaporated under reduced pressure, quantitatively yielding [Cp*$_2$Yb(bimpym)Pd(Me)(py)]$_2$, as an analytically pure brown powder. Crystals suitable for XRD analysis were grown by dissolving the powder in toluene. Thin red-brown needles were formed after a few days by storing the solution at -40 °C.

^{1}H NMR (300 MHz, Tol-d_8): δ (ppm): ^{1}H NMR (300 MHz, Tol) δ 229.08 (s, 2H), 189.21 (s, 2H), 49.59 (s, 2H), 39.99 (s, 2H), 25.16 (s, 2H), 13.44 (s, 2H), 5.48 (s, Cp*, 30H), 2.49 (s, Cp*, 30H), -0.08, -14.45 (s, 2H), -33.38 (s, Me, 6H). The product is thermally sensitive above 70 °C.

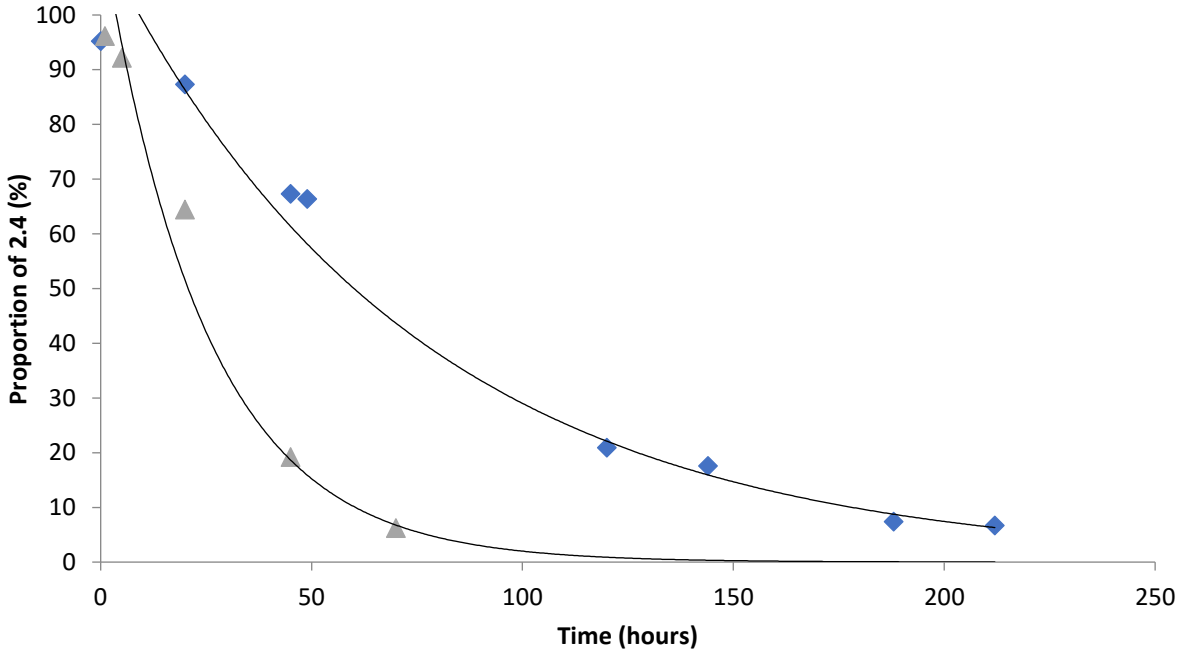

Figure S1: Time evolution (hours) of the clean isomerisation of 2.4 to 2.5 without (blue lozenges) and with stirring (grey triangles).

[(Cp*$_2$Yb)$_2$(μ-Pd(pyridyl)$_2$] (**2.6**):

Toluene (8 mL) was added to a mixture of (bimpym)Pd(Py)(Me) (1.12) (100 mg, 0.25 mmol, 1 eq) and Cp*$_2$Yb(OEt$_2$) (265 mg, 0.51 mmol, 2 eq). Within 5 minutes, the resulting brown suspension gave a black solution. A gaseous evolution was also concurrently observed. The solution was stirred for 30 minutes at room temperature before being filtered. The solution was concentrated and left overnight

in the freezer at -40 °C to obtain brown blocks of [(Cp*$_2$Yb)$_2$(μ-Pd(pyridyl)$_2$]. The crystals were dried, washed 5 times with cold pentane, dried again to yield 2.6 (36 mg, 0.03 mmol, 12 % yield). The washing solutions are evaporated and the solid is re-dissolved in toluene. Upon concentration and crystallisation, further clean crystals can be obtained.

^{1}H NMR (300 MHz, THF-d$_8$): δ (ppm): 228.25 (s, 2H, pyridyl), 116.84 (s, 2H, pyridyl), 25.78 (s, 2H, pyridyl), 24.89 (s, 2H, pyridyl), 9.02(s, 60H, Cp*). Anal. Calculated for $C_{50}H_{68}N_2PdYb_2$: C, 52.24; H, 5.96; N, 2.44; Pd, 9.26; Yb, 30.11. Found: C, 52.08; H, 6.07; N, 3.53.

[(Cp*$_2$Sm)$_2$(μ-Pd(pyridyl)$_2$] (**2.7**):

Toluene (8 mL) was added to a mixture of (bimpym)Pd(Pyr)(Me), 1.12, (100 mg, 0.25 mmol, 1 eq) and Cp*$_2$Sm(OEt$_2$) (250 mg, 0.52 mmol, 2.1 eq). The resulting black solution with yellow hues was formed instantly. A gaseous evolution was also concurrently observed. The solution was stirred for 30 minutes at room temperature before being filtered. The solution was concentrated under reduced pressure and left overnight in the freezer at -40 °C to obtain brown blocks, suitable for XRD. The crystals were dried, washed 5 times with cold pentane, dried again to yield [(Cp*$_2$Sm)$_2$(μ-Pd(pyridyl)$_2$] (28.4 mg, 10% yield). The washing solutions are evaporated and the solid is re-dissolved in toluene. Upon concentration and crystallisation, further clean crystals are obtained in freezer.

^{1}H NMR (300 MHz, THF-d$_8$): δ (ppm)= 4.87 (s, 2H, pyridyl), 4.64 (s, 2H, pyridyl), 1.11 (s, Cp*, 60H), -0.81 (s, pyridyl, 2H), -9.06 (s, pyridyl, 2H). Anal. Calculated for $C_{50}H_{68}N_2PdSm_2$: C, 54.39; H, 6.21; N, 2.54; Pd, 9.64; Sm, 27.23. Found: C, 54.83; H, 6.45; N, 3.33.

[(Cp*$_2$Sm)$_2$(μ-Pd(pyridyl-d$_4$)$_2$] (2.7-pyr-d$_4$). The procedure was identical to 2.7, using 1.12-py-d$_5$ instead of 1.12.

General procedure when synthesising the pyridine analogues **2.8** and **2.9**:

(bimpym)Pd(Pyr)(Me), 1.12, and Cp*$_2$Ln(OEt$_2$) (slight excess) are added in a vial that is placed sideways. A small drop of the pyridine analogue is carefully placed at the rim, so as to not slide towards the compounds. Toluene is then poured so that the pyridine analogue is included in the resulting solution.

2.8: The mixture immediately turns black with yellow hues. After stirring for 30 minutes, the solution is filtered, concentrated under reduced pressure and then stored at -35 °C. Large golden-yellow blocks are grown overnight.

2.9: The mixture immediately turns bright red. The solution is filtered after 15 minutes, concentrated under reduced pressure and then stored at -35 °C. Large crimson blocks are grown overnight.

[Cp*$_2$Yb(bimpym)Pt(py)(Me)]$_2$ (**2.13**):

Toluene (5 mL) was added to a mixture of (bimpym)Pt(Pyr)(Me), 1.14, (27 mg, 0.055 mmol, 1.0 eq) and Cp*$_2$Yb(OEt$_2$) (30 mg, 0.058 mmol, 1.04 eq). The resulting red-black solution is formed rapidly under stirring. The solution was evaporated under vacuum without stirring. The red powder was washed thrice with cold pentane, yielding [Cp*$_2$Yb(bimpym)Pd(py)(Me)]$_2$ as an analytically pure powder (45 mg, 0.044 mmol, 79% yield). Crystals suitable for XRD analysis were grown by dissolving

the powder in THF. Adequate plates were formed overnight by storing a concentrated solution at -40 °C.

^{1}H NMR (300 MHz, THF) δ 198.40 (s, 2H), 191.97 (s, 2H), 52.80 (s, 2H), 28.94 (s, 2H), 20.27 (s, 2H), 9.76 (s, 30H, Cp*), 2.39 (s, 30H, Cp*), 0.66 (s, 2H), -1.67 (s, 6H, py), -14.81 (s, 6H, Me).

$[Cp^*_2Sm(bimpym)Pt(py)(Me)]_2$ (**2.14**):

Toluene (5 mL) was added to a mixture of (bimpym)Pt(Pyr)(Me), 1.14, (27 mg, 0.055 mmol, 1.0 eq) and $Cp^*_2Yb(OEt_2)$ (30 mg, 0.058 mmol, 1.04 eq). The resulting red-black solution is formed rapidly under stirring. The solution was evaporated under vacuum without stirring. The red powder was washed thrice with cold pentane, yielding $[Cp^*_2Yb(bimpym)Pd(py)(Me)]_2$ as an analytically pure powder (45 mg, 0.044 mmol, 79% yield). Crystals suitable for XRD analysis were grown by dissolving the powder in THF. Adequate plates were formed overnight by storing a concentrated solution at -40 °C.

^{1}H NMR (300 MHz, Tol) δ 10.93 (s, 4H, py), 8.18 (s, 2H), 6.32 (s, 2H), 6.03 (s, 2H), 4.52 (s, 2H), 2.64 (s, 4H), 0.98 (s, 30H, Cp*), 0.94 (s, 30H, Cp*), -4.68 (s, 2H), -9.03 (s, 2H).

Magnetism

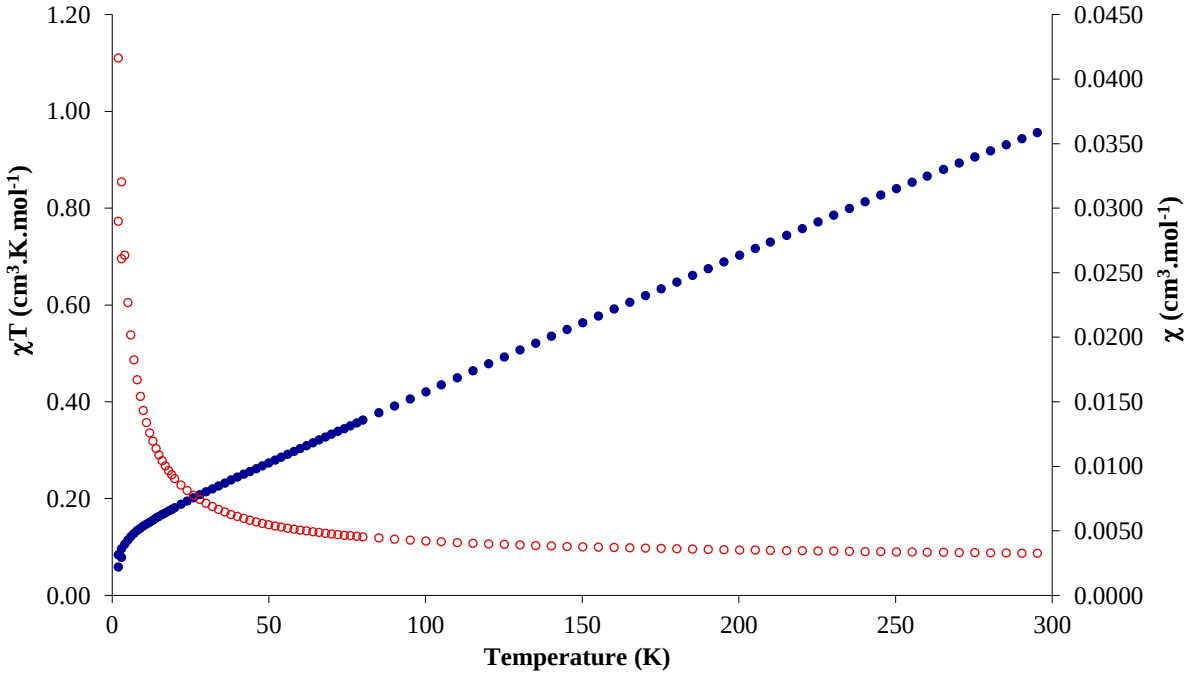

Figure S2: Magnetic susceptibility and the χT product for 2.7.

References

(1) Sheldrick, G. M. *Acta Crystallogr. Sect. Found. Adv.* 2015, *71* (1), 3–8. https://doi.org/10.1107/S2053273314026370.

(2) Sheldrick, G. M. *Acta Crystallogr. A* 2008, *64* (1), 112–122. https://doi.org/10.1107/S0108767307043930.

(3) Sheldrick, G. M. *Acta Crystallogr. Sect. C Struct. Chem.* 2015, *71* (1), 3–8. https://doi.org/10.1107/S2053229614024218.

(4) Dolomanov, O. V.; Bourhis, L. J.; Gildea, R. J.; Howard, J. A. K.; Puschmann, H. *J. Appl. Crystallogr.* 2009, *42* (2), 339–341. https://doi.org/10.1107/S0021889808042726.

(5) Ackermann, M. N.; Interrante, L. V. *Inorg. Chem.* 1984, *23* (24), 3904–3911. https://doi.org/10.1021/ic00192a014.

(6) Haga, M.; Ishizuya, M.; Kanesugi, T.; Yutaka, T.; Sakiyama, D., Feed, J.; Kuim, W. *IJC-A* 2003, *42A*, 2290-2299. http://nopr.niscair.res.in/handle/123456789/20737.

(7) De Graaf, Wim.; Boersma, Jaap.; Smeets, W. J. J.; Spek, A. L.; Van Koten, Gerard. *Organometallics* 1989, *8* (12), 2907–2917. https://doi.org/10.1021/om00114a028.

(8) Hill, G. S.; Irwin, M. J.; Levy, C. J.; Rendina, L. M.; Puddephatt, R. J.; Andersen, R. A.; Mclean, L. In *Inorganic Syntheses*; Darensbourg, Marcetta. Y., Ed.; John Wiley & Sons, Inc.: Hoboken, NJ, USA, 2007; pp 149–153. https://doi.org/10.1002/9780470132630.ch25.

(9) Kang, J. W.; Moseley, K.; Maitlis, P. M. *J. Am. Chem. Soc.* 1969, *91* (22), 5970–5977. https://doi.org/10.1021/ja01050a008.

(10) van der Ent, A.; Onderdelinden, A. L.; Schunn, R. A. In *Inorganic Syntheses*; Wold, A., Ruff, J. K., Eds.; John Wiley & Sons, Inc.: Hoboken, NJ, USA, 2007; pp 92–95. https://doi.org/10.1002/9780470132456.ch18.

(11) Berg, D. J.; Burns, C. J.; Andersen, R. A.; Zalkin, A. *Organometallics* 1989, *8* (8), 1865–1870. https://doi.org/10.1021/om00110a006.

(12) Tilley, T. D.; Boncella, J. M.; Berg, D. J.; Burns, C. J.; Andersen, R. A.; Lawless, G. A.; Edelman, M. A.; Lappert, M. F. In *Inorganic Syntheses*; Ginsberg, A. P., Ed.; John Wiley & Sons, Inc.: Hoboken, NJ, USA, 2007; pp 146–150. https://doi.org/10.1002/9780470132586.ch27.

Résumé général du projet doctoral

Les complexes à base de lanthanides divalents suscitent un intérêt croissant dans le domaine de la chimie organométallique, à cause de leur aptitude à s'engager dans des réactions de réduction mono-électronique. L'ajout de ce type de fragments aux ligands redox actifs, qui coordinent aussi des fragments de métaux de transition, produit des complexes avec des propriétés intéressantes. L'électron transféré par le Ln réduit le LRA et cette densité électronique stockée sur le ligand influe la réactivité de ces espèces.

L'objectif de ce travail doctoral est, dans un premier temps, de synthétiser des adduits hétérométalliques à base de fragments de lanthanides divalents et de métaux de transition, pontés par un ligand redox-actif. Ce concept a été précédemment utilisé dans les travaux de notre groupe. Dans un second temps, ces complexes seront caractérisés par une série de techniques spectroscopiques et par des calculs théoriques, avant d'obtenir de renseignements sur leurs propriétés physico-chimiques et sur leurs structures électroniques.

Ce projet doctoral a exploré l'utilisation de deux LRA conceptuellement différents des ligands précédemment utilisés – le 2-(2-pyrimidyl)benzimidazole (Hbimpym) et la dipyridophenazine (dppz). Les travaux antérieurs se sont servis des ligands neutres et symétriques, où seulement deux métaux pouvaient être coordinés. En contraste, Hbimpym propose deux sites de coordination différents – un site anionique de type LX et un site neutre de type L_2. dppz permet la coordination de deux fragments de lanthanides divalents, en plus du fragment de métal de transition.

Le premier chapitre décrira la synthèse et la caractérisation par les outils précédemment évoqués de complexes à base de ces ligands, où figurent également des fragments de métaux de transition à base d'Ir, de Pd et de Pt. Leurs structures électroniques ont été étudiées par DFT pour jauger leur viabilité en tant qu'accepteurs d'électron. La mauvaise solubilité du dppz a compliqué la réactivité des composés respectifs. Néanmoins, l'ajout de fragments de lanthanides divalents aux composés à base de dppz a permis l'isolation de complexes trimétalliques, où deux fragments de lanthanides divalents ont réduit le ligand, validant la démarche employée.

La présence de deux types de sites de coordination sur Hbimpym confère à l'utilisateur la flexibilité du choix de quel site occupera chaque métal envisagé. C'est ainsi que des complexes ont été obtenus, où le métal de transition occupe soit le site L_2, soit le site LX. Des calculs théoriques ont étudié l'influence de la coordination de métaux sur les orbitales frontières de ce ligand, en démontrant une assez forte influence sur la densité électronique sur chaque atome de l'hétérocycle. En effet, lorsqu'un électron est transféré sur le ligand, il y a une forte accumulation de densité électronique sur un des atomes de carbone sur la partie pyrimidine. Dans la majorité des cas, une réaction de couplage sur la partie pyrimidine du ligand s'ensuit.

Ceci a été observé pour plusieurs complexes lorsqu'un ajout de fragments de lanthanides divalent a été entrepris. Ce type de composés sont décrit dans le deuxième chapitre. Vraisemblablement, la réaction de couplage est très rapide, car aucun intermédiaire bimétallique, où le lanthanide n'a pas transféré son électron, n'a été observé. Cette réactivité particulière n'est pas particulièrement prometteuse pour des éventuelles applications catalytiques, car l'électron transféré par le lanthanide est immédiatement entraîné dans la réaction de couplage et n'influe pas sur les propriétés du métal de transition.

Cependant, pour certains composés à base de Pd, la coordination du Ln et le transfert électronique produit des complexes hétérométalliques atypiques, ayant des courtes distances Pd-Ln. Deux types de tels composés ont été obtenus : deux édifices trimétalliques Ln^{III}-Pd^{0}-Ln^{III} (Ln = Sm, Yb), comportant un arrangement linéaire très rare entre les deux groupements pyridyls sur le Pd et un complexe Yb^{III}-Pd^{II}, où les deux métaux sont pontés par deux groupements méthyle.

Leur mécanisme de formation n'est pas trivial. Une étude expérimentale et théorique exhaustive a été menée pour rationaliser ces comportements, décrite dans le troisième chapitre. Pour les adduits trimétalliques, le mécanisme de formation est intriqué et basé, probablement, sur plusieurs étapes d'interaction avec des fragments réducteurs de lanthanides divalents et des décompositions moléculaires, à la suite desquels les complexes trimétalliques sont isolés. Les calculs théoriques montrent que la distance intermétallique courte n'induit pas d'interactions électroniques fortes entre les métaux.

En revanche, pour le complexe Yb^{III}-Pd^{II}, pontés par les groupements méthyle, les calculs au niveau CASSCF indique la présence de quelques orbitales dans la structure électronique, où figurent simultanément des contributions importantes de la part des électrons 4d du Pd et des électrons 4f de l'Yb. L'accord entre les preuves expérimentales (lorsque possible) et les résultats des études théoriques a été analysé. Les implications pour le domaine des composés hétérométalliques, dont ces complexes appartiennent, sont discutées.

ECOLE DOCTORALE

Titre : Synthèse et études théoriques de complexes hétérométalliques à base de lanthanides divalents et de métaux de transition
Mots clés : Ligands redox actifs, lanthanides divalents, complexes multimétalliques, chimie computationnelle

Résumé : Les complexes à base de lanthanides (Ln) divalents sont un domaine qui suscite un intérêt croissant dans le domaine de la chimie organométallique, à cause de leur aptitude à s'engager dans des réactions de réduction mono-électronique. L'ajout de fragments de Ln divalents aux ligands redox actifs (LRA), qui coordinent aussi des fragments de métaux de transition (MT), produit des complexes avec des propriétés intéressantes. L'électron transféré par le Ln réduit le LRA et cette densité électronique stockée sur le ligand influe le MT, en permettant la stabilisation de configurations réactives.

Ce projet doctoral a exploré l'utilisation de deux LRA différents – le 2-(2-pyrimidyl)benzimidazole (**Hbimpym**) et la dipyridophenazine (**dppz**). Ces ligands ont été utilisés pour coordiner des fragments de MT à base d'Ir, de Pd et de Pt. **Hbimpym** propose deux sites de coordination différents – un site anionique de type LX et un site neutre de type L_2. **dppz** permet la coordination de deux fragments de lanthanides divalents. Les précurseurs à base de ligands et de MT ont été synthétisés et caractérisés par des outils spectroscopiques et théoriques. Leurs structures électroniques ont été étudiées par DFT pour jauger leur viabilité en tant qu'accepteurs d'électron.

En revanche, l'ajout de fragments de lanthanides divalents aux composés à base de bimpym engendre la réduction du ligand. Dans la majorité des cas, une réaction de couplage sur la partie pyrimidine du ligand s'ensuit, à cause de l'accumulation de densité électronique sur l'atome de carbone qui couple. Cette réactivité est cohérente avec la structure électronique prédite par les calculs théoriques. Cependant, pour certains composés à base de Pd, la coordination du Ln et le transfert électronique produit des complexes hétérométalliques atypiques, ayant des courtes distances Pd-Ln.

Leur mécanisme de formation n'est pas trivial. Une étude expérimentale et théorique exhaustive a été menée pour rationaliser ces comportements. Pour un de ces complexes, les calculs au niveau CASSCF indique la présence de quelques orbitales dans la structure électronique, où figurent simultanément des contributions importantes de la part des électrons 4d du Pd et des électrons 4f de l'Yb. L'accord entre les preuves expérimentales (lorsque possible) et les résultats des études théoriques a été analysé. Les implications pour le domaine des composés hétérométalliques, dont ces complexes appartiennent, sont discutées.

Title : Synthesis and theoretical studies of heterometallic complexes based on divalent lanthanides and transition metals
Keywords : Redox-active ligands, divalent lanthanides, multimetallic complexes, computational chemistry

Abstract : Divalent lanthanides complexes are gaining increasing interest in the area of organometallic chemistry, due to their propensity to engage in Single Electron Transfer (SET) reactions. The addition of divalent organolanthanide fragments to redox-active ligands (RAL), which also coordinate a transition metal (TM) fragment, has previously resulted in complexes with promising properties. The electron transferred from the Ln is stored onto the RAL and the electronic contribution towards the TM fragment allows the stabilisation of more reactive oxidation states.

This work explored the use of two conceptually different RAL – the 2-(2-pyrimidyl)benzimidazole (**Hbimpym**) and dipyridophenazine (**dppz**). These ligands were coordinated to TM fragments based on Ir, Pd and Pt. **Hbimpym** offers two different, asymmetric coordination sites – an anionic LX site and a neutral L_2 site, whilst **dppz** allows the coordination of two divalent lanthanide fragments. The corresponding TM precursors, based on the two ligands, were synthesised and characterised using both spectroscopic and theoretical tools. Their electronic structures were analysed at the DFT level to assess their suitability as SET targets.

The addition of divalent lanthanide fragments to bimpym-based complexes results in an immediate electron transfer towards the ligand. What follows in most cases is a coupling reaction on the pyrimidine group between two identical fragments, due to the accumulation of significant electronic density on the coupling carbon. This is consistent with the predicted behaviour, following theoretical computations. However, for some Pd-based precursors, this reactivity results in unusual heterometallic complexes, containing short Pd-Ln distances.

Their formation cannot be explained in a trivial way. An extensive experimental and theoretical study, whose objective is to help clarify the uncertainties associated with these complexes, was performed. Theoretical computations at the CASSCF level of theory for one of these complexes would point to the presence of a number of orbitals with significant participation from both the Pd 4d and Yb 4f electrons. The agreement between spectroscopic evidence (when available) and theory was assessed and the repercussions with respect to the field of Ln-based intermetallics, to which these complexes belong, was discussed.